REPORT NO.
UCB/EERC-88/19
NOVEMBER 1988

EARTHQUAKE ENGINEERING RESEARCH CENTER

STEEL BEAM-COLUMN JOINTS IN SEISMIC MOMENT RESISTING FRAMES

by

KEH-CHYUAN TSAI
EGOR P. POPOV

Report to Sponsors:
National Science Foundation
American Iron and Steel Institute

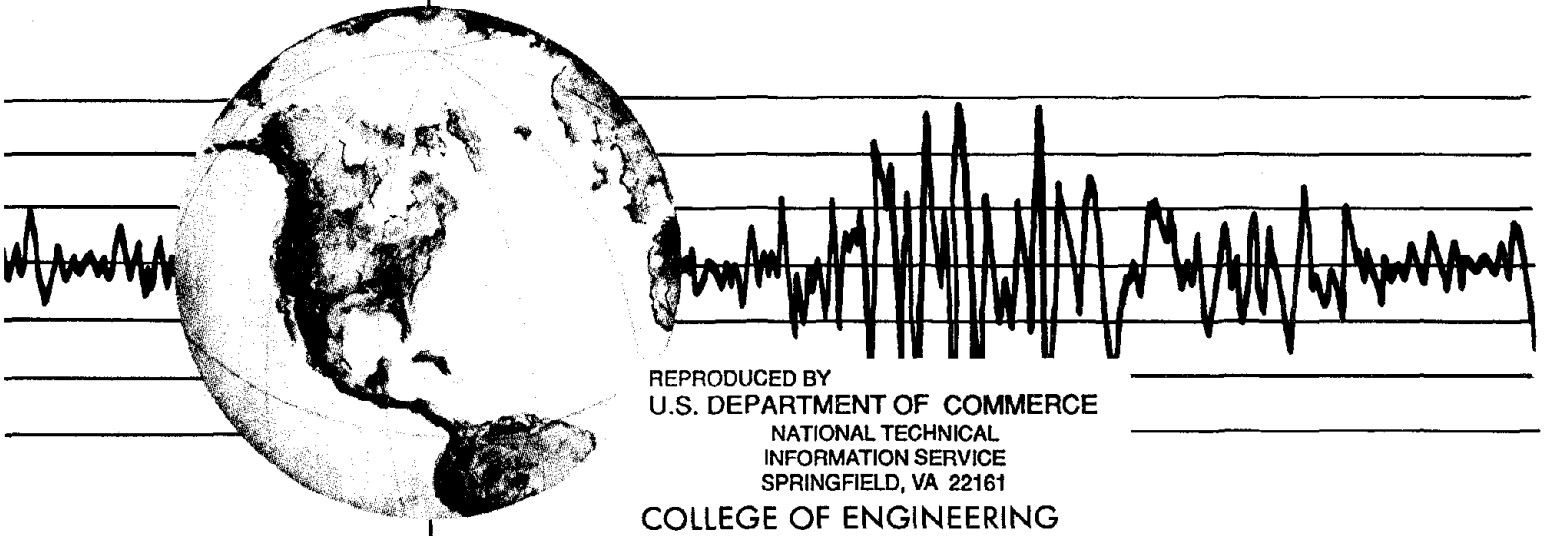

COLLEGE OF ENGINEERING

UNIVERSITY OF CALIFORNIA AT BERKELEY

For sale by the National Technical Information Service, U.S. Department of Commerce, Springfield, Virginia 22161

See back of report for up to date listing of EERC reports.

50272-101

REPORT DOCUMENTATION PAGE	1. REPORT NO. NSF/ENG-88054	2.	3. PB91-217984

4. Title and Subtitle
Steel Beam-Column Joints in Seismic Moment Resisting Frames

5. Report Date
November 1988

6.

7. Author(s)
K-C Tsai and E.P. Popov

8. Performing Organization Rept. No.
UCB/EERC-88/19

9. Performing Organization Name and Address
Earthquake Engineering Research Center
University of California, Berkeley
1301 S 46th St.
Richmond, CA 94804

10. Project/Task/Work Unit No.

11. Contract(C) or Grant(G) No.
(C)
(G) ECE86-03320

12. Sponsoring Organization Name and Address
National Science Foundation
1800 G. St. NW
Washington, DC 20550

13. Type of Report & Period Covered

14.

15. Supplementary Notes

16. Abstract (Limit: 200 words)

Several important aspects of the behavior of MRFs under real earthquake loading are not well understood. This combined experimental and analytical research program addresses some of these important issues, focusing primarily on conventional moment connections with bolted web and welded flange details. Beam sections with a relatively large web plastic moments were used, as experimental data for such sections is very limited. The effects of various connection details and welding procedures on the performance of nineteen full scale beam-column subassemblages were studied. In particular, the effects of reinforcing ribs as well as the use of supplementary welds between the shear tab and the beam web were assessed.

In the analysis the numerical procedure and nonlinear elements used in solving the nonlinear dynamic system were studied, and a special panel zone joint element implemented into the ANSR-1 computer program in order to account for the inelastic shear deformation of panel zone joints. Several steel MRF designs for a six-story and a twenty-story office building were analyzed using various ground acceleration records. It is demonstrated that the panel zone shear deformations in a MRF designed according to the current building code can be significant and should be considered explicitly in the response analyses of a MRF under static or dynamic forces. For MRFs under static lateral forces, a method incorporating actual panel zone flexibilities into the computation of elastic story drifts is developed.

17. Document Analysis a. Descriptors

b. Identifiers/Open-Ended Terms

c. COSATI Field/Group

18. Availability Statement	19. Security Class (This Report)	21. No. of Pages
Release Unlimited	unclassified	452
	20. Security Class (This Page) unclassified	22. Price

(ANSI Z39.18) *See Instructions on Reverse* OPTIONAL FORM 272 (4-77)
Formerly NTIS-35)
Department of Commerce

Steel Beam-Column Joints in Seismic Moment Resisting Frames

by

Keh-Chyuan Tsai
and
Egor P. Popov

A Report to Sponsors:
National Science Foundation
and
American Iron and Steel Institute

Report No. UCB/EERC - 88/19
Earthquake Engineering Research Center
University of California
Berkeley, California
November 1988

ABSTRACT

Although Moment Resisting Frames (MRFs) are the most widely used structural system for seismic-resistant steel buildings, several important aspects of their behavior under real earthquake loading are not well understood. This combined experimental and analytical research program addresses some of these important issues, focusing primarily on the behavior of beam-column joints. The experimental investigation focused primarily on conventional moment connections with bolted web and welded flange details. Beam sections with a relatively large web plastic modulus were used, as experimental data for such sections is very limited. The effects of various connection details and welding procedures on the performance of nineteen full scale beam-column subassemblages were studied. In particular, the effects of reinforcing ribs as well as the use of supplementary welds between the shear tab and the beam web were assessed.

One of the important unresolved issues for steel MRFs is the effects of yielding in the beam-column panel zones on the behavior of the frame as well as the beam-column connections. Analytical research on the dynamic behavior of steel MRFs designed to allow active yielding of panel zone joints is limited. For this reason, an analytical investigation was conducted for steel MRFs designed according to a recently developed seismic building code. In this analytical work, the numerical procedure and nonlinear elements used in solving the nonlinear dynamic system are studied, and a special panel zone joint element is implemented into the ANSR-1 computer program in order to account for the inelastic shear deformation of panel zone joints. Several steel MRF designs for a six-story and a twenty-story office building are analyzed using various ground acceleration records.

From these analyses, the maximum beam inelastic rotation and the dissipated energy demands at critical joints of the frame are compared with the maximum experimentally obtained capacity. The effects of various panel zone designs on the static and dynamic

behavior of the MRF are studied in detail. Based on these analytical results, it is demonstrated that the panel zone shear deformations in a MRF designed according to the current building code can be significant and should be considered explicitly in the response analyses of a MRF under static or dynamic forces.

For MRFs under static lateral forces, a method incorporating actual panel zone flexibilities into the computation of elastic story drifts is developed. Without the use of an additional panel zone element, this method can be used conveniently to predict the story drift contribution due to panel zone shear deformations in a MRF. For MRFs under severe ground excitations, it is found that the high nonliner rotational demand imposed on the beam-to-column connections can be reduced by allowing panel zone joints to effectively participate in nonlinear deformations. It is demonstrated that well proportioned panel zone joints enhance the performance of the MRF under severe ground accelerations. Therefore, it is recommended that the panel zone joints be designed to allow active participation in nonlinear deformations, thereby contributing a stable energy dissipation mechanism to the frame.

ACKNOWLEDGEMENTS

The authors are grateful to the National Science Foundation (Grant No. ECE-8603320), and the American Iron and Steel Institute for their financial support for this research. The continued encouragement of Dr. S.C. Liu of the NSF and A.C. Kuentz of the AISI is greatly appreciated. The opinions expressed in this report are those of the authors and do not necessarily reflect the views of the sponsors.

This research was carried out by the first author in partial fulfillment of the requirements for the degree of Doctor of Philosophy in Engineering under direct supervision of Professor E.P. Popov. This report is largely based on the dissertation submitted in September 1988 to the Graduate Division of the University of California, Berkeley.

The authors sincerely appreciate the assistance offered by Mr. Michael Engelhardt, a Ph. D. candidate, and Dr. James Ricles, an assistant professor of the University of California, San Diego, throughout the study and the writing of this report. Special thanks are due to Ms. Lorraine Lin for her assistance in proof reading the manuscript of this report.

A number of people have made significant contribution to this research and their assistance is appreciated. The support provided by the Department of Civil Engineering machine shop and Mr. Roy Stephen are acknowledged. The donation of some test specimens by the Herrick Corporation is appreciated.

Table of Contents

ABSTRACT i

ACKNOWLEDGEMENTS iii

TABLE OF CONTENTS v

1. INTRODUCTION 1

1.1 General 1

1.2 Moment Resisting Frame 1

1.3 Beam-Column Connections 2

1.4 Objective and Scope 4

2. EXPERIMENTAL PROGRAM 6

2.1 Selection of Subassemblages and Test Specimens 6

2.2 Experimental Set-Up 6

2.3 Description of Test Specimens 7

2.4 Instrumentation 15

2.5 Loading Sequence 15

3. EXPERIMENTAL RESULTS 17

3.1 Material Properties 17

3.2 Test Results 17

3.3 Summary 29

3.4 Conclusions 34

4. CYCLIC BEHAVIOR OF BOLTED END PLATE MOMENT CONNECTIONS 36

4.1 Introduction 36

4.2 Measuring the Bolt Tension Forces 36

4.3 Bolt Tensions in Connected Plates 38

4.4 Bolts Under Cyclic Loading 40

4.5 Design of Bolts 41

4.6 Fracture of Undersized Bolts 42

4.7 Conclusions 44

5. NONLINEAR DYNAMIC ANALYSIS METHOD FOR MRFS 46

5.1 General 46

5.2 Nonlinear Behavior of MRFs 46

5.3 Numerical Procedure for Nonlinear Dynamic Analysis 47

5.3.1 Incremental Equations of Motion 47

5.3.2 Solution of Incremental Equations of Motion 48

5.3.3 Iterative Procedure for Direct Integration 50

5.4 Damping Coefficient 53

5.5 Inelastic Elements for Nonlinear Analysis of MRFs 56

5.6 Beam-Column Element 57

5.6.1 General Description 57

5.6.2 Degree of Freedom 58

5.6.3 Yield Surface for Axial and Flexural Interaction 59

5.6.4 Flexural Stiffness 60

5.6.5 Geometric Stiffness 61

(A) Consistent Geometric Stiffness 62

(B) Linear Approximation 63

5.6.6 State Determination for Beam-Column Element 65

5.6.6.1 General 65

5.6.6.2 Procedure 65

5.7 Beam-Column Panel Zone Element 67

5.7.1 General 67

5.7.2 Force-Deformation Relationships 68

5.7.3 Planar Nonlinear Joint Element 71

5.7.4 Degrees of Freedom 72

5.7.5 Element Stiffness 73

5.7.6 State Determination for Joint Element 74

5.7.6.1 General 74

5.7.6.2 Procedure 74

5.8 Performance of Joint Element 76

5.8.1 General 76

5.8.2 Analytical Model 77

5.8.3 Comparison of Analytical Model and Experimental Result 77

6. NONLINEAR FINITE ELEMENT ANALYSES OF A BEAM-COLUMN JOINT 79

6.1 Introduction 79

6.2 Steel Beam-Column Subassemblage 79

6.3 Finite Element Model 80

6.4 Program of Investigation 81

6.5 Results 82

6.5.1 Distribution of Shear Stress 82

6.5.2 Force-Deformation Relationships and Effects of Column Axial

Force 83

6.6 Large Distortion of Beam-Column Joint 84

6.7 Concluding Remarks 85

7. NONLINEAR STATIC AND DYNAMIC ANALYSES OF SIX-STORY MRFS 87

7.1 Introductory Remarks 87

7.2 Design Procedures 89

7.2.1 ANSR-1 Models 95

7.3 Effects of Panel Zone Joint Flexibilities 96

7.3.1 General 96

7.3.2 Effects of Joint Elements for MRFs under Triangularly Distributed Shear 98

7.3.3 Code Implications 99

7.3.4 Effects of Joint Elements for MRFs under Uniformly Distributed Shear 100

7.4 Simplified Model for Nonlinear Seismic Response of MRF 101

7.4.1 Introduction 101

7.4.2 Equivalent Single-Degree-of-Freedom System 103

7.4.3 Inclusion of $P-\Delta$ Effect 107

7.4.4 Behavior of Equivalent SDOF System 107

7.4.4.1 Effects of Damping 109

7.4.4.2 Effects of Post-Yield Stiffness 109

7.4.5 Response Comparison of Equivalent SDOF System and Original MDOF System 110

7.4.6 Conclusions 112

7.5 Nonlinear Dynamic Analyses of Six-Story MRFs 113

7.5.1 Dynamic Characteristics of the MRFs 113

7.5.2 Selection of Ground Acceleration 114

7.5.3 Response to the Selected Ground Accelerations 114

7.5.3.1 Response to Parkfield Earthquake 115

7.5.3.2 Response to 1.5*El Centro Earthquake 117

7.5.3.3 Response to 3*Taft Earthquake 117

7.5.3.4 Response to Mexico Earthquake 118

7.5.3.5 Other Response Indices 120

7.5.4 The Demand and the Supply 121

Beam Plastic Rotation 122

Energy Dissipation 123

7.6 Summary and Conclusions for the Six-Story MRF Analyses 124

8. NONLINEAR STATIC AND DYNAMIC ANALYSES OF 20-STORY MRFS 128

8.1 Program of Investigation 128

8.2 Design Procedures 129

8.2.1 Static Lateral Force Procedure 130

8.2.2 Dynamic Lateral Force Procedure 134

8.2.3 Beam-Column Panel Zone Designs 138

8.3 ANSR-1 Models 140

8.4 Static Deformation Characteristics of the 20-Story MRFs 143

8.4.1 Effects of Panel Zone Flexibilities 143

8.4.2 Corrections of Elastic Story Drifts to Account for Joint Deformations 144

8.4.3 $P-\Delta$ Effects 146

8.5 Dynamic Characteristics of the MRFs 147

8.6 Dynamic Characteristics of the Selected Ground Accelerations 149

8.6.1 Selection of Ground Acceleration 149

8.6.2 Acceleration Histories, Fourier Amplitudes and the Associated Response Spectrum 150

8.7 Nonlinear Dynamic Analyses of the 20-Story MRFs 151

8.7.1 Response to the Parkfield Earthquake 151

8.7.2 Response to the 1.5*El Centro Earthquake 152

8.7.3 Response to the 1.5*Miyagi-Ken-Oki Earthquake 159

8.7.4 Response to the Mexico Earthquake 162

8.7.5 The Contribution of Panel Zone Deformations to Total Story Drifts 166

8.8 Summary and Conclusions for the Twenty-Story MRF Analyses 167

REFERENCES 172

APPENDIX A. DESIGN OF SPECIMENS 179

TABLES 194

FIGURES 215

1. INTRODUCTION

1.1 General

In the current analysis and design practice of building structures, specific procedures are often followed in establishing the seismic criteria. Usually, a reduced ground acceleration is assumed for a response spectrum. This reduced or scaled response spectrum incorporates specific site conditions such as foundation material, regional tectonics, distance to faults, seismic recurrence information as well as the type of structural system being designed. In selecting such a response spectrum, it is assumed that the minimum ductility supply of the structure will be satisfied [1,2,3]. This response spectrum is then applied using either a static method with seismic forces distributed approximating the first mode shape [1,2], or a dynamic method with modal superposition techniques [2,3]. With either approach, two basic requirements must be satisfied:

1. During a small or moderate earthquake, a building frame must provide the necessary stiffness and strength to prevent damage and to continue to be serviceable after the event.
2. During a major earthquake, a building frame must provide the necessary strength and ductility such that the building will not collapse. This requires the frame to dissipate seismic energy.

This design process is usually based on elastic theory and is likely to remain in use until a suitable inelastic analytical strategy becomes available for design purposes.

1.2 Moment Resisting Frame

A steel moment resisting frame (MRF) is the most widely used building system in seismic resistant design. Besides its architectural and functional advantages, it has demonstrated the required strength and energy absorption characteristics. This system is made of beams rigidly connected to either column flanges or webs (Fig. 1.1). The strength and

ductility of this system depends primarily on the adequacy of beam-column joints and their connections. To better understand the importance of ductility, a typical elastic response spectrum for a strong earthquake may be compared with a building code requirement commonly used (Fig. 1.2). From the figure, it can be seen that the ductility requirement varies and may be high, depending on the natural period of the structure. This applies directly to systems of single degree of freedom and can be applied to regular building systems which vibrate predominantly in first mode. Therefore, the ductility demand of beam-column joints and connections for steel MRFs designed according to the building code may be large and must accordingly be designed and constructed to provide the required strength and ductility.

1.3 Beam-Column Connections

Before the development of high-strength bolts, rivets were used to join angles, channels, I-beams and plates to form larger girders, columns and their connections. With the advancement of welding technology and the availability of weldable steel, welds and high-strength bolts replaced rivets in high-rise buildings. Today, welding is commonly used in the construction of building frames, and has contributed to the development of more compact and economical structural joints as well as providing greater elastic continuity. One particular application of a bolted web and welded flange had gained wide acceptance in the western part of the United States. In this type of connection, the beam web is first field bolted to a shear tab, which initially is shop welded to either the column flange or the column web and continuity plates. Full penetration bevel welds are then applied to join the beam flanges to the column flange or continuity plates (Figs. 1.1a and 1.1d). These welds are usually produced by shielded-metal arc welding (stick-electrode) process or if higher welding speed is desired, self shielded flux-cored welding (innershield) process. Web-copes are required to accommodate the backup plates at the top flange and to permit making the bevel weld at the bottom flange. These web-copes are usually done using torch

cutting and should be ground smooth to reduce stress concentration [4,20]. In this experimental research, the effects of the roughness in the web cope to the performance of the connections is examined.

In a typical steel MRF, beams are generally connected to the column flanges in order to obtain the largest frame stiffness. In three dimensional frames, such as a framed tube, beams often must be framed into column webs as well as flanges. The integrity of this whole structural system strongly depends on corner spandrels and columns. Experimental evidence had shown the successful application of bolted-web and welded-flange for beams connected to column flanges [8]. However, the behavior of this type of connecting beam to column web has not been entirely satisfactory. Various modifications to enhance its performance have been attempted [11]. One alternative design, tested on the Berkeley campus [18], using reinforcing ribs in a beam-to-column web connection which showed a significant improvement in connection behavior will be reviewed in this report.

Experimental evidence also demonstrated some slippage of the beam web relative to the shear tab during severe cyclic loading. This slippage is caused by a large beam moment combined with shear being transmitted through the web and can contribute to the fracture of the beam flange at the connection. For beam sections having relatively large web plastic moduli, the slippage is more vulnerable at the joint and may cause premature fracture of the beam flange. For those beams having a flange moment capacity less than 70% of the total beam plastic moment capacity, SEAOC recommends [47] providing welding between the beam web and the shear tab to develop 20% of the web plastic moment capacity. This web welding is assumed to prevent bolt slippage and thereby develop the full web moment capacity. In such connections, the tightness of the bolts is critical in controlling slippage. To assure good performance of the bolts, the most common way of tightening the bolts is the turn-of-nut method [4]. However, it was found that the required preload using this procedure may be questionable [7]. Therefore, sometimes twist-off bolts and direct tension indicators are used in the field. In this experimental research, some

specimens were made using these special devices to determine their effect on connection capacity.

For areas where field welding is not desired, beam-to-column flange connections can be made by shop welding of a beam to an end plate or directly to a column. The moment frame can then be erected by bolting the end plates to column flanges or splicing beams at mid-span or inflection points (Fig. 1.1e and 1.1f). However, very little information is available on an all-welded beam with an end plate connection under sever cyclic loading. In this research, two specimens of each of the above types were made to determine their performance under cyclic loading. Moreover, in an all-welded beam-column joint, full penetration beam flange welds can be costly when large beam flange thickness is encountered. Therefore, in one test specimen, a new design was employed using partial penetration welds on one side of the flanges and fillet welds on their opposite sides.

1.4 Objective and Scope

Previous experimental research on steel beam-to-column moment connections has been done quite extensively [7-19], however, it was found that a certain type of connection detail commonly used in current practice performed very poorly under cyclic loading. Accordingly, there is a great need to improve present methods used to detail such connections. In order to improve the cyclic performance of large steel beam-column moment connections, an experimental test program was conducted for nineteen full scale beam-column subassemblages using various connection details and welding procedures. The experimental investigation is focused primarily on the steel beam-to-column flange moment connections with bolted web, welded flange connection details and relatively large beam web plastic moduli. With this type of connection, slippage of the bolts and subsequent fracture of the flange welds resulting from the cyclic loading often occurred in previous research.

The scope of the present experimental investigation consists of the following:

(1) To assess the effects of the supplementary welds between the shear tab and the beam web.

(2) To compare the performance of connections of web bolts tightened using tension control devices and turn-of-nut method.

(3) To assess the importance of smoothness of web copes, and to compare the performance of welded connections fabricated using shield metal arc welding and flux-cored arc welding.

(4) To assess the performance of reinforcing ribs in beam-column flange or web connections.

(5) To examine the performance of other moment connection details: the end plate connections and the fully welded beam-column connections.

In order to gain further insight into the nonlinear behaviors of beams, columns and panel zone joints in a steel MRF under strong ground excitations, an analytical investigation was also conducted for steel MRFs designed based on the recently developed building code. In this analytical work, the numerical procedure and nonlinear elements used in solving the nonlinear dynamic system are studied. For this purpose, a special panel zone joint element was developed and incorporated into the ANSR-1 computer program in order to account for the panel zone joint flexibilities. The performance of the proposed panel zone joint element is assessed by correlating the model with the previous experimental test and further substantiated using nonlinear finite element method. Finally, several steel MRF designs for a six-story and a twenty-story office building are analyzed using various ground acceleration records. The result obtained from these analyses are discussed in detail. From this experimental and analytical research, a number of recently developed code provisions for the design of steel MRF are examined, recommendations for the seismic-resistant design of steel beam-column joints in moment resisting frame are provided.

2. EXPERIMENTAL PROGRAM

2.1 Selection of Subassemblages and Test Specimens

A subassemblage made of a single beam connected to a column in either the strong or weak direction was chosen for each specimen to study the connection behavior. To ease the complexity of test equipment, axial force in the column was not considered. The beam size for each specimen was restricted by the capacity of the actuator connected at the end of the beam. The associated column was selected such that no inelastic deformation would be expected under the applied load and to realistically reflect the size used in building frames. The ratio, denoted as r_f, of the beam flange plastic moment capacity to the beam plastic moment capacity of wide flange section can be computed as following:

$$r_f = \frac{bt_f(d - t_f)}{Z}$$

where b and t_f are the flange width and thickness of the beam, respectively; d and Z are the beam depth and plastic section modulus, respectively. For wide flange sections W18×40, W18×35 and W21×44, r_f values are 0.70, 0.66 and 0.62, respectively. These relatively small r_f values imply that the webs relative to the flanges are large and additional web-to-shear tab welding is required if the SEAOC [47] recommendation is followed. Therefore these sections are convenient to use for studying the performance of the additional web-to-shear tab welding.

2.2 Experimental Set-Up

The experiment was conducted by applying cyclic loads to the horizontally mounted specimens at the tip of the cantilever. The experimental set-up, including a testing specimen, is shown in Figs. 2.1 and 2.2(a). The ends of the column were anchored to the flange of a supporting wide flange section that had been attached to a massive concrete

block by post tension rods. Four 1-1/4 in. diameter grade A354-BD bolts were used at each end of the column to take the shearing and tension forces induced by the applied force. In order to allow the column to deform under load, a 3/4-in. gap was provided between the flange of the column and the flange face of the supporting beam by two bearing plates at each end of the column. The bearing plates were tapered at the ends to reduce the column end fixity and prying action of the anchor bolts. To further prevent the longitudinal movement of the column, two steel bars were welded to the supporting beam near each end of the column (Fig. 2.2(b)). The slippage of the column stub could be prevented by tightening the bolts in each bar against the end of the column. A hydraulic actuator was used to apply load to the beam in the horizontal plane. A clevis was bolted to the end of the beam and a 3-in. diameter pin was inserted to connect the clevis to the actuator. The other end of the actuator was attached to a steel pedestal which was bolted to a 1-in. thick steel plate tied to the slab by post-tensioning rods. A pair of angles was installed near the end of the test beam to provide lateral support (Fig. 2.1).

2.3 Description of Test Specimens

The material used for all specimens including beams, columns, shear tabs, continuity plates and reinforcing ribs was ASTM A36. All welding was done using AWS E70 stick electrode unless otherwise indicated. For bolted web connections, four or five bolts were used to connect the web of W18 or W21, respectively to shear tab. These bolts were A325-X of 1-in. diameter tightened by the turn-of-nut method unless otherwise indicated. The bolt holes on the shear tab and beam web were 1/16-in. oversize. All web copes were of about 1-in. width and the back-up plates were 3/8-in. by 1-in. unless otherwise indicated. Web copes, when required, were made by torch-cutting without being ground smooth, unless otherwise indicated. Back-up plates for flange welding of all specimen remained in place after the welds were completed. All welds were visually inspected unless otherwise indicated. Specimen 3 through Specimen 6 were fabricated by a major fabricator in the

area. Specimen 9 through Specimen 18 were fabricated by another local fabricator. The remaining specimens were made in the university shop. Table 2.1 summarize the basic characteristics of each specimen. The design of specimens is given in Appendix A. Detailed information of each specimen is as follows:

Specimen 1

Specimen 1 was made by connecting a W18×40 beam to the web of a W12×133 column. Two pairs of continuity plates and one shear tab were welded to the column with fillet welds. The beam flanges were groove-welded to the continuity plates using full-penetration welds with 1/4-in. root openings. The overall fabrication details are shown in Fig. 2.3. Note that the top continuity plates were 5/8-in. thick while the bottom plates were 3/4-in thick. This arrangement is used by some fabricators and provides good preparation for full-penetration flange welds regardless of the unavoidable variation in beam depth. Finally, two pairs of reinforcing ribs, 1/2-in. by 2-in. by 9-in. each, were welded to the connection as shown in Fig. 2.3. The plates were tapered at the ends to reduce stress concentration in the beam flange. Three 3/8-in. fillet welds each 2-in. long were made to attach the beam web to the shear tab to reduce joint slippage. The welding is designed to develop 22% of the web plastic moment capacity. All welding was visually inspected and appeared to be comparable to that commonly seen in good fabrication shops.

Specimen 2

After Specimen 1 had been tested, the beam was cut off along the plane of the column-flange tips, and a new segment of W18×40 was attached by means of a new shear tab on the opposite side of the column web. The same details were used for Specimen 2 as for Specimen 1, except that no reinforcing ribs nor welding on the beam web-to-shear tab were used. The fabrication details for Specimen 2, shown in Fig. 2.3, are typical of those used in the western part of the United States.

Specimen 3

After the testing of Specimen 2, the beam was cut off. Specimen 3 was then made by connecting W18×35 to the same W12×133 column in the strong direction. The shear tab was 1/2-in. thick and welded to the column flange using 3/8-in. fillet welds. It was noted that both web copes had about 1-1/4 in. radius. The flux-cored arc welding (innershield) process was used for joining the beam to column flange. The flange welding was ultrasonically tested and no defects were found. The overall fabrication details are shown in Fig. 2.4.

Specimen 4

Specimen 4 was made by connecting W18×40 to the same W12×133 column in the weak direction while the beam of Specimen 3 was connected to its strong axis. New continuity plates and shear tab for Specimen 4 were welded after the used ones from previous test were gouged out. The flange weld was made by innershield welding and then ultrasonically tested. Both web copes had about 1-1/4 in. radius. The same details were used for Specimen 4 as for Specimen 2, except two 5/16-in. fillet welds each 2-in. long using stick electrodes were made in the university shop to attach the beam web to the shear tab. The overall fabrication details are shown in Fig. 2.4.

Specimen 5

Specimen 5 was made by connecting a W21×44 beam to a W14×176 column stub in the strong direction. Similar details were used for Specimen 5 as for Specimen 3, except two 5/16-in. fillet weld each 1-in. long were made to attach the beam web to the shear tab using stick electrodes and five bolts were used in connecting the beam web and shear tab. The flange weld was made by innershield welding and then ultrasonically tested. The overall fabrication details are shown in Fig. 2.4.

Specimen 6

Specimen 6 was made by connecting a W21×44 beam to a W14×176 column stub in the weak direction while the beam of Specimen 5 was connected to its strong axis. Note that the top continuity plates were 1/2-in. thick while the bottom plates were 3/4-in. thick. Both top and bottom continuity plates were projected beyond the column flange tips by 1-in. The overall fabrication details are shown in Fig. 2.5. The flange weld was made by innershield welding and then ultrasonically tested. Both web copes were of about 1-1/4 in. radius.

Specimen 7

Specimen 7 was made by connecting a W21×44 beam to the unused flange of the W14×176 column stub used previously. Similar details were used for Specimen 7 as for Specimen 3, except that two pairs of reinforcing ribs, 3/8-in. by 2-in. by 5-in. each, were welded to the column and beam flanges. The overall fabrication details are shown in Fig. 2.4.

Specimen 8

Specimen 8 was made by connecting a W21×44 beam to the web of a W14×176 column stub. A 3/8-in. thick shear tab was first welded to the column web and continuity plates. Similar details were used for Specimen 8 as for Specimen 1, except that the thickness of the reinforcing ribs was reduced to 3/8-in. and no beam web-to-shear tab welding was used. Direct load indicating washers were used under the heads of the bolts to check the tightness of the bolts. The washers were manufactured by Coronet. The overall fabrication details are shown in Fig. 2.3.

Specimen 9

Specimen 9 was made by welding a W18×46 beam directly to the unused flange of the W12×133 column stub of Specimen 3. The flange welding consisted of partial-penetration welds on the exterior sides of the flanges of the beam and continuous fillets weld on both sides of the web and the interior sides of the flanges. The flange partial-penetration welds and the web fillet welds appeared to be oversized by about 1/4-in. due to a fabrication error. The web fillet welds were therefore modified by arcing out the excess weld; but the flange welds were not altered. The overall fabrication details are shown in Fig. 2.6.

Specimen 10

Specimen 10 was made by welding a W18×40 beam to a 1-3/8 in. thick end plate using 3/8-in. and 5/16-in. fillet welds for the flanges and web, respectively. After Specimen 9 had been tested, the beam was cut off from one column flange. Eight 15/16-in. holes had been drilled in the unused flange of the column stub. The end plate was then bolted to the W12×133 column flange using eight 7/8-in. diameter A325-X bolts. The overall fabrication details are shown in Fig. 2.6. During the early stage of the testing of Specimen 10, yielding of the interior bolts and the subsequent fracture of one bolt under cyclic loading were observed. Up until then, no significant inelastic deformation of the beam had occurred. It was decided that the connection of Specimen 10 to be modified and retested.

Specimen 10R

Specimen 10 was disassembled after the test and modified for retesting. The specimen after the modifications is denoted as Specimen 10R. In this specimen, two stiffeners welded to the end plate and beam flanges were made in order to evenly distribute the bolt forces. After the bolt holes were rimmed to 1-1/16 in. diameter, eight 1-in. A354 grade BD bolts, in lieu of A490 bolts, which were not available, were used to connect the end

plate to the column flange. One row of bolts was instrumented using bolt gauges to monitor the bolt forces during assembling and testing of the specimen. The overall fabrication details are shown in Fig. 2.6.

Specimen 11

Specimen 11 was made by welding a W21×44 beam directly to an unused flange of a W14×176 column stub. Similar welding details were used for Specimen 11 as for Specimen 9 except that the flange welding consisted of 3/8-in. fillet weld on both sides of the flanges. The overall fabrication details are shown in Fig. 2.7.

Specimen 12

Specimen 12 was made by welding a W21×44 beam to a 1-1/4 in. thick end plate using the same welding details as those used for Specimen 10. Having observed the bolt fracture in the test of Specimen 10, the connecting bolts for Specimen 12 were changed from 7/8-in. diameter A325-X bolts to 1-in. diameter A354-BD bolts. After Specimen 11 had been tested, the beam was cut off from the column flange. The end plate was then bolted to the unused flange of the W14×176 column stub using eight 1-in. diameter A354 grade BD bolts. The overall fabrication details are shown in Fig. 2.7.

Specimen 13

Specimen 13 was made by connecting a W18×35 beam to a W14×159 column stub flange. The beam was bolted to a 1/2-in. thick shear tab using four A325-X bolts. The bolts were brought to be snug-tight before the flange weld was made. The beam flanges were groove-welded to the column flange using full-penetration welds with 1/4-in. root openings. The bolts in the beam web and shear tab were then tightened as required using the turn-of-nut method. This procedure is used by some fabricators to prevent the flange welding from developing lock in stress due to web bolting. The web copes were of about

7/8-in. radius and the back-up plates were 1/4-in. by 1-1/2 in. Two 5/16-in. fillet welds each 3-in. long were used in attaching the beam web to the shear tab. The overall fabrication details are shown in Fig. 2.4. This web welding was designed to develop 20% of the web plastic moment capacity.

Specimen 14

Specimen 14 was made by connecting a W21×44 beam to a W14×159 column flange. For this specimen similar details were used as for Specimen 13 except that five bolts were used and two 5/16-in. fillet weld each 3-1/2 in. long were used to attach the beam web to the shear tab. This web welding was designed to develop 20% of the web plastic moment capacity. Having observed the failure modes of several specimens, which will be discussed in detail later in Chapter 3, it was decided to grind the web copes smooth of future specimens. After grinding, the bottom web cope had about a 1-in. radius (Fig. 2.8). The top web cope radius was about 7/8-in. and remained unground due to the presence of a back-up plate (Fig. 2.9). The overall fabrication details are shown in Fig. 2.4.

Specimen 15

After Specimen 13 and 14 were tested, the beams were cut-off from the W14×159 column stubs and the columns were sent back to the fabricator for fabrication of Specimen 15 and 16. Specimen 15 was made by welding a new W18×35 beam to the unused flange of the W14×159 column stub previously used for Specimen 13. Similar details were used for Specimen 15 as those for Specimen 13 except that twist-off type bolts were installed and web welding was eliminated. The bolts used were manufactured by LOHR Structural Fasteners Inc. and the bolts were tightened by an electrical wrench supplied by the manufacturer. Two outer bolts were instrumented using bolt gauges to monitor the bolt forces during the assembling of the specimen. The beam flange welding was made using the innershield welding process. The top and bottom web copes were both ground smooth

and their radius measured about 1-in. after grinding. It was noted that both beam flanges had about 1/8 in undercuts near the joint (Fig. 2.10 and 2.11). The overall fabrication details are shown in Fig. 2.4.

Specimen 16

Specimen 16 was made by welding a new W21×44 beam to an unused flange of the W14×159 column stub previously used for Specimen 14. The same details were used for Specimen 16 as for Specimen 15 except that five twist-off type bolts were employed. The beam flange welding was made using the innershield welding process. The top and bottom web copes were both ground smooth and their radius measured about 1-in. after grinding (Fig. 2.12).

Specimen 17

Specimen 15 fractured prematurely at a flange weld. The beam of Specimen 15 was then cut off and the column was ground smooth, and Specimen 17 was fabricated identical to Specimen 15, using a new W18×35 beam and the same W14×159 column stub. However, for this specimen the flange welds were made using stick electrodes. The beam web was bolted using twist-off bolts.

Specimen 18

Specimen 16 also fractured prematurely at a flange weld. Then the beam of Specimen 16 was cut off and the column was ground smooth, and Specimen 18 was fabricated identical to Specimen 16, using a new W21×44 beam and the same W14×159 column stub. However the flange welds were made by using stick electrodes. The beam web was bolted using twist-off bolts.

2.4 Instrumentation

Each specimen was instrumented with various types of deformation measuring device such as strain gages, clip gages, linear potentiometers, and linear voltage displacement transducers (LVDTs). The hydraulic actuator load was monitored by a calibrated load cell which was attached to the end of the rod on the actuator. To obtain information on relative displacements between the beam web and the shear tab due to bolt slippage, a pair of LVDTs and tabs were mounted on the beam webs and shear tabs as shown in Fig. 2.13. A similar set-up was installed to measure the absolute rotation of the column at the joint. In order to obtain the data of forces in the bolts, some bolts used in Specimens 10, 15 and 16 were instrumented using BTM gauges, special bolt gauges which measure the axial strain in the bolts. These gauges were installed by drilling a 2.5-mm diameter hole in the center of the bolt from the head end into the shank of the bolt for 22-mm. During the test, an X-Y recorder, connected to the load cell and the linear potentiometers, was used to display the tip displacement as a function of the applied cantilever force. All specimens were whitewashed in the vicinity of the beam-column joint in order to observe the developing yield pattern during loading. All instruments and the load cell were connected to a multichannel scanner system which read all measurements and recorded the readings onto a computer system for subsequent data reduction.

2.5 Loading Sequence

For each test a zero reading was taken on all instruments before the specimen was loaded. The beam was initially loaded through one complete cycle to about ± 12 ksi bending stress at the column face. This loading cycle was used to verify proper functioning of the instrumentation. One or two additional cycles of reversing loads were then applied to about ± 24 ksi maximum bending stress in the beam. The load was then increased to give approximately a 36-ksi maximum bending stress in the beam assuming elastic behavior. One or two cycles of reversing loads of this magnitude was then slowly applied. For

subsequent loading cycles, the tip displacement was incrementally increased to attain preselected displacements. For each specimen, except at fracture of a beam or yielding of bolts in Specimen 10, the inelastic cyclic displacements were terminated when satisfactory ductility of the connection was observed. During the entire process, the loading was stopped at selected points to take readings with a low-speed scanner. A log was maintained during each test to record critical observations, such as crack or buckling of beam flange, slippage of bolts, flaking of the whitewash, etc.

3. Experimental Results

3.1 Material Properties

All steel shapes and plates used to construct the specimens were of ASTM A36 steel as mentioned previously. Two tensile coupon tests were carried out to determine the steel properties for each specimen using ASTM procedures [21]. Coupons from each shape were taken, one from the beam flange and the other from the web. The test results are listed in Table 3.1. The stress-strain curves for the coupon tests were typical of those for A36 mild steel. The gauge length of the extensiometer used in all tensile coupon tests was 2 in. except for Specimens 1 and 2 in which the gauge length was set at 4 in. Measured elongations at fracture of the test coupons for Specimen 3 through Specimen 18 were therefore larger than those for Specimen 1 and 2. The actual dimensions of the beam sections were measured and found to be in good agreement with the values given in the AISC Manual [4]. The small differences in size of each beam were therefore neglected and the section properties in the AISC manual were adopted. For specimens, in which two pairs of ribs were added at the beam-column connection, the section properties of the beams at the juncture were obtained from the nominal plate dimensions and section properties of the bare beam. The section properties of the W12×133 column stub are given in the AISC Manual, 7th Edition.

3.2 Test Results

For each experiment the load-deformation data were obtained for cyclically applied loads. The resulting hysteretic loops provide the basic data for determining the behavior of the specimens. As cyclic loading progressed, the corresponding areas enclosed by the hysteretic loops indicate the capacity of a member and its connections to absorb and dissipate energy. The maximum attained load, the onset of yielding, and the ultimate inelastic

deformation of the beams were measured in each test and provided the data for assessing the performance of the specimens. A typical plot of cantilever tip load versus column rotation at the beam-column joint is shown in Fig. 3.1. It is to be noted that the column behaved elastically as anticipated during the test. A typical plot for the cantilever tip load versus the beam end deflection is shown in Fig. 3.2. Note that the beam end deflection represents the total displacement contributed by deformation of the beam as well as the column. The column's contribution to the beam end deflection is essentially elastic and can be computed by multiplying the column joint rotation by the cantilever beam length. The beam's contribution can then be obtained by subtracting the column's contribution from the total displacement. These beam deflections can further be divided by the length of the beam specimens and results obtained are denoted as beam rotations. Beam rotations of Specimen 1 through Specimen 18 are shown in Fig. 3.3 through 3.20. In order to obtain the plastic rotation of beam specimens under the load, elastic rotations of the beams have to be subtracted from the beam rotations. Theoretically, the elastic load-deflection relationship of a prismatic cantilever beam under the load can be obtained simply as follows:

$$\Delta = \frac{PL^3}{3EI} \tag{3.1}$$

where Δ is the cantilever tip displacement, P is the cantilever tip load, E and I are modulus of elasticity and moment of inertia of the beam section; L is measured from the support to the point of the applied load. The elastic rotations of beam can then be obtained by dividing Δ by the beam lengths. However, due to the presence of a shear tab, bolt holes and clevis, the beam specimens were not truly prismatic. Hence, a direct application of Eq. 3.1 would lead to inaccurate results. Therefore, experimental data as shown in Fig. 3.3 through Fig. 3.20 were used to obtain the elastic rotations of the beams assuming that the first few cycles of these hysteretic loops show elastic response. The slope of these responses represents the elastic rotational flexibility of the beams and column stubs and can be obtained from experimental data using the least square method. The elastic contribution

of beam rotations was then obtained by multiplying the flexibilities by the applied load. The plastic rotation versus applied load of beam specimens obtained are shown in Fig. 3.21 through 3.38. The experimental result for each specimen is described as follows:

Specimen 1

The hysteretic loops of load versus beam rotation for Specimen 1 are shown in Fig. 3.3. The beam responded elastically until the load was slightly above that required to reach the maximum beam bending stress of 36 ksi (40.2 kips). Flaking of the whitewash was first observed during the third loading cycle on the beam top flange outside the tips of the reinforcing ribs. The loops consistently exhibited stable characteristics. During the sixth cycle, no significant deterioration of the loop occurred, although local buckling of the bottom flange outside the reinforcing ribs developed. Subsequently, both the top and bottom flanges had pronounced local buckling that appeared and disappeared cyclically. However, the beam-column assemblage maintained load-carrying capacity even when severe local buckling occurred in either of the flanges.

The web of the beam beyond the shear tab buckled during the ninth cycle and then became straightened. Thereafter it buckled cyclically. The hysteretic loops remained stable. The cantilever load was terminated after pronounced ductility had been observed. The maximum load applied by the actuator was about 67 kips. A slight reduction of peak load was detected during the last cycle. No visible slippage of the bolts was detected in the shear tab. Cyclic buckling of the top and bottom flanges as well as that of the beam web was observed in the region outside the line connecting the tips of the top and bottom reinforcing ribs. Buckled beam flanges and web are shown in Fig. 3.39. The extent of the yield pattern at the top continuity plate is shown in Fig. 3.40.

Specimen 2

The hysteretic loops of load versus beam rotation for Specimen 2 are shown in Fig. 3.4. The beam again responded elastically up to the load slightly beyond that required to reach the maximum nominal beam bending stress of 36 ksi (37.4 kips). During early cycles, the whitewash on the top continuity plate cracked and relative movement between the beam web and the shear tab was observed. At the end of the eighth cycle, extensive slippage of the beam web, flaking of whitewash on both the top and the bottom flanges as well as on the top continuity plate were noted. During the ninth cycle, the beam top flange near the end of the web-cope cracked beginning at the center of the flange and propagating toward each side of the flange as the load was increased (Figs. 3.41 and 3.42). The beam top flange subsequently fractured and the beam lost its load-carrying capacity. The crack closed and opened when subjected to subsequent cyclic loading. During this test, the maximum load attained by the actuator was about 61 kips. The fractured specimen is shown in Fig. 3.42. Note the severity of the flaking of whitewash on the top continuity plate. The relative movement between the beam web and shear tab due to the bolt-slippage is shown in Fig. 3.43.

Specimen 3

The hysteretic loops of load versus beam rotation for Specimen 3 are shown in Fig. 3.5. The beam again responded elastically up to the load slightly beyond that required to reach the maximum nominal beam bending stress of 36 ksi (32 kips). The flaking of whitewash was first observed during the fifth loading cycle on the beam top and bottom flanges. Up until the tenth cycle, the loops exhibited stable characteristics. During the tenth cycle, a crack initiated at the center of the bottom flange near the web-cope (Fig. 3.44). Before crack was initiated, no pronounced bolt slippage was detectable. The last cycle consisted of one additional downward excursion of loading to close the crack followed by an upward excursion of loading to completely open the crack. During the last

cycle, the cracked flange buckled under reversed loading. Before cracking of the flange, the maximum load attained by the actuator was about 64 kips. The fractured specimen is shown in Fig. 3.45.

Specimen 4

The hysteretic loops of load versus beam rotation for Specimen 4 are shown in Fig. 3.6. The beam again responded elastically up to the load slightly beyond that required to reach the maximum nominal beam bending stress of 36 ksi (37.4 kips). All hysteretic loops exhibited stable characteristics. During the tenth cycle, the specimen failed abruptly with noise. A fracture of the bottom flange weld and a fracture of the lower web weld were noted (Fig. 3.46). An additional reversed loading fractured the upper web weld and the top flange weld (Fig. 3.47). The maximum load reached was about 62 kips. The fractured specimen is shown in Fig. 3.48.

Specimen 5

The hysteretic loops of load versus beam rotation for Specimen 5 are shown in Fig. 3.7. The beam again responded elastically up to the load slightly beyond that required to reach the maximum nominal beam bending stress of 36 ksi (46.7 kips). All hysteretic loops exhibited stable characteristics. Until the tenth cycle, both the upper and the lower web welds were cracked (Fig. 3.49). During the twelfth cycle, a crack of the top flange weld at the edge of the flange was detected (Fig. 3.50), and the direction of the applied load was reversed causing closing of the crack as well as buckling of the bottom flange. An additional reversed excursion of the applied load eventually fractured the top flange. The maximum load reached was about 87 kips. The fractured specimen is shown in Fig. 3.51.

Specimen 6

The hysteretic loops of load versus beam rotation for Specimen 6 are shown in Fig. 3.8. The beam again responded elastically up to the load slightly beyond that required to reach the maximum nominal beam bending stress of 36 ksi (47.7 kips). Up to the end of the ninth cycle, extensive flaking of whitewash on both the top and the bottom flanges as well as on the top continuity plate was observed. During the tenth cycle, the beam top flange cracked near the edge and propagating toward the other side of the flange as the load was increased (Figs. 3.52). The beam top flange subsequently fractured and the beam lost its load-carrying capacity. An additional reversed excursion of the applied load fractured the beam bottom flange. During this test, the maximum load attained by the actuator was about 79 kips. The fractured specimen is shown in Fig. 3.53. Note the severity of the flaking of whitewash on the top continuity plate.

Specimen 7

The hysteretic loops of load versus beam rotation for Specimen 7 are shown in Fig. 3.9. The beam again responded elastically up to the load slightly beyond that required to reach the maximum nominal beam bending stress of 36 ksi (49.1 kips). The flaking of whitewash was first observed during the fifth loading cycle on the beam top flange outside the tips of the reinforcing ribs (Fig. 3.54). The loops consistently exhibited stable characteristics. During the fifteenth cycle, a crack of bottom flange weld as well as the weld connecting the bottom reinforcing rib to the column flange were detected (Fig. 3.55). Significant slippage of the bolts was also observed in the shear tab (Fig .3.55). The beam bottom flange subsequently fractured and the beam lost its load-carrying capacity. The maximum load applied by the actuator was about 90 kips. The test was terminated after one more reversed excursion of the applied load.

Specimen 8

The hysteretic loops of load versus beam rotation for Specimen 8 are shown in Fig. 3.10. The beam again responded elastically up to the load slightly beyond that required to reach the maximum nominal beam bending stress of 36 ksi (50.0 kips). The flaking of whitewash was first observed during the early loading cycles on the beam top flange outside the tips of the reinforcing ribs. The loops consistently exhibited stable characteristics. During the tenth cycle, no significant deterioration of the hysteretic loop occurred, although local buckling of the bottom flange outside the reinforcing ribs developed. Similar to Specimen 1, both the top and the bottom flanges had pronounced local buckling that appeared and decreased in size cyclically. The load-carrying capacity reduced slightly when severe local buckling occurred in either of the flanges. The hysteretic loop remained stable. The web of the beam outside the shear tab buckled during the twelfth cycle. The cantilever load was terminated after pronounced ductility had been observed. The maximum load applied by the actuator was about 95 kips. A slight reduction of peak load was detected during the last cycle. Slippage of the bolts in the shear tab was detectable but not significant (Fig. 3.56). The buckling of beam flanges and web is shown in Fig. 3.57.

Specimen 9

The hysteretic loops of load versus beam rotation for Specimen 9 are shown in Fig. 3.11. The beam again responded elastically up to the load slightly beyond that required to reach the maximum nominal beam bending stress of 36 ksi (45.1 kips). The flaking of whitewash was first observed during the sixth loading cycle on the beam top and bottom flanges. Up until the tenth cycle, significant flaking of whitewash on web was also noted (Fig. 3.58). During the fifteenth cycle, local buckling of bottom flange occurred and the beam load-carrying capacity was slightly reduced. Buckling of beam flanges appeared and disappeared cyclically as the loading progressed. During the seventeenth cycle, buckling of the beam web was observed. The loops consistently exhibited stable characteristics. The

actuator load was terminated after pronounced ductility had been observed. The maximum load applied by the actuator was about 75 kips. The failed specimen is shown in Fig. 3.59.

Specimen 10

The beam again responded elastically up to the load slightly beyond that required to reach the maximum nominal beam bending stress of 36 ksi (40.0 kips). At higher loads, the gap between the end plate and the column flange appeared and disappeared cyclically. Some, but not severe flaking of whitewash on the beam flanges was also observed. Up until the end of the eighth cycle, the beam had not gone through severe inelastic deformation. However, the gap between the end plate and the column flange increased as cyclic loading progressed and the interior bolts between the two beam flanges yielded and elongated (Fig. 3.60). One of these interior bolts eventually fractured. Subsequently, the loading was terminated and it was decided that the specimen should be strengthened and retested. The failure of Specimen 10 will be discussed later in detail in chapter 4. The maximum load attained was about 68 kips. The fracture of the bolt will be studied in Chapter 4 in more detail.

Specimen 10R

As mentioned in Chapter 2, Specimen 10 was disassembled and repaired using end plate stiffeners and eight 1-in. diameter A354-BD bolts. Four bolts outside the beam web were instrumented using special strain gages to monitor the axial load in the bolts during the cyclic loading as well as the assembling of the specimen. The specimen was reload and the beam again responded elastically up to the load beyond that required to reach the maximum nominal beam bending stress of 36 ksi. The plot of cantilever load versus beam rotation relationships for Specimen 10R is shown in Fig. 3.12. All hysteretic loops exhibited stable characteristics. During the eighth cycle of the reloading, beam web buckling

in conjunction with flange buckling occurred near a section along two ends of the stiffeners. Buckling of the flanges and web appeared and decreased in size cyclically. The load-carrying capacity deteriorated after severe flange buckling had occurred. The load was terminated after pronounced ductility and severe buckling had been observed. The maximum load attained was about 80 kips. The failed specimen is shown in Fig. 3.61. In Chapter 4, the behavior of Specimen 10R will be examined with greater detail.

Specimen 11

The hysteretic loops of load versus beam rotation for Specimen 11 are shown in Fig. 3.13. The beam again responded elastically up to the load slightly beyond that required to reach the maximum nominal beam bending stress of 36 ksi (46.5 kips). All hysteretic loops exhibited stable characteristics. Up until the eighth cycle, flaking of whitewash on the beam flanges and web had been observed (Fig. 3.62). During the ninth cycle, the beam bottom flange buckled slightly. Subsequently, beam flange buckling appeared and diminished cyclically as the loading progressed. The load-deformation hysteretic loop lost its reproducibility once severe flange buckling occurred. The beam gradually lost its load-carrying capacity as the hysteretic loops deteriorated. The maximum load attained by the actuator was about 72 kips. The test was terminated when the beam tip displacement reached the travel limit of the linear potentiometer. The failed specimen is shown in Fig. 3.63. Local buckling of the flange occurred at 6 in. (about one flange width), away from the column face. Web buckling occurred at 5 in. from the column flange and at failure was about 1-1/8 in. out of plane.

Specimen 12

The hysteretic loops of load versus beam rotation for Specimen 12 are shown in Fig. 3.14. The beam again responded elastically up to the load slightly beyond that required to reach the maximum nominal beam bending stress of 36 ksi (47.5 kips). The hysteretic

loops exhibited stable characteristics until beam flange buckling occurred. Flaking of whitewash developed on the beam flanges and propagated toward the center of the web as the loading progressed (Fig. 3.64). During the tenth cycle, the beam flanges buckled at about 6 in. away from the end plate. Subsequently, the beam web buckled at about the same distance from the end plate and hysteretic loops started losing their reproducibility. From then on, buckling of the beam flanges and web appeared and diminished cyclically. The test was terminated when the beam tip displacement reached the travel limit of the linear potentiometer. No slippage of bolts in the end plate was observed throughout the test. The maximum load attained by the actuator was about 77 kips. The failed specimen is shown in Fig. 3.65.

Specimen 13

The hysteretic loops of load versus beam rotation for Specimen 13 are shown in Fig. 3.15. The beam again responded elastically up to the load slightly beyond that required to reach the maximum nominal beam bending stress of 36 ksi (32.8 kips). The flaking of whitewash was first observed at the beam flanges near the edge of the shear tab during the fifth cycle. The loops consistently exhibited stable characteristics and excellent reproducibility. During the tenth cycle, the top flange weld near the end of the web-cope cracked beginning at the center of the flange and propagated toward each side of the flange (Fig. 3.66). In the meantime, the upper web weld cracked and was followed by the fracture of the top flange weld and the upper web weld (Fig. 3.67). An additional excursion of the load fractured the bottom flange beginning at the center of the flange near the end of the web-cope and the welded nut which supported instrumentation (Fig. 3.68 and 3.69). The lower web weld together with the shear tab near the lowest bolt hole also cracked (Fig. 3.69). The maximum load applied by the actuator was about 69 kips. No slippage of the bolts was detectable before the fracture of flange welds.

Specimen 14

The hysteretic loops of load versus beam rotation for Specimen 14 are shown in Fig. 3.16. Having gained experience from the failure of Specimen 13 and other specimens, it was decided that both web copes of future specimens should be carefully ground smooth. However, the upper web cope of Specimen 14 was not accessible due to the presence of the back-up plate needed for the top flange weld (Fig. 2.8 and 2.9). The beam again responded elastically up to the load slightly beyond that required to reach the maximum nominal beam bending stress of 36 ksi (46.5 kips). The flaking of whitewash was first observed during the early loading cycles beginning at the beam flanges and propagating toward the center of the web at a region about 7 in. away from the column face (Fig. 3.70). During the eighth cycle, the beam flanges buckled slightly. Up until then, hysteretic loops consistently exhibited stable characteristics and good reproducibility. Local flange buckling became more and more severe as the loading progressed. During the tenth cycle, the web also buckled in the region outside the shear tab and deterioration of the hysteretic loops was observed (Fig. 3.71). During the fifteenth cycle, the beam top flange cracked beginning at center of the flange near the end of the web-cope (Fig. 3.72). Subsequently, beam top flange fractured and the beam lost its load-carrying capacity. The maximum load applied by the actuator was about 76 kips. No cracking of the web welds was observed during the test.

Specimen 15

Both web copes were ground smooth by the fabricator as shown in Fig. 2.10 and 2.11. It was noticed that the beam flanges had unintentional undercuts at the welds of about 1/8 in. The load versus beam rotation hysteretic loops for Specimen 15 is shown in Fig. 3.17. The beam top flange weld fractured abruptly before the beam underwent any inelastic deformation. The fracture of the weld was probably due to the improper application of the innershield welding procedure. The maximum load applied by the actuator was

about 33 kips.

Specimen 16

This specimen was similar to Specimen 15, both web copes were ground smooth as shown in Fig. 2.12. The weld undercuts of the beam flanges were not as obvious as they were in Specimen 15. The beam responded elastically up to the load slightly beyond that required to reach the maximum nominal beam bending stress of 36 ksi (46.5 kips). The load versus beam rotation hysteretic loops for Specimen 16 is shown in Fig. 3.18. The beam top flange weld again failed prematurely. The whole fractured section was right at the edge of the weld away from the column flange as shown in Fig. 3.73. The maximum load applied by the actuator was about 57 kips. It was decided that both Specimen 15 and Specimen 16, fabricated using the same welding procedure, were to be sent back to the fabricating shop to be re-done using the stick-welding procedure.

Specimen 17

The load versus beam rotation hysteretic loops for Specimen 17 is shown in Fig. 3.19. The beam again responded elastically up to the load slightly beyond that required to reach the maximum nominal beam bending stress of 36 ksi (32.8 kips). All hysteretic loops exhibited stable characteristics. Up until the eighth cycle, flaking of whitewash was observed mostly on beam flanges. During the ninth cycle, the beam top flange slightly buckled and noise was heard from slippage of the beam web relative to the shear tab. The noise continued and flaking of whitewash on beam web was still not obvious as the loading progressed (Fig. 3.74). During the tenth cycle, the top flange weld cracked near the lower edge of the flange. However, the beam did not loose its load-carrying capacity. During the reversed excursion of the same loading cycle, the bottom flange weld also cracked beginning at the lower edge of the flange and propagating toward the opposite edge. Subsequently, the whole bottom flange fractured abruptly with noise (Fig. 3.75). Another reversed excursion

of the applied load fractured the top flange. The maximum load attained by the actuator was about 54 kips. The failed specimen is shown in Fig. 3.76.

Specimen 18

The hysteretic loops of load versus beam rotation for Specimen 18 are shown in Fig. 3.20. The beam again responded elastically up to the load slightly beyond that required to reach the maximum nominal beam bending stress of 36 ksi (46.5 kips). Flaking of whitewash at both flanges was observed during the early loading cycles. In this test as well as other test specimens, flaking of whitewash was always started and concentrated in areas where welds had been made. For instance, a tack weld for a back up plate, a tack weld for a nut or a stud which supports the displacement-measuring device (Fig. 3.77), etc. During the tenth cycle, the beam flange slightly buckled. Subsequently, flange buckling appeared and disappeared cyclically. All hysteretic loops maintained stable characteristics. During the twelfth cycle, the top flange cracked beginning at the center of the flange near the end of the web-cope, and slippage of the beam web relative to the shear tab was observed (Fig. 3.78). Subsequently, the crack propagated and the top flange fractured (Fig. 3.79). The maximum load attained by the actuator was about 70 kips.

3.3 Summary

In general, all specimens, except Specimens 15 and 16, carried loads well above the 36 ksi nominal yield strength of the beams. In all experiments, except Specimens 15 and 16, the hysteretic loops exhibited a considerable amount of strain hardening of the material. Specimens in which a crack of a flange or a weld was initiated failed quite abruptly. For bolted web with welded flange connections, welding procedure as well as workmanship are critical to the performance of the connections. Any tack weld or undercut of weld could initiate a crack near a weld. Welded reinforcing ribs helped to ease stress concentration thereby preventing initiation of cracks in the welds. In Specimen 7, the

fracture of a weld on the reinforcing ribs appeared to be caused by poor welding workmanship. During the experiments, bolts tighten by the turn-of-nut method generally did not reach the required bolt preload. Beam web-to-shear tab welding helped to prevent slippage of the bolts, thereby enhancing the performance of the connection. If bolts in the end plate connection were designed and constructed properly, the all-welded beam with bolted end plate connections exhibit superb capacity to absorb and dissipate energy. The specimens having direct all-welded beam-to-column flange connections sustained very large deformations without significant lost of load carrying capacity. Premature failure of Specimens 15 and 16 can be attributed to improper welding procedures.

A summary of experimental results for the nineteen tests is given in Table 3.2. For purpose of discussion, the test result of these specimens will be divided into five groups. In the first two groups, W18×35 beams with $Z_f/Z = 0.66$ and W21×44 beams with $Z_f/Z = 0.62$ are discussed, respectively. Three specimens with beam-to-column web connections form the third group. Two specimens having direct all-welded beam-to-column flange connections are in the fourth group. In the fifth group, three bolted end plate beam-to-column flange connections are discussed.

(1) W18×35 Beam-to-Column Flange Connections

Specimens 3, 17 and 13, using W18×35 with $Z_f/Z = 0.66$, comprise the first group. The force versus beam rotation relationships for these specimens are plotted in Fig. 3.80. As described previously, the beam rotation is obtained by dividing the beam end deflection by the cantilever length L_c as defined in Table 3.2. In all cases, the effect of the elastic column rotation of the joint is excluded. In order to have these results comparable to other tests, the beam rotations are shown as a percentage. As a guide to the lowest acceptable level of performance, the hysteretic loops are bracketed by vertical lines at ±2%.

As shown in the top plot in Fig. 3.80, the early failure of Specimen 3 on a downward stroke occurred. On the reversely applied load, the fracture was closed and excellent

ductility in the opposite direction was observed. This disparity in ductilities in the two directions illustrates the possibility of erratic behavior. As shown in the middle plot in the same figure, Specimen 17 exhibits better behavior. The improved performance of this connection may be attributed to the use of tension control web bolts. As shown in the bottom plot in Fig. 3.80, similar improvement in the cyclic behavior of the connection was attained in Specimen 13 by applying beam web-to-shear tab welding.

As shown in Table 3.2, the maximum total beam rotation of Specimen 3 was 1.61 percent (0.0161 radian) and the corresponding maximum plastic rotation was about one percent. This kind of beam plastic rotation capacity may be inadequate for the general applications in severe seismic environment unless the beam-column panel zone joint can effectively participate the inelastic deformation of the structure. The hysteretic loops shown in Fig. 3.80 for Specimen 17 and Specimen 13 are better than those for Specimen 3. The improvement can be attributed to the use of tension control bolts or supplementary web welding. Moreover, in Specimen 17, the copes for back-up bars were ground smooth.

(2) W21×44 Beam-to-Column Flange Connections

Specimens 5,18 and 14, using W21×44 beams, comprise the second group. The force versus beam rotation relationships for these specimens are plotted in Fig. 3.81. Similar to the first group, the erratic behavior of Specimen 5 was observed and the performance of the connection was significantly improved either by using tension control web bolts or 20 percent supplementary welding as required per SEAOC [47]. Similar improvement can be observed from Specimen 18 as shown in Table 3.2. In this specimen, the copes were also ground smooth. In Specimen 7, using W21×44 beam, the welds for the ribs was noted inadequate.

(3) Beam-to-Column Web Moment Connections

Specimens 1,2 and 8 were selected for this group. The force versus beam rotation relationships for these specimens are plotted in Fig. 3.82. In Specimens 1 and 8, reinforcing ribs were used in the beam-to-column connections. The cyclic performance of these connections was excellent. With regard to these tests, it is useful to note the following:

The test on Specimen 1 with reinforcing ribs was terminated after reaching a very large ductility. Specimen 8, also with reinforcing ribs, exhibited excellent ductile behavior without the occurrence of any weld fracture. However, since the beam flange width-to-thickness ratio for Specimen 8 was relatively large, significant buckling of the beam flanges developed at large beam end displacement. A substantial beam moment continued to be carried by the connection after the beam flanges buckled. In order to better evaluate the performance of this connection, the beam plastic rotational capacities at the nominal plastic moment are given in parentheses in columns 10 and 11. For Specimen 2, although the maximum beam plastic rotations ,θ_p and θ_p^*, were also large, a brittle weld fracture was observed at the end of the test.

(4) All Welded Beam-to-Column Flange Connections

Specimens 9 and 11 comprise the fourth group. The beam load versus beam rotation relationships for these specimens are plotted in Fig. 3.83. As noted previously, both of these connections were fabricated by welding the beams directly to the column flanges. In Specimen 9, partial penetration welds from the outside and fillet welds from the inside were used to connect the beam flanges to the column. Fillet welds were applied on both sides of the beam web. In Specimen 11, continuous fillet welds were used around the entire beam cross-section. In either specimen, no copes in the webs were used in the fabrication of the connections; neither were any stress relief holes made at the junctures of the beam flanges and the webs. The performance of these specimens demonstrates the improvement in joint ductility obtained when no holes for back-up bars are provided. As

shown in both plots in Fig. 3.83, the ductility of these connections is excellent, although a slight decay in load carrying capacity occurred after beam flanges had buckled. As can be noted in Table 3.2, the maximum beam rotation angles were very large. No weld failure occurred in either one of these two specimens.

(5) Bolted End Plate Beam-to-Column Flange Moment Connections

Specimens 10, 10R and 12, using bolted end plate connections, comprise the fifth group. In these specimens, the connections were fabricated by first welding the beam to an end plate and then attaching the end plate to the column flange. In each specimen, continuous fillet welds were used around the entire beam cross-section and no holes and back-up bars were provide. The force versus beam rotation relationships for these specimens are plotted in Fig. 3.84.

As noted previously, the test of Specimen 10 was terminated due to the fracture of a connecting bolt. Specimen 10R was made by modifying Specimen 10 with stronger connecting bolts and two end plate stiffeners. Some of the bolt forces in the connection for Specimen 10R were also recorded during the application of cyclic load. After observing the bolt failure in Specimen 10, the connecting bolts for Specimen 12 were also enlarged. In Fig. 3.84, the maximum beam total rotation for Specimen 10 was also large, however, was attributed to the elongations of the connecting bolts. Therefore, various maximum rotation angles as shown in Table 3.2 were neglected for Specimen 10. In Fig. 3.84, excellent ductility for Specimens 10R and 12 can be observed from their hysteretic loops although a slight decay in load carrying capacity occurred after beam flanges buckling had developed. The behavior of Specimens 10 and 10R will be discussed in detail later in chapter 4.

In this series of experiments, only the flange welds in Specimen 3 through Specimen 6 were inspected ultrasonically and were found to be satisfactory. Specimen 15 and 16 were fabricated by a vendor generally using shielded metal arc welding rather than flux-more arc welding. In conformity with the AWS specification [20], the joints in these two specimens

were not preheated during the fabrication. Although the appearance of the welds was good, they were not ultrasonically inspected. As shown in Table 3.2, the ductility of these two connections was very poor.

On scanning column 10 and column 11 in Table 3.2, the beam plastic rotational capacities for Specimens 1, 2, 7, 8, 9, 10R, 11, 12, 14, 17 and 18 are probably adequate while that for Specimen 13 is marginal. Unless the beam-column panel zone joints can effectively participate in the nonlinear deformation and dissipate earthquake energy, the beam plastic rotational capacities for Specimens 2, 4, 5, and 6, and certainly for the poorly fabricated Specimens 15 and 16, are not acceptable.

3.4 Conclusions

As noted previously, the ductility demand of beam-column connections for steel MRFs designed according to the building code may be large. Therefore, the beam-column connections must be designed and constructed to provide the required strength and ductility. Premature weld fractures in the connections are particular dangerous and should be mitigated. From this limited series of tests, some conclusions can drawn as follows:

(1) As shown in Column 7 of Table 3.2, all nineteen specimens attained their strength at a nominal 36 ksi yield stress. Except for poorly fabricated Specimens 15 and 16, all specimens also exceeded their yield strengths based on tensile coupon tests.

(2) As shown in Column 10 and 11 of Table 3.2, the rotational capacity in beam-to-column flange moment connections in Specimens 7, 8, 9, 10R, 11, 12, 14, 17 and 18 may be considered satisfactory. In some of these specimens, the required ductility was achieved using either reinforcing ribs at the connections, tension control web bolts, or 20 percent supplementary web welds.

(3) Variability in ductility of moment connections was observed in many instances. It is recommended that this be reduced by the following means:

(a) Beam web copes for back-up bars should be ground as smooth as possible. Back-up bars should be tack welded on the inside of the flange cope and away from the edges of the flange.

(b) The use of either tension control web bolts or supplementary web welds are necessary for bolted web connections for beams with Z_f/Z ratio smaller than 0.70.

(c) Careful inspection of the connections. This includes bolts as well as welds.

(4) If it can be demonstrated that the column panel zone joints in the MRF can effectively participate in providing ductility, the requirements for beam connection ductility can be reduced.

(5) Ductility in beam-to-column web moment connections was found to be satisfactory. In Specimens 1 and 8, this was achieved with the aid of reinforcing ribs. Specimen 2 was fabricated with exceptional care using the shielded metal arc welding process and cannot necessarily be duplicated in the field.

(6) Specimen 9 and 11 with fully welded beam-to-column flange having no copes in the beam webs provided exceptionally high ductility.

(7) From the limited number of tests and under laboratory conditions, no essential difference in performance was noted between the two types of tension control devices used for web bolts.

4. Cyclic Behavior of Bolted End Plate Moment Connections

4.1 Introduction

In end plate moment connections, one of the most essential elements is believed to be the connecting bolts, which attach the end plate to the column flange. In the test of Specimen 10, premature fracture of a bolt near the beam web was observed. In order to gain more information for the design of connecting bolts, the cyclic behavior of these bolts under moment reversal needs to be studied. For this purpose, four of the bolts in Specimen 10R were instrumented with bolt gauges in order to monitor the bolt tension forces during the installation of bolts and the application of external load. The locations of these gauged bolts, bolt 1 through bolt 4, are indicated in Fig. 4.1.

4.2 Measuring the Bolt Tension Forces

Inelastic elongation occurs practically in all properly installed bolts and essentially results from local yielding of the threads between the underside of the nut and the gripped material [28]. The bolt gauges used in Specimen 10R, installed in the center of the bolts within the bolt shanks, measured the strains in the bolt shanks and are believed to remain elastic during the application of external load.

Since the bolt gauges measure the strain in the bolts, the bolt tension forces can be obtained by measuring the strain in the bolt after the proper force-strain relationship of bolt is established. Ideally, bolt gauges ought to be calibrated prior to the installations of bolts so that the bolt force-strain relationship can be obtained and therefore the bolt preloads be controlled and monitored. Since calibration of bolt gauges required a special mounting fixture, the gauged bolts were installed for Specimen 10R while the mounting fixture was being fabricated in order to expedite the test program. As a result, the bolt required prestrain, associated with the specified preload, was estimated based on an

assumed modulus of elasticity and monitored during the installation. Note that the specified minimum bolt tension force varies depending on the bolt size and its minimum tensile strength [4]. In this case, a minimum preload of 64 kips was required for each 1-inch diameter A354 grade BD bolt. Therefore, using the assumed modulus of elasticity E = 29000 ksi and bolt cross-sectional area of 0.7854 in^2, the bolt strain, ϵ, corresponds to 64 kips of preload, can be obtained as follows:

$$\epsilon = \frac{\sigma}{E} = \frac{\frac{64}{0.7854}}{29000} = 0.00281$$

Note that if the turn-of-nut tightening method per AISC specification [4] were used to install the bolts, a 1/2 turn of nut would have been required for each bolt after enough bolts have been brought to a snug tight position in order to achieve the specified minimum bolt preload. However, during installation of gauged bolts for Specimen 10R, all bolts were brought to snug tight first. Note that at the snug tight position, all gauged bolts showed about 0.001 tensile strain. Subsequently, bolts were tightened symmetrically progressing from the interior bolts to the exterior ones. When 0.00281 strain was achieved in the gauged bolt, each had about 3/4 turn of nut after it had been brought to snug tight. Based on this observation, the other bolts which were not instrumented were also tightened by a 3/4 turn of nut after they had been brought to snug tight position.

During the test, the applied load, the strain histories as well as other deformation measurements were recorded. After the test of Specimen 10R, the bolts were disassembled from the connection and the tensile strain reading in each gauged bolt was found to be essentially zero. From this observation, the response of the bolt gauges under the applied load appeared to be elastic. Subsequent calibrations of bolt gauges were done by relating the strains under the controlled tension forces. An essentially elastic force-strain relationship is evident for each gauged bolt as shown in Figs. 4.2 and 4.3.

4.3 Bolt Tensions in Connected Plates

Since bolts are tightened prior to the application of the external loading, the bolts are pretensioned as much as the plates are precompressed. As a result of this preload, the externally applied loads primarily change the contact pressure between the plates; very little additional fastener elongation is introduced before the precompression between the plates was exhausted. Therefore there is only a minor increase in bolt tension until the separation of the plates occurs. This behavior can be illustrated by a simple model [27,28] as shown in Fig. 4.4. Tightening of the nut results in a tension in the bolt and compression between the connected plates. Assuming that the bolts and plates remain elastic, the force in each is proportional to its change in length, that is:

$$\Delta B = K_b \Delta e \tag{4-1}$$

$$\Delta C = -K_p \Delta e \tag{4-2}$$

where B represents the bolt preload, C is the sum of contact forces between the plates and K_b and K_p the stiffness of the bolt and the plate, respectively. The term Δe represent the change in bolt elongation due to an externally applied load. Unless separation of the plates occur, the change in bolt elongation is equal to the change of plate in thickness. In the usual case, K_p will be much smaller than K_b, because the bolt force, B_o, is concentrated in the bolt whereas the compression force, C_i, is distributed over the contact area. Under no external load, the bolt preload, B_o, and the contact force, C_i, are equal. When a load T is applied to the connection, the bolt will elongate and the precompressed plate will expand. Under this load, the equilibrium equation becomes:

$$B = C_p + T \tag{4-3}$$

where T is the externally applied load, C_p the sum of the reduced contact forces, and B the bolt force under an applied force T. Under such conditions, an increase in applied load T results in an increase in bolt elongation Δe. For compatibility, the plates must expand by the same amount. Since the plate stiffness is much larger than the bolt stiffness,

the application of external force T results in a greater reduction in the compression, ΔC, in the plates than the increase of tension, ΔB, in the bolt. Before the separation of plates occurs, their relationship at the equilibrium state is:

$$B_o + \Delta B = C_i + \Delta C + T \tag{4-4}$$

Since

$$B_o = C_i \tag{4-5}$$

Therefore,

$$\Delta B - \Delta C = T \tag{4-6}$$

When contact pressure between the plates reduces to zero, separation of plates will start. When this occurs,

$$\Delta C = -C_i = -B_o = -K_p \Delta e \tag{4-7}$$

Therefore,

$$\Delta e = \frac{B_o}{K_p} \tag{4-8}$$

and

$$\Delta B = K_b \Delta e = B_o \frac{K_b}{K_p} \tag{4-9}$$

As a result, for the elastic case, separation of plates takes place at an applied load equal to:

$$T = B_o(1+\frac{K_b}{K_p}) \tag{4-10}$$

which can be obtained by substituting Eq. 4-7 and 4-9 into Eq. 4-4. After the plates are separated, the bolt force B is simply equal to the external load T. Note that the above model can only apply to a single bolt or bolt groups without the effect of prying action. It is well known that the prying force can be neglected if the connecting plates are sufficiently

stiff [28].

4.4 Bolts Under Cyclic Loading

Since bolt prying forces in Specimens 10 and 10R are negligible as estimated in Appendix A, the basic model described in Section 4.3 for a single bolt under tension appeared to be applicable to the bolt groups in end plate connection. However, in Specimens 10 and 10R, each bolt in the bolt groups was subjected to a cyclically instead of monotonically applied force described in the model.

As noted in Section 4.1, the tension force in the bolts can be obtained from the available strain readings and the corresponding bolt force-strain relationships. Cyclic behavior of bolts under tension can be studied by plotting the bolt tensions versus applied beam moment relationships. The results from those four gauged bolts under the cyclic applied beam moment are shown in Figs. 4.5 and 4.6. The locations of the bolts are indicated in Fig. 4.1. In general, degrading of bolt clamping forces was observed in each subsequent cycle of applied beam moment. It appeared that the pretension force combined with the additional applied load on the connection was sufficient to produce yielding of the bolts; reduced clamping forces resulted upon unloading. Note that the degrading of the clamping force was more significant in the first few cycles of the loading than those toward the end of the test. This may well be attributed to the fact that the applied moment was increased cyclically in the early loading cycles whereas the applied moments were more repetitive during the late cycles. As noted in Section 4.2, the stiffness of the end plate and the column flange was much larger than the bolt group and the reduction of the bolt clamping forces was small when the beam moment reversed causing compression to the beam flange near the bolt group.

4.5 Design of Bolts

The design bolt force in the end plate connection can be obtained by dividing the beam moment by an assumed lever arm. In general, the bolt's resisting lever arm is often approximated as the distance between the beam compression flange and the center of bolt or bolt group [4,27,29]. Since the bolt forces and the corresponding beam moment were recorded during the testing of Specimen 10R, the bolt resisting lever arms can be examined experimentally. Assuming that the gauged bolts as shown in Fig. 4.1 subjected to 50% of the externally applied moment, an equilibrium equation for the beam moment and the bolt forces can be established as follows:

$$\frac{M}{2} = T_1 h_1 + T_2 h_2 \tag{4-11}$$

where M is the externally applied moment which causes bolt 1 and bolt 2 to be pulled, T_1 and T_2 are the tension forces in bolt 1 and bolt 2 respectively, h_1 and h_2 are the distances measured from the resulting compressive force to the the center of bolt 1 and bolt 2 respectively. In Specimen 10R, we have:

$$h_1 = h_2 + 4.525 \ \ in.$$

Let h equal to the distance measured from the center of the bolt group to the resulting compressive force, Eq. 4-11 becomes:

$$\frac{M}{2} = T_1 (h + 2.2625) + T_2 (h - 2.2625)$$

or

$$h = \frac{M - 4.525 T_1 + 4.525 T_2}{2 (T_1 + T_2)} \tag{4-12}$$

Similar equations can be derived for bolt 3 and 4 under reversed moment.

Note that Eqs. 4-11 and 4-12 are valid only when the end plate and the column flange are separated at places where bolt 1 and bolt 2 are located. For this reason, only the

peak bolt force and the associated peak moment of each loading cycle were examined when Eq. 4-12 was used. The relationship between the peak beam moment versus the corresponding lever arm determined based on Eq. 4-12 were plotted in Fig. 4.7. Note in the figure that the computed lever arms associated with the lower external moments are significantly smaller than those associated with the higher external moments. This may be due to the fact that the end plate and the column flange still remains in contact during the first few cycles of loading. From these limited data, it appears that the bolt resisting lever arm under the beam moment is only about 80% of the beam depth rather than the full beam depth commonly measured from the beam compression flange to the center of the bolt group.

4.6 Fracture of Undersized Bolts

As mentioned in Chapters 2 and 3, one of the A325 7/8-inch diameter connecting bolts near the beam web in Specimen 10 was fractured before the modification of the specimen was made. As noted in Chapter 2, after the bolt failed, Specimen 10R was made with stiffeners and connected to column with eight 1-inch diameter A354 grade BD bolts. The performances of Specimens 10 and 10R, can be assessed by examining the beam rotation versus beam applied load relationships as plotted in Fig. 4.8. Clearly, in Specimen 10, 7/8 inch diameter A325 bolts were inadequate in developing enough beam plastic rotation. The fracture of the interior bolt, located at where Bolt 2 occurred in Fig. 4.1, brought up the question of the distribution of the resisting bolt forces under the applied moment. It appeared that two interior bolts near the web participated in resisting the applied moment more than the other two exterior bolts did before stiffeners were made. Note, before the stiffeners were added, that the interior bolts were surrounded by the beam flange as well as the beam web whereas the exterior bolts were adjacent to the beam flange only.

In order to access the relative stiffness of the end plate at various bolt locations, a finite element analysis was performed. The finite element model was made of four-node

elastic plate elements and was analyzed using a general purpose finite element analysis program FEAP [31]. In the analysis, only one half of the end plate was modeled as shown in Fig. 4.9b. The bolt holes in the end plate were modeled as square holes and the model consisted of a planar mesh of elements, supported perpendicularly to the plane of the plate at the nodes where the end plate was halved and where the beam flange and the web occurred. The analysis was carried out by applying a total of 60 kips of force normal to the plane of the plate at each bolt location. Each force was distributed into four equal nodal forces at four nodes around each bolt hole as shown in Fig. 4.9b. In order to better approximate the situation that only one bolt exist in each bolt hole, the out of plane translational displacements for each of these four nodes was forced to be identical. The analytical results obtained indicated that the out of plane displacement at the edge of the bolt holes were 0.00355 inch and 0.00156 inch. A larger displacement resulted for the exterior bolt as anticipated.

Taking the advantage of structural symmetry in the end plate, a further halved finite element model as shown in Fig. 4.9c was analyzed using another finite element program SAP80 [32] with its shell element to examine the deformed shape under the same loading pattern. The out of plane displacements at the edges of the bolt holes obtained were very similar to the previous analytical result. The isometric view of the deformed shape is shown in Fig. 4.10.

From these limited analytical studies, it is important to recognized that the actual shape of the bolt hole, the size of the washer, the actual condition and location of the boundaries were not precisely considered. It is believed that these parameters are all essential to the true behavior of the end plate. However, without the help of the stiffeners, a general trend of the relative rigidity in the end plate near both the interior and the exterior bolts was obvious. Clearly, due to a larger rigidity of the plate bounded by the beam web and the flange, the separation of the end plate with respect to the column flange first occurred near the interior bolts. As described in Section 4.2, the bolt force increased

significantly only after the separation of the connecting parts took place. Therefore, in Specimen 10, once this separation occurred near the interior bolt, further applied load was resisted primarily by two interior bolts on each side of the beam web.

Recall the design procedure [27] used as shown in Appendix A, note that the design bolt force was based only on the beam flange area and its nominal yield strength. In Specimen 10 or 10R, plastic moment capacity of the web of W18x40 constitutes 30% of the total beam plastic moment capacity. The fracture of the interior bolt might be due to the undersized bolt resulting from inadequate design force in conjunction with the differential force distribution among the bolt group.

4.7 Conclusions

End plate moment connections are a viable choice for moment resisting connections where field welding is not desired. As mentioned in Chapters 2 and 3, Specimen 10R and Specimen 12 showed excellent ductility and energy dissipation capacity.

Before more experimental results become available, it is important to note that the bolt pretension force due to the tightening of the bolt could drive the bolt to yield before the application of an external load. Subsequently applied cyclic loading increases permanent elongation of bolts and therefore degrades the clamping force of the connection. Moreover, under external load, the distribution of the bolt force within the bolt group may be far from uniform if no stiffeners were devised. Therefore, the connecting bolts in the end plate connection should be conservatively sized; the design bolt force should be based upon a conservative assumption of the resisting lever arm and account for possible strain hardening of the beam section.

From these limited experimental data, it appears that well designed end plate connections are suitable for severe seismic service. However, more experimental work is needed to examine other end plate connections consisting of different proportions of bolt sizes, end plate thickness, stiffeners and beam section; possibly, a thinner end plate with stiffeners.

Nontheless, steel column base plate connections fix-connected to the foundation, a similar yet more important connection, deserves much more attention.

5. NONLINEAR DYNAMIC ANALYSIS METHOD FOR MRFS

5.1 General

Properly designed and constructed steel MRFs are expected to deform well into the inelastic range under strong ground excitations, dissipating seismic energy without collapse of the structure. Inelastic activity can occur in beams, columns or panel zone joints, or any combination of these structural elements. In order to realistically assess the performance and behavior of MRFs under severe seismic ground motions, a nonlinear dynamic analysis procedure must be used. Nonlinear behavior of the structural elements must be realistically modeled considering member post-yielding behavior and material strain hardening. Efficiency and stability of the numerical strategies are also required for practical analysis of nonlinear systems of realistic size.

This chapter presents a procedure used to solve the equations of motion for nonlinear dynamic analysis of MRFs. The element modelings for nonlinear beams, columns and panel zone joints are discussed. Performance of the panel zone joint element is evaluated by comparing the analytical result with an experimental test conducted previously at Berkeley [51].

5.2 Nonlinear Behavior of MRFs

Nonlinearities of MRFs arise from two important sources. First, material nonlinearity gives rise to nonlinear force-deformation relationships for beams, columns, and joints. Second, geometric nonlinearities within the deformation-displacement relationships of the system require that equilibrium conditions be examined in the deformed configuration.

For the most practically designed and constructed MRFs, material nonlinearity is typically the most important source. Geometric nonlinearity, arising from column P-Δ effects, can be significant when column axial loads are high or the frame lateral drift is excessively large. For the MRF models analyzed in this report, both types of nonlinearity are

considered and examined. Material nonlinearity is considered by using bilinear force-deformation relationships for members and joints. Geometric nonlinearity is approximated by including geometric stiffness terms in the element stiffness formulation.

5.3 Numerical Procedure for Nonlinear Dynamic Analysis

5.3.1 Incremental Equations of Motion

Response of a structural system subject to dynamic loading can be obtained by solving the equations of motion for the system. For large elastic systems, response to dynamic loads can be obtained efficiently by superposition of modal responses or Ritz vectors. For nonlinear dynamic analysis, incremental and iterative procedures have been widely used and will be discussed later.

For a typical building frame model, good accuracy can be achieved by using the lumped mass at each floor level and by assuming viscous damping [58]. At any time t, the discrete equations of motion resulting from dynamic force equilibrium are:

$$\underline{M}\cdot\ddot{\underline{U}} + \underline{C}\cdot\dot{\underline{U}} + \underline{K}_t\cdot\underline{U} = \underline{P}_t \tag{5-1}$$

Assuming mass and damping remain unchanged, at time $t+\Delta t$, the equations of motion become:

$$\underline{M}\cdot(\ddot{\underline{U}} + \Delta\ddot{\underline{U}}) + \underline{C}\cdot(\dot{\underline{U}} + \Delta\dot{\underline{U}}) + \underline{K}_t\cdot(\underline{U} + \Delta\underline{U}) = \underline{P}_{t+\Delta t} \tag{5-2}$$

$\underline{K}_t$ represents the tangent stiffness of the system linearized at time t. Because of this linearization, Eq. 5-2 will in general provide only an approximate solution to the response at time $t + \Delta t$. However, through appropriate choice of solution strategy and time step Δt, an accurate solution can be obtained. Let R_t denote the nodal loads in equilibrium with element forces at time t, that is:

$$R_t = \underline{K}_t\underline{U} \tag{5-3}$$

Combining Eq. 5-1 through 5-3, an incremental form of the equations of motion is then:

$$\underline{M}\cdot\Delta\ddot{\underline{U}} + \underline{C}\cdot\Delta\dot{\underline{U}} + \underline{K}_t\cdot\Delta\underline{U} = \underline{P}_{t+\Delta t} - (\underline{M}\cdot\ddot{\underline{U}} + \underline{C}\cdot\dot{\underline{U}} + R_t) \qquad (5\text{-}4)$$

where

$\underline{M}$: mass matrix,

$\underline{C}$: damping matrix,

$\underline{K}_t$: tangent stiffness matrix at time t,

$\underline{U}$, $\dot{\underline{U}}$, $\ddot{\underline{U}}$: nodal displacement, velocity and acceleration at time t,

$\Delta\underline{U}$, $\Delta\dot{\underline{U}}$, $\Delta\ddot{\underline{U}}$: increments of nodal displacement, velocity and acceleration,

$\underline{P}_t$, $\underline{P}_{t+\Delta t}$: external applied loads at time t and $t+\Delta t$.

The left side of Eq. 5-4 can be viewed as the change in response from time t to $t+\Delta t$ due to the unbalance load resulting from time t to $t+\Delta t$ on the right side of the equation. In the case of earthquake excitation, the externally applied dynamic loads on the system are the inertia forces associated with the ground acceleration. If soil-structure interaction and differential support excitations are not considered, the inertia forces of the system can be expressed as:

$$\underline{F}_I(t) = -\underline{M}\cdot\underline{r}\cdot\ddot{\underline{U}}_g(t) \qquad (5\text{-}5)$$

where $\ddot{\underline{U}}_g(t)$ is the ground acceleration of support at time t and $\underline{r}$ is the displacement influence coefficient matrix relating static nodal displacements to the support motions [33]. If only one horizontal ground acceleration is considered for the analysis, $\underline{r}$ reduces to a vector.

5.3.2 Solution of Incremental Equations of Motion

The discrete form of the equations of motion are typically solved by direct integration, in which the time domain is divided into a number of time steps. Various explicit and implicit, single and multiple step integration schemes have been used to solve the incremental equations of motion for linear and nonlinear systems [34-38]. The basic

requirements for any integration scheme are accuracy and stability. Generally, the stability can be assessed by studying the growth of the computed response, while accuracy can be evaluated by measuring the distortion of the computed response amplitude and frequency of the system.

Stability and accuracy of various integration schemes for linear systems have been investigated. However, these stability limits may no longer be valid for nonlinear systems. Moreover, the accuracy of the computed response in a nonlinear system depends on the nature of the nonlinearity, the solution scheme and the iterative procedure used. For example, instability and error can be attributed to equilibrium unbalance and the work done by the unbalanced load. To control this error, it is important to select a sufficiently small time step and remove the unbalanced load within each time step. Because of the complexity involved, accuracy and stability limits of particular integration schemes for non-linear dynamic analysis have not been fully established. Therefore, the performance of a particular integration scheme for nonlinear dynamic analysis can only be evaluated by numerical experimentation.

Several single step, implicit integration schemes used for linear analysis have been adapted to nonlinear systems. An implicit, single step, two-parameter family of integration methods by Newmark have gained wide acceptance in nonlinear analysis [39,40]. Newmark's method, as implemented in the ANSR-1 [40] computer program, is used to analyze the model building described in this report. Basically, in Newmark's method, it is assumed that increments of velocity and acceleration are a function of the increment in displacement and the state of motion at time t. That is:

$$\Delta\dot{\underline{U}} = \frac{\gamma}{\beta\Delta t}\Delta\underline{U} - \frac{\gamma}{\beta}\dot{\underline{U}}_t + \Delta t\left(1 - \frac{\gamma}{2\beta}\right)\ddot{\underline{U}}_t \qquad (5\text{-}6a)$$

$$\Delta\ddot{\underline{U}} = \frac{1}{\beta(\Delta t)^2}\Delta\underline{U} - \frac{1}{\beta\Delta t}\dot{\underline{U}}_t - \frac{1}{2\beta}\ddot{\underline{U}}_t \qquad (5\text{-}6b)$$

where

β, γ = integration parameters

Δt = time step

$\underline{\dot{U}}_t$, $\underline{\ddot{U}}_t$ = nodal velocities and accelerations at time t

Substituting Eq. 5-6 into Eq. 5-4, the incremental equations of motion take the form:

$$\underline{K}_t^* \cdot \Delta U = \underline{P}^* \tag{5-7}$$

in which $\underline{K}_t^*$ is the effective stiffness matrix and $\underline{P}_t^*$ is the effective load vector, where:

$$\underline{K}_t^* = \frac{1}{\beta(\Delta t)^2}\underline{M} + \frac{\gamma}{\beta \Delta t}\underline{C} + \underline{K}_t$$

and

$$\underline{P}^* = \underline{P}_{t+\Delta t} - \underline{M}\left[\left(1-\frac{1}{2\beta}\right)\underline{\ddot{U}}_t - \frac{1}{\beta \Delta t}\underline{\dot{U}}_t\right] - \underline{C}\left[\Delta t\left(1-\frac{\gamma}{2\beta}\right)\underline{\ddot{U}t} + \left(1-\frac{\gamma}{\beta}\right)\underline{\dot{U}}_t\right] - \underline{R}_t$$

The displacement increment ΔU can be solved from Eq. 5-7 and the state of the motion at time $t+\Delta t$ can then be obtained:

$$\underline{U}_{t+\Delta t} = \underline{U}_t + \Delta \underline{U} \tag{5-8a}$$

$$\underline{\dot{U}}_{t+\Delta t} = \left(1-\frac{\gamma}{\beta}\right)\underline{\dot{U}}_t + \frac{\gamma}{\beta \Delta t}\Delta U + \Delta t\left(1-\frac{\gamma}{2\beta}\right)\underline{\ddot{U}}_t \tag{5-8b}$$

$$\underline{\ddot{U}}_{t+\Delta t} = \left(1-\frac{1}{2\beta}\right)\underline{\ddot{U}}_t + \frac{1}{\beta(\Delta t)^2}\Delta U - \frac{1}{\beta \Delta t}\underline{\dot{U}}_t \tag{5-8c}$$

5.3.3 Iterative Procedure for Direct Integration

If nonlinearities developed within the time step, equilibrium will not be satisfied. In this circumstance, an iterative procedure within the time step is required in order to satisfy equilibrium, subject to a specified tolerance. In general, there are two basic types of iterative procedures commonly used in nonlinear analysis, namely Constant Stiffness iteration

and Tangent Stiffness or Newton-Raphson iteration. These procedures are illustrated in Fig. 5.1 for one dimensional load-displacement response.

Constant Stiffness iteration will typically converge more slowly than Newton-Raphson iteration. However, a notable drawback of the Newton-Raphson iteration procedure is the large amount of computational effort required to reform the structural tangent stiffness at every iteration. In some cases, it may be advantageous to combine both procedures. Such a mixed iteration scheme is illustrated in Fig. 5.1c. It was found that Constant Stiffness iteration was more efficient for the dynamic nonlinear analyses of MRFs. Therefore, an iterative algorithm for Newmark's integration method based on iterating with a constant effective stiffness matrix $\underline{K}_t^*$ was incorporated in ANSR-1 program as follows:

(A) Initialization

(1) Specify the parameters β, γ, time step Δt and convergence tolerance TOL.

(2) Compute the integration parameters:

$$a_1 = \frac{1}{\beta(\Delta t)^2} \qquad a_2 = \frac{1}{\beta \Delta t} \qquad a_3 = \frac{1}{2\beta}$$

$$a_4 = \frac{\gamma}{\beta \Delta t} \qquad a_5 = \frac{\gamma}{\beta} \qquad a_6 = \Delta t \left(1 - \frac{\gamma}{2\beta}\right)$$

(3) Form the effective stiffness matrix:

$$\underline{K}_t^* = a_1 \underline{M} + a_4 \underline{C} + \underline{K}_0$$

(4) Decompose the effective stiffness matrix:

$$\underline{L}\ \underline{D}\ \underline{L}^t = \underline{K}_t^*$$

(5) Specify initial conditions at time $t = 0$.

(B) Iteration within Time Step

(1) Form load vector $\underline{P}_{t+\Delta t}$

(2) Set iteration index $i = 0$ and initialize the motion vectors:

$$\underline{U}_{t+\Delta t}^{(i)} = \underline{U}_t$$

$$\dot{\underline{U}}_{t+\Delta t}^{(i)} = (1 - a_5)\,\dot{\underline{U}}_t + a_6\,\ddot{\underline{U}}_t$$

$$\ddot{\underline{U}}_{t+\Delta t}^{(i)} = (1 - a_3)\,\ddot{\underline{U}}_t - a_2\,\dot{\underline{U}}_t$$

(3) Perform state determination for the current configuration and determine the equivalent nodal forces $\underline{R}_{t+\Delta t}^{(i)}$ in equilibrium with the element internal forces.

(4) Solve for the incremental displacement $\Delta \underline{U}^{(i+1)}$ for iteration i:

$$\underline{LDL}^t \cdot \Delta \underline{U}^{(i+1)} = \underline{P}_{t+\Delta t} - \left[\underline{M} \cdot \ddot{\underline{U}}_{t+\Delta t}^{(i)} + \underline{C} \cdot \dot{\underline{U}}_{t+\Delta t}^{(i)} + \underline{R}_{t+\Delta t}^{(i)}\right]$$

(5) Update the motion vectors:

$$\underline{U}_{t+\Delta t}^{(i+1)} = \underline{U}_{t+\Delta t}^{(i)} + \Delta \underline{U}^{(i+1)}$$

$$\dot{\underline{U}}_{t+\Delta t}^{(i+1)} = \dot{\underline{U}}_{t+\Delta t}^{(i)} + a_4 \Delta \underline{U}^{(i+1)}$$

$$\ddot{\underline{U}}_{t+\Delta t}^{(i+1)} = \ddot{\underline{U}}_{t+\Delta t}^{(i)} + a_1 \Delta \underline{U}^{(i+1)}$$

(6) Perform state determination and determine $\underline{R}_{t+\Delta t}^{(i+1)}$ in equilibrium with the element internal forces associated with the updated configuration $\underline{U}_{t+\Delta t}^{(i+1)}$

(7) Compute the residual load vector:

$$\hat{\underline{F}} = \underline{P}_{t+\Delta t} - \left[\underline{M} \cdot \ddot{\underline{U}}_{t+\Delta t}^{(i+1)} + \underline{C} \cdot \dot{\underline{U}}_{t+\Delta t}^{(i+1)} + \underline{R}_{t+\Delta t}^{(i+1)}\right]$$

(8) Check convergence:

$$\text{If } \frac{||\hat{\underline{F}}||}{||\underline{P}_{t+\Delta t}||} < TOL \text{ then proceed to next time step.}$$

$$\text{If } \frac{||\hat{\underline{F}}||}{||\underline{P}_{t+\Delta t}||} \geq TOL \text{ then } i = i+1, \text{ go to Step 4.}$$

It has been shown that for unconditional stability of Newmark's operator in linear analysis, parameters β and γ must meet certain criteria. That is:

$$\gamma \geq 0.5 \tag{5-9a}$$

$$\beta \geq \frac{1}{4}(0.5 + \gamma)^2 \tag{5-9b}$$

For the dynamic analyses of MRFs discussed in this report, the *constant average acceleration* scheme was employed with $\beta = 0.25$ and $r = 0.5$. Other stable integration schemes can be obtained by specifying appropriate values for parameters γ and β. Numerical damping can also be introduced by incorporating a damping parameter δ in the parameter γ as following:

$$\gamma = 0.5 + \delta, \qquad \delta > 0 \tag{5-10}$$

In these ANSR-1 analyses, however, viscous damping is specified explicitly through the damping matrix $\underline{C}$. The selection of the time step Δt is problem dependent. Therefore, several trial analyses using different time step sizes were performed for each MRF model. The final result was based on a time step size which resulted in no significant change in the response compared to the results obtained using a further reduced time step size. The initial stiffness matrix $\underline{K}_0$, referred to in the initialization stage of the procedure may include a geometric stiffness based on the gravity loads applied before the dynamic analysis.

5.4 Damping Coefficient

In linear analysis using the mode-superposition method, it is most convenient to define modal damping for each mode considered. Consequently, the modal equation of motion for n^{th} mode is:

$$M_n \ddot{Y}_n(t) + C_n \dot{Y}_n(t) + \omega_n^2 M_n Y_n(t) = P_n(t) \tag{5-11a}$$

and

$$C_n = 2\xi_n \omega_n M_n \tag{5-11b}$$

where

M_n = generalized modal mass,

C_n = generalized modal damping,

K_n = generalized modal stiffness,

P_n = generalized modal force,

ξ_n = modal damping ratio,

ω_n = circular frequency of mode n,

$\ddot{Y}, \dot{Y}, Y$ = modal acceleration, velocity and displacement.

Note that the motion $\underline{U}(t)$ in geometric coordinates is related to the motion $Y_n(t)$ in modal coordinates through the following transformation:

$$\underline{U}(t) = \sum_n \underline{\Phi} n Y_n(t) \tag{5-12}$$

where $\underline{\Phi}_n$ is the n^{th} mode shape.

In the step-by-step integration of a multi-degree of freedom (MDOF) system, one potential difficulty is that the damping matrix $\underline{C}$ must be defined explicitly rather than in terms of modal damping ratios. In general, it is difficult to estimate the magnitude of the damping influence coefficients of a complete damping matrix. The most effective means for deriving a suitable damping matrix has been to assume appropriate values of modal damping ratios for the modes which are considered to be important and then to compute an orthogonal damping matrix possessing those properties. This orthogonal damping matrix for the MDOF system is typically defined to be proportional to the mass matrix and stiffness matrix: That is:

$$\underline{C} = a_0\underline{M} + a_1\underline{K} \tag{5-13}$$

It is referred to as Rayleigh damping and can be diagonalized in the modal coordinates. That is:

$$\underline{C}^* = \underline{\Phi}^T \underline{C} \underline{\Phi} \tag{5-14}$$

and its *nth* diagonal term is:

$$C_n = a_0 M_n + a_1 K_n = a_0 M_n + a_1 \omega_n^2 M_n \tag{5-15}$$

Combining Eq. 5-11b and Eq. 5-15, it follows:

$$\xi_n = \frac{1}{2}\left(\frac{a_0}{\omega_n} + a_1\omega_n\right) \tag{5-16}$$

The first term of Eq. 5-15 is related to mass-proportional damping while the second term corresponds to stiffness proportional damping. The relationships of damping ratio and frequency for given proportionality factors a_0 and a_1 are illustrated in Fig. 5.2. It is clear that for mass-proportional damping, the damping ratio is inversely proportional to the frequency while for stiffness-proportional damping, the damping ratio is directly proportional to the frequency. In Eq. 5-16, the damping ratio for the whole frequency range is determined, once either a_0 or a_1 has been specified. If both mass- and stiffness-proportional damping are desired, it is necessary to establish two modal damping ratios in order to evaluate the proportionality factors a_0 and a_1. In matrix form:

$$\begin{bmatrix}\xi_m \\ \xi_n\end{bmatrix} = \frac{1}{2}\begin{bmatrix}\frac{1}{\omega_m} & \omega_m \\ \frac{1}{\omega_n} & \omega_n\end{bmatrix}\begin{bmatrix}a_0 \\ a_1\end{bmatrix} \tag{5-17}$$

Therefore:

$$\begin{bmatrix}a_0 \\ a_1\end{bmatrix} = 2\frac{\omega_m\omega_n}{\omega_n^2 - \omega_m^2}\begin{bmatrix}\omega_n & -\omega_m \\ -\frac{1}{\omega_n} & \frac{1}{\omega_m}\end{bmatrix}\begin{bmatrix}\xi_m \\ \xi_n\end{bmatrix} \tag{5-18a}$$

where ω_m and ω_n are circular frequencies of m^{th} and n^{th} modes. In terms of periods T_m and T_n of m^{th} and n^{th} modes, Eq. 5-18a can be rewritten as:

$$\begin{bmatrix}a_0 \\ a_1\end{bmatrix} = 4\pi\frac{T_nT_m}{T_m^2 - T_n^2}\begin{bmatrix}\frac{1}{T_n} & -\frac{1}{T_m} \\ -T_n & T_m\end{bmatrix}\begin{bmatrix}\xi_m \\ \xi_n\end{bmatrix} \tag{5-18b}$$

For example, assuming periods T_1 and T_2 of first two modes are 1.0 sec. and 0.3 sec., respectively, the factors a_0 and a_1 are 0.2896 and 0.087, respectively, for a lightly damped system with damping ratios of 3% for the first two modes. Note that if periods are doubled to 2 sec. and 0.6 sec., the proportionality factor a_0 is halved while a_1 is doubled. Once proportionality factors a_0 and a_1 are determined, the structural damping matrix can be derived using Eq. 5-13. In general, this type of damping progressively filters out the participation of higher modes and is widely used for seismic analysis of building structures in which lower modes dominate the motion. In step-by-step integration, there is no need to uncouple the equations of motion. Therefore, the structural damping matrix can be selected without satisfying modal orthogonality conditions. In ANSR-1, the damping matrix $\underline{C}$ is assembled by summing the global mass-proportional term and the stiffness-proportional term of each element. That is:

$$\underline{C} = a_0\underline{M} + \sum_i a_{1i}\underline{K}^{elmi} + \sum_i a_{2i}\underline{K}_t^{elmi} \tag{5-19}$$

where $\underline{K}^{elmi}$ and $\underline{K}_t^{elmi}$ are the elastic and tangent stiffness matrix associated with global degrees of freedom for element i. Nonproportional damping can be used by specifying different stiffness-proportional factors for different elements [41]. For the nonlinear dynamic analyses of MRFs presented in this report, a damping matrix proportional to both mass and elastic stiffness were used based on the damping ratios of 3% for the first two modes. It is believed that the error in the damping matrix approximated in this manner is within the range of the uncertainty of the real damping for the structure. The analytical results for various damping ratios were also studied in this report.

5.5 Inelastic Elements for Nonlinear Analysis of MRFs

As noted previously, inelastic activity of steel MRFs under severe seismic excitation can occur in beams, columns and/or joint panel zones. It is essential that the nonlinear behavior of these structural elements is realistically modeled considering post-yield behavior

and material strain hardening. In ANSR-1, several nonlinear elements based on bilinear force-deformation relationships are available. These include a three-dimensional truss element, a continuum finite element for plane stress, plane strain or axisymmetric analysis, a two-dimensional beam-column element, and a three-dimensional beam-column element [42]. For the nonlinear analysis of MRFs discussed in this report, the two-dimensional beam-column element was used to model the beams and columns for the model building. In order to account for the panel zone deformation of the beam-column joint, a joint element similar to the semi-rigid connection element implemented in the DRAIN-2D [39] program was developed. The mathematical models for these elements are discussed in the following sections.

5.6 Beam-Column Element

5.6.1 General Description

A two component model is used to simulate the moment rotation relationship of the column or beam elements. The model consists of elastic and elasto-plastic components in parallel. Yielding may take place only in concentrated plastic hinges at the element ends. Hinge formation is affected by the axial force through a simplified axial force-moment interaction relationship. Strain hardening is approximated by specifying an appropriate strain-hardening ratio to the elastic stiffness for the moment-rotation relationship after yielding. Note that in this approximation, the moment-curvature relationship will have the same shape as the moment-rotation relationship for a prismatic member with constant moment as shown in Fig. 5.3a. It follows that rotation and curvature are directly proportional in this case. However, for other cases such as shown in Fig. 5.3b, the curvature and rotation are no longer directly proportional for members with nonuniform moment or strength.

Elements of various cross-section can be modeled by specifying the appropriate flexural stiffness coefficient. Shear deformation of the member is accounted for by specifying an effective shear area. The finite size of the joints are modeled using member end eccentricities. Second order effects, referred to $P-\Delta$ effects, are approximated by including a geometric stiffness in the element stiffness formulation.

5.6.2 Degree of Freedom

The two-dimensional beam-column element has three local degrees of freedom, namely axial extension, and rotations at each end of the element as shown in Fig. 5.4a. Each end of the element is connected to the structure and has three degrees of freedom in the global coordinates as shown in Fig. 5.4b. The transformation of global displacement increments $d\underline{r}$ to the local deformation increments $d\underline{v}$ is accomplished by:

$$d\underline{v} = \underline{a}\ d\underline{r} \tag{5-20a}$$

or

$$\begin{Bmatrix} dv_1 \\ dv_2 \\ dv_3 \end{Bmatrix} = \begin{bmatrix} -\frac{x}{L} & -\frac{y}{L} & 0 & \frac{x}{L} & \frac{y}{L} & 0 \\ -\frac{y}{L^2} & \frac{x}{L^2} & 1 & \frac{y}{L^2} & -\frac{x}{L^2} & 0 \\ -\frac{y}{L^2} & \frac{x}{L^2} & 0 & \frac{y}{L^2} & -\frac{x}{L^2} & 1 \end{bmatrix} \begin{Bmatrix} dr_1 \\ dr_2 \\ dr_3 \\ dr_4 \\ dr_5 \\ dr_6 \end{Bmatrix} \tag{5-20b}$$

where L is the length of the element, x and y are its component in the x and y axis. L, x and y are assumed to remain constant.

As mentioned previously, the complete beam-column element is modeled as two components in parallel. A plastic hinge is introduced at the end of the elasto-plastic component when the corresponding end moment reaches its yield moment. The flexural plastic deformation is defined as the plastic rotations of the hinge. For any flexural rotation

increment at the element end, the plastic rotation increment will be zero if yielding has not occurred. However, the plastic rotation increments will be the same as the total flexural rotation increments once a hinge is formed at the corresponding node. That is, for given flexural rotation increments dv_2 and dv_3 at the ends of the element, the plastic hinge rotation increments dv_{p2} and dv_{p3} can be computed as follows:

$$\begin{Bmatrix} dv_{p2} \\ dv_{p3} \end{Bmatrix} = \begin{bmatrix} A & B \\ C & D \end{bmatrix} \begin{Bmatrix} dv_2 \\ dv_3 \end{Bmatrix} \tag{5-21}$$

in which A, B, C and D are defined in Table 5.1.

5.6.3 Yield Surface for Axial and Flexural Interaction

The yield surface for the beam-column element considering the interaction of moment and axial force is shown in Fig. 5.5a. In this approach, for any combination of axial force and bending moment within the yield surface, the member is assumed to be elastic. If the force-moment combination at an end of the element lies on or outside the surface, yielding has occurred and a plastic hinge is introduced at the corresponding nodal point. Force-moment combinations falling outside the yield surface are not permitted and are corrected by applying corrective moments in the next time step or iteration as shown in Fig. 5.5b. It is assumed that the axial stiffness remained unchanged after flexural yielding occurs. Therefore, this approach is only an approximation of the actual axial-flexural interaction. However, this procedure is believed to be reasonable for practical applications. For a beam type member where axial force is negligible, the yield surface can be specified as shown in Fig. 5.6.

For the beam and column of steel MRFs studied in this analytical investigation, maximum yield moments in both directions were assumed to be the plastic moment capacity of the section. The maximum column yield strength in both axial tension and compression was assumed to be the product of the steel yield strength and the cross-sectional area. The column moment yield strength was assumed to remain constant until a column axial force

of $0.15P_y$, tension or compression, is reached. The buckling of any form in the column was not considered in the beam-column element.

5.6.4 Flexural Stiffness

The complete element stiffness matrix is decomposed into two parts, namely an elastic component and an elasto-plastic component. That is:

$$\underline{k}_b = \rho \begin{bmatrix} \frac{EA}{L} & 0 & 0 \\ 0 & \frac{EI}{L}k_{ii} & \frac{EI}{L}k_{ij} \\ 0 & \frac{EI}{L}k_{ij} & \frac{EI}{L}k_{jj} \end{bmatrix} + (1-\rho) \begin{bmatrix} \frac{EA}{L} & 0 & 0 \\ 0 & \frac{EI}{L}k_{ii}^{ep} & \frac{EI}{L}k_{ij}^{ep} \\ 0 & \frac{EI}{L}k_{ij}^{ep} & \frac{EI}{L}k_{jj}^{ep} \end{bmatrix} \tag{5-22}$$

or

$$\underline{k}_b = \underline{k}^{el} + \underline{k}^{ep} \tag{5-23}$$

where

$\underline{k}_b$ = stiffness matrix of beam-column element,

EI = elastic flexural rigidity,

EA = elastic axial rigidity,

L = length of the beam-column element,

k_{ii}, k_{ij}, k_{jj} = elastic flexural stiffness coefficient,

k_{ii}^{ep}, k_{ij}^{ep}, k_{jj}^{ep} = elasto-plastic flexural stiffness coefficient,

ρ = ratio of strain hardening modulus to elastic modulus,

$\underline{k}^{el}$ = stiffness matrix of elastic component

$\underline{k}^{ep}$ = stiffness matrix of elasto-plastic component.

For a prismatic member, the elastic flexural stiffness coefficients k_{ii}, k_{ij} and k_{jj} are 4, 2 and 4 respectively. However, the stiffness coefficients of $\underline{k}^{ep}$ vary, depend on the yielding state of the member. They are computed as follows:

$$\underline{k}_{ii}^{ep} = k_{ii}(1 - A) - k_{jj}C \tag{5-24a}$$

$$\underline{k}_{ij}^{ep} = k_{ij}(1 - D) - k_{ii}B \tag{5-24b}$$

$$\underline{k}_{jj}^{ep} = k_{jj}(1 - D) - k_{ii}B \tag{5-24c}$$

in which A, B, C and D are defined in Table 5.1. When no plastic hinge exists, A, B, C and D are zero as defined in Table 5.1, and the elasto-plastic stiffness coefficients in Eq. 5-24 become identical to the elastic stiffness coefficients.

Rigid end offsets are accounted for by applying end eccentricities in computing the length L for the member. In the analyses of MRFs presented in this report, the finite size of beam-column joints was modeled by specifying actual end eccentricities for each beam and column. The joint deformations were accounted for by using additional joint elements. An effective shear area is used to further modify the elastic flexural stiffness coefficients in order to account for elastic shear deformation of the member.

The stiffness matrix $\underline{K}_b$ of the element in the global coordinates can be obtained using displacement transformation matrix $\underline{a}$ as defined in Eq. 5-20. This transformation is well known as:

$$\underline{K}_b = \underline{a}^T \, \underline{k}_b \, \underline{a} \tag{5-25}$$

5.6.5 Geometric Stiffness

In general, geometric stiffness can be obtained using two different levels of approximation. In a consistent approach, both translational and rotational degrees of freedom are accounted for. On the other hand, in the linear approach, only translational degrees of freedom are considered.

(A) Consistent Geometric Stiffness

In this approach, the finite element concept is employed to achieve a higher-order approximation of the geometric stiffness. Consider a beam as shown in Fig. 5.7. If only transverse plane displacements are considered, it has vertical and rotational degrees of freedom at each end. Two deflected shape functions resulting from applying a unit displacement of each type at the left end of the member while constraining the other three degrees of freedom are shown in Fig. 5.7. The shape functions could be any shape that satisfy nodal and internal continuity requirements. In general, cubic hermitian polynomials are assumed for these shape functions. They can be expressed as:

$$\Psi_1(x) = 1 - 3\left(\frac{x}{L}\right)^2 + 2\left(\frac{x}{L}\right)^3 \tag{5-26a}$$

$$\Psi_2(x) = 3\left(\frac{x}{L}\right)^2 - 2\left(\frac{x}{L}\right)^3 \tag{5-26b}$$

$$\Psi_3(x) = x\left(1 - \frac{x}{L}\right)^2 \tag{5-26c}$$

$$\Psi_4(x) = \frac{x^2}{L}\left(\frac{x}{L} - 1\right) \tag{5-26d}$$

The complete deflected shape of this element is a combination of these shape functions. That is:

$$v(x) = \Psi_1(x)v_1 + \Psi_2(x)v_2 + \Psi_3(x)v_3 + \Psi_4(x)v_4 \tag{5-27}$$

The stiffness matrix associated with the nodal displacement as shown in Fig. 5.7 can be obtained by using the principle of virtual work. The expression for the stiffness coefficient k_{ij} is as follows [33]:

$$k_{ij} = \int_0^L EI(x)\Psi_i''(x)\Psi_j''(x)dx \tag{5-28}$$

These stiffness coefficients are the exact values for an elastic prismatic beam without shear deformation because the shape functions expressed in Eq. 5-26 are the true shapes for this case. Similarly, a geometric stiffness matrix can be established using appropriate shape functions. In particular, for the results to be properly called consistent, the shape functions selected must be the same as those used to define the element stiffness coefficients. The geometric stiffness coefficients in terms of shape functions can be expressed as follows [33]:

$$k_{Gij} = \int_0^L N(x)\Psi_i'(x)\Psi_j'(x)dx \tag{5-29}$$

where $N(x)$ is the axial load in the member. If the hermitian polynomials are used for a member with constant axial force N, the consistent geometric stiffness matrix associated with the nodal displacement shown in Fig. 5.7 is:

$$k_G = \frac{N}{30L}\begin{bmatrix} 36 & -36 & 3L & 3L \\ -36 & 36 & -3L & -3L \\ 3L & -3L & 4L^2 & -L^2 \\ 3L & -3L & -L^2 & 4L^2 \end{bmatrix} \tag{5-30}$$

Note that this geometric stiffness matrix is not strictly exact for the element in which shear deformation is considered. Moreover, the cubic hermitian shape functions are no longer the true shapes for the element once the yielding of the element takes place. Another simplified approach is possible.

(B) Linear Approximation

In this approach, only translational displacements are considered for establishing geometric stiffness matrix coefficients. Consider a beam as shown in Fig. 5.8. The deflected shapes resulting from applying a unit translation at one end while constraining the translation of the other end are linear. Therefore, the shape functions associated with the translational degrees of freedom as shown in Fig. 5.8 are as follows:

$$\Psi_1(x) = 1 - \frac{x}{L} \tag{5-31a}$$

$$\Psi_2(x) = \frac{x}{L} \tag{5-31b}$$

Using these shape functions in Eq. 5-29, the geometric stiffness matrix associated with the translational degrees of freedom as shown in Fig. 5.8, for a beam-column element of length L with constant axial force N is as follows:

$$\underline{k_G} = \frac{N}{L}\begin{bmatrix} 1 & -1 \\ -1 & 1 \end{bmatrix} \tag{5-32}$$

In principle, the consistent approach should lead to greater accuracy in the results for linear system. However, the improvement is often slight. As noted previously, once yielding occurs the assumption of cubic shape functions is no longer valid. Therefore, in ANSR-1, linear shape functions are adopted in order to establish the geometric stiffness coefficients effectively. As beam-column elements yield, the accuracy of the linear approximation for $P-\Delta$ correction becomes more pronounced.

As shown previously, transformation of the element stiffness matrix from local to global degrees of freedom is as follows:

$$\underline{K_G} = \underline{a}_1^T \, \underline{k_G} \, \underline{a}_1 \tag{5-33}$$

where

$$\underline{a}_1 = \begin{bmatrix} -\frac{y}{L} & \frac{x}{L} & 0 & 0 \\ 0 & 0 & -\frac{y}{L} & \frac{x}{L} \end{bmatrix} \tag{5-34}$$

K_G is the geometric stiffness matrix in global coordinates associated with four translational degrees of freedom as shown in Fig. 5.4. L is the length of the element, x and y are its component in x and y axis as shown in Fig. 5.4. In ANSR-1, end eccentricities of the element for derivation of geometric stiffness coefficients are not considered.

Note that the geometric stiffness as defined in Eq. 5-32 requires the member axial force to be supplied. Therefore, the geometric stiffness can be included only after the application of gravity load. Since the lateral load increases the axial forces in some columns, while reducing it by the same amount in others, the total column axial forces for the entire story being considered remains unchanged after the application of gravity load. In the subsequent application of lateral load, if no yielding of member occurs within the load step, the solution will converge in one iteration. When member yielding occurs within the load step, an iterative procedure is required in order to reduce the unbalanced loads to a specified tolerance. In either case, the unbalance loads are evaluated at the deformed configuration where $P-\Delta$ corrections are considered by formulating equivalent nodal forces based on the updated axial forces and the relative end displacements.

5.6.6 State Determination for Beam-Column Element

5.6.6.1 General

As summarized in Section 5.3.3, a state determination is required for each element in order to compute the element internal resisting forces in equilibrium with the updated configuration. Subsequently, the global unbalanced load can be computed. An additional iteration may be required if the unbalanced load does not satisfy the convergence criterion.

5.6.6.2 Procedure

Having obtained the global displacement increment $d\underline{r}$, the state determination procedure is as follows:

(1) Calculate the deformation increments $d\underline{v}$ of the element based on Eq. 5-20.

(2) Calculate the linear action increments for the element as follows:

(a) Elastic Component:

$$d\underline{S}^{el} = \underline{k}^{el} \cdot d\underline{v} \tag{5-35a}$$

(b) Elasto-Plastic Component:

$$d\underline{S}^{ep} = \underline{k}^{ep} \cdot d\underline{v} \tag{5-35b}$$

where

$d\underline{S}^{el}$ = linear action increment for the elastic component,

$d\underline{S}^{ep}$ = linear action increment for the elasto-plastic component,

$\underline{k}^{el}$, $\underline{k}^{ep}$ = element stiffness matrices as defined in Eq. 5-23 based on current state.

(3) Calculate plastic rotation increments using Eq. 5-21.

(4) Check for the event of yielding and compute the corresponding event factors for both ends of the elasto-plastic component. The event factor $FACT$ is calculated as a proportion of the deformation increment obtained in Step 1. Possible events at each end of the elasto-plastic component are:

(a) The proportion of the deformation increment to cause the end moment to reach the yield moment is greater than one. Set $FACT$ equal to one. The end of the component remains elastic.

(b) The proportion of the deformation increment to cause the end moment to reach the yield moment is less than one. A hinge is formed at the end of the component, and $FACT$ is set equal to the calculated proportion.

(c) Set $FACT$ equal to zero if unloading occurs. Unloading from the yield surface can be detected when the plastic rotation increment and the end moment of the elasto-plastic component are opposite in sign.

(5) Update moments and hinge rotations at both ends of the elasto-plastic component:

$$\underline{S}^{ep} = \underline{S}^{ep} + FACT \cdot d\underline{S}^{ep} \tag{5-36a}$$

$$\underline{\Theta}_p = \underline{\Theta}_p + FACT \cdot d\underline{\Theta}_p \tag{5-36b}$$

(6) Calculate the complement of the event factor as follows:

$$FACAC = 1 - FACT \tag{5-37}$$

(7) Calculate the remaining deformation increment:

$$d\underline{v} = FACAC \cdot d\underline{v} \tag{5-38}$$

(8) If the deformation increment obtained in Step 1 has not been exhausted, go to Step 2b.

(9) Calculate the yield moment for the next step based on the current element action and check for overshoot of the yield surface.

(10) Combine actions of both the elastic and elasto-plastic components:

$$\underline{S}^{el} = \underline{S}^{el} + d\underline{S}^{el} \tag{5-39a}$$

$$\underline{S}^{ep} = \underline{S}^{ep} + d\underline{S}^{ep} \tag{5-39b}$$

$$\underline{S} = \underline{S}^{ep} + \underline{S}^{el} \tag{5-39c}$$

(11) Transform the element actions $\underline{S}$ to global coordinates and compute the equivalent nodal loads including P-Δ corrections.

5.7 Beam-Column Panel Zone Element

5.7.1 General

In linear structural analysis, the finite size of the member joints is generally recognized and the stiffness of the member is formulated based on the clear span of the member. In order to further account for the joint deformations in the structure without using additional elements, a reduced rigid end offset as a fraction of the actual joint size at both ends of the beams and columns can be specified [43]. In a steel frame, the joint may be reinforced with or without doubler plates or continuity plates. Using this approximate approach, it is difficult to specify the appropriate fraction of actual joint sizes for the member end offsets to account for the flexibilities of these joints. Moreover, in nonlinear analysis, the beam-column joint can yield in shear due to the large moment transferred through the joint. The hinge formation pattern of the structure will be incorrect without

considering the relative flexibilities of joints with respect to other elements. Therefore, a separate element that realistically characterizes the behavior of the beam-column joint is needed. For this purpose, a panel zone joint element for modeling steel beam-column joints for nonlinear analyses of MRFs using ANSR-1 was developed and is described in the following sections.

5.7.2 Force-Deformation Relationships for Steel Beam-Column Panel Zone Joint

For a steel beam-column joint subject to loads as shown in Fig. 5.9, with beams of equal depth on both sides of the joint, the average shear stress in the column web due to the beam moment can be calculated as follows:

$$\tau_{av} = \frac{V}{(d_c - t_c^f)t_w} \tag{5-40}$$

where

$$V = \frac{\Sigma M_b}{d_b} - H = \frac{\Sigma M_b}{d_b} - \frac{\Sigma M_b}{L_h} = \frac{\Sigma M_b}{d_b}(1 - \alpha) \tag{5-41a}$$

and

$$\alpha = \frac{d_b}{L_h} \tag{5-41b}$$

where L_h is approximately the story height, and t_w includes the thickness of doubler plates. The other terms are as shown in Fig. 5.9. Combining Eq. 5-40 and 5-41, the average shear strain, γ_{av}, in the panel zone before reaching the yield strain γ_y is:

$$\gamma_{av} \leq \gamma_y \tag{5-42a}$$

$$\gamma_{av} = \frac{\Sigma M_b (1 - \alpha)}{G(d_c - t_c)t_w d_b} \tag{5-42b}$$

The relationship between the average shear deformation and the external beam moments is then:

$$k_e = \frac{\Sigma M_b}{\gamma_{av}} = \frac{G(d_c - t_c)t_w d_b}{(1-\alpha)} \tag{5-43}$$

where G is the elastic shear modulus of steel and k_e can be viewed as the elastic rotational stiffness associated with shear deformation of the panel zone.

Using the von Mises yield criterion, the yield shear stress τ_y can be obtained as follows [44]:

$$\tau_y = \frac{\sigma_y}{\sqrt{3}}\left[1 - (\frac{P}{P_y})^2\right]^{\frac{1}{2}} \tag{5-44a}$$

and

$$\gamma_y = \frac{\sigma_y}{G\sqrt{3}}\left[1 - (\frac{P}{P_y})^2\right]^{\frac{1}{2}} \tag{5-44b}$$

in which P and P_y are the axial load and axial yield strength of the column, respectively, and σ_y is the tensile yield strength of steel. The yield moment ΣM_y that causes shear yielding of the panel zone can be obtained by combining Eqs. 5-43 and Eq. 5-44a. That is:

$$\Sigma M_y = \frac{\sigma_y t_w (d_c - t_c^f) d_b}{\sqrt{3}}\left[\frac{\left[1 - (\frac{P}{P_y})^2\right]^{\frac{1}{2}}}{(1-\alpha)}\right] \tag{5-45}$$

or

$$\Sigma M_y = \frac{\sigma_y t_w d_c d_b}{\sqrt{3}}\beta \tag{5-46a}$$

where

$$\beta = \left[\frac{1 - \frac{t_c^f}{d_c}}{1-\alpha}\left[1 - (\frac{P}{P_y})^2\right]^{\frac{1}{2}}\right] \tag{5-46b}$$

Evidently, the magnitude of β depends on the ratio of column flange thickness to column depth, the ratio of beam depth to story height, and the column axial stress ratio. In order to simplify Eq. 5-46, β is examined below.

For a 12.5 feet long W14×193 column with W27 beams, and assuming the column axial stress ratio is 0.3:

$$\beta = \frac{1 - \frac{1.44}{15.68}}{1 - \frac{27/12}{12.5}}(1 - 0.3^2)^{\frac{1}{2}} = \frac{0.91}{0.82}0.95 = 1.05$$

In general, the value of β is less sensitive to the column axial stress ratio and more sensitive to the overall geometric parameters of the panel zone with respect to the frame. For practical applications, the effect of β can be neglected and simplified equations can be obtained as shown below:

$$\gamma_{av} \leq \gamma_y \tag{5-47a}$$

$$k_e = G d_c t_w d_b \tag{5-47b}$$

$$\Sigma M_y = \frac{\sigma_y t_w d_c d_b}{\sqrt{3}} \tag{5-47c}$$

where

$$\gamma_y = \frac{\sigma_y}{G\sqrt{3}} \tag{5-47d}$$

Krawinkler et al. [9,10] developed the relationship for panel zone behavior after yield.

In the post-elastic range, the rotational tangent stiffness associated with shear deformation of the panel zone is:

$$\gamma_y < \gamma_{av} \leq 4\gamma_y \tag{5-48a}$$

$$k_t = \frac{24EI_c^f}{(1-\alpha)5t_c} \tag{5-48b}$$

where I_c^f is the moment of inertia of one column flange.

In the strain-hardening range, the rotational stiffness for the panel zone is simply:

$$\gamma_{av} > 4\gamma_y \tag{5-49a}$$

$$k_s = k_e \frac{E_{sh}}{E} \tag{5-49b}$$

where E_{sh} is the tangent modulus of the steel at the onset of stain-hardening. In all cases, t_w includes the thickness of the doubler plates if they are effectively attached to the column web. In order to simplify the stiffness formulation, it was assumed that the steel grade of the doubler plate is identical with the steel grade of the column.

5.7.3 Planar Nonlinear Joint Element

As noted previously, the elastic $\Sigma M - \gamma_{av}$ relationship of the panel zone joint is completely characterized by the applied moment, and the dimensions of the joint and the beam that connected to the joint. Experimental evidence [9,10] had shown that the elastic stiffness associated with panel zone shear deformation can be accurately predicted using Eq. 5-43. If axial and flexural deformations of the panel zone are not considered, a two degree of freedom joint element can be introduced at the beam-column intersection to model the $\Sigma M - \gamma_{av}$ relationship.

As depicted in Fig. 5.10a, the joint element is placed between two nodes and is influenced by the relative rotational displacement between the nodes only. The moment transmitted by the element is the unbalanced moment transferred from beams to columns. The deformation of the element represents the angle changes between the connected beams and columns or the shear deformation of the panel zone joint for the steel beam-column connection. In this approach, translational displacements of the nodes at both end of the element are constrained to be identical. Therefore, these nodes also have identical coordinates in order to satisfy equilibrium.

For the joint element to be compatible with the beam-column element previously described, a two component model similar to the beam-column model is used for the joint element. A bilinear relationship for $\Sigma M - \gamma_{av}$ as shown in Fig. 5.10b is used. The model basically consists of an elastic and an elasto-plastic component in parallel. A shear hinge is introduced in the elasto-plastic component once the corresponding yield moment is reached. Kinematic hardening of the joint is modeled by specifying the appropriate strain-hardening ratio for the $\Sigma M - \gamma_{av}$ relationship. This joint element can be used to model other connections which possess semi-rigid characteristics under applied moment.

5.7.4 Degrees of Freedom

The planar joint element has two global degrees of freedom, namely the rotation at each end of the element. The only deformation of the element is measured as the relative rotation between the two ends. The transformation of the nodal displacement increment $d\underline{r}$ to the local deformation increment $d\varnothing$ of the element is:

$$d\varnothing = \underline{a}\ d\underline{r} \tag{5-50a}$$

or

$$d\varnothing = \begin{bmatrix} 1 & -1 \end{bmatrix} \begin{Bmatrix} d\theta_1 \\ d\theta_2 \end{Bmatrix} \tag{5-50b}$$

where $d\varnothing$ is the rotation increment of the joint element and $d\theta_1$, $d\theta_2$ are the rotation increments of the connected nodes. The inelastic rotation increment of the joint element $d\varnothing_p$ is the relative rotation increment between the nodes beyond yield of the elasto-plastic component. That is:

$$d\varnothing_p = A\ d\varnothing \tag{5-51}$$

where A equals one when the moment in the elasto-plastic component reaches the corresponding yield moment, otherwise A is set to zero.

5.7.5 Element Stiffness

As noted previously, the $\Sigma M - \gamma_{av}$ relationship for the panel zone is less sensitive to the column axial stress ratio. Alternatively, the axial force and the shear force in the column may be included in deriving the element stiffness and yield moment as shown in Eq. 5-43 and Eq. 5-45. However, as demonstrated earlier, the effects of the column axial stress, shear forces and flange thickness to depth ratio tend to cancel each other. Subsequently, the axial-shear force interaction is not considered in the formulation of the yield moment for the joint element. The element elastic stiffness is based on Eq.5-47b. The strain hardening effect is obtained by specifying an appropriate stiffness after yield. Similar to the beam-column element, the complete element stiffness is decomposed into elastic and elasto-plastic components in parallel. That is:

$$k = k^{el} + k^{ep} \tag{5-52a}$$

or

$$k = \rho\,[k_e^*] + (1 - \rho)\,[k_e^*] \tag{5-52b}$$

and

$$k_e^* = a_o\,(G d_c t_w^c d_b) \tag{5-52c}$$

$$M_y^* = a_o \frac{\sigma_y t_w^c d_c d_b}{\sqrt{3}} \tag{5-52d}$$

where

k = rotational stiffness for joint element,

M_y^* = yield moment of joint element,

σ_y = yield stress of column and doubler plate,

G = elastic shear modulus,

ρ = ratio of strain-hardening modulus to elastic modulus,

d_c = depth of column,

d_b = depth of beam,

a_o = ratio of total panel zone thickness to column web thickness,

t_w^c = thickness of column web.

Specification of a_o allows the element stiffness to be easily generated for the same column with different doubler plate thicknesses. The global stiffness matrix $\underline{K}$ of the joint element associated with the nodal rotations can be obtained using the standard transformation.

$$\underline{K} = \underline{a}^T \, k \, \underline{a} \tag{5-53}$$

in which $\underline{a}$ is defined in Eq. 5-50.

5.7.6 State Determination for Joint Element

5.7.6.1 General

A state determination procedure is required in each iteration for each element in order to compute the element internal resisting forces in equilibrium with the updated configuration. The global unbalanced load can then be computed. An additional iteration may be required if the unbalanced load vector does not satisfy the convergence criterion.

5.7.6.2 Procedure

Having obtained the global displacement increment $d\underline{r}$, the state determination procedure is as follows:

(1) Calculate the deformation increment $d\varnothing$ of the element based on Eq. 5-50:

$$d\varnothing = \underline{a} \, d\underline{r}$$

(2) Calculate the linear moment increments for both components as follows:

(a) Elastic Component:

$$dM^{el} = k^{el} \cdot d\varnothing \tag{5-54a}$$

(b) Elasto-Plastic Component:

$$dM^{ep} = k^{ep} \cdot d\varnothing \tag{5-54b}$$

where

dM^{el} = linear moment increment for the elastic component.

dM^{ep} = linear moment increment for the elasto-plastic component.

k^{el} = elastic stiffness as defined in Eq. 5-52.

k^{ep} = elasto-plastic stiffness as defined in Eq. 5-52.

(3) Check for the event of yielding and compute the corresponding event factor for the elasto-plastic component. The event factor $FACT$ is calculated as a proportion of the deformation increment obtained in Step 1. Possible events in the elasto-plastic component are:

(a) The proportion of the deformation increment to cause the moment to reach yield is greater than one. Set $FACT$ equal to one. The elasto-plastic component remains elastic.

(b) The proportion of the deformation increment to cause the moment to reach yield is less than one. A hinge is formed in the elasto-plastic component, and $FACT$ is set equal to the calculated proportion.

(c) Set $FACT$ equal to zero if unloading occurs. Unloading can be detected when the plastic rotation increment and the moment of the elasto-plastic component are opposite in sign.

(4) Calculate plastic rotation increments $d\varnothing_p$ using Eq. 5-51.

(5) Update the moment and the hinge rotation in the elasto-plastic component:

$$M^{ep} = M^{ep} + FACT \cdot dM^{ep} \tag{5-55a}$$

$$\varnothing_p = \varnothing_p + FACT \cdot d\varnothing_p \tag{5-55b}$$

(6) Calculate the complement of the event factor as follows:

$$FACAC = 1 - FACT \tag{5-56}$$

(7) Calculate the remaining deformation increment:

$$d\varnothing = FACAC \cdot d\varnothing \tag{5-57}$$

(8) If the deformation increment obtained in Step 1 has not been exhausted, go to Step 2b.

(9) Combine both elastic and elasto-plastic components of moment:

$$M^{el} = M^{el} + dM^{el} \tag{5-58a}$$

$$M^{ep} = M^{ep} + dM^{ep} \tag{5-58b}$$

$$M^{Total} = M^{el} + M^{ep} \tag{5-58c}$$

(10) Transform the element actions to global coordinates and compute the equivalent nodal loads $\underline{R}$. That is:

$$\underline{R} = \underline{a}\ M^{Total} \tag{5-59}$$

5.8 Performance of Joint Element

5.8.1 General

In order to evaluate the joint element, a simple model was analyzed and compared with results obtained from an experimental research program conducted previously at Berkeley [51]. For this purpose, Specimen No.2, as shown in Figs. 5.11 and 5.12, was selected among a total of eight specimens in that experimental investigation. This specimen deformed well into the inelastic range and demonstrated stable hysteretic characteristics under cyclic loading. The performance of the joint element was evaluated by studying the hysteretic loops obtained from ANSR-1 analyses compared to experimental results.

5.8.2 Analytical Model

The mechanical properties of the joint model for Specimen 2 were computed based on the geometric properties as shown in Figs. 5.11 and 5.12 using Eqs. 5-47 to 5-49. Note that the tensile yield strength of the column web was found to be 48.2 ksi from the tensile coupon test. Assuming $E = 29{,}000\ ksi$ and $G = 11{,}200\ ksi$:

$$\gamma_y = 0.0025\ \ radian$$

for $\gamma_{av} \leq \gamma_y$:

$$k_e = 2040 \times 10^3\ \ k-in/radian$$

$$M_y = 5070\ \ k-in$$

for $\gamma_y < \gamma_{av} \leq 4\gamma_y$:

$$k_t = 37.4 \times 10^3\ \ k-in/radian$$

and for $\gamma_{av} > 4\gamma_y$:

$$k_s = 0.015 \times k_e$$

The trilinear force-deformation relationships computed above were modeled by using two joint elements connected in parallel. The joint model was further connected in parallel to an elastic torsional spring with very high stiffness. The cyclic moments were determined by multiplying the stiffness of the spring by the cyclic peak panel zone deformations recorded during the test. In this process, the deformation of the ANSR-1 model could be controlled with applied cyclic moment.

5.8.3 Comparison of Analytical Model and Experimental Result

In Fig. 5.13, the applied moment versus panel zone deformation relationships are plotted for the ANSR-1 model and for the the experimental results obtained for the specimen [51]. From this figure, it is concluded that the analytical model performed satisfactorily, especially in modeling the elastic stiffness of the panel zone. Moreover, the

analytical model closely resembles the effects of kinematic hardening when the panel zone deformed well into the inelastic range. Also from the overall agreement of the hysteretic loops, it is evident that the isotropic hardening of the panel zone was insignificant, since the analytical model simulated kinematic hardening only. It is worth noting that the column was axially loaded to 21 ksi during the experimental test while the analytical model excluded the effects of axial force as described in Section 5.7.

6. Nonlinear Finite Element Analyses of a Beam-Column Joint

6.1 Introduction

As shown in Eq. 5-40, the shear stress in the steel beam-column panel zone joint is assumed to be uniformly distributed in the derivation of the force-deformation relationship for the joint element. An analytical elastic solution using an Airy stress function showed that the distribution is a parabolic variation from a constant stress at the edge of the joint [30]. Shear stress distributions in beam-column joints have also been studied experimentally where it was shown that the shear stress is higher at center of the joint than at the corner [9]. In order to gain additional analytical data on the effect of column axial force on panel zone behavior and on the shear stress distribution within the joint, nonlinear finite element analyses were performed for a beam-column subassemblage.

Note that the proposed force-deformation relationship for the joint element as shown in Eq. 5-47 excludes the effects of the axial-shear interaction as well as the column shear transferred from outside the panel zone.

6.2 Steel Beam-Column Subassemblage

A subassemblage as shown in Fig. 6.1a was considered in order to study the behavior of beam-column joint using the finite element method. The subassemblage, consisting of W30×99 beams and a W30×173 column with 3/8-inch thick doubler plate, is part of a six-story steel MRF design which will be analyzed in chapter 7 with greater detail. The beam-column joint in the subassemblage was designed to yield prior to the development of any plastic hinge in the beam or column. The finite element models of the subassemblage were analyzed using two-dimensional plane stress elastoplastic elements [57], implemented on the general purpose finite element analysis program FEAP [31]. The plane stress elastoplastic element is based on the von Mises yield condition with nonlinear isotropic and

linear kinematic hardening. Although a plane stress model is not strictly correct for the three dimensional beam-column assemblage, this particular element is believed to be suitable for analyzing panel zone behavior. The flanges and webs of the members can be modeled by varying the element thickness.

6.3 Finite Element Model

The finite element mesh for the beam-column subassemblage is shown in Fig. 6-1b. For convenience, the mesh was based on the location of the flanges of the beams and column or the edges of the continuity plates and doubler plate. The thickness of the continuity plate was assumed to be the same as the beam flange. The mesh was somewhat coarse, however, it is believed to be adequate for the purpose of this investigation.

The continuity plates were assumed to be flush with the edges of the column flange. The complete beam-column subassemblage was modeled using the elements described previously with varying thickness for flanges and webs. Their thicknesses were assumed to be the full dimensions in the direction perpendicular to the plane of the model. The overall thickness of the element for the panel zone, or where doubler plate extension occurred, was specified to be the total thickness of column web and the doubler plate. With this mesh, the optional six-inch extensions of the doubler plate beyond the continuity plate were modeled conveniently. A total of 1027 nodes, 700 elements and 5 different element thicknesses were used to define the model.

The top and bottom ends of the column were supported by pins or rollers at the end nodal points. Material properities needed for the element [31,57] were taken as follows:

Young's modulus = 29,000 ksi

Poisson ratio = 0.3

Initial tensile yield stress = 36 ksi

Tensile yield stress at infinite effective plastic strain = 45 ksi

Exponential coefficient in saturation hardening = 0

Linear isotropic hardening coefficient = 10

Linear kinematic hardening coefficient = 500

6.4 Program of Investigation

The finite element model of the subassemblage with the doubler plate extended six-inches beyond the continuity plates was subject to monotonically applied cantilever loads, equal and opposite in sign at each end of the cantilever beams. The response of the model was studied in detail when the beam moments reached certain values; namely $0.66M_y$, $1.33\times\ 0.66M_y$, M_y and M_p, where M_y and M_p are the yield moment and plastic moment of W30×99 beam. For each case, the shear stress contours in the panel zone joint were plotted in order to ascertain the shear stress distribution. Similarly, another analysis was performed for the model assuming the doubler plate terminated at the continuity plates. Again, shear stress contours were plotted at the load points as noted previously. Plots of contours were conveniently obtained by using the graphic capabilities of the FEAP program.

In order to study the effects of column axial force on the overall behavior of the beam-column joint, two additional analyses, with and without axial force, were performed for finite element model having the six-inch extended doubler plate. The effect of axial force was considered by loading the column to a stress level of $0.4F_y$ prior to the application of monotonically increasing cantilever loads. Finally, two more analyses, including and excluding column axial load, were performed for the same finite element model, in which the cantilever beam loads were applied cyclically. In each analysis, the nodal displacements at the four corners of the panel zone along with the applied cantilever load were reported at certain load intervals. The panel zone shear deformation is estimated geometrically as follows:

$$\gamma_{av} = \frac{\Delta_1 - \Delta_2}{2} \frac{D}{d_c} d_b \qquad (6\text{-}1)$$

where D is the diagonal dimension across the panel zone joint, Δ_1 and Δ_2 are the computed relative displacements of each two corners diagonally across the panel zone, d_c and d_b are the width and height of the panel zone. The effects of column axial load on the panel zone behavior were studied by examining the moment-shear deformation relationships of the joints obtained from these analyses.

6.5 Results

6.5.1 Distribution of Shear Stress

For the subassemblage, the average shear stress based on the assumption of uniformly distributed shear in the beam-column joint is as follows:

$$V = \frac{2M_b}{0.95d_b} - \frac{2M_b}{(L_h - d_b)} \tag{6-2}$$

and

$$\tau_{av} = \frac{V}{d_c(t_w + t_p)} \tag{6-3}$$

where V and τ_{av} are the total shear force and average shear stress in the panel zone, M_b is the cantilever beam moment at the column face, d_b and L_h are the beam depth and the column height. The average panel zone shear stresses computed in this manner were 10.7, 14.2, 16.0 and 18.7 ksi at the instants where beam moments reached $0.66M_y$, $1.33\times0.66M_y$, M_y and M_p respectively. They were compared with the stress contours obtained from finite element analyses.

In general, the stress contours in the panel zone joint were almost identical whether or not the doubler plate was extended beyond the continuity plate. Therefore, only the contours for the model with the extended doubler plate are presented. These are shown in Figs. 6-2 to 6-5 for load points listed previously. In each of these figures, the shear stress computed according to Eqs. 6-2 and 6-3 is also shown on the bottom-right corner. Note

that in deriving these equations it was assumed that beam moments are transferred through the beam flanges only. In the finite element model the beam moments are transferred to beam-column joint through both beam flanges and web. In general, the average shear stress obtained by Eq. 6-3 is about 20% lower than the stress shown in contour near the center of the joint while it is about 20% higher than the stresses shown at the edges of the joint. Note that the effects of residual stress resulting from fabrication of the assemblage have not been taken into consideration in the finite element model. The assumption of uniformly distributed shear has been shown to be acceptable in estimating the strength of steel beam-column joints from numerous experimental investigations [9,14,49,51]. However, attaching the center of the doubler plate to the column web by using plug welds appears to be a sound practice. Better participation of the doubler plate in resisting the panel zone shear was achieved [51].

6.5.2 Force-Deformation Relationships and Effects of Column Axial Force

The beam moment-shear deformation relationships for the finite element models, with or without column axial force, are plotted in Fig. 6.6 for monotonically increased cantilever load. The elastic stiffness, k_e^*, and the yield moment, M_y^*, for the proposed ANSR-1 joint element as defined in Eqs. 5-52c and 5-52d were computed for the subassemblage and shown on the figure. The computed elastic stiffness was $k_e^* = 107 \times 10^5$ k-in/radian while the initial stiffness obtained from the finite element model was 121×10^5 k-in/radian. Moreover, by comparing M_y^* with the onset of yielding of the finite element model, as shown in Fig. 6-6, it is evident that the finite element model correlates well with the simplified model described in Section 5.7. It is believed that the initial stiffness of the finite element model would be reduced if a more refined mesh had been used. Note also that the full column flange width was considered in the thickness of the two dimensional plane stress element. This may have also contributed additional stiffness to the finite element model.

The column axial force has no effect on the initial stiffness of the joint as evidenced by the force-deformation relationships. However, the column axial force reduces the yield moment of the panel zone and increases the joint plastic deformation, although the differences were not significant for the applied axial load and deformations. As noted previously, the theoretical shear yield stress considering shear-axial interaction using the von Mises criterion can be determined based on Eq. 5-44. In this case, the reduction factor due to the the effect of column axial force is:

$$\left[1 - \left(\frac{P}{P_y}\right)^2\right]^{\frac{1}{2}} = 0.92$$

However, the effect of axial force was found to be smaller than theoretically obtained as shown in Fig. 6-6. This phenomena may be due to the higher shear stress at the center of the joint and the subsequent strain hardening after yielding in this region. The effects of column axial force on the force-deformation relationships of the finite element model under cyclic loading are depicted in Fig. 6.7. Again, the effects were not very significant for the level of axial load and deformation considered. Based on these limited analyses, it appears that the effect of column axial force may be negligible for columns moderately loaded with axial force particularly in light of other uncertainties associated with the analysis of the structure.

6.6 Large Distortion of Beam-Column Joint

As inelastic deformation of the beam-column panel zone is increased, local kinks can develop in the column flanges near the beam flanges due to high curvature outside the panel zone [9,51]. In experiments, the beam flange welds often fractured in the experimental tests [9,51], apparently due to the simultaneous effects of tension in beam flange together with concentrations of high curvature near the edge of the distorted panel zone (Fig. 6.8). In situations where beam-to-column moment connections were made by web

bolting and flange welding, the beam flange welds became even more vulnerable to these local kinks once bolt slippage occurred.

The finite element models for the subassemblage, both with and without extensions of doubler plate, were loaded up to a panel zone deformation of 0.03 radian with beam moments reaching 1.5 M_p on both side of the joint. The deformed meshes were almost identical for both models within the panel zone as well as in the regions outside the joint. Attempts to identify these local kinks from the deformed finite element meshes were not successful. A much more refined mesh may be required for this purpose.

For the model without the extended doubler plate, Fig. 6.9 shows the as-computed deformed mesh with no amplification of the computed displacements, when the panel zone deformation reached 0.03 radian. An exaggerated deformed mesh is plotted in Fig. 6.10 with a displacement amplification factor of 4. Note that the beam web was modeled as fully connected to the column flange. Therefore, the possible separation of the beam web from the column flange due to bolt slippage was not considered in the analyses. The shear action across the entire panel zone is evident from the deformed meshes. The pronounced shear deformation at the center of the joint is characteristized by the parallelogram shape of the deformed element as shown in Fig. 6.10. Moreover, it is evident in Fig. 6.10 that the top and bottom continuity plates remained essentially horizontal even during large deformations of the panel zone joint.

6.7 Concluding Remarks

The purpose of the above finite element analyses was intended to gain some further insight into the behavior of steel beam-column panel zone joint. In addition, the assumptions made for the proposed joint element described in Chapter 5 was justified. From these limited analyses, following conclusions are noted with respect to the behavior of the beam column panel zone joint.

(1) It was demonstrated that the assumptions of uniformly distributed shear predicted the average shear stress developed within the panel zone joint quite satisfactorily. However, the shear stress at center of the panel zone can be substantially higher than the average shear stress. Therefore, attaching the center of the doubler plate to the column web appears to be good practice to assure better participation of the doubler plate in resisting the panel zone shear.

(2) The simple force-deformation relationship derived in Chapter 5 for the proposed joint element well predicted the elastic stiffness and the onset of yielding of the finite element model for the panel zone joint analyzed. The effects of the moderate column axial force on the the force-deformation relationship of the finite element model were found insignificant. These suggest that the simple joint element model developed in Chapter 5 is likely to predict the behavior of panel zone joints in steel MRF quite satisfactorily.

(3) The top and bottom continuity plates in the joint remained essentially horizontal even during large deformations of the panel zone joint. It appears that the flexural deformation within the panel zone joint can be neglected.

7. Nonlinear Static and Dynamic Analyses of Six-Story MRFs

7.1 Introductory Remarks

In practice, the earthquake-resistant design of building structures is generally carried out based on code requirements for design seismic force and detailing of structural elements [2,3]. In this process, it can be seen that there are two basic categories of code provisions for earthquake-resistant design. The first category includes primarily the design lateral forces and their distribution throughout the structure. The limits of stress and drift under the action of these code prescribed forces are also specified. Building structures designed according to building codes are expected to deform into the inelastic range during severe earthquakes, thereby dissipating earthquake energy. Since inelastic action is actually being counted upon, there is the requirement that this yielding or inelastic action be distributed to as many different elements as possible that possess stable energy absorbing characteristics. The second category, detailing provisions, addresses primarily this requirement for ductile behavior of the earthquake resisting system.

During the past few decades, the Seismology Committee of the Structural Engineers Association of California (SEAOC) has prepared the model seismic design code provisions used in the United States. In response to the unacceptable structural damage experienced in the 1971 San Fernando earthquake, the Applied Technology Council (ATC), set up in early 1970s, began a systematic review of the entire approach to seismic-resistant design. In 1978, the document known as ATC 3-06, titled "*Tentative Provisions for the Development of Seismic Regulations for Buildings*" [3] was published. In developing ATC 3-06, SEAOC provisions were used as a source, and many new innovative and improved provisions were added. Soon after that, the Building Seismic Safety Council (BSSC), established in 1979, began extensive reviews and modifications to ATC 3-06. In 1985, the result of these BSSC modifications was released known as the *NEHRP Recommended Provisions for the*

Development of Seismic Regulations for New Buildings [45]. In the meantime, using the 1980 edition of SEAOC's *Blue Book* together with ATC 3-06 for source documents, SEAOC also began a total reevaluation of their provisions. In January 1987, the new SEAOC seismic provisions, after minor revisions were taken up by the ICBO seismology committee and subsequently approved in September 1987 for inclusion in the 1988 Uniform Building Code [59].

In the new UBC seismic provisions, the design lateral force equation has a format patterned after ATC 3-06 [2] and NEHRP [45]. However, the design lateral forces are still at a working stress level rather than at a yield level. Moreover, for most structural systems, the level of base shear remains essentially unchanged from the 1985 UBC. Other important changes incorporated into the 1988 UBC include requirements for irregular structures, requirements for dynamic lateral force procedures and requirements for consideration of $P-\Delta$ effects. However, the most significant change is the addition of comprehensive requirements for the detailing of steel structures. These include a special section on the seismic design of steel columns. These new provisions, apply to steel columns in all structural systems, and require steel columns and their splices to provide axial strength to resist a largely magnified seismic force. Other important new provisions for special moment resisting space frames (SMRSF) include requirements covering panel zone doubler plates and the possibility for weak column-strong girder designs. Within certain constraints, these new code provisions allow hinging to occur in beams, columns and panel zone joints.

In order to gain some insight into the nonlinear behavior of MRFs designed according to these new provisions, an analytical investigation was carried out and is described herein. Nonlinear dynamic analyses were performed using ANSR-1 [40] for various MRF designs of a 6-story office building. Preliminary designs of the MRF were based upon the equivalent lateral force procedure recommended in the new provisions. Joint panel zone elements, as described in Chapter 5, were incorporated into the ANSR-1 program in order to realistically model the joint flexibilities. These designs were analyzed for responses to

different earthquake excitations. The effects of strain hardening, damping ratio, and geometric stiffness, as discussed in Chapter 5, were included in the study. The study of each MRF design involved examining the story shears and floor displacement of the frame, the plastic deformation of critical elements as well as the story drift index obtained from the analyses.

7.2 Design Procedures

For the purpose of this analytical study, the structure selected was a 6-story, three-bay by four-bay rectangular office building to be built in Berkeley, California. As shown in Figs. 7.1 and 7.2, the lateral load resisting system for the building consists of a 3-dimensional moment resisting frame on the perimeter of the building. The gravity load is supported by interior core columns in conjunction with the perimeter frame. The composite floor framing is made of 2.5-inch regular weight concrete fill over 3-inch metal deck on steel wide flange sections. Since the perimeter lateral resisting framing system provides structural efficiency and large unobstructed interior space, it has gained wide acceptance as a structural system for office buildings [24].

The floor-to-floor height of the building was selected as 12.5 feet for typical floors and 18 feet for the ground floor as shown in Fig. 7.2. The weight of a building floor, including partitions, ceiling and mechanical piping, was assumed to be 100 pounds per square foot (psf) for typical floors and the roof. The exterior window wall system was assumed to weight 35 psf average over the exterior surface of the building. The design live loads were 80 psf and 20 psf for the typical floor and roof, respectively. Note that the 80 psf design live load is higher than 50 psf usually specified [1,46]. This higher design live load is often adopted by design offices in order to accommodate various tenants' needs. However, the live load reduction per ANSI [46] was used to design individual members. The magnitude of the wind load and its effects on the proposed building were assumed to be less significant than the earthquake force and were not considered in the design.

As mentioned previously, the design seismic force was based on the new equivalent lateral force procedure recommended by SEAOC [47]. The design base shear was determined as follows:

$$V = \frac{Z\ I\ C}{R_w} W \tag{7-1}$$

where

V = Design base shear,

Z = Seismic zone factor,

I = Importance factor,

R_w = Numerical coefficient related to the structural system,

W = Total seismic dead load,

C = Numerical coefficient determined as follows:

$$C = \frac{1.25S}{T^{2/3}} \tag{7-2}$$

and

S = Site coefficient for soil characteristics,

T = Fundamental period of vibration of the structure for the direction under consideration.

The fundamental period of the building can be determined using either method A or B described as follows:

Method A:

$$T = C_t(h_n)^{3/4} \tag{7-3}$$

where

C_t = 0.035 for steel moment resisting frame,

h_n = Height, in feet, of building above the base.

Method B:

T = Fundamental period, within certain limits, calculated in a properly substantiated analysis.

However, the value of C in Eq. 7-2 based on the period obtained analytically from method B shall not be less than 80% of the value obtained by using the period obtained from method A.

The total dead load considered includes the dead load on the floor and the weight of the facade. Live load was not considered in calculating the lateral force. For the purposes of this analytical investigation, only one transverse frame was studied. Without considering torsional effects, it was assumed that 50% of the lateral force was resisted by the frame in line 1 as shown in Fig. 7.1. Therefore,

W = 3110 kips, (for one half of the building)

Z = 0.4,

I = 1,

R_w = 12 for special moment resisting space frame,

T = 0.94 second, based on method A,

S = 1.5

C = 1.95

V = 0.065 W

The base shear force was vertically distributed as recommended in SEAOC's provisions. The base of the columns were assumed as fixed in order to economically satisfy the story drift requirement. The preliminary column sizes for the frame were first selected according to the tributary gravity load carried by each column. The beams were then chosen such that the strong-column and weak-beam relationship was maintained. The steel beams and columns were assumed to be A36 material. An elastic, first order analysis of the structure was performed using the ETABS [43] computer program. The lateral forces were applied in conjunction with the gravity load. The stress ratios for all members were

checked based on the 1978 AISC [4] specifications (Sections 1.6.1 and 1.6.2) for the following load combinations:

(1) DL + LL

(2) DL + LL + EQ

(3) DL - EQ

The effective length factor for columns were based on the alignment chart procedure recommended in the AISC commentary [4]. The allowable stresses for the beams and columns were increased by 33% for load conditions including seismic force. Member sizes were evaluated based on the stress ratios and story drifts obtained from the analysis. New member sizes were selected and subsequent analyses were iterative in nature. Finally, the column compression strength, defined as $1.7F_aA$, and the tension strength, defined as F_yA, were checked for two additional load combinations:

(a) Axial Compression

$$1.0 \times DL + 0.7 \times LL + 4.5 \times EQ \tag{7-4a}$$

(b) Axial Tension

$$0.85 \times DL + 0.7 \times LL + 4.5 \times EQ \tag{7-4b}$$

However, the effective length factor was taken as unity in computing the allowable stress, F_a, for the column compressive strength as defined above. Note that the MRF in line 1 carries 50% of the lateral force in the transverse direction while carrying only about 12.5% of the floor gravity load. Most member sizes were found to be governed by the story drifts of the frame under the prescribed lateral force. In these analyses using ETABS, the structural stiffness was formulated based on the clear spans of beams and columns plus 50% of the sizes of the panel zone in order to account for the joint flexibilities. The member properties were based on bare steel sections. In each analysis, the fundamental period of the frame was also examined in order to refine the design lateral force. The periods obtained from these analyses were often found to be significantly higher than the 0.94 sec.

calculated based on SEAOC method A. Therefore, an upper bound for the period determined based on method B was determined as follows:

Since

$$\frac{C_B}{C_A} = \left(\frac{T_A}{T_B}\right)^{2/3} \geq 0.8$$

Therefore

$$T_B^{\max} = 1.40T_A = 1.31 \; seconds$$

where subscripts A and B indicate the corresponding period obtained from method A and method B, respectively. The minimum design base shear for the frame based on $T = 1.31$ seconds can be determined as follows:

$$C = \frac{1.25\,(1.5)}{(1.31)^{2/3}} = 1.56$$

$$V = \frac{0.4\times 1.0\times 1.56}{12} W = 0.052W$$

The allowable story drift under the specified lateral force is 0.03 divided by R_w for structures having a fundamental period greater than 0.7 seconds. In our case, it is 0.0025. However, the lateral force for computing story drift can be based upon a period obtained from method B without the 80% limit.

Based on these provisions, there could be several design possibilities which would satisfy these minimum requirements just mentioned. For the purposes of this analytical investigation, four final MRF designs were selected as follows:

Design 1

The period of the frame was determined as the average of the values obtained from methods A and B. A period of $T = 1.1$ sec. and a corresponding base shear of $0.059W$ or 183.5 kips was used for calculating member forces and story drifts. The story drifts of the frame were limited to within 0.0025. The final selections of the beams and the columns are shown in Fig. 7.3. Note that the fundamental period

obtained from ETABS analysis was 1.53 seconds. The doubler plate thickness, as shown in Fig. 7.3, were determined based on SEAOC provisions as follows:

The panel zone design shear force is:

$$V_E = \frac{\Sigma M}{0.95 d_b} - H \tag{7-5a}$$

and

$$M = M_{DL} + M_{LL} + 1.85 \times M_E \tag{7-5b}$$

where d_b is the beam depth, M_{DL}, M_{LL} and M_E are the bending moments due to dead, live and the prescribed seismic load, respectively. The doubler plates were sized so that the panel zone shear force did not exceed the strength:

$$V = 0.55 F_y d_c t \left[1 + \frac{3 b_c t_{cf}^2}{d_b d_c t} \right] \tag{7-6}$$

In Eq. 7-6, t includes the thickness of doubler plate and other terms are as defined in Fig. 5.9.

Design 2

A period of $T = 1.31$ sec. and a corresponding base shear of 0.052W or 161.7 kips was used for calculating member forces. However, the story drifts were calculated based on a reduced base shear corresponding to a period of 1.6 sec. The final selections of the beams and the columns are shown in Fig. 7.4. The fundamental period for the frame was 1.81 sec. obtained from the ETABS analysis. The doubler plate thickness as shown near the beam-column intersections were determined based on SEAOC provisions mentioned in Design 1.

Design 3

The same beams and columns as used in Design 2 were used for Design 3. However, the doubler plate thicknesses were increased. The doubler plate thicknesses were determined based on the flexural strength of the beams framed into the joint, ΣM_p,

rather than the bending moments as defined in Eq. 7-5b. The member sizes and the doubler plate thickness are shown in Fig. 7.5.

Design 4

The same beams and columns were used for Design 4 as for Designs 2 or 3, but the doubler plates were resized. Doubler plate thicknesses were chosen similar to the ones for Design 3 for the lower two stories and similar to Design 2 for the upper four stories. This arrangement was an attempt to form relatively stronger panel zone joints in the lower floors and to allow the joints in the upper levels to participate in non-linear activity and energy dissipation to a greater extent. The beam, the column and the doubler plate sizes are shown in Fig. 7.6.

In all designs, doubler plate thicknesses were rounded to the nearest 1/16 inch with a a minimum thickness of 3/8 inch whenever a doubler plate was required. As a result, the joint strength was always greater than that required by Eq. 7-5a. As mentioned previously, the actual flexibility of the joints was not considered in the formulation of structural stiffness when the ETABS analyses were performed. Instead of modeling the joints explicitly, it was assumed in ETABS that the member lengths were the clear spans plus a certain portion of the panel zone dimensions. Therefore, the elastic mode shapes and the vibration periods obtained were identical for MRF Designs 2, 3 and 4 analyzed using the ETABS computer program based on the 50% rigid end offsets. As mentioned in Chapter 5, a non-linear joint element was implemented and incorporated in ANSR-1 [40] computer program where the effects of joint flexibilities can be considered. The validity of the above assumptions in the ETABS analyses can therefore be substantiated.

7.2.1 ANSR-1 Models

The beam, column and joint element properties for the ANSR-1 analyses of the above MRF designs were determined using the methods described in Chapter 5. Their results are based on the steel yield strength of 36 ksi tabulated in Tables 7.1 through 7.6. As noted in

Eq. 5.52, the specification of a_o, the ratio of total panel zone thickness to column web thickness, allows various joint stiffnesses to be formulated conveniently. The Modulus of Elasticity and Poisson's Ratio for steel were assumed to be 29,000 ksi and 0.25, respectively. The strain hardening ratios were set at 4% for all beams, columns and joints, unless otherwise noted. As mentioned in Chapter 5, the viscous damping for the MRF models were assumed to be 3% of their critical dampings of the first two modes, unless otherwise stated.

7.3 Effects of Panel Zone Joint Flexibilities

7.3.1 General

In the early development of general structural analysis procedures, structural member stiffness was formulated based on the center line to center line distance of the members [48]. This often led to a flexible structure where the effects of beam-column intersections were not considered. In order to account for the finite sizes of joints, an alternative approach was often adopted. As mentioned previously, the member stiffness can be formulated based on the member clear span plus a certain portion of the joints. Since the beam-column intersections are not perfectly rigid, stiffness formulation based only on the member clear spans appeared to be unrealistic. In lieu of definitive research evidence, it has been widely accepted in practice that 50% of the joint size can be considered rigid and the member stiffness can be formulated accordingly in order to account for the joint flexibility. Since there is no additional element or extra degree of freedom involved in the stiffness formulation, this simplified approach is favored in practical linear structural analysis procedures [43].

Although the 1985 UBC did not require that the panel zone shear yield be precluded, the previous SEAOC provisions [2] recommended that panel zones be capable of developing beam strength. As a result, heavy doubler plates were often needed for the beam-

column joints. Experimental evidence [9,10,14,49] has shown that panel zone joints possess substantial reserve strength beyond first yield. An increased panel zone strength was subsequently proposed to account for the contribution of column flanges to the panel zone shear capacity in the inelastic range [50]. Moreover, well detailed panel zone joints have exhibited stable hysteretic characteristics and excellent energy dissipation capacity after first yield.

In light of this research, the concept of permitting panel zone shear yielding was recognized and implemented in the current SEAOC provisions. Currently, a load factor of 1.85 for the prescribed seismic force is required (Eq. 7-5b) to design the panel zone joints based on an increased joint shear capacity as defined in Eq. 7-6. This new provision leads to the design of panel zone joints with substantially reduced doubler plate requirements. Consequently, the frame is more flexible and, with exceptions, the panel zone deformations must be considered in the drift calculations for steel MRFs per SEAOC recommendations. While permitting the panel zone to yield in shear, it is important to note that larger panel zone deformation may create severe kinks as shown in Figure 6.6 and tend to cause cracking of the flange welds as cited in experimental tests [9,51].

In the nonlinear analyses of steel MRFs, it is obvious that the nonlinearity can occur in the panel zone joints in addition to the beams or the columns. Therefore, the nonlinear kinematics for MRF models with joint elements included can be quite different from a MRF model without them. The nonlinear joint elements which had realistically modeled the panel zone joints were therefore essential in assessing the post-yield behavior of steel MRFs. In order to gain some insight into the behavior of steel MRFs using the assumed beam column rigid end offsets as opposed to the joint elements, an analytical investigation was conducted, as described below.

7.3.2 Effects of Joint Elements for MRFs under Triangularly Distributed Shear

In order to examine the effects of the rigid end offsets and the flexible joint element, MRF Design 1 as described in Section 7.2 was used as the primary model. Several static nonlinear analyses were performed for the MRF models with or without modifications. In each analysis triangularly distributed lateral force was applied monotonically. Gravity load consisting of 100% of the dead load and the reduced live load as defined in Section 7.2 was applied and remained constant during the application of the lateral force. The base shear versus roof displacement relationships for four MRF models with different configurations of panel zone joints were studied. The beam and the column sizes for these four MRF models are identical and shown in Fig. 7.7.

The member stiffnesses for two of the MRF models, denoted as 50% rigid and 0% rigid, modeled without using a joint element, were formulated based on the member clear span plus 50% and 100% of the beam-column intersections, respectively. The MRF model with 0% rigid joints corresponds to the formulation of the stiffness based on the member center-line to center-line distance. The other two MRF models used joint elements. The doubler plates for these two MRF models, denoted as 1.85E and 0.8Mp, were sized to resist the beam moments under the load combination as defined in Eq. 7-5b and to develop 80% of the beam flexural, strength, respectively. Their doubler plate thicknesses along with the beam and the column sizes are shown in Fig. 7.3 and 7.8 for the MRF models of 1.85E and 0.8Mp, respectively. As noted previously, doubler plate thicknesses were rounded to the nearest 1/16 inch with a minimum thickness of 3/8 inch where the need for a doubler plate was indicated. As a result, the joint strength was always greater than the minimum required.

The base shear versus roof displacement relationships for these four MRF models are shown in Fig. 7.9. In general, the MRF models with joint elements included exhibited larger lateral flexibility, especially in the nonlinear range, than those without joint elements included. Moreover, the MRF models with joint elements included showed much earlier

yielding of the frame than the models using the concept of partial rigid end offsets. This is because the nonlinear kinematics of the joints were unaccounted for by using the simple rigid end offsets or the member center-line to center-line stiffness. In spite of this, elastic lateral displacements of the MRF model with the doubler plates designed to develop 80% of the beam strength were accurately predicted by using the member center line stiffnesses without the use of a joint element. However, it is important to note that the actual doubler plates as specified for the MRF model of 0.80Mp are slightly thicker than the minimum required to develop 80% of the beam strength. The minimum required doubler plate thickness as well as the actual thickness provided for the MRF model of 0.8Mp are shown in Table 7.7.

7.3.3 Code Implications

Current SEAOC provisions require, with exceptions, that the panel zone joint distortions must be included in the drift calculations [47]. However, drift calculations may be based on the member center-to-center distance if either of the following conditions are met:

(a) It can be demonstrated that the drift so computed for similar frames is typically within 15% of that determined with joint distortions considered.

(b) The column panel zone strength can develop 80% of the flexural strength of the beams framing into the joint.

In order to better appraise this provision, the force-displacement relationships as shown in Fig. 7.9 were normalized with respect to the code values. A base shear force of 182.5 kips as defined in Section 7.2 and a roof displacement of 2.379 in. under the triangularly distributed shear for MRF model with 0% rigid end offsets were used as the normalizing factors for the vertical and the horizontal axis, respectively. The normalized base shear versus roof displacement relationships are shown in Fig. 7.10. Based on these limited analytical results, several observations from this particular example can be summarized as follows:

(1) Under the prescribed lateral force, the elastic roof displacement of the MRF model using member center line stiffnesses closely matched that of the MRF model with joint elements designed to develop 80% of the beam flexural strength.

(2) Under the prescribed lateral force, the elastic roof displacement of the MRF model with joint elements designed to resist 1.85 times the code prescribed force is larger than that calculated based on the member center line distances. But the difference is within 15%.

(3) The elastic drift calculation based on the member clear spans plus 50% of the joint size was unconservative. The roof drift under the prescribed force was 20% smaller than the frame drift obtained for MRF model with 1.85E joint elements.

(4) The MRF model with the 1.85E joint elements exhibited frame yielding soon after 1.85 times the 182.5 kips base shear was exceeded. As mentioned previously, the panel zone joint in this model was designed to resist the beam moments due to the gravity load plus 1.85 times the prescribed seismic force. It indicates that the overall frame strength is strongly governed by the weakest element in the frame, the panel zone joints in this case, and agrees well with the design procedure where force distributions and member proportions were based on the triangularly distributed shear.

7.3.4 Effects of Joint Elements for MRFs under Uniformly Distributed Shear

Similar force-displacement relationships, as shown in Fig. 7.11 and 7.12, were obtained for the uniformly distributed lateral force. In Fig. 7.12, a base shear of 182.5 kips and a roof displacement of 1.932 in. corresponding to the MRF model with 0% rigid end offsets were used as the normalizing factors.

In general, the trend of the base shear versus roof displacement relationships were similar to those under the triangularly distributed lateral force as described in the previous section. Note that in Fig. 7.12, the yield base shear forces for all MRF models are substantially larger than those shown in Fig 7.10. This is because the overturning moment for the

uniformly distributed shear in this case is significantly smaller than that under the triangularly distributed shear.

7.4 Simplified Model for Nonlinear Seismic Response of MRF

7.4.1 Introduction

As mentioned in Chapter 5, determining the dynamic response for a nonlinear structural system requires an iterative integration procedure. For systems having a large number of degrees of freedom, the convergence of the solution within each time step may require substantial computational effort. Moreover, the dynamic response of multi-degree-of-freedom (MDOF) systems is generally complex and sensitive to the mechanical properties of the model as well as the input ground excitations. Therefore, simplified equivalent single-degree-of-freedom (SDOF) models are useful to assess the sensitivity of the overall response of a proposed design to various uncertainties within the structural model or the ground excitations. For this purpose, an SDOF system subjected to dynamic forces is developed below.

For an SDOF system subjected to an external forcing function as shown in Fig. 7.13(a). the equilibrium equation at time t is:

$$M\ddot{u}(t) + C\dot{u}(t) + R(t) = P(t) \tag{7-7}$$

where

M = Mass of the system,

C = Damping coefficient of the system,

$R(t)$ = Restoring force,

$P(t)$ = External load acting on the system.

In the case of horizontal ground motion excitation as shown in Fig. 7-13(b), Eq. 7-7 can be rewritten as follows:

$$M\ddot{u}(t) + C\dot{u}(t) + R(t) = -M\ddot{u}_g(t) \tag{7-8}$$

In this case, $u(t)$ denotes the displacement of the system relative to the ground and $\ddot{u}_g(t)$ is the ground acceleration relative to a fixed reference axis. A normalized equation of motion can be obtained by using the system mass as the normalizing factor. That is:

$$\ddot{u}(t) + 2\xi\omega\dot{u}(t) + \frac{1}{M}R(t) = \frac{1}{M}P(t) \tag{7-9}$$

$$\ddot{u}(t) + 2\xi\omega\dot{u}(t) + \frac{1}{M}R(t) = -\ddot{u}_g(t) \tag{7-10}$$

where ξ is the viscous damping ratio expressed as a fraction of the critical damping and ω is the natural circular frequency. A nonlinear SDOF model can be solved economically using either general purpose nonlinear analysis programs as mentioned previously [39,40] or programs specially developed for this purpose[52]. For elastic systems, these two equations can be rewritten as:

$$\ddot{u}(t) + 2\xi\omega\dot{u}(t) + \omega^2 u(t) = \frac{1}{M}P(t) \tag{7-11}$$

$$\ddot{u}(t) + 2\xi\omega\dot{u}(t) + \omega^2 u(t) = -\ddot{u}_g(t) \tag{7-12}$$

In general, closed form solutions to these equations of motion only exist for certain types of forcing functions. In most cases, numerical integration must be employed.

For a linear elastic MDOF system, it is often advantageous to decompose the system into ts modal components and use the principle of superposition of the resulting decoupled equations of motion. It can be found that the first few modes often dominate the response for structures with regularly distributed geometric and mechanical properties. Even though modal analysis does not apply in the nonlinear case, member forces and deformations for nonlinear structures have been determined using the linear modal analysis method based on an inelastic response spectra with elastic mode shapes and periods.

Alternatively, it has been proposed that an equivalent nonlinear SDOF system be substituted for the original MDOF system [53,54]. In particular, the Q-model method [54]

basically assumes a one-shape response of the equivalent SDOF system, as shown in Fig. 7.14, to approximate the response history of a reference point on the original structure. This method can be used to compute the displacement histories of multi-story structures subjected to seismic excitations. In order to assess the performance of this equivalent SDOF model for a steel MRF, the resulting equivalent SDOF nonlinear dynamic responses were compared with those obtained using the general purpose nonlinear analysis program ANSR-1 [40]. For the purposes of this investigation, MRF Design 2 was chosen as the model structure.

7.4.2 Equivalent Single-Degree-of-Freedom System

There are two interdependent steps of approximation required in the application of the Q-model method. Firstly, the original MDOF model of the structure must be reduced to an SDOF oscillator. Secondly, the nonlinearly varying stiffness properties of the entire structure must be simplified to a single bilinear spring.

The transformation of a MDOF system to an equivalent SDOF system is accomplished based on an assumed deflected shape of the original structure. The shape function might be taken as the fundamental mode shape of the original structure or the deflected shape resulting from the static application of certain patterns of lateral load. In particular, it was found [54] advantageous to compute the assumed deflected shape, $\hat{x}$, based on a triangularly distributed lateral force, that is, the force in each level is proportional to the product of the height and mass at that level. The bilinear spring stiffness for the equivalent system is established by approximating the base-moment versus roof displacement relationship resulting from a nonlinear analysis of the original structure under this monotonically applied lateral load. Such a base moment-roof displacement relationship is generally nonlinear due to the nonlinearities in the structure, as shown in Fig. 7.15. The curve may be reduced to two straight lines, the knee of the resulting bilinear relationship implying a synthetic yield point (Fig. 7.15). The shape function $\hat{x}$ is taken as the deflected shape when

the knee of the bilinear force-displacement relationship curve occurs.

Note that it may be difficult to determine the location of the synthetic yield point on the force-displacement relationship curve. Although prescriptive rules have been suggested for the concrete test structures considered in the literature [54], this important decision is left to the judgement of the analyst. In order to establish the bilinear spring stiffness and the corresponding shape function for MRF Design 2, the location of the synthetic yield point was determined as follows.

(1) Perform a nonlinear analysis for MRF Design 2 under triangularly distributed load using 4% of the elastic stiffness as the strain hardening stiffness for all structural elements (see Chapter 5). Obtain the base moment-roof displacement relationship as shown in Fig. 7.16.

(2) Plot the equivalent period, T_e, versus roof displacement relationship as shown in Fig. 7.17, where

$$T_e = 2\pi \left(\frac{\hat{\underline{x}}^T \underline{M} \hat{\underline{x}}}{\hat{\underline{x}}^T \underline{K} \hat{\underline{x}}} \right)^{1/2} \tag{7-13}$$

Locate the significant roof displacement, $\hat{x}_r$, when T_e started increasing.

(3) Locate the synthetic yield point on the base moment-roof displacement curve at a point where $\hat{x}_r$ is reached.

(4) The bilinear approximation of the force-displacement relationship is obtained by connecting two straight lines as shown in Fig. 7.16.

Using this approach, the roof yield displacement, $\hat{x}_r$, was found to be 5.11 inches and the resulting shape function is:

$$\hat{\underline{x}}^T = \begin{Bmatrix} \hat{x}_r \\ \hat{x}_6 \\ \hat{x}_5 \\ \hat{x}_4 \\ \hat{x}_3 \\ \hat{x}_2 \end{Bmatrix} = \begin{Bmatrix} 5.11 \\ 4.51 \\ 3.69 \\ 2.87 \\ 1.96 \\ 1.09 \end{Bmatrix} \tag{7-14}$$

The strain hardening stiffness of the spring was found to be 8 % from step (4), by computing the stiffness after yielding as a fraction of the elastic stiffness.

The MDOF system of the original structure can be transformed to an SDOF system using the shape vector, $\underline{\hat{x}}$ obtained above. The equation of motion for the original structure under ground acceleration, $\ddot{u}_g(t)$, is:

$$\underline{M}\ddot{\underline{v}}(t) + \underline{C}\dot{\underline{v}}(t) + \underline{R}(t) = \underline{M}\,\underline{\hat{1}}\ddot{u}_g(t) \tag{7-15}$$

Let

$$\underline{v}(t) = \underline{\hat{x}}u(t) \tag{7-16}$$

Substitute Eq. 7-16 into Eq. 7-15 and premultiply the transpose of $\underline{\hat{x}}$ to each side of the equation. The equation of motion becomes:

$$M_e\ddot{u}(t) + C_e\dot{u}(t) + R_e(t) = F_e \tag{7-17}$$

where

$$M_e = \underline{\hat{x}}^T\underline{M}\underline{\hat{x}} \tag{7-18}$$

$$C_e = \underline{\hat{x}}^T\underline{C}\underline{\hat{x}} \tag{7-19}$$

$$R_e = \underline{\hat{x}}^T\underline{R} \tag{7-20}$$

$$F_e = \underline{\hat{x}}^T\underline{M}\,\underline{\hat{1}}\ddot{u}_g(t) \tag{7-21}$$

The nonlinear seismic response of the equivalent system can be obtained conveniently by solving Equation 7-17 using the NONSPEC [52] computer program. Several parameters needed for the program were determined as follows.

In the elastic range,

$$R_e = \underline{\hat{x}}^T\underline{K}\underline{\hat{x}}u(t) \tag{7-22}$$

and Eq. 7-17 can be normalized as:

$$\ddot{u}(t) + 2\xi_e\omega_e\dot{u}(t) + \omega_e^2u(t) = \alpha_1\ddot{u}_g \tag{7-23}$$

where

$$\alpha_l = \frac{\hat{x}^T \underline{M} \hat{1}}{\hat{x}^T \underline{M} \hat{x}} \tag{7-24}$$

$$\omega_e = \left(\frac{\hat{x}^T \underline{K} \hat{x}}{\hat{x}^T \underline{M} \hat{x}} \right)^{1/2} \tag{7-25}$$

ξ_e and ω_e denote the damping ratio and initial circular frequency of the equivalent system, respectively. Comparing Eq. 7-23 with Eq. 7-12, note that the ground acceleration must be scaled by a factor of α_l for the equivalent SDOF system. Substitute $\hat{x}^T$ as defined in Eq. 7-14 and the mass of 1.339 $k-sec^2/in$ for each floor into Eqs. 7-24, 7-25. Let

$$\underline{K}\hat{x} = \underline{P}$$

where $\underline{P}$ is the the triangularly distributed lateral force when $\hat{x}$ occurred. It can be shown that:

$$\alpha_l = 0.263$$

and

$$\omega_e = 3.27 \ \ radian/sec$$

or

$$T_e^o = 1.92 \ \ second$$

where T_e^o denotes the initial period of the equivalent SDOF system. In applying the NONSPEC program, these parameters together with the unit yield displacement were specified for the equivalent SDOF system. The yield displacement of unity for the SDOF system, specified for the bilinear model(Fig. 7.13(c)) in NONSPEC, corresponds to the roof yield displacement of 5.11 inches for the original structure through the transformation as defined in Eq. 7-16. From the equivalent SDOF system, the effects of damping ratio, strain hardening stiffness, and various ground accelerations can be conveniently studied.

7.4.3 Inclusion of $P-\Delta$ Effect

Note that the equivalent period obtained by using Eq. 7-13 is an application of the Rayleigh method based on an assumed deflected shape. In general, the natural vibration period calculated by the Rayleigh method is smaller than the actual natural period of the system. The actual natural period can be obtained by substituting the actual mode shape into Eq. 7-13. When $P-\Delta$ effects are considered for the system, the initial period will be increased resulting from a reduced lateral stiffness.

Note that the force-displacement relationship of the original structure as shown in Fig. 7.16 is a result of a nonlinear static analysis using the ANSR-1 program in which the $P-\Delta$ approximation, as described in Chapter 5, was considered. Therefore, the corresponding deflected shape, $\hat{x}$, and the initial period, T_e^o, reflect the $P-\Delta$ effect. This also explains the reason why the initial period, $T_e^o = 1.92\ sec.$ obtained from the Rayleigh method, is larger than the fundamental period of 1.90 sec. for MRF Design 2 reported by the ANSR-1 program in which the undamped fundamental period was determined based on the initial structural stiffness without the $P-\Delta$ effect.

If the deflected shape and the associated equivalent period are obtained from the force-displacement relationship excluding the $P-\Delta$ effect, the elastic stiffness or the initial period, T_e^o for the equivalent SDOF system can be modified using a stability coefficient [52,55].

7.4.4 Behavior of Equivalent SDOF System

Several earthquake records were used to assess the performance of the equivalent SDOF system. Moreover, in order to realistically assess the effects of nonlinearities within the structure on the validity of the assumed one-shape response, the earthquakes selected had to be representatives of real strong earthquake motions. Accordingly, three ground acceleration inputs were chosen as follows.

(1) The original 1940 El Centro Earthquake NS component was scaled to a peak ground acceleration of 0.5 g by a factor of 1.5. This event is denoted as *1.5EC*. The original record of this earthquake was recorded in the epicentral area during the earthquake and is considered to be a strong motion record [56] and has been widely used in earthquake engineering.

(2) The original 1966 Parkfield Earthquake N65E component possessed a peak ground acceleration of 0.49 g. This event is denoted as *PK*. The original record was recorded at a site 200 feet away from the ruptured fault. Therefore, the event exhibited near-fault ground motion characteristics with impulsive types of excursions.

(3) The original 1952 Taft Lincoln School Tunnel Record N21E component was scaled to a peak ground acceleration of 0.47 g by a factor of 3. This event is denoted as *3TF*.

In analyses series 1, the equivalent SDOF system for MRF Design 2 with properties obtained in Section 7.4.2 was first analyzed for all three earthquake events using 3% damping. The post yield stiffness of the spring was taken as 8% of its elastic stiffness.

In order to assess the effects of various damping ratios, the SDOF model was reanalyzed, in analyses series 2, with a damping ratio of 5% for the three prescribed earthquake events.

In lieu of a step-by-step nonlinear static analysis, an assumed strain hardening effect for the equivalent SDOF system may be needed. This situation can occur when the yield strength of the structure is obtained from a limit analysis or from linear extrapolation of an elastic analysis. In such cases, the structural strain hardening effect can only be obtained by arbitrary guessing. Therefore, in analyses series 3, the equivalent SDOF model with a damping ratio of 3% and a reduced post-yield stiffness taken as 4% of its elastic stiffness was analyzed for the three prescribed earthquake events, again in order to examine the effects of post-yield stiffness.

In each analysis, the seismic response time history of the SDOF system during the first sixteen seconds of the event was obtained. Each analysis was performed using the

NONSPEC [52] program in which a step-by-step direct integration technique was employed. A total of nine computer runs described above was conveniently accomplished on a VAXstation II/GPX workstation. The execution time for each computer run was only about 1 minute, depending on the number of users on the computer system. Displacement response histories for each floor of the original structure were obtained by the displacement transformations as defined in Eq. 7-16, where $u(t)$ is the computed response history of the equivalent SDOF system and $\hat{x}$ is the assumed deflected shape as defined in Eq. 7-14. The results of these nine runs are summarized below.

7.4.4.1 Effects of Damping

The effects of different damping ratios on the response of the equivalent SDOF system under various ground acceleration records was examined by comparing the plots of the roof displacement histories obtained from the analyses series 1 and series 2. The roof response histories of the equivalent SDOF system during the first sixteen seconds of each event are shown in Fig. 7.18 for models having both 3% and 5% damping ratios. In general, the roof response histories for the 5% damped system are very similar to that of the 3% damped system. In all events, the 5% damped system exhibited reduced responses as anticipated, but the reductions are almost negligible.

7.4.4.2 Effects of Post-Yield Stiffness

The roof displacement histories of the equivalent SDOF system were plotted for analyses series 1 and series 3 in order to examine the effects of post-yield stiffness on the response histories. Their results are shown in Fig. 7.19 for all three events. Roof displacement histories for the SDOF system using post-yield stiffnesses of 8% and 4% of the elastic stiffness are plotted. In all three events, the nonlinear response history of the softer system was identical to the stiffer system until significant yielding occurred. The maximum displacements are found to be the same for both systems. However, after significant yielding

occurred, each system was characterized by oscillation about an offset. The system with a 4% post-yield stiffness was oscillating about a larger offset in all events, especially in event *PK* where larger permanent deformation had developed.

It is interesting to note that maximum roof displacements of the equivalent SDOF systems were found to be independent of the post-yield stiffness in the three prescribed events. The softer system may have attracted less force resulting in the same maximum response as the stiffer system. This appears to be the case for the prescribed earthquake excitations where only a few and one-directional large excursions were embedded in the ground acceleration. However, this requires further verification for other earthquake events in order to better assess the relationship between the post-yield stiffness and the maximum response for the equivalent SDOF system.

7.4.5 Response Comparison of Equivalent SDOF System and Original MDOF System

As noted in Section 7.4.2, the response history of each floor of the equivalent system can be obtained by the displacement transformation as defined in Eq. 7-16. The complete frame response histories derived from this transformation can be compared with the response of the original MDOF system in order to assess the performance of the equivalent SDOF system. For this purpose, the results of analyses series 1, as described in Section 7.4.4, were compared with the response of the original MDOF system. Later, the complete seismic response of the MDOF system for MRF Design 2 will be discussed with greater detail. In this section, only the floor displacement histories in the MDOF system during the first fifteen seconds are used for comparison. Note that the damping ratio for both the equivalent SDOF system and the original MDOF system were 3%. The post yield stiffness of the SDOF system was taken as 8% of its elastic stiffness as obtained in Section 7.4.2. In the analyses of the MDOF system for MRF Design 2 using the ANSR-1 [40], Rayleigh damping of 3% was assumed for the first and second modes, as described in Chapter 5.

The complete floor displacement histories for the original MDOF system and the equivalent SDOF systems are plotted in Figs. 7.20 to 7.22 for events *1.5EC*, *PK* and *3TF*, respectively. The scaled ground acceleration recorded of the first sixteen seconds for each event is also shown on the bottom of each figure. Note that a roof displacement of 5.11 inches or larger roughly indicates the yielding of the frame as described in Section 7.4.2. As depicted in Figs. 7.20 to 7.22, the floor displacement histories for both systems were very similar until significant yielding occurred. During event *PK*, where more severe yielding had occurred in the systems, deviations of floor displacement histories between two systems were found to be more pronounced. The roof response histories for both the MDOF and the SDOF systems during each event are summarized in Fig. 7.23.

In order to further evaluate the performance of the equivalent SDOF system in predicting the peak response indices, story drifts were calculated for both the MDOF and the equivalent SDOF systems. Frame lateral deflections and the associated story drifts of both systems are plotted in Fig. 7.24 for each event at instants when peak roof displacements occurred. In the figure, the distributions of floor displacements are plotted on the left-hand side while the corresponding story drifts are shown on the right-hand side. The instance when the maximum roof displacement occurred in the original MDOF system and the equivalent SDOF system, denoted as Tm and Ts, respectively, are also indicated on Fig. 7.24. From the figure, it is evident that the response of the equivalent SDOF system is similar to that from the analyses of the original MDOF system. In general, except for event *3TF*, the equivalent SDOF model predicted the instants, the magnitudes of the maximum frame displacement, as well as its associated story drifts for the original MDOF system quite satisfactorily. Clearly, event *3TF* is not the most severe earthquake among the three prescribed earthquake events for the given structure. However, as shown in Fig. 7.23 for event *3TF*, the overall discrepancy between the two floor displacement histories demonstrates the complexities of the nonlinear response of MDOF systems and their sensitivities to the ground excitations. The participation of higher modes to the response of the MDOF

system at the instant of maximum roof displacement in event *3TF* can be observed in Fig. 7.24.

7.4.6 Conclusions

The dynamic response of MDOF systems is generally complex and sensitive to the mechanical properties of the model as well as the input ground excitations. Considering the uncertainty within these parameters, a simplified model renders not all, but sufficient information for a proposed structure under given ground excitations, and may therefore be well justified.

The preceding comparisons, made for the MRF Design 2, suggest that an equivalent SDOF model employing the Q-model [54] concept is quite likely to predict the overall response of similar MDOF planar frames satisfactorily. The synthetic yield point for the equivalent SDOF model can be determined as described in Section 7.4.2. The $P-\Delta$ effect can also be included for the equivalent SDOF system in the derivation of equivalent period as described in Section 7.4.3. The nonlinear dynamic analysis program NONSPEC [52] provides a useful tool to perform nonlinear dynamic analyses for SDOF systems. It appears that the one-shape formulation, as described in Section 7.4.2, for the equivalent SDOF model is effective in producing acceptable approximations to frame displacement histories for a multi-story steel MRF system without abrupt changes of stiffness and mass along its height. For MDOF systems with irregularities in distribution of stiffness or mass, further substantiations are needed.

Ideally, building should be proportioned to resist earthquake effects without the use of nonlinear time history analysis. In certain cases when such analyses are desired, simplified equivalent SDOF systems appear to be justifiable. Nevertheless, in spite of providing the displacement histories, the equivalent SDOF system failed to provide the distribution of nonlinearities within the structure. In cases where complete information about the nonlinear kinematics of the system are desired, general nonlinear dynamic analysis procedures

are still required.

7.5 Nonlinear Dynamic Analyses of Six-Story MRFs

In order to assess the nonlinear behavior of the proposed MRF designs under earthquake excitation, several nonlinear dynamic analyses using the ANSR-1 program were performed. As described in Section 7.2.1, all MRF models incorporate the actual panel zone stiffness with joint elements in formulating the structural stiffness. Therefore, the effects of the panel zone flexibilities on the beam plastic rotation demand as well as the overall structural response can be studied. In all analyses, the $P-\Delta$ effects due to the gravity load in the MRF were included.

7.5.1 Dynamic Characteristics of the MRFs

As mentioned in Section 7.2, the member sizes of MRF Design 1 were designed based on a larger base shear than that for MRF Designs 2, 3 and 4. While retaining the same member sizes for MRF Designs 2, 3 and 4, the panel zone joints in these MRFs were designed based on various levels of bending moment of beams framed into the joint. Therefore, the effects of the relative member stiffness and the panel zone joint flexibilities on the dynamic characteristics of the MRF can be studied by examining the vibration mode shapes and periods of each MRF design. In Table 7.8, the first three vibration periods of each MRF design are tabulated. It can be seen from the table that MRF Design 1, designed based upon a larger base shear, possesses a larger lateral stiffness and significantly smaller vibration periods than do the other MRF designs. Moreover, the vibration periods are shortened as panel zone stiffness increases. However, the effects of panel zone flexibilities on the vibration period are not very significant. As a result, the first mode periods for MRF Designs 1, 2, 3 and 4 are 1.65, 1.90, 1.84 and 1.86 seconds, respectively. The first three vibration mode shapes for MRF Designs 1, 2, 3 and 4 are tabulated in Tables 7.9 and 7.10. In these two tables, it can be seen that the corresponding mode

shapes of all MRF designs are essentially the same. It can be concluded that the effects of the relative lateral stiffness and the panel zone stiffness on the vibration mode shapes are insignificant in the proposed MRF designs.

7.5.2 Selection of Ground Acceleration

Several earthquake ground acceleration records were used to assess the dynamic behavior of the six-story MRF designs. In addition to the three earthquake events as described in Section 7.4.4, the EW component of the first eighty seconds of the original 1985 Mexico Earthquake which possessed a peak ground acceleration of 0.17 g was also used. This earthquake is denoted as event MX. The ground acceleration histories of these four events are plotted in Fig. 7.25. The corresponding elastic pseudo-acceleration spectrum for these events are plotted compositely in Fig. 7.26 using 3% damping. The range of the first three vibration periods of the MRF designs is also identified in the figure. As can be seen from Fig. 7.26, unscaled events MX and PK possess relatively larger spectral pseudo-acceleration near the period range for the first mode. This is true especially for event MX, the participation of the first mode is expected to be more pronounced for this event than for any other event.

7.5.3 Response to the Selected Ground Accelerations

Recall that the design of beams and columns for MRF Design 1 was based on a base shear of 0.059W or 183.5 kips while it was 0.052W or 161.7 kips for MRF Designs 2, 3 and 4. In both MRF Designs 1 and 2, the design of panel zone joints, using Eqs. 7-5 and 7-6, was based on factored beam moments due to the prescribed lateral forces, $1.85M_E$, plus the effects of gravity loads. As described in Section 7.2, the design of panel zone joints for MRF Design 3 is based on the beam flexural strength, M_p. Moreover, the design of panel zone joints for MRF Design 4 is based on the beam flexural strength for joints at lower floors while based on beam moments of $1.85M_E$ for joints at higher floors.

Therefore, the effects of beam-column stiffness and stiffness on the response of the MRF designs can be studied by comparing the response of MRF Designs 1 and 2. The effects of panel zone joint flexibilities on the response of the MRF designs can be studied by comparing the response of MRF Designs 2, 3 and 4. In all analyses, the $P-\Delta$ effects due to the gravity load in the MRF were included. The resulting story shears, story displacements and story drifts obtained from these analyses were studied. During each event, the extent of the maximum plastic hinge rotation of the beams, the columns and the panel zone joints of each model were also examined.

In examining the extent of the maximum hinge rotation of beams, columns or panel zone joints, these deformations were plotted on the frame elevation at the corresponding location using circles of radius proportional to the associated deformation. While the center of the circle for a panel zone joint is located at the center of the beam-column intersection, the center of the circle for a beam or column is located at a point two feet from the associated beam-column intersection. In general, a circle of one-eighth-inch radius is equivalent to 0.01 radians of deformation as indicated in these plots. The results of these analyses are summarized for each events as follows.

7.5.3.1 Response to Parkfield Earthquake

Maximum Floor Displacements, Story Shears and Story Drifts for Event *PK*

The floor displacement envelope and maximum floor displacements at instant when the maximum roof displacement that occurred during the event are plotted in Fig. 7.27 for MRF Designs 1 and 2. From the figure, it can be seen that the least stiff MRF, Design 2, exhibited larger lateral displacement at each floor. Moreover, the shape of the plot for the maximum floor displacement as shown in Fig. 7.27a suggests that the response of the frame is dominated by its first mode. The maximum story shear and story drift that occurred during the event are plotted in Fig. 7.28. From the figure, it can be seen that MRF Design

1 was subjected to a significantly larger base shear while it experienced a smaller story drift at most of the floors. The story shear that occurred in each floor of MRF Design 1 is substantially larger than that which occurred in MRF Design 2. The maximum base shear occurred in MRF Designs 1 and 2 are 575 and 414 kips, about 3.1 and 2.6 times the corresponding code prescribed base shear, respectively. The maximum story drifts occurred in the MRF Designs 1 and 2 are 2.3% and 2.6%, 9.2 and 10.4 times that allowed under the code prescribed lateral forces, respectively.

Similarly, plots of maximum floor displacements, story shears and story drifts for MRF Designs 2, 3 and 4 are shown in Figs. 7.29 and 7.30. It can be seen from these two figures that the least stiff design, MRF Design 2, was subjected to the smallest floor displacements and smallest story shears in most of the floors. Although the maximum story drift that occurred in upper floors of MRF Design 2 is relatively larger, the distribution of the maximum story drift that occurred among all floors are more uniform. The maximum story drifts occurred in MRF Designs 2, 3 and 4 are 2.6%, 3.3% and 2.9%, respectively. These maximum story drifts all occurred at the ground floor.

Maximum Beam, Column and Panel Zone Joint Plastic Hinge Rotations

The maximum beam, column and panel zone joint plastic hinge rotations occurred during the event are plotted in Figs. 7.31 through 7.34 using circles of various radius as mentioned previously for MRF Designs 1 through 4, respectively. It can be seen from Figs. 7.31 and 7.32 that the plastic hinge formations and the maximum plastic rotations of MRF Designs 1 and 2 are similar. Four hinges with the largest plastic rotation were formed at the bottom end of columns at the ground floor, the rest of the plastic hinges were concentrated in panel zone joints. Comparing Figs. 7.32 and 7.33, it can be seen that once panel zone stiffness and strength increase, the rotational demands of the beams and columns also increase. Comparing Figs. 7.33 and 7.34, it can be seen that those relatively weaker panel zone joints as designed for the upper floors of MRF Design 4 help to

distribute the plastic hinge formations more evenly. The extent and the distribution of the maximum plastic rotations in MRF Design 4 appear to be the most uniform among all MRF designs. During event PK, a maximum column plastic hinge rotation of 0.03 radians occurred at the bottom end of the ground floor column in MRF Design 3, a maximum beam plastic hinge rotation of 0.015 radians occurred at the second floor beam in MRF Design 3, a maximum panel zone joint plastic hinge rotation of 0.021 radians occurred in the MRF Design 2.

7.5.3.2 Response to 1.5*El Centro Earthquake

Similar to the case for event PK, plots of maximum floor displacements, story shears, story drifts as well as plastic hinge deformations for beams, columns and panel zone joints are shown in Figs. 7.35 through 7.42. Although the peak ground acceleration in event $1.5EC$ is about the same as that in event PK, the response of all MRF designs to event $1.5EC$ is considerably smaller than to event PK. This is anticipated after inspecting the linear pseudo-acceleration spectra as shown in Fig. 7.26. Nevertheless, the general trend of the response observed for event $1.5EC$ is similar to those for event PK. During event $1.5EC$, a maximum story drift of 2% occurred in the ground floor in MRF Design 3, a maximum base shear of 502 kips, 2.7 times the code prescribed base shear, occurred in MRF Design 1. The maximum beam, column and panel zone joint plastic hinge rotations that occurred during event $1.5EC$ are 0.004, 0.017 and 0.015 radians, respectively.

7.5.3.3 Response to 3*Taft Earthquake

Similar to the case for the previous two events, plots of maximum floor displacements, maximum story shears, story drifts as well as plastic hinge deformations for beams, columns and panel zone joints are shown in Figs. 7.43 through 7.50. Although the peak ground acceleration during this event is 0.47g and a sharp increase of spectral acceleration near the period range for the third mode is evident, the response of all MRF designs to

event $3TF$ is smaller than to previous two events. The trend of the response observed in this event is generally similar to those in the previous two events. However, the arrangement of the panel zone strength in MRF Design 4 results larger panel zone plastic hinge rotations occurred in the upper floors. This may well attribute to the sharp increase of spectral acceleration near the period range for the third mode (Fig. 7.26).

7.5.3.4 Response to Mexico Earthquake

Maximum Floor Displacements, Story Shears and Story Drifts

The floor displacement envelope and maximum floor displacements at the instant when the maximum roof displacement occurred during event MX are plotted in Fig. 7.51 for MRF Designs 1 and 2. The maximum story shear and story drift that occurred in MRF Designs 1 and 2 are plotted in Fig. 7.52. From these figures, it can be seen that the least stiff MRF, Design 2, exhibited significantly larger lateral displacement at each floor. Moreover, the shape of the plot for the maximum floor displacement as shown in Fig. 7.51a suggests that the response of the frame is dominated by its first mode. From Fig. 7.52, it can be seen that MRF Design 1 was subjected to a significantly larger base shear while experienced a smaller story drift at most of the floors. The story shear that occurred in each floor of MRF Design 1 is substantially larger than that which occurred in MRF Design 2. The maximum base shear that occurred in MRF Designs 1 and 2 are 530 and 411 kips, about 2.9 and 2.5 times the corresponding code prescribed base shear, respectively. The maximum story drifts which occurred in the MRF Designs 1 and 2 are 2.1% and 2.9%, respectively.

Plots for maximum floor displacements, story shears and story drifts for MRF Designs 2, 3 and 4 are shown in Figs. 7.53 and 7.54. From Fig. 7.53, it can be seen in MRF Design 3 that relatively large floor displacement occurred in the lower floors while smaller floor displacements occurred at upper floors. From Figs 7.53 and 7.54, it appears that the

soft story was formed in the ground floor, and larger story drifts had concentrated on lower floors. In MRF Designs 2, 3 and 4, the maximum base shear which occurred during event *MX* is 484 kips, in MRF Design 3. The maximum story drifts which occurred are 2.8%, 3.4% and 2.9% for MRF Designs 2, 3 and 4, respectively.

Maximum Beam, Column and Panel Zone Joint Plastic Hinge Rotations for Event *MX*

The maximum beam, column and panel zone joint plastic hinge rotations occurred during the event are plotted in Figs. 7.55 through 7.58 using circles of various radius for MRF Designs 1 through 4, respectively. It can be seen from Figs. 7.55 and 7.56 that the plastic hinge formations and the maximum plastic rotations of MRF Designs 1 and 2 are no longer similar. MRF Design 2 exhibited relatively larger hinge rotations in members and joints at the lower floors. This may attribute to the sharp increase of spectral pseudo-acceleration near the first mode period of MRF Design 2. Comparing Figs. 7.56 and 7.57, it can be seen again that once panel zone stiffness and strength increase, the rotational demands of the beams and columns also increase. Comparing Figs. 7.57 and 7.58, it can be seen that these relatively weaker panel zone joints designed for the upper floors of MRF Design 4 help to distribute the plastic hinge formations more uniformly. The extent and the distribution of the maximum plastic rotations in MRF Design 4 appear to be most uniform among MRF Designs 2, 3 and 4. During event *MX*, the largest column plastic hinge rotation of 0.031 radians occurred in the bottom end of the ground floor column in MRF Design 3, the largest beam plastic hinge rotation of 0.014 radians occurred in second floor beam in MRF Design 3. The largest panel zone joint plastic hinge rotation of 0.023 radians occurred in the MRF Design 2.

7.5.3.5 Other Response Indices

From the preceding discussions on the response of the MRFs, it is apparent that events $1.5*EC$ and $3*TF$ are not severe earthquakes for the proposed six-story MRFs. During a severe earthquake, the column maximum bending moment and axial force can be several times larger than those resulting from code prescribed lateral forces. In Fig. 7.59, the maximum bending moments and maximum axial forces that occurred during event *PK* for one interior and one exterior column are plotted. In this figure, the forces and moments resulting from code prescribed lateral forces are also plotted with dotted lines. It can be seen from Fig. 7.59 that the maximum column forces that occurred during the event are two to three times greater than those resulting from the code prescribed lateral forces.

The maximum column end moments shown in Fig. 7.59 do not occur at the same time. However, it is evident that under the dynamic excitation the unbalanced beam moment is often distributed unequally to the columns above and below a joint. This phenomena was also found in the analyses of eccentrically braced frames conducted by other researchers [41]. As a result of this unequal distribution of column moment, the inflection point may be far from the mid-height of the column or may not even occur within the column [65]. In order to better account for this unequal distribution of moment in the design of columns, a dynamic amplification factor has been proposed by other researchers [65] and incorporated in one of the building code [66].

In order to examine the distribution of maximum column moments during event *PK*, the bending moment diagram for columns of MRF Design 2 at instants when the maximum moment occurred at the bottom and the top ends of each column are plotted in Fig. 7.60 and 7.61, respectively. In these figures, the bending moments resulting from code prescribed lateral forces are also indicated with dotted lines. An examination of these two figures indicates that the location of the inflection point is not stationary and the bending moment at a point near the mid-height of the column may be large. Similar phenomena are found in other MRF designs during other events. In view of the above, great care

must be taken for the design of column splices.

The plot of the story shear versus story drift hysteretic loops, shown in Fig. 7.62 for MRF Design 2 during event *PK*, is useful in assessing the general behavior of the MRF. In general, event *PK* imposed a large impulse to the MRF, resulting in a large permanent deformation. The MRF then essentially oscillated elastically about this permanent offset. This behavior can also be observed in the hysteretic loops for the individual members. In Fig. 7.63, the beam moment versus beam plastic rotation hysteretic loops for the first floor beams of MRF Design 3 during event *PK* are plotted. Similarly, the panel zone rotation versus applied moment hysteretic loops for one interior and one exterior columns of MRF Design 2 during event *PK* are plotted in Fig. 7.64 and 7.65, respectively. The member designation used in these plots can be found in the frame elevation shown in Fig. 7.2. Since the area enclosed by the hysteretic loops is directly related to the energy dissipated in each member or joint, the general trend observed in these plots indicates that the hysteretic energy dissipated during event *PK* is not very large. Unlike the response to event *PK*, the MRF design was subjected to many cycles of large excursion during event *MX*. This can be observed in Fig. 7.66 where the beam moment versus beam plastic rotation hysteretic loops of the first floor beams in MRF Design 3 during event *MX* are plotted. As a result, the hysteretic energy dissipated during event *MX* is much larger than during event *PK*.

7.5.4 The Demand and the Supply

As mentioned previously, event *PK* imposed a single large impulsive excursion while event *MX* imposed many large excursions to the MRF designs. The MRF was subjected to large member forces and deformations during both events. However, the deformation and the energy dissipation demands imposed by events *PK* and *MX* are quite different.

Beam Plastic Deformations

In order to study the beam plastic rotation demand imposed by events *PK* and *MX*, the experimental results of nineteen specimens as described in Chapters 3 and 4 are plotted against the maximum deformations observed during events *PK* and *MX*. For this purpose, the maximum beam plastic rotation demands, 0.015 and 0.0145 radians, which occurred during events *PK* and *MX* are plotted against the plastic rotation capacity, θ_p, as tabulated in column 10 of Table 3.2. In this application, it is noted that the specimens tested and reported herein correspond to the half scale model of a prototype MRF with 12 ft. column heights and 24 ft. beam-bay length. Therefore, the results of these experimental tests as tabulated in Table 3.2 are comparable with the maximum demand observed in the analyses of the six-story MRF designs. The definition of various plastic rotation capacities for Table 3.2 can be found in the footnote of the table. In Fig. 7.67, in which the beam plastic rotations are measured from the initial point of zero deformation, it can be seen that only Specimens 1, 2, 7, 8, 10R, 11, and 14 are considered to be adequate in providing the needed rotation capacity. Specimens 3, 4, 5, 6, 13, 15, 16 and 18 are apparently inadequate and Specimens 7, 12 and 17 are marginal. As mentioned in Chapters 3 and 4, Specimen 10 with an end plate moment connection was subjected to large bolt elongations and subsequent fracture of one connecting bolt. The beam rotation of Specimen 10, shown in Fig. 4.8, is due primarily to the elongation of bolts and is therefore not incorporated in Table 3.2 and Fig. 7.67.

As tabulated in column 11 of Table 3.2, another important measure of beam rotation capacity is the measurement of the maximum beam plastic rotation θ_p^*, where θ_p^* is the deformation measured from the point of zero load during a half cycle. In Fig. 7.68 the maximum beam plastic rotations, measured from the point of zero load, during events *PK* and *MX* are plotted against the experimental results as tabulated in column 11 of Table 3.2. From Fig. 7.68, Specimens 1, 2, 7, 8, 9, 10R, 11, 12, 14, 17 and 18 are considered to be adequate for event *MX*. Specimens 5, 6, 15, and 16 are considered to be inadequate

for both events *PK* and *MX*.

Energy Dissipation

As mentioned previously, the energy dissipated in the MRF is primarily hysteretic energy dissipated in beams, columns and panel zone joints. The total story hysteretic energy dissipated in each floor can be estimated simply by intergrating the area within the hysteretic loops of all members and joints in the corresponding floor. In a well designed MRF, member strength is progressively reduced along the frame height, The total story dissipated energy along the frame height should therefore also be reduced proportionally if a uniform deformation demand along the frame height is achieved.

In order to assess the energy dissipated in a beam where large plastic rotation demand occurred during events *PK* and *MX*, the hysteretic loops for the left end of beam B1A at the first floor of MRF Design 3 are integrated. The resulting dissipated energies at the left end of the beam are 153 and 1451 kip-inch during the first twenty seconds of event *PK* and the first sixty seconds of event *MX*, respectively. These dissipated energies are further normalized with respect to the beam flexural strength of 10008 kip-inch. The resulting normalized dissipated energies provide a measure of the cumulative plastic deformations and can be compared with the experimental results described in Chapters 3. For this purpose, the hysteretic energy dissipated in the nineteen test specimens is computed from the hysteretic loops as shown in Figs. 3.21 through 3.38. The results are then normalized with respect to the corresponding beam flexural strength M_p^*, where M_p^* is based on the corresponding coupon tensile strength. In Fig. 7.69, it can be seen that the normalized dissipated energy demand occurred for event *PK* is very small. However, only Specimens 1, 2, 8, 9, 10R, 11, 12, 13, 14, 17 and 18 meet the demands incurred during event *MX*.

7.6 Summary and Conclusions for the Six-Story MRF Analyses

From the preceding discussions, it is evident that the nonlinear dynamic response of the proposed MRF designs is very sensitive to the input ground accelerations as well as to the mechanical properties of the model. From these analyses, the behavior of the six-story MRFs is better understood and the following conclusions are noted with respect to the analyses and design of the six-story MRFs.

(1) As demonstrated in Section 7.3, the effects of the panel zone joint flexibilities on story drifts can be significant. Depending on the design of the panel zone joints, the elastic drift calculation based on the member clear span plus 50% of the joint size may be too unconservative. The error may be as large as 20%. The elastic drift calculation based on the member center line distances still underestimated the total drift incorporating the actual panel zone joint deformation for MRF with panel zone joints designed for the effects of gravity load plus 1.85 times the prescribed lateral force.

(2) As noted in Section 7.4, an equivalent SDOF model employing one shape displacement function is likely to predict the overall nonlinear response of a planar MRF quite satisfactorily. The equivalent SDOF system appears to be effective in producing acceptable approximations to nonlinear frame displacement histories for the proposed steel MRF design when the response is dominated by the first vibration mode. However, the equivalent SDOF system failed to provide the information about the distribution of nonlinearities within the structure.

(3) The effects of panel zone flexibilities also change the dynamic mode shapes and periods, but the effect is insignificant for the six-story MRF designs. The effects of beam and column stiffness on the dynamic characteristic of the MRFs are more pronounced as indicated in the periods of MRF Designs 1 and 2 in Table 7.8.

(4) The dynamic response of the six-story MRF designs to the selected earthquake excitations, except event $3^{*}TF$, is primarily dominated by the first vibration mode. The participation of the third mode in the response of MRF designs is more pronounced

during event $3*TF$ due to its sharp increase of spectral pseudo-acceleration near the period range for the third mode. As a result, the maximum story drift and maximum panel zone joint deformation which occurred during event $3*TF$ are primarily at upper floors of the MRF designs.

(5) Although events $1.5*EC$ and $3*TF$ possess peak ground accelerations of about 0.5g, the associated response of the MRF designs are not as large as that during events *PK* and *MX*. This can be anticipated by examining the pseudo-acceleration spectrum for the selected events as shown in Fig. 7.26. However, column plastic hinges formed at the column bases during each event in most of the MRF designs. Moreover, the plastic hinge rotations at these column bases are often large. In view of this, great care should be taken in the design of the column base plate and anchor bolts for this type of MRF.

(6) Under the prescribed lateral force, it is anticipated that the story drift of MRF design 3, the stiffest design among MRF Designs 2, 3 and 4, will be smaller than that of the other two MRF Designs. However, an examination of Figs. 7.30, 7.38, 7.46 and 7.54 indicates that the stiffer design, MRF Design 3, attracted relatively larger story shears in each floor and was therefore not necessarily subjected to the smallest story drift in each floor. In fact, it can be seen from these figures that MRF Design 3 was subjected to a larger first story drift than were the other two MRF designs during the selected earthquake events. The maximum story drifts that occurred in MRF design 2 are 3.3%, 2.0%, 1.1% and 3.4% during events *PK*, $1.5*EC$, $3*TF$ and *MX*, respectively. During event *PK*, the maximum story drift which occurred in MRF Designs 1 and 2 are 2.3% and 2.6%, respectively. They are often substantially larger than the elastic drift under the code prescribed lateral force. The maximum base shears that occurred in MRF Designs 1, 2, 3 and 4 are 574, 414, 495 and 471 kips during event *MX*. These base shear are two to three times the corresponding code prescribed base shear.

(7) During most of the selected earthquake events, the special arrangement of panel zone joint strength adopted in MRF Design 4, stronger panel zone joints for lower floors with relatively weaker panel zone joints for the upper floors, appears to smooth the extent of maximum panel zone joint deformations quite effectively.

(8) In general, the extent of the maximum panel zone deformations were more severe in MRF Designs 1 and 2, in which the panel zone joints were designed for the effects of the gravity load plus 1.85 times the prescribed lateral load, than in other two designs. The maximum panel zone deformations that occurred at the first floor of MRF Design 2 are 0.021 and 0.022 radians during events *PK* and *MX*, respectively. As the panel zone joint strength approaches the beam flexural strength, the extent of the maximum panel zone deformations is reduced while the the extent of the maximum beam and column plastic rotations are greatly increased. As noted in Section 7.5.3, the maximum beam plastic rotations are 0.0145 and 0.015 radians in the first floor beam of MRF Design 3 during events *PK* and *MX*, respectively. It appears that a beam rotation bench mark of 0.02 radians, used in evaluating the performance of beam specimens as described in Chapter 3, is justifiable.

(9) An examination of Figs. 7.59, 7.60 and 7.61 indicates that the column bending moment and axial force can be two to three time the forces resulting from the prescribed lateral forces. Moreover, the unbalanced beam moment is often distributed unequally to the column above and below a joint. As a result, the inflection point may be far from the mid-height of the column and the moment at mid-height of the column can be large. In view of above, one must take great care to detail the column splices.

(10) As demonstrated in Section 7.5.4, an examination of the experimental data obtained from nineteen specimens indicates that the ductility capacity of beams in MRF Design 3 may be exceeded during events *PK* and *MX* if the beam-column connections in the MRF are not detailed and constructed appropriately. Since experimental evidence

has shown that well designed panel zone joints posses stable hysteretic behavior and excellent energy dissipation capacity, it is recommended that beam column panel zone joints should be carefully proportioned to allow their participation in dissipating energy in order to reduce, but not totally eliminate the beam and column plastic rotation demand.

From the preceding discussion, the complexities of nonlinear dynamic response of a MDOF system are apparent. In these analyses, it was demonstrated that the ductility demands on beams, columns and their connections for MRFs designed according to the current building code can be very large. Therefore, one must take great care in detailing various parts of the MRF. The analytical results summarized in this chapter should aid in the further development of earthquake resistant design procedures for low-rise steel MRFs. The nonlinear dynamic response reported herein is obtained from the six-story MRF designs analyzed using selected ground accelerations. For MRFs with irregularities in the distribution of stiffness or mass, the dynamic response to specific ground accelerations requires further research. Moreover, experimental investigation of MRF systems under dynamic loading is needed in order to substantiate these analytical results. In these analyses, it was assumed that the stability of the beams, columns and their connections were adequate for seismic resistant design and the effects of soil structure interaction were not considered.

8. Nonlinear Static and Dynamic Analyses of 20-Story MRFs

8.1 Program of Investigation

As mentioned previously, building structures designed according to building codes are expected to deformed into the inelastic range during a severe earthquake. In Chapter 7, the nonlinear behavior of various MRFs, designed according to the new SEAOC provisions for a six-story building, have been studied in detail. However, MRFs of a larger vibration period for taller buildings may behave differently. In order to gain some insight into the nonlinear behavior of MRFs for taller buildings, an analytical investigation was carried out and is described herein.

In Section 8.2 of this Chapter, a twenty-story MRF is designed according to the new SEAOC provisions [47] and 1988 UBC [59] using both the static and dynamic lateral force procedures. At this stage of the design, the beam column panel zone joints are assumed partially rigid. The designs of beams and columns are primarily based on the associated stress ratios and story drifts under the prescribed lateral forces. The beam column panel zone joints are then designed for various levels of bending moments of beams framed into the joints. Traditionally, the panel zone joints have been designed for the beam flexural strength.

In order to assess the effects of the panel zone flexibility on the static and dynamic characteristics of the MRF, the MRF models of various panel zone designs are analyzed using the ANSR-1 [40] program in which a joint element was incorporated as described in Chapter 5. The resulting frame deformations, vibration mode shapes and periods were studied and compared with those obtained from the approximate method commonly used in design offices. In Section 8.4, a method which incorporates the actual panel zone stiffness into the calculations of story drifts is also introduced and can be used for situations when a joint element cannot be defined in the computer program commonly used in the building

industry.

In Section 8.6, the ground acceleration, the associated Fourier amplitude and linear response spectra are studied for selected earthquake ground motions. In Section 8.7, nonlinear dynamic responses of various MRF designs to the selected earthquake events are described. The study of each MRF design involves examining the story deformations, story shears of the MRF, the maximum plastic deformations of each element, as well as the distribution of the maximum plastic deformations obtained from the analyses.

From this analytical investigation, the nonlinear behavior of the proposed MRF designs are better understood. It can be found from these analyses that panel zone flexibilities in the MRF greatly change the static and dynamic characteristics of the whole frame. The dynamic response of each MRF design is highly dependent upon the ground acceleration characteristics: the Fourier amplitude and response spectra. Higher vibration modes may well participate in the response of the structure to a specific ground acceleration. The lengthening of structural periods due to the development of nonlinearities may also change the relative participation of various modes. In assessing the nonlinear behavior of multi-degree-of-freedom systems, the application of the linear response spectra is found useful.

8.2 Design Procedures

For the purpose of this analytical study, the structure selected was a twenty-story, three-bay by four-bay rectangular office building to be built in San Francisco, California. As shown in Figs. 8.1 and 8.2, the lateral load resisting system for the building consists of a three-dimensional moment resisting frame on the perimeter of the building. The gravity load is supported by interior core columns in conjunction with the perimeter frame. The structural system employed in this building is similar to the one used in the six-story office building described in Chapter 7. However, the column spacings in the twenty-story structure are smaller than those in the six-story structure. Perimeter frame or framed tubular systems with columns spaced closer than ten feet have gained wide acceptance as the major

lateral force resisting system for tall buildings [60].

The floor-to-floor height of the building was selected as 12.5 feet for typical floors and 18 feet for the ground floor and the basement floor as shown in Fig. 8.3. The total building height is 255.5 feet above the ground floor. The composite floor framing is made of 2.5-inch regular weight concrete fill over a 3-inch metal deck on steel wide flange sections. The weight of a building floor, including partitions, ceiling and mechanical piping, was assumed to be 100 pounds per square foot (psf) for typical floors and the roof. The exterior window wall system was assumed to weight 35 psf average over the exterior surface of the building. The design live loads were 80 psf and 20 psf for the typical floor and roof, respectively. As noted in Chapter 7, the 80 psf design live load is higher than 50 psf as usually specified [1,46]. This higher design live load is often adopted by design offices in order to accommodate various tenants' needs. However, the live load reduction per ANSI [46] was used to design individual members. The magnitude of the wind load and its effects on the proposed building were assumed to be less significant than the earthquake force and were not considered in the design.

8.2.1 Static Lateral Force Procedure

In the preliminary design, the design seismic force was based on the new equivalent lateral force procedure recommended by SEAOC [47]. As described in Chapter 7, the design seismic force coefficient can be determined by using Eqs. 7-1 and 7-2. The fundamental period of the building can be determined using either method A or B as described in Section 7.2. That is:

Method A:

$$T_A = C_t(h_n)^{3/4} = 0.035\ (255.5)^{3/4} = 2.24\ \ sec.$$

Method B:

T_B = Fundamental period, within certain limits, calculated in a properly substantiated analysis.

As demonstrated in Section 7.2, the upper bound value for the period determined using method B is 1.4 times the period obtained from method A. However, the minimum ratio for $\frac{C}{R_w}$ of 0.075 also limits the period allowed in deriving the design base shear. In our case,

$$T_B^{max} = 1.40 \times T_A = 3.13 \; sec.$$

Let the site coefficient for soil characteristics, S, equal to 1.5. From Eq. 7-2 and the minimum ratio for $\frac{C}{R_w}$ of 0.075:

$$T^{max} = \left(\frac{1.25 \; S}{0.075 \; R_w} \right)^{3/2} = 3.0 \; sec.$$

Therefore, the minimum ratio for $\frac{C}{R_w}$ governs.

The total dead load considered includes the dead load on the floor and the weight of the facade. Live load was not considered in calculating the lateral force. As a result, the total seismic dead load, W, is 15,000 kips, based on the weight of twenty floors above the ground floor. Therefore, the base shear can be computed as follows:

$Z = 0.4$,

$I = 1$,

$R_w = 12$ for special moment resisting space frame,

$T = 3.0$ seconds,

$S = 1.5$,

$C = 0.90$,

$V = \frac{Z \; I \; C}{R_w} W = 0.0292 \; W = 438$ kips.

The base shear force derived above was vertically distributed in both principal directions as recommended in SEAOC's provisions between the second floor and the roof floor. The concentrated force, F_T, applied at the roof level was found to be 0.25V.

The preliminary column sizes for the frame were first selected according to the tributary gravity load carried by each column. The beams were then chosen such that the strong-column and weak-beam relationship was roughly maintained. The steel beams and columns were assumed to be A36 material. Assuming rigid floor diaphragms, an elastic analysis of the three dimensional model was performed using the ETABS [43] computer program. The member properties were based on bare steel sections. The effect of the finite joint size was considered by formulating member stiffnesses with member clear spans plus 50% of the panel joint sizes. Since the story drift at the basement level was insignificant, the base of the columns were assumed pinned. The rigidities of the basement wall were taken into account using external springs of large stiffness located at the first floor level. The lateral forces were applied in conjunction with the gravity load. The accidental torsional effect was accounted for by appling the lateral force in each direction at an eccentricity equal to 5% of the building dimension at each level perpendicular to the direction of the force considered. The resulting stress ratios for all members were checked based on the 1978 AISC [4] specifications (Sections 1.6.1 and 1.6.2) for the following load combinations:

(1) DL + LL

(2) DL + LL + EQX

(3) DL + LL + EQY

(4) DL - EQX

(5) DL - EQY

The four corner columns were check for additional load combinations:

(6) DL + LL + 1.0×EQY + 0.3×EQY

(7) DL + LL + 0.3×EQY + 1.0×EQY

The effective length factor for columns were based on the alignment chart procedure recommended in the AISC commentary [4]. The allowable stresses for the beams and columns were increased by 33% for load conditions including seismic force. Moreover, the

column compression strength, defined as $1.7F_aA$, and the tension strength, defined as F_yA, were checked for two additional load combinations as defined in Eqs. 7-4a and 7-4b. In applying these two equations, the effective length factor was taken as unity in computing the allowable stress, F_a, for the column compressive strength as defined above. Member sizes were evaluated based on the stress ratios and story drifts obtained from the analysis. New member sizes were selected and subsequent analyses were iterative in nature. All members were to satisfy the compact section requirements [4]. In each analysis, the fundamental period of the frame was also assessed in order to examine the design lateral force.

Similar to the six-story building described in Chapter 7, the twenty-story MRF in line 1 carries 50% of the lateral force in the transverse direction while carrying only about 12.5% of the floor gravity load. The allowable story drift under the specified lateral force is $\frac{0.03}{R_w}$ or 0.0025. Most member sizes were found to be governed by the story drifts of the frame under the prescribed lateral force. The periods obtained from these analyses were often found to be about 3.6 seconds. Since limitations of the fundamental period in seismic force calculations for member strength designs do not apply to the case for story drift calculations, the design seismic force was relaxed for drift calculations. In the final stage of the preliminary design, the design seismic force was reduced based on a fundamental period of 3.6 seconds for story drift calculations. That is:

T = 3.6 seconds,

S = 1.5,

C = 0.80,

$V = \frac{Z\ I\ C}{R_w} W = 0.0266\ W = 400$ kips.

In summary, the member strength of the MRF were sized based on a base shear of 0.0292W or 438 kips and the frame stiffness was evaluated based on a base shear of 0.0266W or 400 kips. Finally, a set of beams and columns was selected for the proposed

twenty-story structure as shown in Fig. 8.3. For the purpose of discussion, only the results in the transverse frame are presented. It was found that most of the members in the higher levels were governed by the stiffness requirement while the member in the lower levels were governed by the strength demand. The story forces and shears based on a base shear of 400 kips and the associated floor displacements and story drifts are tabulated in Table 8.1.

8.2.2 Dynamic Lateral Force Procedure

It is required per SEAOC's [47] provision and 1988 UBC [59] that buildings over 240 feet in height and in seismic zones 3 and 4 require the dynamic lateral force procedure. Therefore, a three-dimensional elastic dynamic response spectrum analysis was performed for the proposed structure obtained above using the normalized response spectra recommended in the SEAOC's provision.

Number of Modes

The number of modes considered was the first nine modes. Note that the proposed twenty-story structure possesses sixty vibration modes in its three-dimensional model. It is required per SEAOC [47] provision that at least 90% of the participating mass in each direction of the structure be included in the calculation of the response. This requirement represents an approximated basis for providing an acceptable degree of accuracy in the computation of dynamic base shear using the first few modes. The adequacy of the number of modes considered can be examined by summing the ratio of the effective modal mass to the total mass for each mode being considered in each principal direction.

It can be shown [33] that the base shear, $V(t)$, in each translational direction at time t is:

$$V(t) = \sum_{n=1}^{N} \frac{\alpha_n^2}{M_n} \omega_n^2 u_n(t)$$

where α_n, M_n and ω_n are the modal participation factor, modal mass and modal

frequency, respectively. The maximum n_{th} contribution to the total base shear is:

$$V_n^{\max} = \frac{\alpha_n^2}{M_n} S_{an}$$

where S_{an} is the spectral acceleration associated with the n^{th} mode. Hence each modal contribution V_n to the base shear is directly proportional to the effective modal mass, $\frac{\alpha_n^2}{M_n}$, for a constant unit spectral acceleration. It can be proved [33] that, in the k^{th} principal direction:

$$\sum_{n=1}^{N} \left(\frac{\alpha_n^2}{M_n} \right)_k = M_{Tk}$$

where the total mass in the k^{th} principal direction, M_{Tk}, is given [33] as:

$$M_{Tk} = [1]\, m_k\, 1$$

in which m_k is the mass matrix for the k^{th} principal direction. Therefore, in each principal direction, if all modes are included in the summation, it can be proved [33] that:

$$\sum_{n=1}^{N} \frac{\left(\frac{\alpha_n^2}{M_n} \right)_k}{M_{Tk}} = 1$$

The effective modal mass ratios for the first nine modes are tabulated in Table 8.2. It can be found that the total effective modal masses of the first nine modes are 92.9, 91.4 and 97.2 percent of the corresponding total mass in the longitudinal, transverse and torsional directions, respectively. Table 8.2 also shows the participation factor in three principal directions, the vibration periods and the circular frequencies of the first nine modes. It can be seen that the first, the fifth and the eighth modes are primarily in the transverse direction.

Modal Combination

The normalized response spectra given by SEAOC [47] was first scaled with a factor of $\frac{1}{R_w}$ (Fig. 8.4) and applied in both translational directions for the three-dimensional ETABS model. The peak floor displacements, story drifts, story forces, story shears and member forces were combined in a statistical manner using the Complete Quadratic Combination (CQC) procedure [61] with 5% damping for all modes considered. The CQC method is based on random vibration theories and requires that all modal response terms be combined using the following equation:

$$q_k = \left[\sum_i \sum_j q_{ki}\ \rho_{ij}\ q_{kj}\right]^{1/2} \tag{8-1}$$

where q_{ki} is the k^{th} component of the i^{th} spectral modal response vector, $Q_i^{\max}$. The spectral modal response vector, $Q_i^{\max}$, can be the displacement vector or any associated force vector. The cross-modal coefficients, ρ_{ij}, are functions of the duration and frequency content of the loading and of the modal frequencies and damping ratios of the structure. If the duration of an earthquake is relatively long compared to the fundamental period of the structure, and if the response spectrum is smooth over a wide range of frequencies, then these coefficients can be approximated as cross-correlations between modal responses. For constant modal damping, ζ, the cross-modal coefficient, ρ_{ij}, reduces to:

$$\rho_{ij} = \frac{8\zeta^2(1+r)r^{3/2}}{(1-r^2)^2 + 4\zeta^2 r(1+r)^2} \tag{8-2}$$

where $r = \frac{\omega_i}{\omega_j}$, is the ratio of the corresponding modal frequencies. The complete development of the CQC method for more general cases can be found in reference [62]. Note that when $r = 1$, Eq. 8-2 gives $\rho_{ij} = 1.0$. For $r \leq 0.67$ and $\zeta = 0.05$, $\rho_{ij} \leq 0.055$. This demonstrates that the cross correlation between modal responses diminishes rapidly when the corresponding modal frequencies are well separated. The well

known Square-Root-of-Sum-of-Square (SRSS) is merely a special case when the cross correlations between two different modes approach zero. For our case, the cross-modal coefficients for the first nine modes are tabulated as follows:

Mode	1^{st}	2^{nd}	3^{rd}	4^{th}	5^{th}	6^{th}	7^{th}	8^{th}	9^{th}
1^{th}	1	0.7576	0.0419	0.0069	0.0065	0.0027	0.0024	0.0021	0.0013
2^{nd}	0.7576	1	0.0542	0.0079	0.0074	0.0030	0.0027	0.0024	0.0014
3^{rd}	0.0419	0.0542	1	0.0251	0.0227	0.0070	0.0061	0.0053	0.0029
4^{th}	0.0069	0.0079	0.0251	1	0.9184	0.0423	0.0332	0.0258	0.0108
5^{th}	0.0065	0.0074	0.0227	0.9184	1	0.0483	0.0374	0.0287	0.0116
6^{th}	0.0027	0.0030	0.0070	0.0423	0.0483	1	0.7414	0.3779	0.0519
7^{th}	0.0024	0.0027	0.0061	0.0332	0.0374	0.7414	1	0.6769	0.0696
8^{th}	0.0021	0.0024	0.0053	0.0258	0.0287	0.3779	0.6769	1	0.1035
9^{th}	0.0012	0.0014	0.0029	0.0108	0.0116	0.0519	0.0696	0.1035	1

The most significant cross-correlations can be seen between the fourth and fifth modes. The resulting maximum base shears obtained by the CQC procedure were 756.8 kips and 739.7 kips in the longitudinal and the transverse directions, respectively. Therefore, the response maximums were scaled as follows:

(1) The maximum story displacements and the maximum story drifts were scaled down with factors of 400/756.8 and 400/739.7 for the event in the longitudinal and transverse directions, respectively. The resulting maximum story forces, story shears, floor displacements and story drifts for the transverse frame are tabulated in Table 8.1 along with the specified static lateral forces and the associated responses described previously.

(2) The maximum forces in each member were scaled down with factors of 438/756.8 and 438/739.7 for the event in the longitudinal and transverse directions, respectively.

From Table 8.1, it can be seen that the maximum story shear force distribution, column 6, obtained from the CQC procedure is more of an uniform type rather than a triangular distribution with a concentrated force at the roof level, column 2, obtained from the prescribed static force procedure. As a result, the floor displacement, column 8, and the story drift, column 9, of each floor obtained from the CQC procedure are substantially larger than those, columns 4 and 5, obtained from the static force procedure. The scaled maximum member forces obtained above were checked as for the static cases. The stress ratios of all members were found to be well below that allowed. In all ETABS analyses, the $P-\Delta$ effects were considered approximately using linearized geometric stiffness terms in the structural stiffness matrix [63]. Therefore, the lengthening of the period and the change of mode shapes due to $P-\Delta$ effects were accounted for.

8.2.3 Beam-Column Panel Zone Designs

Based on the results from these elastic analyses, the member sizes of the MRF described above were taken. The sizes of the beam and the column are shown in Fig. 8.3. The frame is symmetrical with respect to the frame center line. The floor girders shown in the center bays were also used in two end bays. All members are of A36 grade steel. However, for the purposes of this analytical investigation, three final MRF designs for the transverse frame with different panel zone designs were determined as follows:

Design 1

The doubler plate thicknesses were determined based on SEAOC provisions as follows:

The panel zone design shear force is:

$$V_E = \frac{\Sigma M}{0.95 d_b} - H \tag{8-3a}$$

where the column shear, H, is:

$$H = \frac{\Sigma M}{L_h} \tag{8-3b}$$

and

$$\Sigma M = M_{DL} + M_{LL} + 1.85 \times M_E \tag{8-4}$$

where d_b and L_h are the beam depth and column height, M_{DL}, M_{LL} and M_E are the bending moments due to dead, live and the prescribed seismic load respectively. The doubler plates were sized so that the panel zone shear force did not exceed the strength given as:

$$V = 0.55 F_y d_c t \left[1 + \frac{3 b_c t_{cf}^2}{d_b d_c t} \right] \tag{8-5}$$

In Eq. 8-5, t includes the thickness of doubler plate and other terms are as defined in Fig. 5.9. The resulting doubler plate requirement is shown in Table 8.3 for one typical exterior and interior columns. Since the requirement is negligible, it was decided that no doubler plate was to be provided for MRF Design 1. The member sizes for MRF Design 1 can be found in Fig. 8.3.

Design 2

The design shear force for the panel zone joints was increased using the flexural strength of the beams framed into the joint, ΣM_p, rather than the bending moments as defined in Eq. 8-4. The required and the as-provided doubler plates are shown in Table 8.3. The doubler plates provided are also shown in Fig. 8.6 near the intersections of beams and columns along with the member sizes.

Design 3

The doubler plate thicknesses were determined based on 80% flexural strength of the beams framed into the joint, $0.8 \times \Sigma M_p$, rather than the bending moments as defined in Eq. 8-4. The required and the as-provided doubler plates are tabulated in Table 8.3. The doubler plate thicknesses and the member sizes are shown in Fig. 8.7.

In all designs, except Design 1, doubler plate thicknesses were rounded to the nearest 1/16 inch with a minimum thickness of 3/8 inch whenever a doubler plate was required.

As a result, except in Design 1, the joint shear strength was always greater than that required by Eq. 8-3. As mentioned previously, the actual flexibility of the joints was not considered in the formulation of structural stiffness when the ETABS analyses were performed. Instead of modeling the joints explicitly, it was assumed in ETABS that the member lengths were the clear spans plus a certain portion of the panel zone dimensions. Therefore, the elastic mode shapes and the vibration periods obtained would be identical for all three MRF designs if the ETABS computer program was used with the same rigid end offsets. As mentioned in Chapter 5, a nonlinear joint element was implemented and incorporated in the ANSR-1 [40] computer program where the effects of joint flexibilities can be considered. The effects of the flexible joints can be examined.

8.3 ANSR-1 Models

In order to assess the nonlinear behavior of tall steel MRFs, the proposed twenty-story MRFs, having fundamental periods larger than 3.5 seconds, were further studied using the ANSR-1 [40] program. For the purposes of this analytical investigation, only two dimensional models for the transverse frame were studied in order to reduce the amount of data which would have been generated from the analyses of complete three-dimensional models. Without considering torsional effects, it was assumed that 50% of the lateral force was resisted by the transverse frame. Each floor diaphragm was assumed to be rigid in its own plane, and the ground floor was laterally restrained with rollers to account for the rigidity of the basement wall (Fig. 8.5).

As mentioned in Chapter 5, the value of viscous damping for the MRF models was assumed to be 3%, unless otherwise noted, of the values of the critical damping of the first two modes. The properties of the beam, column and joint elements of the MRF designs for the ANSR-1 analyses were determined using the methods described in Sections 5.6.3 and 5.7.4. These results are based on a steel yield strength of 36 ksi. The strain hardening ratios were set at 4% for all beams, columns and joints, unless otherwise noted. The

Modulus of Elasticity and Poisson's Ratio for steel were assumed to be 29,000 ksi and 0.25, respectively. As noted in Eq. 5.52, the specification of a_o, the ratio of the total panel zone thickness to column web thickness, allows various joint stiffnesses to be formulated conveniently.

As described in Section 5.7, the yield strength of the joint element was given in Eq. 5-52d:

$$M_y^* = a_o \frac{\sigma_y}{\sqrt{3}} t_w^c \, d_c \, d_b$$

It was assumed that the effects of the column axial force, the column shear force and the column flange thickness canceled each other out. This approximate yield strength well agrees with the results found in the nonlinear finite element studies described in Chapter 6. It also agrees with the strength at first yield of the beam-column panel zone subassemblages tested in the past experimental studies [9,14,49,51]. In these experimental studies, panel zone joints also exhibited significant reserve strength after the first yield. It may seem conservative in defining the yield strength of the joint element at first yield of the panel zone while specifying the beam yield strength as the plastic moment capacity, M_p, of the bare steel section. However, since the strength contribution of the floor slab is not included in the strength of the girder, the conservatism of the yield strength for the joint element is believed to be insignificant.

For MRF Design 2, in which the panel zone joint design incorporated the beam plastic moment capacity, the relationship of the yield strength of the joint element and the beam element in the ANSR-1 model can be evaluated as follows:

Equating the design strength and the design force for MRF Design 2 gives:

$$0.55\sigma_y d_c t = \frac{\Sigma M_p}{0.95} d_b - \frac{\Sigma M_p}{L_h} \qquad \text{(8-6a)}$$

or

$$\frac{\sigma_y}{\sqrt{3}} d_c d_b t = (1.11 - 1.05 \frac{d_b}{L_h}) \Sigma M_p \tag{8-6b}$$

where t is the total thickness of the panel zone joint. For typical $W27$ beams and a typical floor-to-floor height, L_h, of 12.5 feet, the value in the parenthesis is about 0.92. Clearly, depending upon the panel zone thickness provided, the yield strength for the joint element, M_y^*, given in Eq. 5-52d may be smaller than the sum of the plastic moment capacity of beams framed into the joint. Therefore, in ANSR-1 model for MRF Design 2, the joint element may still have yielded before the hinge formed in the beams framed into the joint unless the joint strength or the doubler plate provided is significantly larger than it was designed for.

Therefore, in order to assess the plastic rotational demand of floor beams and the effects of overstrength of panel zone joints in the proposed MRF, joint elements with a larger yield strength were considered for MRF Model 4 as follows:

Model 4

Using the member sizes and the doubler plates of MRF Design 2, MRF Model 4 incorporated the column flange contributions into the formulation of the yield strength for the joint element. That is:

$$M_y^* = a_o \frac{\sigma_y}{\sqrt{3}} t_w^c d_c d_b \left[1 + \frac{3 b_c t_{cf}^2}{d_b d_c t} \right] \tag{8-6}$$

Since the stiffness of the joint element remained unchanged as given in Eq. 5-52c, the elastic mode shapes and periods were identical to those of MRF Design 2.

The gravity load was based on the tributary beam load taken by the transverse frame, and the weight of the facade was assumed uniformly distributed to the spandrels. The gravity load was applied to the MRF models by specifying fixed end forces at the beam-column intersections. As noted previously, the transverse frame in line 1 carries 50% of the lateral force in the transverse direction while carrying only about 12.5% of the floor

gravity load. Since the floor was assumed rigid and the lateral force is completely resisted by the perimeter frame, the $P-\Delta$ effects of the interior core columns have to be taken by the perimeter frame. In order to account for the complete $P-\Delta$ effects of the structure, a special modeling technique is employed: an additional column line is introduced as shown in Fig. 8.5. The column is pin ended and connected to the two-dimensional frame at each floor level by a truss bar transferring only axial force. In the ANSR-1 model, the pin ended columns and the truss bars are members with very large cross-sectional areas and small moments of inertia. The $P-\Delta$ effects from the leaning core columns can be included by loading the pin ended columns at each floor level with the tributary gravity load from the leaning columns.

8.4 Static Deformation Characteristics of the 20-Story MRFs

8.4.1 Effects of Panel Zone Flexibilities

As mentioned previously, the effects of panel zone flexibility can be approximately accounted for by formulating the member stiffness based on the member clear span plus certain portions of the beam-column joints. This approximate method, which requires no additional joint element and minimizes the total number of equations that has to be solved, has been widely accepted in the industry without considering the relative stiffness and the dimension of the panel zone joint with respect to the connecting members. The accuracy of the approximation is believed to be dependent on the ratio of the panel zone dimension to the member length as well as the panel zone relative stiffness. The effectiveness of this approximated method can be studied by using the joint element incorporated in the ANSR-1 program [40] and the results can be compared with that obtained by adjusting the member length in formulating member stiffness [43].

In order to examine the effects of the various doubler plate designs in MRF Designs 1, 2 and 3 and the approximated method in computing lateral displacements, the results of

several static analyses using both the ANSR-1 and the ETABS [43] programs can be compared. The member stiffness of two MRF models in ETABS analyses, denoted as 50% Rigid and 0% Rigid, were based on the member clear span plus 50% and 100% of the panel zone dimensions, respectively. As described in Sections 8.2.3 and 8.3, panel zone joints designed for $1.85E$, M_p and $0.8M_p$ have been incorporated into the ANSR-1 models for MRF Designs 1, 2 and 3, respectively. These ANSR-1 models incorporated the actual panel zone thickness in formulating the stiffness for each joint element. The frame lateral displacements of these models resulting from the prescribed seismic forces described previously are tabulated in Table 8.4. The resulting lateral displacements along the height of the building are also plotted in Fig. 8.8. Note that the $P-\Delta$ effects were incorporated in computing the lateral displacements for all models. Table 8.4 also shows the first five vibration periods for each model obtained from the associated analysis.

From Table 8.4 and Fig. 8.8, it can be seen that the ETABS model considering 50% rigid beam-column intersections grossly underestimated the lateral displacements of all MRF designs while the model with center-to-center line stiffness predicted the lateral displacements of MRF Design 2 in which panel zone joints were designed for M_p of the beams. The roof displacement obtained from the ETABS 50% Rigid model is about 73%, 87% and 82% of that obtained from the ANSR-1 models for MRF of Designs 1, 2 and 3, respectively. Obviously, the ETABS 0% Rigid model showed better performance. The roof displacement obtained with this model is about 83%, 99% and 94% of that obtained with MRF models for Designs 1, 2 and 3, respectively. The error is still large when the panel zone joints are relatively flexible as in the model for MRF Design 1.

8.4.2 Corrections of Elastic Story Drifts to Account for Joint Deformations

Since most of the structural analysis programs currently used in the building industry [32,43] do not allow the panel zone joint to be modeled explicitly, a methodology which incorporates the panel zone deformations into the drift calculations is useful. For this

reason, a method which incorporates average panel zone joint deformations in each floor into the corresponding story drift was examined.

In this study, MRF Design 3 was used as the model structure. First, the modified ANSR-1 model for MRF Design 3 was statically loaded with the prescribed seismic forces in the analysis Run 1. The modifications made for the ANSR-1 model, using a very large stiffness for all joint elements, are meant to exclude the panel zone deformations from the frame lateral displacement. This makes it equivalent to a MRF model whose member stiffness formulation is based strictly on the member clear span. The resulting story drift for the analysis RUN 1 is tabulated in column 7 of Table 8.5. Secondly, using the beam end moments obtained from the analysis RUN 1, the panel zone deformation, γ, of each joint was then estimated as follows:

$$\gamma = \frac{\Sigma M}{G\ d_b\ d_c\ t} \tag{8-7}$$

where ΣM is the sum of the bending moments due to the gravity and lateral load of beams which framed into the joint, d_b, d_c, and t are the beam depth, the column depth and the panel zone thickness, respectively. The resulting panel zone deformation in each joint is tabulated in columns 2 through 5 of Table 8.5. In column 6 of the table, the average of the four joint deformations for each floor is also tabulated. The sum of the components in columns 6 and 7 for each floor is tabulated in column 8. The story drifts tabulated in column 8 can be viewed as the corrected story drifts for the inclusion of panel zone deformations.

Finally, an unmodified ANSR-1 model, using the actual panel zone thickness in formulating the joint stiffness, was analyzed in the analysis RUN 2. The resulting story drift is tabulated in column 9 of the Table 8.5. In both analyses RUN 1 and RUN2, the $P-\Delta$ effects were deliberately excluded. Therefore, the performance of the method described above can be assessed by directly comparing the results tabulated in columns 7, 8 and 9. Story drift ratios, obtained from dividing the value in column 7 by that in column 9 are

tabulated in column 10, indirectly demonstrate the participation of panel zone deformations in the total story drift of each floor. It can be seen in column 10 of Table 8.5 that panel zone deformations can contribute as much as 27% of the total story drift in the fifth floor of MRF Design 3. Story drift ratios, obtained by dividing the value in column 8 by that in column 9 are tabulated in column 11, indicate that the simple method described above can provide satisfactory results in correcting the story drifts. A better result can be expected if the average panel zone deformations, tabulated in column 6, of two adjacent floors can be further averaged for the associated story drift correction.

In summary, the method incorporates the actual panel zone stiffness provided in each joint in calculating the story drifts under any prescribed lateral forces. It can be applied easily in the design offices where panel zone joint stiffness can not be modeled directly using regular structural analysis programs.

8.4.3 $P-\Delta$ Effects

The significance of the joint flexibilities and the $P-\Delta$ effects in computing the total lateral displacement for the proposed 20-story MRF can be examined by plotting the lateral displacements obtained from various MRF models.

In this study, the lateral displacements under the prescribed lateral force obtained from previous analyses RUN 1 and RUN 2 are plotted in Fig. 8.9 together with the analysis RUN 3 which incorporated the joint element as well as the $P-\Delta$ effects for the MRF Design 3. It can be seen in Fig. 8.9 that the $P-\Delta$ effect is significant. In order to further assess its significance, the total story drift can be divided into three components, namely: the beam-column component, components due to panel zone flexibilities and the $P-\Delta$ effects. The story drift components due to the beam-column deformations can be computed directly from the relative story displacements obtained from the analysis RUN 1 and is tabulated in column 2 of Table 8.6. The story drift components due to the panel zone deformations and the $P-\Delta$ effects can be obtained by taking the differences of the

lateral displacements obtained between RUN 2 and RUN 1, RUN 3 and RUN 2, respectively. These three drift components of each floor are shown in columns 2 to 4 of Table 8.6 and are plotted in Fig. 8.9. Their relative contributions to the total story drift were further computed and are shown in column 5 to 7 of Table 8.6. It can be seen from Fig. 8.9 and Table 8.6 that the contributions due to the panel zone deformations and the $P-\Delta$ effects are quite significant, especially toward the lower floors of the MRF. From Table 8.6, it can be seen that the contribution of the panel deformations to the total story drift is as high as 23.7% in fifth floor while that of the $P-\Delta$ effects contribute as much as 10% of the total story drifts in the lower floors.

Note that the panel zone joints of MRF Design 1, with doubler plates designed for $1.85M_p$, are even more flexible than those of MRF Design 3 in which $0.8M_p$ of beams have been used to design the panel zone joints. These clearly indicated that both the panel zone deformations and the $P-\Delta$ effects can be significant and should be considered in the analysis and design of the proposed MRF.

8.5 Dynamic Characteristics of the MRFs

The panel zone joint flexibilities also affect the vibration periods of the whole structure. As mentioned previously, Table 8.4 shows the first five periods of each model. Note that the $P-\Delta$ effects were incorporated [63] in the ETABS models. However, in the ANSR-1 models, the vibration periods and mode shapes were computed prior to the calculation of column axial forces, therefore, the $P-\Delta$ effects were not considered. In order to account for the $P-\Delta$ effects in computing the period for the ANSR-1 model, an alternative using Rayleigh method, as described in Section 7.4.3, can be adopted. In general, the $P-\Delta$ effects lengthen the period but are negligible in comparison with the effects of the flexible joint. From Table 8.4, it can be seen that the first mode period for the ETABS 0% Rigid model is about 1.08 times that for the 50% Rigid model. Similarly, the first mode period of the ANSR-1 model for MRF Design 1 is about 1.08 and 1.05 times those

for MRF Designs 2 and 3, respectively. Similar ratios for other modes can be found between these models. Without using the joint element explicitly, there seems no direct way of incorporating panel zone flexibilities into the calculations of vibration period. Incidently, the ETABS model with 0% rigid joints predicted the first five periods of the ANSR-1 model for MRF Design 3 well, as shown in Table 8.4.

The first three mode shapes of the ANSR-1 models for MRF Designs 1, 2 and 3 are shown in Table 8.7 and Fig. 8.11. It can be seen from the figure that the shapes for Designs 1, 2 and 3 of any of these three modes are similar to each other. It somewhat indicates that the effects of the panel zone stiffness in the computations of mode shapes for the proposed twenty-story MRF are relatively insignificant.

In order to evaluate the distribution of floor lateral deformations in each mode shape, a relative story drift index was computed for each floor using the mode shape components as the floor lateral displacements. For this purpose, the first three mode shapes of the ANSR-1 model for MRF Design 3 were used. The intent of this work is to examine the relative deformation demands among all floors when the frame oscillates in each specific mode. The resulting normalized relative story drift indices for the first three modes are plotted in Fig. 8.12. These drift indices shown in the figure have been normalized and indicate the relative deformation demand in each floor for the associated vibration mode. It can be seen from the figure that larger story deformations can be expected at the third floor through tenth floor if the MRF is vibrating in its first mode. Larger deformation demands occur at the fourteenth through seventeenth floors and the ninth to tenth or seventeenth to nineteenth floors for the second and third modes, respectively. The deformations of members or joints are expected to be more severe in these floors when the frame is excited predominately in the corresponding mode.

8.6 Dynamic Characteristics of the Selected Ground Accelerations

8.6.1 Selections of Ground Acceleration

Several earthquake records were used to assess the dynamic performance of the 20-story MRF designs. Moreover, in order to realistically assess the extent of nonlinearities within the structure, the earthquakes selected had to be representatives of actual, strong earthquake motions. Accordingly, four ground acceleration inputs were chosen as follows.

(1) The N65E component of the first twenty seconds of the original 1966 Parkfield Earthquake possessed a peak ground acceleration of 0.49 g. This event is denoted as *PK*. The original record was recorded at a site 200 feet away from the fault rupture. Therefore, the event exhibited near-fault ground motion characteristics with impulsive types of excursions.

(2) The NS component of the first twenty seconds of the original 1940 El Centro Earthquake was scaled to a peak ground acceleration of 0.5 g by a factor of 1.5. This event is denoted as *1.5EC*. The original record of this earthquake was recorded in the epicentral area during the earthquake and is considered to be a strong motion record [56] and has been widely used in earthquake engineering.

(3) The NS component of the first ten seconds of the original 1978 Miyagi-Ken-Oki Earthquake which possessed a peak ground acceleration of 0.26 g was scaled to a peak ground accceleration of 0.39 g by a factor of 1.5. This event is denoted as *1.5MO*.

(4) The EW component of the first eighty seconds of the original 1985 Mexico Earthquake possessed a peak ground acceleration of 0.17 g. This event is denoted as *MX*.

8.6.2 Acceleration Histories, Fourier Amplitudes and the Associated Response Spectrum

The peak ground acceleration can be obtained directly from the acceleration history of the corresponding earthquake. However, the magnitude of the peak ground acceleration has no direct indication of its frequency contents and the response that the given structure may undergo. Therefore, it is useful to obtain the associated Fourier amplitudes and the response spectra for a range of structures with a certain damping ratio. For this reason, the ground acceleration history, the associated Fourier amplitude and the linear elastic pseudo-acceleration spectra for 2 and 5 percent damping ratios were computed and plotted in Figs. 8.13 through 8.16 for events PK, $1.5EC$, $1.5MI$ and MX, respectively. In Figs. 8.17 through 8.20, three response spectra quantities of various damping ratios are also plotted on a tripartite diagram for events PK, $1.5EC$, $1.5MI$ and MX, respectively.

In these linear elastic response spectra, the extent of response to the ground acceleration can be readily obtained for any given elastic single-degree-of-freedom (SDOF) system with specific period and damping. However, the limitation in its application is that the response is assumed to be linearly elastic. Nonlinear response spectra can be constructed using a strength ratio for the bilinear SDOF system [52]. Nevertheless, the amount of each elastic modal response to be expected is still a very significant indication of the ground-motion intensity to a multi-degree-of-freedom system. In Fig. 8.21, elastic response spectra for 3% damping system are plotted compositely for all selected earthquake events. In this figure, the vibration periods of the first three modes for MRF Designs 1, 2 and 3 are also indicated. Note that the vibration period will be lengthened somewhat once the nonlinearities in the system take place as observed in some experimental research [58].

By inspecting the periods of the proposed MRFs and the corresponding spectral pseudo-accelerations, it can be seen from Fig. 8.21 that the second and the third modes are expected to be well excited by event PK and event $1.5MO$. Moreover, event $1.5EC$, widely used in earthquake engineering research, appears to possesses least damage potential to the proposed MRFs among the selected earthquake events. Event MX, the original

1985 Mexico Earthquake, possesses the largest spectral pseudo-acceleration value for the first mode of the given MRFs while excites the second and the third modes relatively insignificantly. However, the effects of one key element in the earthquake motion, the duration of the significant accelerations, is of particular interest in our study.

8.7 Nonlinear Dynamic Analyses of the 20-Story MRFs

In order to assess the nonlinear behavior of the proposed MRF designs, several nonlinear dynamic analyses using the ANSR-1 program were performed. The selected earthquake events mentioned in Section 8.6 were used as the input ground motions for each ANSR-1 model. As described previously, the analytical models for MRF Designs 1, 2, and 3 incorporate panel zone joints designed for $1.85M_E$, M_p and $0.8M_p$, respectively. The MRF Model 4 possesses the same panel zone joint stiffness as that for the model of MRF Design 2 but with a larger yield strength for joint elements. In all analyses, the $P-\Delta$ effects incorporating the interior leaning core columns were considered. The resulting story shears, story displacements and story drifts obtained from these analyses were studied. The extent of the panel zone joint deformation, the maximum plastic hinge rotations of the beams, the columns and the panel zone joints of each model during each earthquake event were also examined. In examining the dynamic behavior of the proposed MRF designs, it was found that the plots of mode shapes, the associated story drift indices and the pseudo-acceleration spectrum for the selected earthquakes as shown in Figs. 8.11, 8.12, and 8.21, respectively, are particularly useful. The results are summarized for each event as follows.

8.7.1 Response to the Parkfield Earthquake

8.7.1.1 Maximum Floor Displacements During Event *PK*

In Fig. 8.22, the floor displacement envelopes of each MRF design and the corresponding floor displacements at instances when the maximum roof displacement occurred during the event are plotted. It can be found in Fig. 8.22a that the participation of the second and the third modes in floor displacements was quite obvious for all MRF designs. The stiffest model, MRF Design 2, experienced the largest roof displacement while the roof of the least stiff model, MRF Design 1, deformed least severely among all of the MRF designs. However, the relatively larger floor displacements which occurred in the lower floors of MRF Design 1 indicate that the participation of the second mode is more pronounced in MRF Design 1 than in the other two MRF designs. This can be concluded by inspecting the plot of the second mode shape in Fig. 8.11 and the corresponding drift indices shown in Fig. 8.12.

8.7.1.2 Maximum Story Shears and Maximum Story Drifts During Event *PK*

The maximum story shears and maximum story drifts that occurred during the event in each MRF design are plotted in Fig. 8.23. The shapes of the maximum story shears also suggest the strong participation of the second and third modes. Moreover, MRF Design 2, the stiffest MRF of all designs, attracted more story shear in each floor than did the other two MRF designs. On the other hand, MRF Design 1, the least stiff design, was subjected to the least story shears among those observed in the three MRF designs. This can be rationalized from the psuedo-acceleration spectra, as plotted in Fig. 8.21, even though the difference in the story shears for MRF Designs 1 and 2 is quite substantial in the tenth floor through the fifteenth floor. This may well attribute to the sharp decrease of the spectral pseudo-acceleration within the period range for the third mode. Note that MRF Design 2 is subjected to a maximum base shear of about 600 kips, almost three times the code prescribed base shear noted in Section 8.2. Moreover, the shape of the maximum story shear envelopes do not suggest a high concentrated force applied at the roof level as

required by the static lateral force procedure in the code.

The maximum story drifts of each floor which occurred during the event are plotted in Fig. 8.23 for MRF Designs 1, 2, and 3. From the figure, it can be found that the maximum story drift that occurred among all MRF designs is about 1.7 percent or 0.017 radians. Although the variation of the maximum story drifts along the building height is large in all MRF designs, all designs are considered to have performed adequately. MRF Design 1, the least stiff design, exhibited smaller story drifts at most floors than did the other two MRF designs. The maximum story drift that occurred during the event is at the twelfth floor of MRF Design 2 and is about 6.8 times that allowed under the code prescribed lateral force.

8.7.1.3 Effects of Panel Zone Joint Overstrength on Floor Displacements and Story Shears During Event *PK*

The effects of panel zone joint overstrength on maximum response can be studied by plotting the response envelopes for MRF Design 2 and Model 4. In Fig. 8.24, it can be found that MRF Model 4 experienced slightly larger floor displacements. However, the maximum floor displacements for MRF Model 4 are almost identical to those for MRF Design 2. In Fig. 8.25, it can be seen that the maximum story shears and the maximum story drifts for MRF Model 4 are somewhat larger than those for MRF Design 2, but the differences are negligible.

8.7.1.4 Maximum Panel Zone Deformations During Event *PK*

The maximum panel zone joint deformations of each MRF design are tabulated in Table 8.8. It can be found in the table that the maximum total panel zone deformation which is as high as 0.0119 radians occurred at the thirteenth floor on the column line C of MRF Design 1. The maximum panel zone deformations of MRF Designs 2 and 3 are 0.0095 and 0.01186 radians, respectively. The extent of the maximum panel zone

deformations in the frame can be best understood by plotting each panel zone deformation on the frame elevation. As shown in Fig. 8.26, maximum panel zone deformations of each MRF design are plotted using circles of radii corresponding to the associated panel zone deformation. The center of the circle is located at the center of the beam-column intersection.

In Fig. 8.26, a circle of one quarter-inch radius is equivalent to 0.01 radians of panel zone deformation as indicated above the plot for MRF Design 2. Note that the panel zone deformations shown in Table 8.8 and Fig. 8.26 are the total deformation that occurred in each joint. The yield deformation of the panel zone joint is defined as the average shear yield strain of the panel zone. Therefore, the yield deformations for all panel zone joints are identical and can be computed as follows:

$$\gamma_y = \frac{M_y^*}{k_e^*} = \frac{\sigma_y}{G\sqrt{3}} = 0.00186 \ \ radians \tag{8-8}$$

where M_y^* and k_e^* are the yield moment and the elastic stiffness of the joint as defined in Eqs. 5-52c and 5-52d, σ_y and G are the yield strength and the elastic shear modulus, respectively. A yield circle of radius corresponding to the yield joint rotation is also shown in Fig. 8.26 above the plot for MRF Design 3. In Fig. 8.26, a circle of radius larger than that of the yield circle implies the formation of a plastic hinge at the corresponding joint.

In Table 8.8, it can be found that the largest panel zone deformations occurred during the event are about 6.4, 5.1 and 6.4 times the yield deformation for MRF Designs 1, 2 and 3, respectively. Moreover, the extent of the panel zone deformations is more severe at the tenth floor through fifteenth floor for each MRF design. The extent of the panel zone plastic rotations can be obtained by subtracting the yield rotations from the total panel zone deformations.

8.7.1.5 Maximum Beam, Column and Panel Zone Joint Plastic Hinge Rotations During Event *PK*

Using circles of various radius, the extent of the plastic hinge rotations for the beams, columns and panel zone joints in MRF Designs 1, 2, 3 and Model 4 are plotted in Figs. 8.27, 8.28, 8.29, and 8.30, respectively. The center of the circle for a beam or a column end hinge rotation is located at a point two feet from the associated beam-column intersection. In Figs. 8.26 through 8.30, a circle of one-quarter inch radius has been deliberately chosen to represent a plastic deformation of 1% or 0.01 radians. Therefore, the extent of the element deformations among various MRF designs as shown in Figs. 8.26 through 8.30 can be directly cross-compared. Note that the circles in Fig. 8.26 indicate the total panel zone deformations.

From these figures, the number of the panel zone hinges formed during the event are found to be 49, 42, 39 and 37 for MRF Designs 1, 2, 3 and Model 4, respectively. Although MRF Design 1, designed to have the weakest panel zone strength, developed more panel zone hinges than any other MRF design did, the extent of the hinge deformations and their distribution through the entire frame is more uniform when compared with other MRF designs. It can be seen from these figures, the largest panel zone joint plastic rotation, about 1% or 0.01 radians, occurred in both MRF Designs 1 and 3. Comparing Figs. 8.28 and 8.30 for MRF Design 2 and Model 4, respectively, the effects of the panel zone overstrength on the extent and distribution of hinge formations can be found insignificant.

The extent of the beam and column hinge formations vary greatly between different MRF designs. When the panel zone joint strength approaches the corresponding beam flexural strength, as in MRF Design 2, the beam plastic rotation demand greatly increases. Even in MRF Design 2 and MRF Model 4, where the panel zone joint strength approaches the beam strength, only a few plastic hinges were formed in the columns. In regards to the strong-column/weak-girder principle, the beam and the column strength for the proposed

twenty-story MRF appears to be well proportioned. The maximum beam plastic rotation of 0.712% or 0.00712 radians occurred in the twelfth floor of MRF Model 4. During the event, most of the beam plastic hinges were formed on beams located between the tenth and the fifteenth floors of MRF Design 2 and Model 4. Very few beam plastic hinges were formed in MRF Designs 1 and 3 and their plastic rotations are small.

8.7.2 Response to the 1.5*El Centro Earthquake

8.7.2.1 Maximum Floor Displacements During Event $1.5EC$

In Fig. 8.31, the floor displacement envelopes of each MRF design and the corresponding floor displacements at instances when the maximum roof displacement occurred during the event are plotted. As can be expected from the psuedo-acceleration spectra as shown in Fig. 8.21, the maximum displacement of each floor as shown in Fig. 8.31 is substantially smaller than that which occurred during event PK. Moreover, the participation of the second and the third modes in floor displacements appears to be less pronounced. Similar to what occurred during event PK, the stiffest model, MRF Design 2, experienced the largest roof displacement while the roof of the least stiff model, MRF Design 1, deformed least severely among all the MRF designs.

8.7.2.2 Maximum Story Shears and Maximum Story Drifts During Event $1.5EC$

The maximum story shears and maximum story drifts that occurred during the event in each MRF design are plotted in Fig. 8.32. MRF Design 2, the stiffest of all MRFs, attracted more story shear in each floor, except in the ground floor, than did the other two MRF designs. MRF Design 1, the least stiff design, was subjected to the least story shears among those observed in the three MRF designs. Similar to the case in event PK, this can be rationalized from the psuedo-acceleration spectra as plotted in Fig. 8.21. The difference in the story shears for MRF Designs 1 and 2 is also quite substantial in the seventh floor

through the thirteenth floor. This may attribute to the relatively larger spectral pseudo-acceleration near the period range for the third mode. Note that MRF Design 3 is subjected to a maximum base shear of about 470 kips, about 2.35 times the code prescribed base shear.

The maximum story drifts of each floor which occurred during the event are also plotted in Fig. 8.32 for MRF Designs 1, 2, and 3. From the figure, it can be found that the maximum story drift of most floors is well below 1.0 percent or 0.010 radians for all MRF designs. Although the variation of the maximum story drifts along the building height is large in all MRF designs, this event is not considered to be a strong earthquake for the proposed MRF designs. MRF Design 1, the least stiff design, exhibited smaller story drifts at most floors than did the other two MRF designs. The maximum story drift that occurred during the event is at the ninth floor of MRF Design 2 and is about 3.8 times that allowed under the code prescribed lateral force.

8.7.2.3 Effects of Panel Zone Joint Overstrength on Floor Displacements and Story Shears During Event $1.5EC$

The maximum floor displacements which occurred during event $1.5EC$ are plotted in Fig. 8.33 for MRF Design 2 and Model 4. From the figure, it can be seen that the maximum floor displacements for both MRF Design 2 and Model 4 are almost identical. Since MRF Design 2 and Model 4 possess identical elastic stiffness and vibration periods, the response of these two MRF models will be very similar when the nonlinearities within each model are limited. The maximum story shears and maximum story drifts which occurred during event $1.5EC$ are plotted in Fig. 8.34 for MRF Design 2 and Model 4. It can be found from the figure that the difference in these responses can be neglected.

8.7.2.4 Maximum Panel Zone Deformations During Event $1.5EC$

In Fig. 8.35, maximum total panel zone deformations of each MRF design are plotted using circles of radius corresponding to the associated panel zone deformation. Similar to the plots for event PK, a circle of one quarter-inch radius is equivalent to 0.01 radians of panel zone deformation as indicated in the figure. A yield circle of radius corresponding to the yield joint rotation as defined in Eq. 8-8 is also shown in Fig. 8.35. In this figure, it can be found that the extent of the maximum panel zone deformations is well below 0.01 radians in most of the joints. Moreover, the extent of the maximum panel zone deformations among all floors is fairly uniform. The exception is in MRF Design 3 where relatively larger panel zone deformations are observed near the tenth floor.

8.7.2.5 Maximum Beam, Column and Panel Zone Joint Plastic Hinge Rotations During Event $1.5EC$

The extent of the panel zone plastic rotations was obtained by subtracting the yield rotations from the total panel zone deformations. Using circles of various radii, the extent of the plastic hinge rotations for the beams, columns and panel zone joints in MRF Designs 1, 2, 3 and Model 4 are plotted in Figs. 8.36, 8.37, 8.38, and 8.39, respectively. In Figs. 8.36 through 8.39, a circle of one-quarter inch radius also represents a plastic deformation of 0.01 radians as indicated in each figure.

From these figures, it can seen that the number of the panel zone plastic hinges decreases rapidly once the panel zone design strength increases. The number of the panel zone hinges formed during the event are found to be 47, 5, 22 and 2 for MRF Designs 1, 2, 3 and Model 4, respectively. Although MRF Design 1 developed more panel zone hinges than any other MRF design did, the extent of the plastic hinge deformations and their distribution through the entire frame is quite uniform. It can be seen from these figures, the largest panel zone plastic hinge rotation, occurred in both MRF Designs 1 and 3, is well below 0.01 radians. In all MRF designs and Model 4, none of the panel zone joints

was yielded and strain-hardened enough to cause a plastic hinge to be formed in a beam or column.

8.7.3 Response to the 1.5*Miyagi-Ken-Oki Earthquake

8.7.3.1 Maximum Floor Displacements During Event $1.5MI$

In Fig. 8.40, the floor displacement envelopes of each MRF design and the corresponding floor displacements at instances when the maximum roof displacement occurred during the event are plotted. From both Figs. 8.40a and 8.40b, it can be seen that the participation of the third mode in floor displacements was very significant. This behavior can be related to the pseudo-acceleration spectra which are shown in Figs. 8.15, 8.19 and 8.21 for event $1.5MI$. As shown in these response spectra, a sharp increase of the spectral value occurred at a period of about one second. Once nonlinearities occurred in the structure, the vibration period was lengthened, and the third mode period of MRF Design 1 may have been very close to one second during the event. Similar to the previous two earthquake events, the stiffest model, MRF Design 2, experienced the largest floor displacements, while the least stiff model, MRF Design 1, still deformed least severely among all of the MRF designs, in the direction of the negative displacement.

8.7.3.2 Maximum Story Shears and Maximum Story Drifts During Event $1.5MI$

The maximum story shears and maximum story drifts that occurred during the event in each MRF design are plotted in Fig. 8.41. The shape of the plots for the maximum story shears and story drifts also suggest the strong participation of the third mode. Similar to the case in previous events, MRF Design 2, the stiffest MRF in all designs, attracted more story shear in each floor than did the other two MRF designs; and MRF Design 1, the least stiff design, was subjected to the least story shears among those observed in the three MRF designs. The difference in the maximum story shears and story drifts among

various MRF designs is quite substantial in most of the floors. This may well attribute to the sharp changes in the spectral pseudo-acceleration within the period range for both the second and third modes. Note that MRF Design 2 is also subjected to a maximum base shear of about 600 kips, almost three times the code prescribed base shear. Moreover, the shape of the maximum story shear envelopes do not suggest a high concentrated force applied at the roof level as required by the static lateral force procedure in the code.

From Fig. 8.41, it can be found that the maximum story drift that occurred among all MRF designs is about 0.015 radians. The event appears to be a strong earthquake for the proposed MRF, and all MRF designs are considered to have performed adequately. The maximum story drift occurred at the sixteenth floor of MRF Design 2 and is about six times that allowed under the code prescribed lateral force.

8.7.3.3 Effects of Panel Zone Joint Overstrength on Floor Displacements and Story Shears During Event $1.5MI$

The maximum floor displacements of MRF Design 2 and Model 4 which occurred during the event are plotted in Fig. 8.42. In this figure, it can be found that MRF Model 4 experienced slightly larger floor displacements. In Fig. 8.43, where maximum story shears and story drifts are plotted, it can be seen that the maximum story shears and the maximum story drifts for MRF Model 4 are somewhat larger than those for MRF Design 2. As shown in both Figs. 8.42 and 8.43, the difference in response of MRF Design 2 and Model 4 at every floor is insignificant.

8.7.3.4 Maximum Panel Zone Deformations During Event $1.5MI$

The maximum total panel zone deformations of each MRF design are plotted in Fig. 8.44 using circles of radius corresponding to the associated panel zone deformation. Similar to the previous events, a circle of one quarter-inch radius is equivalent to 0.01 radians of panel zone deformation. The maximum panel zone deformation which was found to be

about 0.01 radians occurred in the column line C at the eleventh floor of MRF Design 1. Although the extent of the maximum panel zone deformations in MRF Design 1 is larger than those of the other two designs, the distribution of the maximum panel zone deformations in MRF Designs 2 and 3 is not as uniform and is concentrated in lower and higher floors, as shown in Fig. 8.44.

8.7.3.5 Maximum Beam, Column and Panel Zone Joint Plastic Hinge Rotations During Event 1.5*MI*

The extent of the panel zone plastic rotations was obtained by subtracting the yield rotations from the total panel zone deformations. Using circles of various radius, the extent of the plastic hinge rotations for the beams, columns and panel zone joints in MRF Designs 1, 2, 3 and Model 4 are plotted in Figs. 8.45, 8.46, 8.47, and 8.48, respectively. A circle of one-quarter inch radius was chosen to represent a plastic deformation of 1% or 0.01 radians as indicated in the figures.

From these figures, the number of the panel zone hinges formed during the event are found to be 60, 40, 52 and 33 for MRF Designs 1, 2, 3 and Model 4, respectively. Although MRF Design 1, designed to have the weakest panel zone strength, developed more panel zone hinges than did any other MRF design, the extent of the hinge deformations and their distribution through the entire frame is more uniform when compared with other MRF designs. It can be seen from these figures, the largest panel zone joint plastic rotation, about 0.9% or 0.009 radians, occurred in MRF Design 1. Comparing Figs. 8.46 and 8.48 for MRF Design 2 and Model 4, respectively, the effects of the panel zone overstrength on the extent and distribution of hinge formations can be found insignificant.

The extent of the beam and column hinge formations vary greatly between different MRF designs. When the panel zone joint strength approaches the corresponding beam flexural strength, as in MRF Design 2, the beam plastic rotation demand greatly increases. Even in MRF Design 2 and MRF Model 4, where the panel zone joint strength approaches

the beam strength, only a few plastic hinges were formed in the columns. In regards to the strong-column/weak-girder principle, the beam and the column strength for the proposed twenty-story MRFs appears to have been well proportioned. The maximum beam or column plastic rotations can be found well below 0.01 radians. During the event, most of the beam plastic hinges were formed on beams located between the second and the seventh floors, and the fifteenth through the nineteenth floors of MRF Design 2 and Model 4. Very few beam plastic hinges were formed in MRF Designs 1 and 3, and their plastic rotations are small.

8.7.4 Response to the Mexico Earthquake

8.7.4.1 Floor Displacement Histories During Event *MX*

In order to assess the effects of the long duration of this event, the frame lateral displacement histories of selected floors are plotted for MRF Designs 1, 2, 3 and Model 4 in Figs. 8.49 through 8.52, respectively. It can be seen from these figures that the sixth, eleventh, sixteenth and roof floors in each MRF design and Model 4, except in Design 1, are vibrating in the same phase. As shown in Figs. 8.49 through 8.52, the response of each MRF design and Model 4, except MRF Design 1, appears to be dominated by its first mode. By inspecting the pseudo-acceleration spectrum for the event, this seems to be justifiable from the fact that the spectral pseudo-acceleration near the period range for the second and third mode are not distinctively larger than that for the first mode. Moreover, they are not as large as those for the previous events. In MRF Design 1, however, once nonlinearities developed, the participation of the second mode in the response became more pronounced due to a rapid increase of the spectral pseudo-acceleration for the lengthened second vibration period of MRF Design 1 (Fig. 8.21).

In order to examine the effects of various panel zone designs, the roof displacement histories of MRF Designs 1, 2 and 3 are plotted in Fig. 8.53. It can be seen from the

figure that once large roof displacements occur, the roof displacement history differs from one design to another quite significantly. About 38 seconds after the start of the event, the roof displacement of the stiffest design, MRF Design 2, is almost 2.8 times that of MRF Design 1, the least stiff design. From Fig. 8.53, large variations in roof displacements of various designs can be observed at many instances. An attempt of correlating this with the linear response spectrum was not very successful. The complexities of the nonlinear dynamic behavior in the multi-degree-of-freedom system are evident. From Fig. 8.53, however, the effects of the duration of a severe event is distinguished. It can be seen from the figure that the roof displacement histories of MRF Designs 1 and 2 deviate greatly after forty seconds of shaking during which several large displacement cycles have occurred in MRF Design 2. During this event, the largest roof displacement which occurred in MRF Design 2 is about 28.3 inch, 120 percent of that which occurred during event *PK*.

8.7.4.2 Base Shear Histories During Event *MX*

The base shear history of each MRF design is plotted in Fig. 8.54. It can be seen from the figure that the divergence of the base shear histories of the designs is significant especially after the occurrence of a large number of base shear reversals. Moreover, MRF Design 2, the stiffest MRF of all designs, attracted more base shear at most instances than did the other two MRF designs. In the meantime, the MRF Design 1, the least stiff design, was subjected to the least base shear among those observed in the three MRF designs. A maximum base shear of about 520 kips or 2.6 times the code prescribed base shear occurred in MRF Design 2. This is about 14 percent smaller than the maximum base shear that occurred during events *PK* and 1.5*MI*.

8.7.4.3 Effects of Panel Zone Joint Overstrength on Roof Displacement and Base Shear During Event *MX*

The effects of panel zone joint overstrength on the response can be studied by plotting the roof displacement and base shear histories for MRF Design 2 and Model 4. In Fig. 8.55, it can be found that MRF Model 4 experienced slightly larger roof displacement peaks at instances after the first large displacement cycle had occurred. In Fig. 8.56, it can be found that the base shear peaks that occurred in MRF Model 4 are somewhat larger than those in MRF Design 2. However, in both figures, the differences in these responses are insignificant.

8.7.4.4 Maximum Panel Zone Deformations During Event *MX*

The maximum panel zone joint deformations of each MRF design are plotted in Fig. 8.57 using circles of radius corresponding to the associated panel zone deformation. In Fig. 8.57, a circle of one quarter-inch radius is equivalent to 0.01 radians of panel zone deformation and is indicated in the figure. From Fig. 8.57, it can be seen that larger panel zone deformations occurred at joints near the fourteenth floor of MRF Design 1 and their distribution is not uniform. The maximum total panel zone deformation which occurred is as high as 0.0138 radians, about sixteen percent larger than that during event *PK*, occurred at the fourteenth floor on the column line C of MRF Design 1. The extent of the maximum panel zone deformations of MRF Designs 2 and 3 is less severe and is 0.0068 and 0.0082 radians, respectively.

A yield circle of radius corresponding to the yield joint rotation as defined in Eq. 8-8 is also shown in Fig. 8.57. It can be found that the largest panel zone deformations that occurred during the event are about 7.4, 3.6 and 4.4 times the yield deformation for MRF Designs 1, 2 and 3, respectively. The concentration of relatively larger panel zone deformations that occurred in each design appears to vary from one design to another.

8.7.4.5 Maximum Beam, Column and Panel Zone Joint Plastic Hinge Rotations During Event *MX*

The extent of the maximum panel zone plastic rotations can be obtained by subtracting the yield rotations from the maximum total panel zone deformations described above. Using circles of various radii, the extent of the plastic hinge rotations for the beams, columns and panel zone joints in MRF Designs 1, 2, 3 and Model 4 are plotted in Figs. 8.58, 8.59, 8.60, and 8.61, respectively. A circle of one-quarter inch radius represents a plastic deformation of 1% or 0.01 radians.

From these figures, the number of panel zone hinges formed during the event are found to be 51, 41, 48 and 26 for MRF Designs 1, 2, 3 and Model 4, respectively. MRF Design 1, designed to have the weakest panel zone strength, developed more panel zone hinges than did any other MRF design, and the hinge deformations are concentrated in floors near the fourteenth floor. The largest panel zone joint plastic rotation, about 0.012 radians, occurred in MRF Design 1. Comparing Figs. 8.59 and 8.61 for MRF Design 2 and Model 4, respectively, the effects of the panel zone overstrength on the extent and distribution of hinge formations can be found insignificant.

When the panel zone joint strength approaches the corresponding beam flexural strength, as in MRF Design 2 and Model 4, beam plastic hinges developed as shown in Fig. 8.59 and 8.61. However, even in MRF Design 2 and MRF Model 4, where the panel zone joint strength approaches the beam strength, only a few plastic hinges were formed in the columns. The maximum beam plastic rotations can be found well below 1.0 percent radians in most of the floors of MRF Design 2 and Model 4. Very few plastic hinges were formed in MRF Designs 1 and 3, and their plastic rotations is negligible.

8.7.5 The Contribution of Panel Zone Deformations to Total Story Drifts

In order to gain some insight on the contribution of panel zone deformations to story drifts, the maximum deformation in each of the four panel zone joints at each floor were averaged and compared with the story drift that occurred during each event. The resulting maximum average story panel zone deformations and the maximum story drifts of each MRF design and Model 4 are tabulated in Tables 8.9, 8.10 and 8.11 for event PK, $1.5EC$ and $1.5MI$, respectively. Recall that the panel zone joints of MRF Designs 1, 2 and 3 were designed for beam moments of $1.85M_E$, M_p and $0.8M_p$, respectively. From these tables, it can be seen that in general the least stiff design, MRF Design 1, experienced relatively larger average story panel zone deformations while exhibited relatively smaller story drifts. The panel zone joints in the least stiff MRF design clearly demonstrate a larger contribution of deformations to story drifts.

In order to assess the effectiveness of the panel zone contributions, a γ/θ ratio of each floor for each MRF design was obtained by dividing the maximum average panel zone deformation by the corresponding maximum story drift. The resulting average joint deformation to story drift ratios, γ/θ, for the selected earthquake events are shown in Table 8.12 and plotted in Figs. 8.62 through 8.65 for MRF Design 1, 2, 3 and Model 4, respectively. From Table 8.12 and these figures, it can be seen that the least stiff design, MRF Design 1, exhibited a substantially larger contribution from the panel zone deformations to story drifts. Moreover, in each MRF design, the average γ/θ ratios for the selected events can be found to be about the same. From Table 8.12, the average γ/θ ratios can be found to be about 0.49, 0.30, 0.38 and 0.25 for MRF Designs 1, 2, 3 and Model 4, respectively. From Figs. 8.62 through 8.65, the distribution of the γ/θ ratios along the height of the frame is found to be earthquake dependent. In MRF Design 1, however, the distribution is more uniform.

8.8 Summary and Conclusions for the Twenty-Story MRF Analyses

The preceding analyses, made for the proposed twenty-story MRF designs, suggest that the nonlinear dynamic response of a high-rise MRF is very sensitive to the panel zone joint flexibilities as well as the input ground accelerations. From these analyses, the behavior of the twenty-story MRF is better understood and the following conclusions are noted with respect to the design and analyses of the twenty-story MRFs.

(1) Depending on the design of panel zone joints, the effects of the panel zone flexibilities on story drifts can be significant and therefore should be included explicitly in the calculations of story drifts under the prescribed lateral forces. As demonstrated in Section 8.4.1, if the MRF model is based on the assumption that panel zone joints are 50% rigid, the errors in estimating the roof displacements are 27, 13 and 18 percent of those obtained from models considering the actual panel zone stiffness for MRF Designs 1, 2 and 3, respectively. The MRF model using the center-to-center line stiffness still failed to estimate the floor displacements of most of the MRF designs satisfactorily.

(2) In cases where panel zone joints cannot be modeled directly, elastic story drifts of the twenty-story MRF designs can be accurately estimated using the method described in Section 8.4.2. The method incorporates the actual panel zone stiffness provided in each joint and the average panel zone deformation that would occur in each floor. Therefore, under any prescribed lateral forces, the elastic story drifts can be conveniently corrected.

(3) The $P-\Delta$ effect on story drifts was found to be significant in the lower floors of the MRF designs. Under code prescribed lateral forces, the contribution of the $P-\Delta$ effects to the total elastic story drift can be found as high as 10%. $P-\Delta$ effects would be more pronounced once nonlinearities developed or larger panel zone deformations occurred in the MRF. Therefore, both $P-\Delta$ effects and panel zone joint flexibilities should be considered in analyses, especially when nonlinearities in the

members are anticipated under the applied forces.

(4) Panel zone joint flexibilities and $P-\Delta$ effects also alter the dynamic properties of the MRF designs. An MRF with lightly reinforced panel zone joints can have a fundamental period substantially larger than that of an MRF using a traditional panel zone joint design. The fundamental period of MRF Design 1 is 4.21 seconds while that of MRF Design 2 is 3.89 seconds. The difference between the two is about 8 percent. However, the effects of the panel zone joint flexibilities on vibration mode shapes were found insignificant.

(5) Unlike the results obtained from the analyses of the six-story MRF, in which the dynamic response of the MRF was dominated by its first mode, higher vibration modes participate relatively more in the total response of the twenty-story MRFs. As a result, depending on the characteristics of the ground motion, relatively larger story drifts, larger story shears and larger element plastic deformations often occurred in the upper floors of the twenty-story MRFs, rather than the lower floors as occurred in the six-story MRF. The nonlinear dynamic behavior of the twenty-story MRF can be better understood by using the linear response spectrum for the corresponding earthquake ground accelerations. Moreover, the lengthening of the vibration periods due to the development of nonlinearities in the MRF could significantly change the participation of a specific mode when a sharp variation of spectral pseudo-acceleration exists near the period range for the corresponding mode.

(6) Under code prescribed lateral forces, it is expected that the floor displacements of the least stiff design, MRF Design 1, are larger than those of other designs. However, during most of the selected earthquake events, the stiffest design, MRF Design 2, was subjected to the largest story shears and experienced the largest floor lateral displacements among all MRF designs. In general, it can be seen from these analyses that the stiffer the panel zone joint is, the larger the dynamic response of the MRF design is. During the selected earthquake events, the maximum base shear that occurred in

MRF Design 2 was about 600 kips, almost three times the code prescribed base shear. The maximum story drifts that occurred in each MRF design can be obtained from Tables 8.9 through 8.11 for the selected events. It can be seen from these tables that the maximum story drifts are 1.77, 0.92 and 1.49 percent during events *PK*, 1.5*EC* and 1.5*MI*, respectively. All of these values occurred either in the middle or upper floors of the MRF.

(7) The effects of panel zone overstrength, as considered in MRF Model 4, on the maximum story displacements and story shears are not significant. Thus, the ANSR-1 models as defined in Sections 8.3 should be reasonable in estimating the response of the proposed twenty-story MRF designs.

(8) A typical distribution of maximum panel zone joint deformations in each MRF is shown in Table 8.8. The extent of the maximum panel zone deformations is found to be more severe in the interior columns than in the exterior columns. The maximum panel zone deformation that occurred in each MRF design can be found in Figs. 8.26, 8.35, 8.44 and 8.57 for events *PK*, 1.5*EC*, 1.5*MI* and *MX*, respectively. During each event, the extent of the maximum panel zone deformations is more severe in MRF Design 1 than in any other designs. The maximum panel zone deformations which occurred in MRF Design 1 are 0.0119, 0.0053, 0.010 and 0.0138 radians during events *PK*, 1.5*EC*, 1.5*MI* and *MX*, respectively. The maximum panel zone deformations which occurred in the stiffest design, MRF Design 2, are reduced to 0.0095, 0.0036, 0.0077 and 0.0064 radians, respectively. Note that a deformation of 0.00186 radians corresponds to the yield rotation of the panel zone joint made of A36 grade steel. These maximum panel zone deformations occurred all in the middle or upper floors of the MRF and their locations vary greatly from one MRF design to another in each event. While the panel zone joints in MRF Design 1 were subjected to larger panel zone deformations than were the other designs, the corresponding maximum story drifts are smaller than those of others. Moreover, as shown in Figs.

8.62 through 8.65, the average maximum story panel zone deformation to maximum story drift ratios of MRF Design 1 are most uniformly distributed.

(9) Once the panel zone joint strength approaches the beam flexural strength, the beam or column plastic rotation demand greatly increases. In MRF Designs 1 and 3, beam and column plastic rotations are insignificant during the selected events. However, in MRF Design 2, the maximum plastic rotations that occurred in the beam are 0.0043, 0.0033 and 0.0042 radians during events PK, $1.5MI$ and MX, respectively. In general, the effects of the panel zone overstrength as considered in MRF Model 4 increase the beam plastic rotation demands. The maximum beam plastic rotations that occurred in MRF Model 4 are 0.0071, 0.0039 and 0.0046 radians during events PK, $1.5MI$ and MX, respectively. These maximum beam plastic hinge rotations occurred either in the lower or upper floors of the MRF and varied from event to event. During event PK, $1.5MI$ and MX, very few column plastic hinge formed in each MRF and the maximum column plastic hinge rotations all occurred in the bottom end of the ground floor interior columns. During event PK, $1.5MI$ and MX, these maximum column plastic hinge rotations that occurred in MRF Design 2 are 0.0040, 0.0034 and 0.0036 radians, respectively. For MRF Model 4, they are 0.0041, 0.0042 and 0.0036 radians for events PK, $1.5MI$ and MX, respectively. During event $1.5EC$, no beam or plastic hinges formed in any one of the MRF designs.

(10) The extent and distribution of maximum panel zone deformations vary greatly from event to event, therefore, it is recommended that the design strength of the panel zone joints be based on a site dependent response spectrum in which the response due to higher modes can be incorporated in the preliminary design. If the CQC method as summarized in Section 8.2 is to be used, the maximum beam end moments obtained from the response spectrum method, would not occur at the same time, therefore, the direct use of the maximum beam moments for the design of panel zone joints could lead to an unsatisfactory distribution of panel zone strength. Instead, each modal

unbalanced moment of beams framed into the joint should be combined [64] using procedures as described in Eqs. 8-1 and 8-2 in order to obtain the design strength for the panel zone joint more appropriately.

(11) Experimental results summarized in Chapter 3, show that well detailed beam-column moment connections can sustain a plastic rotation of 0.02 radians. Since the beams and columns of the proposed twenty-story MRF satisfy the compact section requirements, judging the plastic rotation demand imposed on the beams and columns, it is anticipated that ductility problems would not occur in these members for all MRF designs. Other experimental data [51] have shown that well detailed panel zone joints could sustain a total panel zone deformation larger than 0.02 radians. Thus, the maximum panel zone deformation developed in MRF Design 1 is possible if appropriate panel zone joint details are used.

The analytical results summarized in this chapter should aid in the development of earthquake resistant design for high-rise MRF. The nonlinear dynamic response reported herein is obtained from the twenty-story MRF designs analyzed using specified ground accelerations. For high-rise MRF with irregularities in distribution of stiffness or mass, the dynamic response to specific ground accelerations requires further substantiations. Moreover, experimental investigation of MRF under dynamic loading is needed in order to substantiate these analytical results. In these analyses, it was assumed that the stability of the beams, columns and their connections were adequate for seismic resistant design and the effects of soil structure interaction were not considered.

REFERENCES

[1] *Uniform Building Code*, International Conference of Building Officials, Whittier, California, 1985.

[2] SEAOC, *Recommended Lateral Force Requirements*, Seismology Committee, Structural Engineering Association of California, San Francisco, 1980.

[3] ATC (Applied Technology Council), *Tentative Provisions for the Development of Seismic Regulations for Buildings*, Publication ATC 3-06, June, 1978.

[4] AISC, "Specifications for the Design, Fabrication and Erection of Structural Steel for Buildings," *Manual of Steel Construction*, 8th ed., American Institute of Steel Construction, Chicago, 1980.

[5] Newmark, N. M., "Design Specifications for Earthquake Resistance," *Civil Engineering Frontiers in Environmental Technology*, Dept. of Civil Engineering, University of California, Berkeley, 1971.

[6] Newmark, N. M., Hall, W. J., "Earthquake Spectra and Design," Earthquake Engineering Research Institute, El Cerrito, 1982

[7] Notch, J. S., *A Field Problem with Preload of Large A490 Bolts,* The Structural Engineer/Volume 64A/No.4/April 1986

[8] Popov, E. P. and Stephen, R. M., "Cyclic Loading of Full-Scale Steel Connections," *Report No. UCB/EERC-70-3*, Earthquake Engineering Research Center, University of California, Berkeley, 1970.

[9] Krawinkler, H., Bertero, V. V., and Popov, E. P., "Inelastic Behavior of Steel Beam-to-Column Subassemblages," *Report No. UCB/EERC-71/7*, Earthquake Engineering Research Center, University of California, Berkeley, 1971.

[10] Bertero, V. V., Popov, E. P., and Krawinkler, H., "Further Studies on Seismic Behavior of Steel Beam-Column Subassemblages," *Report No. UCB/EERC-73/27*,

Earthquake Engineering Research Center, University of California, Berkeley, 1973.

[11] Rentschler, G. P., Chen, W. F., and Driscoll, G. C., "Test of Beam-to-Column Web Moment Connections," *Journal of Structural Division*, ASCE, Vol. 106, No. ST5, 1980.

[12] Rogec, J. E., Huang, J. S., and Chen, W. F., "Test of a Fully-Welded Beam-to-Column Connection," *Publication No. 188*, Welding Research Council, 1973.

[13] Chen, W. F. and Patel, K. V., "Static Behavior of Beam-to-Column Moment Connections," *Journal of Structural Division*, ASCE, Vol. 107, No. ST9, September 1981.

[14] Slutter, R. G., "Test of Panel Zone Behavior in Beam-Column Connections," *Report No. 200.81.403.1*, Fritz Engineering Laboratory, Lehigh University, Bethlehem, Pennsylvania, 1981.

[15] Popov, E. P. and Pinkney, R. B., "Behavior of Steel Building Connections Subjected to Inelastic Strain Reversal," *SESM Report No. 67-30*, Structures and Materials Research, Dept. of Civil Engineering, University of California, Berkeley, 1967.

[16] Popov, E. P. and Pinkney, R. B., "Behavior of Steel Building Connections Subjected to Inelastic Strain Reversal—Experimental Data," *SESM Report No.67-31*, Structures and Materials Research, Dept. of Civil Engineering, University of California, Berkeley, 1967.

[17] Rentschler, G. P., "Analysis and Design of Steel Beam-to-Column Web Connections," Ph.D. Dissertation, Dept. of Civil Engineering, Lehigh University, Bethlehem, Pennsylvania, 1979.

[18] Tsai, K. C. and Popov, E. P., "Two Beam-to-Column Web Moment Connections," *Report No. UBC/EERC/86-05*, Earthquake Engineering Research Center, University of California, Berkeley, 1986.

[19] Pourbohloul, A., Wang, X., and Driscoll, G. C., "Test on Simulated Beam-to-Column Web Moment Connection Details," *Report No. 469.7, Fritz Engineering*

Laboratory, Lehigh University, Bethlehem, Pennsylvania, 1983.

[20] "AWS Structural Welding Code-Steel," AWS D1.1-80, American Welding Society, Miami, 1980.

[21] American Society for Testing and Materials, *Standard Methods of Tension Testing of Metallic Materials,* ASTM Designation E8-79, Philadelphia, Pennsylvania, 1980.

[22] Popov, E. P., "Seismic Moment Connections for Moment-Resisting Steel Frames," *Report No. UBC/EERC/83-02*, Earthquake Engineering Research Center, University of California, Berkeley, 1983.

[23] Popov, E. P. and Pinkney, R. B., "Cyclic Yield Reversal in Steel Building Connections," *Journal of the Structural Division*, ASCE, Vol. 95, No. ST3, 1969.

[24] Wang, C., "Structural System—Getty Plaza Tower," *Engineering Journal*, American Institute of Steel Construction, Chicago, Vol. 21, No. 1, 1984.

[25] Galambos, T. V., "Deformation and Energy Absorption Capacity of Steel Structures in the Inelastic Range," *Bulletin No. 8*, American Iron and Steel Institute, New York, 1968.

[26] Lee, S.-J. and Lu, L.-W., "Cyclic Tests of Full-Scale Composite Beam-to-Column Joints," *Report 467.6*, Fritz Engineering Laboratory; also in *Proceedings*, U.S.-Japan Cooperative Research.

[27] Salmon, C. G. and Johnson, J. E., "Steel Structures, Design and Behavior," 2nd Edition; Harper & Row, Publishers, New York, 1980.

[28] Kulak, G. L.,Fisher, J. W., Struik, J. A., "Guide to Design Criteria for Bolted and Riveted Joints," 2nd Edition; John Wiley & Sons, Inc. 1987.

[29] Blodgett, O. M., "Design of Welded Structures," The James F. Lincoln Arc Welding Foundation, Cleveland, 1976.

[30] Maka, T., Kato, B., and Watabe, M., "Research on The Behavior of Steel Beam-to-Column Connections", Laboratory for Steel Structures, Department of Architecture, University of Tokyo, 1966.

[31] Zienkiewicz, O. C., "The Finite Element Method," 3rd Edition; McGraw-Hill, 1977 (see Chapter 24 "Computer Procedures for Finite Element Analysis" by R. L. Taylor).

[32] Wilson, E. L. and Habibullah, A., "SAP80-Structural Analysis Programs," Computers and Structures, Inc., Berkeley, California, 1986.

[33] Clough, R. W.,and Penzien, J., "Dynamics of Structures," McGraw-Hill Book Company, Inc., New York, 1975.

[34] Newmark, N. M., "A Method of Computing for Structural Dynamics," *Journal of Engineering Mechanics Division*, ASCE, vol. 85, 1959.

[35] Nickell, R. E., "On the Stability of Approximation Operators in Problems of Structural Dynamics," *International Journal of Solids and Structures*, Vol. 7, 1971.

[36] Wilson, E. L., Farhoomad, I., and Bathe, K. J., "Nonlinear Dynamic Analysis of Complex Structures," *International Journal of Engineering and Structural Dynamics*, vol. 1, 1973.

[37] Hilber, H. M., Hughes, T. J. R., and Taylor, R. L., "Improved Numerical Dissipation of Time Integration Algorithm in Structural Dynamics," *Earthquake Engineering and Structural Dynamics*, vol. 5, 1977.

[38] Hughes, T. J. R., Caughey, T. K., and Liu, W. K., "Finite Element Method for Nonlinear Elastodynamics which Conserve Energy", *Journal of Applied Mechanics*, vol. 45, 1978.

[39] Powell, G. H., "DRAIN-2D User's Guide," *Report No. UCB/EERC-73/22*, Earthquake Engineering Research Center, University of California, Berkeley, 1973.

[40] Mondkar, D. P., and Powell, G. H., "ANSR-1 General Purpose Computer Program for Analysis of Non-Linear Structural Response", *Report No. UCB/EERC-75/37*, Earthquake Engineering Research Center, University of California, Berkeley, 1975.

[41] Ricles, J. M., and Popov, E. P., "Dynamic Analysis of Seismically Resistant Eccentrically Braced Frames," *Report No. UCB/EERC-87/07*, Earthquake

Engineering Research Center, University of California, Berkeley, 1987.

[42] Riahi, A., Row, D. G. and Powell, G. H., "Three Dimensional Inelastic Frame Elements for the ANSR-1 Program," *Report No. UCB/EERC-78/06*, Earthquake Engineering Research Center, University of California, Berkeley, 1978.

[43] Wilson, E. L., Hollings, J. P., and Dovey, H. H., "Three Dimensional Analysis of Building Systems (Extend Version)," *Report No. UCB/EERC-75/13*, Earthquake Engineering Research Center, University of California, Berkeley, 1978.

[44] Popov, E. P., "Introduction to Mechanics of Solids," Prentice-Hall, Englewood Cliffs, N.J., 1968.

[45] NEHRP (National Earthquake Hazards Reduction Program), *Recommended Provisions for the Development of Seismic Regulations for New Buildings*, Building Seismic Safety Council, Federal Emergency Management Agency, Washington, D.C. 1985.

[46] ANSI, "American National Standard Minimum Design Loads for Buildings and Other Structures," ANSI A58.1-1982, New York, New York, 1982.

[47] SEAOC, *Recommended Lateral Force Requirements*, Seismology Committee, Structural Engineering Association of California, San Francisco, 1987.

[48] Bathe, K. J., Wilson, E. L., Peterson, F. E., "SAP IV: A Structural Analysis Program for Static and Dynamic Response of Linear Systems," *Report No. UCB/EERC-73/11*, Earthquake Engineering Research Center, University of California, Berkeley, 1973.

[49] Fielding, D. J., Huang, J. S., "Shear in Steel Beam-to-Column Connections," *Welding Journal*, Vol. 50, No.7, Research Supplement, 1971.

[50] Krawinlker, H., "Shear in Beam-Column Joints in Seismic Design of Steel Frames," *Engineering Journal*, AISC, Volume 15, No.3, 1978.

[51] Popov, E. P., Amin, N. R., Louis, J. J. C. and Stephen, R. M., "Cyclic Behavior of Large Beam-Column Assemblies," *Earthquake Spectra*, 1, No.2, 1985.

[52] Mahin, S.A., and Lin, J., "Construction of Inelastic Response Spectra for Single Degree of Freedom System," *Report No. UCB/EERC-83/17*, Earthquake Engineering Research Center, University of California, Berkeley, 1983.

[53] Newmark, N. M. and Hall, W. J., "Procedures and Criteria for Earthquake Resistant Design", *Building Practices for Disaster Mitigation*, Building Science Series 46, U.S. Department of Commerce, National Bureau of Standard, Washington, D.C. February 1973.

[54] Saiidi, M. and Sozen, M. A., "Simple Nonlinear Seismic Analysis of R/C Structures", *Journal of the Structural Division*, ASCE, Vol. 107, No. ST5, May 1981.

[55] Bernal, D., "Amplification Factors for Inelastic Dynamic $P-\Delta$ Effects in Earthquake Analysis", *Earthquake Engineering and Structural Dynamics*, Vol. 15, 635-651, 1987.

[56] Jennings, P. C., Housner, G. W. and Tsai, N. C., "Simulated Earthquake Motions", California Institute of Technology, California, Pasadena, 1968.

[57] Simo, J. C. and Taylor, R. L., "A Consistent Return Mapping Algorithm for Plane Stress Elastoplasticity", Report No. UCB/SESM-85/04, Department of Civil Engineering, University of California, Berkeley, 1985.

[58] Uang, C.-M., and Bertero, V. V. "Earthquake Simulation Tests and Associated Studies of a 0.3-Scale Model of a Six-Story Concentrically Braced Steel Structures," *Report No. UCB/EERC-86/10*, Earthquake Engineering Research Center, University of California, Berkeley, 1986.

[59] *Uniform Building Code*, International Conference of Building Officials, Whittier, California, 1988.

[60] "Tall Building Systems and Concepts," *Monograph on Planning and Design of Tall Buildings*, Council on Tall Buildings and Urban Habitat, American Society of Civil Engineers, New York, 1980.

[61] Wilson, E. L., Der Kiureghian, A. and Bayo, E., "A Replacement for the SRSS Method in Seismic Analysis," *Earthquake Engineering and Structural Dynamics*, Vol. 9, 1981.

[62] Der Kiureghian, A., "On Response of Structures to Stationary Excitation," *Report No. UCB/EERC-79/32*, Earthquake Engineering Research Center, University of California, Berkeley, 1979.

[63] Wilson, E. L. and Habibullah, A. "Static and Dynamic Analysis of Multi-Story Buildings, Including P-Delta Effects," *Earthquake Spectra*, Earthquake Engineering Research Institute, Vol. 3, No. 2, May 1987.

[64] Der Kiureghian, A., Private Communications.

[65] Pauley, T., "Deterministic Seismic Design Procedures for Reinforced Concrete Buildings," *Engineering Structures*, Vol. 5, No. 1, January 1983.

[66] Standards Association of New Zealand, "Code of Practice for the Design of Concrete Structures," Draft, New Zealand Standard NZS 3101, Parts 1 and 2, 1982.

[67] Popov, E. P., Bertero, V. V., and Chandramouli, S., "Hysteretic Behavior of Steel Columns," *Report No. UCB/EERC-75/11*, Earthquake Engineering Research Center, University of California, Berkeley, 1975.

APPENDIX A. Design of Specimens

A.1 Bolts in Beam Web

Use 1-in. diameter A325-X bolts to connect the beam web to the shear tab. The ultimate shear, V_{ult}, in the beam web occurs when the peak moment, M_{ult}, of the cantilever beam is reached. The ultimate shear force in the cantilever beam is therefore:

$$V_{ult} = \frac{M_{ult}}{L_b}$$

where L_b is the cantilever beam length measured from the applied load to the column flange. Without considering strain hardening, M_{ult} can be approximated as the plastic moment capacity of the beam section based on F_y=36ksi. In order to determine the number of web bolts required, specifications of plastic design in the AISC manual [4] are applied. The number of bolts required, n, rounded up to an integer, is then:

$$n \approx \frac{V_{ult}}{1.7V_{bolt}}$$

where V_{bolt} equals 22.7 kips, the allowable shear force for 1-in. diameter A325-X bolts with 3-in. center to center spacing governed by the web bearing strength of W21×44. L_b is about 60-in. for all specimens. Table A.1 shows the calculations and the the resulting bolt schedule. In column 5 of the table, gives the number of bolts used based on details commonly used in industry for the given beam sizes.

Beam Size [1]	M_p (kip-in) [2]	V_{ult} (kips) [3]	n $[4]=\frac{[2]}{[3]}$	No. of Bolts* Used [5]
W18×35	2400	40	1	4
W18×40	2820	47	2	4
W21×44	3432	57	2	5

* (A325-X 1-in. diameter)

Table A.1 Bolt Schedule for Bolted Web Connections

A.2 Beam Web to Shear Tab Welding

Using E70 electrode, the allowable stress of the fillet weld is 21 ksi, in the design of weldings.

Specimen 1 W18×40 beam with three 3/8-in. by 2-in. web weld, 10.5-in. center-to-center apart.

The maximum size of fillet weld along the edge of 3/8-in. shear tab is 5/16-in.

The ultimate moment capacity of the weld group can be approximated as:

$$M_{weld} = 1.7\times21\times0.707\times Z_{weld}$$

$$= 1.7\times21\times0.707\times\left[3\left(\frac{1}{4}\times\frac{5}{16}\times2^2\right)+\frac{5}{16}\times2\times5.25\times2\right]$$

$$= 189 \text{ kip–in}$$

Based on F_y=36ksi, the plastic moment capacity of the beam web is:

$$M_{web} = 36\times Z_{web}$$

$$= 36\times\left[\frac{t_w(d-2t_f)^2}{4}\right]$$

$$= 36\times\left[\frac{0.315(16.85)^2}{4}\right]$$

$$= 805$$

$$\frac{M_{weld}}{M_{web}} = \frac{189}{805} \approx 23\%$$

Specimen 4 W18×40 beam with two 5/16-in. by 2-in. web weld, 10.5-in. center-to-center apart.

The ultimate moment capacity of the weld group can be approximated as:

$$M_{weld} = 1.7\times21\times0.707\times Z_{weld}$$

$$= 1.7\times21\times0.707\times\left[2(\frac{1}{4}\times\frac{5}{16}\times2^2) + \frac{5}{16}\times2\times5.25\times2\right]$$

$$= 181 \text{ kip–in}$$

As in Specimen 1, the plastic moment capacity of beam web is 805 kip–in.

$$\frac{M_{weld}}{M_{web}} = \frac{181}{805} \approx 22\%$$

Specimen 5 W21×44 beam with two 5/16-in. by 1.25-in. web weld, 14-in. center-to-center apart.

The ultimate moment capacity of the weld group can be approximated as:

$$M_{weld} = 1.7\times21\times0.707\times Z_{weld}$$

$$= 1.7\times21\times0.707\times\left[2(\frac{1}{4}\times\frac{5}{16}\times1.25^2) + \frac{5}{16}\times1.25\times7\times2\right]$$

$$= 144 \text{ kip–in}$$

Based on F_y=36ksi, the plastic moment capacity of the beam web is:

$$M_{web} = 36 \times Z_{web}$$

$$= 36 \times \left[\frac{t_w(d-2t_f)^2}{4} \right]$$

$$= 36 \times \left[\frac{0.35(19.76)^2}{4} \right]$$

$$= 1230$$

$$\frac{M_{weld}}{M_{web}} = \frac{144}{1230} \approx 12\%$$

Specimen 13 W18×35 beam with three 5/16-in. by 3-in. web weld, 9.5-in. center-to-center apart.

The ultimate moment capacity of the weld group can be approximated as:

$$M_{weld} = 1.7 \times 21 \times 0.707 \times Z_{weld}$$

$$= 1.7 \times 21 \times 0.707 \times \left[2\left(\frac{1}{4} \times \frac{5}{16} \times 3^2\right) + \frac{5}{16} \times 3 \times 4.75 \times 2 \right]$$

$$= 260 \text{ kip–in}$$

Based on F_y=36ksi, the plastic moment capacity of the beam web is:

$$M_{web} = 36 \times Z_{web}$$

$$= 36 \times \left[\frac{t_w(d-2t_f)^2}{4} \right]$$

$$= 36 \times \left[\frac{0.30(16.85)^2}{4} \right]$$

$$= 767$$

$$\frac{M_{weld}}{M_{web}} = \frac{260}{767} \approx 34\%$$

Specimen 14 W21×44 beam with three 5/16-in. by 3.5-in. web weld, 11.5-in. center-to-center apart.

The ultimate moment capacity of the weld group can be approximated as:

$$M_{weld} = 1.7\times21\times0.707\times Z_{weld}$$

$$= 1.7\times21\times0.707\times\left[2(\frac{1}{4}\times\frac{5}{16}\times3.5^2) + \frac{5}{16}\times3\times5.75\times2\right]$$

$$= 320 \text{ kip–in}$$

As in Specimen 5, the plastic moment capacity of beam web is 1230 kip–in.

$$\frac{M_{weld}}{M_{web}} = \frac{320}{1230} \approx 26\%$$

A.3 End Plate Design

Plastic design and procedures outlined by Salmon and Johnson [27] are used.

Specimen 10 W18×40 beam, all welded to end plate.

(a) **Bolting of End Plate**

Without considering stain hardening of the beam section, the force to be developed in the tension flange is:

$$T_f = F_y\times A_f = 36\times b_f\times t_f$$

$$= 36\times6.015\times0.525$$

$$= 114 \text{ kips}$$

For $\frac{7}{8}$-in. diameter A325-X bolts,

the allowable tension force of each bolt = R_t = 26.5 kips

$$\text{number of bolts required} = \frac{T_f}{1.7R_t} = \frac{105}{45} = 2.53$$

Try 4 bolts for symmetrical placement of bolts above and below the flange. Use another 4 bolts around the opposite flange to develop the beam cyclic moment capacity. To determine the shear capacity of the connection under applied load, assume four bolts near the tension flange resist the tension force while the other four bolts around the opposite flange resist the shear force.

Shear Capacity of four $\frac{7}{8}$ A325-X bolts is:

$$V_{ult} = 1.7 \times 4 \times 18.0 = 122 \text{ kips}$$

Examine the tabulated values shown in Section A-1; the maximum cantilever shear, based on F_y=36 ksi, is about 47 kips. Four $\frac{7}{8}$-in. diameter A325-X bolts are adequate to resist the shear force.

(b) **Welding Requirement**

Fillet welds are used to develop the flange and web plastic moment capacities.

Flange

Beam flange weld length = L_w

$$= 2b_f - t_w = 11.72 \text{ in.}$$

$$\text{Flange fillet weld size} = \frac{T_f}{L_w(1.7)(0.707)21}$$

$$= \frac{36 \times b_f \times t_f}{L_w(1.7)(0.707)21}$$

$$= 0.38 \text{ in.} \quad \text{use } \frac{3}{8}\text{-in. fillet weld}$$

Web

$$Z_{web} = \frac{0.315}{4}(17.90-2\times0.525)^2$$

$$= 22.36 \text{ in.}^3$$

$$\text{Web fillet weld size} = \frac{\frac{1}{2}\times36\times Z_{web}}{1.7\times21\times0.707\times\frac{(d-2t_f)^2}{6}}$$

$$= \frac{\frac{1}{2}\times36\times22.36}{1.7\times21\times0.707\times\frac{16.85^2}{6}}$$

$$= 0.34 \text{ in.} \quad \text{use } \frac{3}{8}\text{-in. fillet weld}$$

(c) **Dimension** of End Plate

Installation clearance required for the $\frac{7}{8}$ -in. diameter bolt is 1.375 in.

Total clearance required for end plate installation

$= 1.375 +$ flange fillet weld size

$= 1.375 + 0.375$

$= 1.75$ in.

Use 2-in. clearance between the center of bolt to the beam flange and $1\frac{1}{2}$-in. distance between center of bolt to the edge of end plate.

Minimum longitudinal dimension of the end plate

$= 2\times(2.0+1.5) + 17.90$

$= 24.90$ in.

Use 25-in. plate length.

For the W12×133 column. k_1 = 1-in. The diameter of the washer for $\frac{7}{8}$-in. diameter bolt is $1\frac{3}{4}$-in.

Minimum horizontal spacing of bolts

$= 2\times1 + 1\frac{3}{4}$

$= 3\frac{3}{4}$ in.

Use 4-in. spacing between the bolts and $1\frac{1}{2}$-in. for bolt edge distance.

The resulting end plate width is $= 2\times1.5 + 4$

$= 7$ in.

(d) **Thickness** of end plate

Distance from the center of bolt to the critical section of bending

$= 2 - \frac{1}{16}$

$= 1.94$ in.

Assume there is no prying action for now and check it later

Total force in two exterior bolts is then

$$P = \frac{T_f}{2} = \frac{114}{2} = 57$$

Moment at critical section

$M_{ult} = 57\times1.94$

$$= 105 \text{ kip–in.}$$

$$\text{End plate thickness} = \left[\frac{4M_{ult}}{b_f F_y}\right]^{\frac{1}{2}}$$

$$= \left[\frac{4\times 105}{7(36)}\right]^{\frac{1}{2}}$$

$$= 1.29 \text{ in. Use } 1\frac{3}{8}\text{–in. thick plate}$$

(e) Check Prying Action

Using equations in AISC manual, prying action can be estimated as follows:

$$\delta = 1 - \frac{d'}{p} \tag{A-1}$$

$$M = \frac{M_p}{2} = \frac{pt_p^2 F_y}{8} \tag{A-2}$$

$$\alpha = \frac{\frac{Tb}{M} - 1}{\delta} \tag{A-3}$$

$$B_c = T\left[1 + \frac{\delta\alpha}{(1+\delta\alpha)}\frac{b'}{a'}\right] \tag{A-4}$$

where

δ = Ratio of net area (at bolt line) to the gross area (at the face of the beam flange),

d' = Width of bolt hole in end plate parallel to beam flange, in.

p = Length of end plate, parallel to beam flange tributary to each bolt, in.

t_p = End plate thickness, in.

M = Allowable bending moment tributary to end plate by one bolt,

α = Moment ratio, if $\alpha > 1.0$, use $\alpha = 1.0$

T = Applied tension per bolt (exclusive of initial tightening), kips

B_c = Load per bolt including prying action, kips

d = Bolt diameter,

a = Distance from bolt center line to edge of end plate, but no more than 1.25-in.

$b' = b - \frac{d}{2}$, in.

$a' = a + \frac{d}{2}$, in.

For Specimen 10, We have:

$d' = \frac{15}{16}$ in.

$p = 3.5$ in.

$t_p = 1.375$ in.

$F_y = 36$ ksi

$T = \frac{114}{4} = 28.5$ kips

$d = \frac{7}{8}$ in.

$b = 2$ in.

$a = 1.25$ in.

$b' = b - \frac{d}{2} = 1.5625$ in.

$a' = a + \frac{d}{2} = 1.6875$ in.

Enter the above values into equations (A-1) through (A-4); we then have:

$\delta = 0.732$

$M = 29.8$ kip–in

$\alpha = 1.25$, use $\alpha = 1.0$

$$B_c = 1.39T = 1.39 \times 28.5 = 39.6 \text{ kips} < 1.7 \times R_t = 45 \text{ kips (OK)}$$

Specimen 12 W21×44 beam, all welded to end plate.

(a) **Bolting of End Plate**

Without considering stain hardening of the beam section, the force to be developed in the tension flange is:

$$T_f = F_y \times A_f = 36 \times b_f \times t_f$$

$$= 36 \times 6.5 \times 0.45$$

$$= 105 \text{ kips}$$

For $\frac{7}{8}$-in. diameter A325-X bolts,

allowable tension force of each bolt = $R_t = 26.5$ kips

$$\text{number of bolts required} = \frac{T_f}{1.7R_t} = \frac{105}{45} = 2.33$$

Similar to Specimen 10, try four bolts for symmetrical placement of bolts above and below the flange. Use another four bolts around the opposite flange to develop the beam cyclic moment capacity. To determine the shear capacity of the connection under applied load, assume four bolts near the tension flange resist the tension force while the other four bolts around the opposite flange resist the shear force.

Shear Capacity of four $\frac{7}{8}$ A325-X bolts is:

$$V_{ult} = 1.7 \times 4 \times 18.0 = 122 \text{ kips}$$

Examine the tabulated values shown in Section A-1; the maximum cantilever shear, based on F_y=36 ksi, is about 57 kips. Four $\frac{7}{8}$-in. diameter A325-X bolts are adequate to resist the shear force.

(b) **Welding Requirement**

Fillet welds are used to develop the flange and web plastic moment capacities.

Flange

Beam flange weld length = L_w

$$= 2b_f - t_w = 12.65 \text{ in.}$$

$$\text{Flange fillet weld size} = \frac{T_f}{L_w(1.7)(0.707)21}$$

$$= \frac{36 \times b_f \times t_f}{L_w(1.7)(0.707)21}$$

$$= 0.33 \text{ in.} \quad \text{use } \frac{3}{8}\text{-in. fillet weld}$$

Web

$$Z_{web} = \frac{0.35}{4}(20.66 - 2 \times 0.45)^2$$

$$= 34.17 \text{ in.}^3$$

$$\text{Web fillet weld size} = \frac{\frac{1}{2} \times 36 \times Z_{web}}{1.7 \times 21 \times 0.707 \times \frac{(d - 2t_f)^2}{6}}$$

$$= \frac{\frac{1}{2} \times 36 \times 34.17}{1.7 \times 21 \times 0.707 \times \frac{19.76^2}{6}}$$

$$= 0.37 \text{ in.} \quad \text{use } \frac{3}{8}\text{-in. fillet weld}$$

(c) **Dimension** of End Plate

Similar to Specimen 10, use 2-in. clearance between the center of bolt to the beam flange and $1\frac{1}{2}$-in. distance between the center of bolt to the edge of the end plate..

Minimum longitudinal dimension of end plate

$= 2\times(2.0+1.5) + 20.66$

$= 27.66$ in.

Use 28-in. plate length.

For W14×176 column. $t_w = 0.83$ in. and $k_1 = 1\frac{1}{16}$ in. Diameter of washer for $\frac{7}{8}$-in. diameter bolt is $1\frac{3}{4}$-in.

Minimum horizontal spacing of bolts

$= 2\times1\frac{1}{16} + 1\frac{3}{4}$

$= 3\frac{7}{8}$ in.

Use 4-in. spacing between bolts and $1\frac{1}{2}$-in. for bolts edge distance.

The resulting end plate width is $= 2\times1.5 + 4$

$= 7$ in.

(d) **Thickness** of end plate

Distance from the center of bolt to the critical section of bending

$= 2 - \frac{1}{16}$

$= 1.94$ in.

Assume there is no prying action for now and check it later

Total force in two exterior bolts is then

$$P = \frac{T_f}{2} = \frac{105.3}{2} = 52.7$$

Moment at critical section

$$M_{ult} = 52.7 \times 1.94$$

$$= 102 \text{ kip–in.}$$

$$\text{End plate thickness} = \left[\frac{4M_{ult}}{b_f F_y}\right]^{\frac{1}{2}}$$

$$= \left[\frac{4 \times 102}{7(36)}\right]^{\frac{1}{2}}$$

$$= 1.27 \text{ in. Use } 1\frac{1}{4}\text{–in. thick plate}$$

(e) Check Prying Action

Similar to Specimen 10, using equations in AISC manual, prying action can be estimated. As defined for Specimen 10, in this specimen, We have

$$d' = \frac{15}{16} \text{ in.}$$

$$p = 3.5 \text{ in.}$$

$$t_p = 1.25 \text{ in.}$$

$$F_y = 36 \text{ ksi}$$

$$T = \frac{105.3}{4} = 26.3 \text{ kips}$$

$$d = \frac{7}{8} \text{ in.}$$

$$b = 2 \text{ in.}$$

$a = 1.25$ in.

$b' = b - \frac{d}{2} = 1.5625$ in.

$a' = a + \frac{d}{2} = 1.6875$ in.

Enter the above values into equations (A-1) through (A-4); we then have:

$\delta = 0.732$

$M = 24.6$ kip–in

$\alpha = 1.56$, use $\alpha = 1.0$

$B_c = 1.39T = 1.39 \times 26.3 = 36.6$ kips $< 1.7 \times R_t = 45$ kips (OK)

Specimen [1]	Beam[1] Size [2]	Column Size [3]	Connecting Direction [4]	Connection Detail [5]	No. of Connection Bolts[2] [6]	Remarks [7]
1	W18×40 (0.70)	W12×133	Weak	Bolted Web Welded Flg	4	Reinforcing Ribs 20% Web Weld
2	W18×40 (0.70)	W12×133	Weak	Bolted Web Welded Flg	4	---
3	W18×35 (0.66)	W12×133	Strong	Bolted Web Welded Flg	4	Flux-Cored Arc Welding
4	W18×40 (0.70)	W12×133	Weak	Bolted Web Welded Flg	4	Flux-Cored Arc Welding 20% Web Welding
5	W21×44 (0.62)	W14×176	Strong	Bolted Web Welded Flg	5	Flux-Cored Arc Welding 10% Web Weld
6	W21×44 (0.62)	W14×176	Weak	Bolted Web Welded Flg	5	Flux-Cored Arc Welding Extended Continuity Plates
7	W21×44 (0.62)	W14×176	Strong	Bolted Web Welded Flg	5	Reinforcing Ribs
8	W21×44 (0.62)	W14×176	Weak	Bolted Web Welded Flg	5	Reinforcing Ribs Load Indicating Washers
9	W18×46 (0.71)	W12×133	Strong	All Welded	NA	Partial Penetration and Fillet Flange Welds
10	W18×40 (0.70)	W12×133	Strong	End Plate	8	Fillet Welds to End Plate
10R	W18×40 (0.70)	W12×133	Strong	End Plate	8	Fillet Welds to End Plate with Stiffeners
11	W21×44 (0.62)	W14×176	Strong	All Welded	NA	Fillet flange Weld All Around
12	W21×44 (0.62)	W14×176	Strong	End Plate	8	---
13	W18×35 (0.66)	W14×159	Strong	Bolted Web Welded Flg	4	20% Web Weld
14	W21×44 (0.62)	W14×159	Strong	Bolted Web Welded Flg	5	20% Web Weld
15	W18×35 (0.66)	W14×159	Strong	Bolted Web Welded Flg	4	Flux-Cored Arc Welding Twist-Off Bolts
16	W21×44 (0.62)	W14×159	Strong	Bolted Web Welded Flg	5	Flux-Cored Arc Welding Twist-Off Bolts
17	W18×35 (0.66)	W14×159	Strong	Bolted Web Welded Flg	4	Twist-Off Bolts
18	W21×44 (0.62)	W14×159	Strong	Bolted Web Welded Flg	5	Twist-Off Bolts

[1] Values in parenthesis give ratios of $\frac{Z_f}{Z}$

[2] All bolts 1 in. diam. A325-X, except 7/8-in. diam. A325-X for Specimen 10 and 1-in. diam. A354-BD for Specimens 10R and 12.

Table 2.1 Specimen Schedule

Specimen [1]	Coupon Location [2]	Yield Strength (ksi) [3]	Tensile Strength (ksi) [4]	Elongation at Fracture (%) [5]
1	Flange	38.2	60.6	25
	Web	50.3	64.3	28
2	Same as Specimen 1			
3	Flange	51.6	69.6	44
	Web	56.4	74.3	31
4	Flange	47.1	65.9	44
	Web	54.5	68.9	43
5	Flange	48.6	69.4	44
	Web	56.0	72.4	41
6	Same as Specimen 5			
7	Flange	48.9	65.6	42
	Web	59.0	71.6	41
8	Flange	48.3	65.6	42
	Web	59.5	71.7	41
9	Flange	37.2	60.9	37
	Web	41.5	64.5	42
10	Flange	45.0	67.6	43
	Web	55.8	72.4	42
10R	Same as Specimen 10			
11	Same as Specimen 9			
12	Flange	46.0	64.6	35
	Web	46.0	64.8	43
13	Flange	51.2	70.3	44
	Web	63.5	78.5	29
14	Flange	44.6	65.8	41
	Web	45.8	66.1	42
15	Same as Specimen 13			
16	Same as Specimen 14			
17	Flange	46.3	68.6	41
	Web	55.7	73.2	42
18	Flange	42.0	65.0	39
	Web	42.0	64.7	40

Table 3.1 Mechanical Properties of Tensile Coupon Specimens

Specimen	L_c (in)	M_p^* (kip–in)	P_p^* (kip)	P_{36} (kip)	P_{max} (kip)	$\frac{P_{max}}{P_{36}}$	$\frac{P_{max}}{P_p^*}$	θ_{max} (%)	θ_p (%)	θ_p^* (%)
[1]	[2]	[3]	$[4]=\frac{[3]}{[2]}$	[5]	[6]	$[7]=\frac{[6]}{[5]}$	$[8]=\frac{[6]}{[4]}$	[9]	[10]	[11]
1	61.3	3280	53.5	40.2	67	1.67	1.25	5.84	5.24	8.66
2	65.8	3280	49.8	37.4	61	1.63	1.22	2.53	1.95	3.29
3	64.8	3540	54.6	32.0	61	1.91	1.12	1.61	0.94	1.53
4	65.8	3807	57.9	37.4	62	1.66	1.07	1.65	0.92	1.71
5	62.9	4905	77.9	46.7	81	1.73	1.04	1.31	0.68	1.39
6	61.6	4905	79.7	47.7	79	1.66	1.01	1.33	0.73	1.41
7	59.8	5031	84.1	49.1	90	1.83	1.07	2.11	1.46	2.42
8	58.8	5014	85.3	50.0	95	1.90	1.11	2.43	1.75 (4.82)	3.39 (7.60)
9	62.9	3487	55.4	45.1	75	1.66	1.35	5.03	4.49	6.93
10	61.6	3782	61.4	40.0	68	1.70	1.10	--	--	--
10R	56.6	3782	66.8	43.5	80	2.01	1.20	3.33	2.73	4.76
11	63.2	4388	69.0	46.5	72	1.55	1.04	1.77	1.26 (3.21)	1.95 (5.65)
12	61.9	4388	70.9	47.5	77	1.66	1.09	2.01	1.51	2.65
13	63.2	3683	58.3	32.8	69	2.10	1.18	2.02	1.27	2.12
14	63.2	4298	68.0	46.5	76	1.63	1.12	2.80	2.39	4.16
15	63.2	3683	58.3	32.8	33	1.01	0.57	0.43	0.04	0.04
16	63.2	4298	68.0	46.5	57	1.23	0.84	0.83	0.39	0.78
17	63.2	3291	52.1	32.8	54	1.65	1.04	2.12	1.48	2.70
18	63.2	4006	63.4	46.5	70	1.51	1.10	1.81	1.36	2.63

L_c = Distance from applied load to face of column or edge of stiffener
M_p^* = Plastic moment capacity based on tensile coupon strength
P_{36}, P_{max} = Nominal cantilever load at yield stress of 36 ksi, maximum attained load during test
θ_{max} = Maximum beam rotation before failure occurs or moment capacity M_p^* is exhausted
θ_p = Maximum beam plastic rotation before failure occurs or moment capacity M_p^* is exhausted
θ_p^* = Beam plastic rotation measured from zero intercept to the same point as defined in θ_p
Values of θ_p and θ_p^* in parenthesis give rotations at M_p, where M_p = plastic moment at 36ksi

Table 3.2 Summary of Experimental Results

Yield Condition	A	B	C	D
Elastic	0	0	0	0
Plastic Hinge at end i only	1	$\frac{k_{ij}}{k_{ii}}$	0	0
Plastic Hinge at end j only	0	0	$\frac{k_{ij}}{k_{jj}}$	1
Plastic Hinge at both ends	1	0	0	1

TABLE 5.1 Coefficients for Determining Stiffness Matrix and Plastic Hinge Rotation of Elasto-Plastic Component[40]

Section [1]	I (in^4) [2]	A (in^2) [3]	A_v (in^2) [4]	M_p $(k-in)$ [5]	P_y $(kips)$ [6]
W14×109	1240	32.00	7.52	6912	1152
W14×159	1900	46.70	11.16	10332	1494
W14×193	2400	56.80	13.78	12840	2054
W24×104	3100	30.60	12.03	10404	1102
W27×146	5630	42.90	16.56	16560	1544
W30×173	8200	50.80	19.94	21840	1829
W24×76	2100	22.40	10.52	7200	-
W27×94	3270	27.70	13.19	10008	-
W30×99	3990	29.10	15.42	11230	-

TABLE 7.1 Column and Beam Element Properties for MRF Design 1

Column Section [1]	Beam Section [2]	M_y $(k-in)$ [3]	k_e $(\frac{k-in}{radian}\times 10^3)$ [4]	Doubler Plate Thickness (in) [5]	a_o [6]
W14×109	W24×76	3513	1885	-	1.0
W14×159	W24×94	5748	3085	-	1.0
W14×193	W30×99	7700	4132	-	1.0
W24×104	W24×76	5795	3110	-	1.0
W27×146	W27×94	8937	4796	3/8	1.62
W30×173	W30×99	11860	6365	3/8	1.57

TABLE 7.2 Panel Zone Joint Element Properties for MRF Design 1

Section [1]	I (in^4) [2]	A (in^2) [3]	A_v (in^2) [4]	M_p $(k-in)$ [5]	P_y $(kips)$ [6]
W14×99	1110	29.10	6.97	6228	1048
W14×132	1530	38.80	9.46	8424	1400
W14×159	1900	46.70	11.16	10332	1680
W18×86	1530	25.30	8.83	6696	911
W21×122	2960	35.90	13.01	11052	1290
W24×146	4580	43.00	16.08	15048	1550
W21×68	1480	20.00	9.09	5760	-
W24×94	2700	27.70	12.52	9144	-
W27×94	3270	27.70	13.19	10008	-

TABLE 7.3 Column and Beam Element Properties for MRF Design 2

Column Section [1]	Beam Section [2]	M_y $(k-in)$ [3]	k_e $(\frac{k-in}{radian}\times 10^3)$ [4]	Doubler Plate Thickness (in) [5]	a_o [6]
W14×99	W21×68	2850	1530	3/8	1.77
W14×132	W24×94	4442	2384	3/8	1.58
W14×159	W27×94	5748	3085	3/8	1.50
W18×86	W21×68	3776	2026	3/8	1.78
W21×122	W24×94	6391	3430	3/8	1.62
W24×146	W27×94	8610	4616	3/8	1.58

TABLE 7.4 Panel Zone Joint Element Properties for MRF Design 2

Column Section [1]	Beam Section [2]	M_y $(k-in)$ [3]	k_e $(\frac{k-in}{radian}\times 10^3)$ [4]	Doubler Plate Thickness (in) [5]	a_o [6]
W14×99	W21×68	2850	1530	3/8	1.77
W14×99	W21×68	2850	1530	7/16	1.90
W14×132	W24×94	4442	2384	1/2	1.78
W14×159	W27×94	5748	3085	3/8	1.50
W14×159	W27×94	5748	3085	1/2	1.67
W18×86	W21×68	3776	2026	3/4	2.56
W18×86	W21×68	3776	2026	1	3.08
W21×122	W24×94	6391	3430	1	2.67
W24×146	W27×94	8610	4616	3/4	2.15

TABLE 7.5 Panel Zone Joint Element Properties for MRF Design 3

Column Section [1]	Beam Section [2]	M_y $(k-in)$ [3]	k_e $(\frac{k-in}{radian}\times 10^3)$ [4]	Doubler Plate Thickness (in) [5]	a_o [6]
W14×99	W21×68	2850	1530	3/8	1.77
W14×132	W24×94	4442	2384	3/8	1.58
W14×159	W27×94	5748	3085	1/2	1.67
W18×86	W21×68	3776	2026	1/2	2.04
W21×122	W24×94	6391	3430	1/2	1.83
W24×146	W27×94	8610	4616	3/4	2.15

TABLE 7.6 Panel Zone Joint Element Properties for MRF Design 4

Floor	Column Line A		Column Line B		Column Line C		Column Line D	
	Req'd	Prov'd	Req'd	Prov'd	Req'd	Prov'd	Req'd	Prov'd
Roof	0.1	3/8	0.2	3/8	0.2	3/8	0.1	3/8
6^{th}	0.2	3/8	0.4	1/2	0.4	1/2	0.2	3/8
5^{th}	0.1	3/8	0.4	1/2	0.4	1/2	0.1	3/8
4^{th}	0.1	3/8	0.4	1/2	0.4	1/2	0.1	3/8
3^{rd}	-	-	0.2	3/8	0.2	3/8	-	-
2^{nd}	-	-	0.2	3/8	0.2	3/8	-	-

TABLE 7.7 Doubler Plate Thickness Required versus Provided for MRF Design 1 of 0.8Mp

MRF Model [1]	Vibration Periods (second)		
	1^{st} Mode [2]	2^{nd} Mode [3]	3^{rd} Mode [4]
Design 1	1.65	0.58	0.30
Design 2	1.90	0.68	0.37
Design 3	1.84	0.65	0.35
Design 4	1.86	0.66	0.36

TABLE 7.8 Vibration Periods of MRF Models

Floor	Vibration Mode Shapes					
	Design 1			Design 2		
	Φ_1	Φ_2	Φ_3	Φ_1	Φ_2	Φ_3
[1]	[2]	[3]	[4]	[5]	[6]	[7]
Roof	1.000	-1.000	-0.815	1.000	-1.000	-0.826
6^{th}	0.881	-0.255	0.642	0.883	-0.259	0.659
5^{th}	0.717	0.495	1.000	0.723	0.476	1.000
4^{th}	0.551	0.833	-0.072	0.562	0.812	0.088
3^{rd}	0.371	0.824	-0.879	0.384	0.815	-0.867
2^{nd}	0.200	0.531	-0.910	0.214	0.541	-0.918

TABLE 7.9 Vibration Mode Shapes of MRF Design 1 and Design 2

Floor	Vibration Mode Shapes					
	Design 3			Design 4		
	Φ_1	Φ_2	Φ_3	Φ_1	Φ_2	Φ_3
[1]	[2]	[3]	[4]	[5]	[6]	[7]
Roof	1.000	-1.000	-0.809	1.000	-1.000	-0.810
6^{th}	0.892	-0.296	0.595	0.889	-0.289	0.597
5^{th}	0.734	0.461	1.000	0.726	0.475	1.000
4^{th}	0.576	0.815	0.136	0.563	0.831	0.122
3^{rd}	0.397	0.834	-0.830	0.384	0.842	-0.836
2^{nd}	0.224	0.563	-0.913	0.216	0.566	-0.902

TABLE 7.10 Vibration Mode Shapes of MRF Design 3 and Design 4

Floor [1]	Static Analysis				Response Spectrum Analysis (CQC)			
	Story Force (kip) [2]	Story Shear (kip) [3]	Floor Displ. (in) [4]	Story Drift (%) [5]	Story Force (kip) [6]	Story Shear (kip) [7]	Floor Displ. (in) [8]	Story Drift (%) [9]
Roof	128.2	128.2	8.15	0.20	51.6	51.6	5.87	0.11
20^{th}	26.7	154.8	7.78	0.23	45.9	97.4	5.72	0.15
19^{th}	25.3	180.1	7.35	0.22	38.9	135.5	5.53	0.16
18^{th}	23.9	204.1	6.95	0.24	33.6	166.7	5.32	0.18
17^{th}	22.6	226.6	6.51	0.25	30.6	191.5	5.09	0.20
16^{th}	21.2	247.8	6.09	0.25	30.5	211.6	4.84	0.20
15^{th}	19.8	267.6	5.66	0.25	31.8	228.9	4.57	0.20
14^{th}	18.5	286.1	5.23	0.25	32.8	245.0	4.31	0.21
13^{th}	17.1	303.2	4.78	0.26	32.9	260.5	4.03	0.21
12^{th}	15.7	318.9	4.34	0.26	32.3	275.3	3.74	0.22
11^{th}	14.3	333.2	3.91	0.26	31.6	289.3	3.43	0.22
10^{th}	12.9	346.2	3.51	0.25	31.7	302.4	3.12	0.23
9^{th}	11.6	357.7	3.10	0.26	32.7	315.0	2.80	0.22
8^{th}	10.2	367.9	2.72	0.25	34.1	327.8	2.49	0.22
7^{th}	8.8	376.8	2.34	0.25	35.1	341.2	2.20	0.22
6^{th}	7.5	384.3	1.96	0.25	34.6	355.3	1.84	0.23
5^{th}	6.1	390.4	1.58	0.25	32.3	369.4	1.51	0.23
4^{th}	4.7	395.1	1.21	0.24	27.9	382.3	1.17	0.23
3^{rd}	3.4	398.5	0.84	0.24	21.3	393.1	0.83	0.23
2^{nd}	1.0	400.0	0.50	0.23	13.3	400.0	0.49	0.23

Table 8.1 Lateral Forces and the Associated Responses

Mode	Period	Circular	Participation Factor			Effective Modal Mass Ratio (%)		
	(sec)	Frequency	X^1	Y^2	Z^3	X^1	Y^2	Z^3
[1]	[2]	[3]	[4]	[5]	[6]	[7]	[8]	[9]
1^{st}	3.78	1.66	0	5.576	0	0	76.3	0
2^{nd}	3.60	1.76	5.595	0	0	76.8	0	0
3^{rd}	2.37	2.65	0	0	2443.719	0	0	89.8
4^{th}	1.30	4.82	-2.098	0	0.003	10.8	0	0
5^{th}	1.27	4.97	0	-2.189	0.003	0	11.7	0
6^{th}	0.82	7.67	0	0	-700.646	0	0	7.4
7^{th}	0.77	8.14	1.198	0	-0.003	3.6	0	0
8^{th}	0.72	8.72	0	1.170	0.002	0	3.4	0
9^{th}	0.54	11.67	0.837	0	-0.010	1.7	0	0
Σ						92.9	91.4	97.2

[1] X direction is the longitudinal direction

[2] Y direction is the transverse direction

[3] Z direction is the torsional direction

Table 8.2 Dynamic Characteristics of the 20-Story MRF

Floor	Design 1				Design 2				Design 3			
	Exterior Column		Interior Column		Exterior Column		Interior Column		Exterior Column		Interior Column	
[1]	Req'd (in) [2]	Pro'd (in) [3]	Req'd (in) [4]	Pro'd (in) [5]	Req'd (in) [6]	Pro'd (in) [7]	Req'd (in) [8]	Pro'd (in) [9]	Req'd (in) [10]	Pro'd (in) [11]	Req'd (in) [12]	Pro'd (in) [13]
Roof	--	--	--	--	0.28	3/8	0.47	1/2	0.06	3/8	0.18	3/8
20*th*	--	--	--	--	0.49	1/2	0.74	3/4	0.21	3/8	0.37	3/8
19*th*	--	--	--	--	0.47	1/2	0.67	3/4	0.17	3/8	0.31	3/8
18*th*	--	--	--	--	0.47	1/2	0.67	3/4	0.17	3/8	0.31	3/8
17*th*	--	--	--	--	0.35	3/8	0.67	3/4	0.05	3/8	0.31	3/8
16*th*	--	--	--	--	0.35	3/8	0.67	3/4	0.05	3/8	0.31	3/8
15*th*	--	--	--	--	0.45	1/2	0.86	1	0.10	3/8	0.43	1/2
14*th*	--	--	--	--	0.45	1/2	0.86	1	0.10	3/8	0.43	1/2
13*th*	--	--	0.01	--	0.26	3/8	0.86	1	--	--	0.43	1/2
12*th*	--	--	0.04	--	0.26	3/8	0.86	1	--	--	0.43	1/2
11*th*	--	--	0.07	--	--	--	0.86	1	--	--	0.43	1/2
10*th*	--	--	0.10	--	--	--	0.86	1	--	--	0.43	1/2
9*th*	--	--	--	--	--	--	0.68	3/4	--	--	0.30	3/8
8*th*	--	--	--	--	--	--	0.68	3/4	--	--	0.30	3/8
7*th*	--	--	--	--	--	--	0.68	3/4	--	--	0.30	3/8
6*th*	--	--	--	--	--	--	0.68	3/4	--	--	0.30	3/8
5*th*	--	--	0.05	--	--	--	0.68	3/4	--	--	0.30	3/8
4*th*	--	--	0.05	--	--	--	0.68	3/4	--	--	0.30	3/8
3*rd*	--	--	0.01	--	--	--	0.56	5/8	--	--	0.22	3/8
2*nd*	--	--	0.07	--	--	--	0.62	5/8	--	--	0.25	3/8
1*st*	--	--	--	--	--	--	0.65	5/8	--	--	0.28	3/8

Note: All doubler plates are A36 grade steel

Table 8.3 Doubler Plate Schedule (Required and As-Provided) for The 20-Story MRF Designs

Floor	Lateral Displacements (in) and Vibration Periods (sec)				
	ETABS [43]		ANSR-1 [40]		
	50% Rigid[a]	0% Rigid[b]	Design 1	Design 2	Design 3
(1)	(2)	(3)	(4)	(5)	(6)
Roof	7.395	8.468	10.150	8.528	9.026
20*th*	7.082	8.126	9.766	8.196	8.684
19*th*	6.731	7.739	9.327	7.822	8.292
18*th*	6.395	7.366	8.892	7.458	7.909
17*th*	6.038	6.966	8.427	7.067	7.497
16*th*	5.666	6.549	7.937	6.656	7.065
15*th*	5.289	6.124	7.431	6.236	6.623
14*th*	4.921	5.708	6.927	5.827	6.186
13*th*	4.543	5.279	6.406	5.404	5.733
12*th*	4.162	4.845	5.877	4.974	5.266
11*th*	3.773	4.401	5.333	4.529	4.787
10*th*	3.386	3.957	4.788	4.077	4.306
9*th*	2.996	3.507	4.242	3.619	3.820
8*th*	2.624	3.079	3.715	3.174	3.347
7*th*	2.252	2.649	3.186	2.726	2.872
6*th*	1.886	2.223	2.659	2.281	2.399
5*th*	1.522	1.798	2.132	1.836	1.926
4*th*	1.165	1.380	1.611	1.398	1.460
3*rd*	0.815	0.967	1.100	0.965	1.003
2*nd*	0.480	0.569	0.615	0.549	0.567
T_1	3.732	4.018	4.214	3.895	4.000
T_2	1.236	1.340	1.433	1.311	1.348
T_3	0.698	0.762	0.823	0.750	0.773
T_4	0.486	0.532	0.571	0.521	0.537
T_5	0.373	0.408	0.433	0.398	0.408

[a] Member stiffness formulation based on the clear span plus 50% panel zone sizes
[b] Member stiffness formulation based on the center-line dimensions

Table 8.4 Static Lateral Displacements and Vibration Periods of the MRFs

Floor	Panel Zone Deformations γ (% rad)					Story Drifts θ (%)			Effects of Joints	
	Column Line				Average	With Rigid Joint	Corrected	With Joint Element	Drift Ratios	
	A	B	C	D			[6]+[7]		[7]/[9]	[8]/[9]
[1]	[2]	[3]	[4]	[5]	[6]	[7]	=[8]	[9]	=[10]	=[11]
Roof	0.022	0.034	0.034	0.022	0.029	0.195	0.223	0.220	0.89	1.02
20*th*	0.000	0.051	0.060	0.000	0.028	0.231	0.258	0.251	0.92	1.03
19*th*	0.037	0.057	0.059	0.037	0.048	0.212	0.259	0.245	0.87	1.06
18*th*	0.046	0.065	0.060	0.046	0.055	0.236	0.290	0.261	0.90	1.11
17*th*	0.059	0.071	0.040	0.059	0.058	0.243	0.300	0.273	0.89	1.10
16*th*	0.025	0.060	0.054	0.025	0.042	0.209	0.250	0.278	0.75	0.90
15*th*	0.048	0.059	0.059	0.048	0.054	0.212	0.266	0.273	0.78	0.98
14*th*	0.049	0.064	0.064	0.049	0.057	0.218	0.274	0.283	0.77	0.97
13*th*	0.064	0.067	0.067	0.064	0.066	0.220	0.286	0.290	0.76	0.99
12*th*	0.068	0.071	0.070	0.068	0.070	0.225	0.294	0.296	0.76	1.00
11*th*	0.059	0.073	0.073	0.059	0.066	0.224	0.290	0.296	0.76	0.98
10*th*	0.062	0.075	0.075	0.062	0.069	0.226	0.294	0.298	0.76	0.99
9*th*	0.056	0.077	0.077	0.056	0.067	0.216	0.282	0.289	0.75	0.98
th	0.057	0.080	0.080	0.057	0.069	0.216	0.284	0.289	0.75	0.98
7*th*	0.053	0.081	0.081	0.053	0.067	0.213	0.280	0.287	0.74	0.98
6*th*	0.050	0.083	0.083	0.054	0.069	0.212	0.280	0.286	0.74	0.98
5*th*	0.049	0.084	0.084	0.049	0.067	0.207	0.274	0.281	0.74	0.98
4*th*	0.050	0.084	0.084	0.050	0.067	0.204	0.271	0.275	0.74	0.99
3*rd*	0.046	0.080	0.080	0.046	0.063	0.195	0.258	0.262	0.74	0.99
2*nd*	0.050	0.084	0.084	0.050	0.067	0.193	0.260	0.237	0.81	1.10
1*st*	0.018	0.032	0.032	0.018	0.026	--	--	--	--	--

Table 8.5 Panel Zone Deformations and Story Drift Corrections for MRF Design 3

Floor [1]	Story Drift Components (% rad)			Story Drift Contributions (%)		
	Beam Column [2]	Panel Zone [3]	$P-\Delta$ Effect [4]	Beam Column [5]	Panel Zone [6]	$P-\Delta$ Effect [7]
Roof	0.195	0.025	0.008	85.5	10.9	3.6
20*th*	0.231	0.020	0.010	88.5	7.6	3.9
19*th*	0.212	0.033	0.011	82.8	12.9	4.3
18*th*	0.236	0.025	0.013	86.1	9.1	4.8
17*th*	0.243	0.030	0.015	84.3	10.4	5.3
16*th*	0.209	0.069	0.017	70.8	23.4	5.8
15*th*	0.212	0.061	0.018	72.9	20.9	6.2
14*th*	0.218	0.065	0.019	72.1	21.6	6.3
13*th*	0.220	0.070	0.021	70.7	22.5	6.8
12*th*	0.225	0.071	0.023	70.5	22.2	7.3
11*th*	0.224	0.072	0.025	69.7	22.5	7.8
10*th*	0.226	0.072	0.026	69.7	22.2	8.1
9*th*	0.216	0.073	0.026	68.5	23.1	8.4
8*th*	0.216	0.073	0.028	68.1	23.0	8.9
7*th*	0.213	0.074	0.029	67.4	23.4	9.2
6*th*	0.212	0.074	0.029	67.3	23.4	9.3
5*th*	0.207	0.070	0.030	66.5	23.8	9.7
4*th*	0.204	0.070	0.030	66.8	23.2	10.0
3*rd*	0.195	0.067	0.029	67.0	23.0	10.0
2*nd*	0.193	0.044	0.026	73.3	16.8	9.9

Table 8.6 Story Drift Components for MRF Design 3

Floor [1]	Design 1			Design 2			Design 3		
	Mode 1 [2]	Mode 2 [3]	Mode 3 [4]	Mode 1 [5]	Mode 2 [6]	Mode 3 [7]	Mode 1 [8]	Mode 2 [9]	Mode 3 [10]
Roof	1.000	-1.000	1.000	1.000	-1.000	1.000	1.000	-1.000	1.000
20th	0.977	-0.881	0.729	0.976	-0.880	0.736	0.976	-0.882	0.738
19th	0.948	-0.716	0.353	0.946	-0.715	0.365	0.947	-0.717	0.366
18th	0.915	-0.532	-0.021	0.913	-0.533	-0.002	0.914	-0.536	-0.003
17th	0.877	-0.324	-0.380	0.874	-0.327	-0.359	0.876	-0.329	-0.362
16th	0.834	-0.105	-0.665	0.832	-0.110	-0.650	0.834	-0.112	-0.653
15th	0.788	0.109	-0.837	0.786	0.101	-0.832	0.789	0.099	-0.834
14th	0.740	0.303	-0.874	0.740	0.288	-0.881	0.742	0.289	-0.882
13th	0.689	0.476	-0.786	0.691	0.458	-0.810	0.692	0.462	-0.807
12th	0.635	0.621	-0.591	0.640	0.602	-0.631	0.639	0.610	-0.621
11th	0.579	0.734	-0.318	0.585	0.717	-0.368	0.584	0.727	-0.353
10th	0.522	0.808	-0.010	0.529	0.797	-0.061	0.528	0.806	-0.046
9th	0.464	0.844	0.292	0.472	0.840	0.252	0.470	0.847	0.264
8th	0.408	0.841	0.540	0.415	0.844	0.520	0.413	0.849	0.526
7th	0.351	0.803	0.723	0.358	0.812	0.724	0.355	0.815	0.725
6th	0.293	0.732	0.821	0.300	0.746	0.840	0.298	0.746	0.834
5th	0.235	0.631	0.823	0.242	0.649	0.858	0.239	0.646	0.846
4th	0.178	0.506	0.733	0.184	0.526	0.776	0.182	0.521	0.760
3rd	0.122	0.361	0.560	0.127	0.381	0.605	0.125	0.375	0.589
2nd	0.069	0.209	0.337	0.073	0.225	0.371	0.071	0.220	0.358
Period (sec)	4.214	1.4330	0.823	3.895	1.311	0.750	4.000	1.348	0.773

Table 8.7 Vibration Mode Shapes and Periods for MRF Designs 1,2 and 3

Floor	Design 1				Design 2				Design 3			
	Column Line				Column Line				Column Line			
[1]	A (% rad) [2]	B (% rad) [3]	C (% rad) [4]	D (% rad) [5]	A (% rad) [6]	B (% rad) [7]	C (% rad) [8]	D (% rad) [9]	A (% rad) [10]	B (% rad) [11]	C (% rad) [12]	D (% rad) [13]
Roof	0.093	0.131	0.170	0.150	0.078	0.103	0.122	0.107	0.069	0.104	0.128	0.103
20*th*	0.163	0.254	0.392	0.319	0.131	0.152	0.173	0.168	0.131	0.181	0.268	0.175
19*th*	0.147	0.220	0.356	0.257	0.140	0.164	0.184	0.176	0.137	0.194	0.301	0.179
18*th*	0.111	0.156	0.301	0.183	0.132	0.158	0.180	0.171	0.124	0.177	0.265	0.170
17*th*	0.114	0.235	0.412	0.184	0.123	0.156	0.189	0.182	0.109	0.150	0.286	0.156
16*th*	0.152	0.385	0.545	0.304	0.162	0.187	0.323	0.294	0.153	0.360	0.512	0.241
15*th*	0.240	0.609	0.745	0.488	0.195	0.251	0.408	0.408	0.188	0.481	0.614	0.407
14*th*	0.527	0.897	1.031	0.764	0.391	0.418	0.563	0.568	0.394	0.718	0.843	0.613
13*th*	0.563	1.057	1.193	0.800	0.499	0.622	0.706	0.592	0.821	0.986	1.108	1.050
12*th*	0.525	0.995	1.128	0.758	0.570	0.710	0.784	0.662	0.904	1.066	1.186	1.129
11*th*	0.233	0.827	0.962	0.450	0.822	0.672	0.739	0.950	0.599	0.912	1.029	0.768
10*th*	0.181	0.714	0.842	0.356	0.644	0.522	0.603	0.809	0.397	0.671	0.787	0.607
9*th*	0.154	0.580	0.717	0.214	0.263	0.383	0.494	0.393	0.181	0.502	0.619	0.315
8*th*	0.154	0.564	0.695	0.207	0.180	0.268	0.367	0.313	0.168	0.421	0.536	0.260
7*th*	0.154	0.608	0.726	0.180	0.156	0.207	0.296	0.180	0.154	0.398	0.505	0.180
6*th*	0.169	0.681	0.775	0.183	0.159	0.214	0.293	0.180	0.164	0.434	0.525	0.181
5*th*	0.161	0.738	0.813	0.165	0.156	0.260	0.322	0.163	0.159	0.485	0.555	0.164
4*th*	0.163	0.769	0.832	0.165	0.162	0.305	0.354	0.164	0.161	0.509	0.567	0.165
3*rd*	0.150	0.776	0.827	0.152	0.149	0.384	0.439	0.151	0.149	0.489	0.542	0.151
2*nd*	0.151	0.762	0.801	0.152	0.151	0.475	0.516	0.153	0.150	0.518	0.565	0.151
1*st*	0.063	0.117	0.123	0.067	0.070	0.074	0.076	0.074	0.061	0.085	0.089	0.066

Table 8.8 Maximum Panel Zone Deformations (Parkfield Earthquake)

Floor	Design 1		Design 2		Design 3		Model 4	
	Story Drift θ (% rad)	Joint Deform γ (% rad)	Story Drift θ (% rad)	Joint Deform γ (% rad)	Story Drift θ (% rad)	Joint Deform γ (% rad)	Story Drift θ (% rad)	Joint Deform γ (% rad)
[1]	[2]	[3]	[4]	[5]	[6]	[7]	[8]	[9]
Roof	0.57	0.13	0.69	0.10	0.66	0.10	0.70	0.10
20*th*	0.72	0.28	0.89	0.15	0.84	0.18	0.89	0.15
19*th*	0.62	0.24	0.83	0.16	0.79	0.20	0.83	0.16
18*th*	0.57	0.18	0.78	0.16	0.71	0.18	0.78	0.16
17*th*	0.65	0.23	0.83	0.16	0.82	0.17	0.84	0.16
16*th*	0.80	0.34	1.03	0.24	1.00	0.31	1.03	0.21
15*th*	1.04	0.52	1.15	0.31	1.11	0.42	1.16	0.24
14*th*	1.31	0.80	1.38	0.48	1.41	0.64	1.40	0.35
13*th*	1.36	0.90	1.61	0.60	1.64	0.99	1.67	0.41
12*th*	1.23	0.85	1.70	0.68	1.61	1.07	1.77	0.48
11*th*	1.05	0.61	1.54	0.79	1.35	0.82	1.57	0.60
10*th*	0.95	0.52	1.25	0.64	1.11	0.61	1.25	0.48
9*th*	0.87	0.41	0.99	0.38	0.95	0.40	0.99	0.27
8*th*	0.87	0.40	0.87	0.28	0.88	0.34	0.87	0.22
7*th*	0.92	0.41	0.80	0.20	0.87	0.30	0.81	0.19
6*th*	0.97	0.45	0.81	0.21	0.89	0.32	0.80	0.19
5*th*	1.00	0.46	0.83	0.22	0.90	0.34	0.81	0.19
4*th*	1.00	0.48	0.85	0.24	0.90	0.35	0.83	0.21
3*rd*	1.00	0.47	0.88	0.28	0.87	0.33	0.84	0.23
2*nd*	0.85	0.46	0.92	0.32	0.81	0.34	0.90	0.27

Table 8.9 Total Story Drifts and Average Panel Zone Deformations for Designs 1, 2, 3 and Model 4 (Parkfield Earthquake)

Floor	Design 1		Design 2		Design 3		Model 4	
	Story Drift θ (% rad)	Joint Deform γ (% rad)	Story Drift θ (% rad)	Joint Deform γ (% rad)	Story Drift θ (% rad)	Joint Deform γ (% rad)	Story Drift θ (% rad)	Joint Deform γ (% rad)
[1]	[2]	[3]	[4]	[5]	[6]	[7]	[8]	[9]
Roof	0.41	0.12	0.45	0.07	0.43	0.08	0.45	0.07
20*th*	0.55	0.24	0.59	0.12	0.57	0.14	0.59	0.12
19*th*	0.62	0.24	0.62	0.13	0.58	0.15	0.62	0.13
18*th*	0.71	0.35	0.71	0.14	0.67	0.17	0.71	0.14
17*th*	0.67	0.33	0.76	0.15	0.73	0.17	0.76	0.15
16*th*	0.65	0.28	0.75	0.16	0.72	0.20	0.75	0.16
15*th*	0.69	0.32	0.68	0.14	0.63	0.16	0.68	0.14
14*th*	0.68	0.33	0.68	0.14	0.63	0.17	0.68	0.14
13*th*	0.63	0.28	0.71	0.14	0.67	0.19	0.72	0.14
12*th*	0.61	0.28	0.79	0.16	0.81	0.27	0.80	0.16
11*th*	0.69	0.30	0.84	0.22	0.90	0.34	0.83	0.20
10*th*	0.69	0.32	0.85	0.24	0.92	0.39	0.84	0.21
9*th*	0.63	0.26	0.78	0.22	0.83	0.33	0.77	0.19
8*th*	0.66	0.28	0.71	0.18	0.74	0.27	0.71	0.18
7*th*	0.67	0.29	0.66	0.16	0.61	0.20	0.67	0.17
6*th*	0.66	0.29	0.61	0.15	0.63	0.20	0.61	0.15
5*th*	0.62	0.27	0.60	0.15	0.62	0.20	0.60	0.15
4*th*	0.58	0.25	0.59	0.15	0.59	0.19	0.59	0.15
3*rd*	0.53	0.21	0.57	0.14	0.54	0.15	0.57	0.14
2*nd*	0.48	0.21	0.52	0.14	0.52	0.15	0.52	0.14

Table 8.10 Total Story Drifts and Average Panel Zone Deformations for Designs 1, 2, 3 and Model 4 (1.5*El Centro Earthquake)

Floor	Design 1		Design 2		Design 3		Model 4	
	Story Drift θ (% rad)	Joint Deform γ (% rad)	Story Drift θ (% rad)	Joint Deform γ (% rad)	Story Drift θ (% rad)	Joint Deform γ (% rad)	Story Drift θ (% rad)	Joint Deform γ (% rad)
[1]	[2]	[3]	[4]	[5]	[6]	[7]	[8]	[9]
21*th*	0.45	0.11	0.74	0.10	0.58	0.08	0.76	0.11
20*th*	0.66	0.26	1.00	0.17	0.81	0.16	1.02	0.17
19*th*	0.81	0.39	1.16	0.29	0.99	0.30	1.17	0.25
18*th*	0.93	0.57	1.43	0.55	1.24	0.53	1.44	0.40
17*th*	0.91	0.55	1.49	0.68	1.29	0.64	1.49	0.49
16*th*	0.87	0.47	1.29	0.63	1.15	0.59	1.28	0.45
15*th*	0.91	0.51	1.00	0.32	0.89	0.38	1.00	0.24
14*th*	0.94	0.53	0.88	0.23	0.74	0.24	0.89	0.20
13*th*	1.02	0.52	0.77	0.18	0.67	0.20	0.79	0.18
12*th*	1.16	0.65	0.69	0.16	0.74	0.22	0.71	0.16
11*th*	1.18	0.68	0.69	0.15	0.85	0.28	0.73	0.16
10*th*	1.08	0.65	0.73	0.18	0.96	0.38	0.77	0.19
9*th*	0.92	0.46	0.77	0.19	0.95	0.39	0.78	0.20
8*th*	0.98	0.51	0.82	0.24	0.89	0.38	0.85	0.23
7*th*	0.98	0.49	0.82	0.25	0.84	0.30	0.84	0.23
6*th*	0.95	0.48	0.78	0.23	0.95	0.37	0.78	0.21
5*th*	0.95	0.47	0.85	0.24	0.97	0.39	0.87	0.21
4*th*	0.94	0.47	0.92	0.28	0.90	0.38	0.94	0.25
3*rd*	0.89	0.44	0.91	0.30	0.80	0.32	0.96	0.29
2*nd*	0.73	0.41	0.85	0.30	0.71	0.30	0.90	0.29

Table 8.11 Total Story Drifts and Average Panel Zone Deformations for Designs 1, 2, 3 and Model 4 (1.5*Miyagi-Ken-Oki Earthquake)

Floor	Design 1			Design 2			Design 3			Model 4		
	Event			Event			Event			Event		
	PK	*1.5EC*	*1.5MI*	*PK*	*1.5EC*	*1.5MI*	*PK*	*1.5EC*	*1.5MI*	*PK*	*1.5EC*	*1.5MI*
[1]	γ/θ [2]	γ/θ [3]	γ/θ [4]	γ/θ [5]	γ/θ [6]	γ/θ [7]	γ/θ [8]	γ/θ [9]	γ/θ [10]	γ/θ [11]	γ/θ [12]	γ/θ [13]
21*th*	0.23	0.30	0.26	0.14	0.17	0.14	0.15	0.19	0.14	0.14	0.17	0.14
20*th*	0.39	0.44	0.39	0.17	0.20	0.17	0.22	0.26	0.20	0.17	0.20	0.17
19*th*	0.39	0.39	0.48	0.19	0.20	0.25	0.25	0.26	0.30	0.19	0.20	0.21
18*th*	0.32	0.48	0.61	0.20	0.19	0.38	0.25	0.25	0.42	0.20	0.19	0.28
17*th*	0.36	0.49	0.61	0.19	0.20	0.45	0.21	0.24	0.49	0.19	0.20	0.32
16*th*	0.42	0.43	0.53	0.23	0.21	0.48	0.31	0.27	0.51	0.20	0.21	0.35
15*th*	0.49	0.46	0.56	0.27	0.20	0.32	0.37	0.25	0.42	0.21	0.20	0.24
14*th*	0.61	0.49	0.56	0.35	0.21	0.26	0.45	0.27	0.33	0.24	0.21	0.22
13*th*	0.66	0.45	0.51	0.37	0.20	0.23	0.60	0.28	0.30	0.24	0.20	0.22
12*th*	0.69	0.46	0.56	0.39	0.20	0.23	0.66	0.33	0.30	0.27	0.20	0.23
11*th*	0.58	0.43	0.57	0.51	0.26	0.22	0.61	0.37	0.33	0.38	0.24	0.22
10*th*	0.54	0.47	0.60	0.51	0.29	0.24	0.55	0.42	0.39	0.38	0.25	0.25
9*th*	0.47	0.42	0.50	0.38	0.28	0.25	0.42	0.40	0.41	0.28	0.24	0.25
8*th*	0.46	0.43	0.51	0.32	0.26	0.30	0.39	0.37	0.42	0.25	0.25	0.27
7*th*	0.45	0.43	0.49	0.26	0.25	0.31	0.35	0.32	0.36	0.23	0.25	0.28
6*th*	0.46	0.44	0.50	0.26	0.25	0.29	0.36	0.32	0.39	0.24	0.25	0.27
5*th*	0.46	0.43	0.49	0.27	0.24	0.28	0.37	0.32	0.40	0.24	0.24	0.25
4*th*	0.47	0.43	0.50	0.28	0.25	0.30	0.38	0.32	0.42	0.25	0.25	0.27
3*rd*	0.47	0.40	0.49	0.31	0.25	0.33	0.38	0.29	0.39	0.27	0.25	0.30
2*nd*	0.54	0.44	0.56	0.35	0.28	0.35	0.42	0.29	0.42	0.30	0.28	0.32

Table 8.12 Average Panel Zone Deformation to Story Drift Ratios

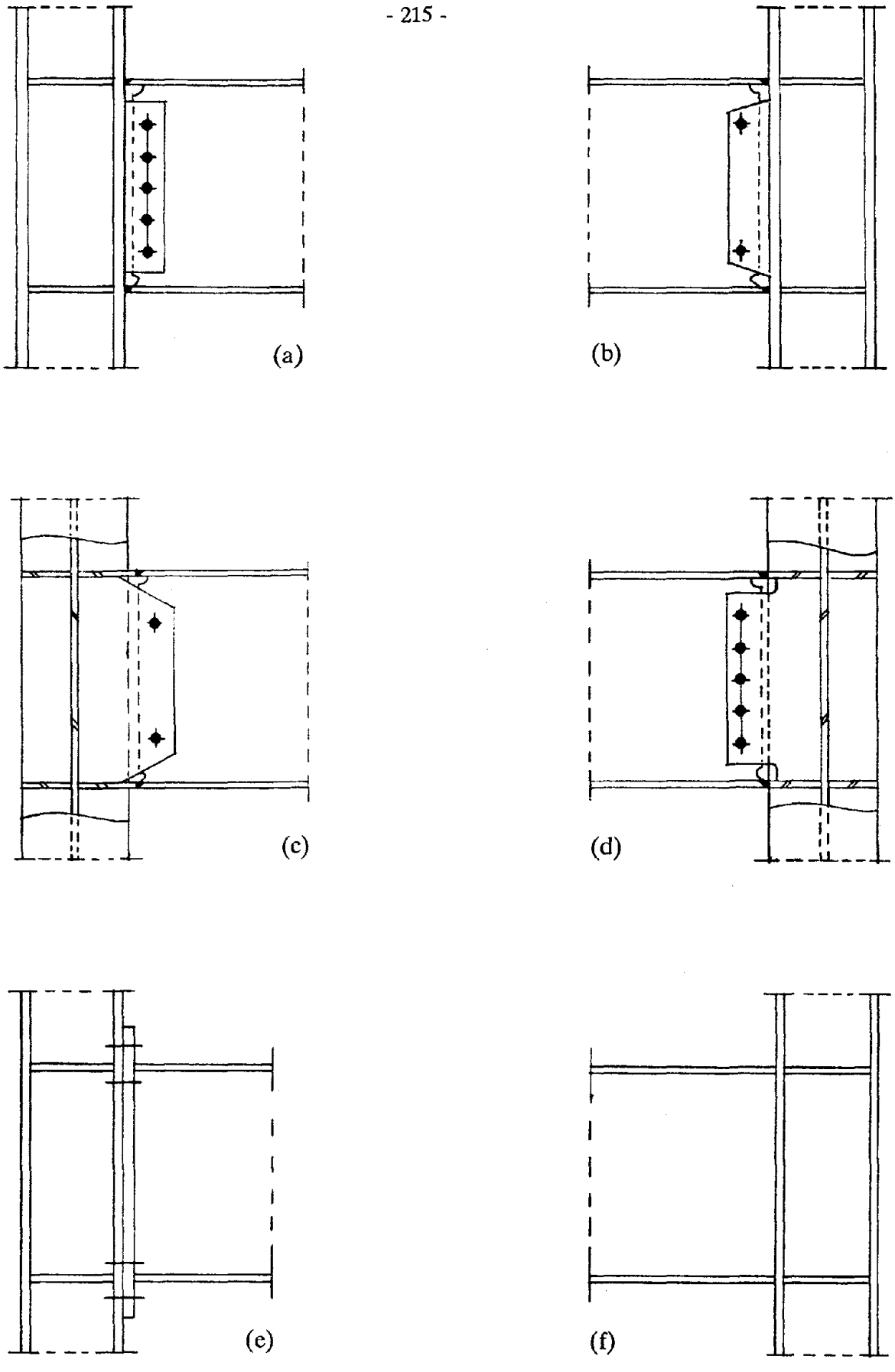

Figure 1.1 Various Beam-to-Column Moment Connections

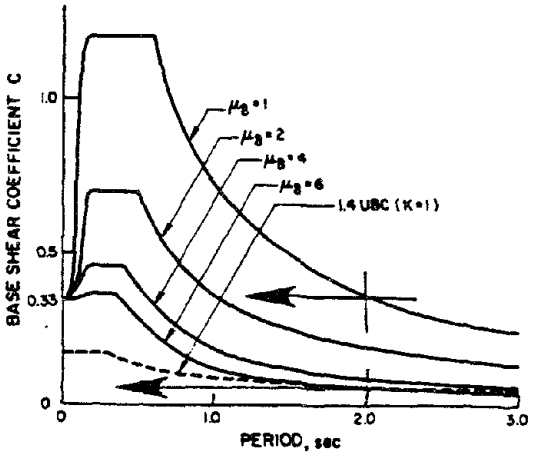

Figure 1.2 Base Shear Coefficient Spectra for Single DOF Systems with different ductilities

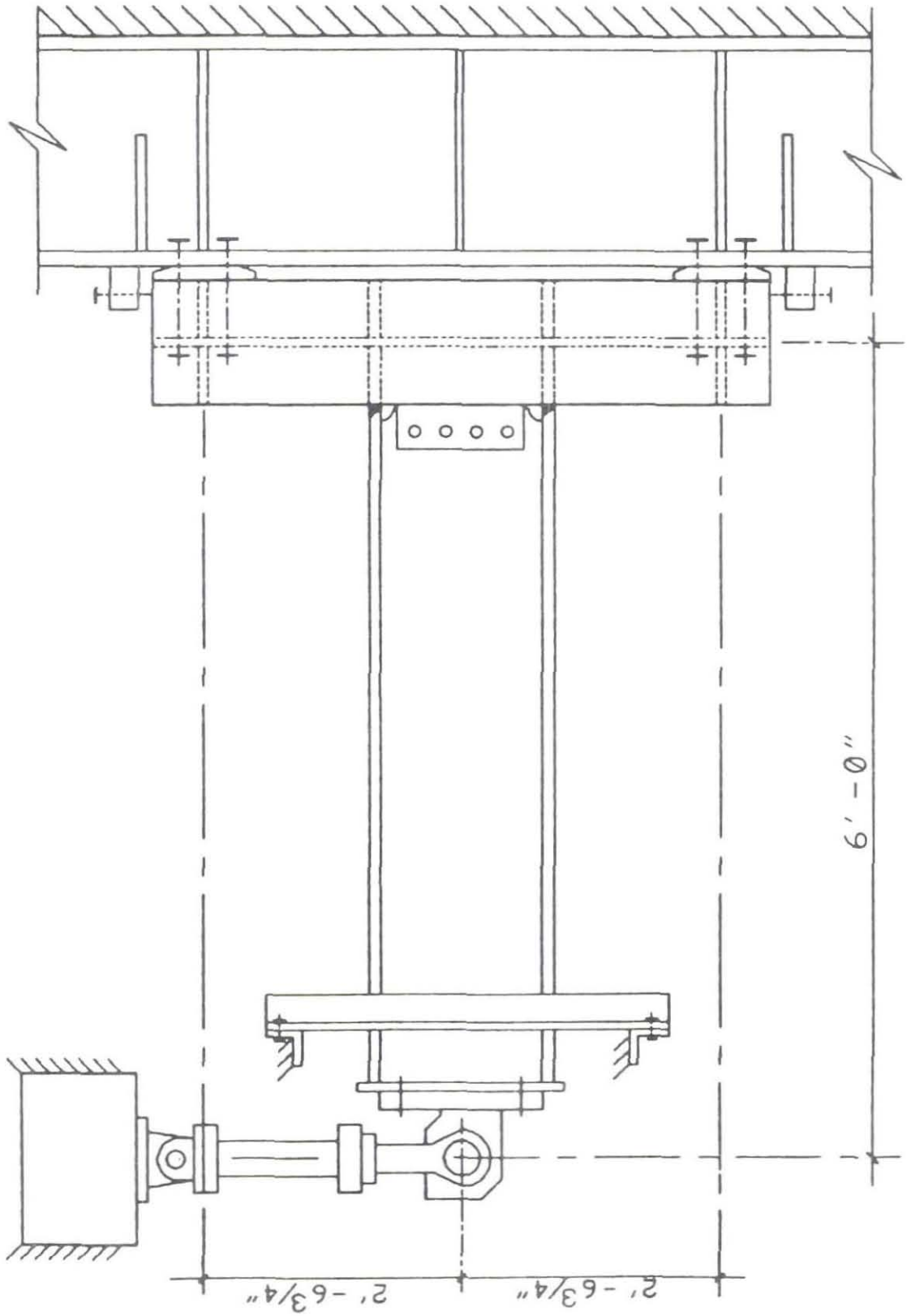

Figure 2.1 General View of Experimental Set-Up

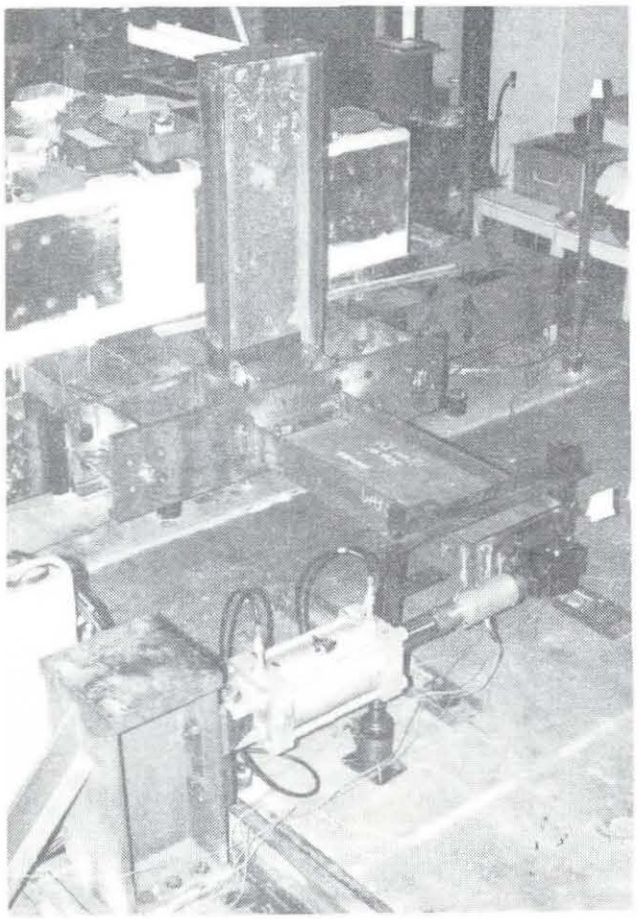

(a)

(b)

Figure 2.2 End Bearing Block with Adjustable Bolts

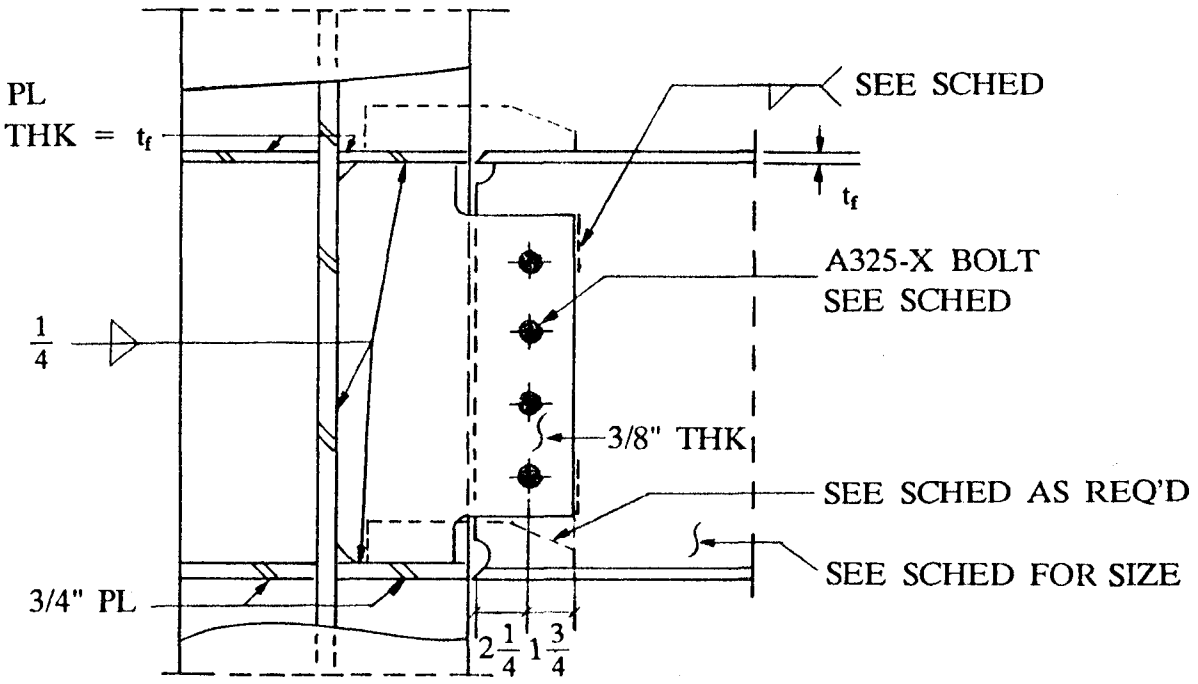

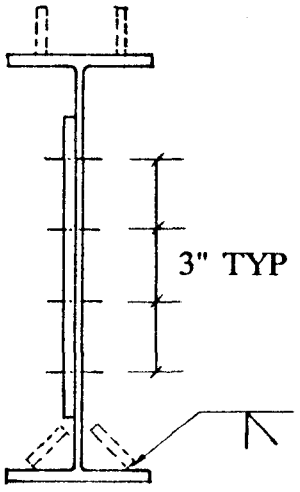

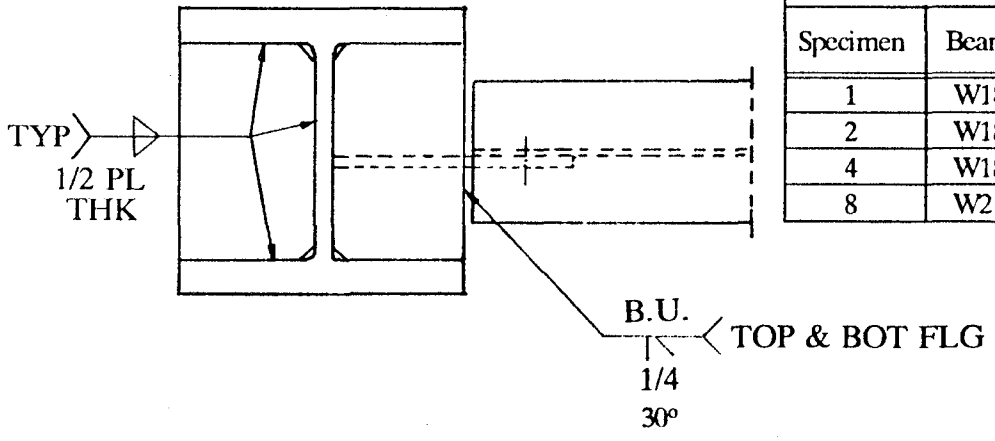

BEAM SCHEDULE				
Specimen	Beam Size	No. of Bolts 1" Φ A325-X	Reinforcing Ribs	Remarks
1	W18×40	4	1/2"×2"×9"	3-5/16"×2 1/2" Web Welding
2	W18×40	4	---	---
4	W18×40	4	---	---
8	W21×44	5	3/8"×2"×9"	Load Indicating Washers

Figure 2.3 Connection Details: Specimens 1, 2, 4 and 8

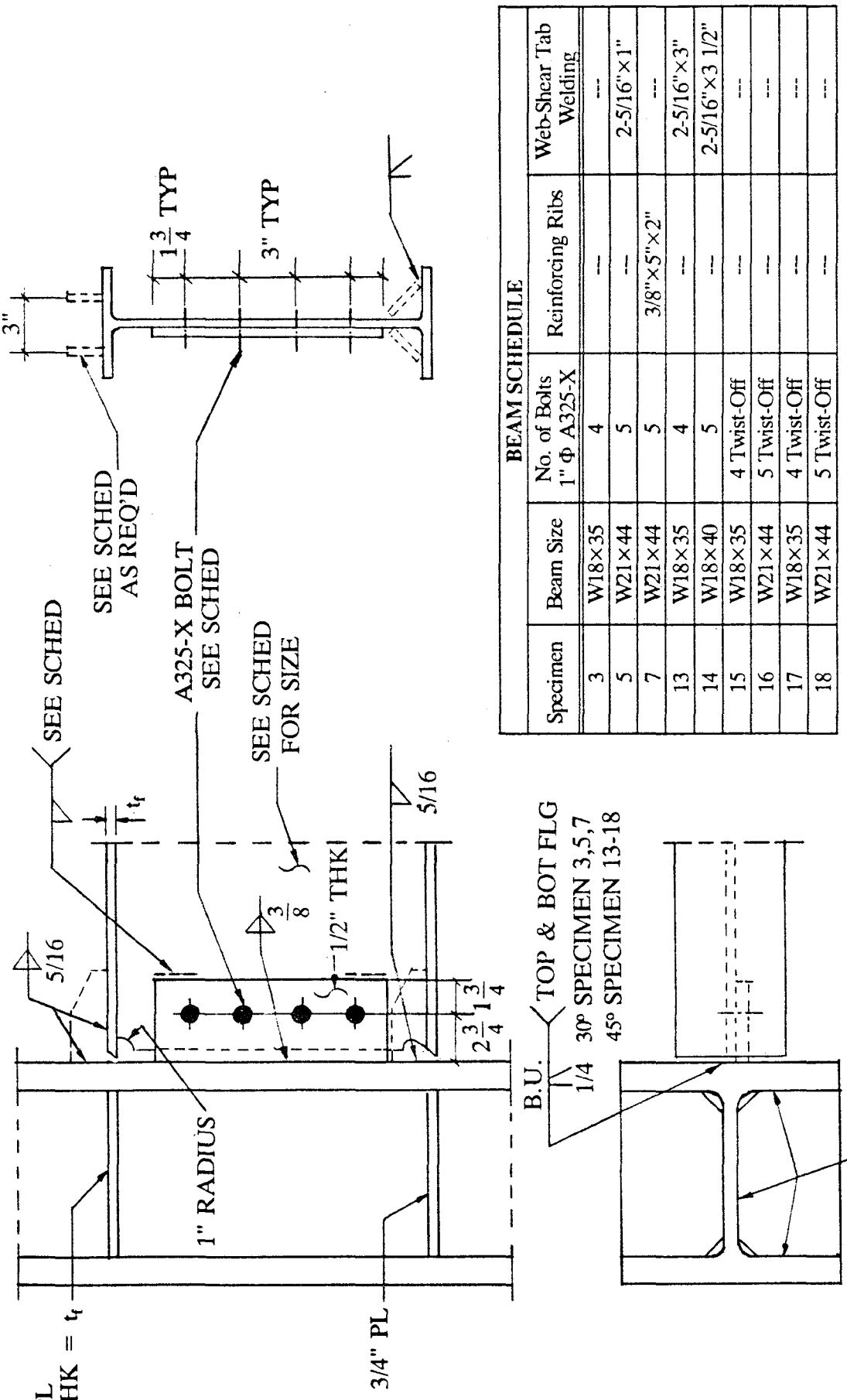

BEAM SCHEDULE

Specimen	Beam Size	No. of Bolts 1" Φ A325-X	Reinforcing Ribs	Web-Shear Tab Welding
3	W18×35	4	---	---
5	W21×44	5	---	2-5/16"×1"
7	W21×44	5	3/8"×5"×2"	---
13	W18×35	4	---	2-5/16"×3"
14	W18×40	5	---	2-5/16"×3 1/2"
15	W18×35	4 Twist-Off	---	---
16	W21×44	5 Twist-Off	---	---
17	W18×35	4 Twist-Off	---	---
18	W21×44	5 Twist-Off	---	---

Figure 2.4 Connection Details: Specimens 3, 5, 7, 13, 14, 15, 16, 17 and 18

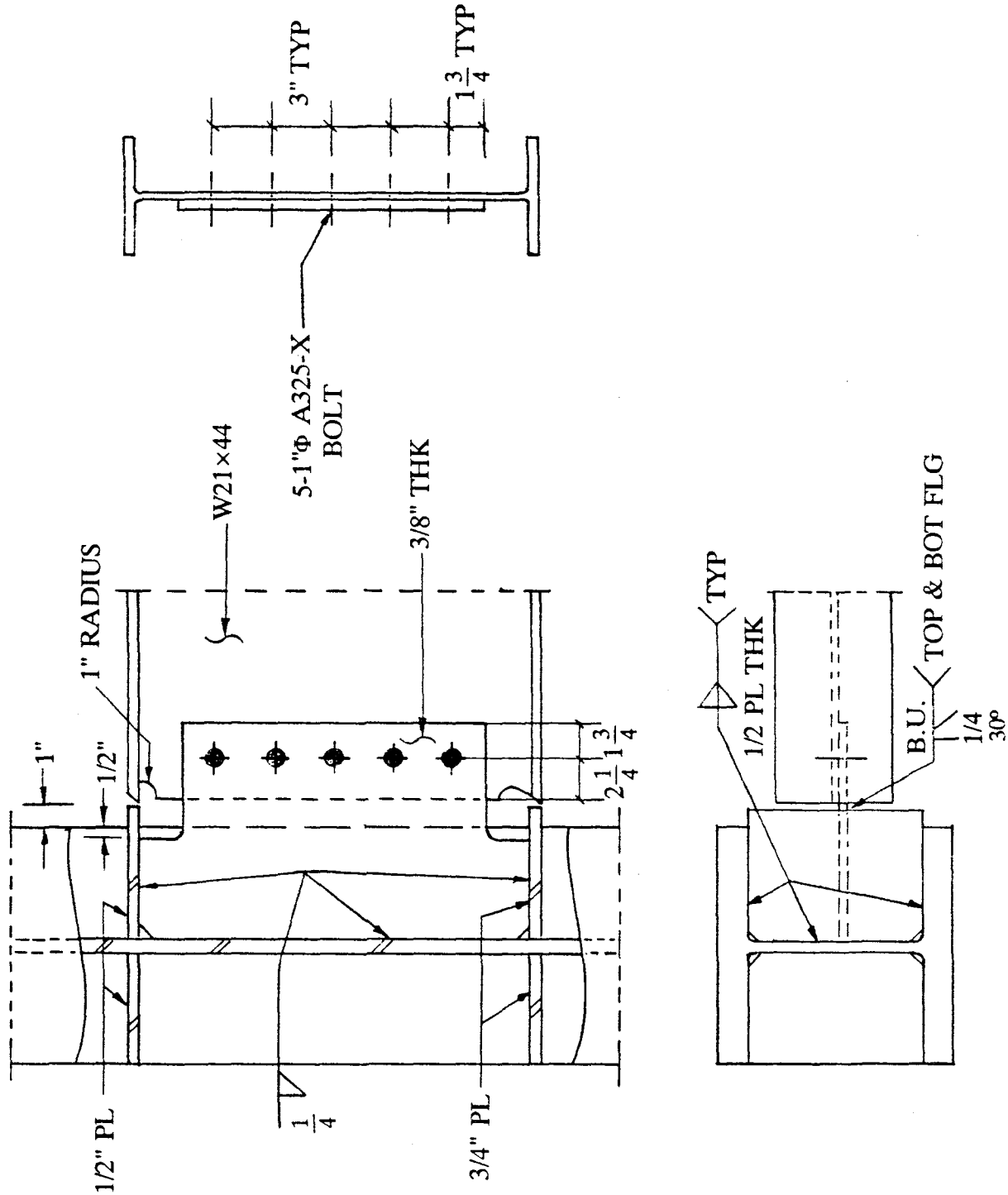

Figure 2.5 Connection Details: Specimen 6

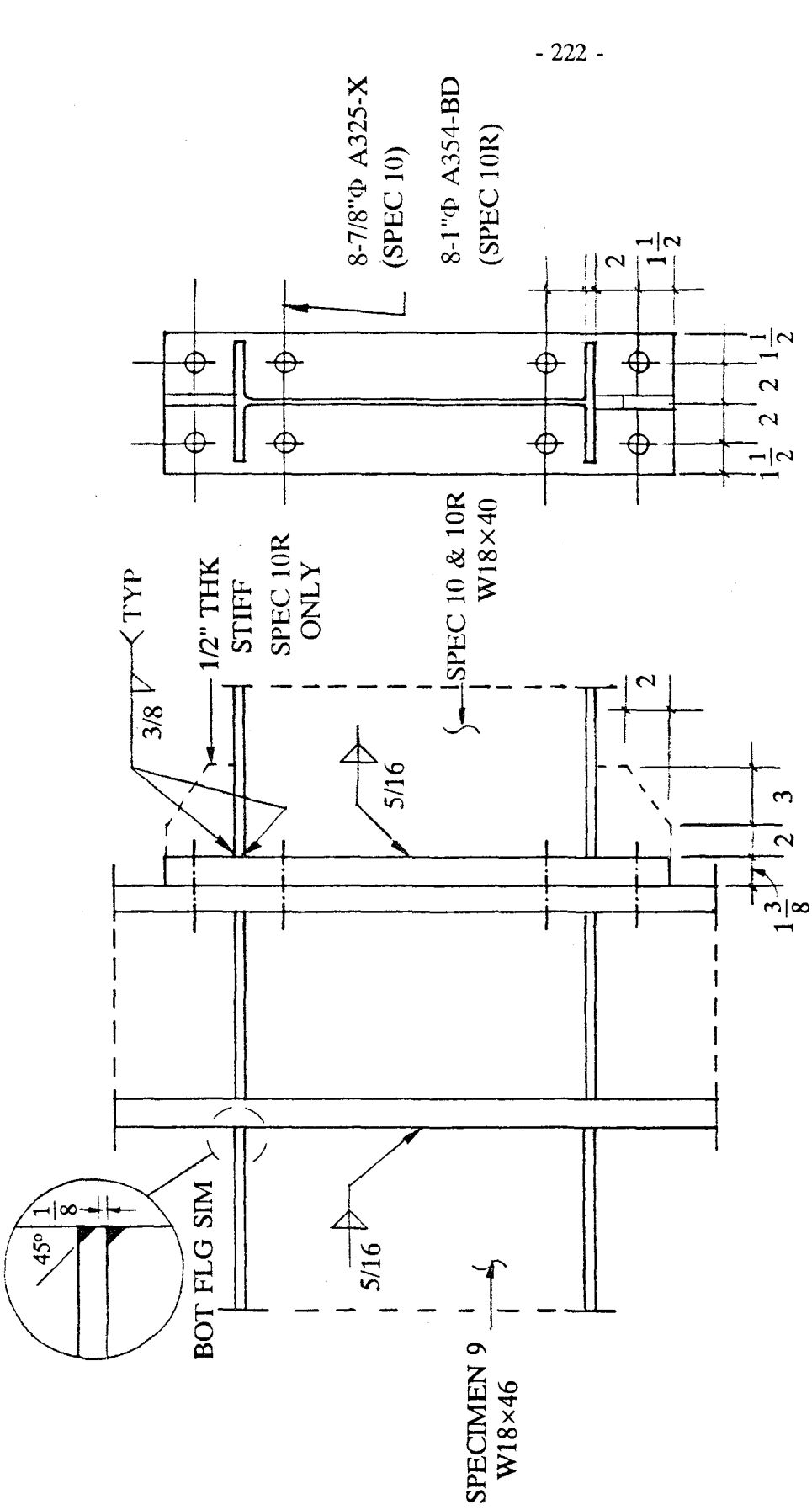

Figure 2.6 Connection Details: Specimens 9,10 and 10R

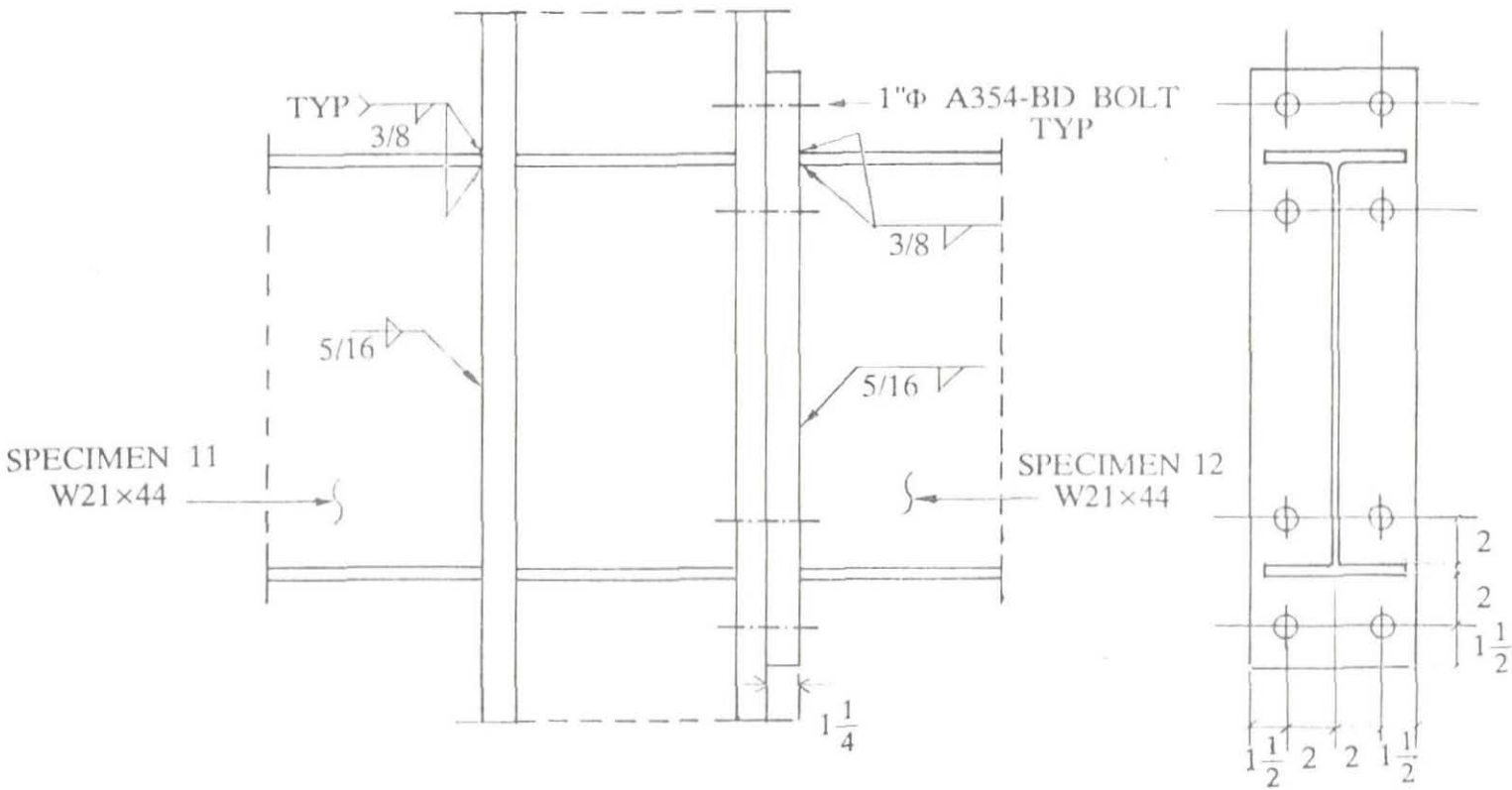

Figure 2.7 Connection Details: Specimens 11 and 12

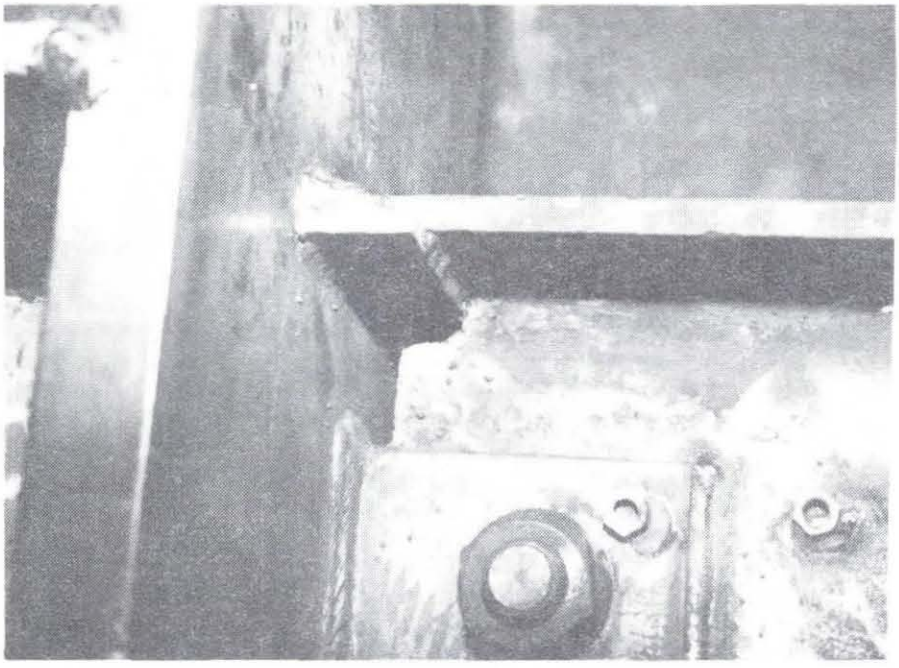

Figure 2.8 Upper Web Cope (Specimen 14)

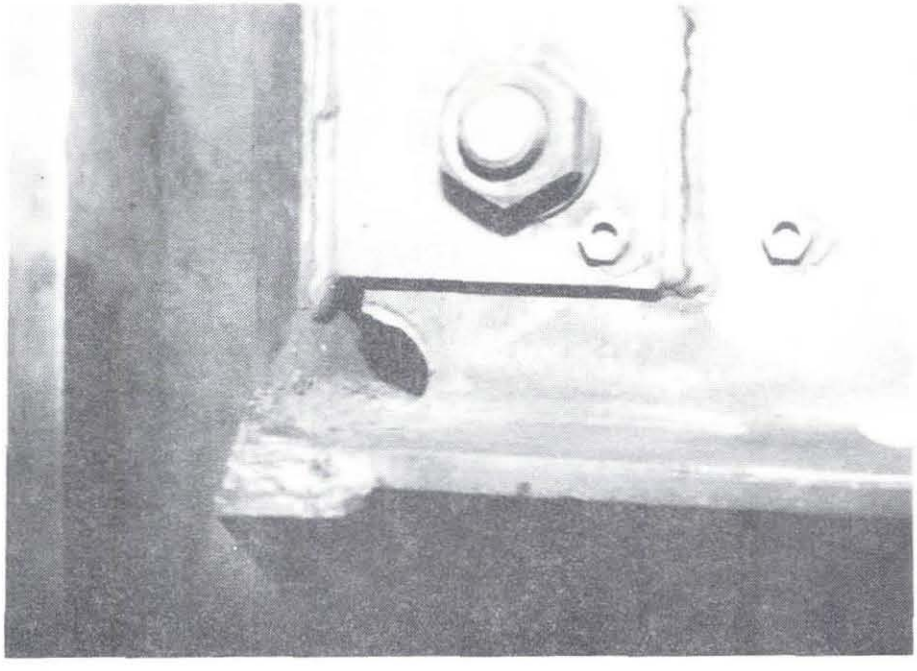

Figure 2.9 Lower Web Cope (Specimen 14)

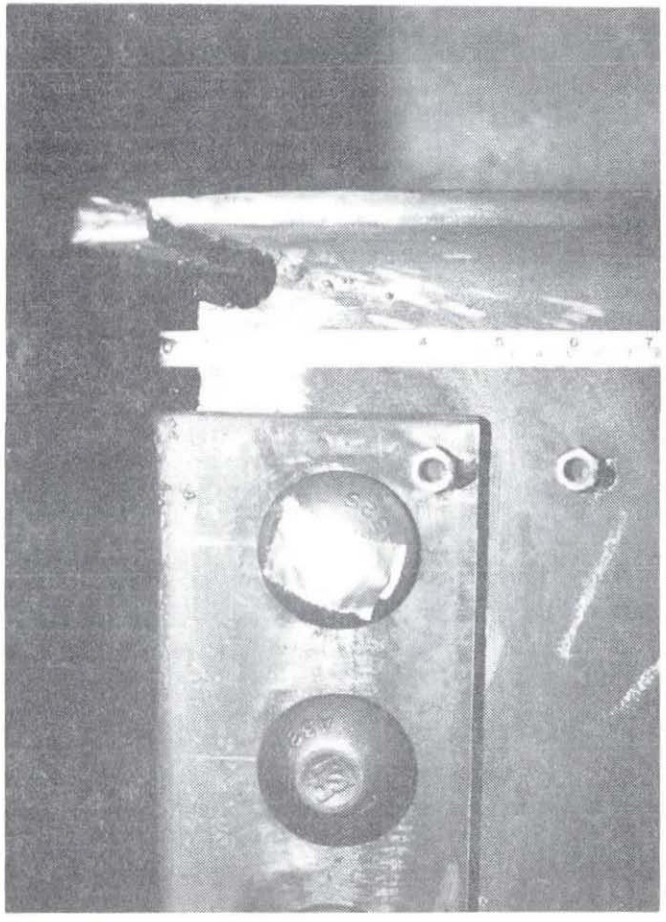

Figure 2.10 Upper Web Cope (Specimen 15)

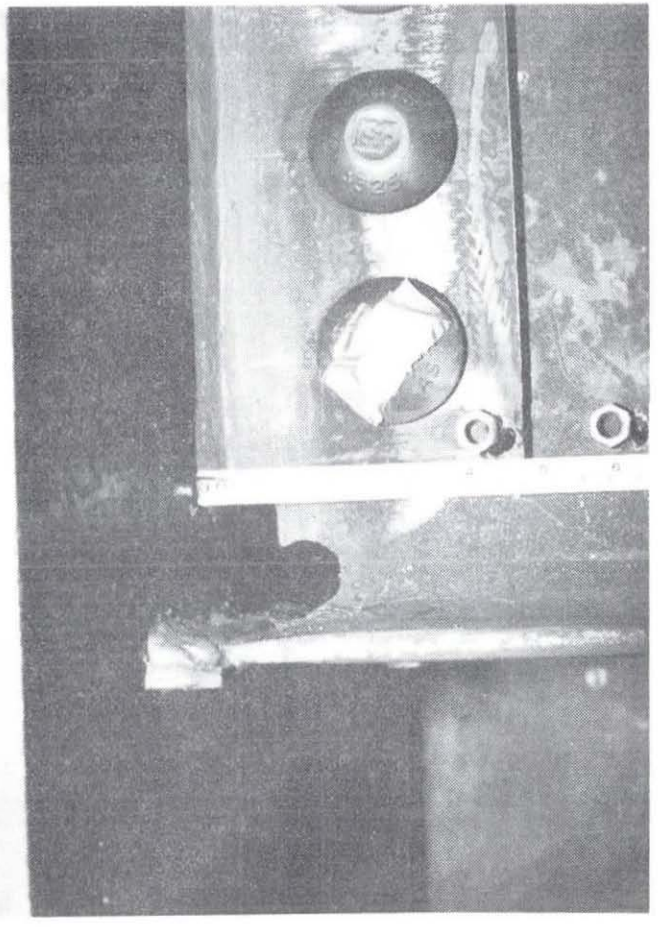

Figure 2.11 Lower Web Cope (Specimen 15)

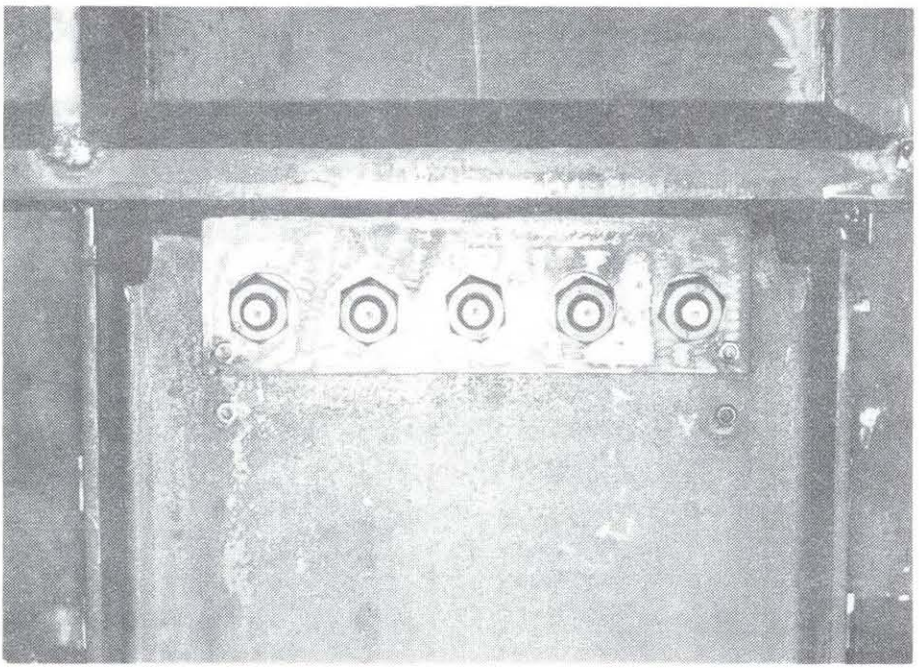

Figure 2.12 Upper and Lower Web Copes (Specimen 16)

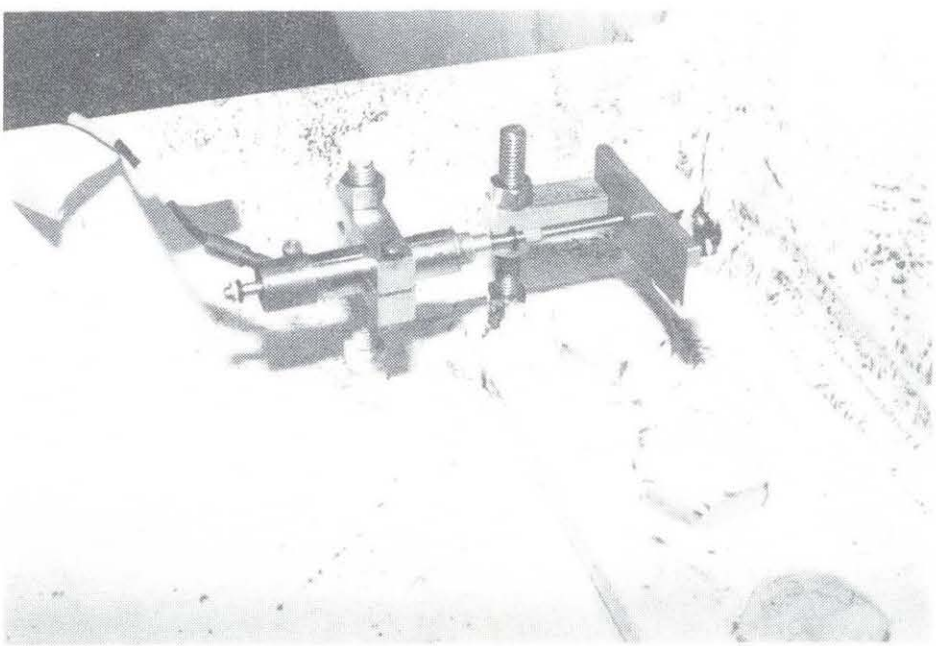

Figure 2.13 Typical Slip Gage

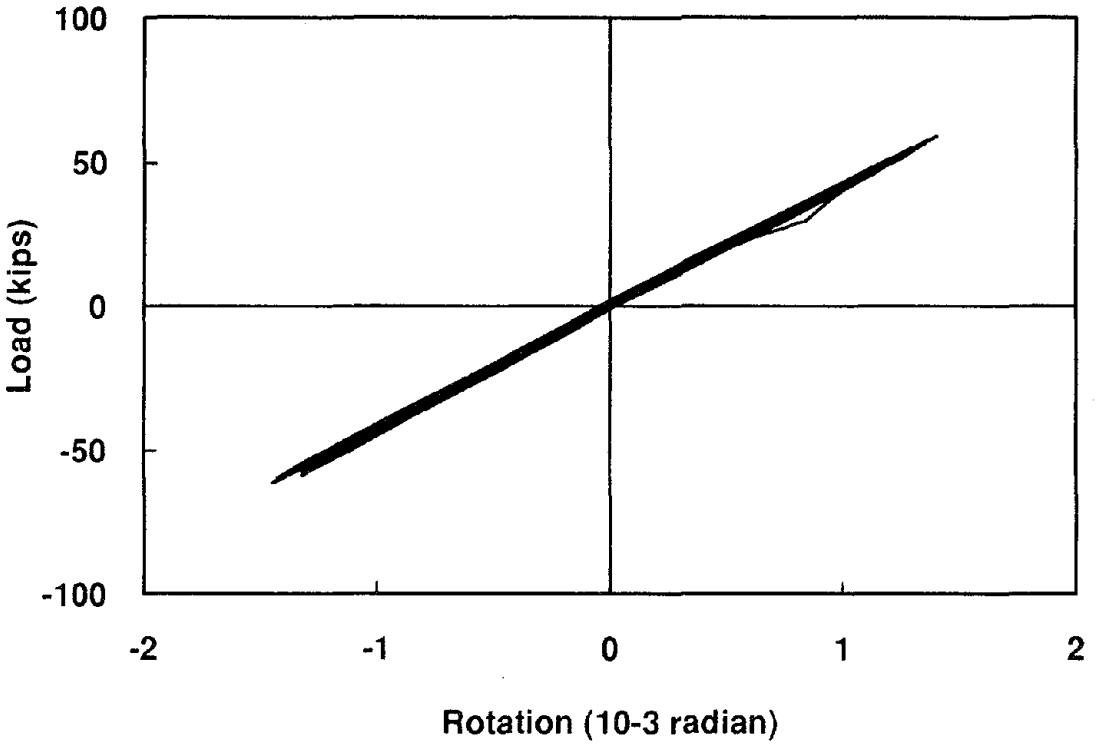

Figure 3.1 Cantilever Beam Load vs. Column Joint Rotation (Typical)

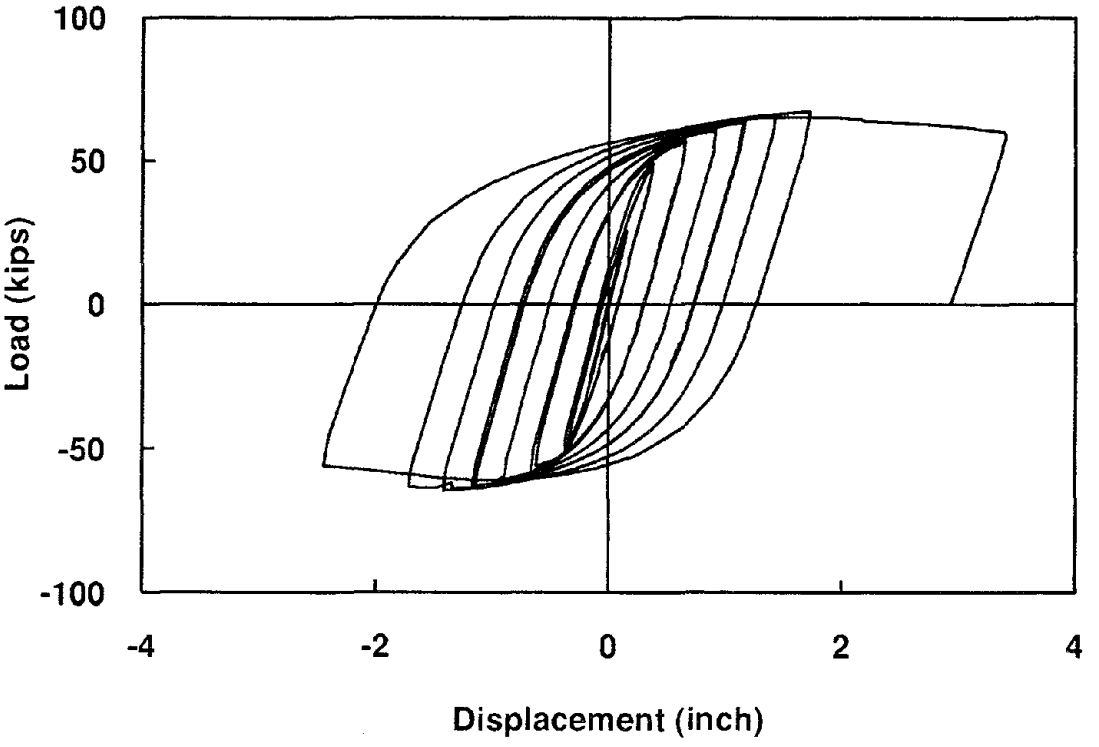

Figure 3.2 Cantilever Beam Load vs. Beam End Displacement (Typical)

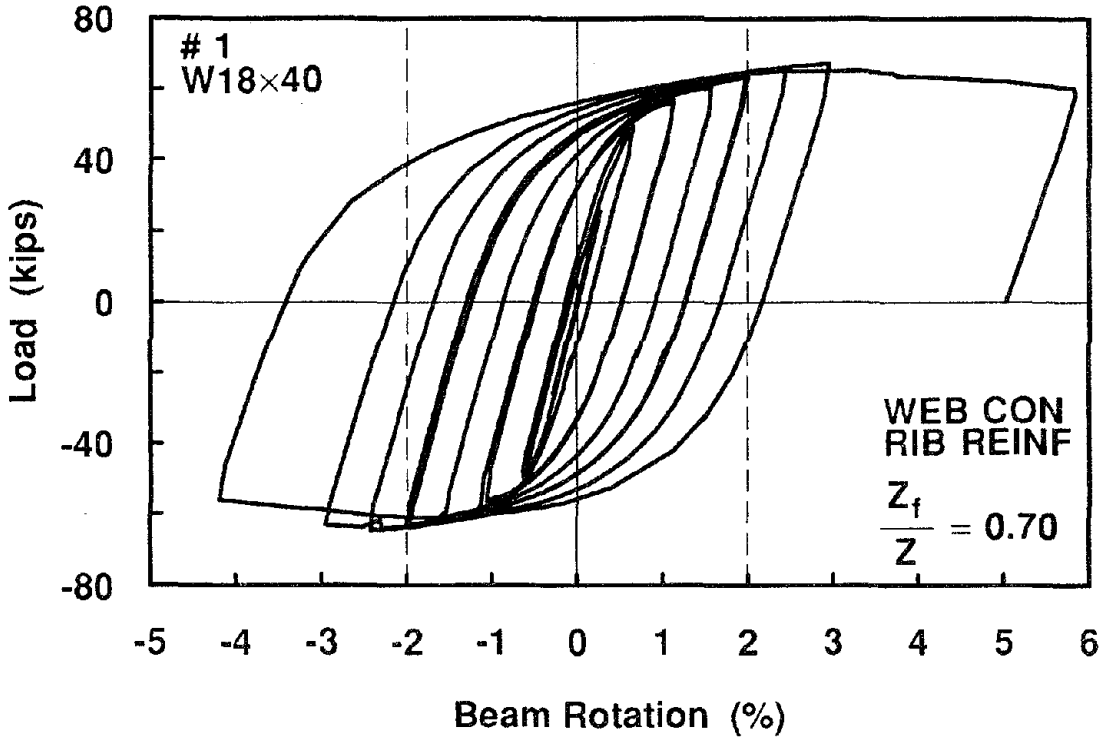

Figure 3.3 Cantilever Beam Load vs. Beam Rotation (Specimen 1)

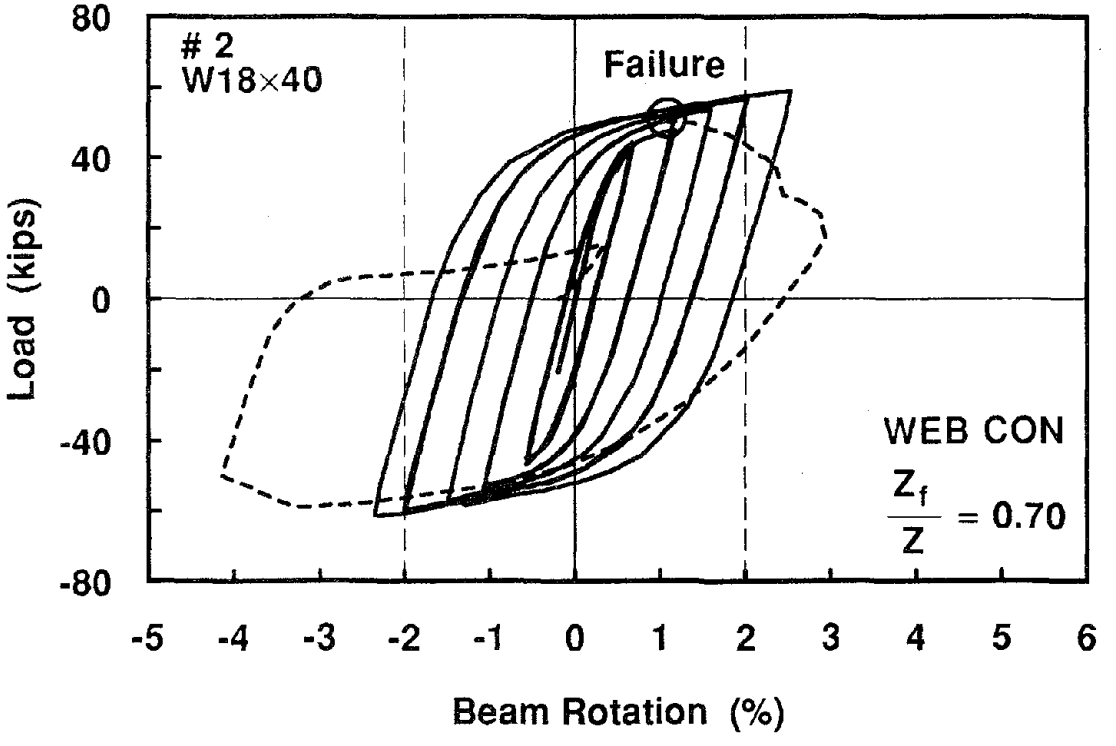

Figure 3.4 Cantilever Beam Load vs. Beam Rotation (Specimen 2)

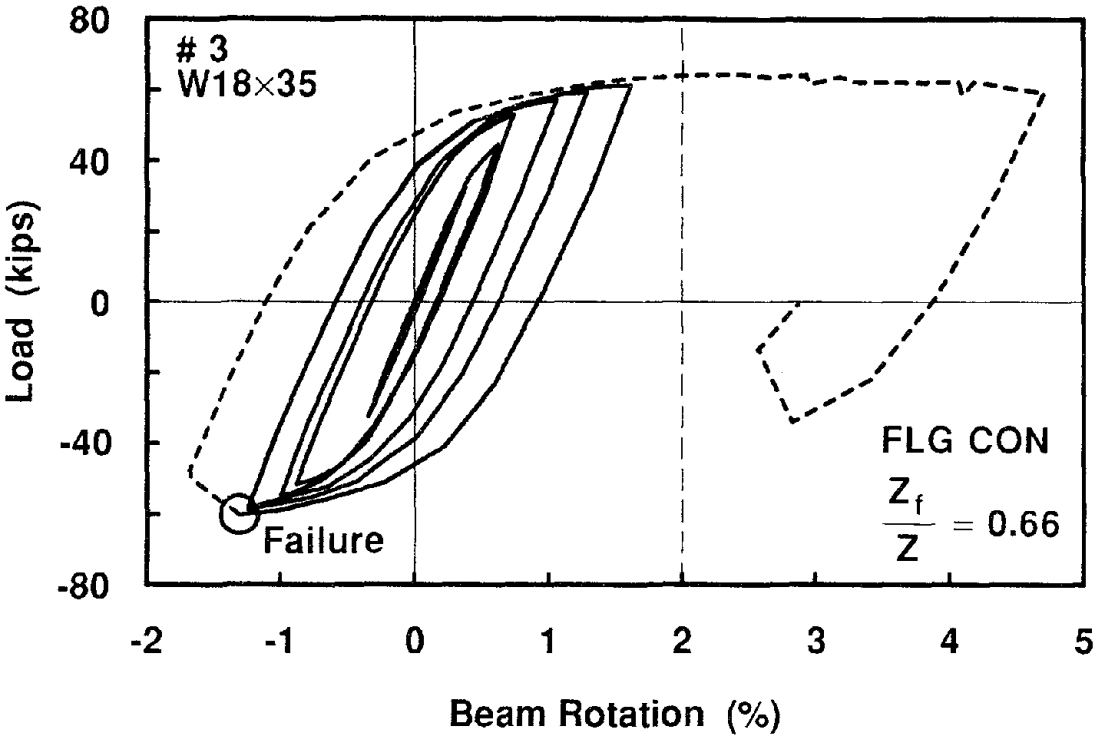

Figure 3.5 Cantilever Beam Load vs. Beam Rotation (Specimen 3)

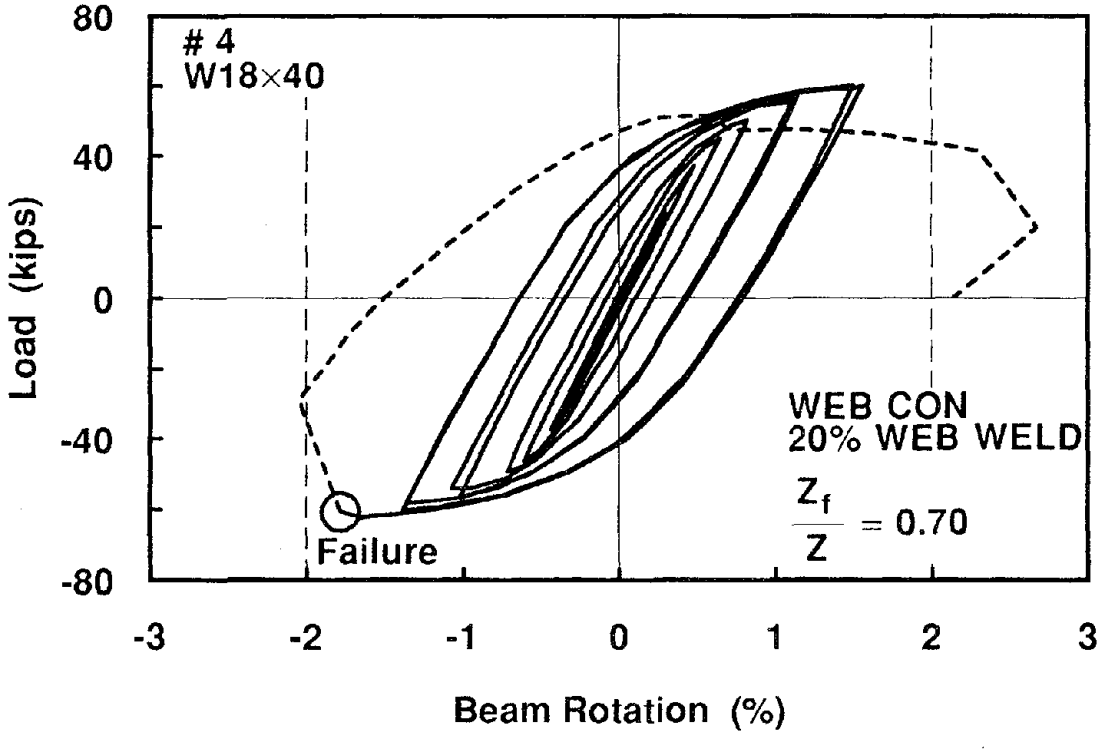

Figure 3.6 Cantilever Beam Load vs. Beam Rotation (Specimen 4)

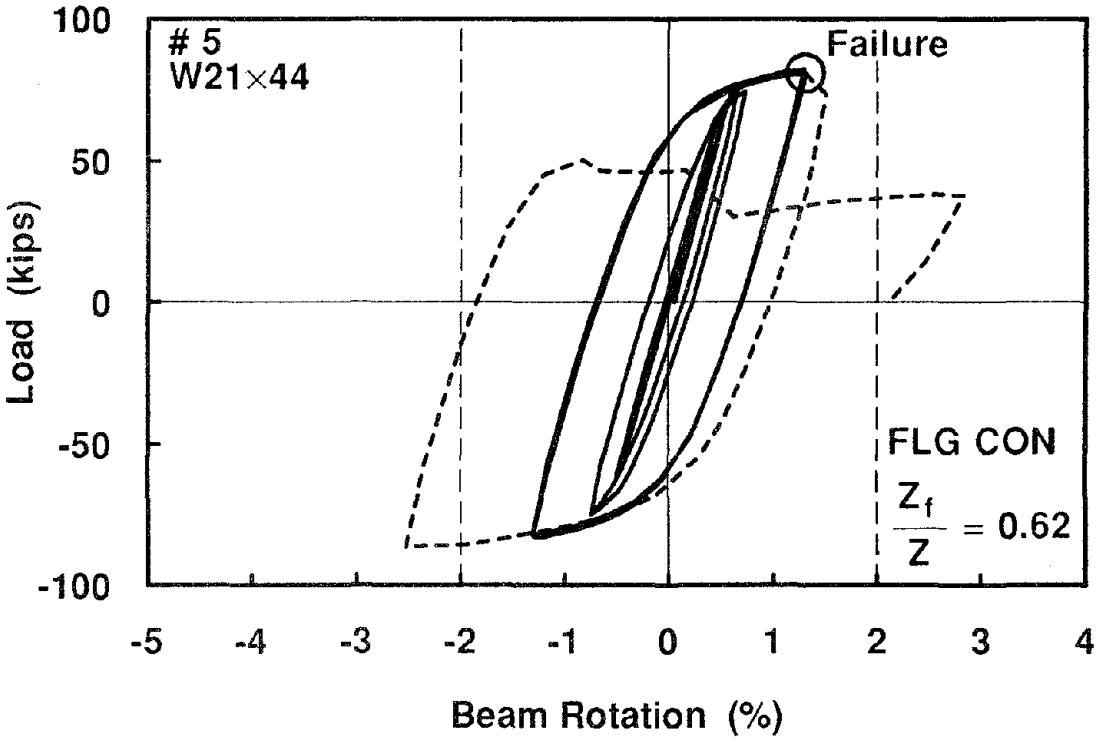

Figure 3.7 Cantilever Beam Load vs. Beam Rotation (Specimen 5)

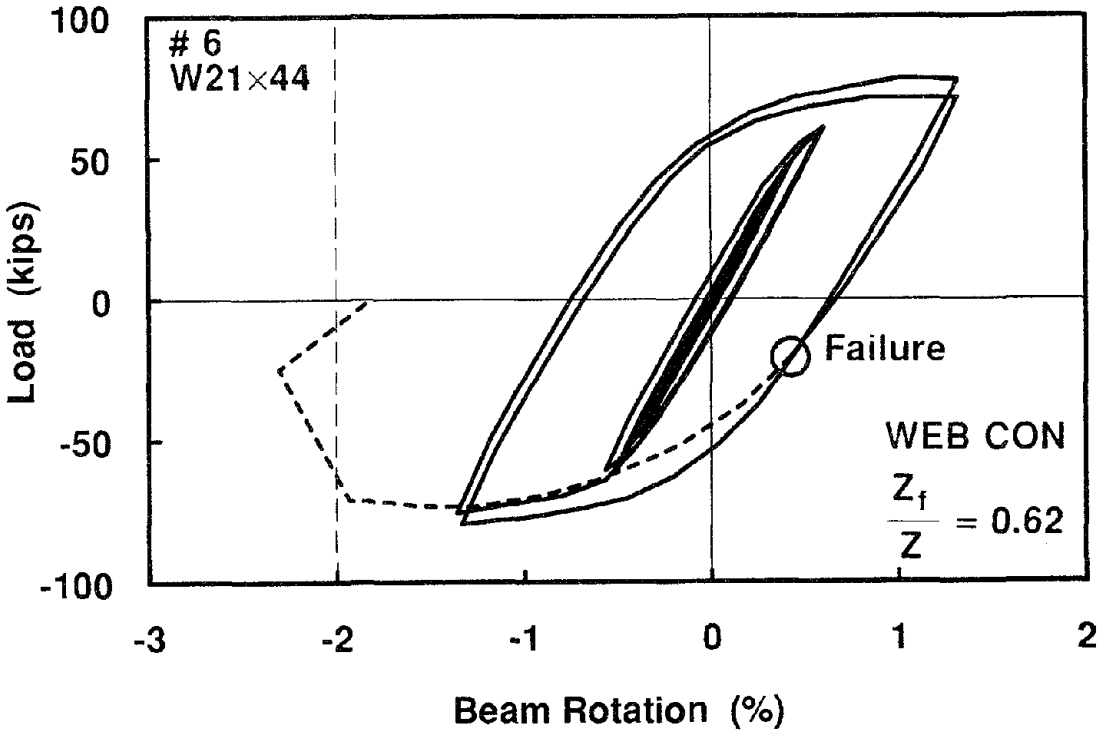

Figure 3.8 Cantilever Beam Load vs. Beam Rotation (Specimen 6)

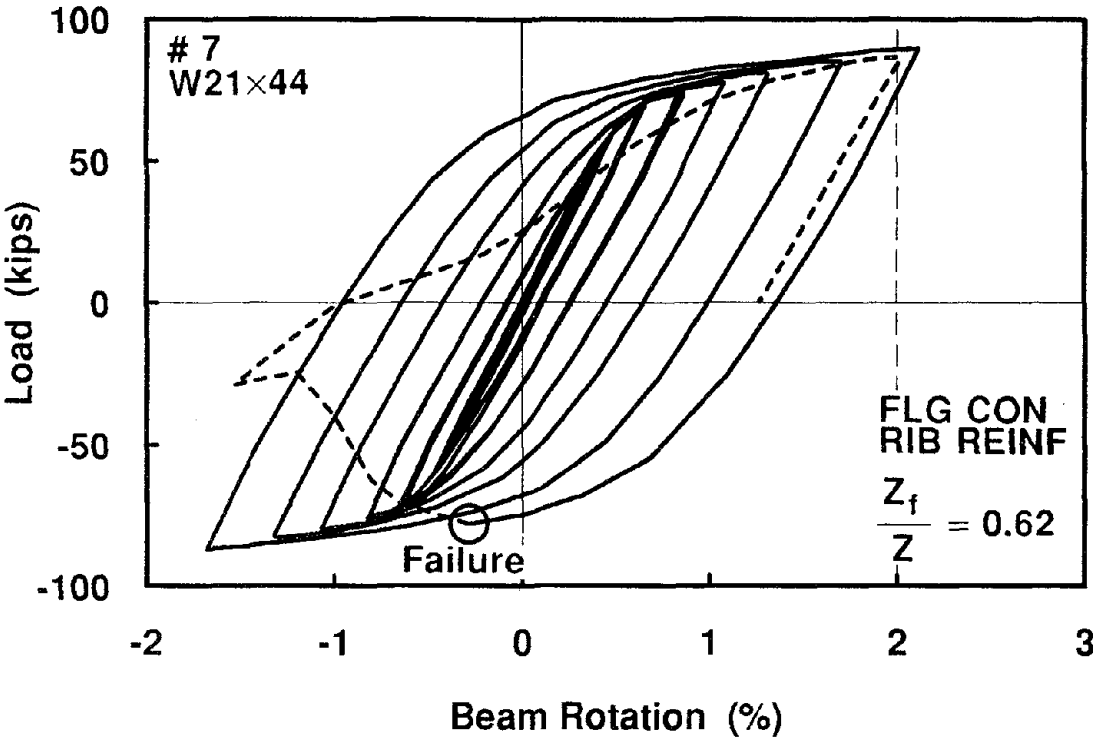

Figure 3.9 Cantilever Beam Load vs. Beam Rotation (Specimen 7)

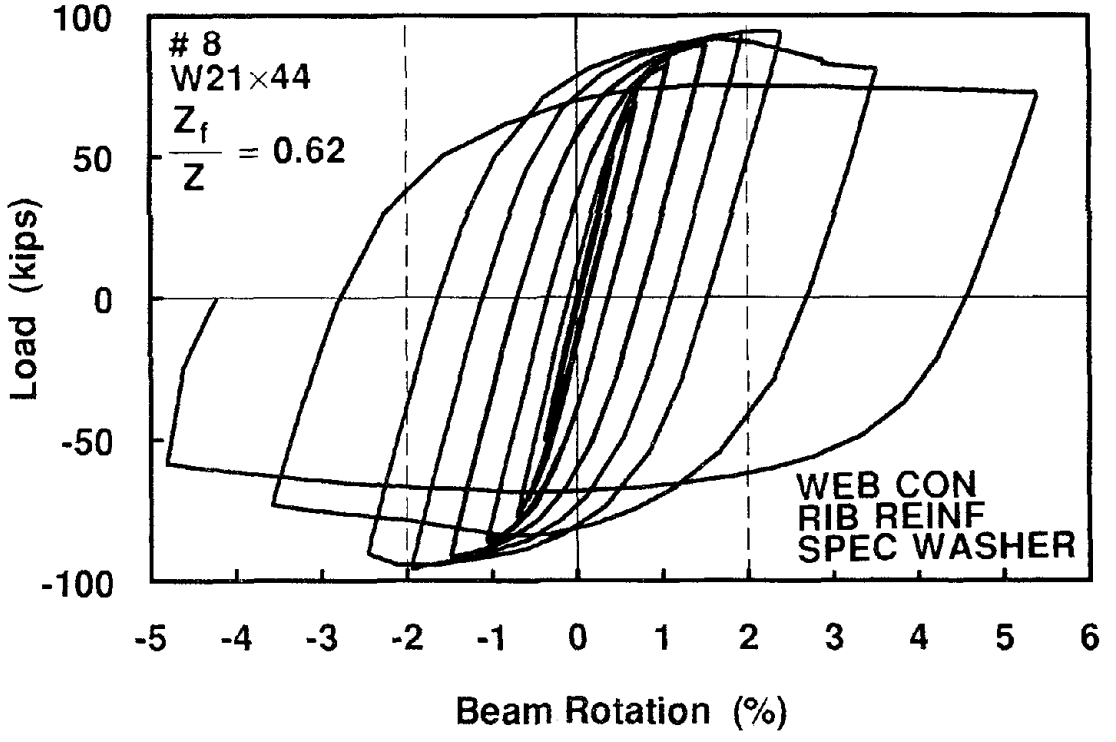

Figure 3.10 Cantilever Beam Load vs. Beam Rotation (Specimen 8)

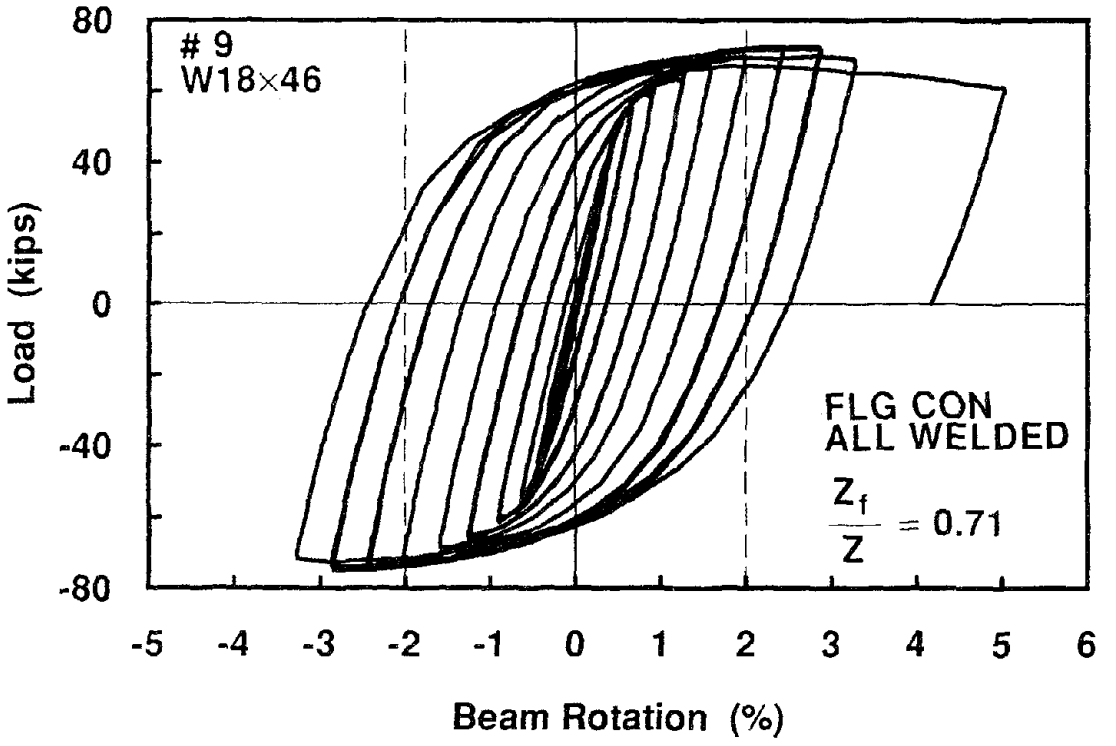

Figure 3.11 Cantilever Beam Load vs. Beam Rotation (Specimen 9)

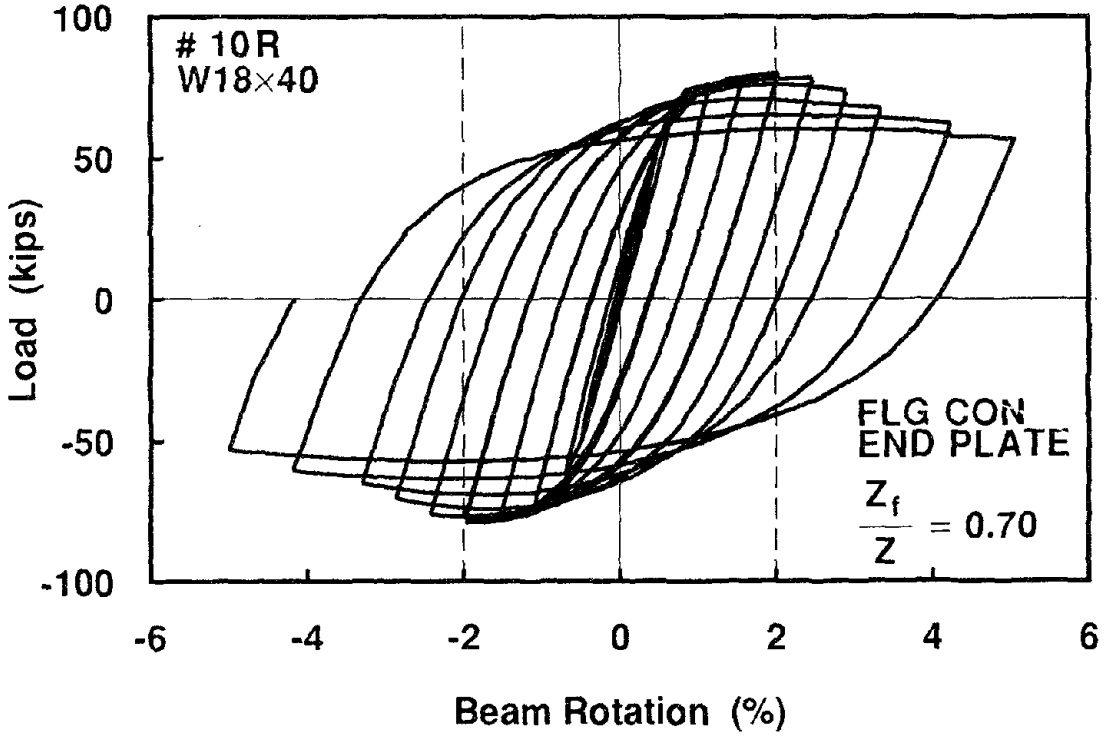

Figure 3.12 Cantilever Beam Load vs. Beam Rotation (Specimen 10R)

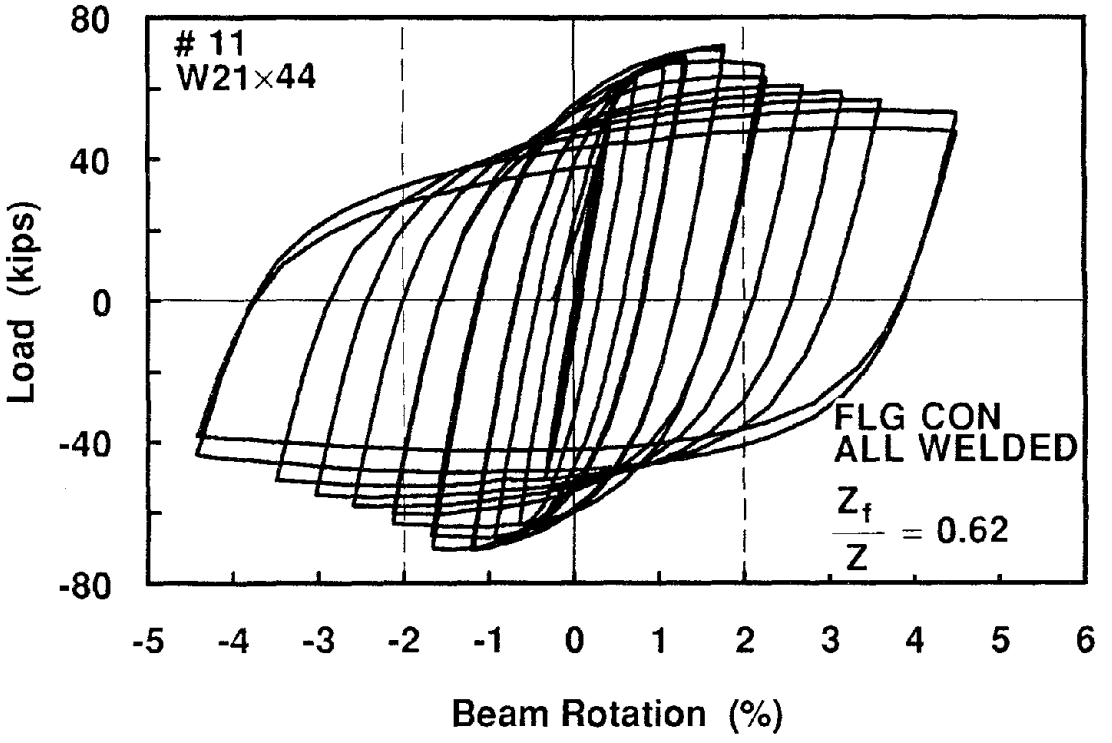

Figure 3.13 Cantilever Beam Load vs. Beam Rotation (Specimen 11)

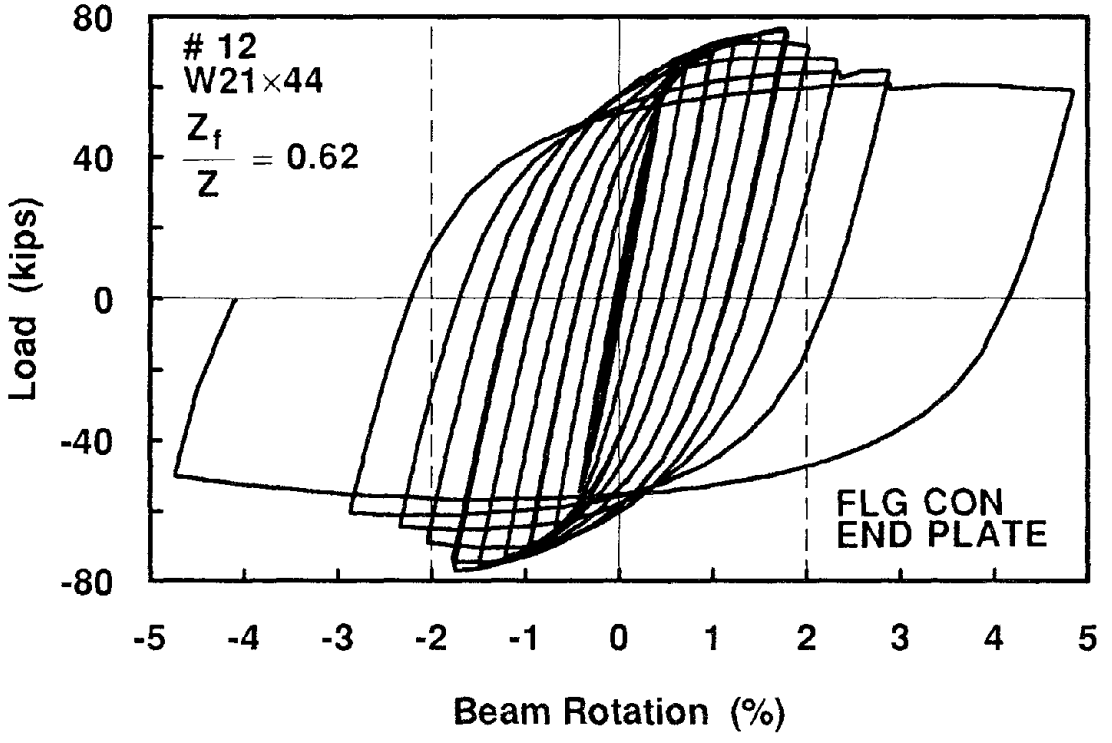

Figure 3.14 Cantilever Beam Load vs. Beam Rotation (Specimen 12)

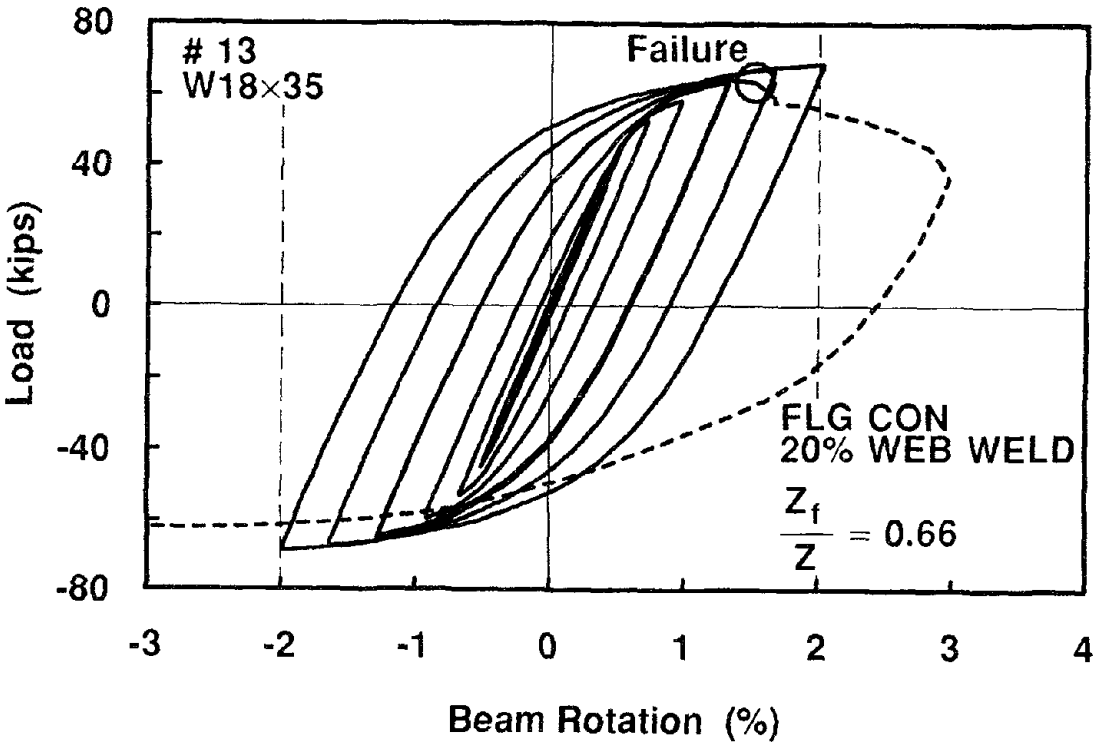

Figure 3.15 Cantilever Beam Load vs. Beam Rotation (Specimen 13)

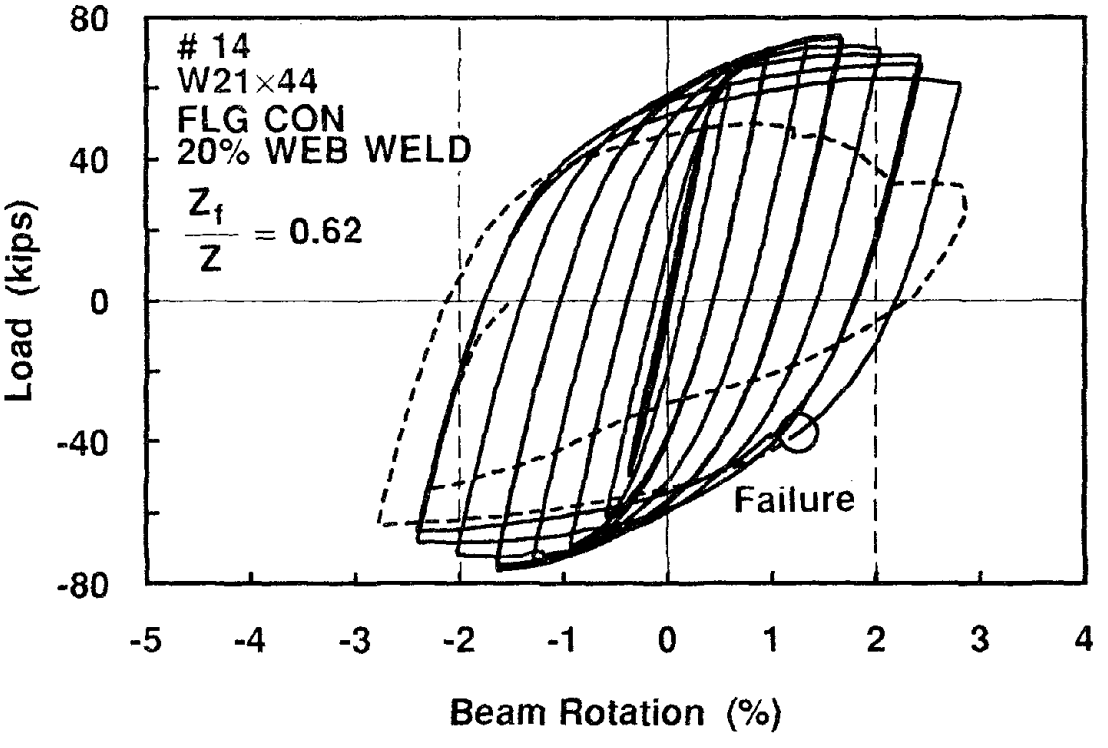

Figure 3.16 Cantilever Beam Load vs. Beam Rotation (Specimen 14)

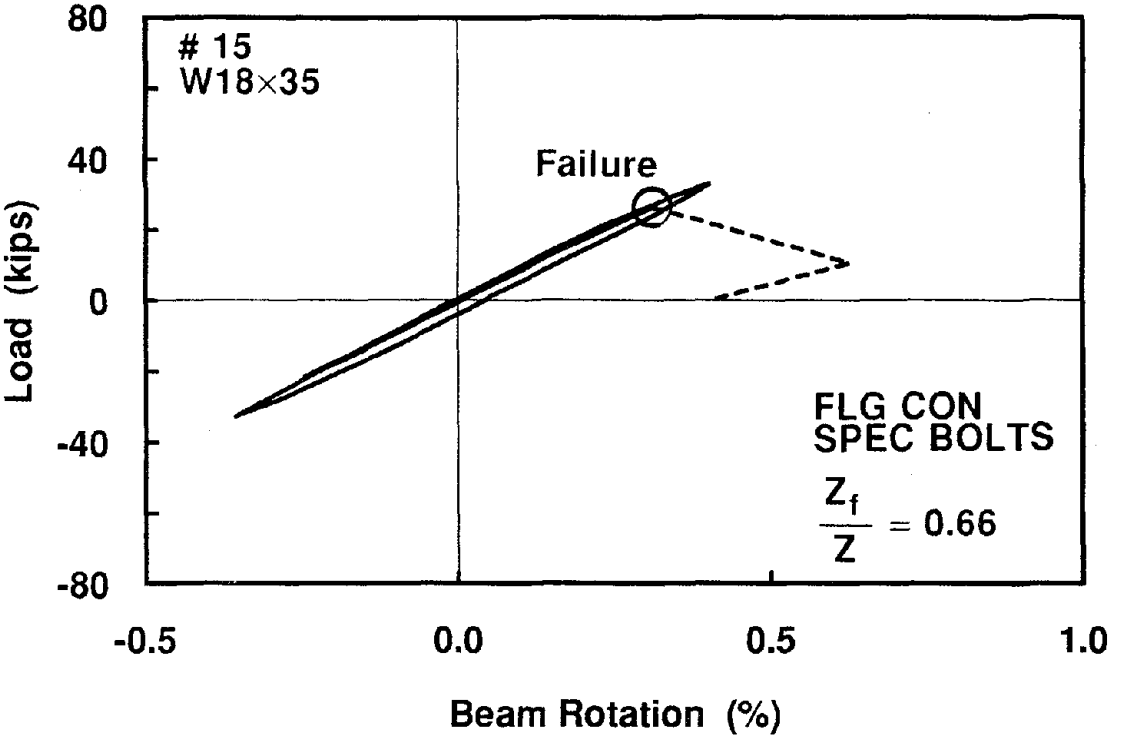

Figure 3.17 Cantilever Beam Load vs. Beam Rotation (Specimen 15)

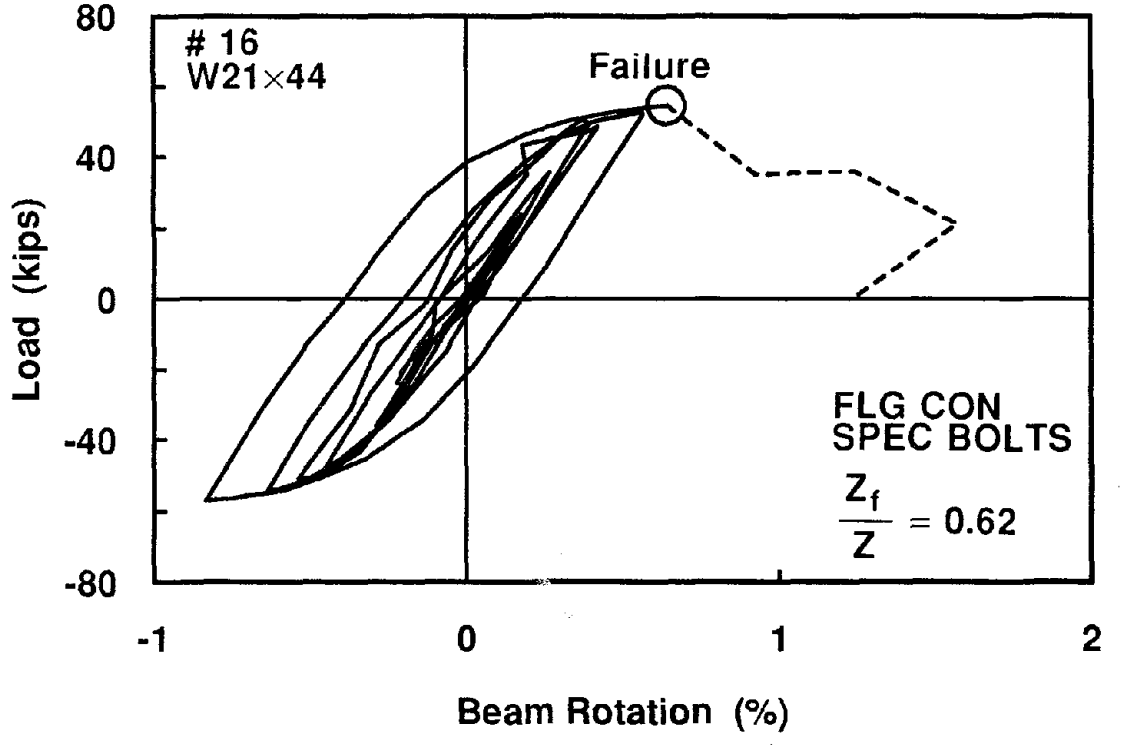

Figure 3.18 Cantilever Beam Load vs. Beam Rotation (Specimen 16)

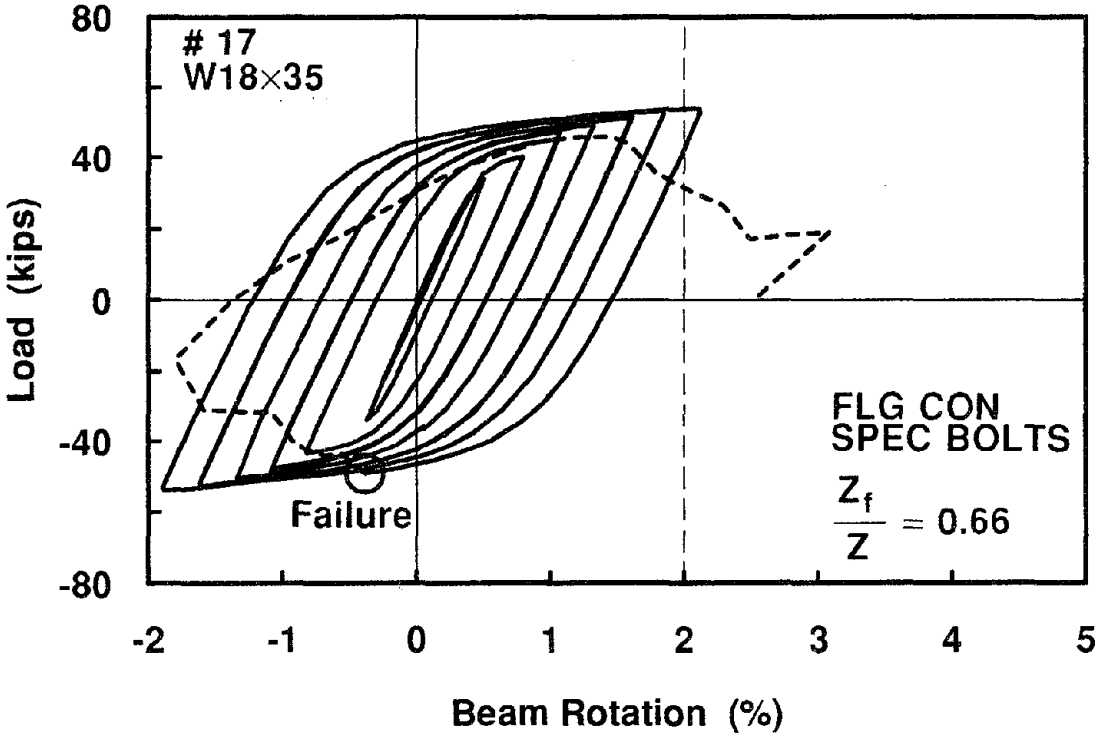

Figure 3.19 Cantilever Beam Load vs. Beam Rotation (Specimen 17)

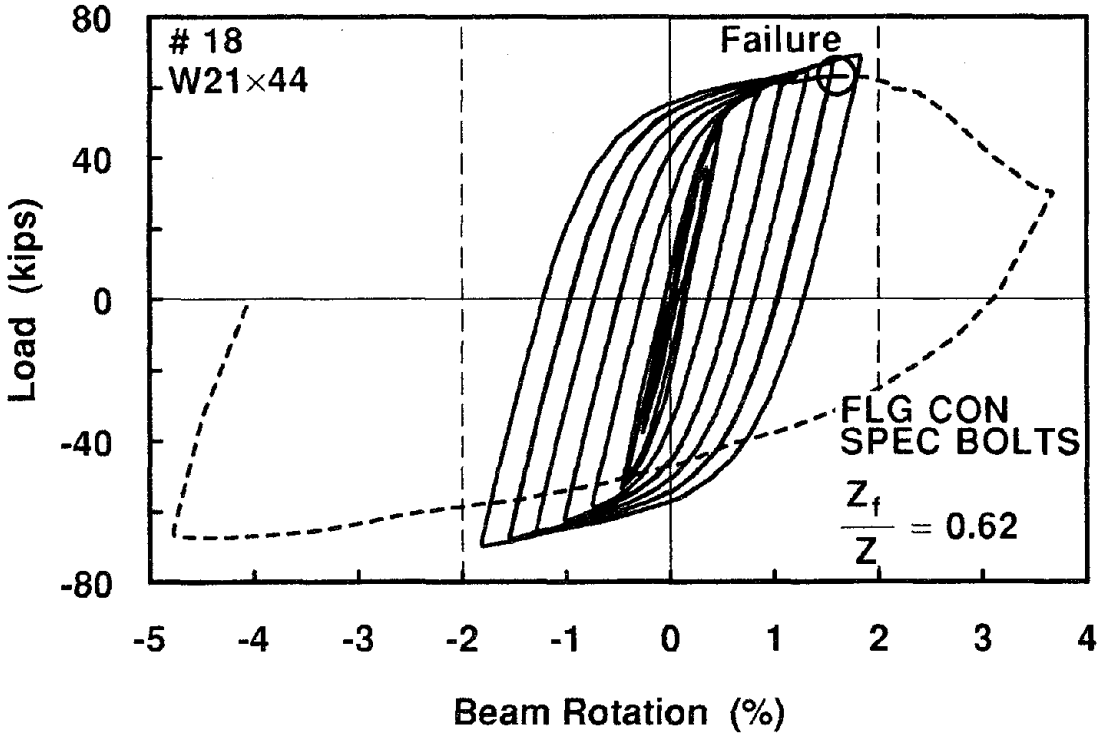

Figure 3.20 Cantilever Beam Load vs. Beam Rotation (Specimen 18)

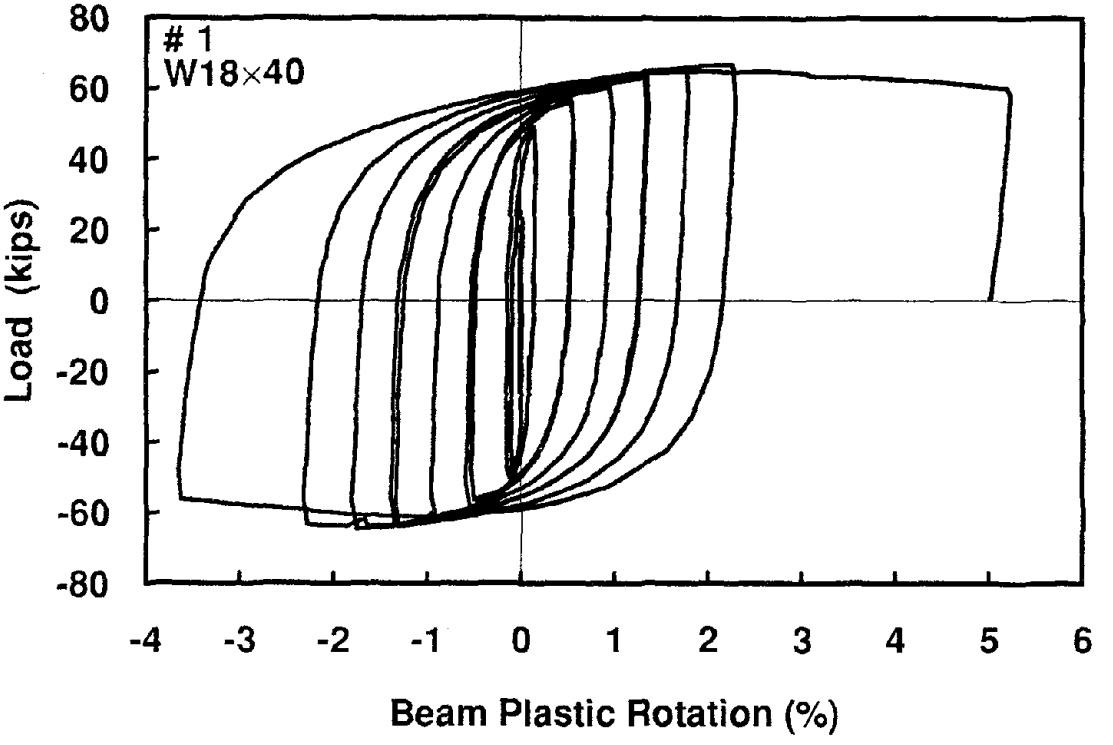

Figure 3.21 Cantilever Beam Load vs. Beam Plastic Rotation (Specimen 1)

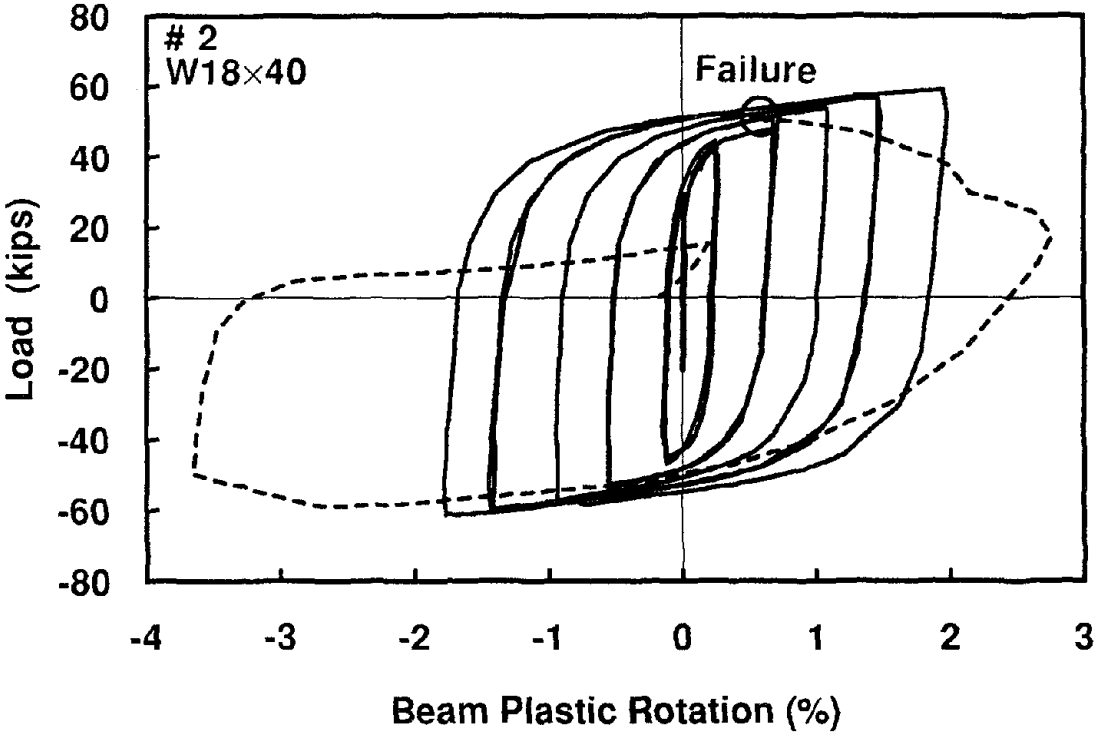

Figure 3.22 Cantilever Beam Load vs. Beam Plastic Rotation (Specimen 2)

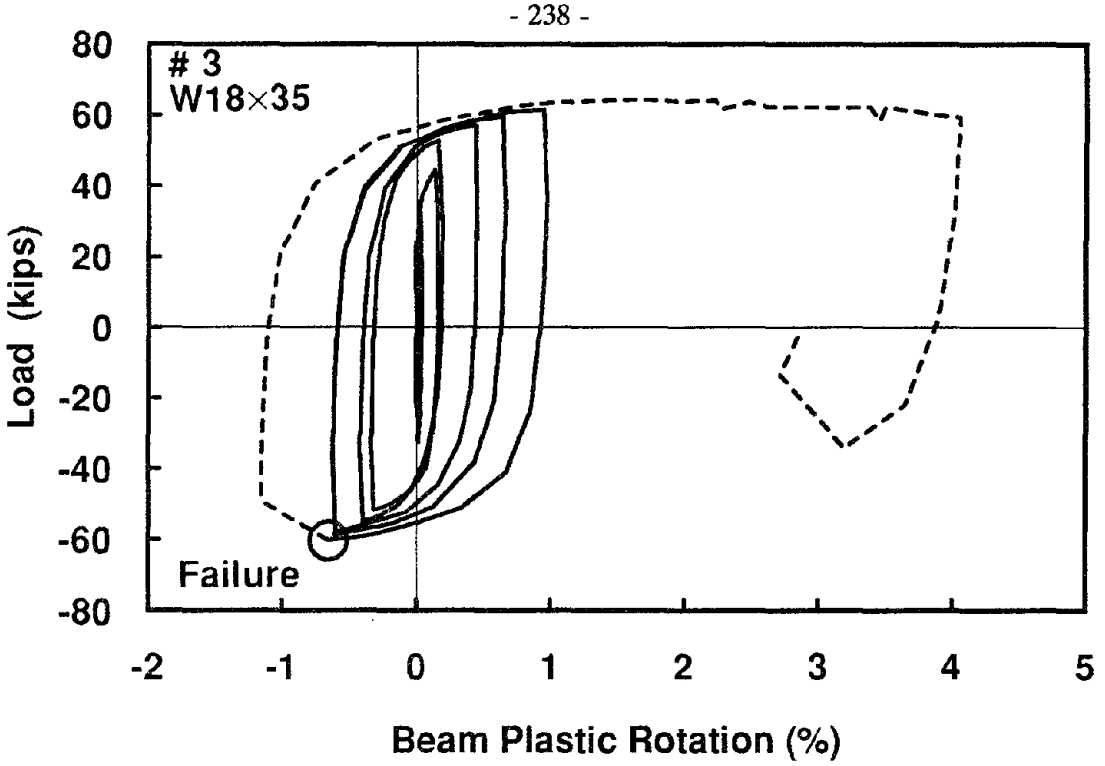

Figure 3.23 Cantilever Beam Load vs. Beam Plastic Rotation (Specimen 3)

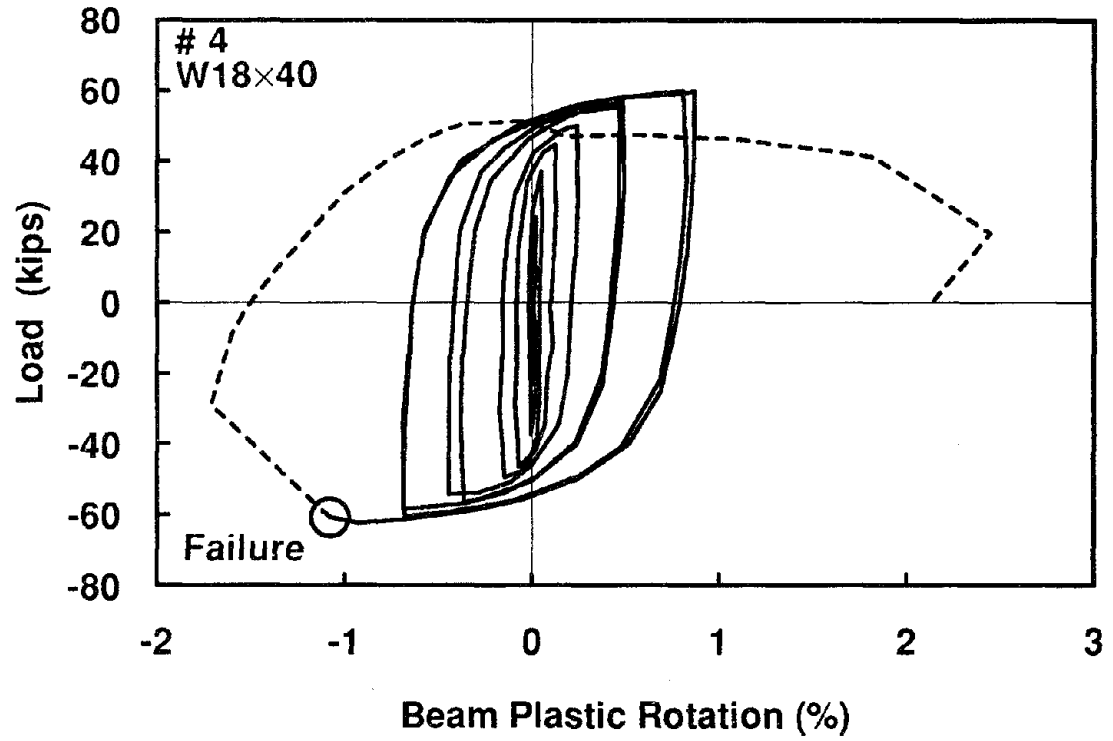

Figure 3.24 Cantilever Beam Load vs. Beam Plastic Rotation (Specimen 4)

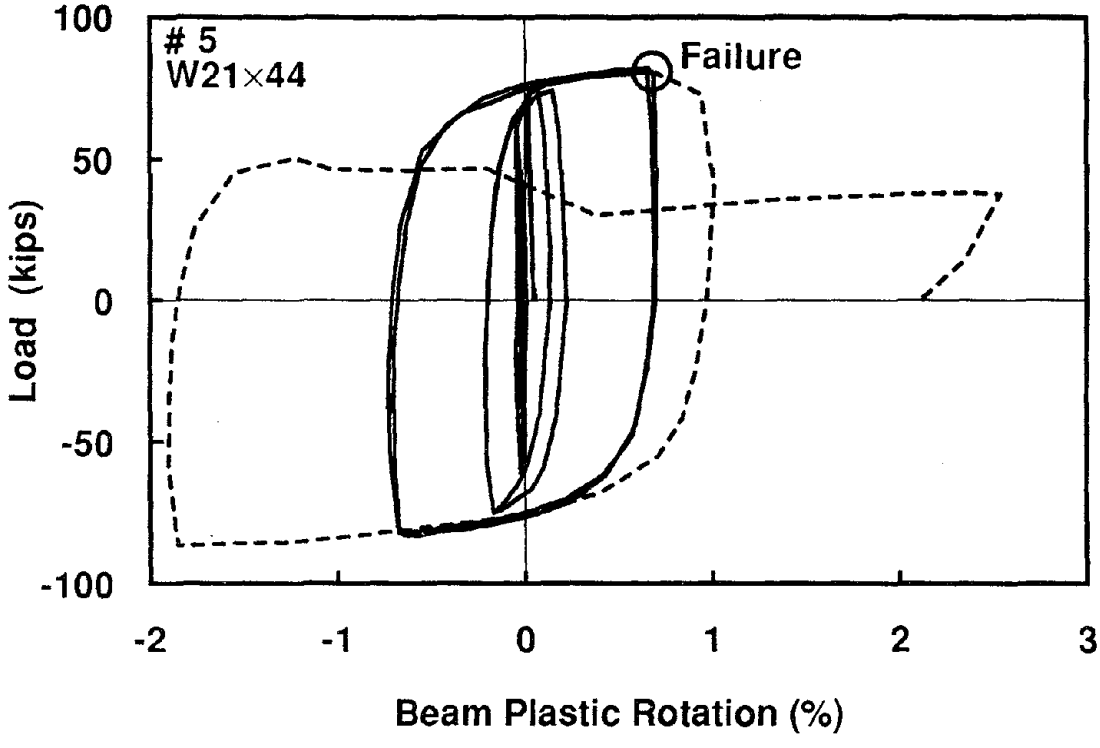

Figure 3.25 Cantilever Beam Load vs. Beam Plastic Rotation (Specimen 5)

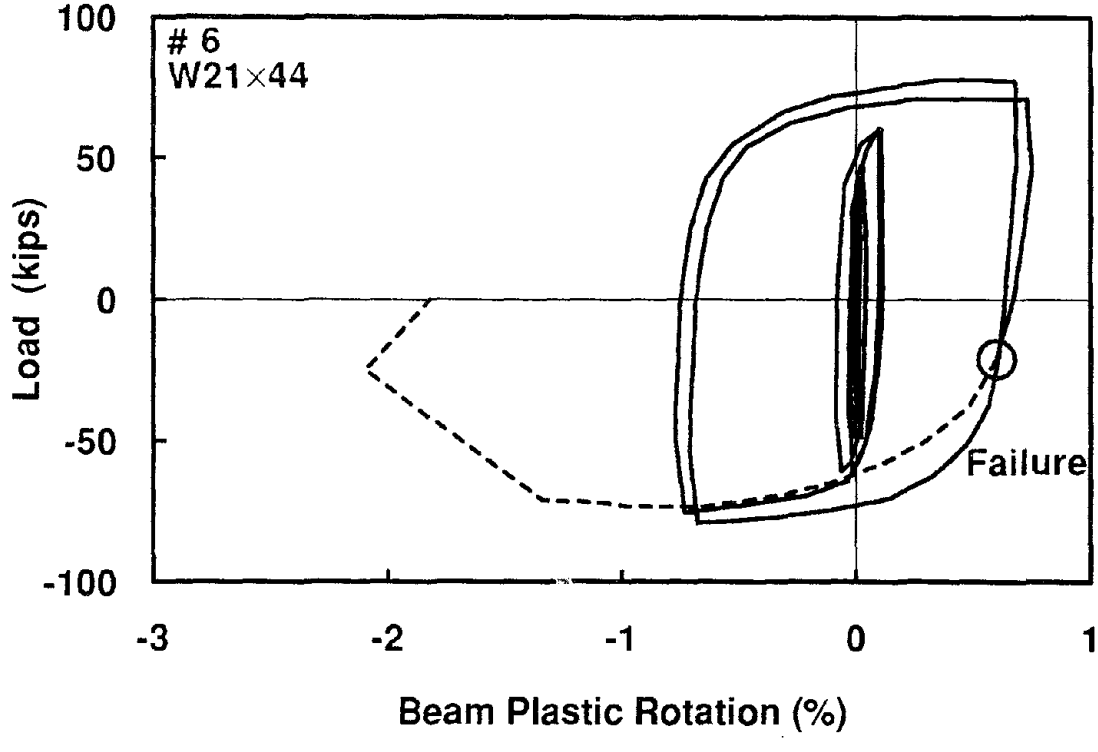

Figure 3.26 Cantilever Beam Load vs. Beam Plastic Rotation (Specimen 6)

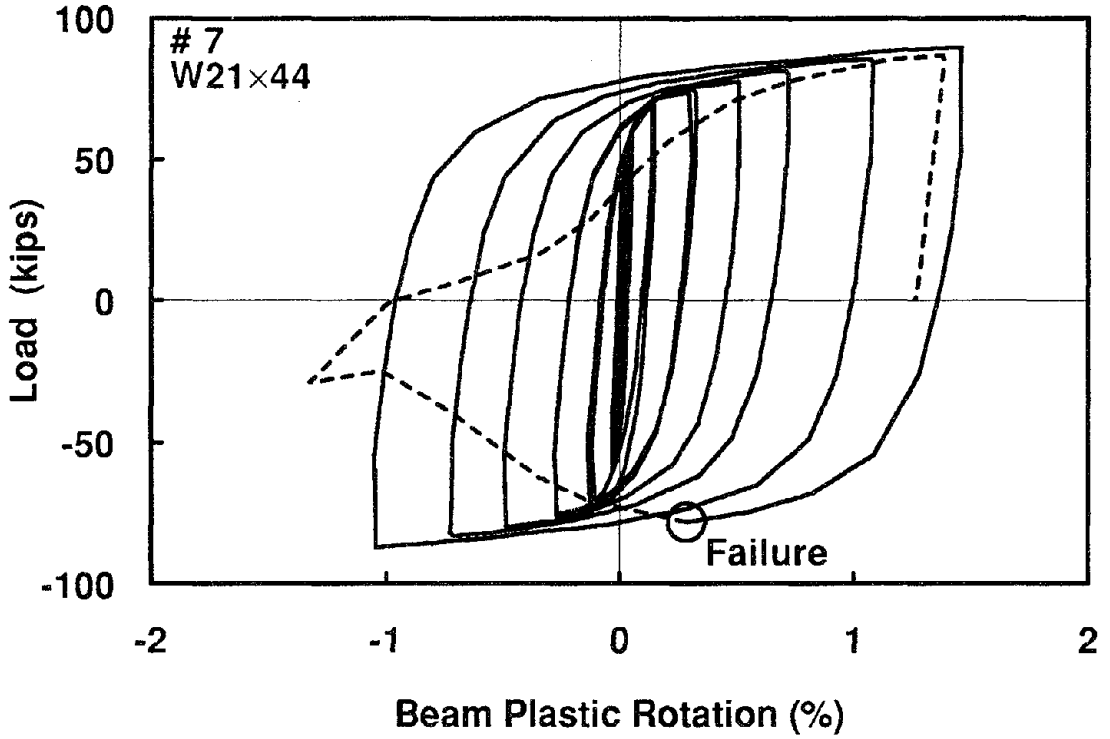

Figure 3.27 Cantilever Beam Load vs. Beam Plastic Rotation (Specimen 7)

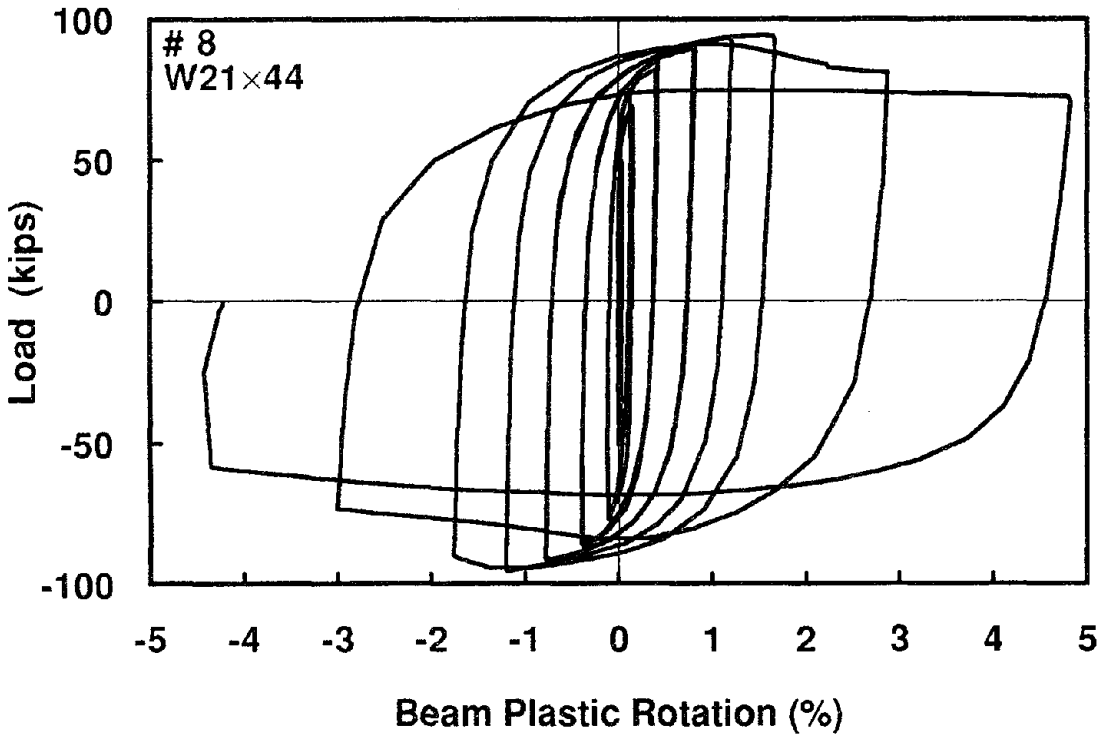

Figure 3.28 Cantilever Beam Load vs. Beam Plastic Rotation (Specimen 8)

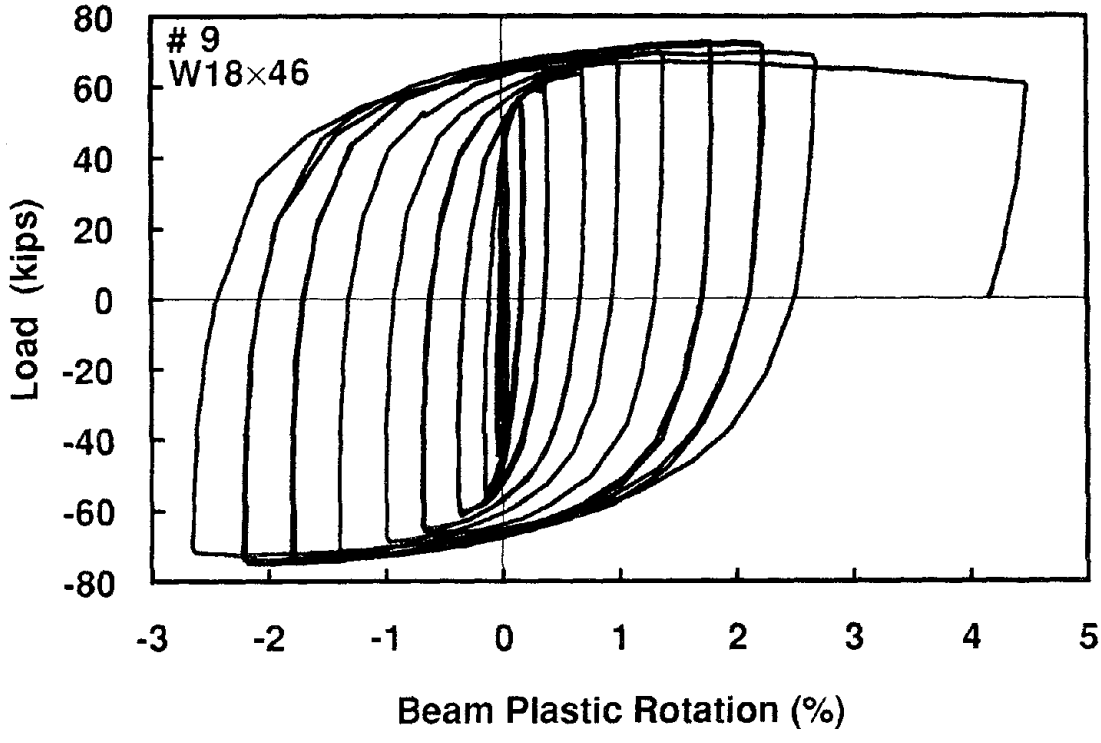

Figure 3.29 Cantilever Beam Load vs. Beam Plastic Rotation (Specimen 9)

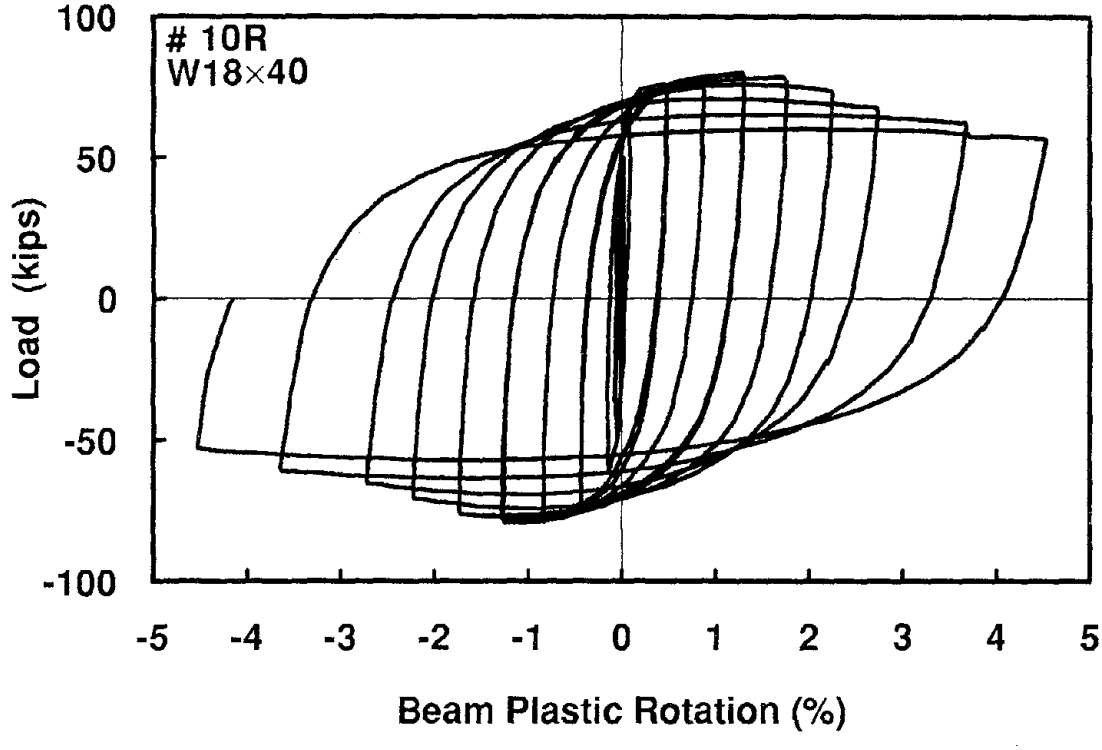

Figure 3.30 Cantilever Beam Load vs. Beam Plastic Rotation (Specimen 10R)

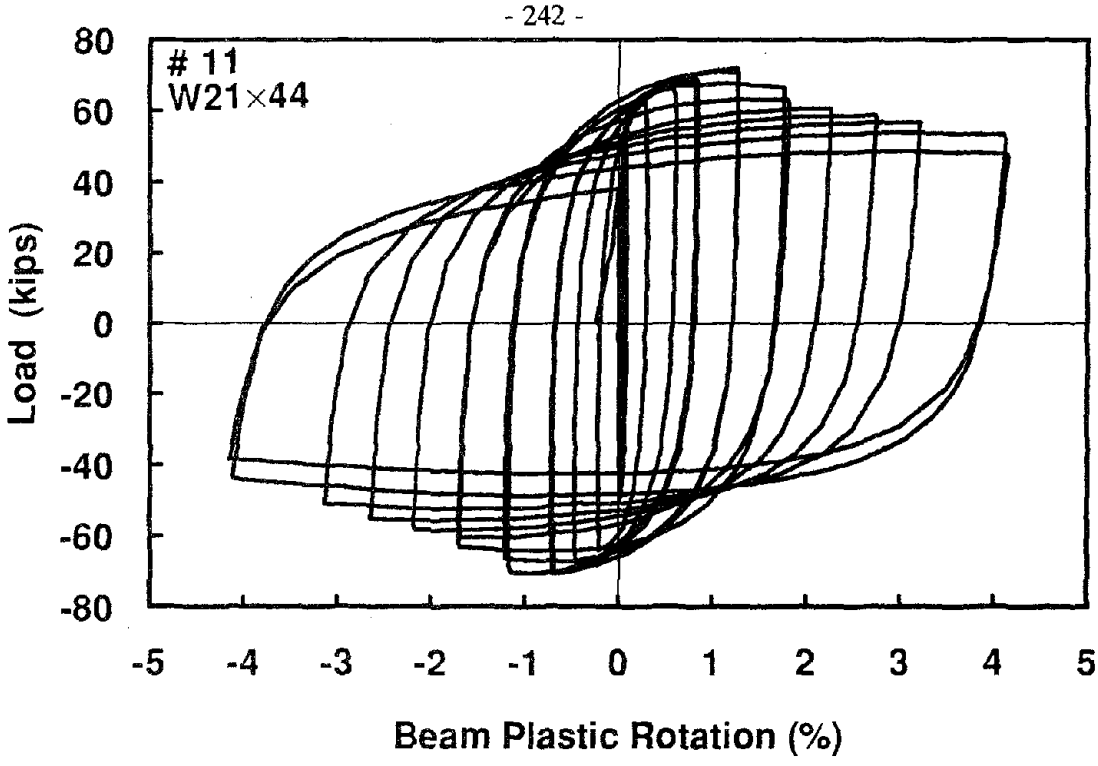

Figure 3.31 Cantilever Beam Load vs. Beam Plastic Rotation (Specimen 11)

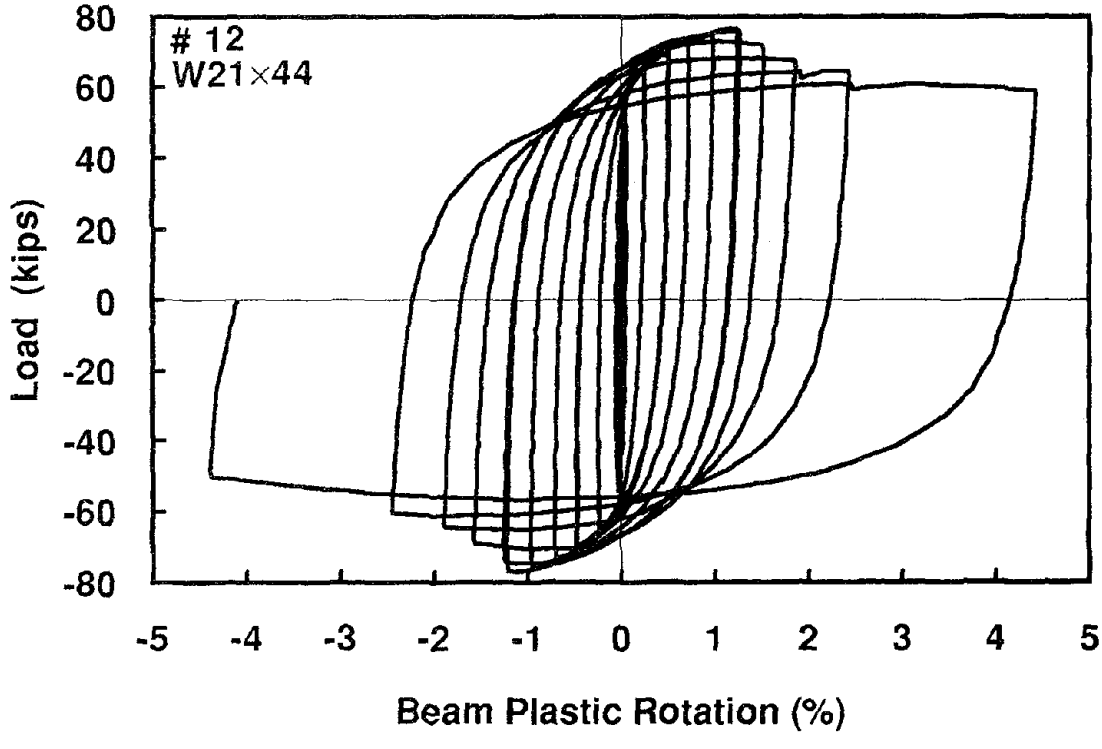

Figure 3.32 Cantilever Beam Load vs. Beam Plastic Rotation (Specimen 12)

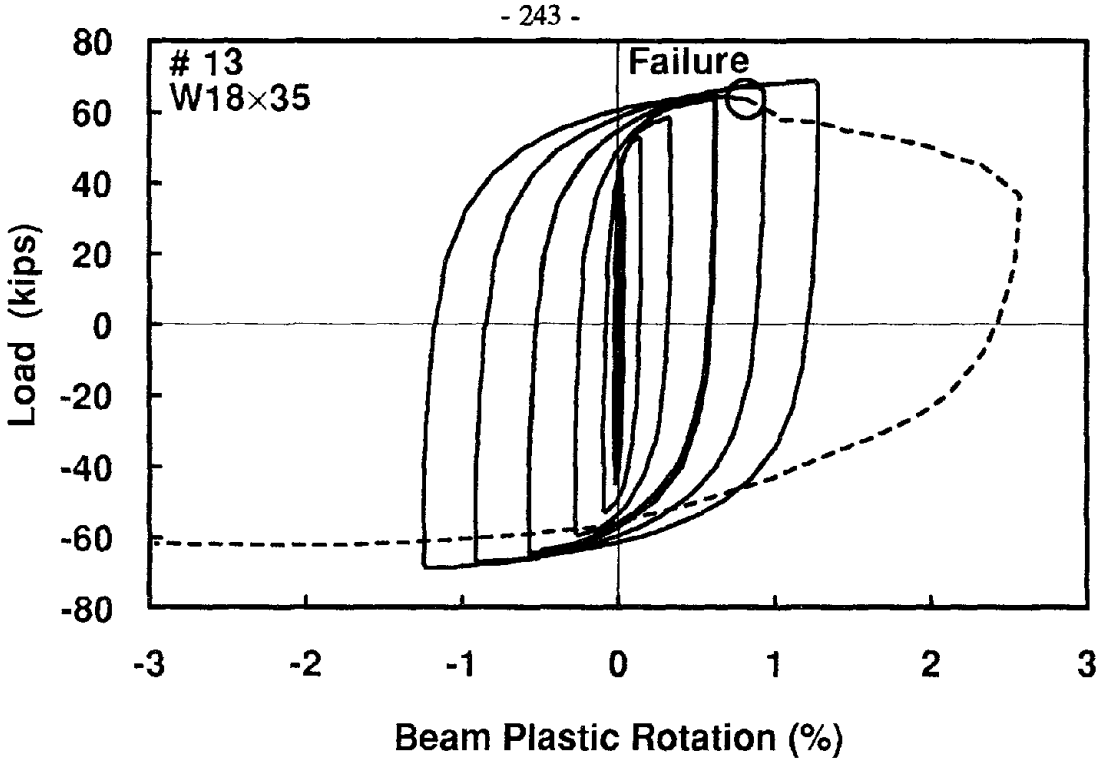

Figure 3.33 Cantilever Beam Load vs. Beam Plastic Rotation (Specimen 13)

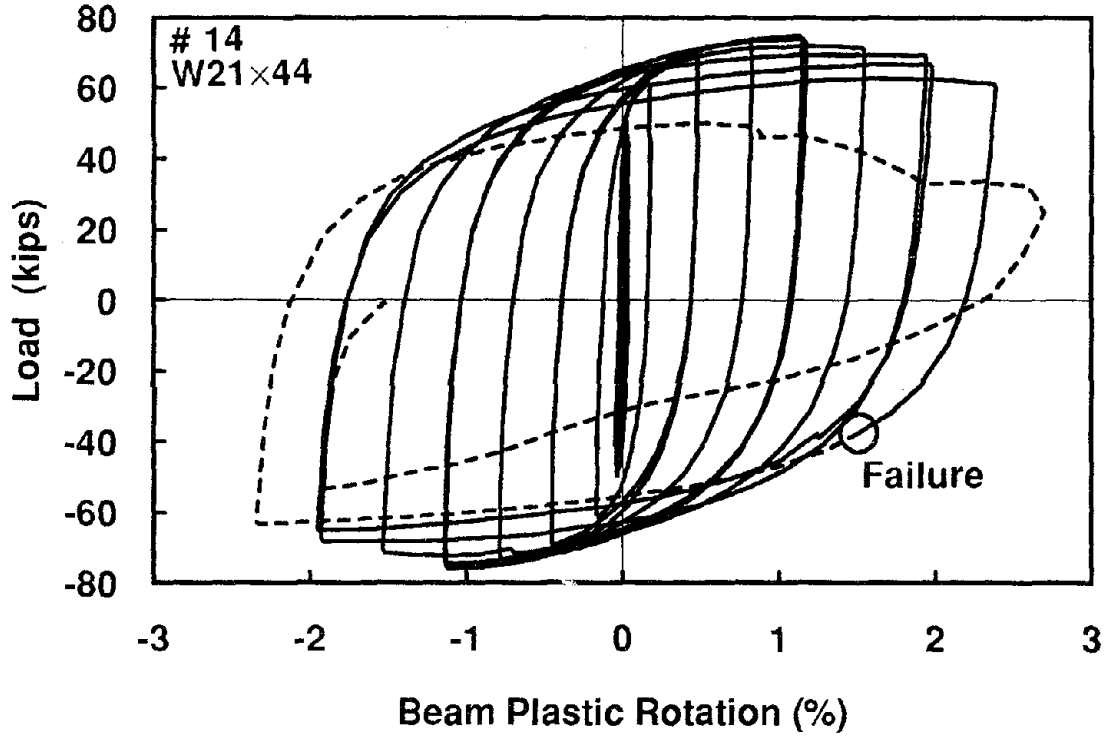

Figure 3.34 Cantilever Beam Load vs. Beam Plastic Rotation (Specimen 14)

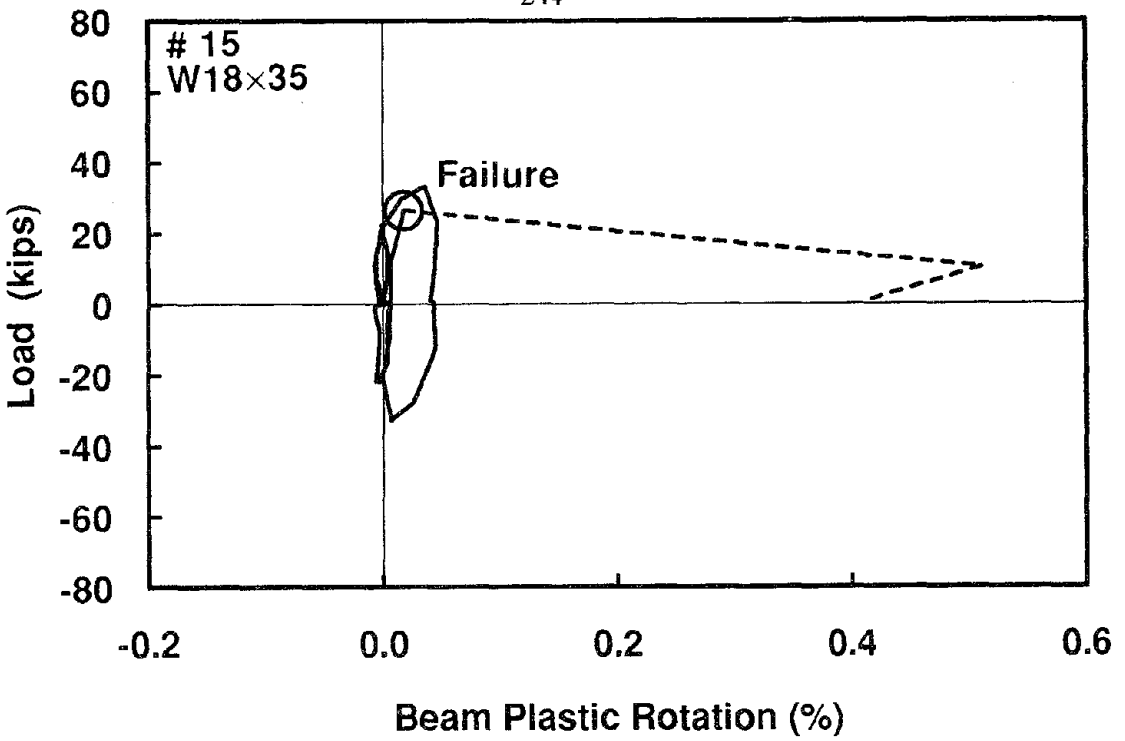

Figure 3.35 Cantilever Beam Load vs. Beam Plastic Rotation (Specimen 15)

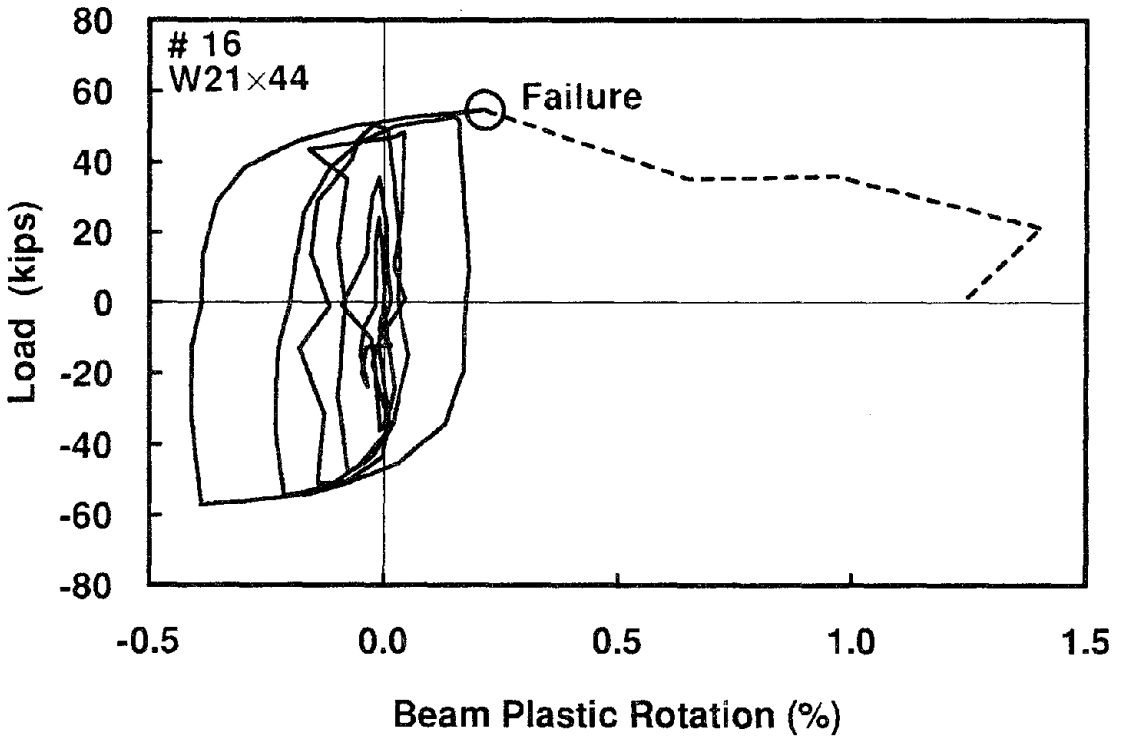

Figure 3.36 Cantilever Beam Load vs. Beam Plastic Rotation (Specimen 16)

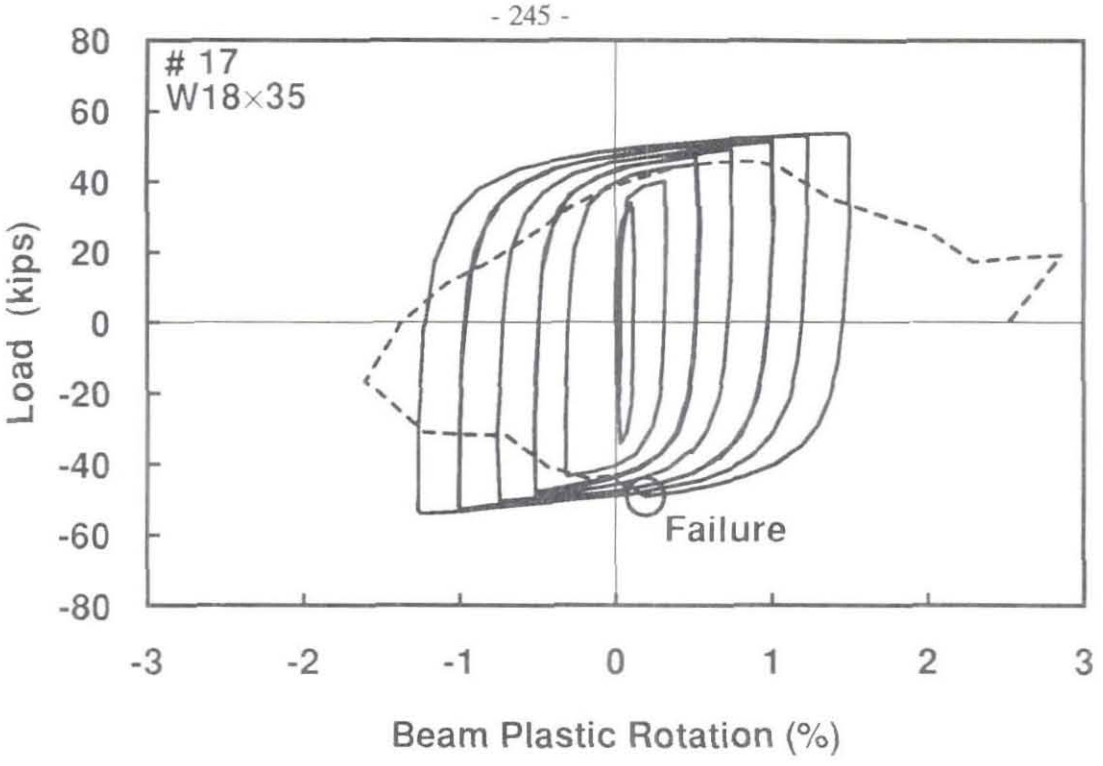

Figure 3.37 Cantilever Beam Load vs. Beam Plastic Rotation (Specimen 17)

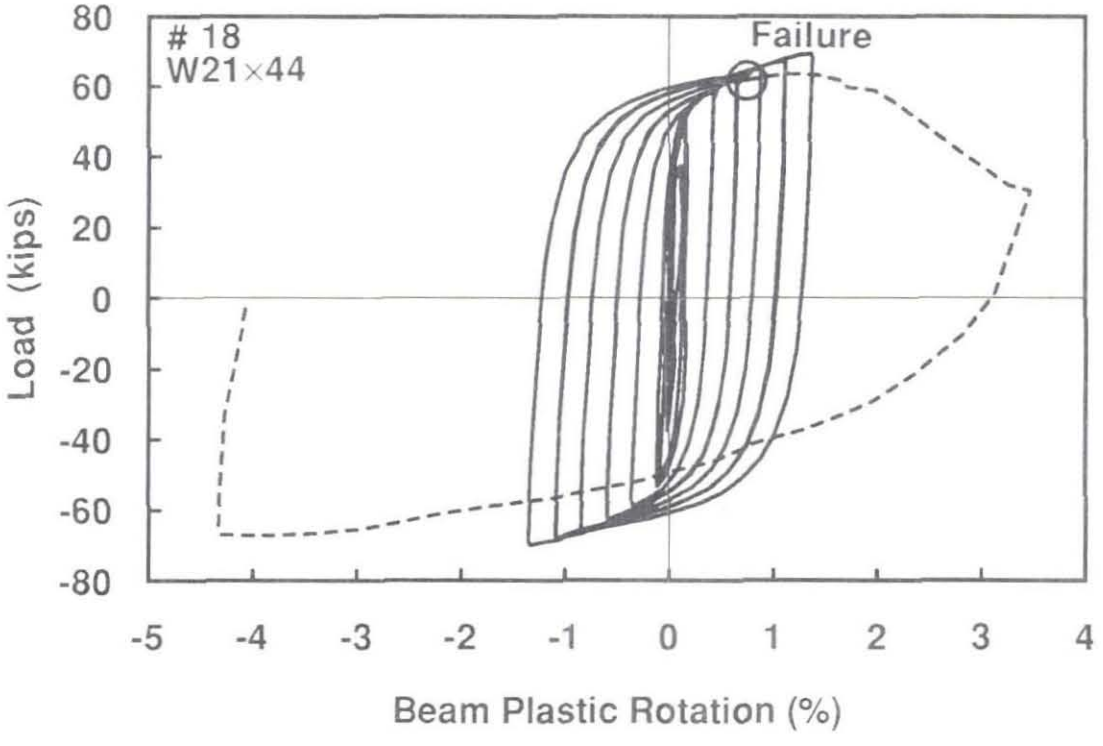

Figure 3.38 Cantilever Beam Load vs. Beam Plastic Rotation (Specimen 18)

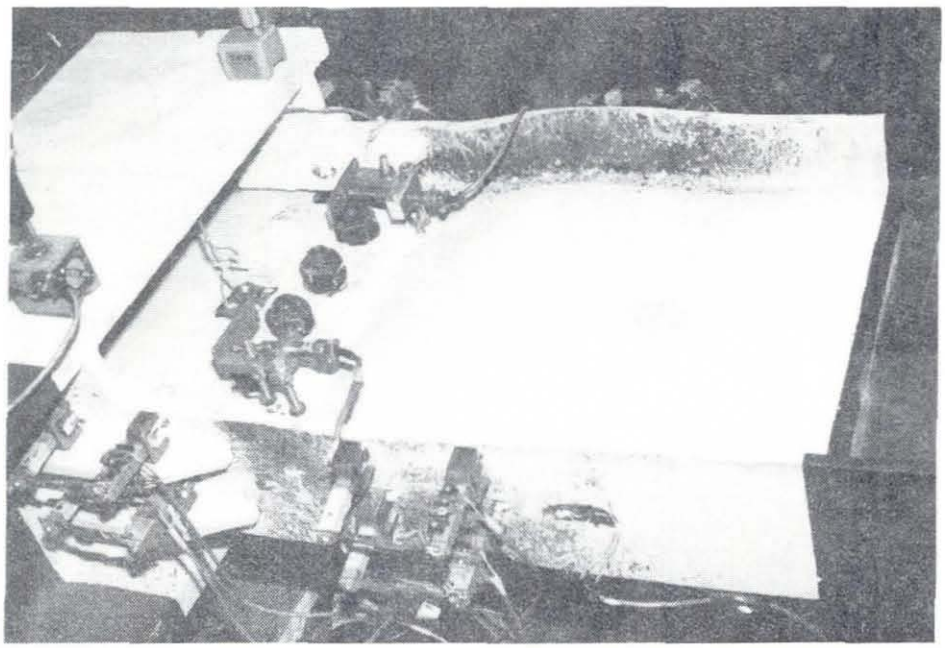

Figure 3.39 Local Buckling of Beam Flanges (Specimen 1)

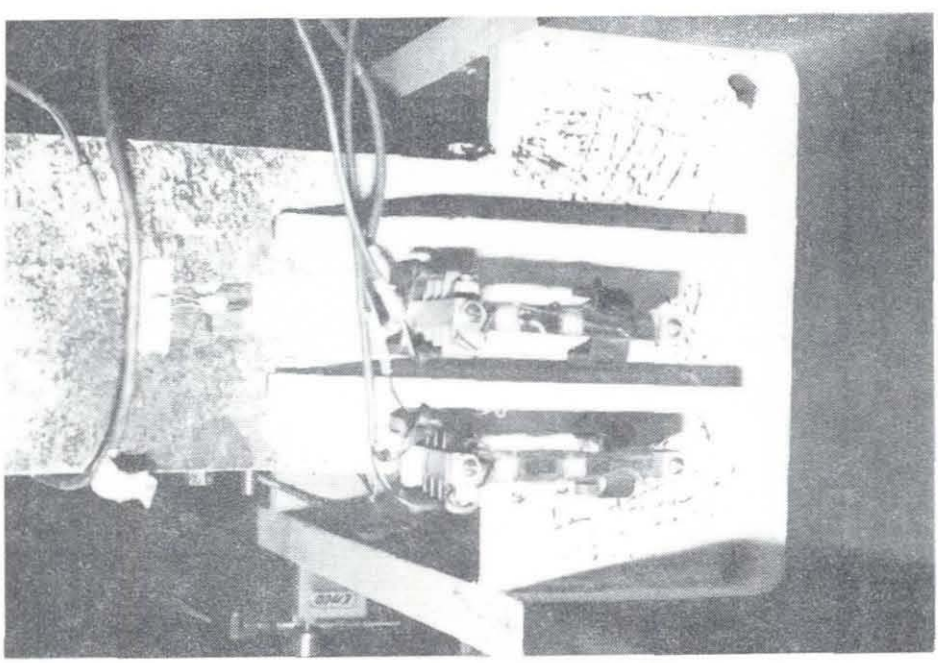

Figure 3.40 Yield Pattern at Top Continuity Plate (Specimen 1)

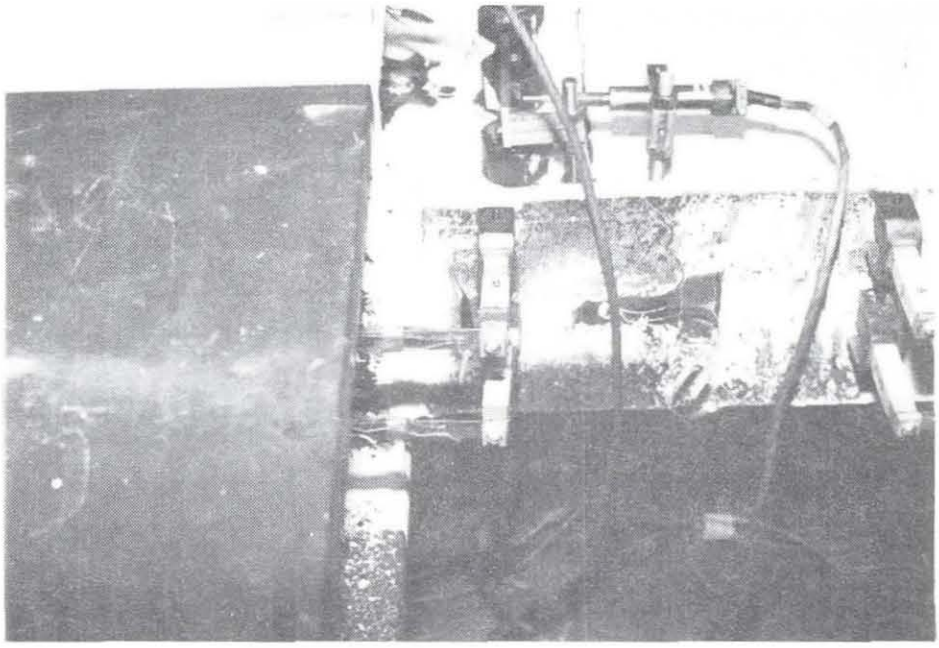

Figure 3.41 Crack Opened at Center of Top Flange (Specimen 2)

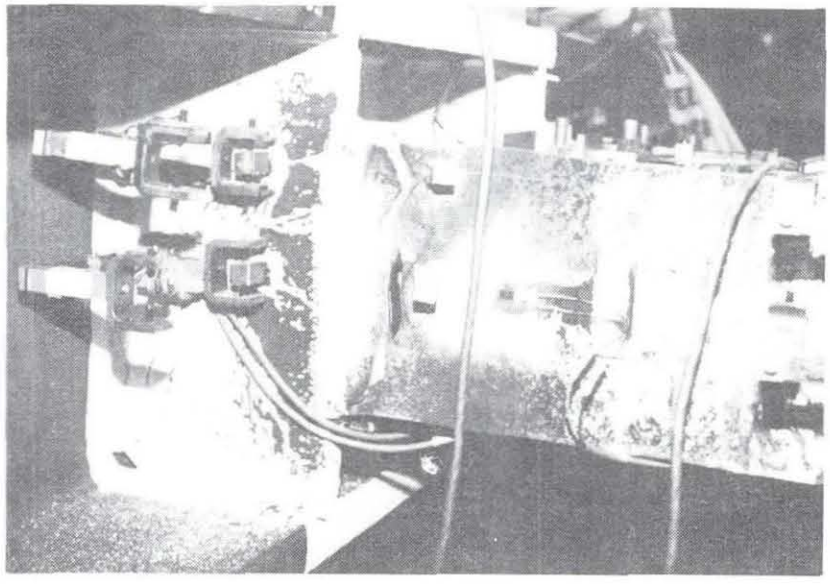

Figure 3.42 Specimen 2 after Failure

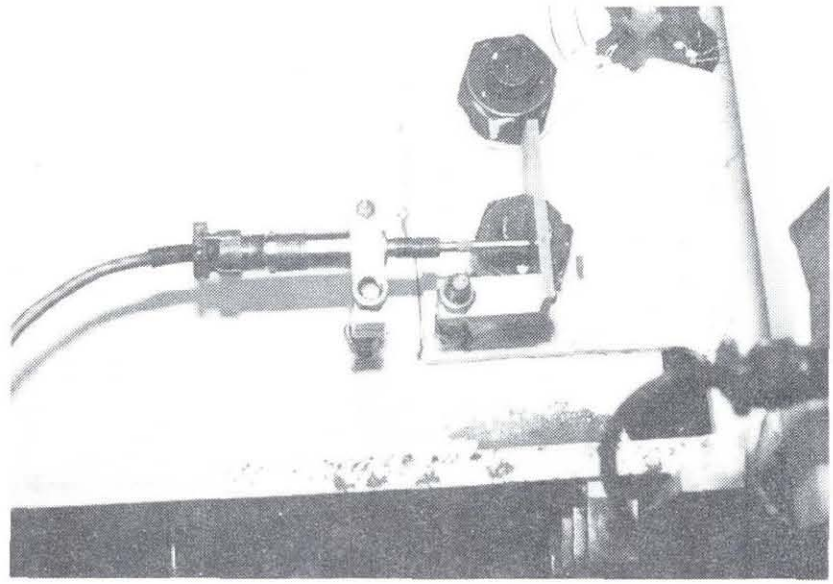

Figure 3.43 Bolt Slippage of Specimen 2

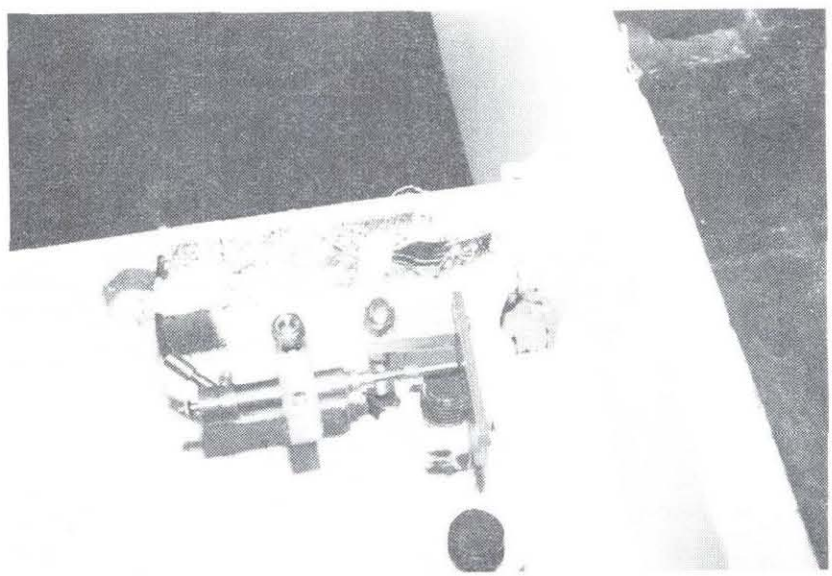

Figure 3.44 Weld Cracked at Center of Bottom Flange (Specimen 3)

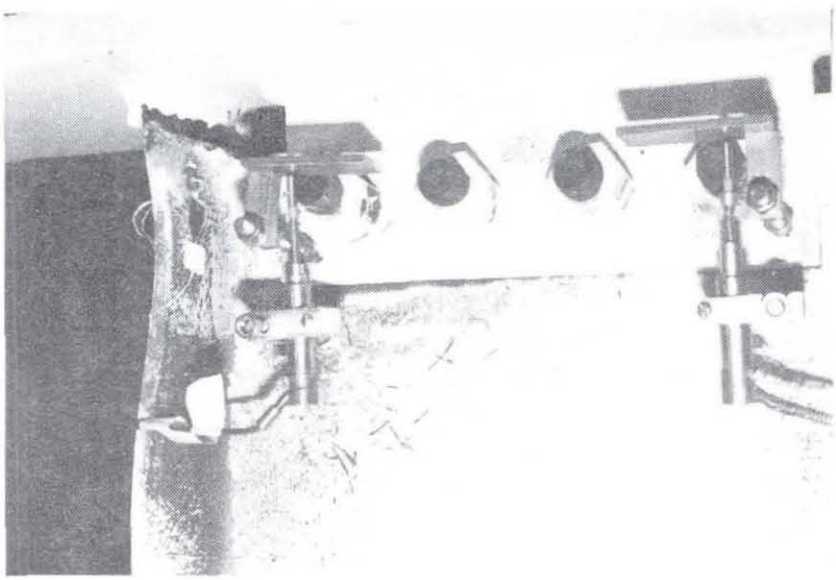

Figure 3.45 Specimen 3 after Failure

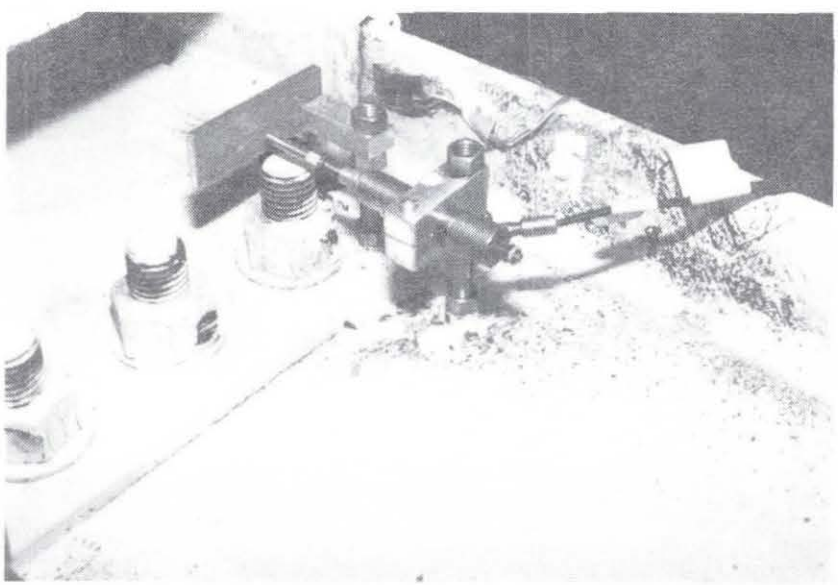

Figure 3.46 Fracture of Bottom Flange and Lower Web Weld (Specimen 4)

Figure 3.47 Fracture of Top Flange and Upper Web Weld (Specimen 4)

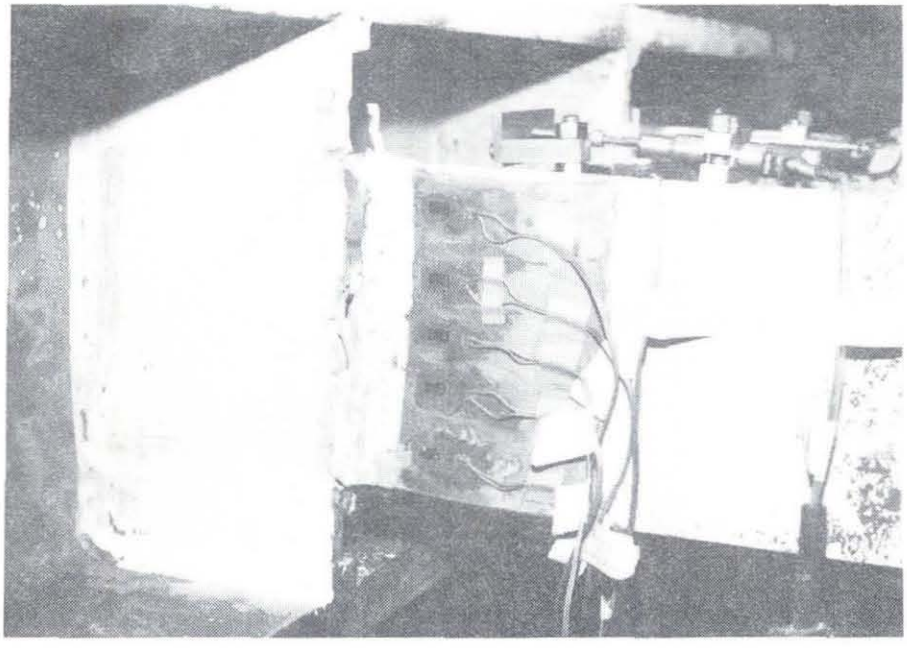

Figure 3.48 Specimen 4 after Failure

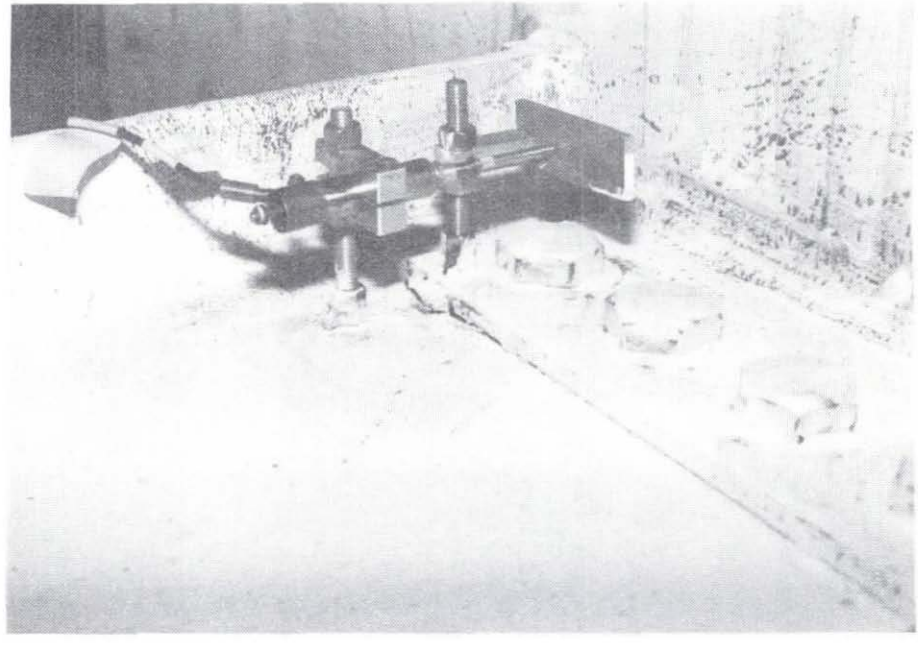

Figure 3.49 Fracture of Web Weld (Specimen 5)

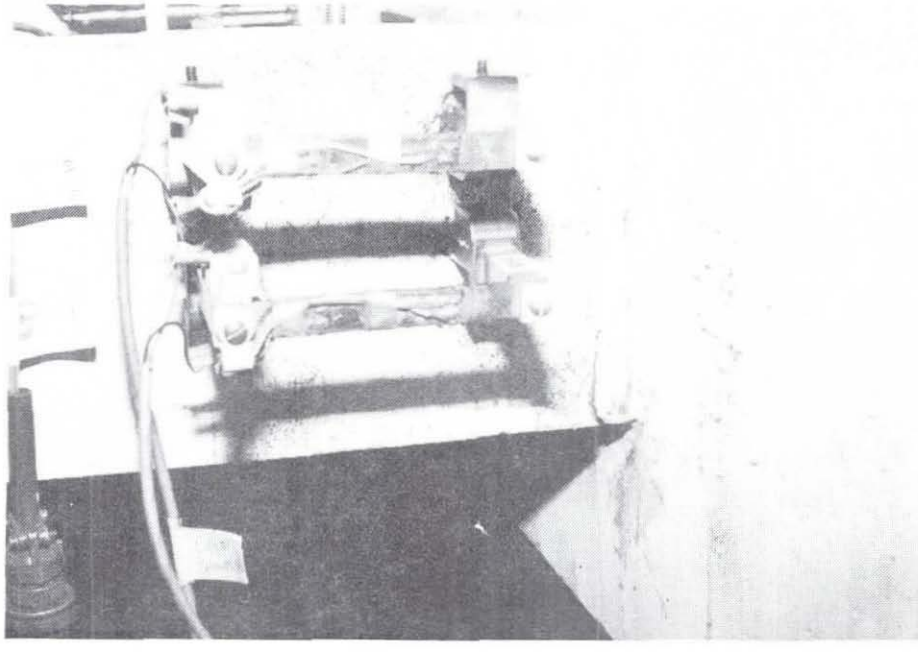

Figure 3.50 Top Flange Weld cracked at The Lower Edge (Specimen 5)

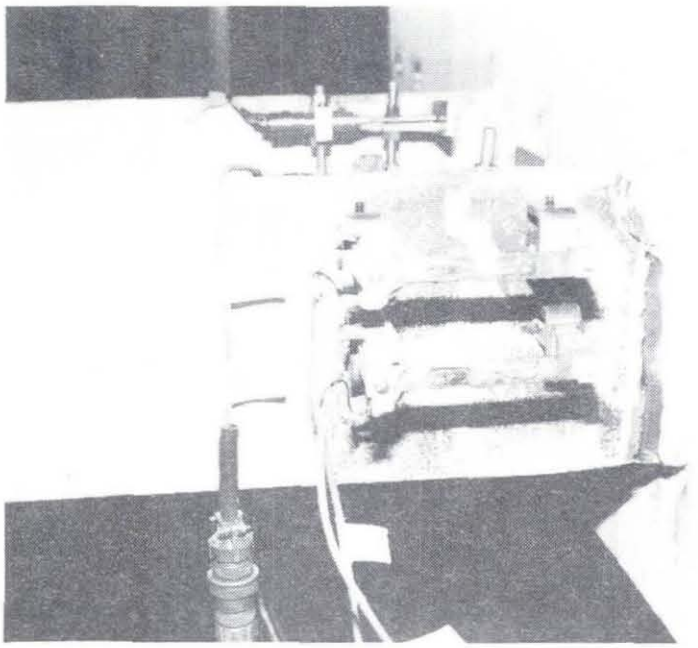

Figure 3.51 Specimen 5 after Failure

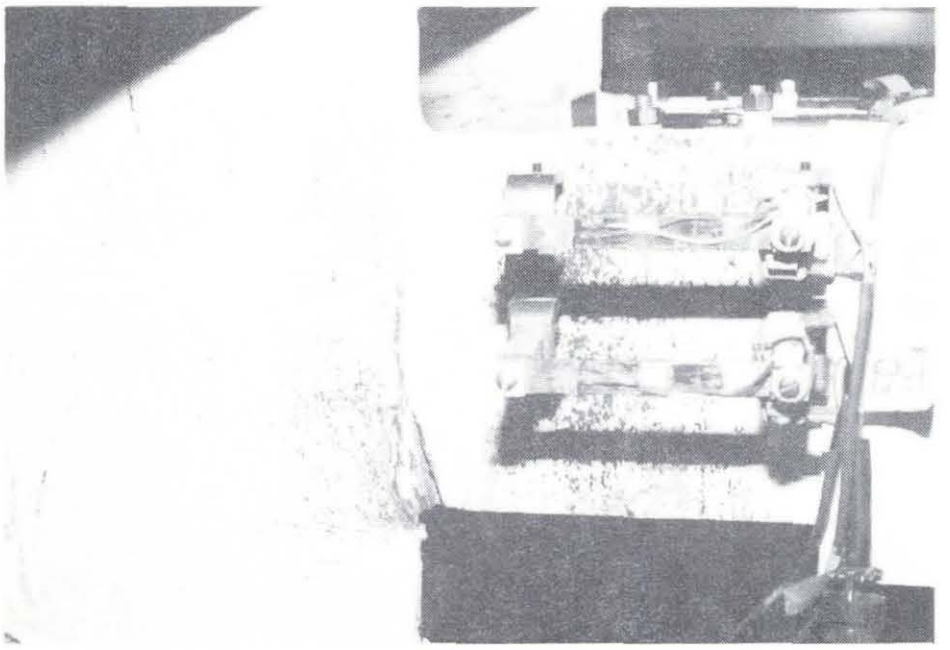

Figure 3.52 Top Flange Weld cracked at The Lower Edge (Specimen 6)

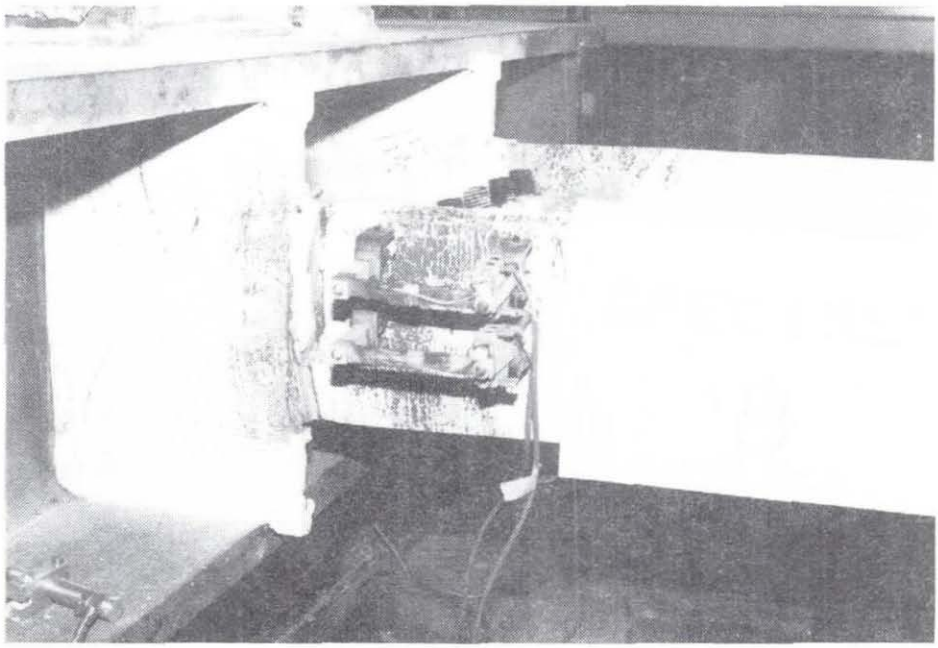

Figure 3.53 Fracture of Top Flange Weld (Specimen 6)

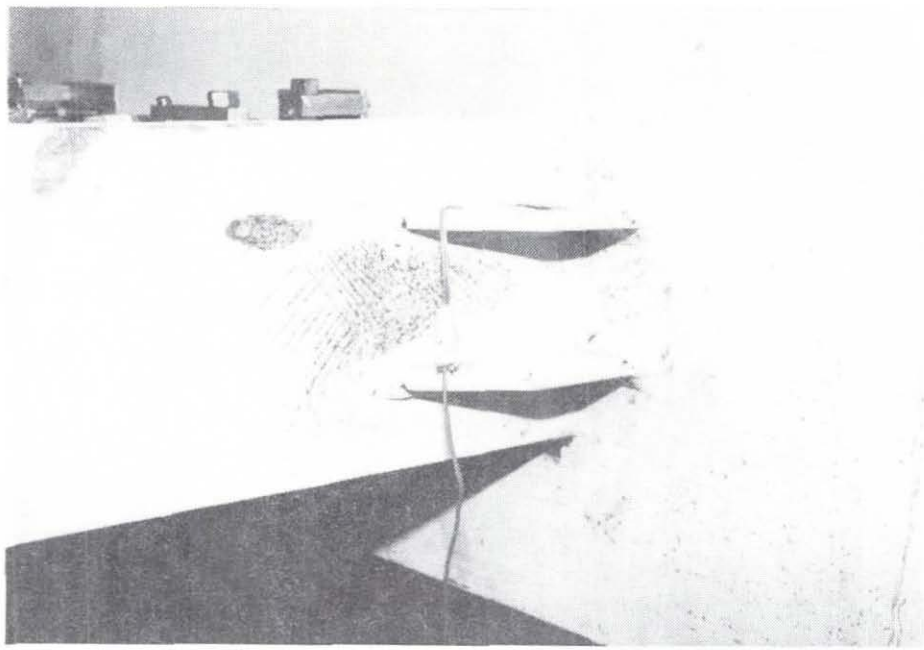

Figure 3.54 Flaking of Whitewash at Top Flange (Specimen 7)

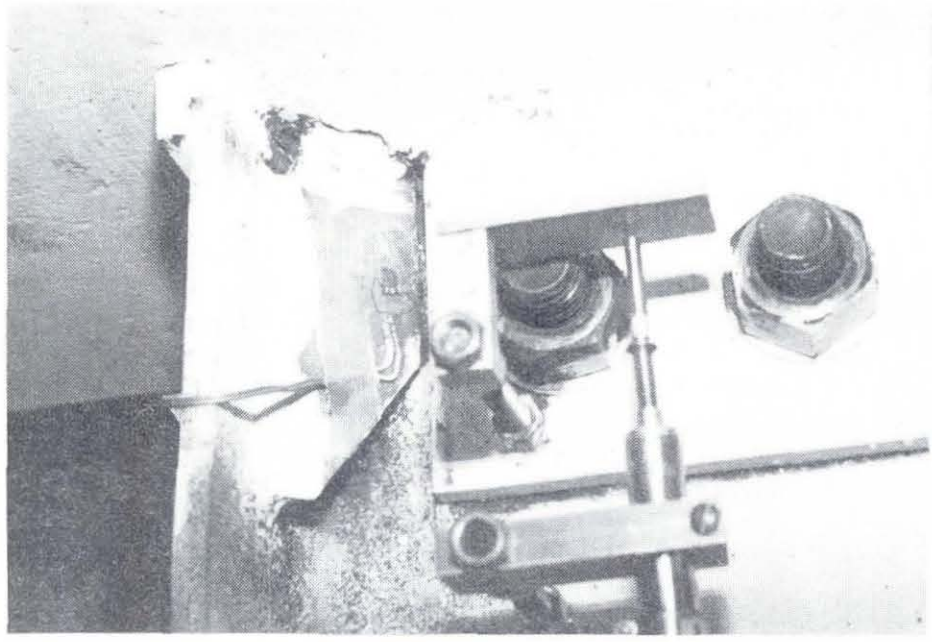

Figure 3.55 Cracking of Welds and Slippage of Bolts (Specimen 7)

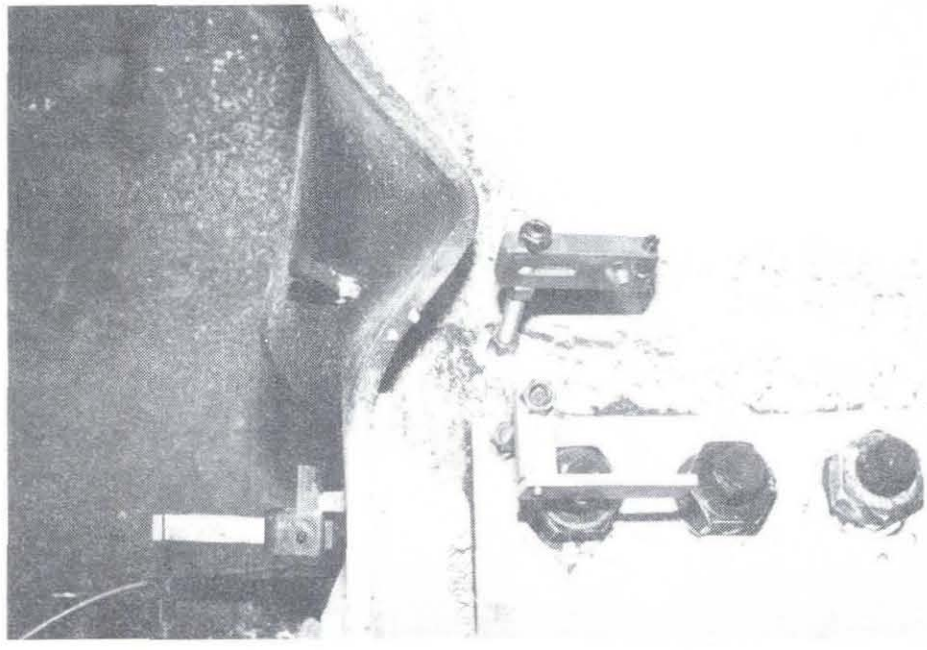

Figure 3.56 Slippage of Bolts (Specimen 8)

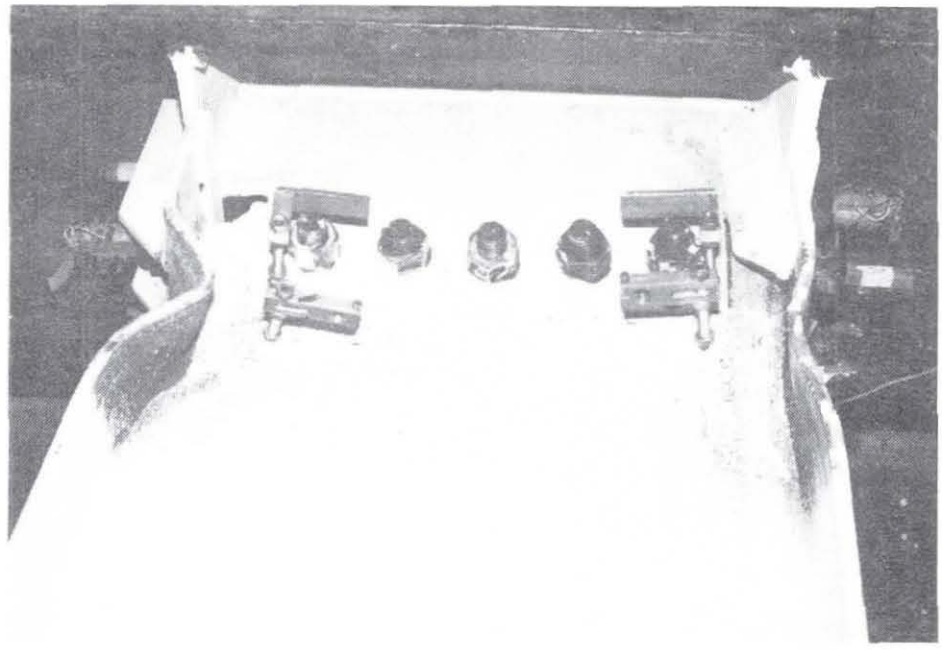

Figure 3.57 Beam Flange and Web Buckling (Specimen 8)

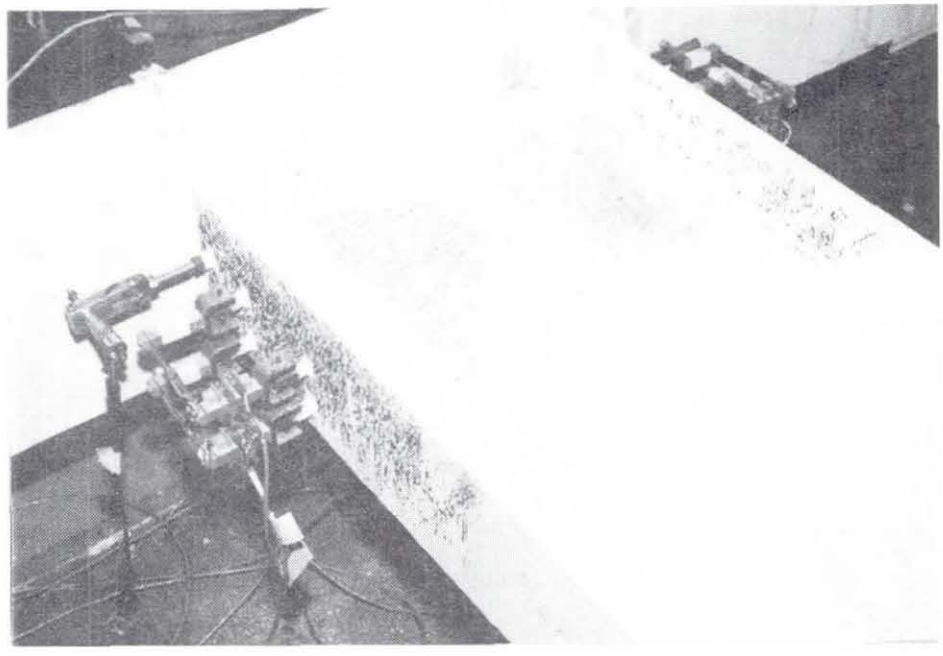

Figure 3.58 Flaking of Whitewash on Beam Flange and Web (Specimen 9)

Figure 3.59 Specimen 9 after Failure

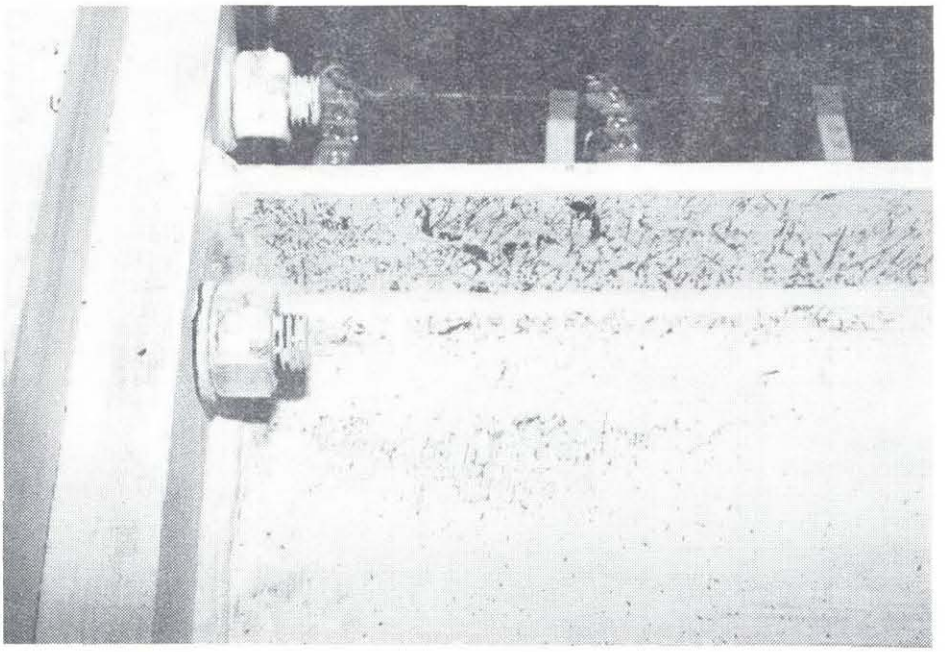

Figure 3.60 Yielding and Elongation of a Bolt (Specimen 10)

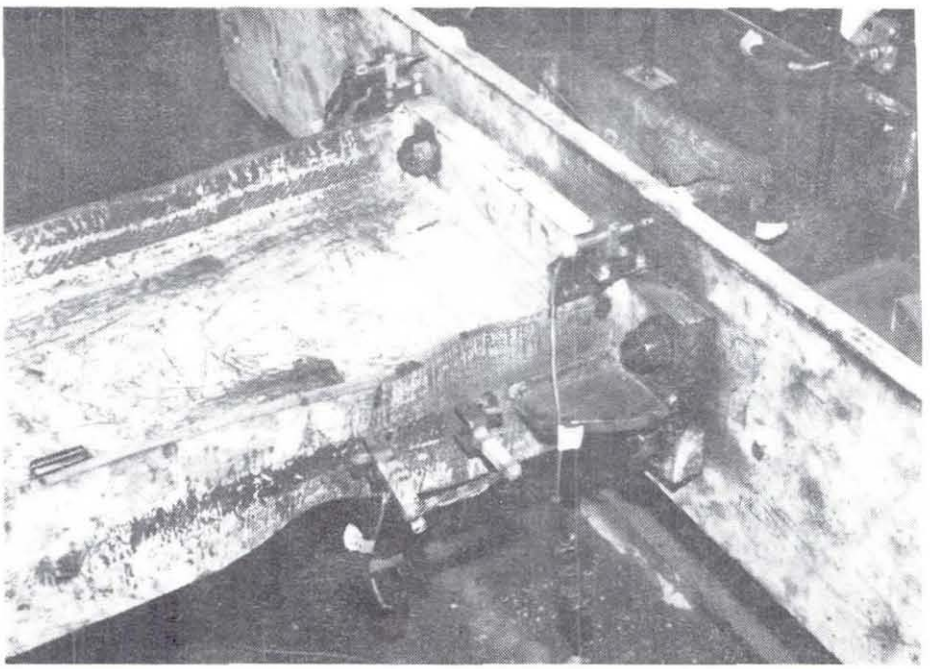

Figure 3.61 Specimen 10R after Failure

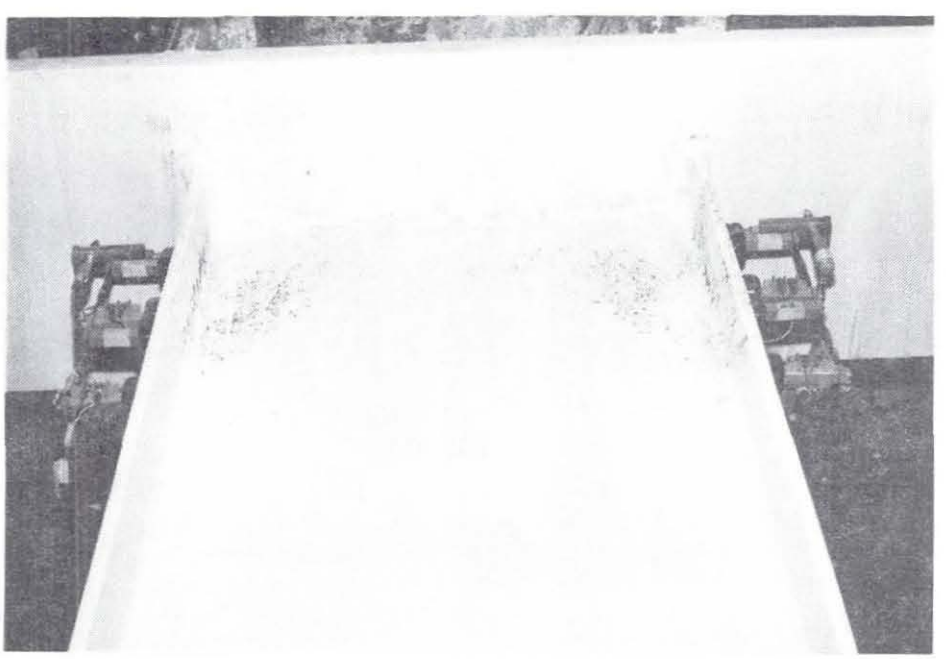

Figure 3.62 Flaking of Whitewash on Beam Flange and Web (Specimen 11)

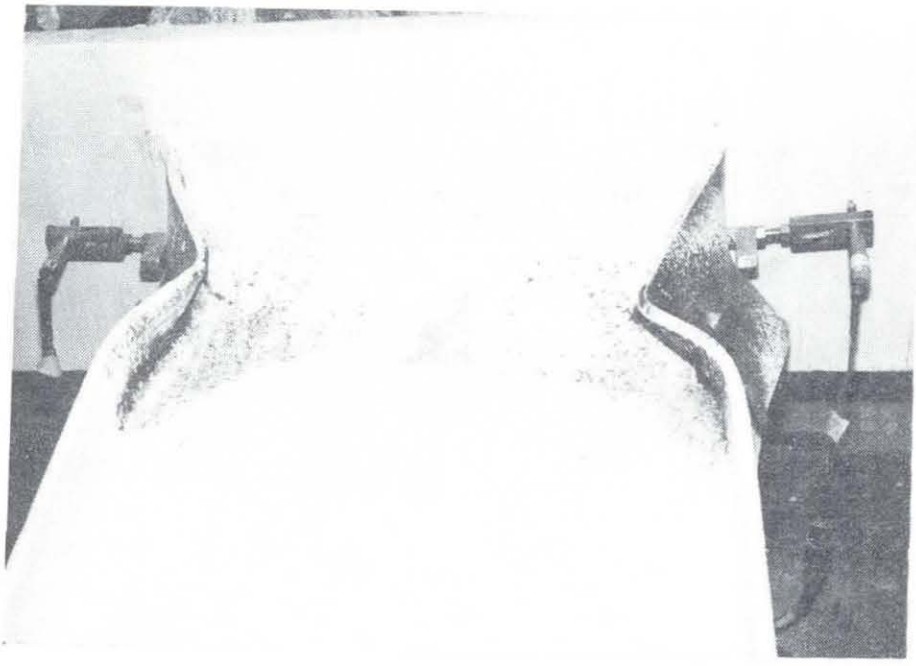

Figure 3.63 Specimen 11 after Failure

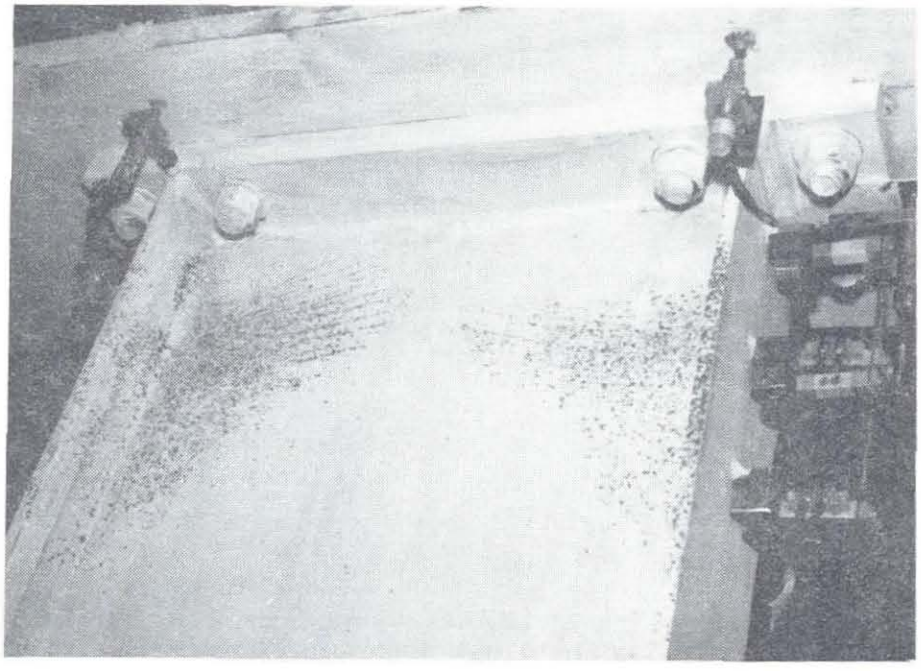

Figure 3.64 Flaking of Whitewash on Beam Flange and Web (Specimen 12)

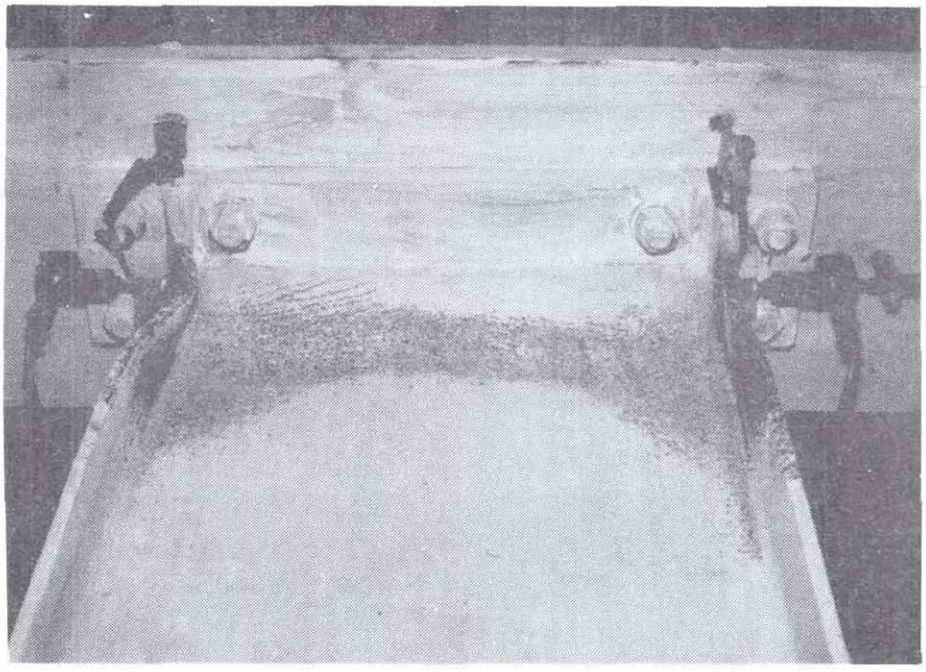

Figure 3.65 Specimen 12 after Failure

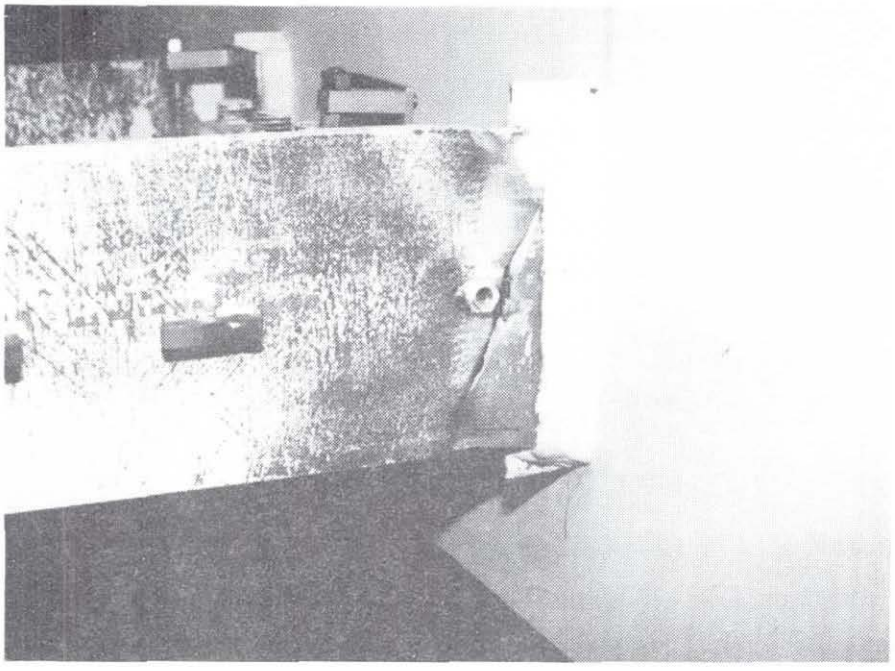

Figure 3.66 Top Flange Cracked at the Center of The Flange (Specimen 13)

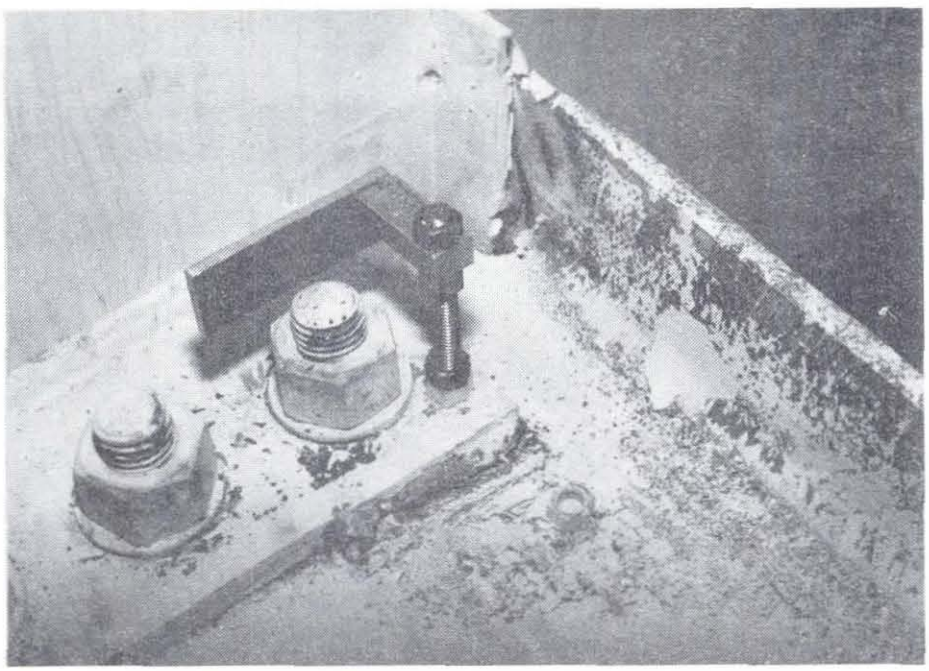

Figure 3.67 Fracture of Beam Top Flange and Upper Web Weld (Specimen 13)

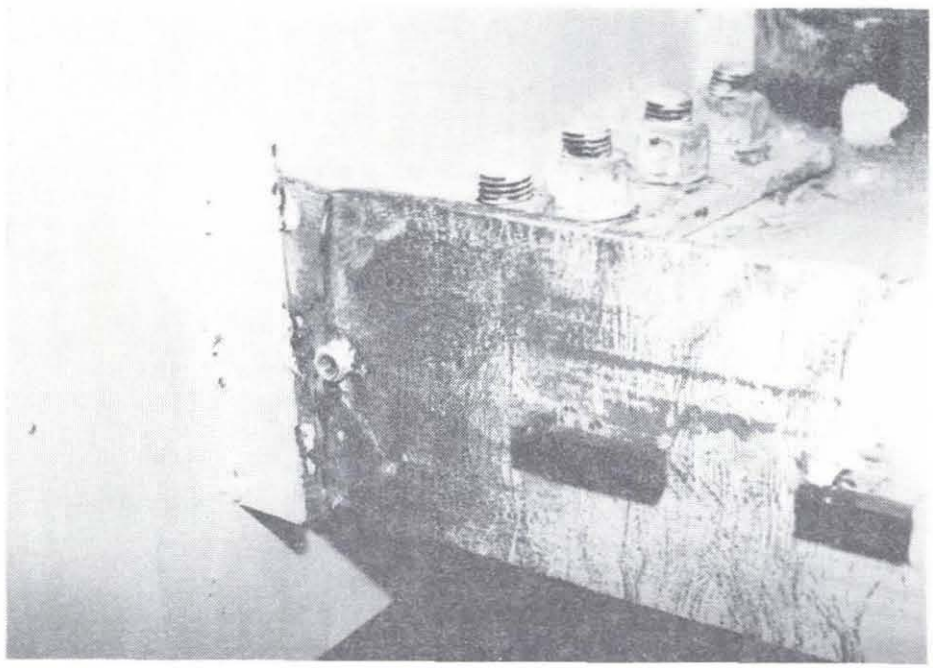

Figure 3.68 Fracture of Beam Bottom Flange (Specimen 13)

Figure 3.69 Fracture of Bottom Flange and Lower Web Weld (Specimen 13)

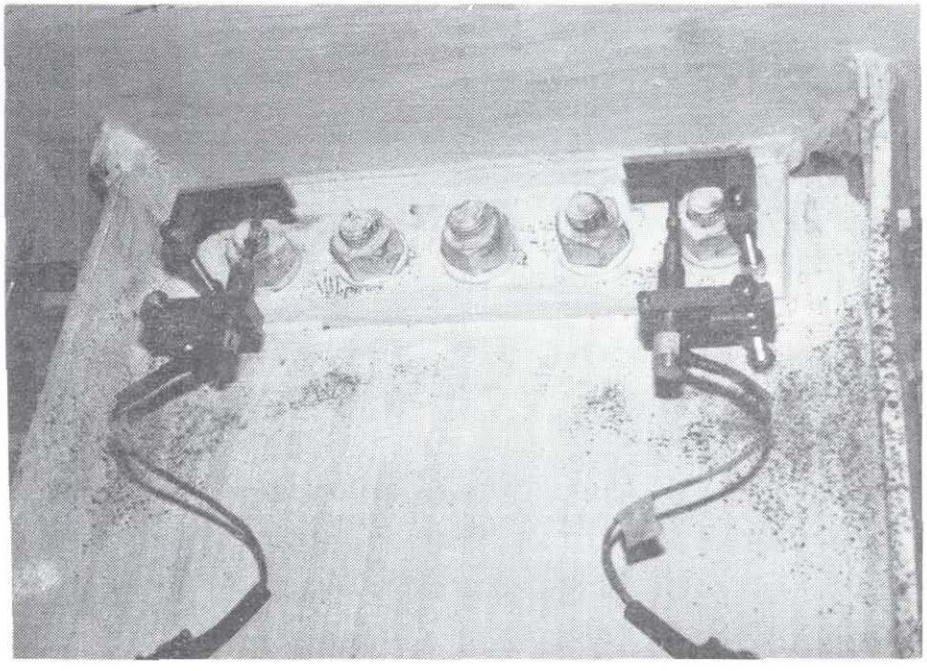

Figure 3.70 Flaking of Whitewash on Beam Flange and Web (Specimen 14)

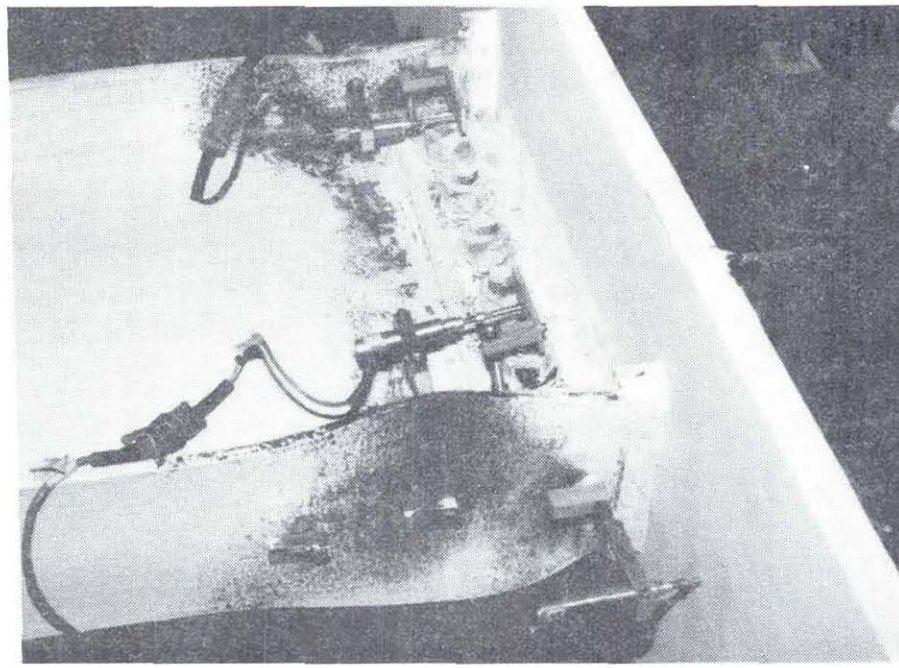

Figure 3.71 Buckling of Beam Flanges and Web (Specimen 14)

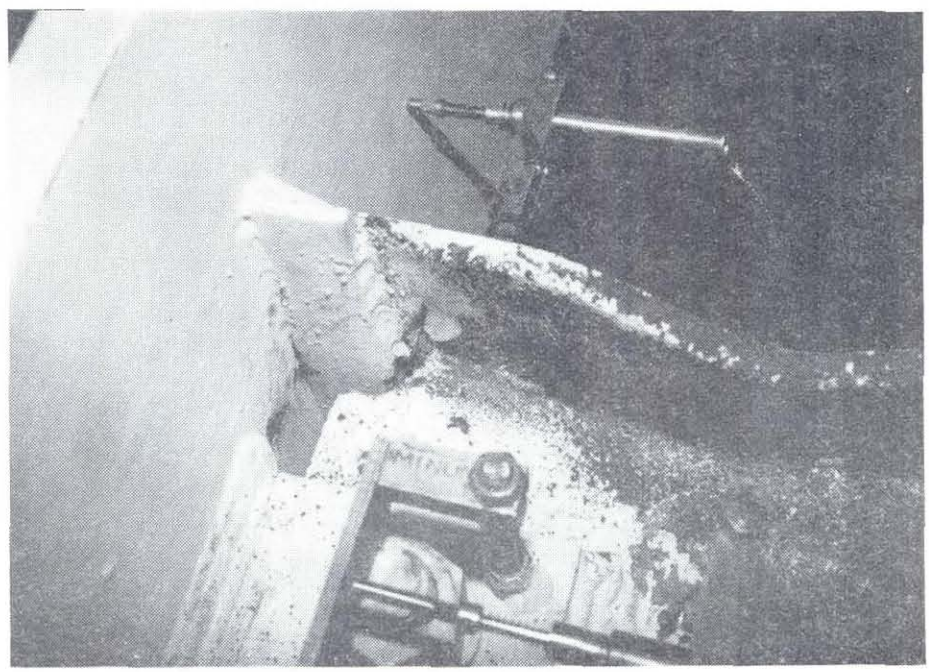

Figure 3.72 Beam Top Flange Cracked at the Center (Specimen 14)

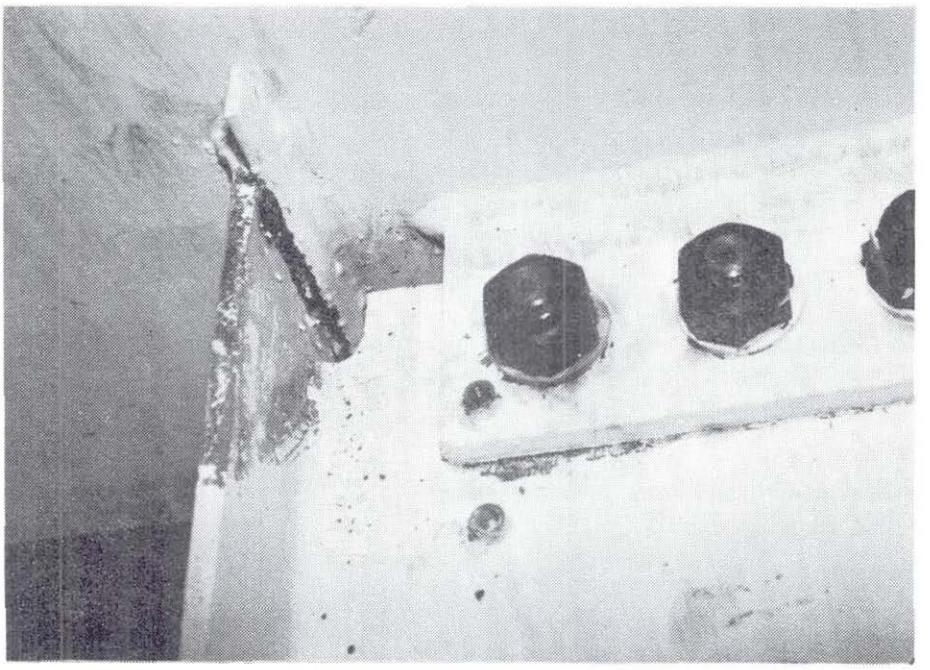

Figure 3.73 Fracture of Flange Weld (Specimen 16)

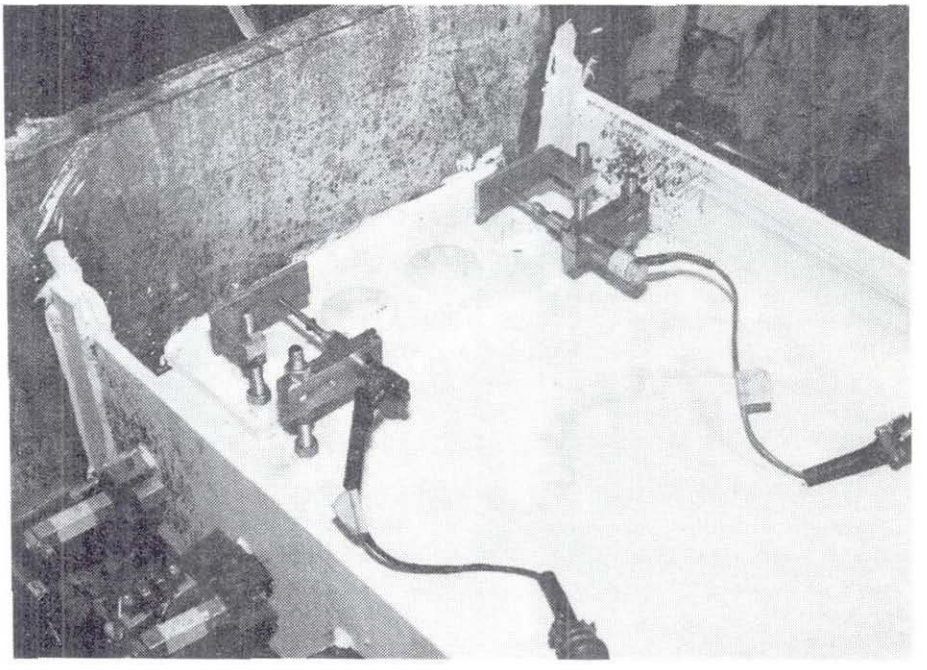

Figure 3.74 Flaking of Whitewash on Beam Flange (Specimen 17)

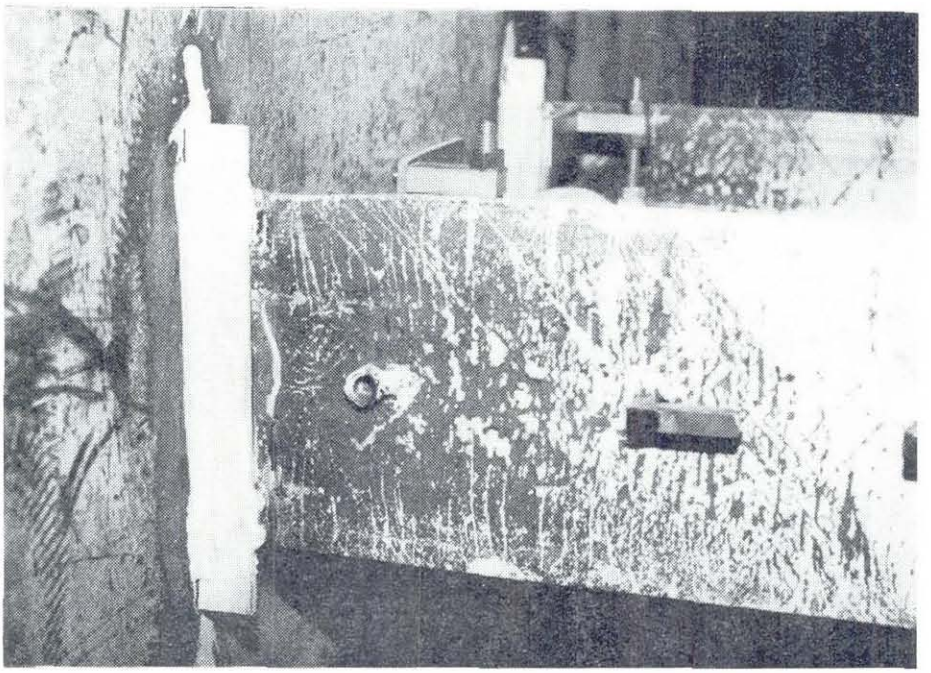

Figure 3.75 Fracture of Beam Bottom Flange (Specimen 17)

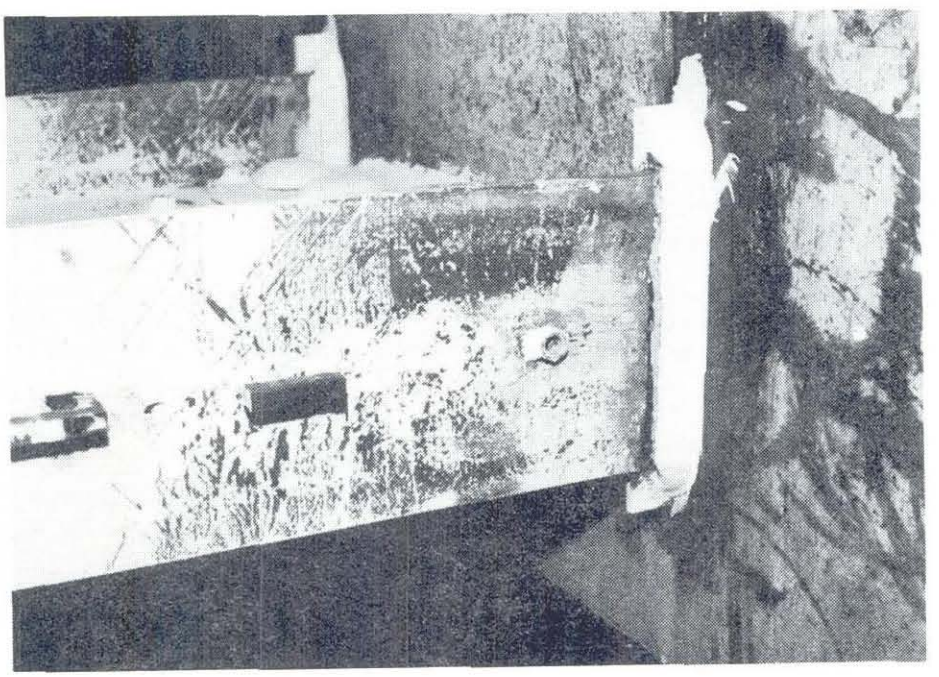

Figure 3.76 Fracture of Beam Top Flange (Specimen 17)

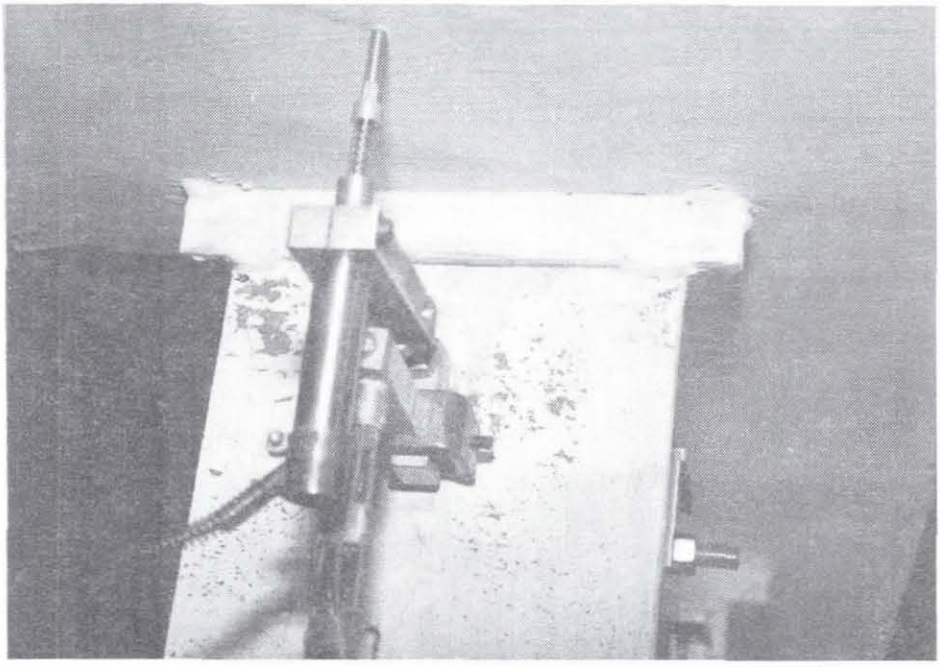

Figure 3.77 Flaking of Whitewash Started in the Area Where Welds Occurred (Specimen 18)

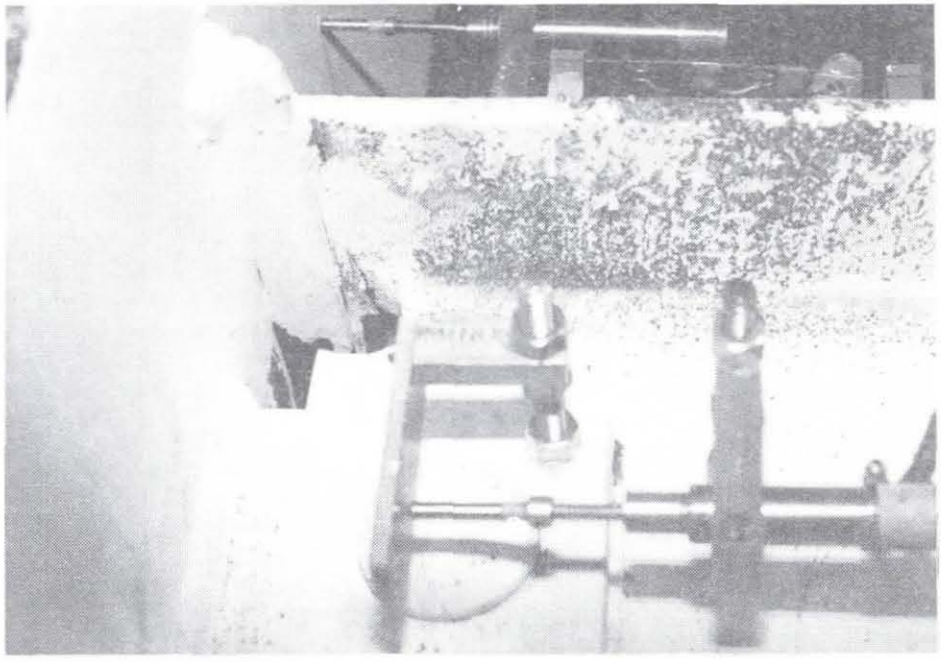

Figure 3.78 Beam Top Flange Cracked at The Center (Specimen 18)

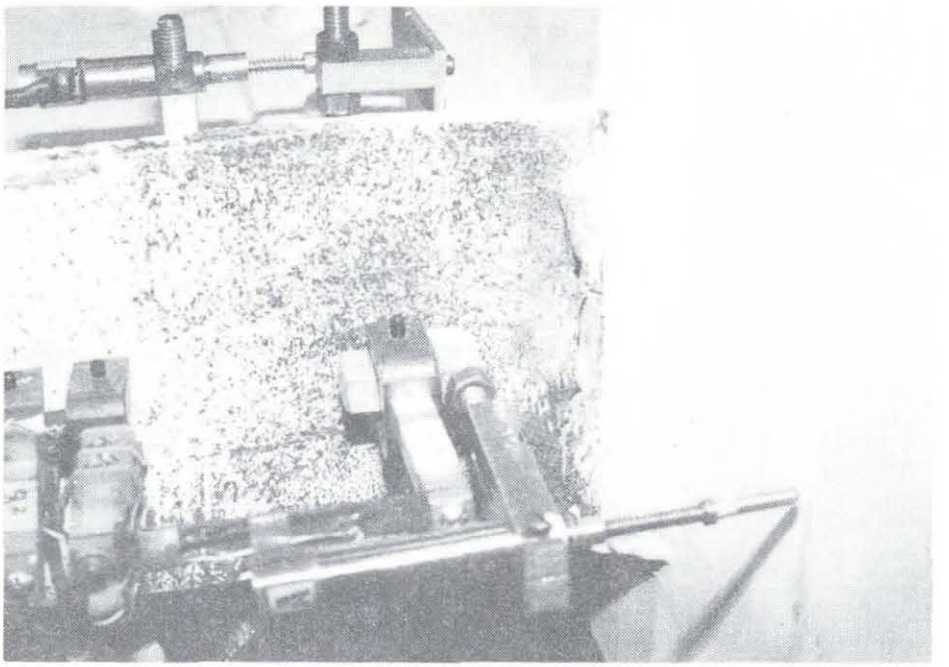

Figure 3.79 Fracture of Top Flange (Specimen 18)

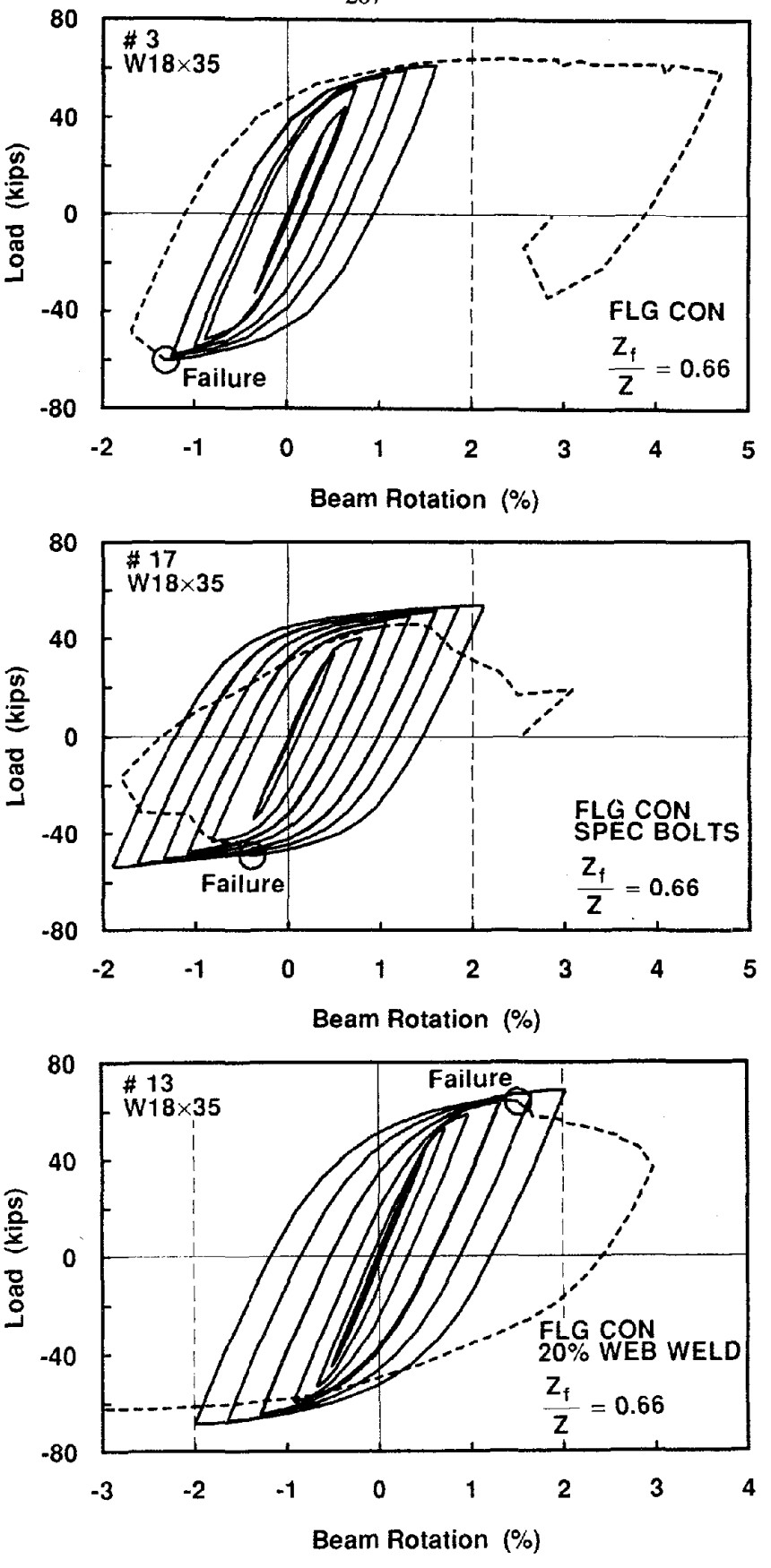

Figure 3.80 Hysteretic Loops for W18x35 Beams Connected to Column Flange

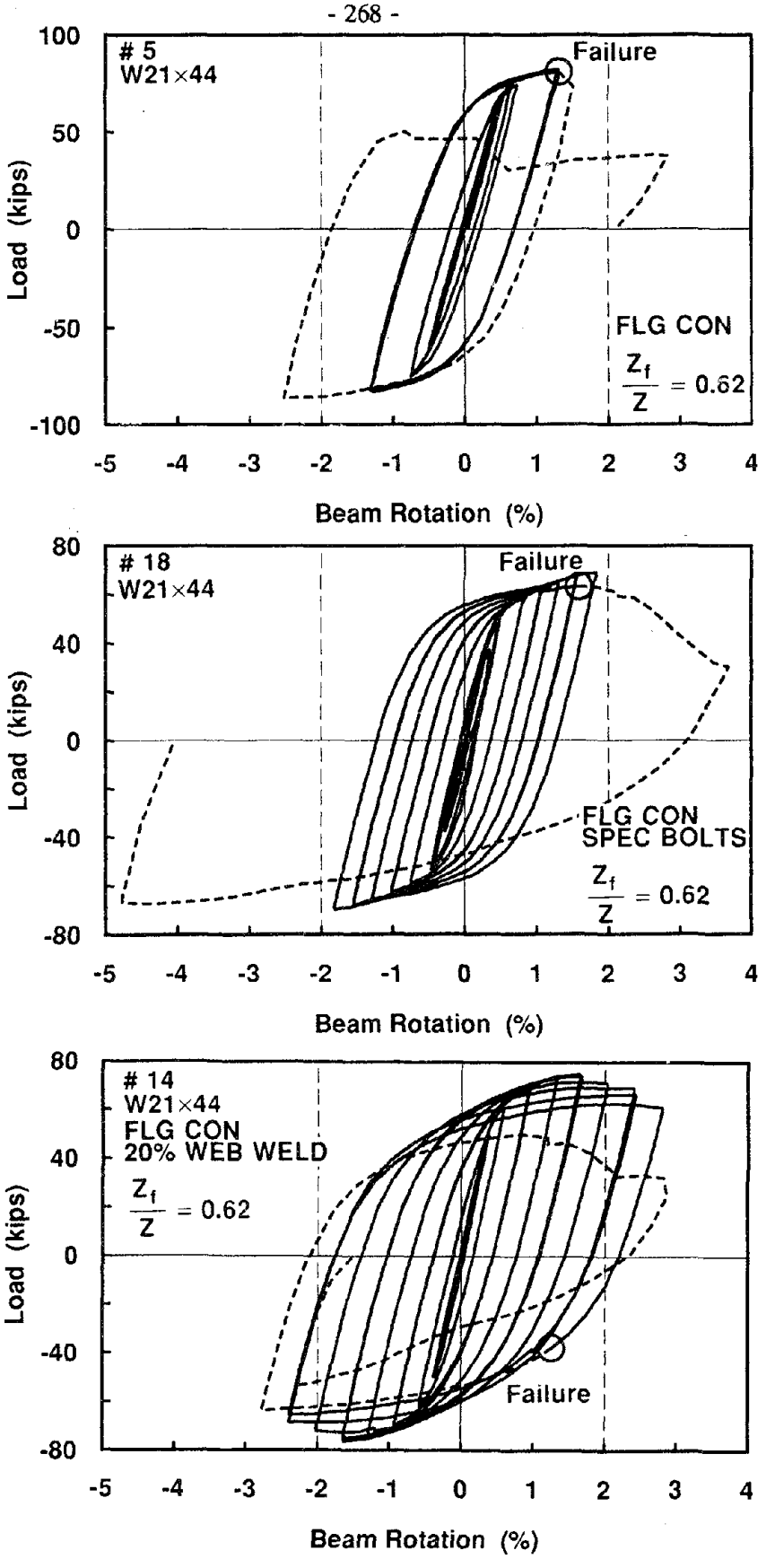

Figure 3.81 Hysteretic Loops for W21x44 Beams Connected to Column Flange

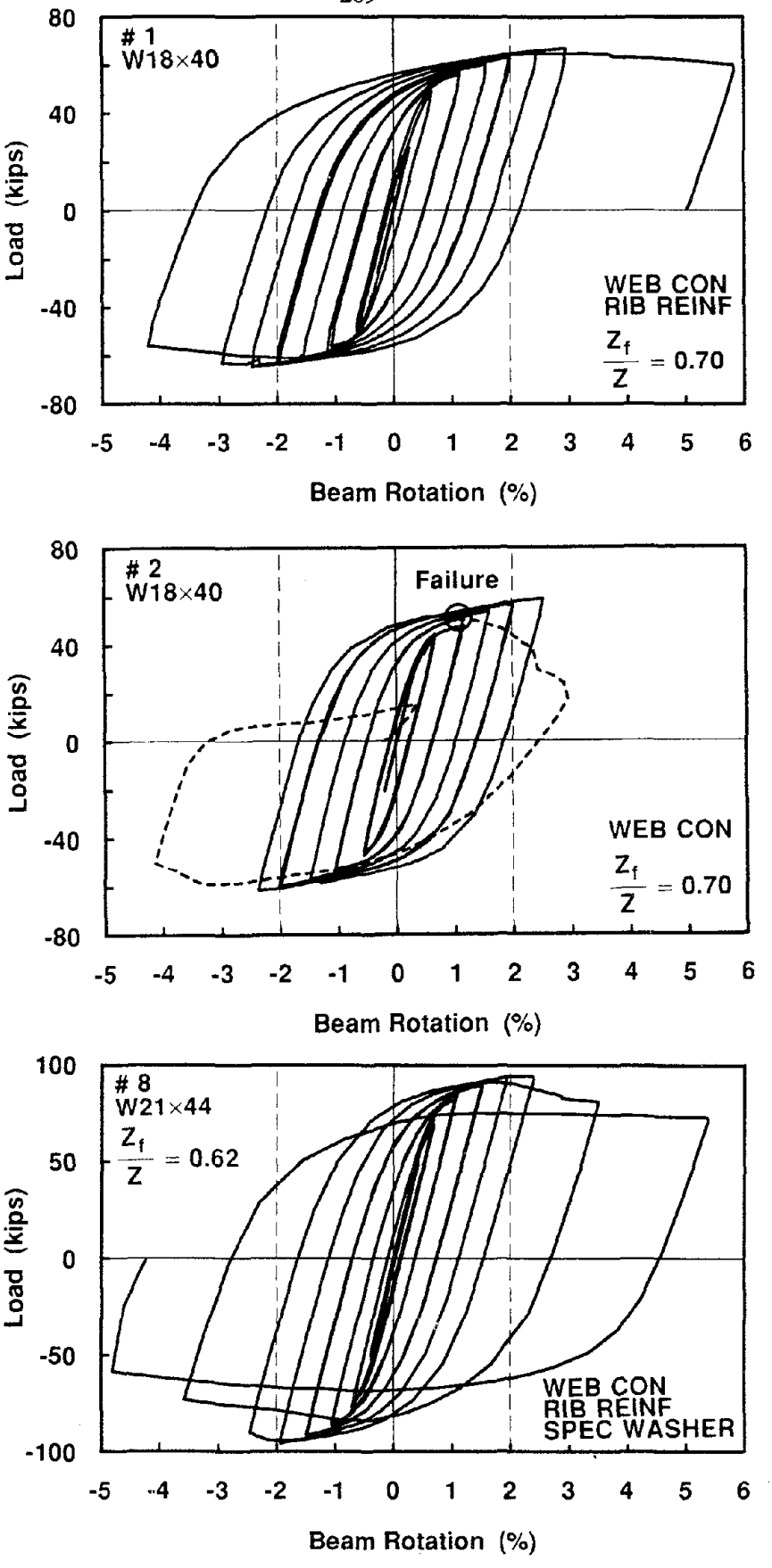

Figure 3.82 Hysteretic Loops for Selected Beam-to-Column Web Connections

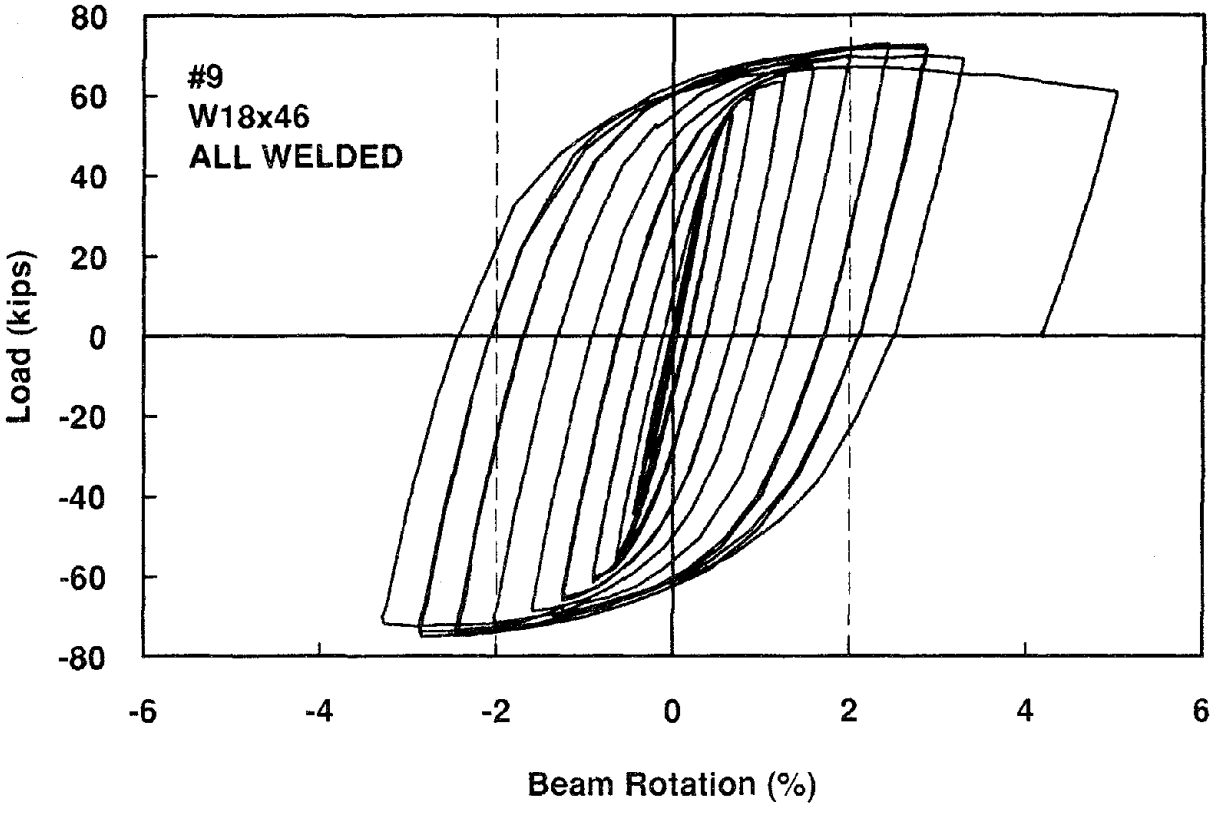

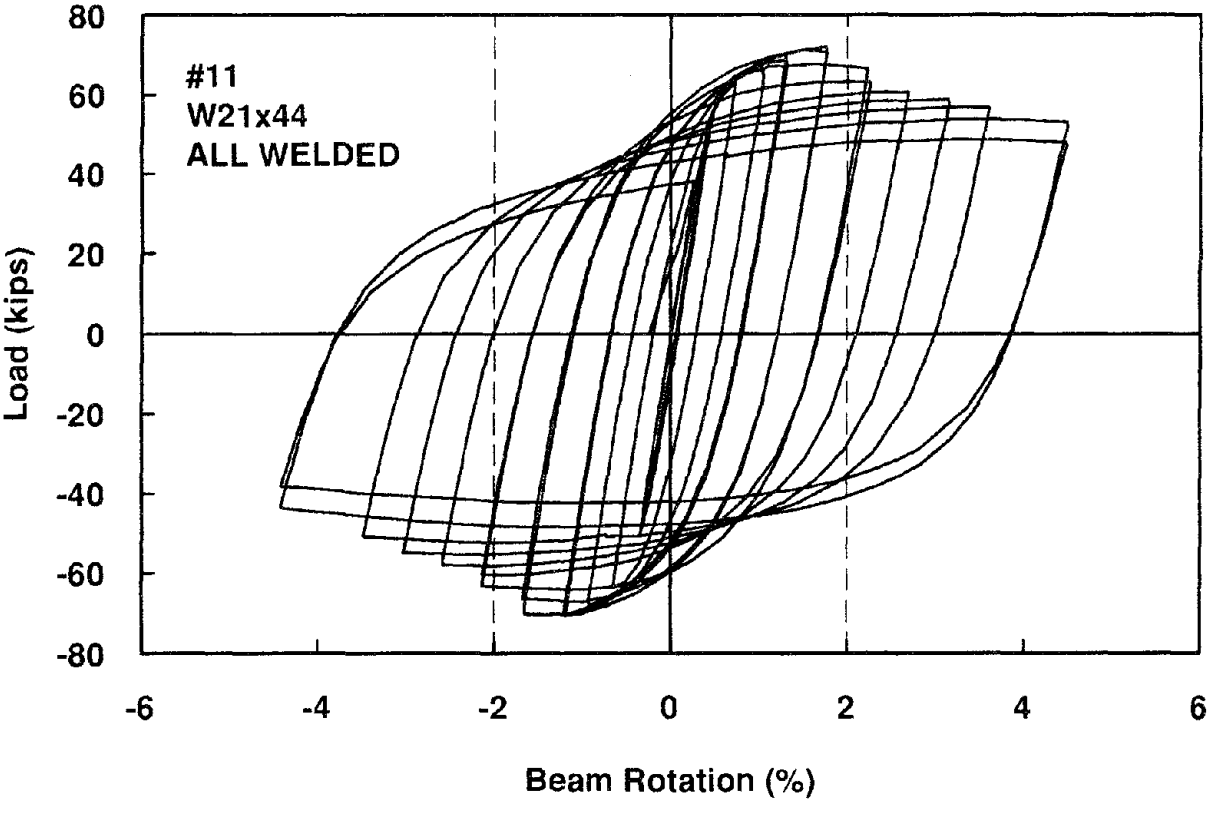

Figure 3.83 Hysteretic Loops for Two Direct All-Welded Beam Connections

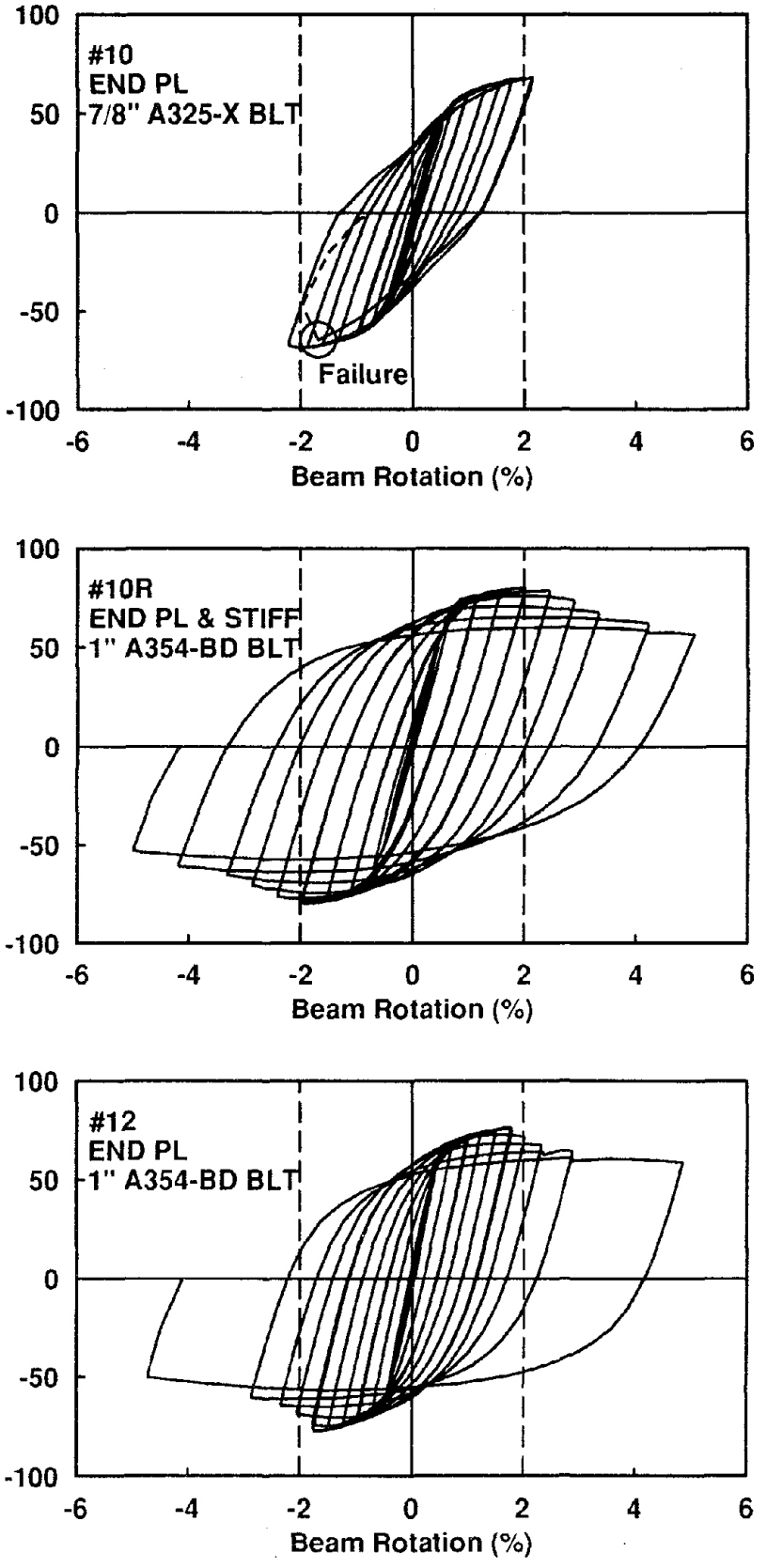

Figure 3.84 Hysteretic Loops for Three Beam End Plate Moment Connections

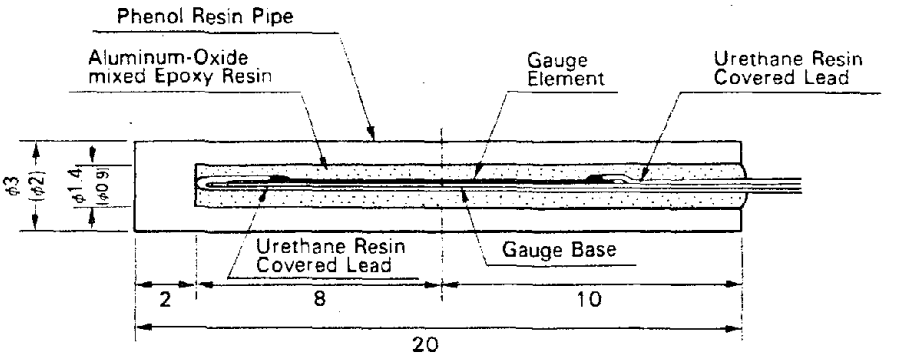

CONSTRUCTION of BTM-8B(A)

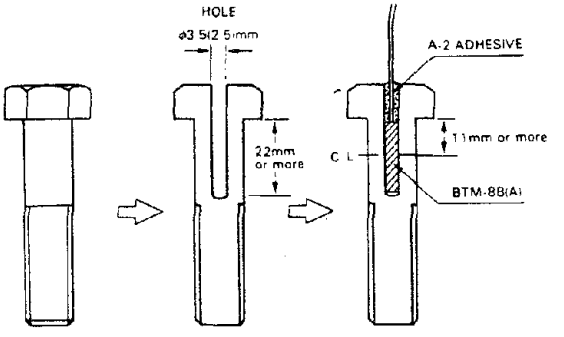

INSTALLATION OF BTM GAUGE

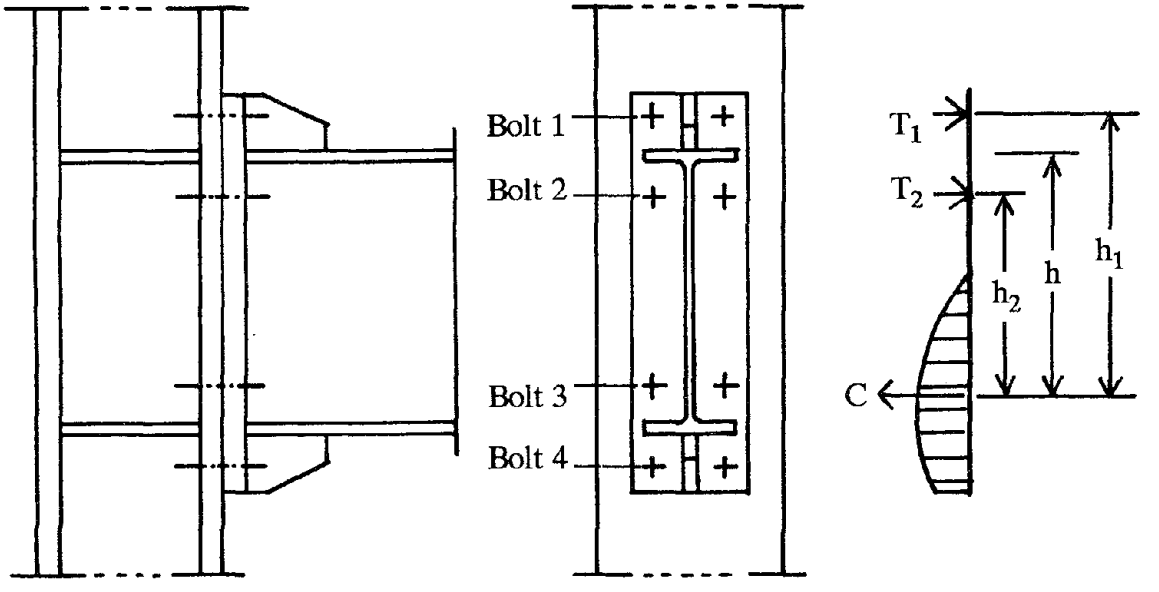

Figure 4.1 Bolt Gauge and Location of Gauged Bolts

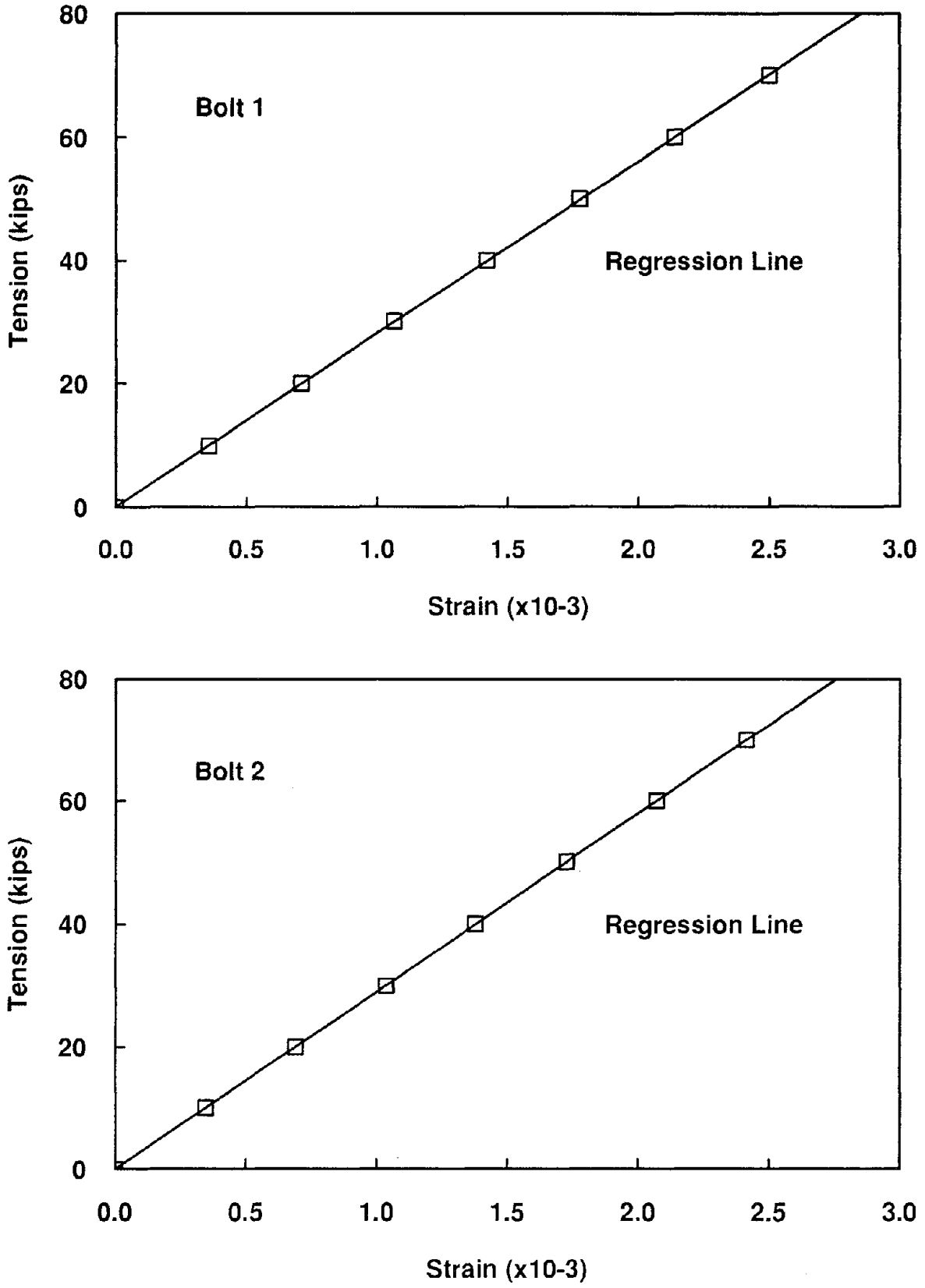

Figure 4.2 Bolt Tension Force vs. Bolt Strain (Bolt 1 and 2)

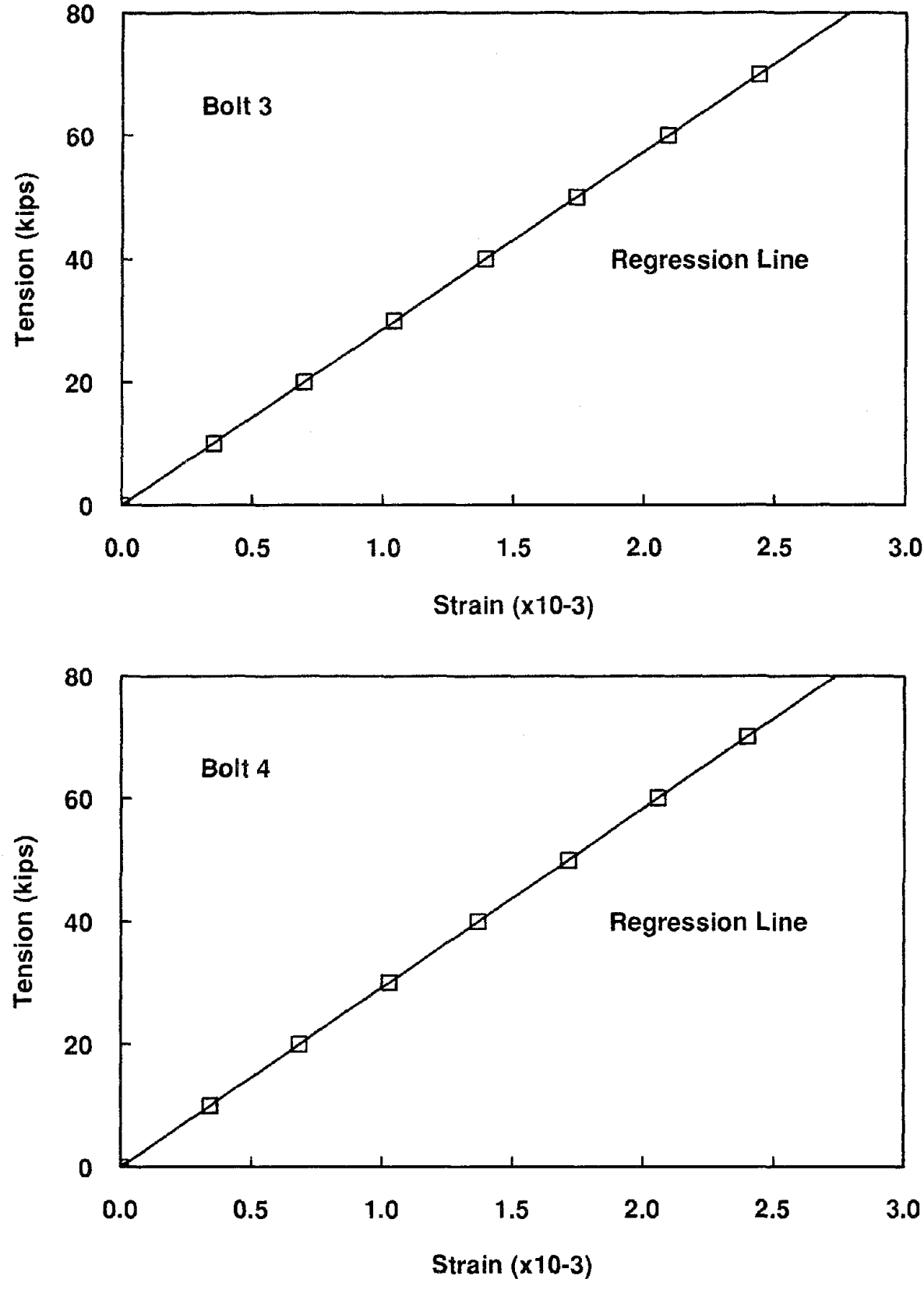

Figure 4.3 Bolt Tension Force vs. Bolt Strain (Bolt 3 and 4)

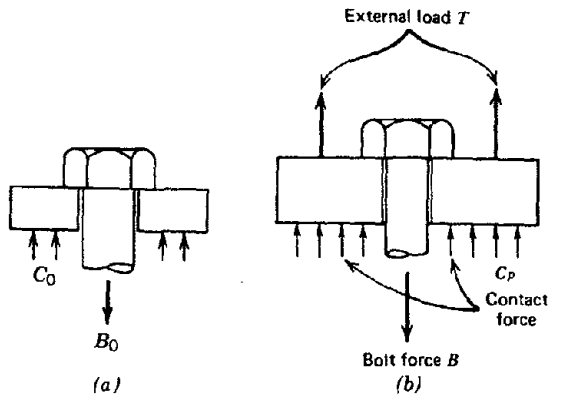

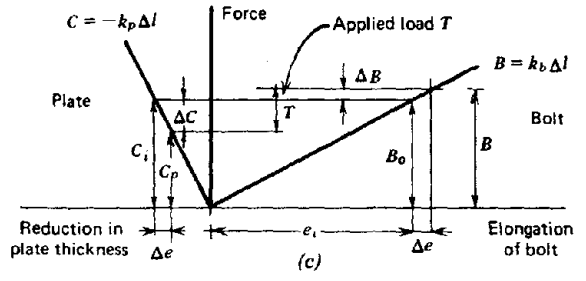

Figure 4.4 Force in Pretensioned Bolt [28]

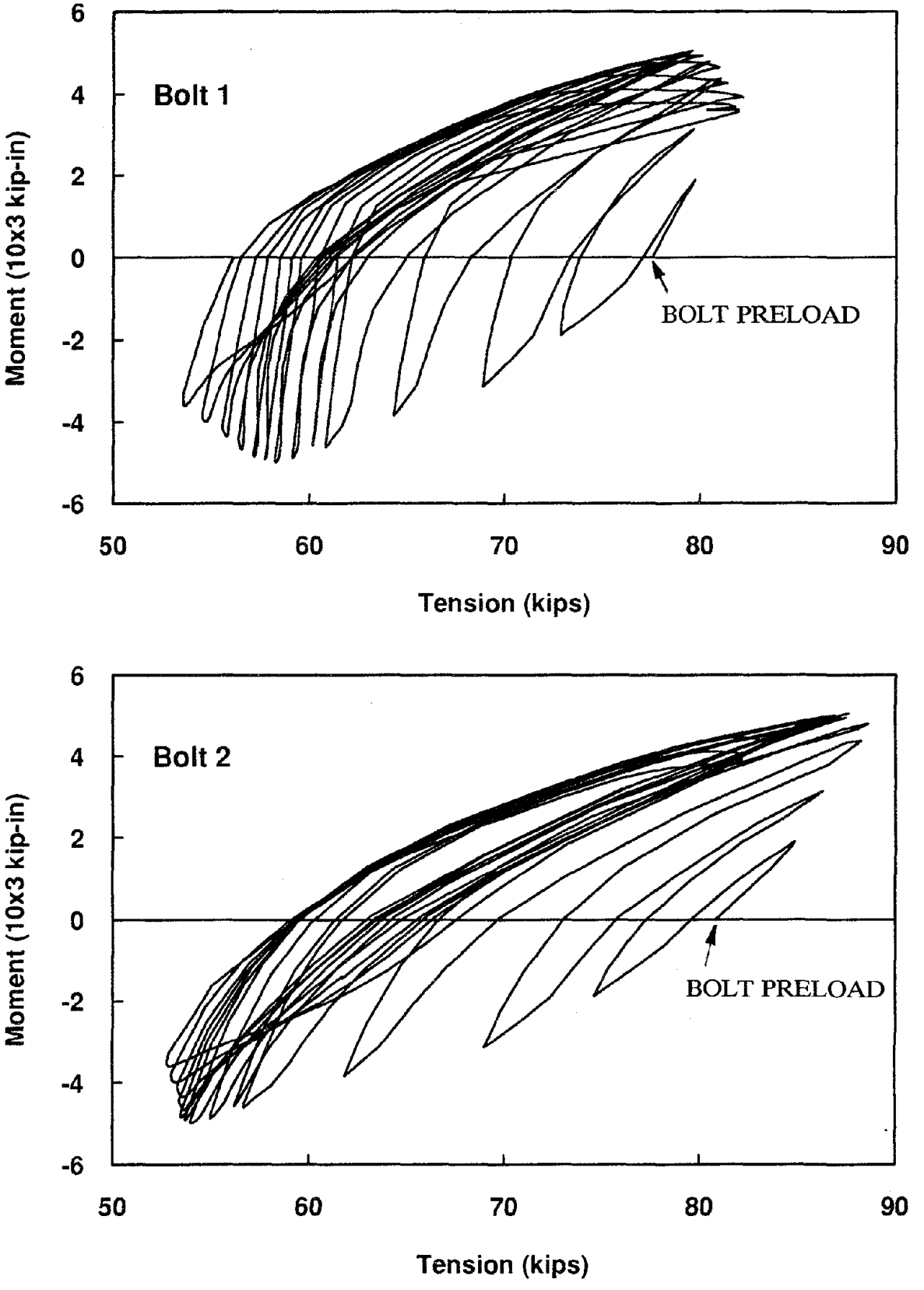

Figure 4.5 Bolt Force vs. Beam Moment (Bolt 1 and 2)

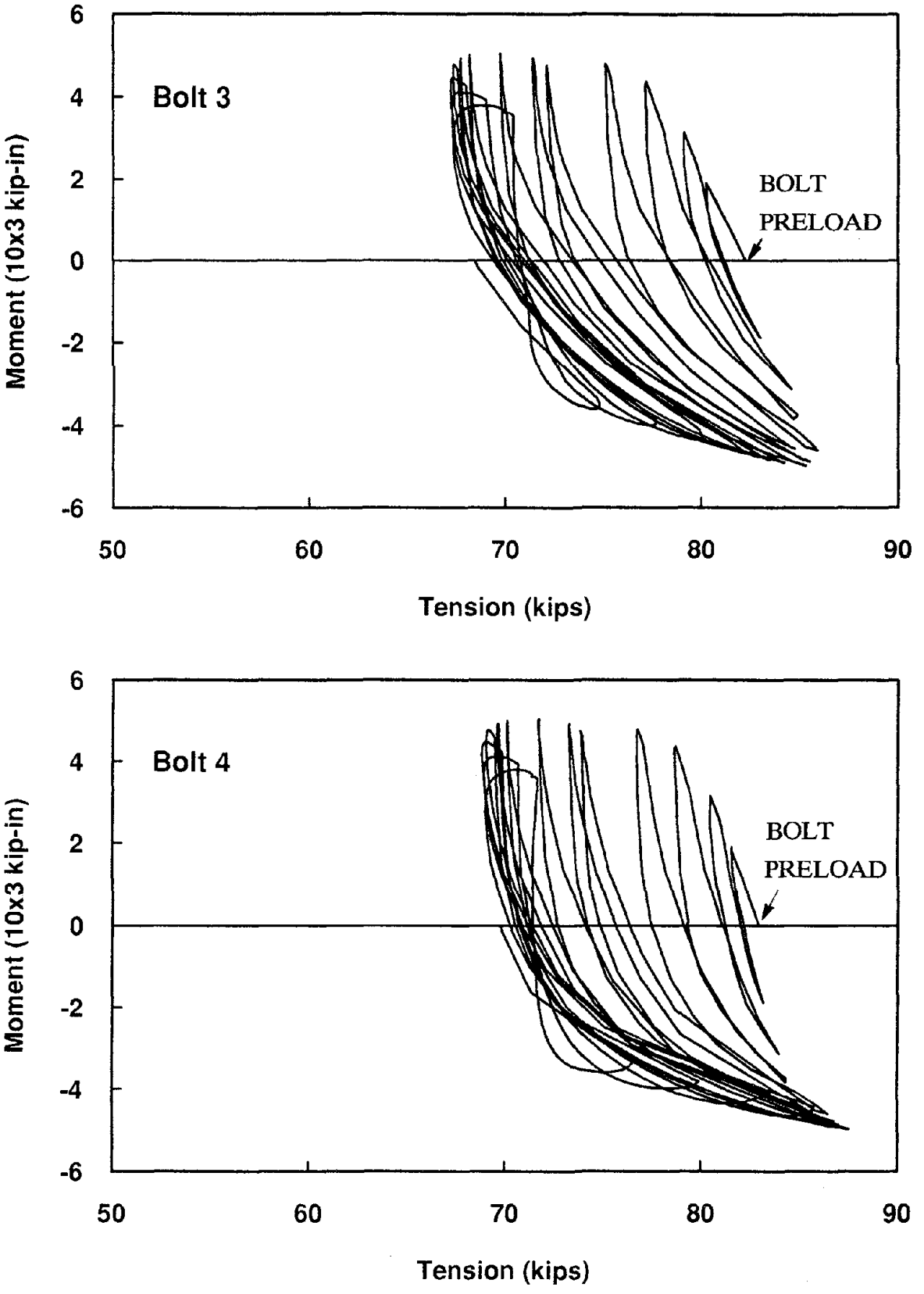

Figure 4.6 Bolt Force vs. Beam Moment (Bolt 3 and 4)

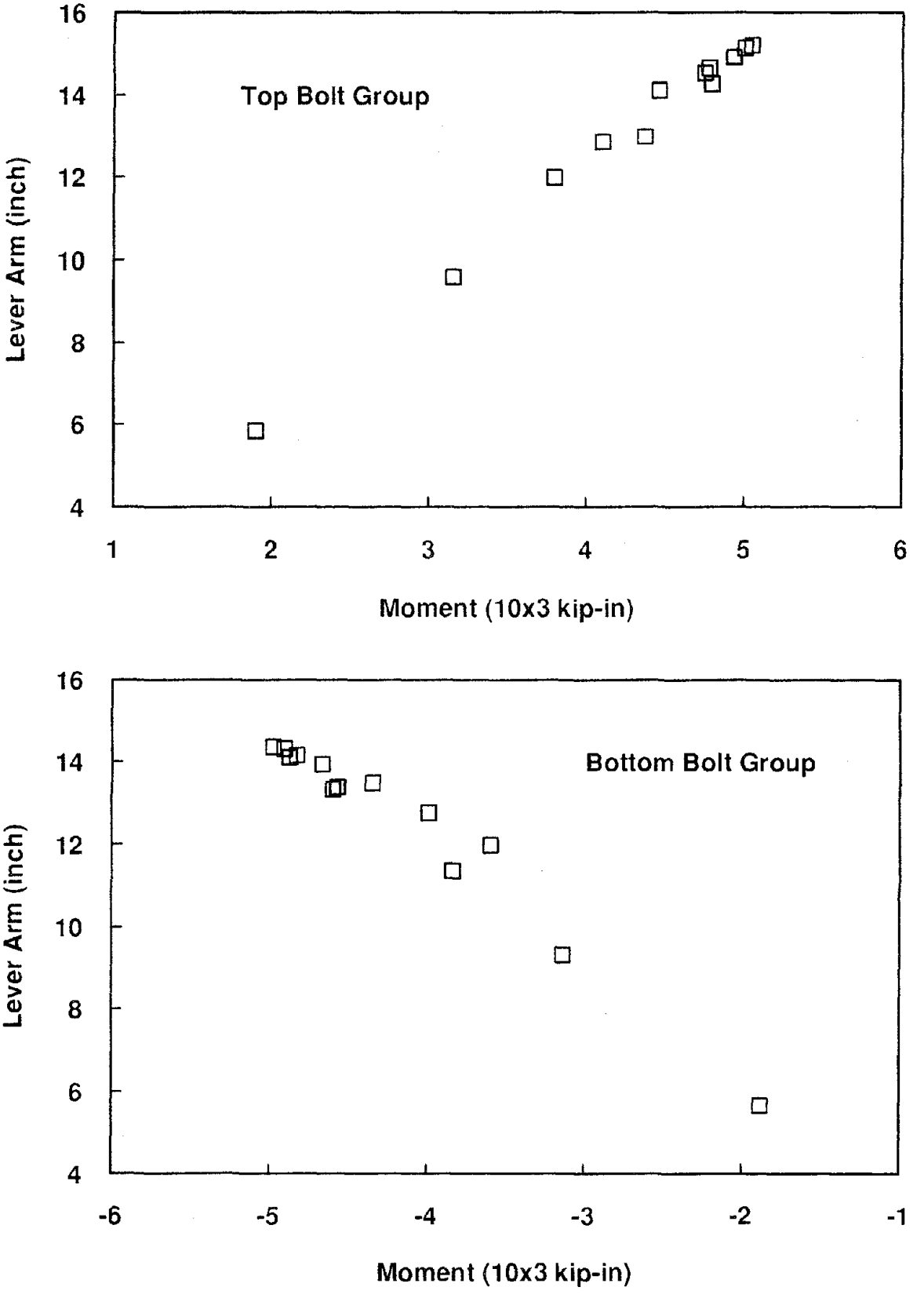

Figure 4.7 Bolt Resisting Lever Arm vs. Beam Moment

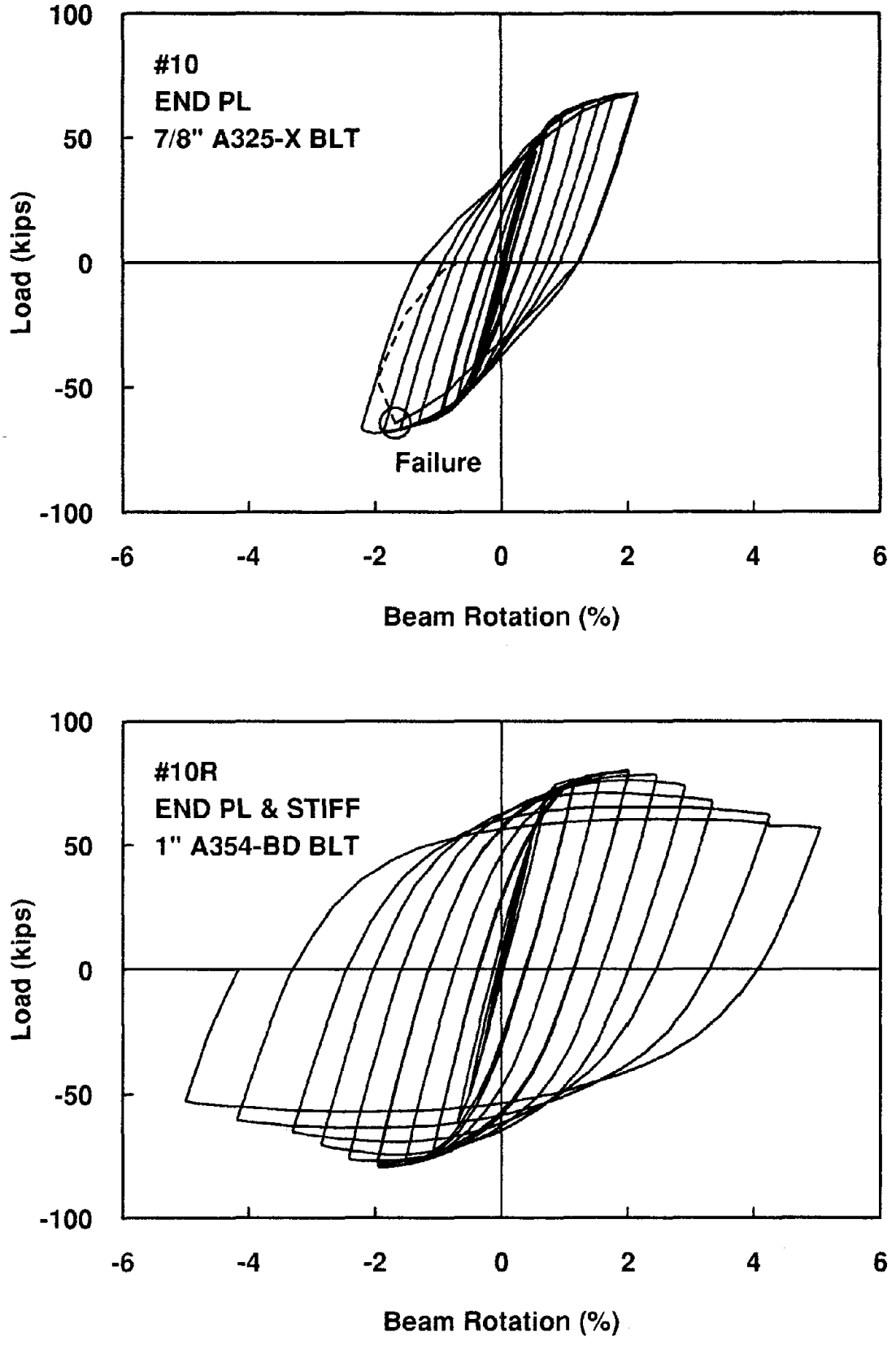

Figure 4.8 Beam Rotation vs. Beam Cantilever Load (Specimens 10 and 10R)

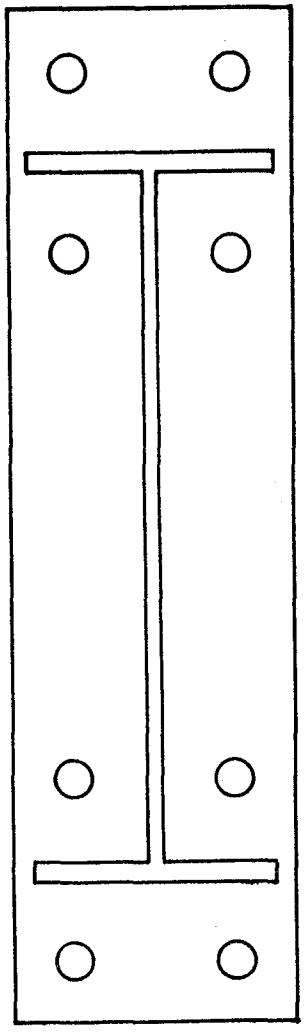

(a) End Plate Configuration

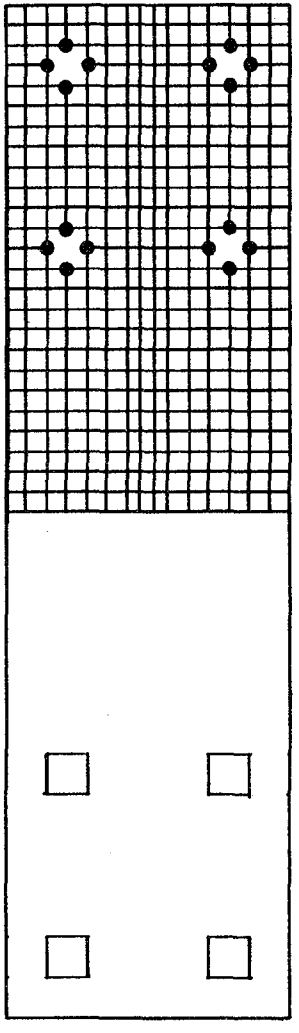

(b) Undeformed Mesh (One Half of The Plate)

● Location of Load

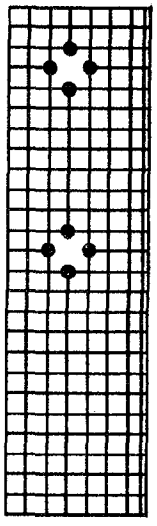

(c) Undeformed Mesh (One Quarter of The Plate)

Figure 4.9 Finite Element Model for The End Plate

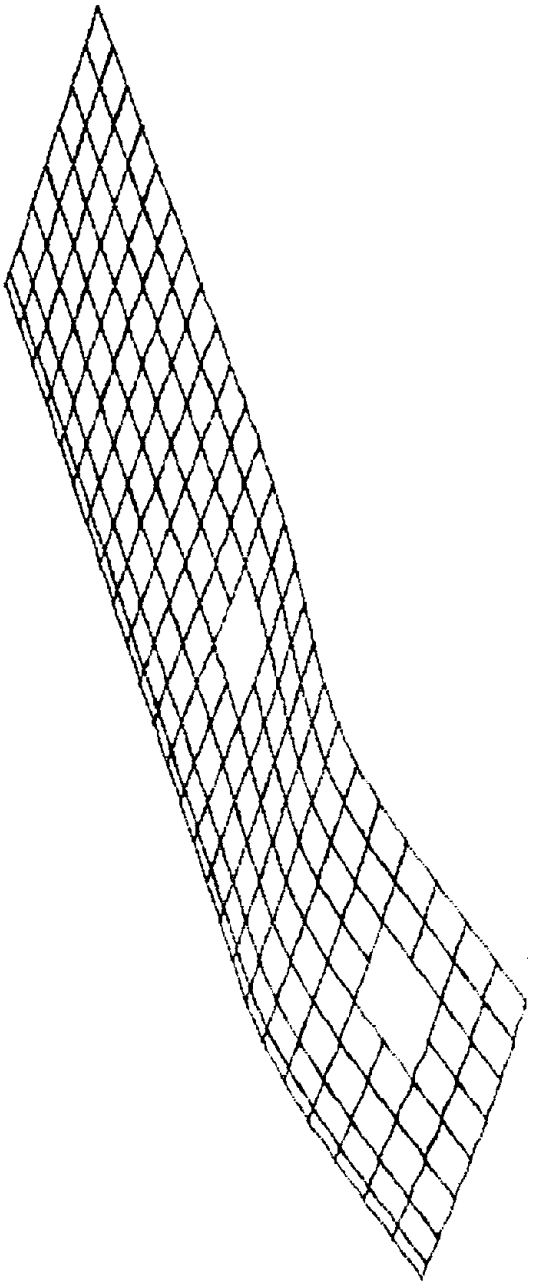

Figure 4.10 Deformed Mesh for One Quarter of The End Plate

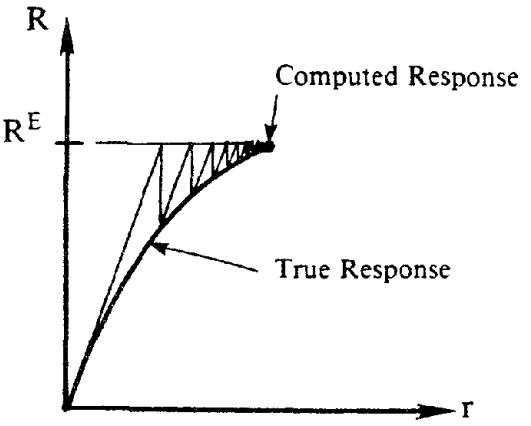

(a) Constant Stiffness Iteration

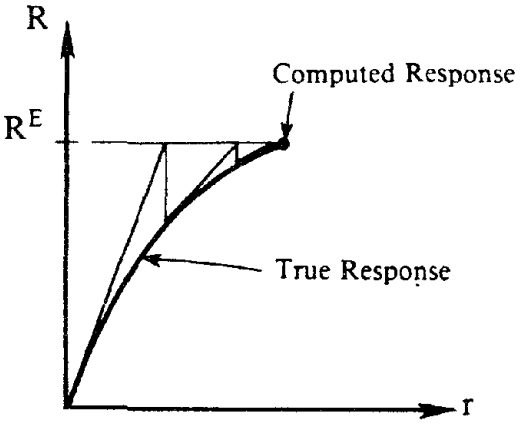

(b) Tangent Stiffness Iteration

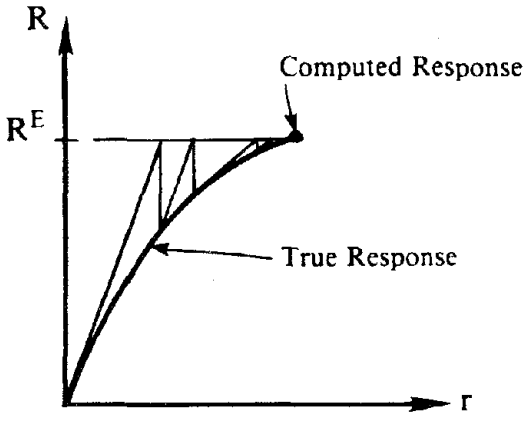

(c) Mixed Scheme

Figure 5.1 Iteration Schemes for Nonlinear Softening System

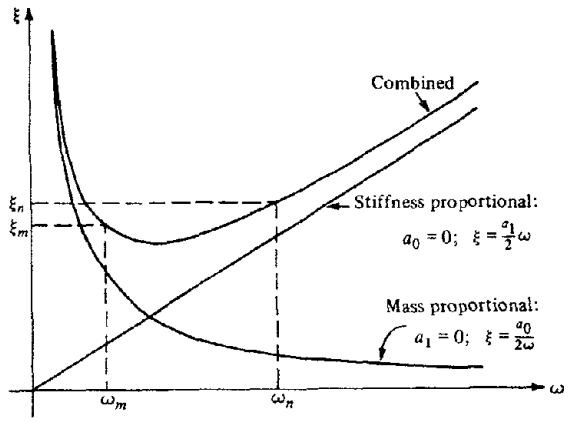

Figure 5.2 Relationship between Damping Ratio and Frequency for Rayleigh Damping [33]

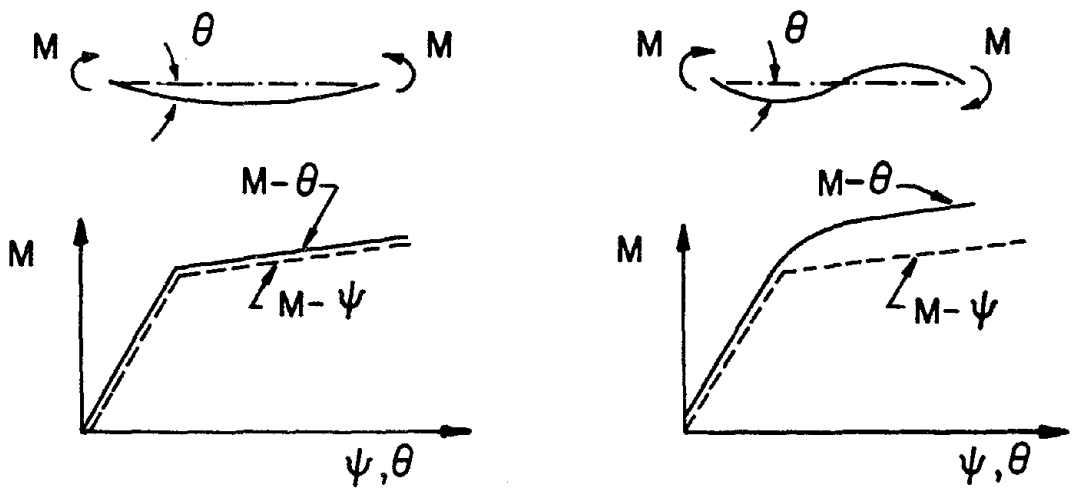

Figure 5.3 Moment-Rotation and Moment-Curvature Relationships

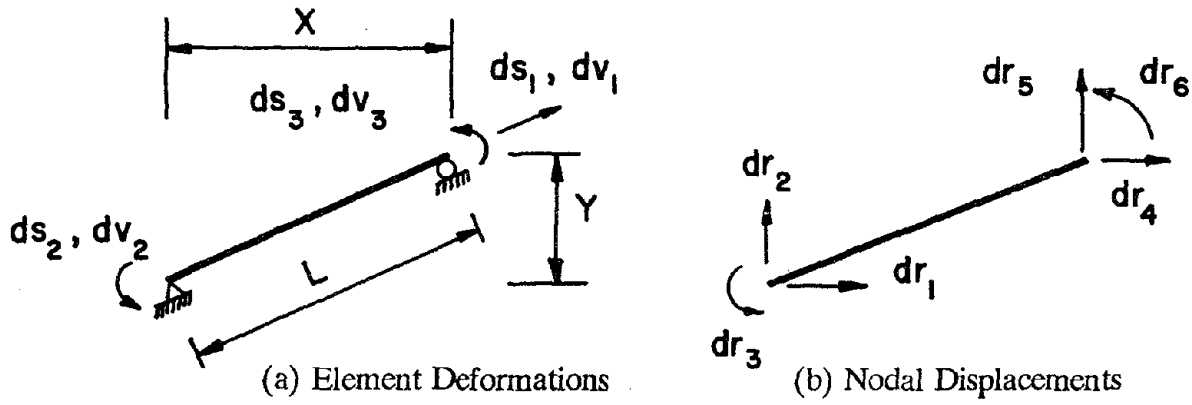

(a) Element Deformations (b) Nodal Displacements

Figure 5.4 Element Deformations and Nodal Displacements

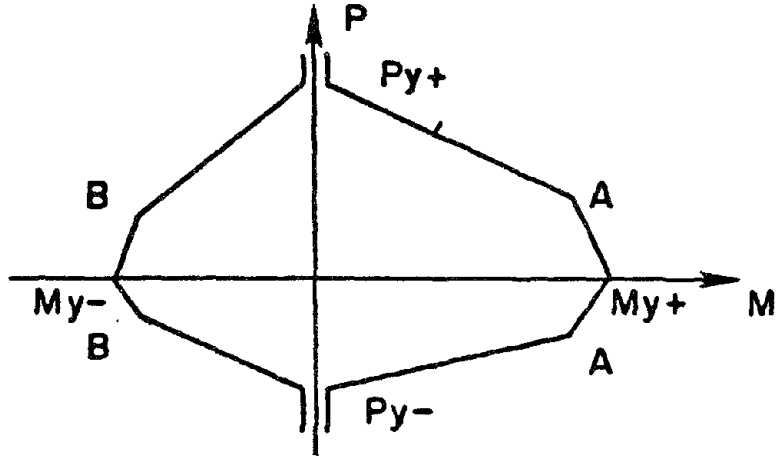

(a) Yield Surface

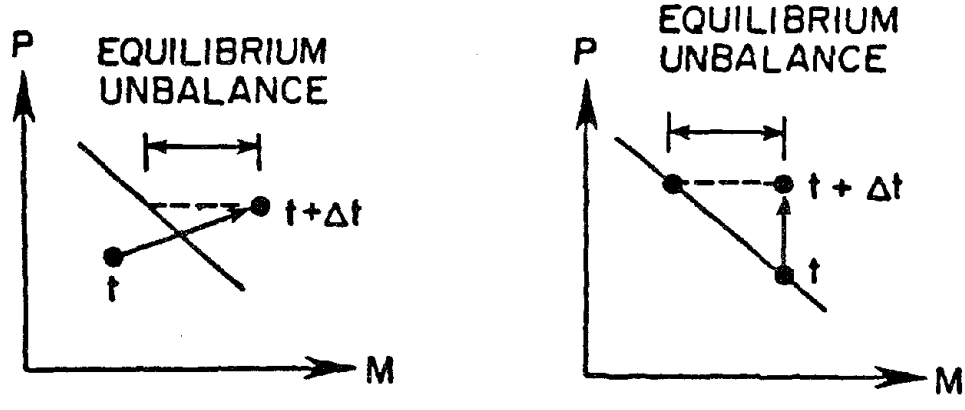

(b) Overshoot Corrections

Figure 5.5 Yield Surface for Beam-Column Element and Overshoot Corrections

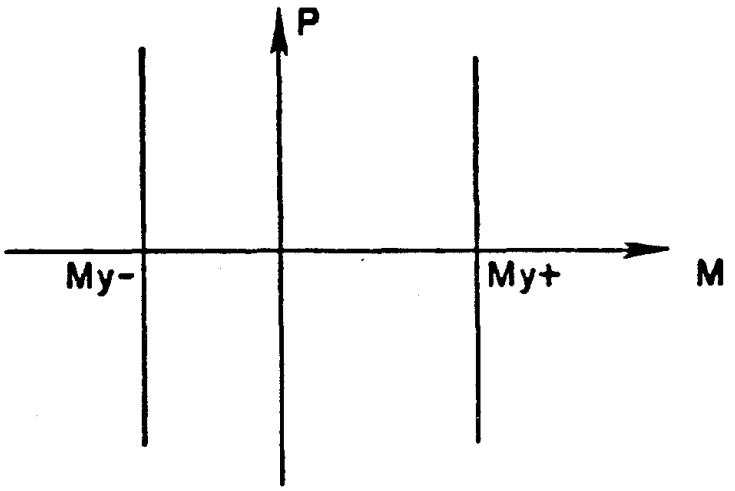

Figure 5.6 Yield Surface for Beam Element

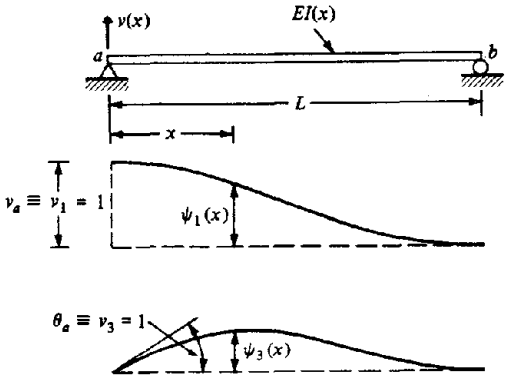

Figure 5.7 Beam Deflections due to Unit Nodal Displacements at Left End[33]

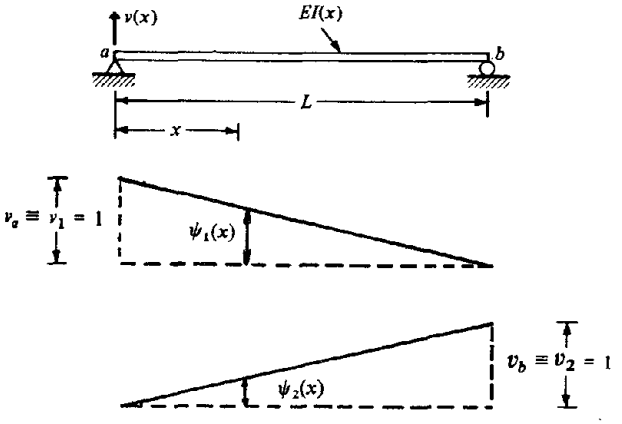

Figure 5.8 Beam Deflections due to Unit Translation at Each End

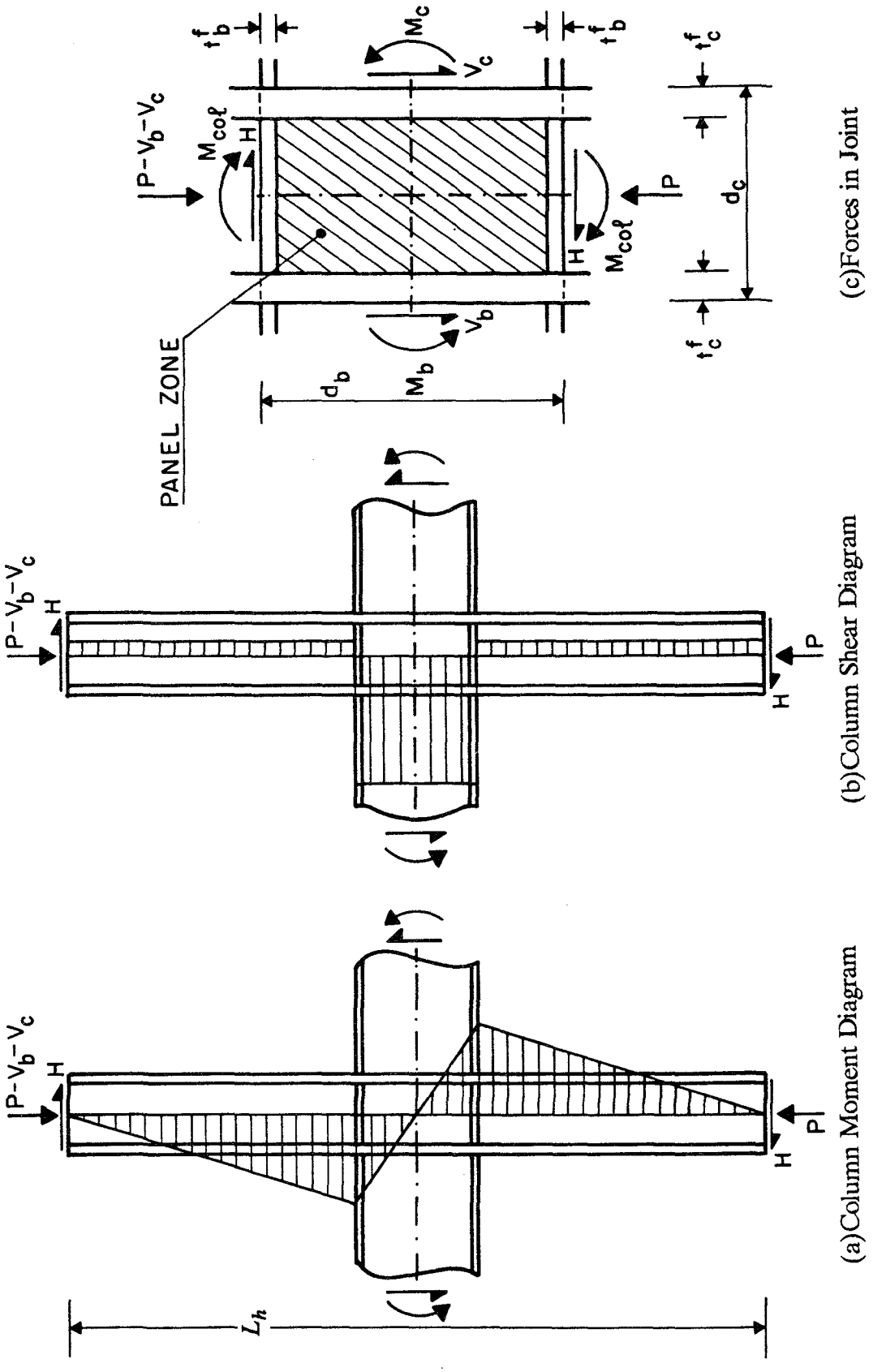

Figure 5.9 Internal Forces in Column and Joint[10]

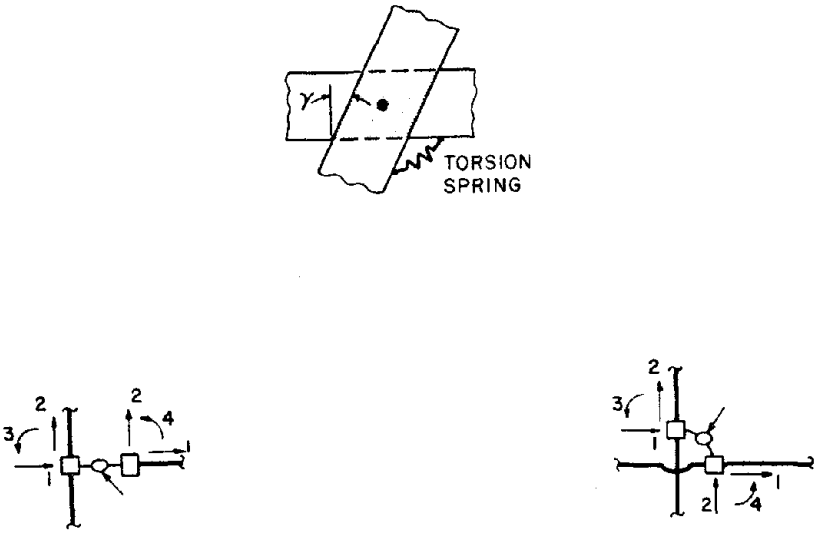

(a) Joint Idealization

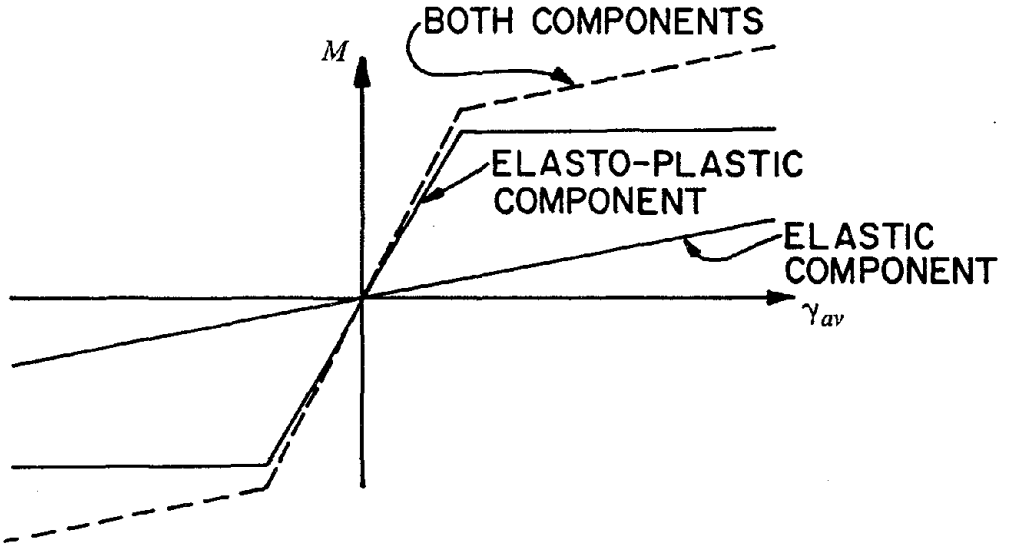

(b) $M - \gamma_{av}$ Relationship

Figure 5.10 Panel Zone Joint Idealization and $M - \gamma_{av}$ Realtionship

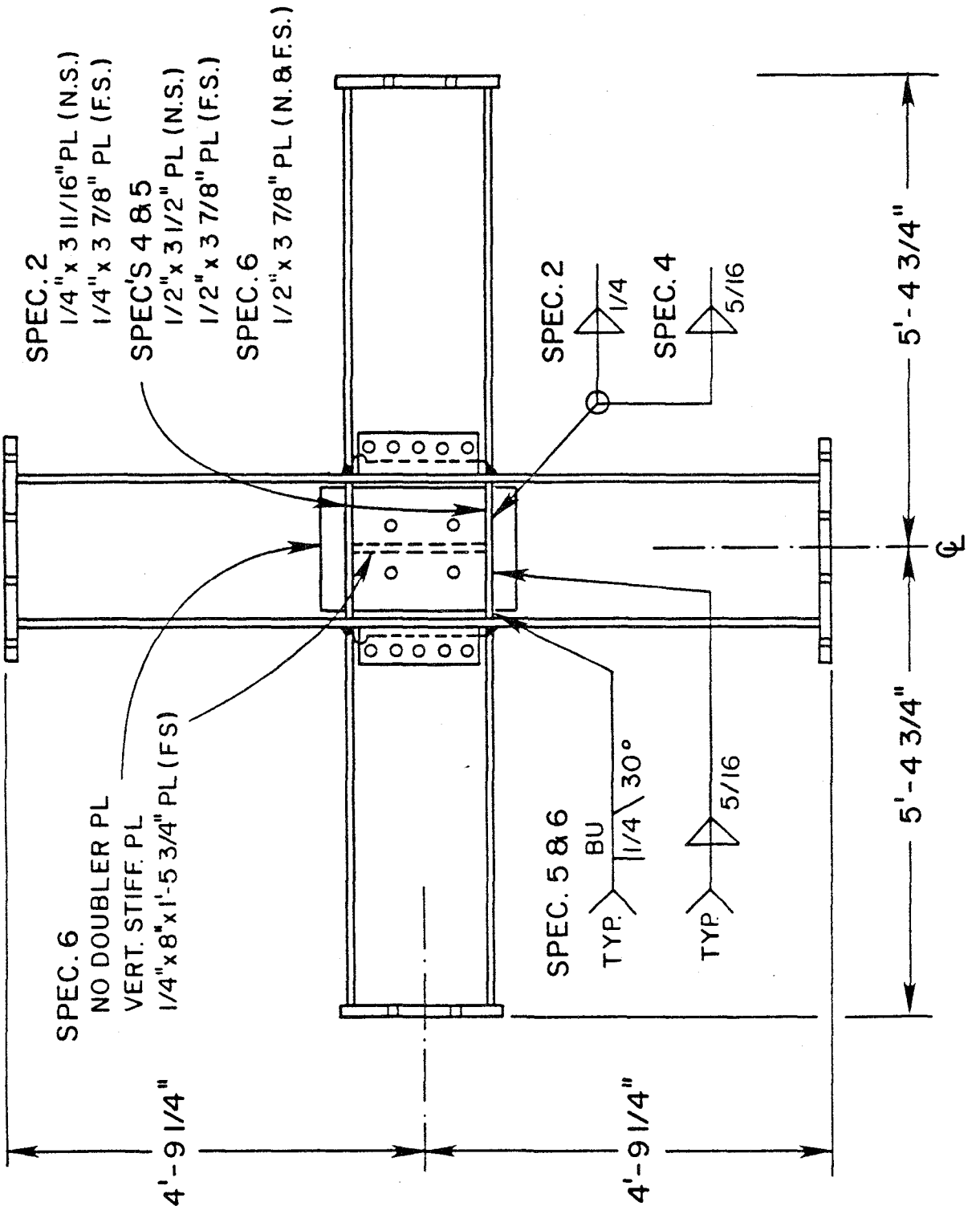

SPEC. 2, EXCEPT AS SHOWN, SAME AS SPEC. 1

Figure 5.11 Details of Beam-Column Subassemblage[51]

Specimen 1

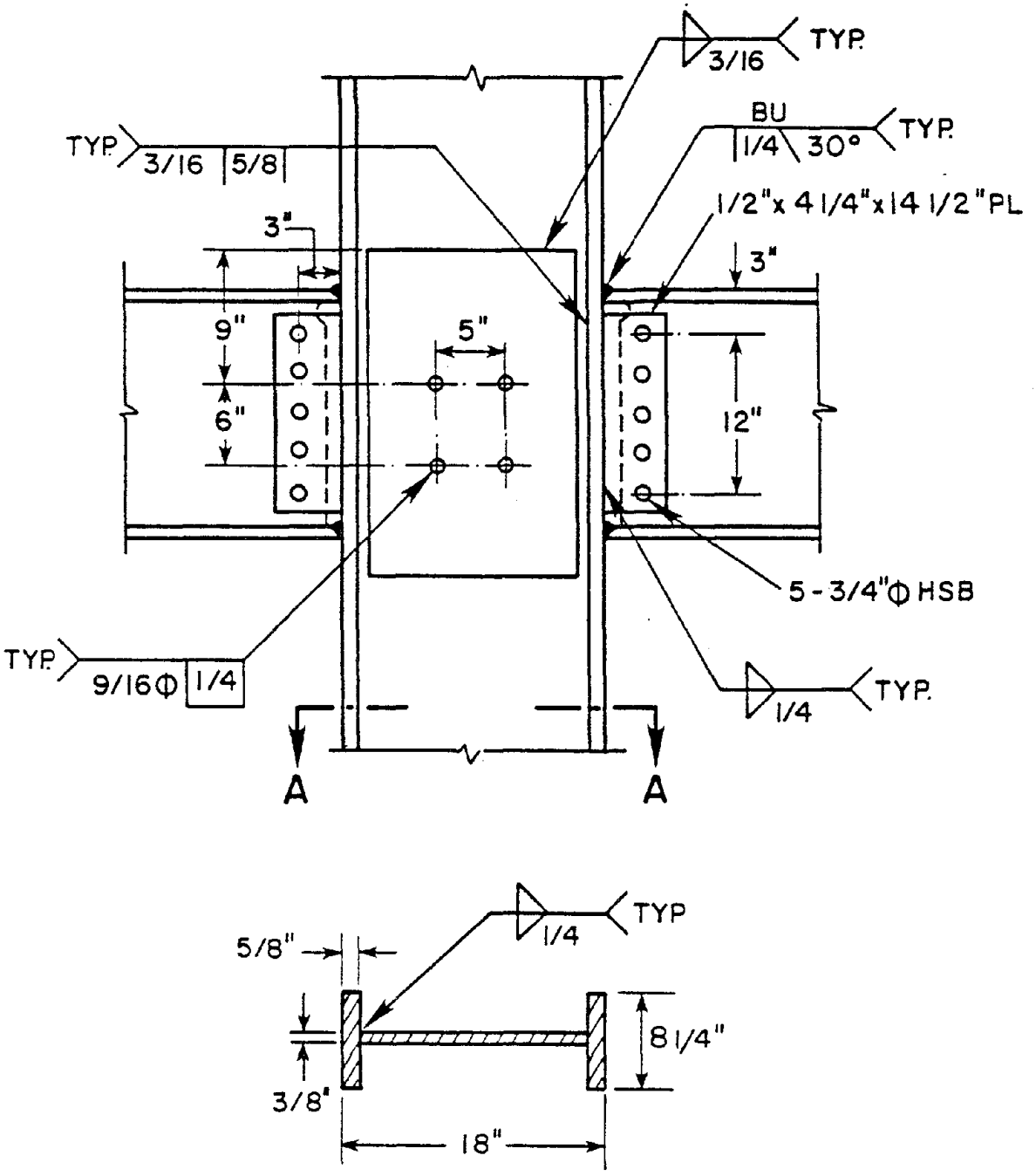

Figure 5.12 Details of Beam-Column Panel Zone Joint (Specimen 1 in Ref. 51)

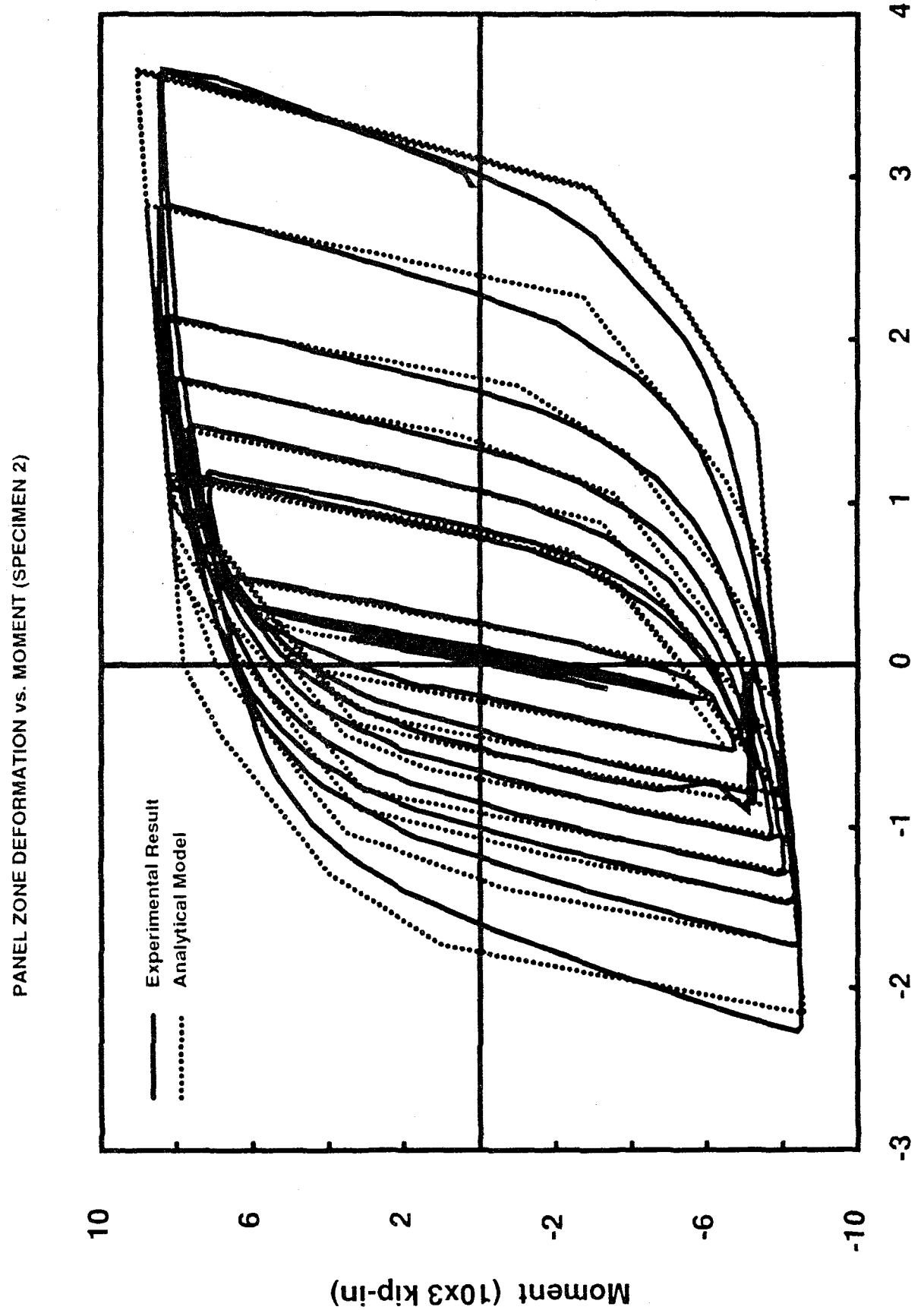

Figure 5.13 Panel Zone Deformation versus Applied Moment (Experimental and Analytical)

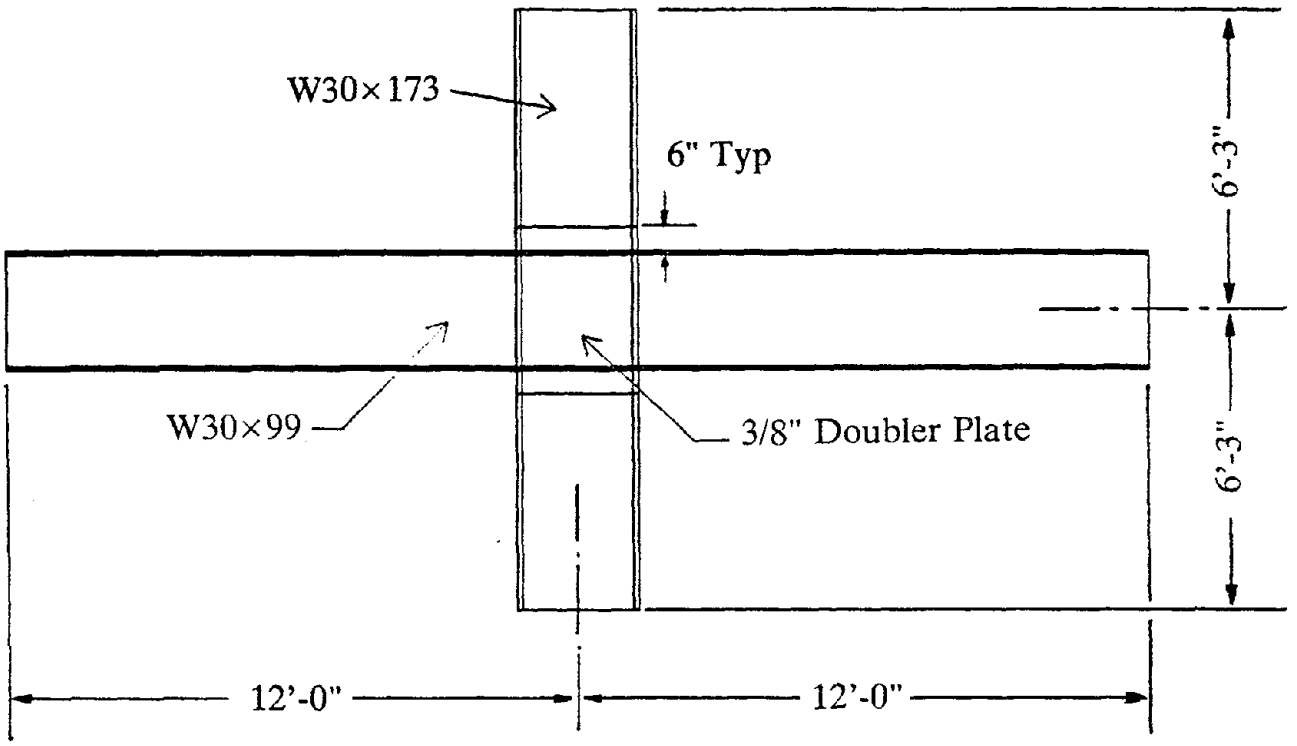

(a) Beam-Column Subassemblage

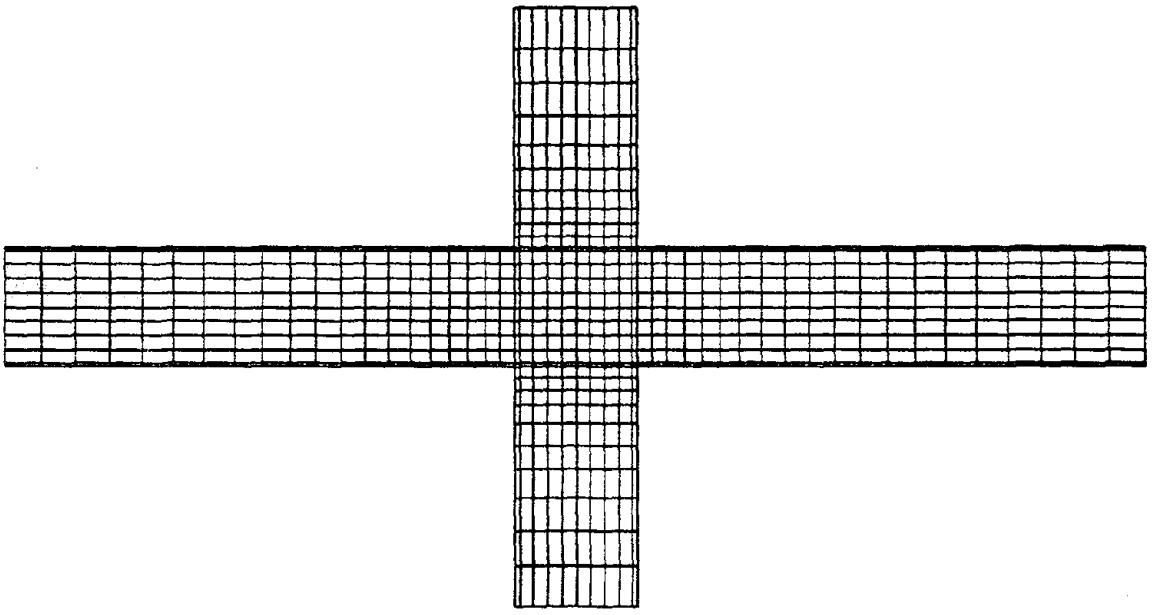

(b) Undormed Mesh

Figure 6.1 Beam-Column Subassemblage and Finite Element Model

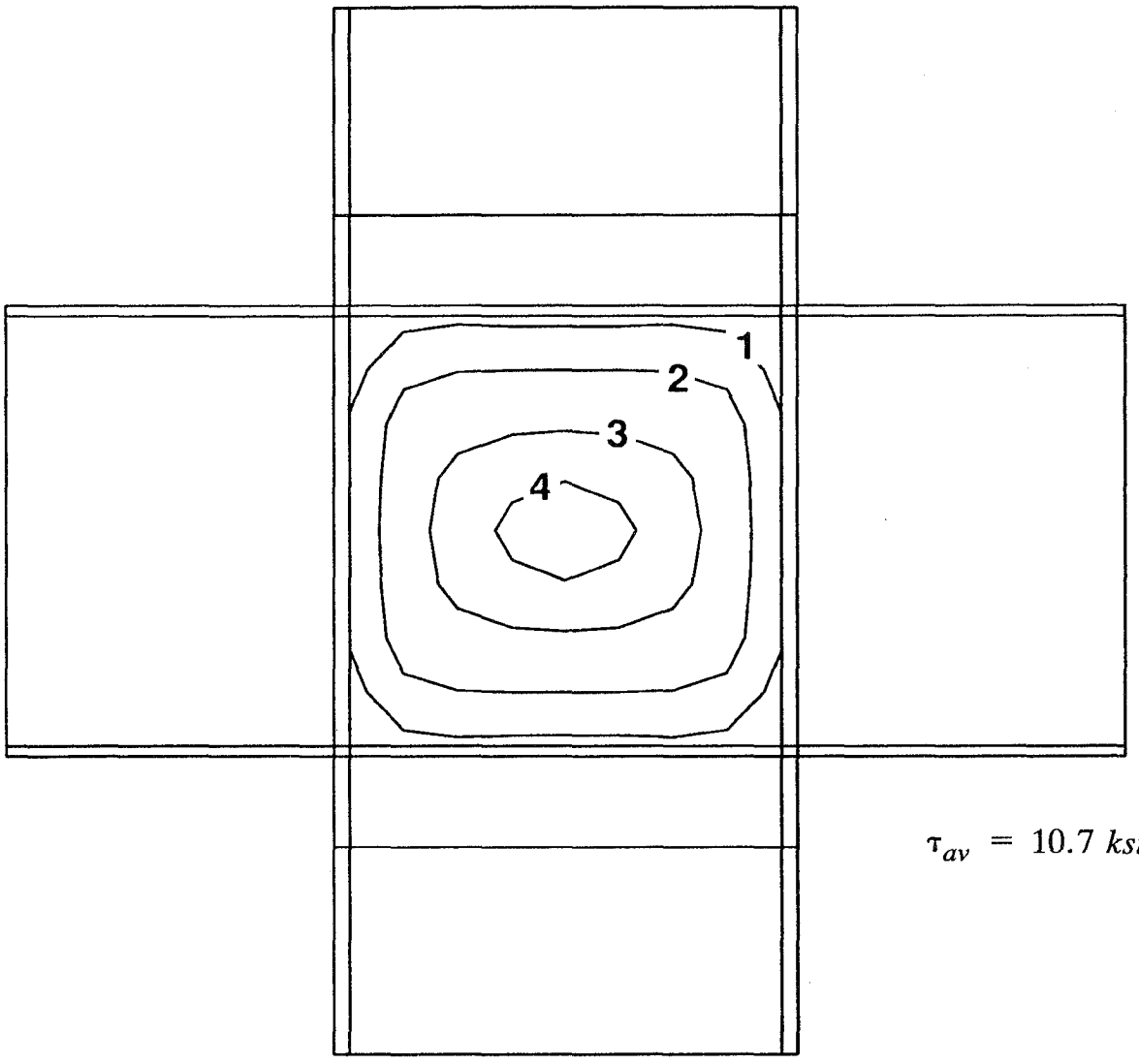

STRESS 2

1 8.000e+00

2 1.000e+01

3 1.200e+01

4 1.300e+01

$\tau_{av} = 10.7\ ksi \quad @\ M_b = 0.66M_y$

Figure 6.2 Joint Shear Stress Contours @ Beam Moments $M_b = 0.66M_y$

FEAP

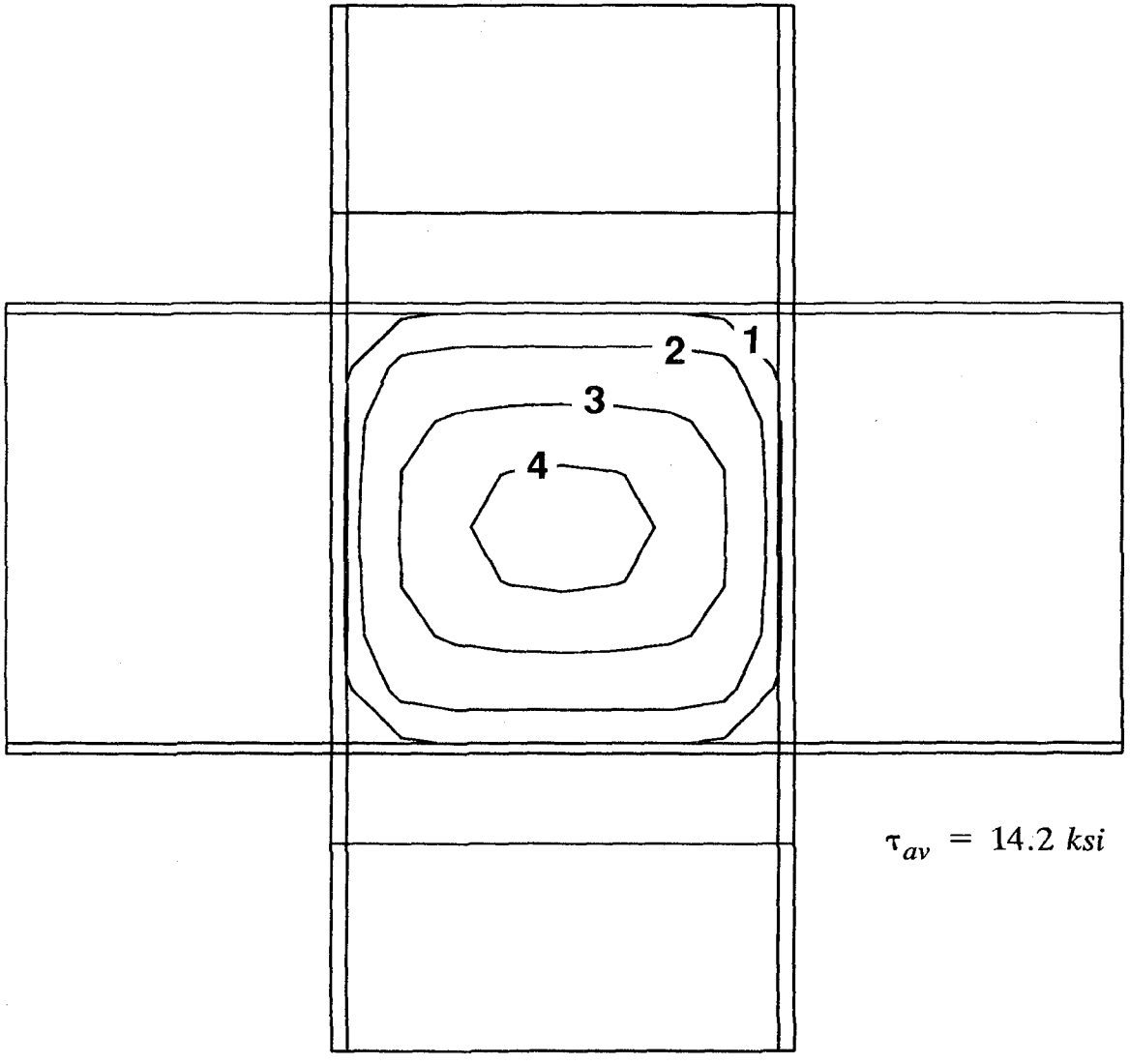

$\tau_{av} = 14.2\ ksi \quad @\ M_b = 1.33 \times 0.66 M_y$

Figure 6.3 Joint Shear Stress Contours @ Beam Moments $M_b = 0.88 M_y$

FEAP

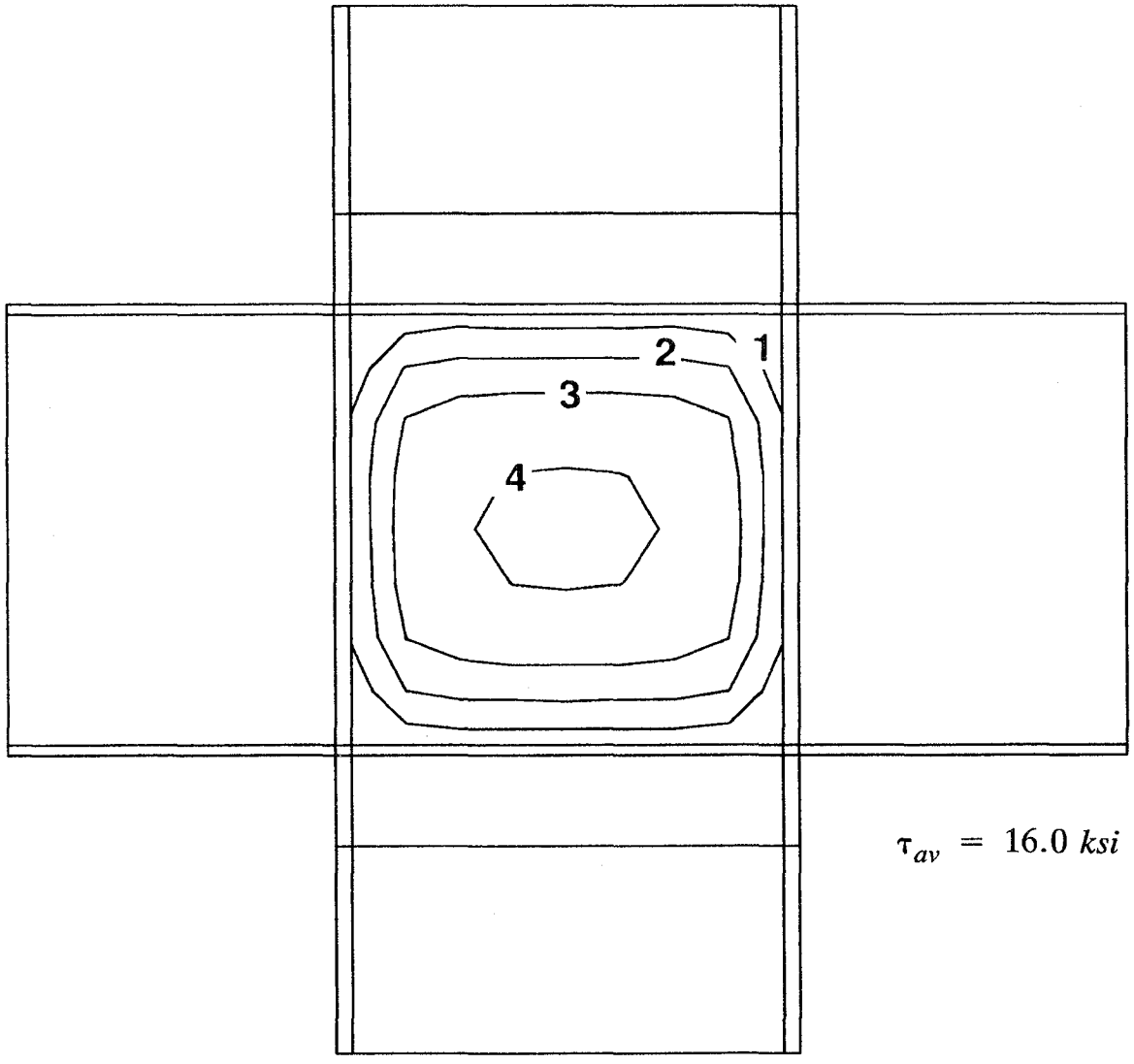

$\tau_{av} = 16.0\ ksi \quad @\ M_b = M_y$

Figure 6.4 Joint Shear Stress Contours @ Beam Moments $M_b = M_y$

FEAP

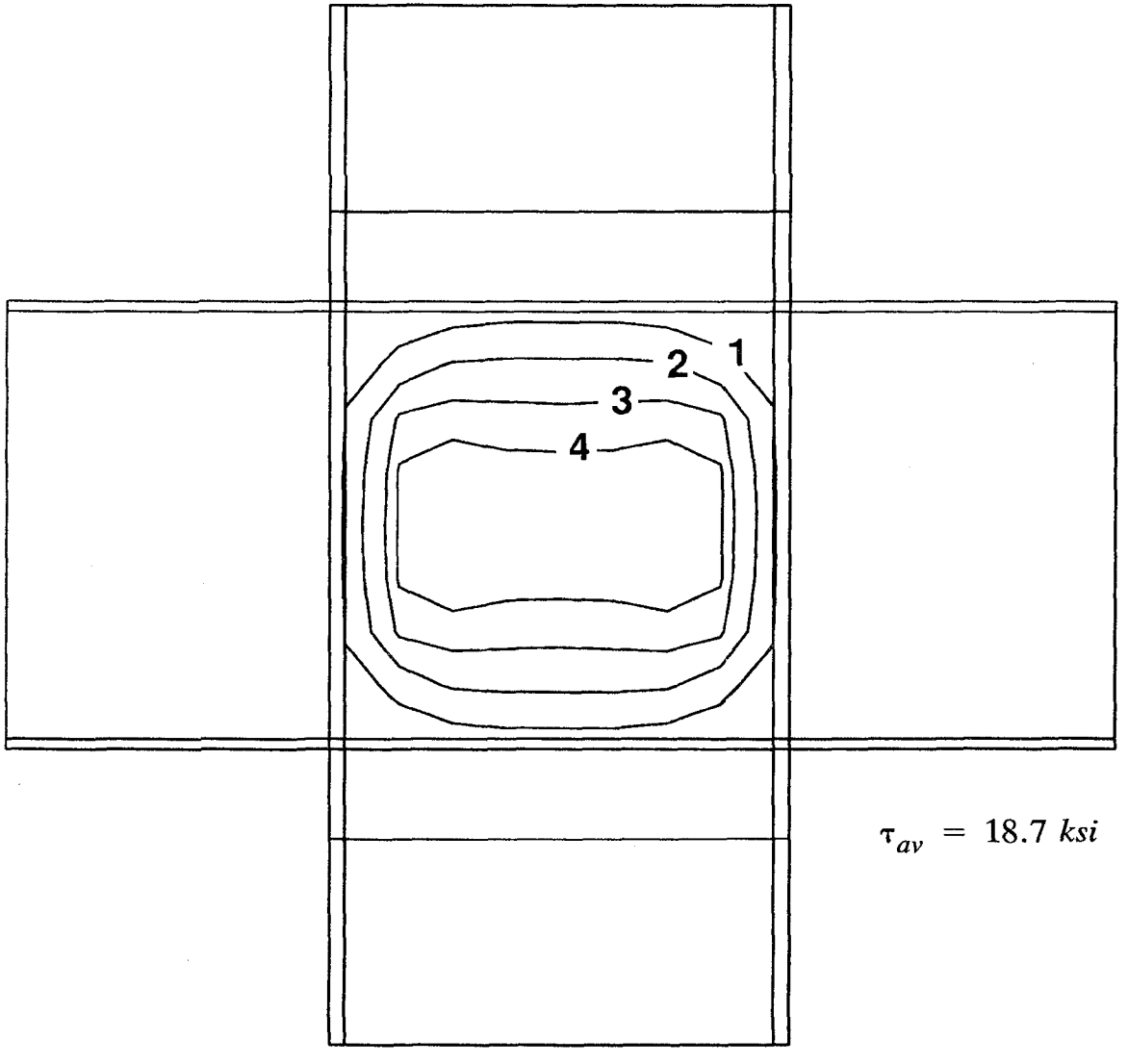

$\tau_{av} = 18.7\ ksi \quad @\ M_b = M_p$

Figure 6.5 Joint Shear Stress Contours @ Beam Moments $M_b = M_p$

FEAP

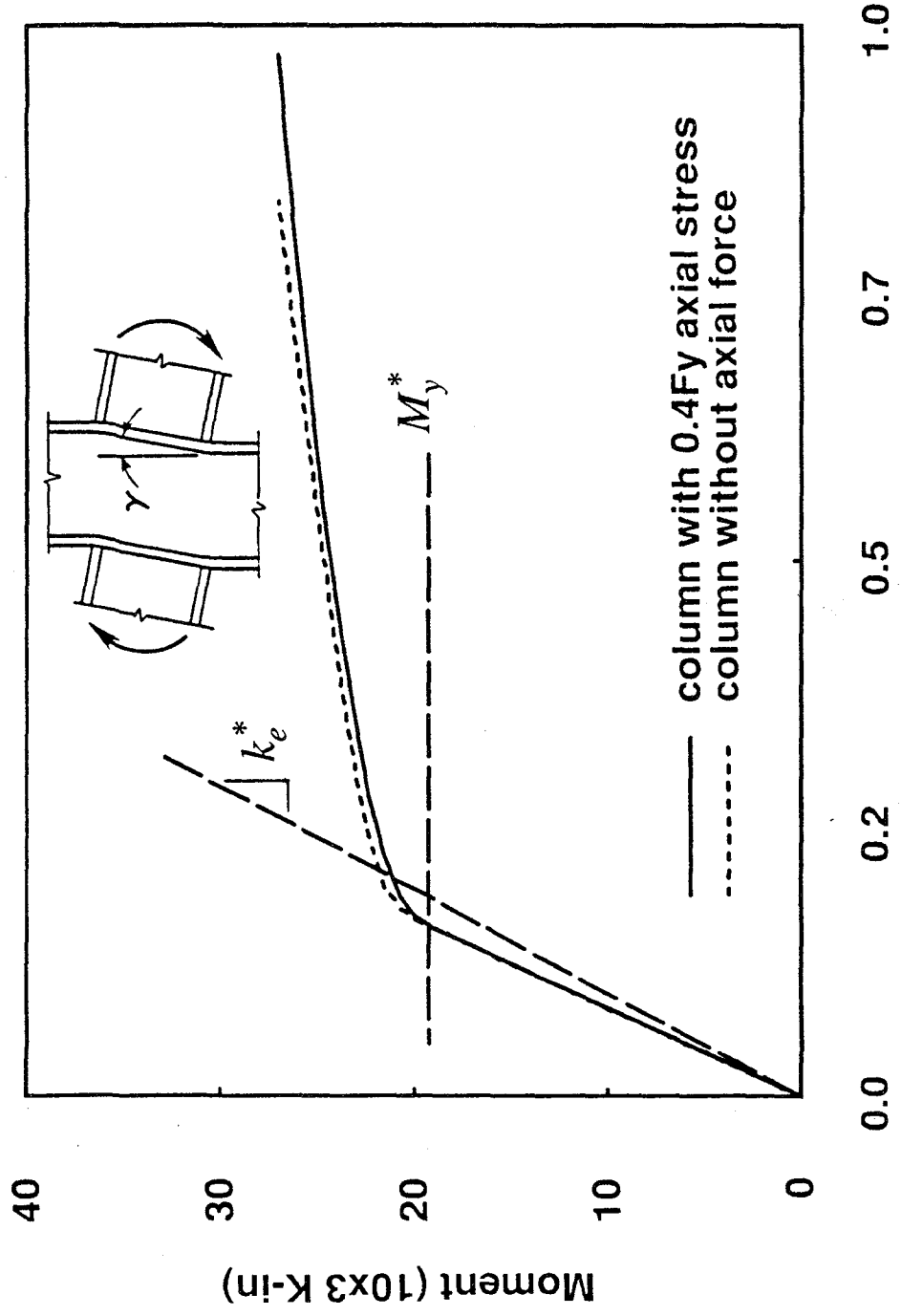

Figure 6.6 Force-Deformation Relationships of Joint under Monotonically Applied Moment

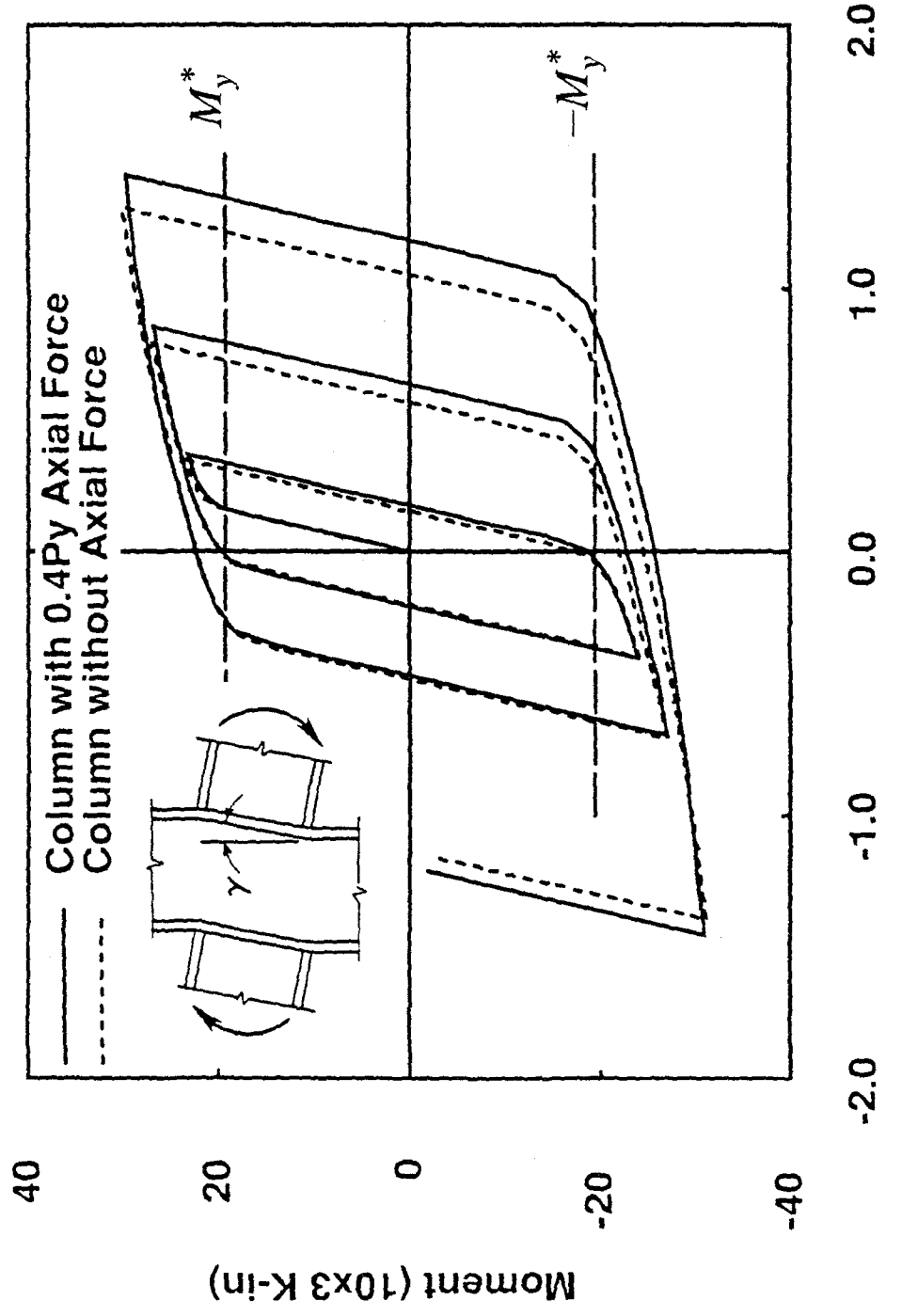

Figure 6.7 Force-Deformation Relationships of Joint under Cyclic Applied Moment

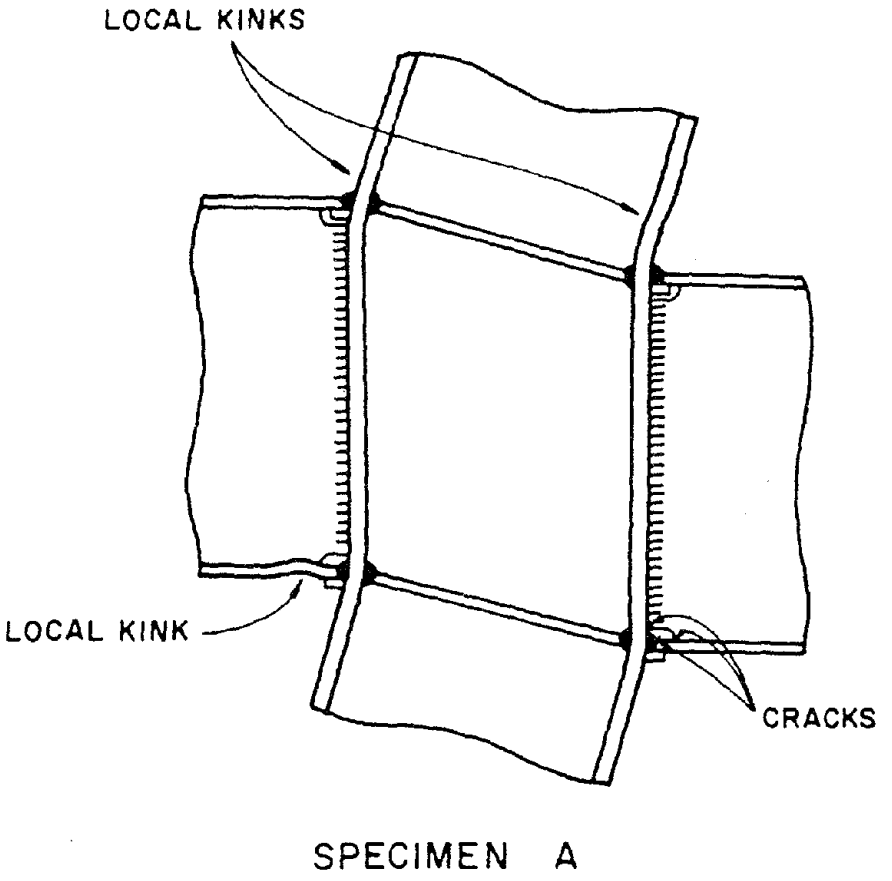

Figure 6.8 Effects of Excessive Panel Zone Deformation[9]

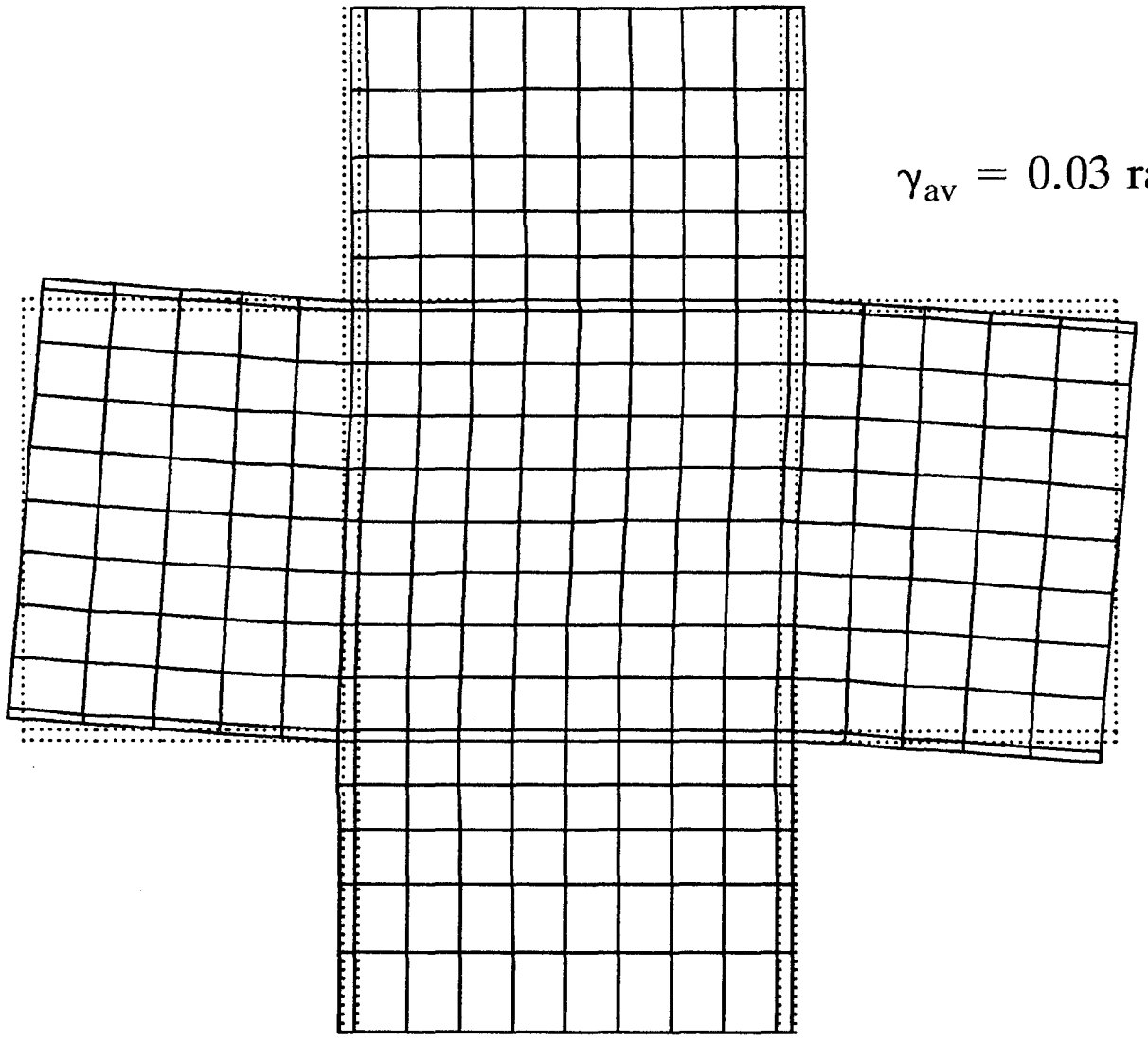

$\gamma_{av} = 0.03$ radians

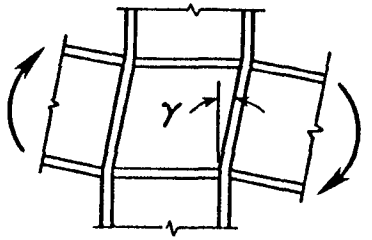

Figure 6.9 Deformed Mesh for Panel Zone Joint(As Computed)

FEAP

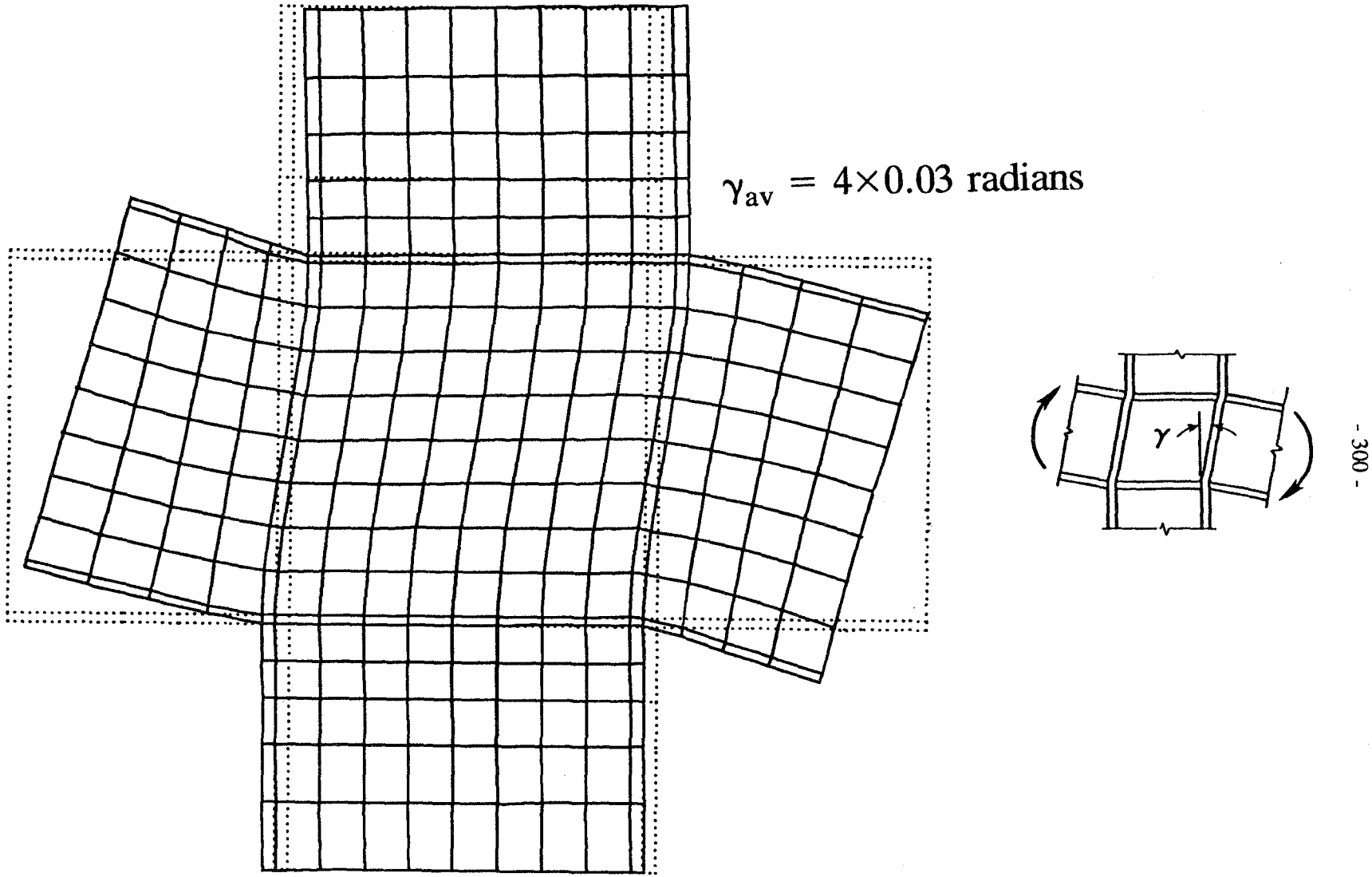

Figure 6.10 Amplified Deformed Mesh for Panel Zone Joint(4 times Amplified)

FEAP

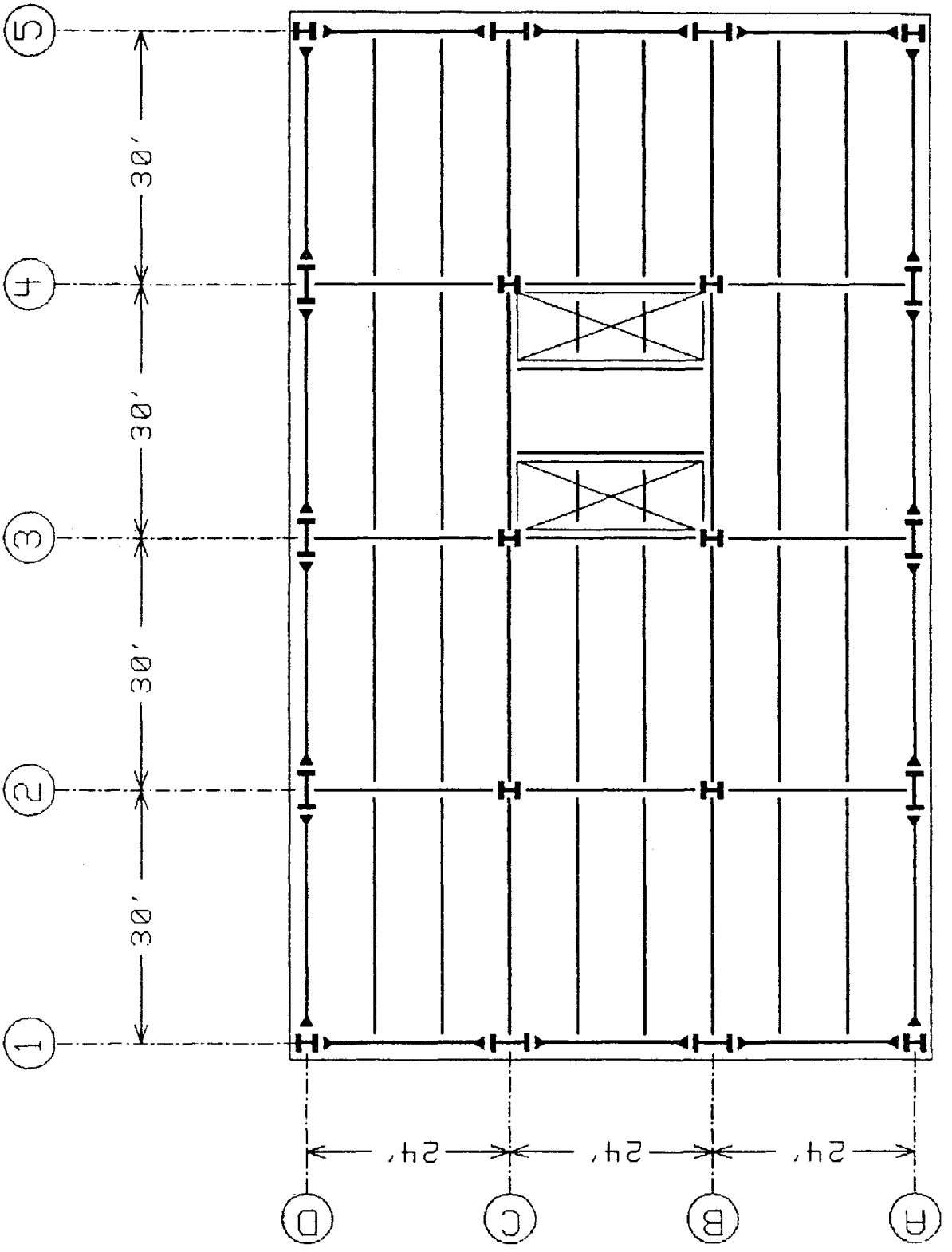

Figure 7.1 Typical Floor Framing Plan for A Six-Story Office Building

3 Bay, 6 Story

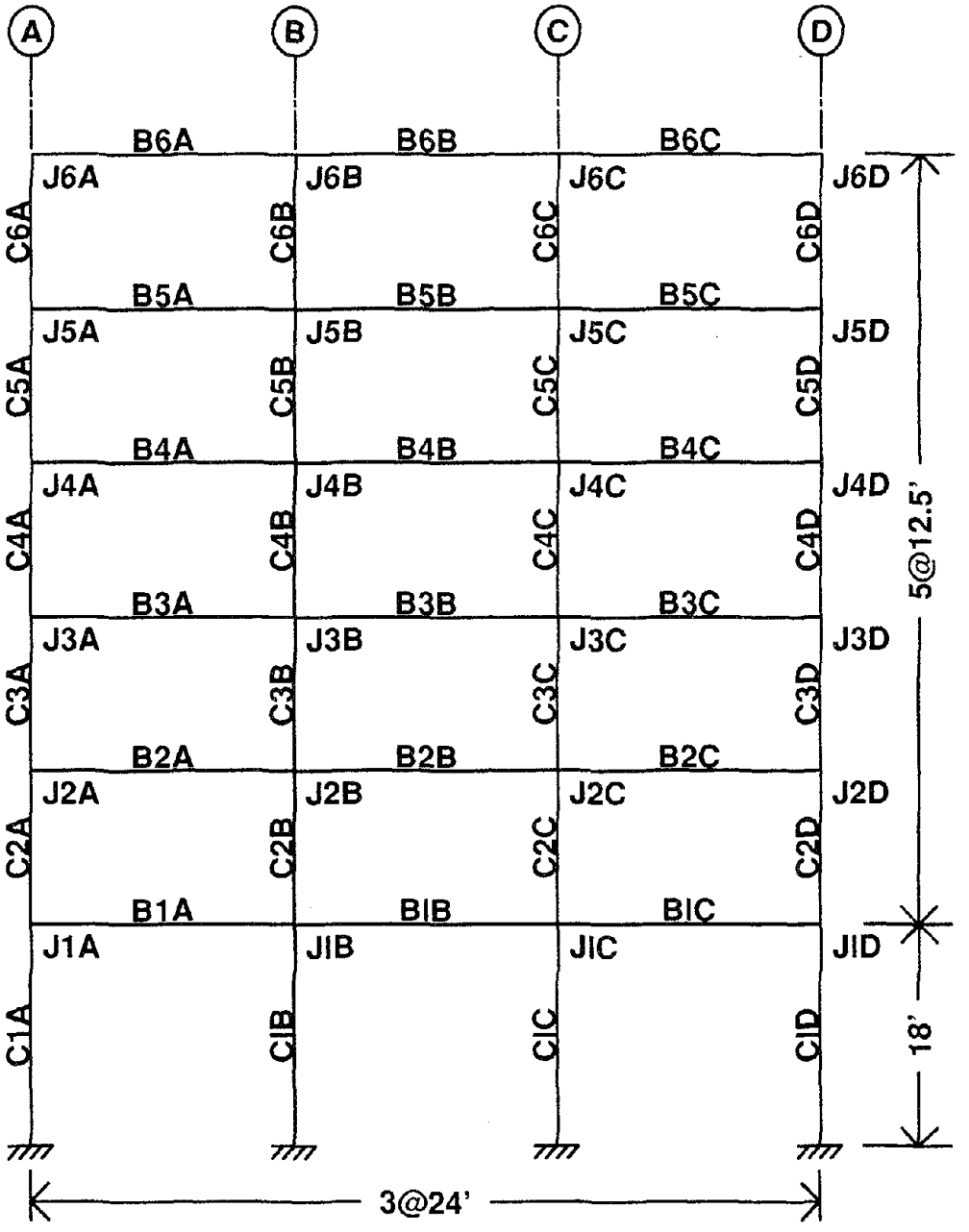

Figure 7.2 Transverse MRF Elevation and Element Designations

Design 1

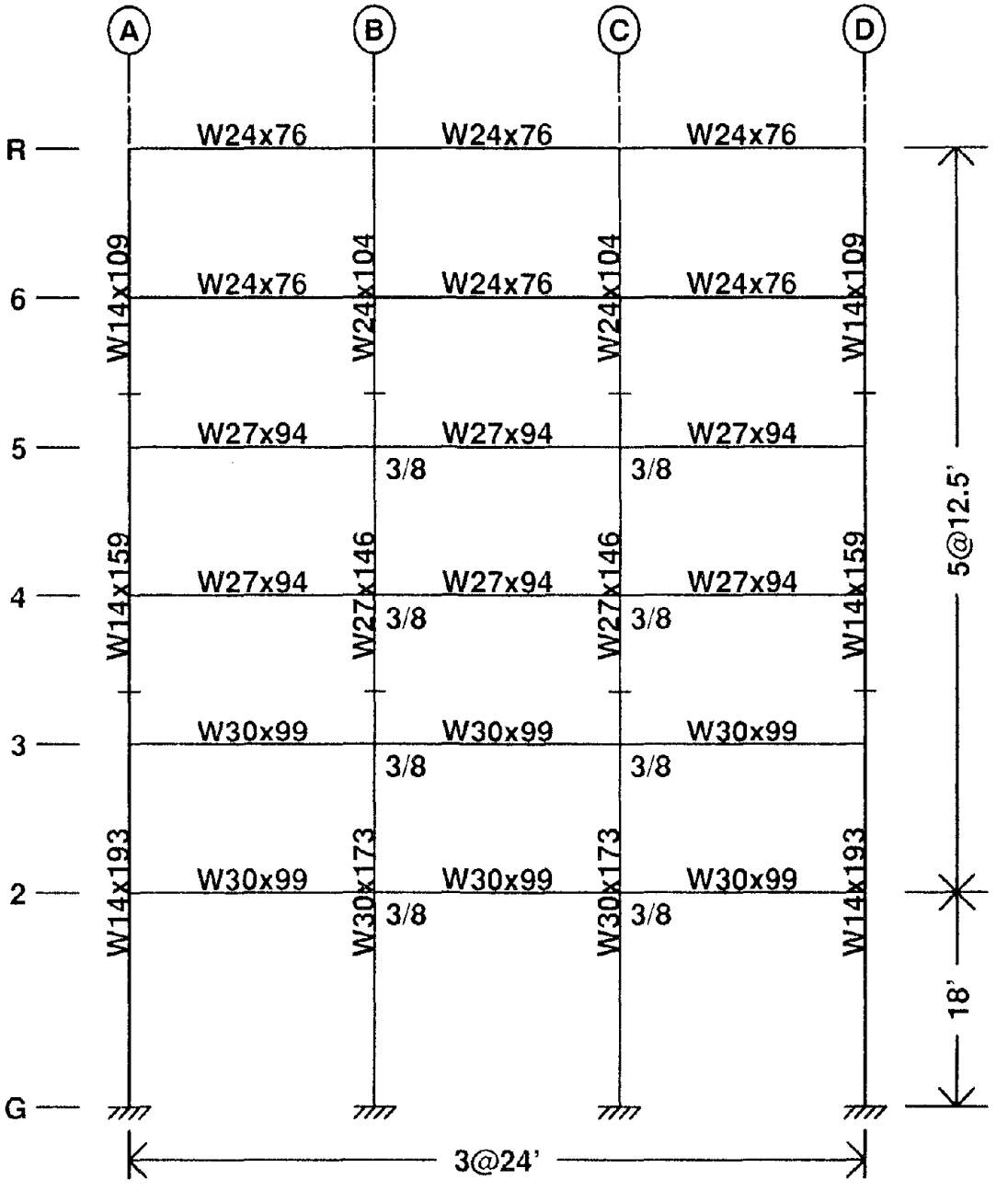

Figure 7.3 Member Sizes and Doubler Plate Thicknesses for MRF Design 1

Design 2

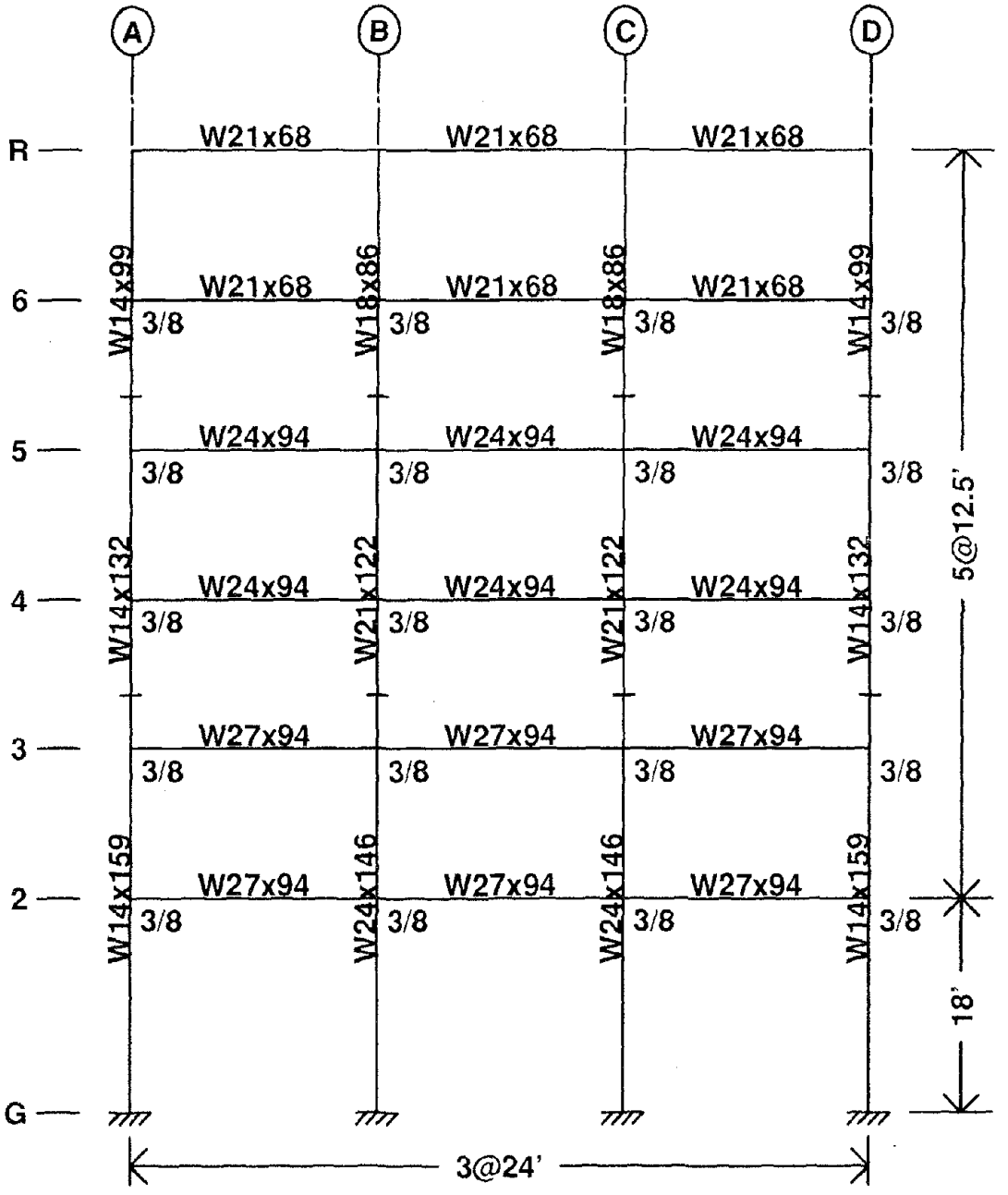

Figure 7.4 Member Sizes and Doubler Plate Thicknesses for MRF Design 2

Design 3

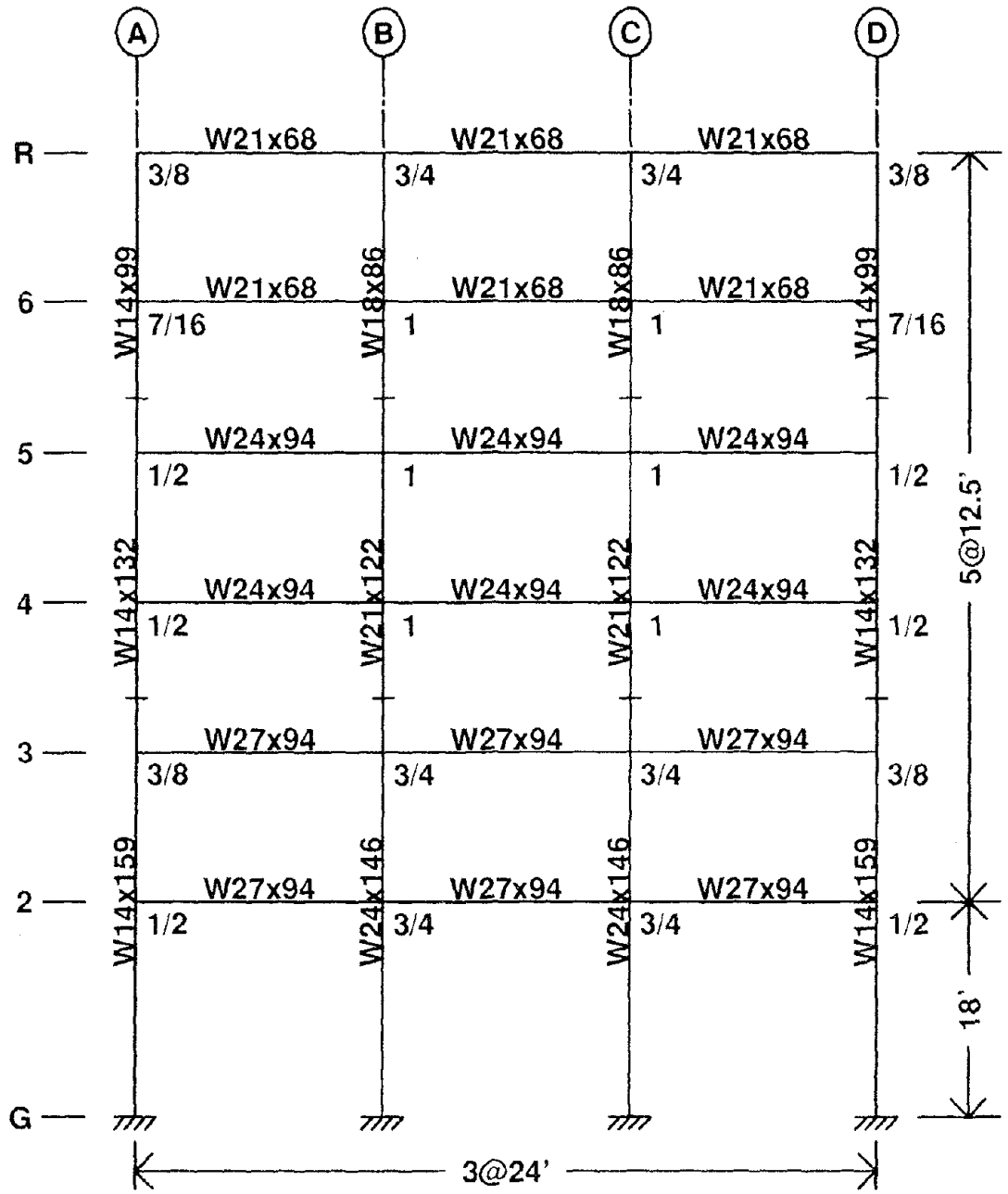

Figure 7.5 Member Sizes and Doubler Plate Thicknesses for MRF Design 3

Design 4

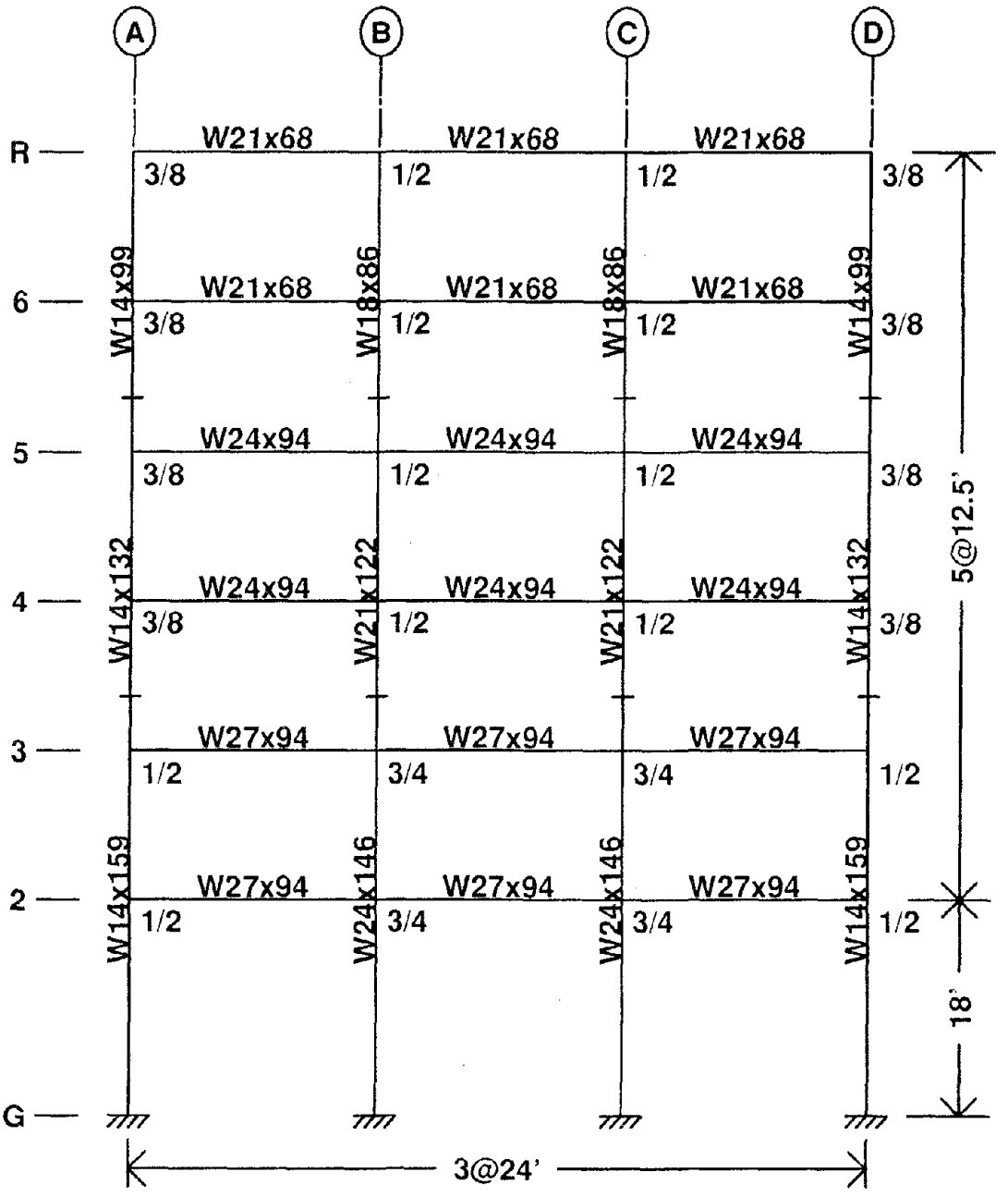

Figure 7.6 Member Sizes and Doubler Plate Thicknesses for MRF Design 4

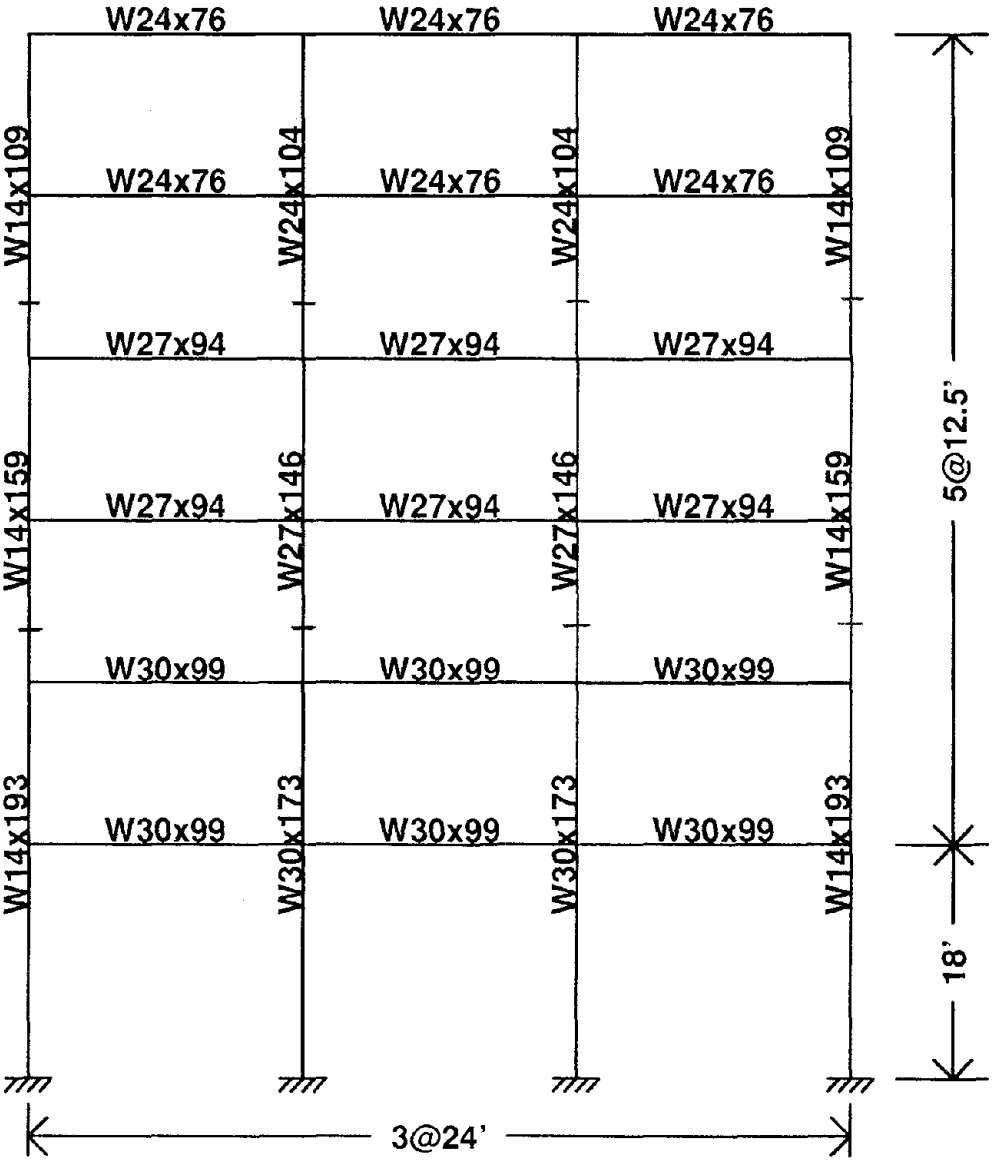

Figure 7.7 Beam and Column Sizes for MRF Design 1

Design 1

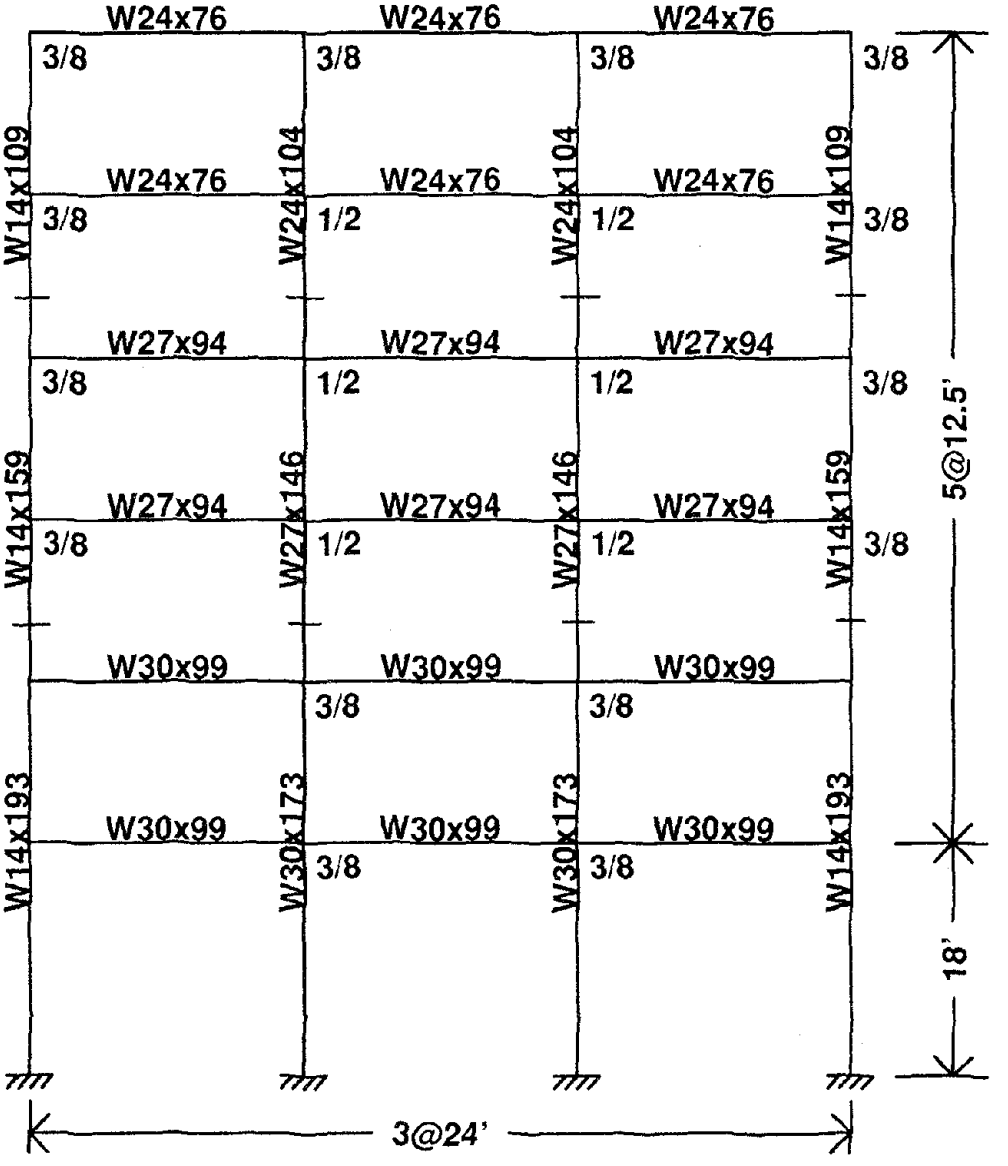

Figure 7.8 Member Sizes for MRF Design 1 with Doubler Plate Thicknesses for 0.8Mp

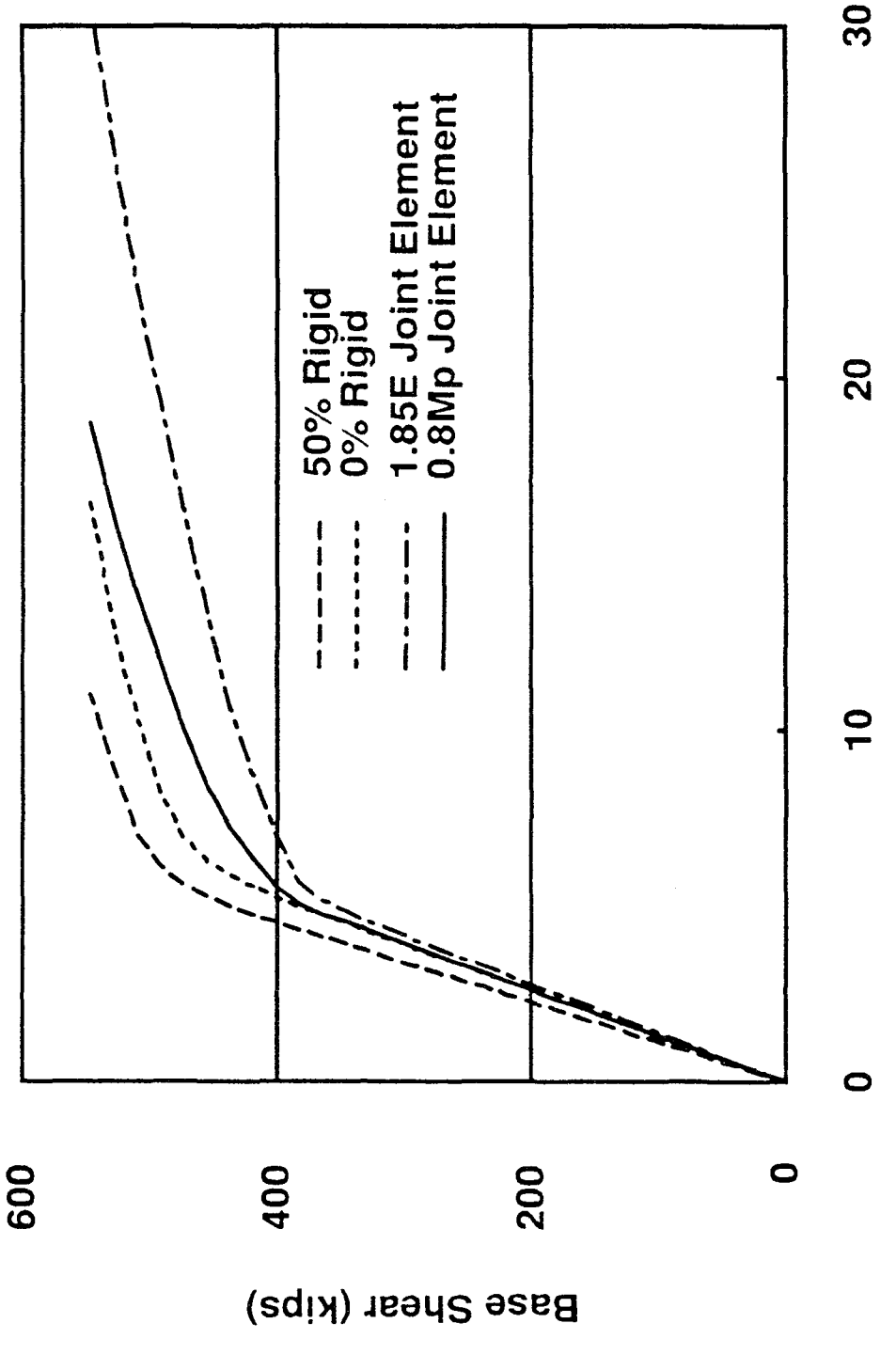

Figure 7.9 Base Shear versus Roof Displacement Relationships for MRF Design 1 (Triangularly Distributed Shear)

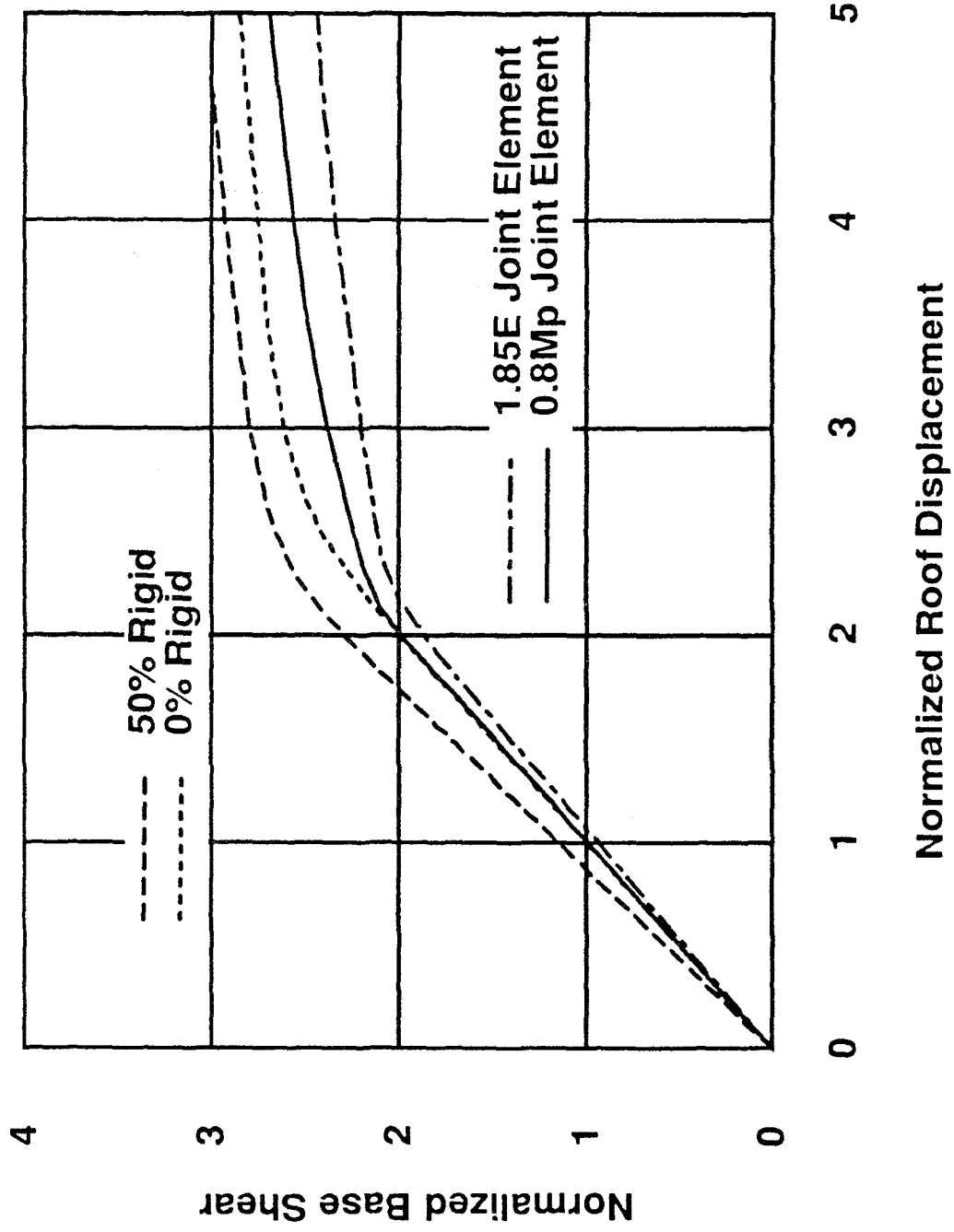

Figure 7.10 Normalized Base Shear versus Roof Displacement Relationships for MRF Design 1 (Triangularly Distributed Shear)

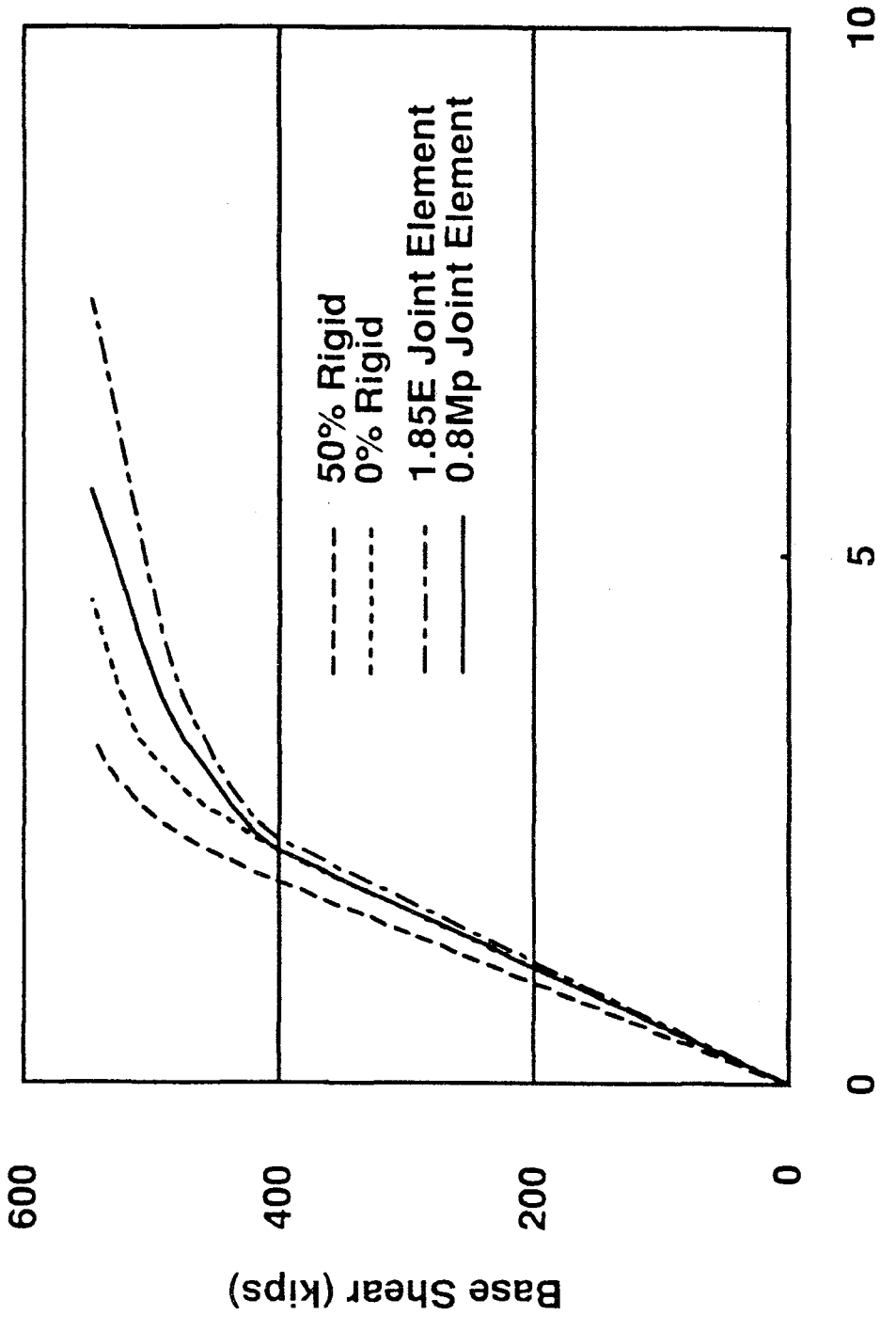

Figure 7.11 Base Shear versus Roof Displacement Relationships for MRF Design 1 (Uniformly Distributed Shear)

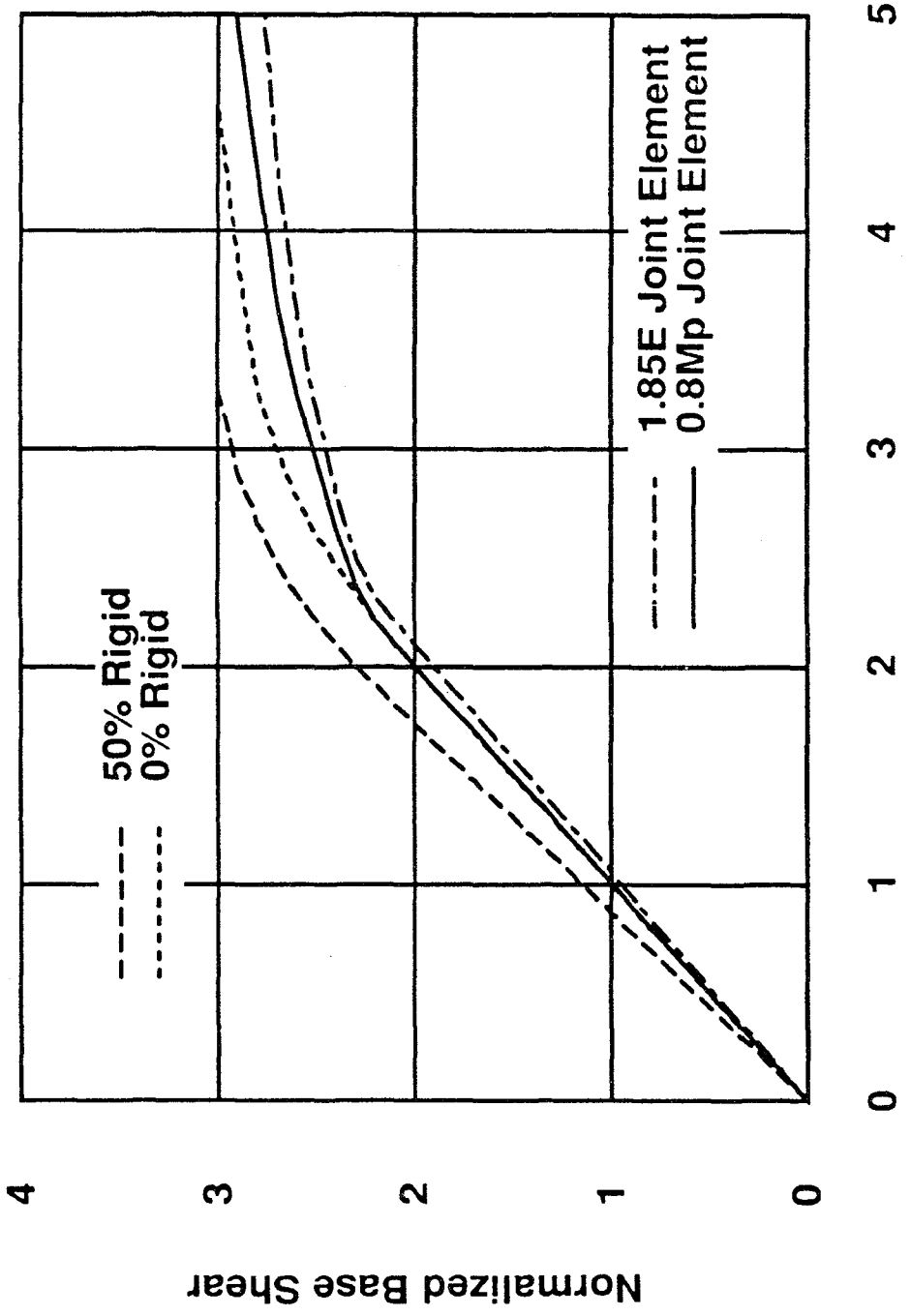

Figure 7.12 Normalized Base Shear versus Roof Displacement Relationships for MRF Design 1 (Uniformly Distributed Shear)

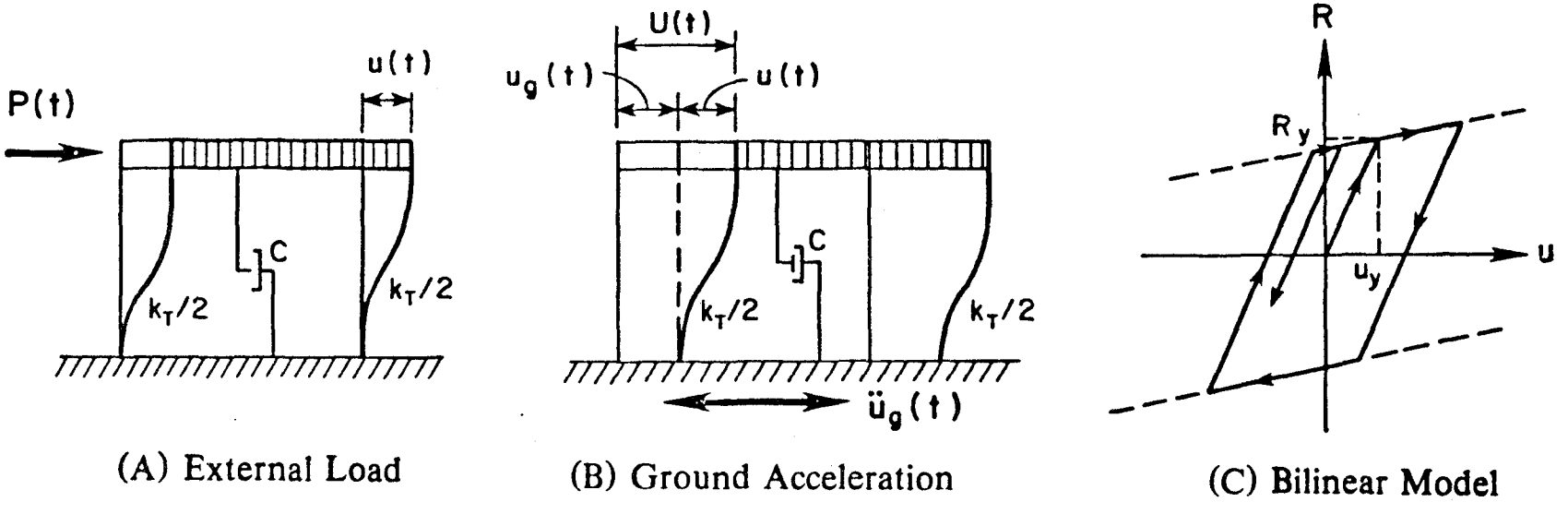

(A) External Load (B) Ground Acceleration (C) Bilinear Model

Figure 7.13 Models of SDOF System and Bilinear Stiffness Model

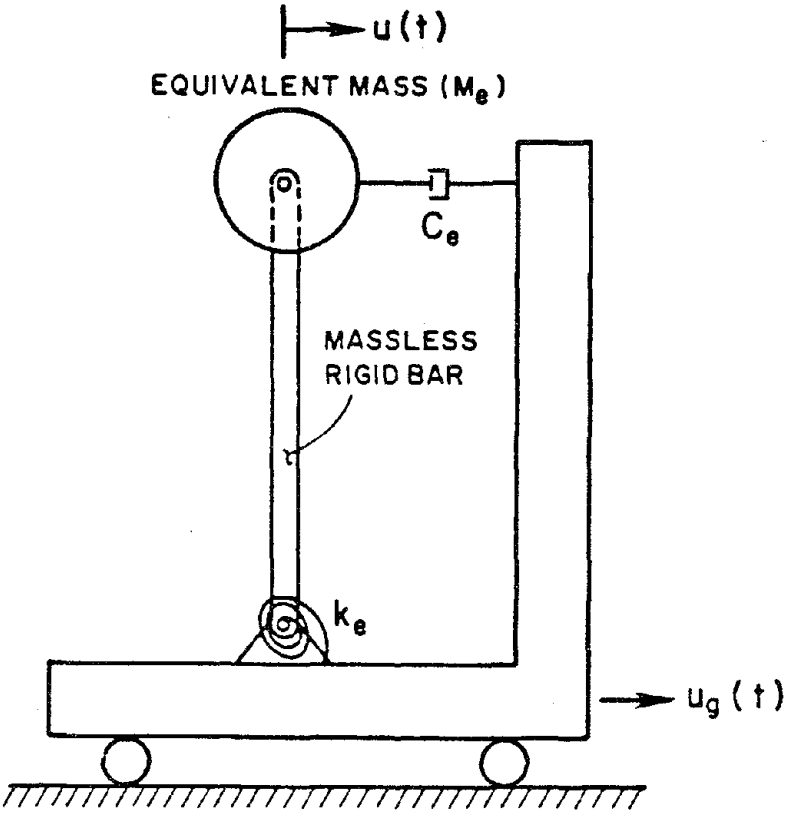

Figure 7.14 Equivalent SDOF System, Q Model [54]

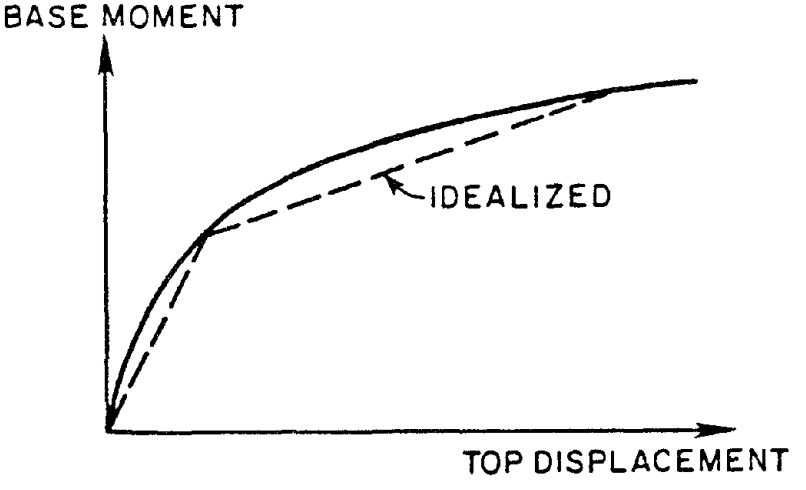

Figure 7.15 Nonlinear Force-Displacement Relationship and Bilinear Idealization

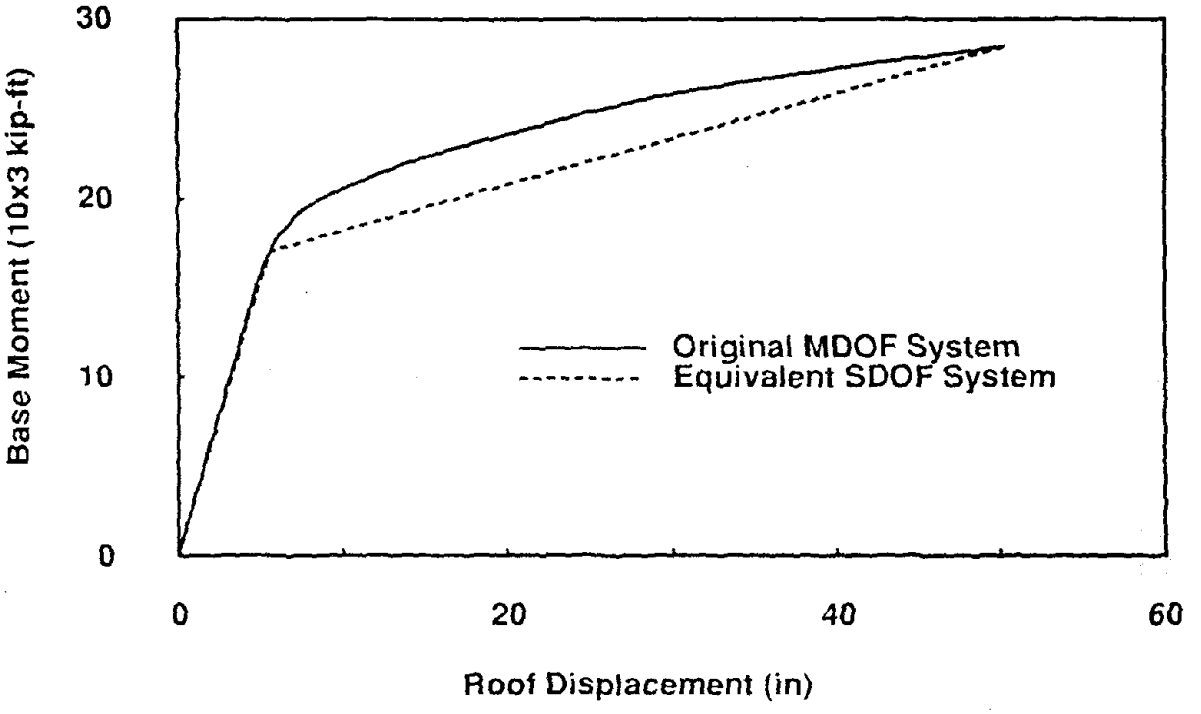

Figure 7.16 Nonlinear Force-Displacement Relationship and Bilinear Idealization (MRF Design 2)

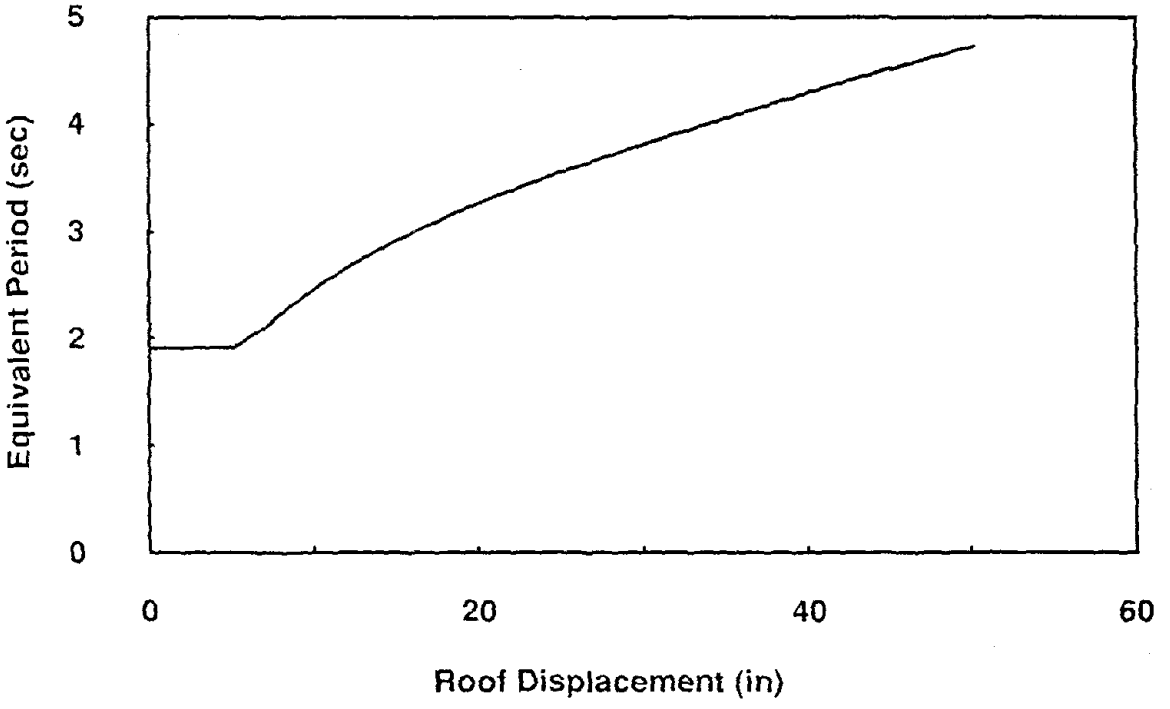

Figure 7.17 Equivalent Period-Roof Displacement Relationship

Equivalent SDOF System for Design 2

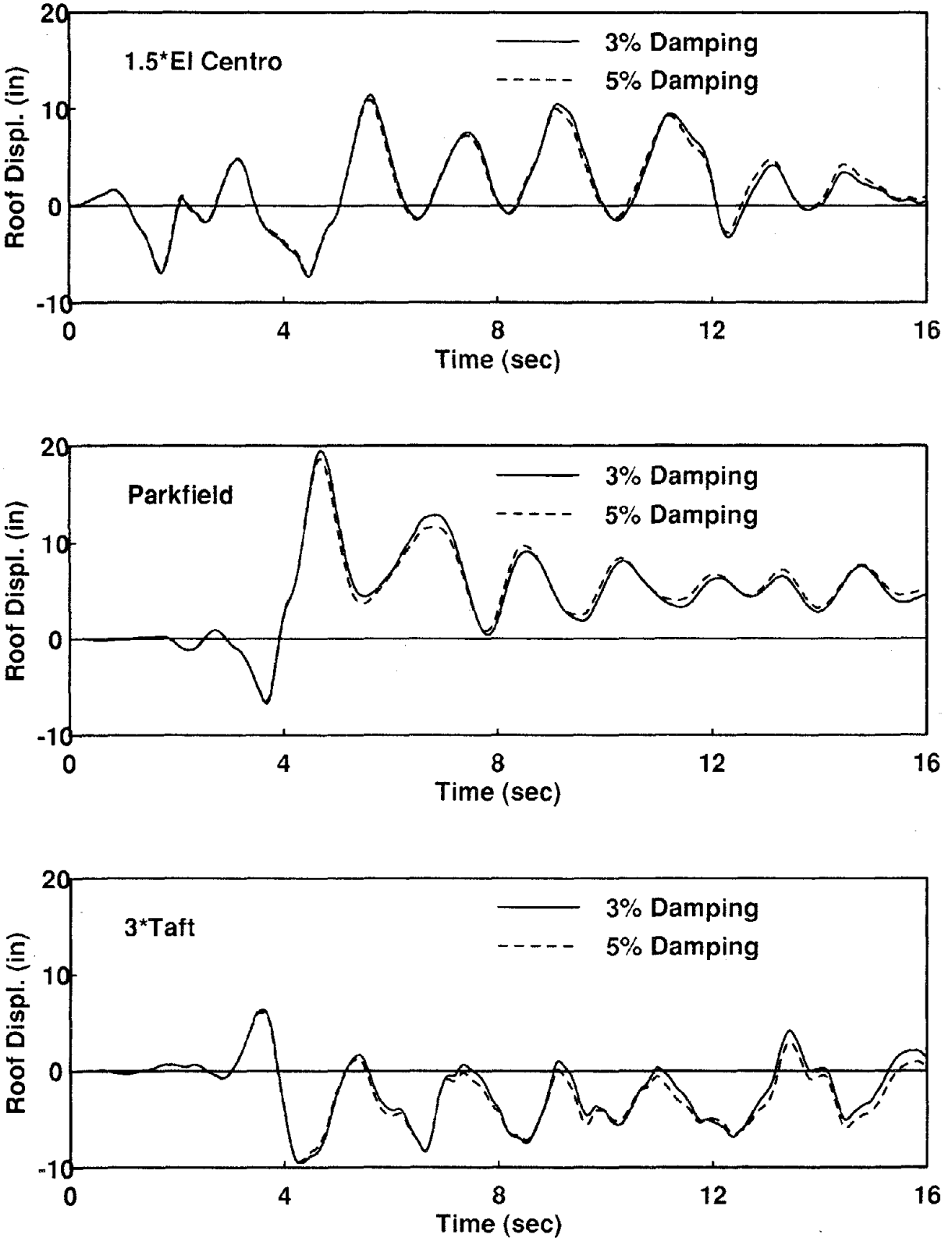

Figure 7.18 Effects of Damping Ratios to Response of Equivalent SDOF System

Equivalent SDOF System for Design 2

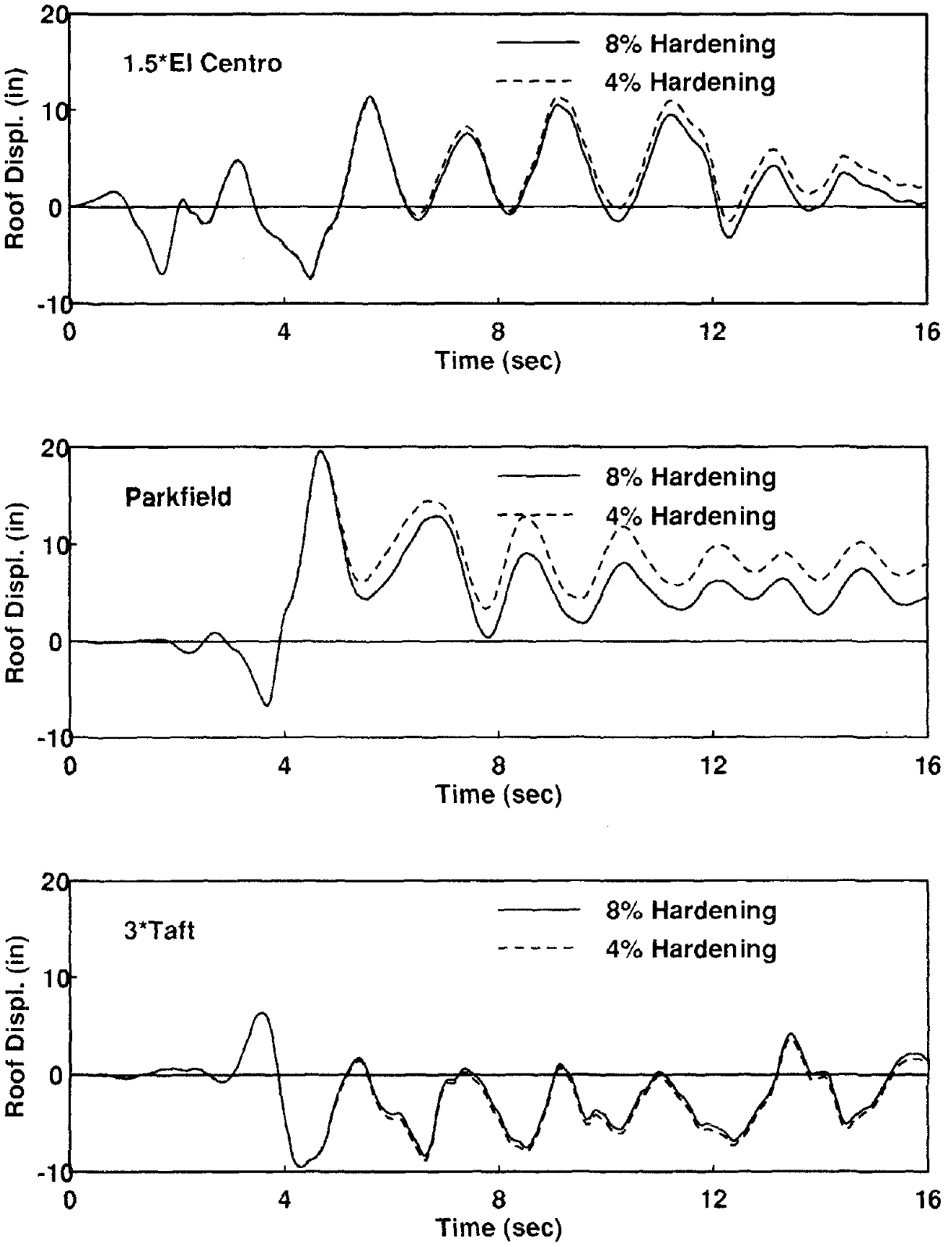

Figure 7.19 Effects of Post Yield Stiffness to Response of Equivalent SDOF System

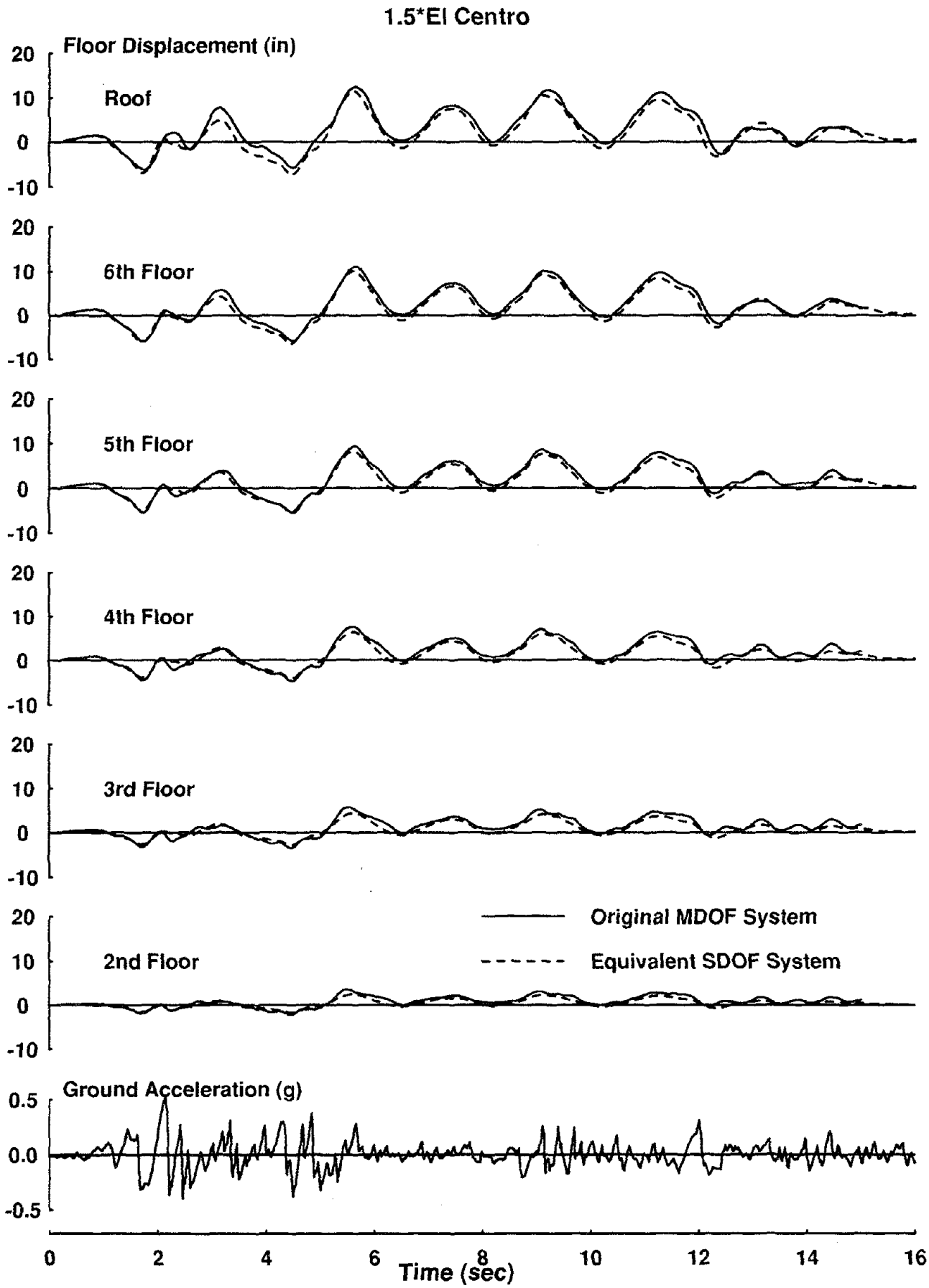

Figure 7.20 Response Comparisons of MDOF System and SDOF System(1.5*El Centro)

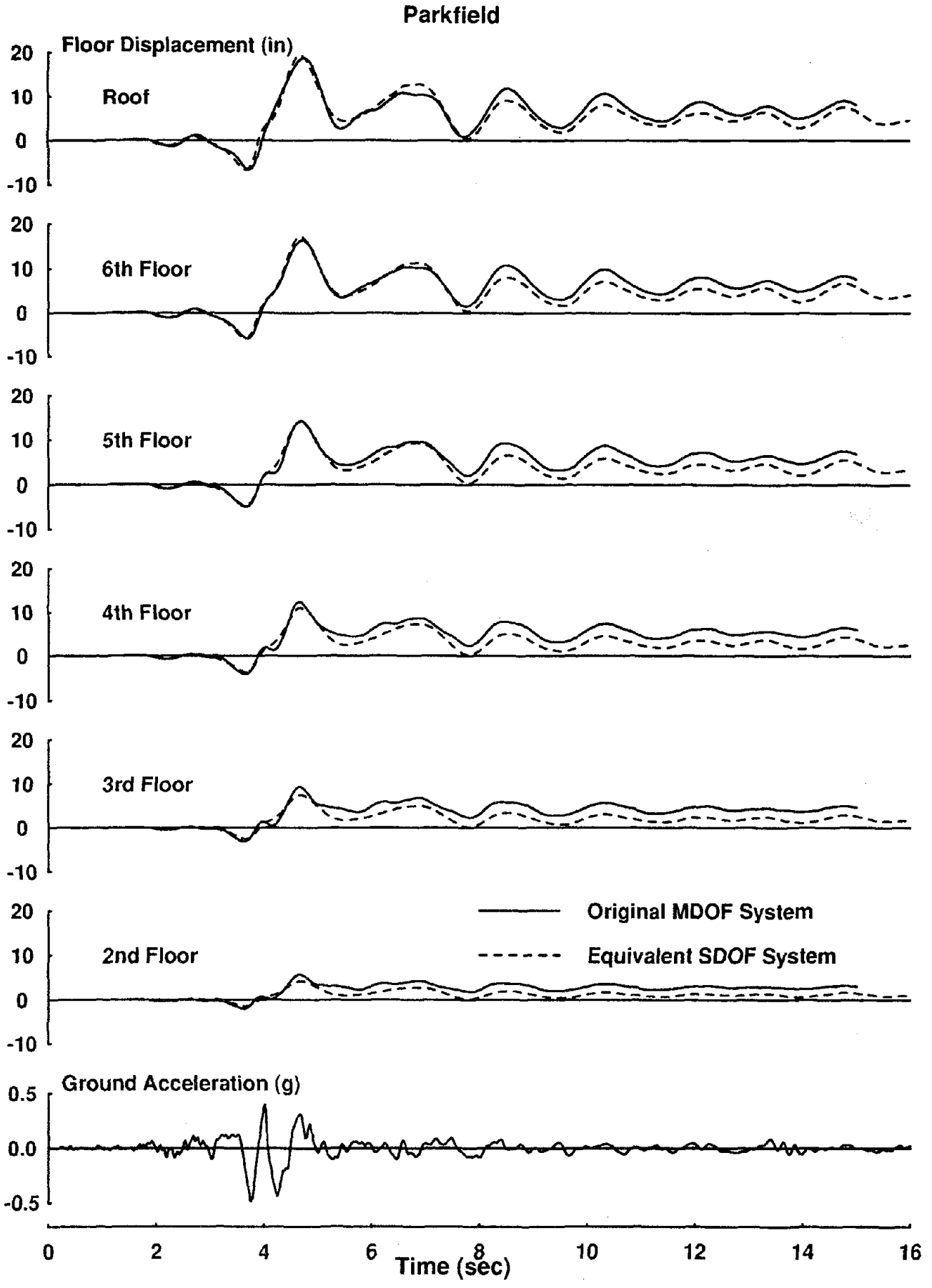

Figure 7.21 Response Comparisons of MDOF System and SDOF System (Parkfield)

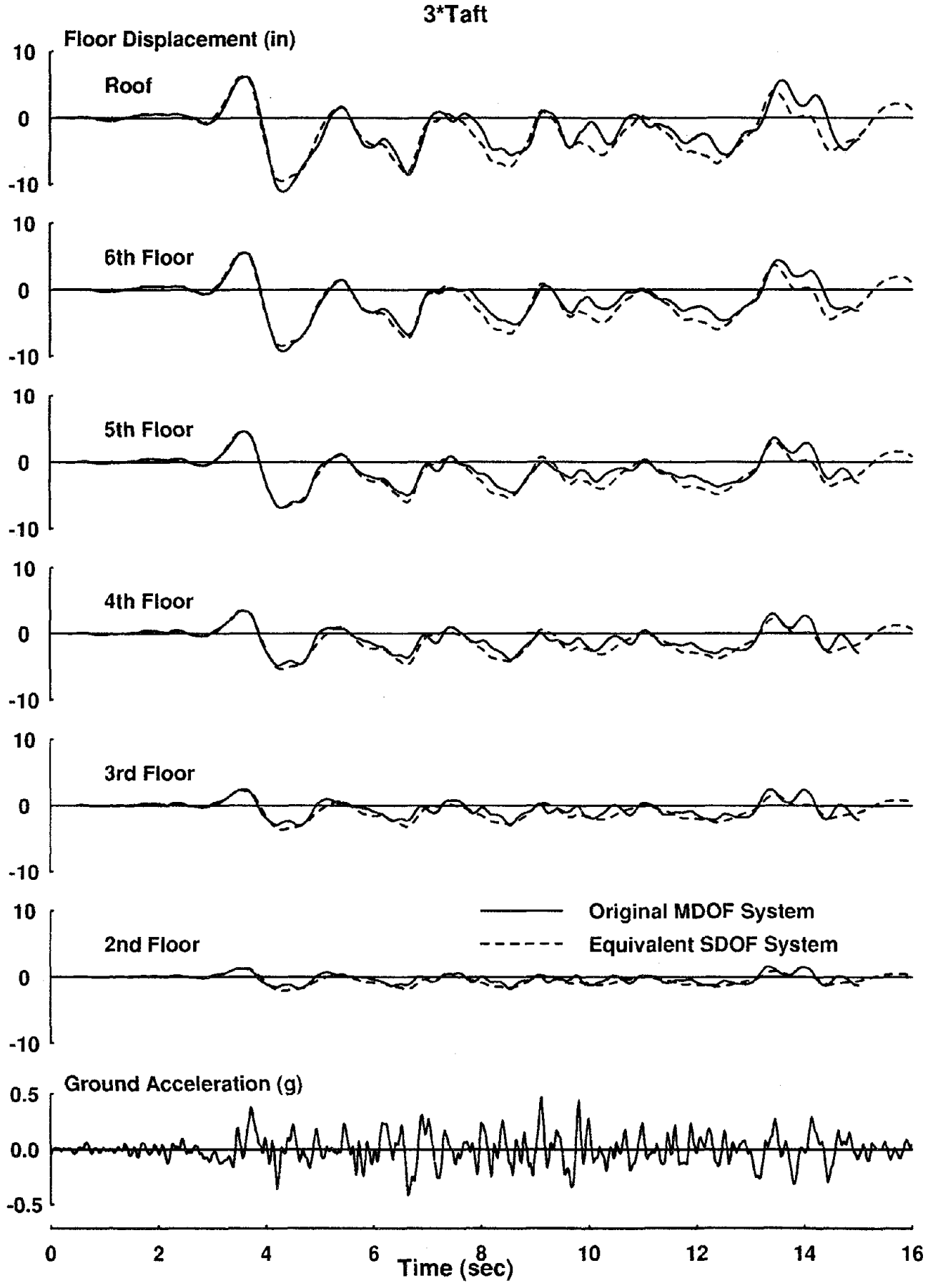

Figure 7.22 Response Comparisons of MDOF System and SDOF System (3*Taft)

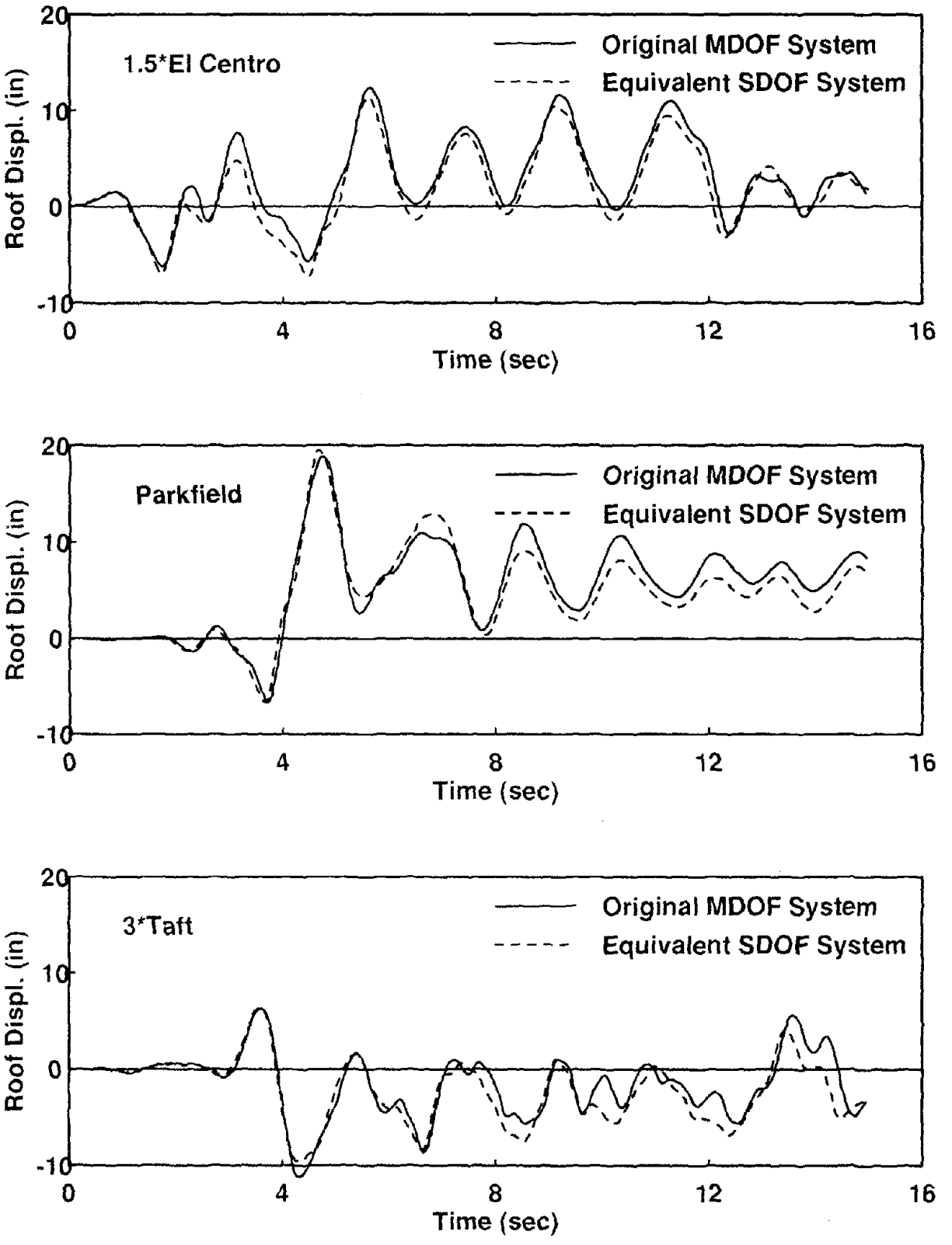

Figure 7.23 Roof Displacement Comparisons of MDOF System and SDOF System

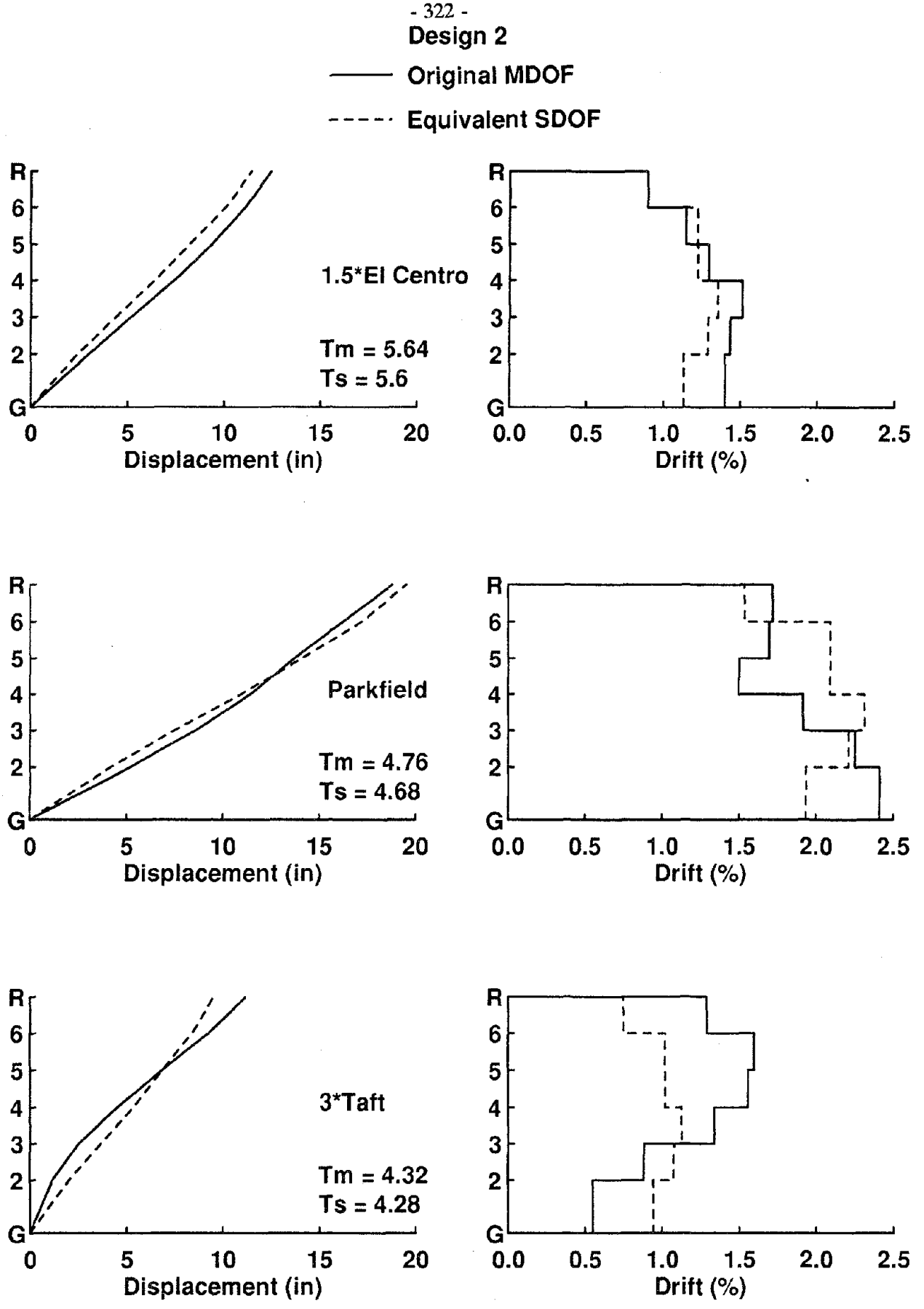

Figure 7.24 Frame Displacements and Story Drifts at Instant of Maximum Roof Displacements

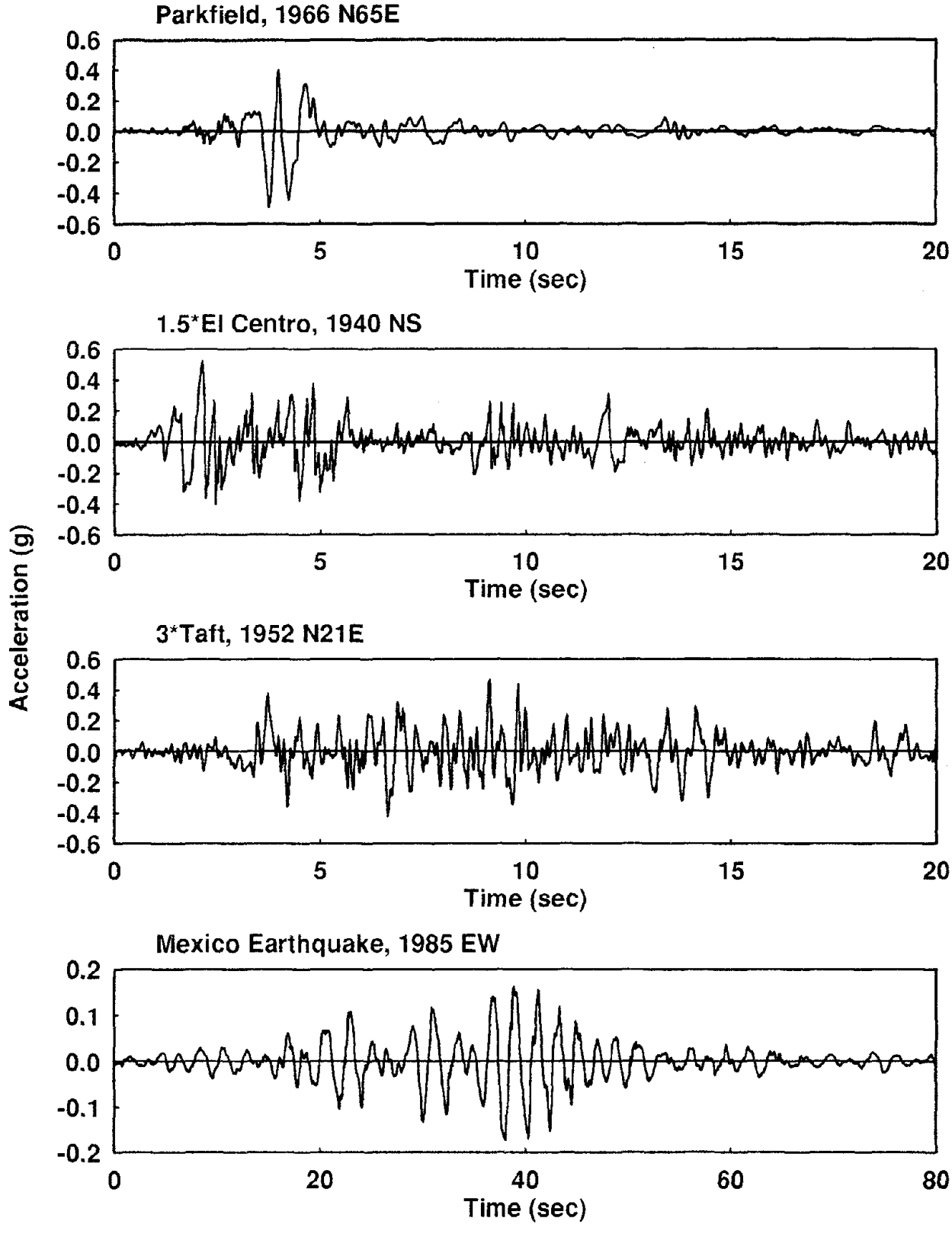

Figure 7.25 Ground Acceleration History of Selected Earthquakes

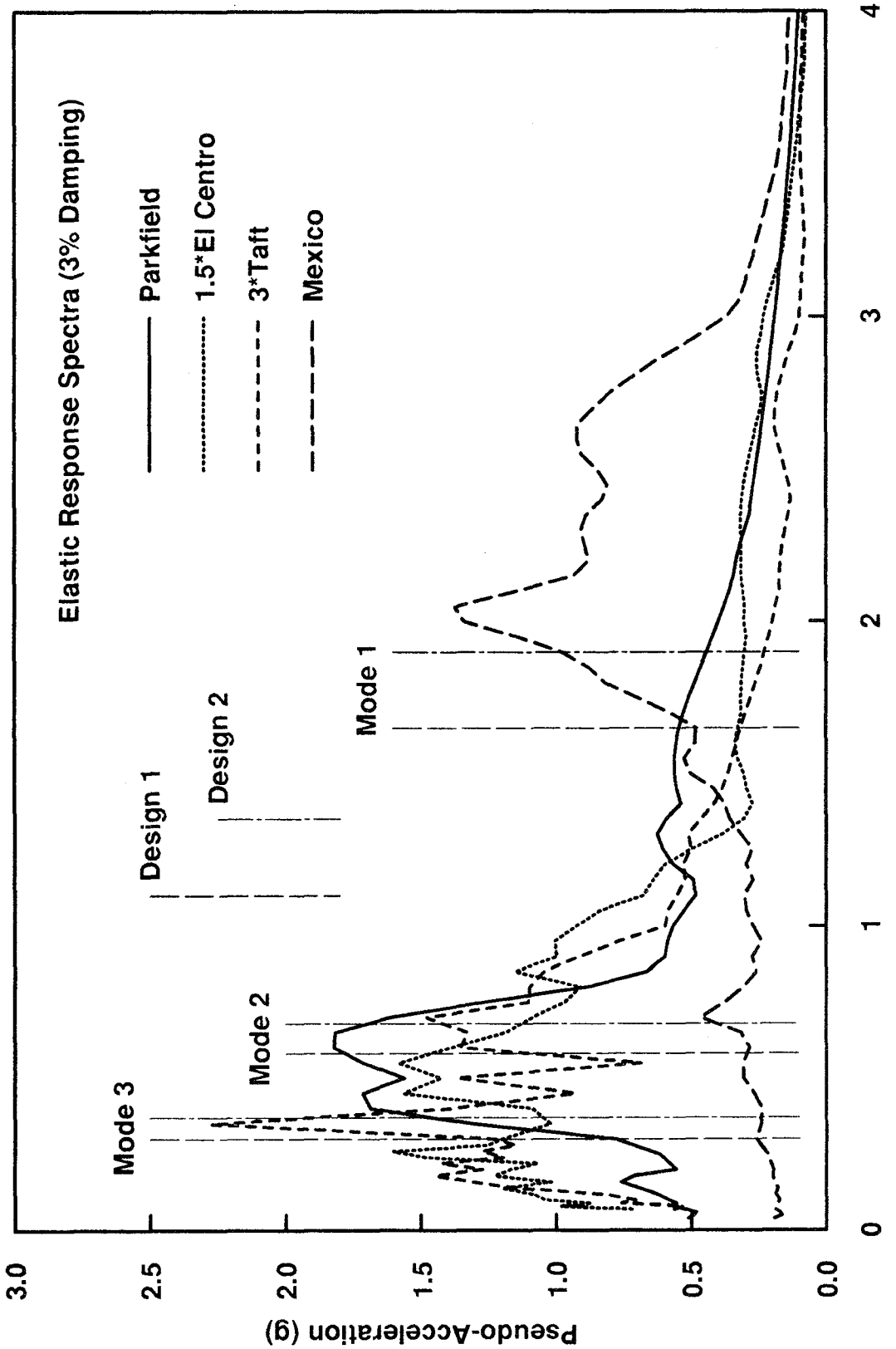

Figure 7.26 Linear Elastic Pseudo-Acceleration Spectra for the Selected Ground Accelerations (3% Damping)

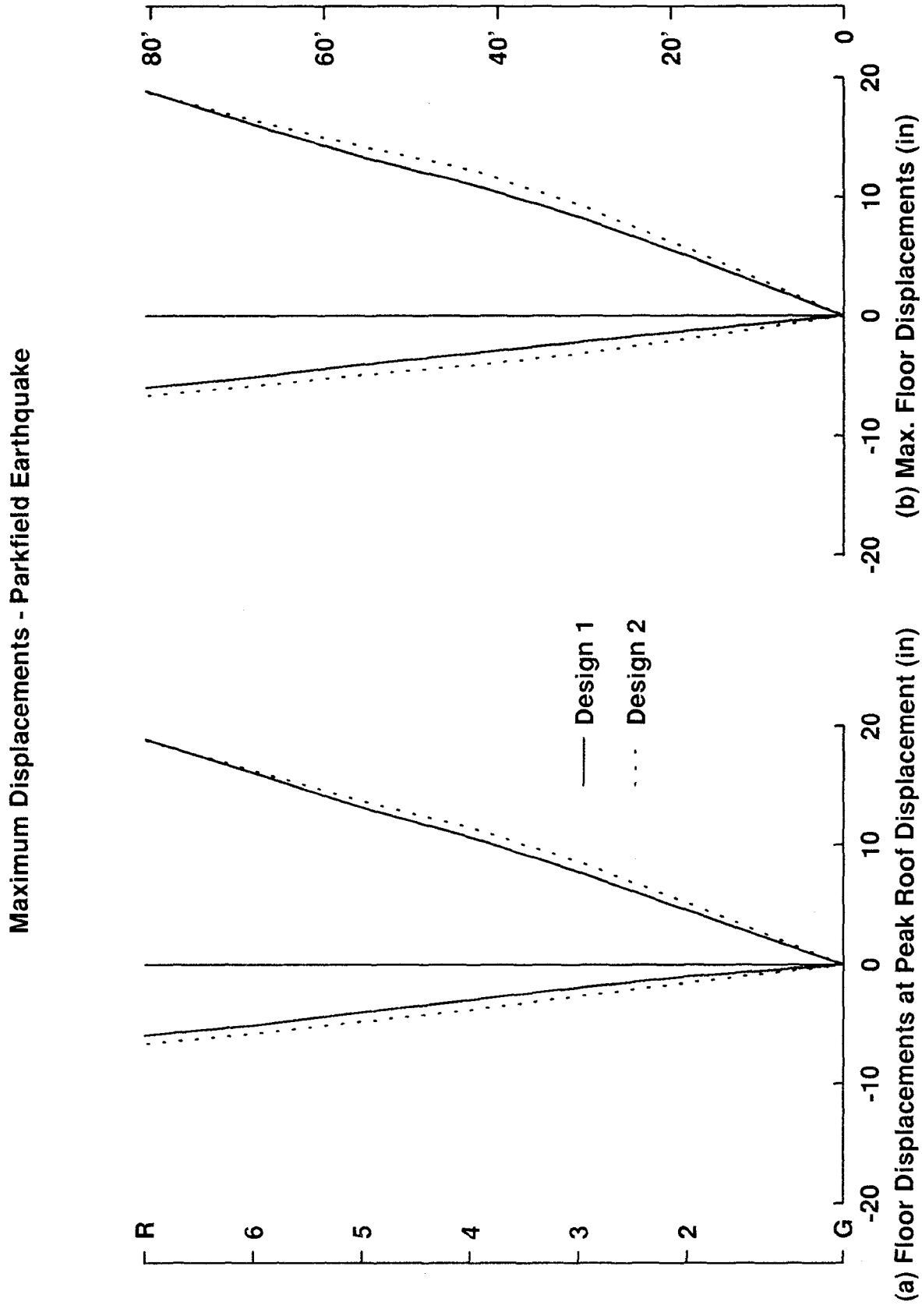

Figure 7.27 Maximum Floor Displacements for MRF Designs 1 and 2 (Parkfield Earthquake)

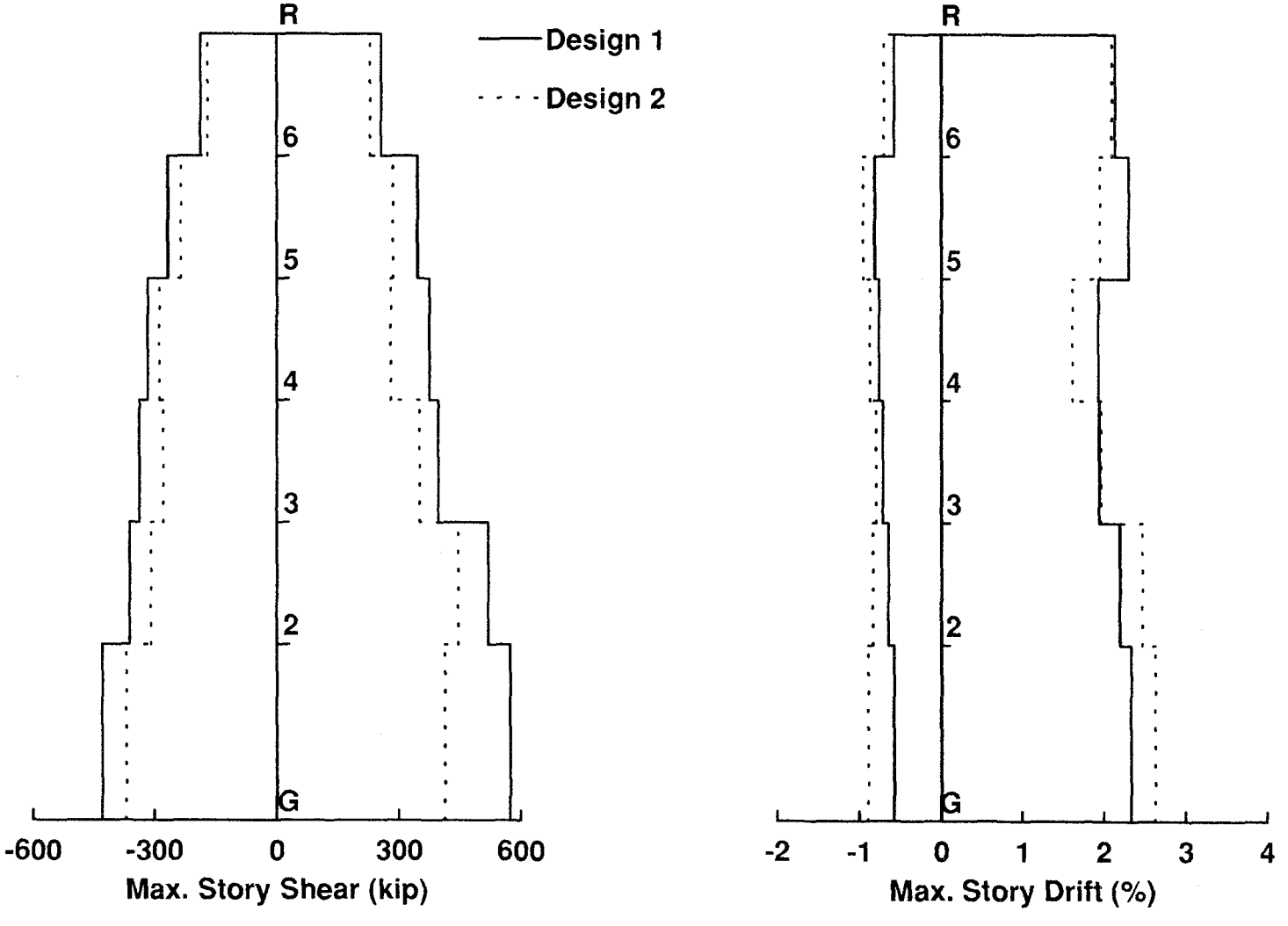

Figure 7.28 Maximum Story Shears and Story Drifts for MRF Designs 1 and 2 (Parkfield Earthquake)

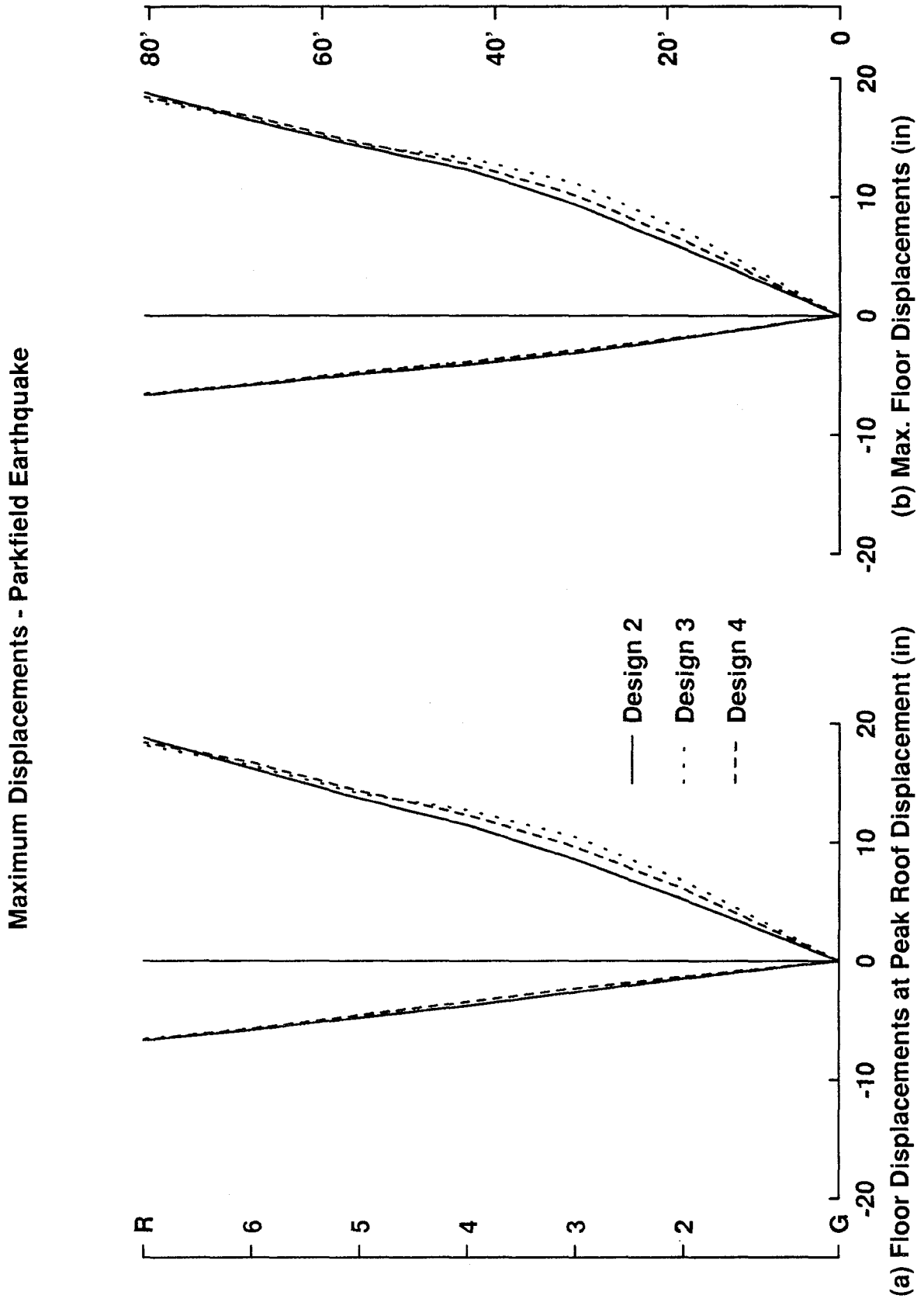

Figure 7.29 Maximum Floor Displacements for MRF Designs 2, 3 and 4 (Parkfield Earthquake)

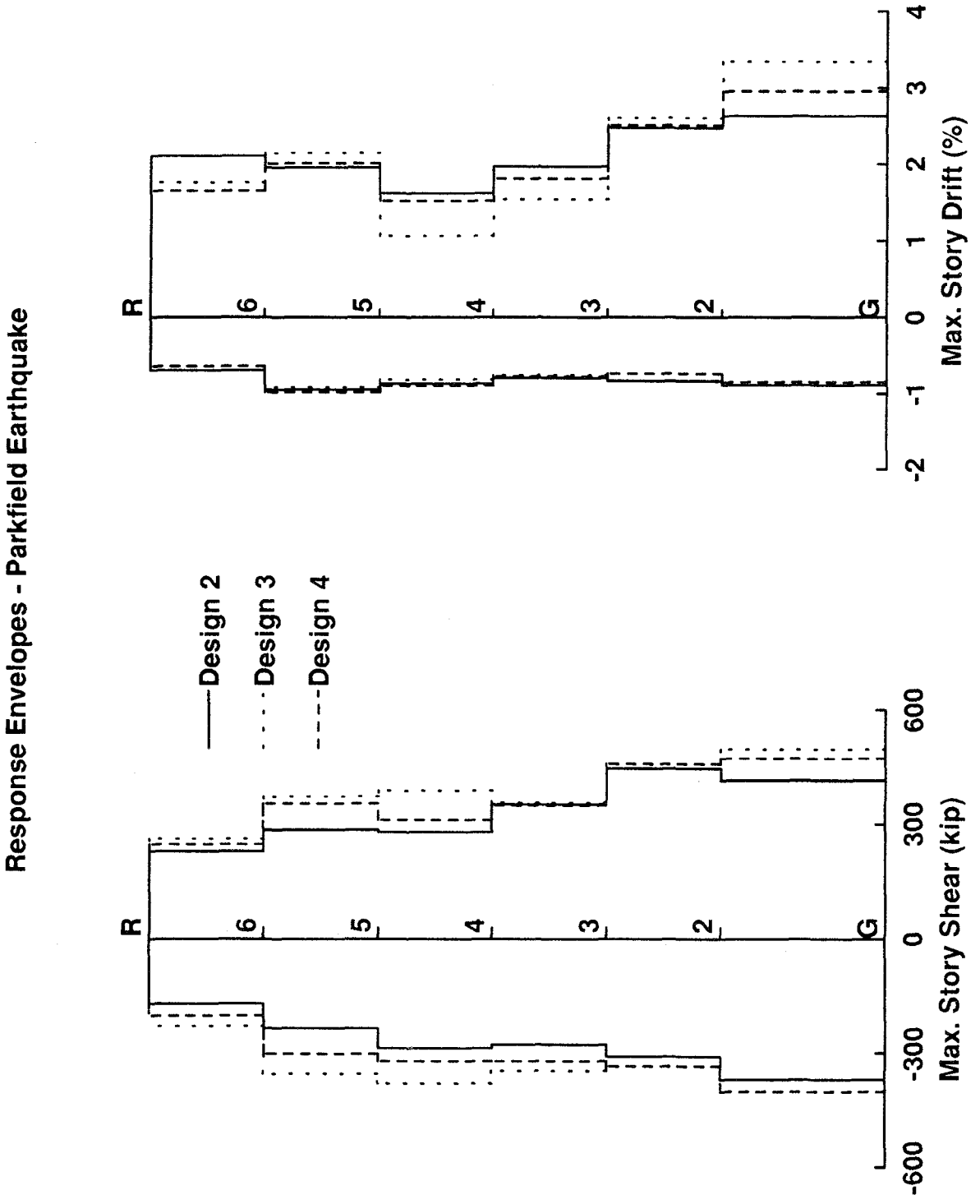

Figure 7.30 Maximum Story Shears and Story Drifts for MRF Designs 2, 3 and 4 (Parkfield Earthquake)

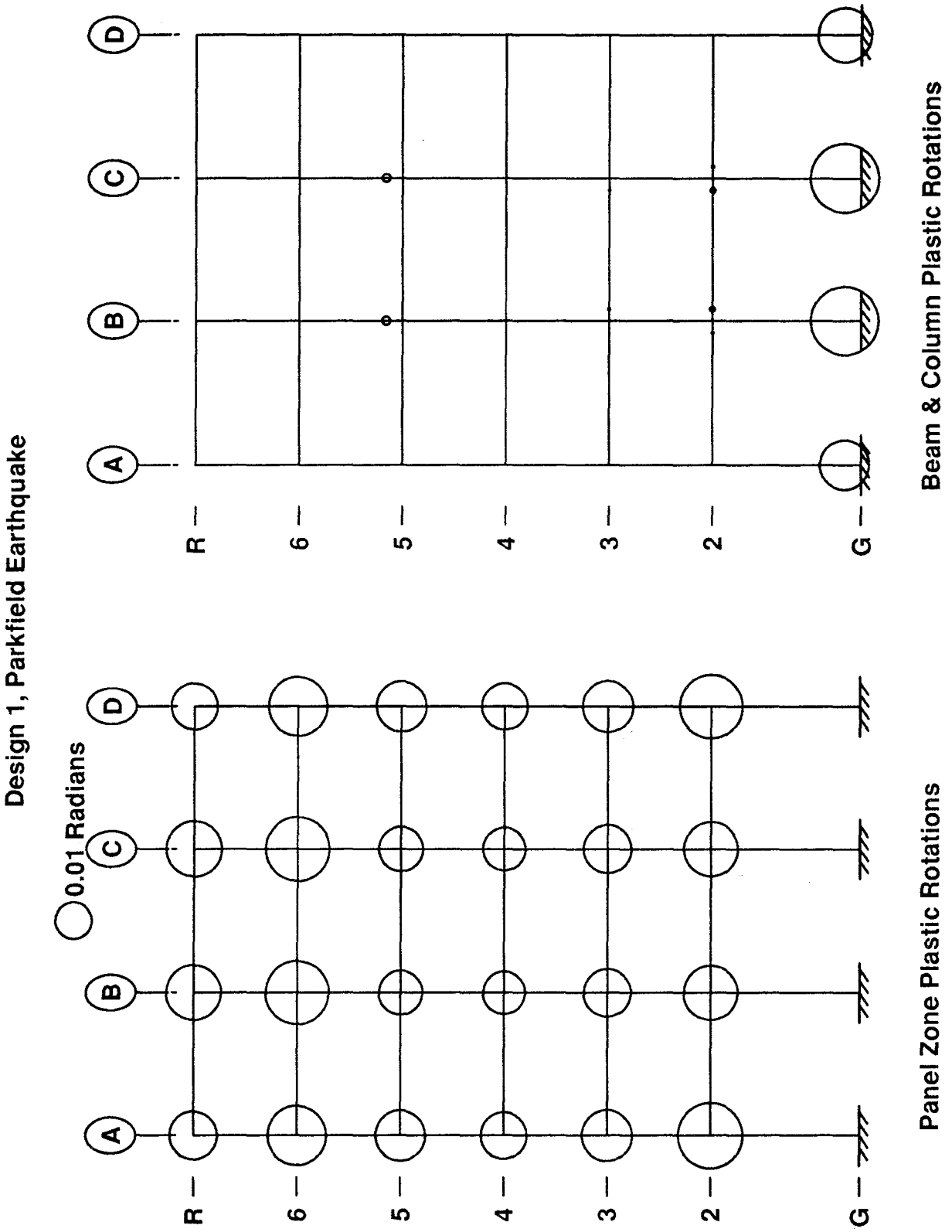

Figure 7.31 Maximum Beam, Column and Panel Zone Joint Plastic Rotations for MRF Design 1

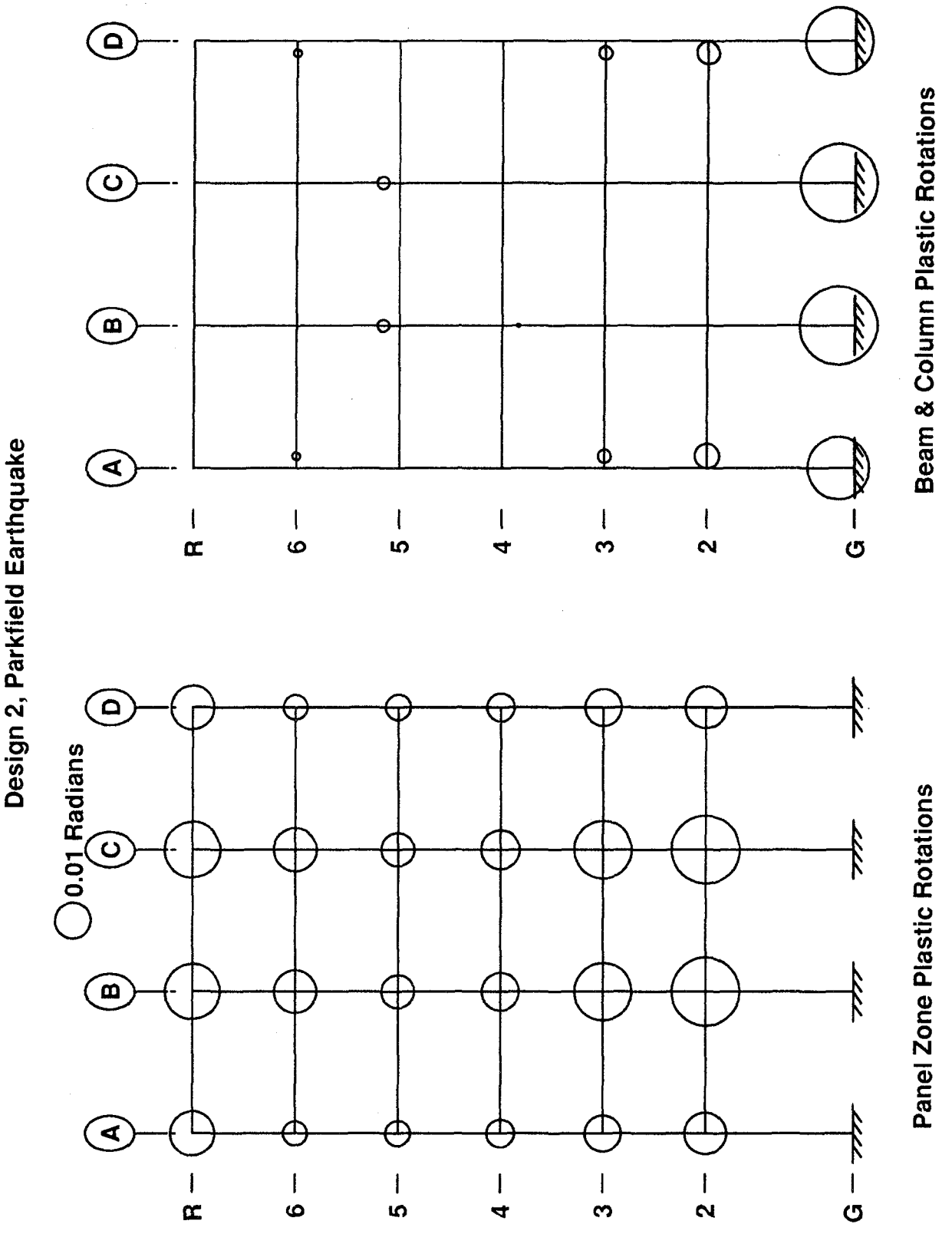

Figure 7.32 Maximum Beam, Column and Panel Zone Joint Plastic Rotations for MRF Design 2

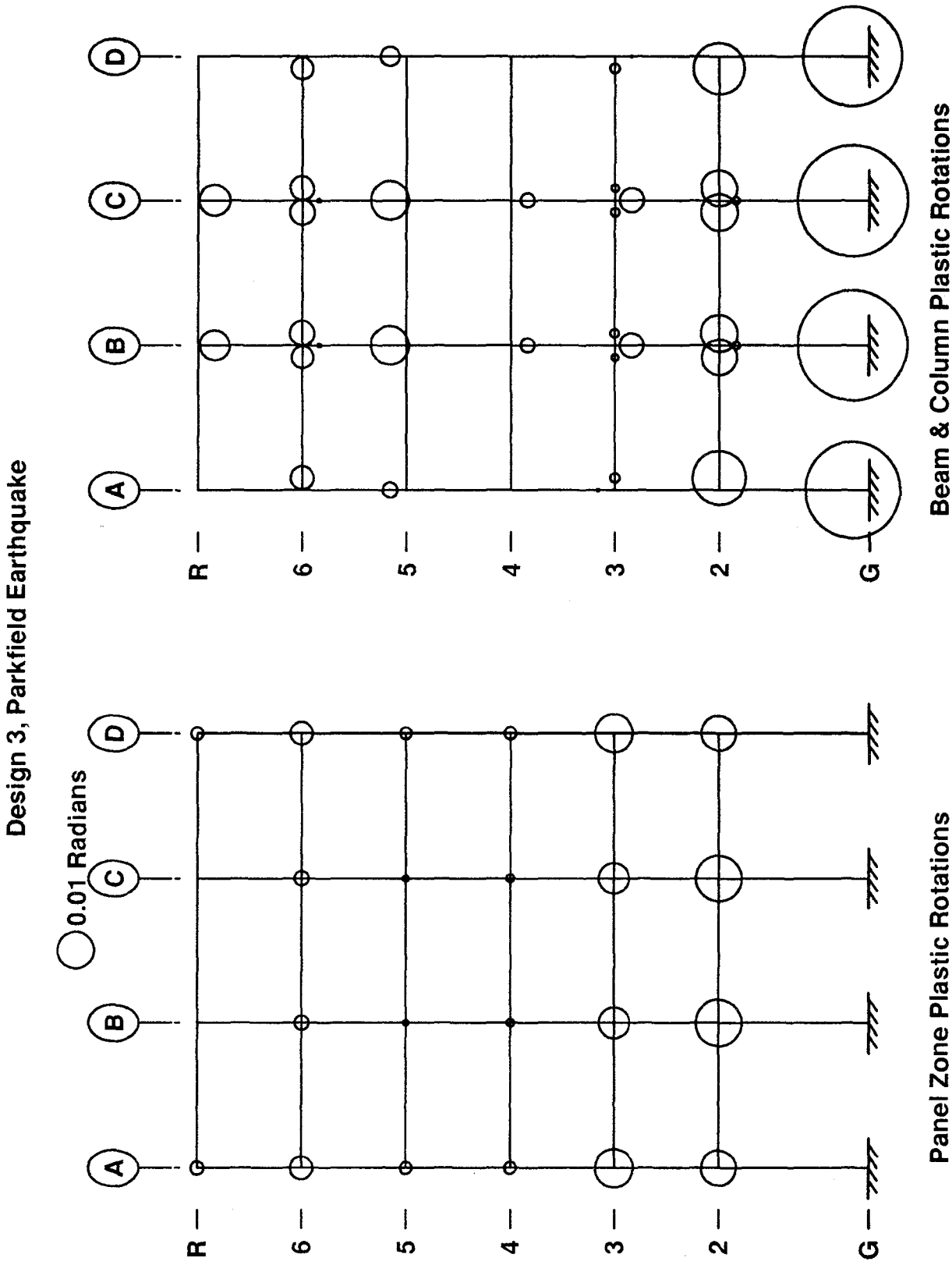

Figure 7.33 Maximum Beam, Column and Panel Zone Joint Plastic Rotations for MRF Design 3

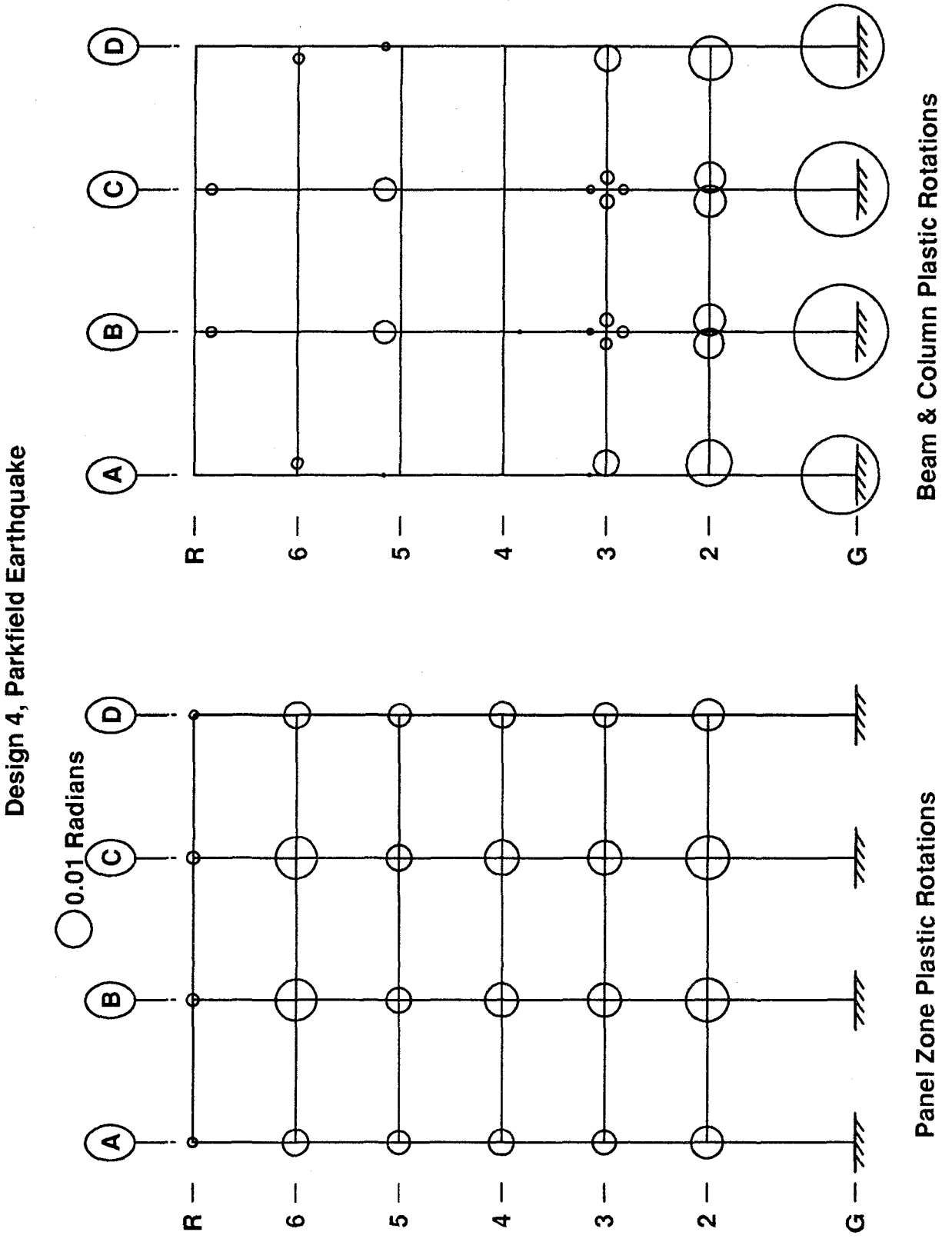

Figure 7.34 Maximum Beam, Column and Panel Zone Joint Plastic Rotations for MRF Design 4

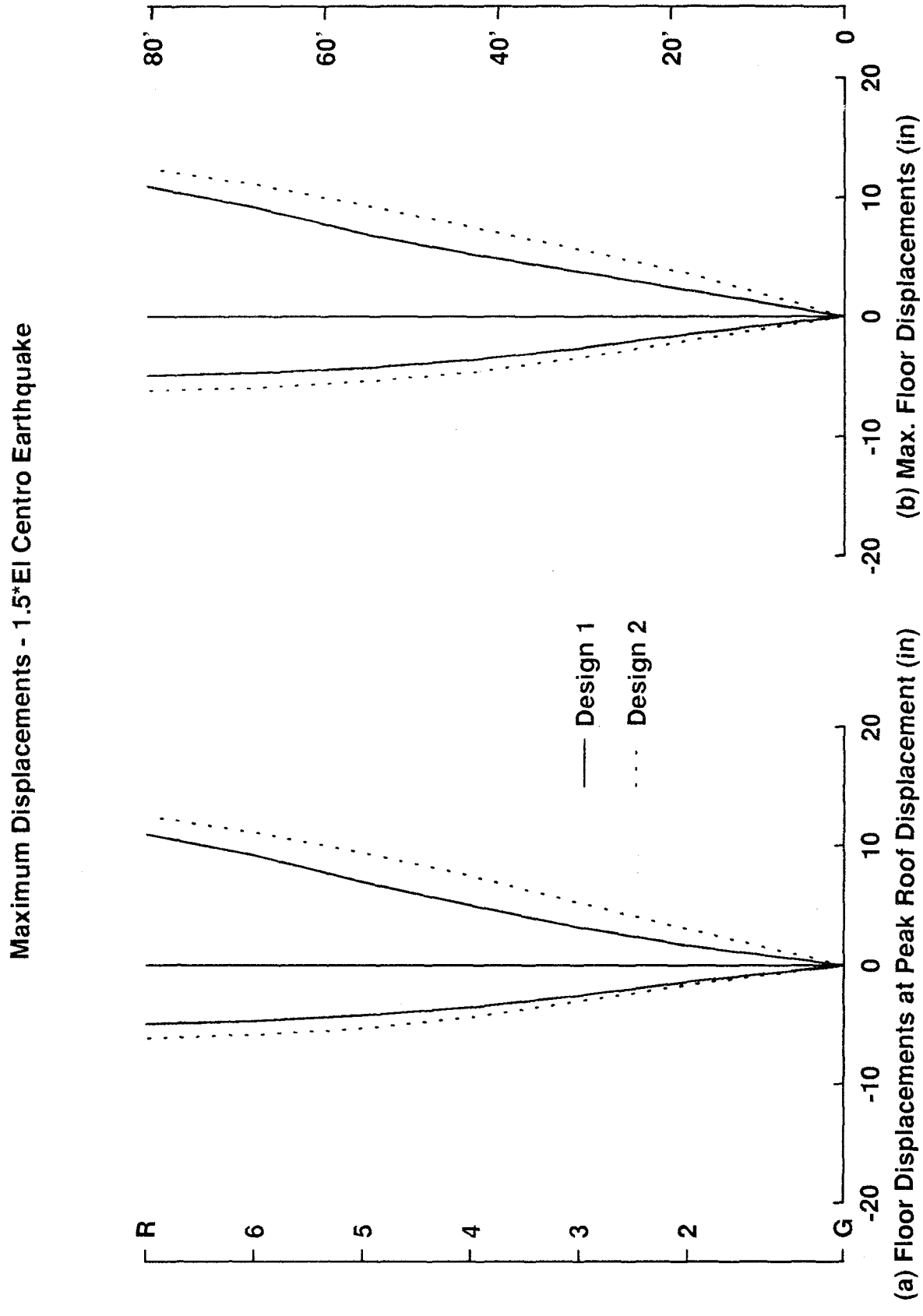

Figure 7.35 Maximum Floor Displacements for MRF Designs 1 and 2 (1.5*El Centro Earthquake)

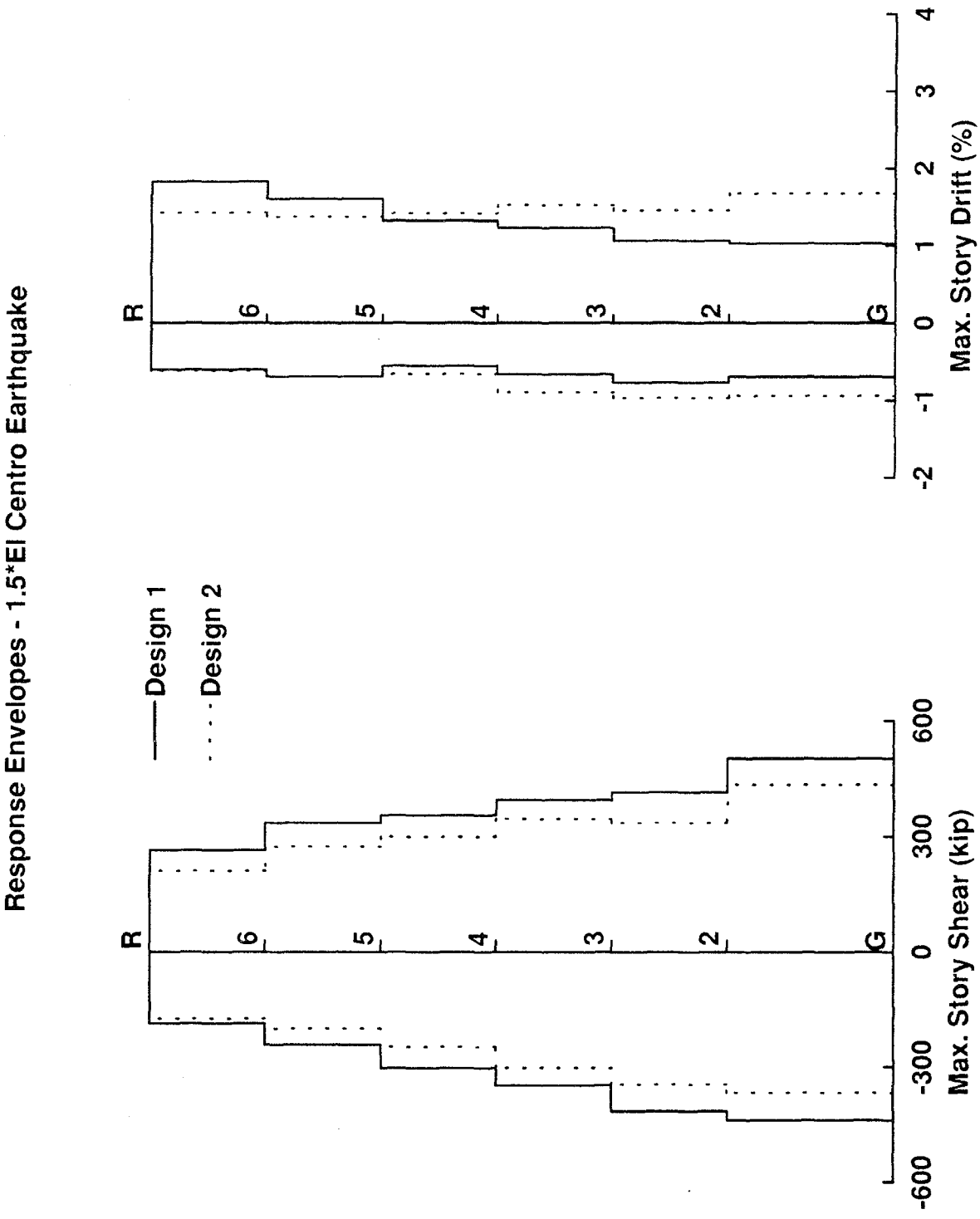

Figure 7.36 Maximum Story Shears and Story Drifts for MRF Designs 1 and 2 (1.5*El Centro Earthquake)

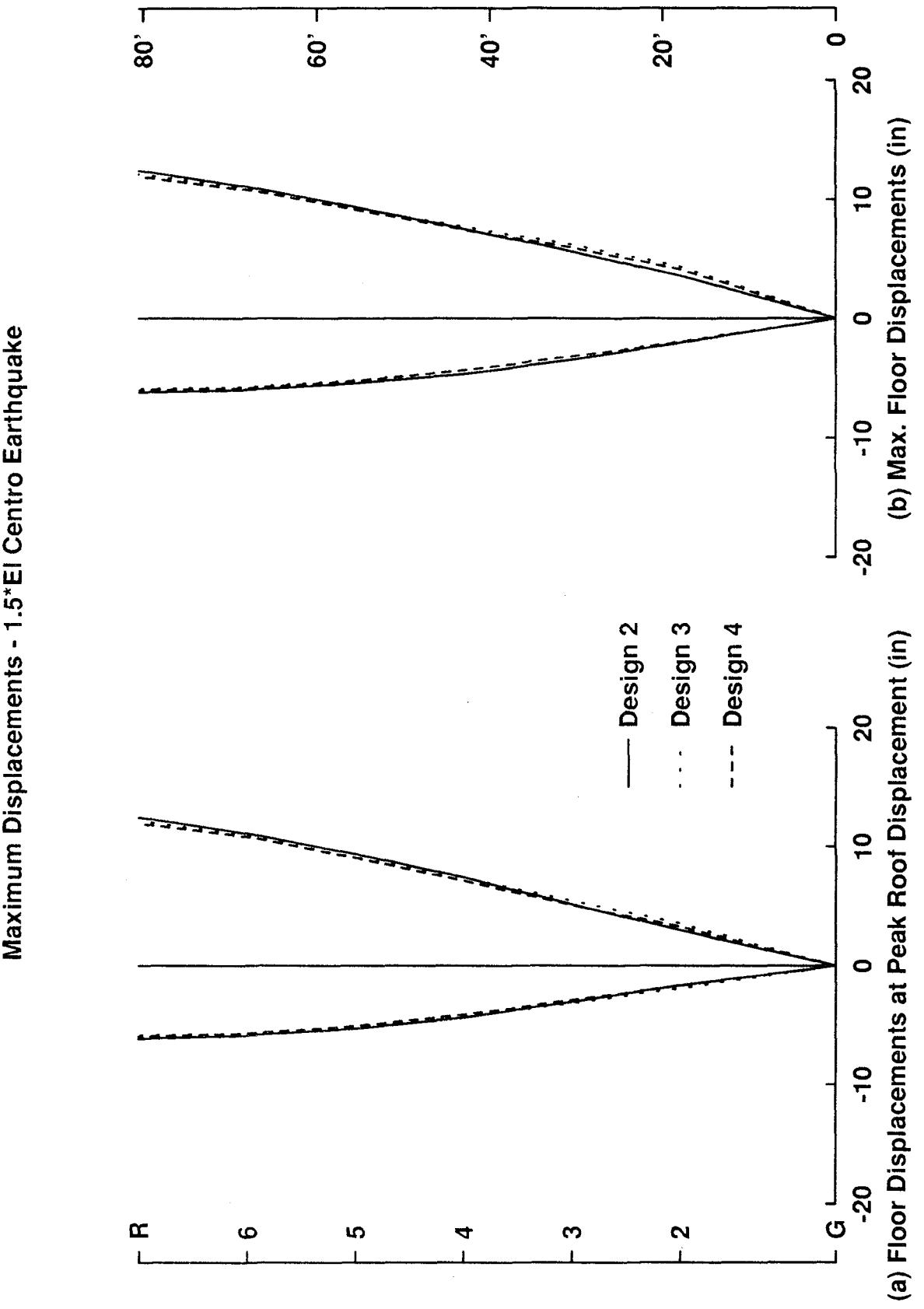

Figure 7.37 Maximum Floor Displacements for MRF Designs 2, 3 and 4 (1.5*El Centro Earthquake)

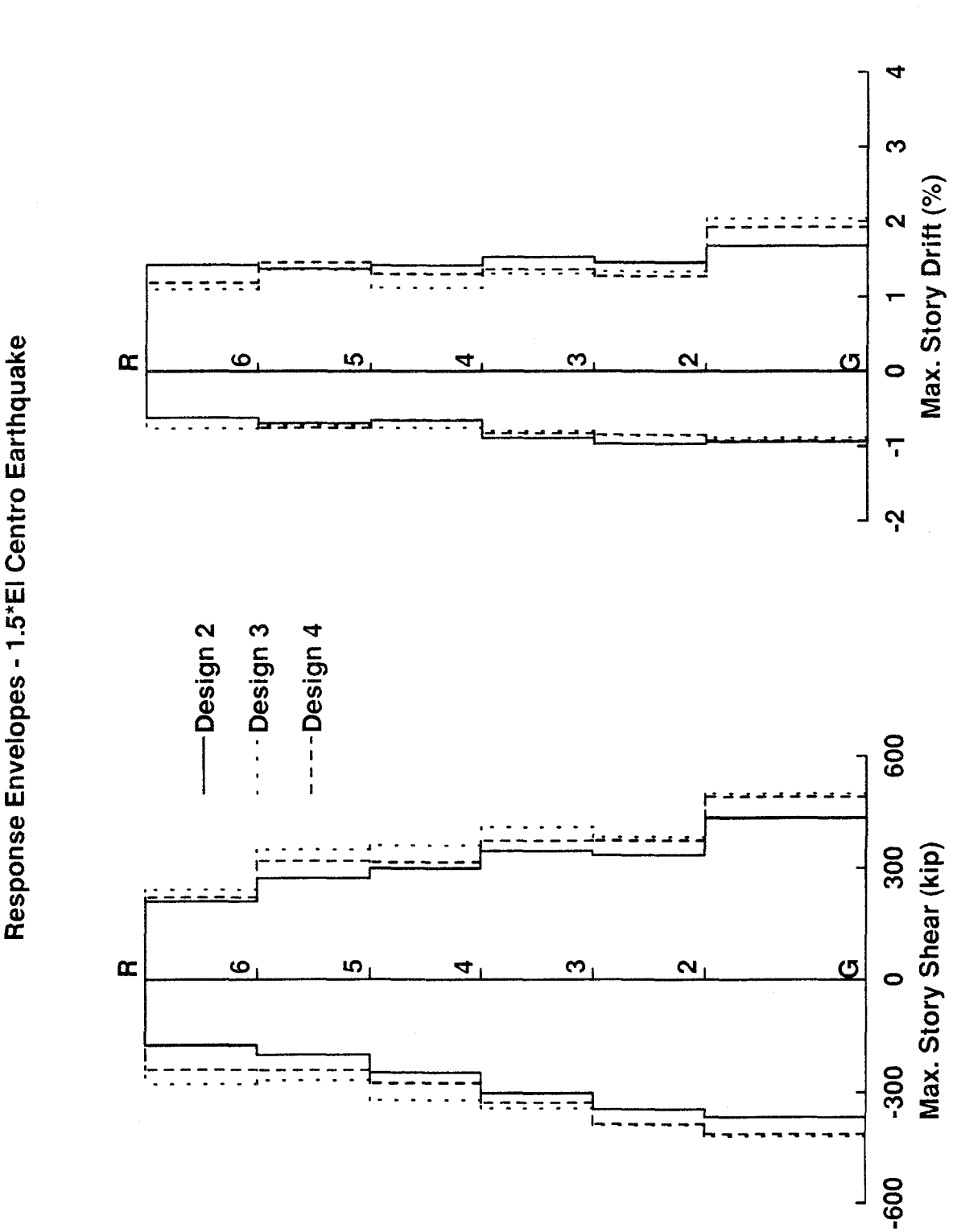

Figure 7.38 Maximum Story Shears and Story Drifts for MRF Designs 2, 3 and 4 (1.5*El Centro Earthquake)

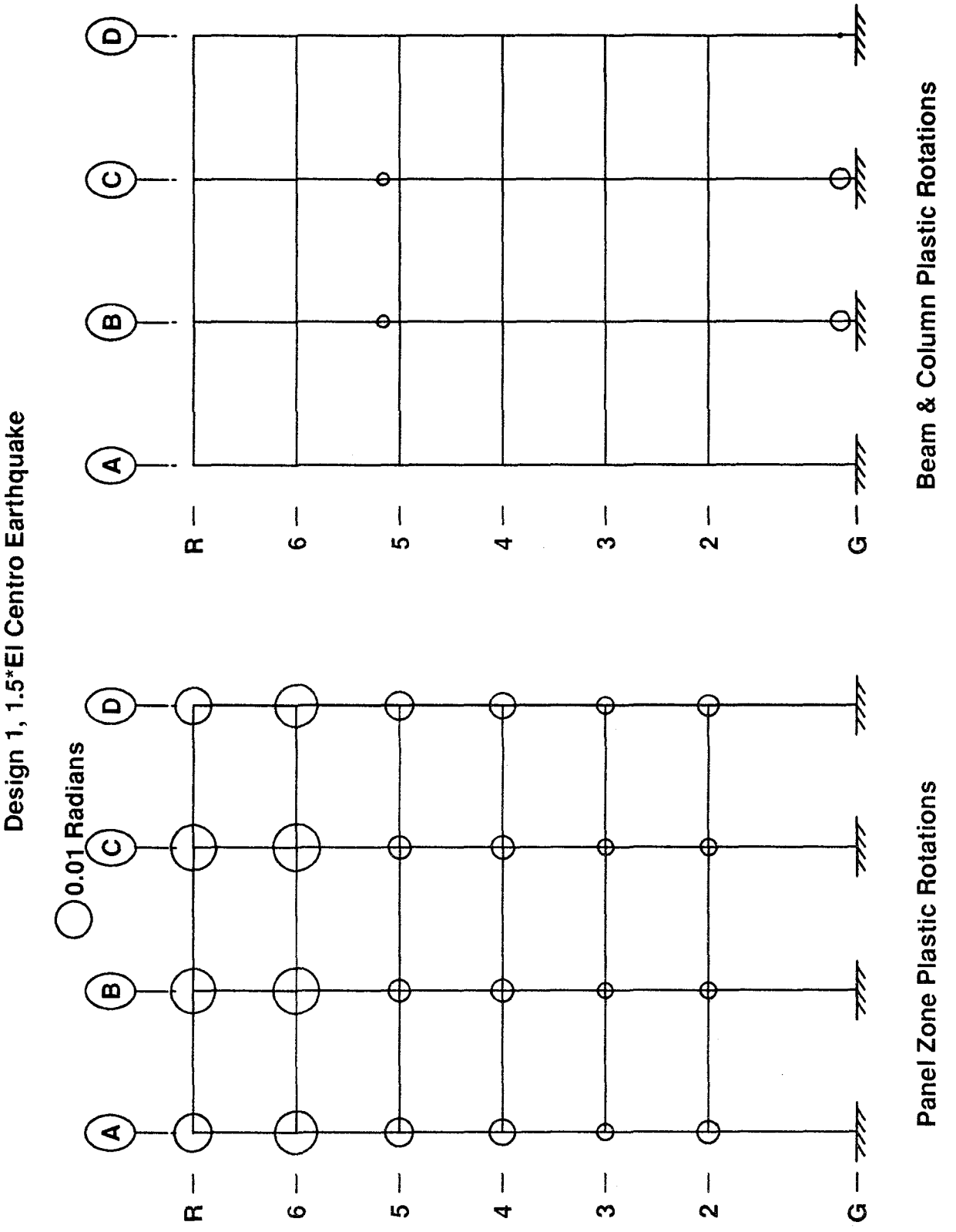

Figure 7.39 Maximum Beam, Column and Panel Zone Joint Plastic Rotations for MRF Design 1

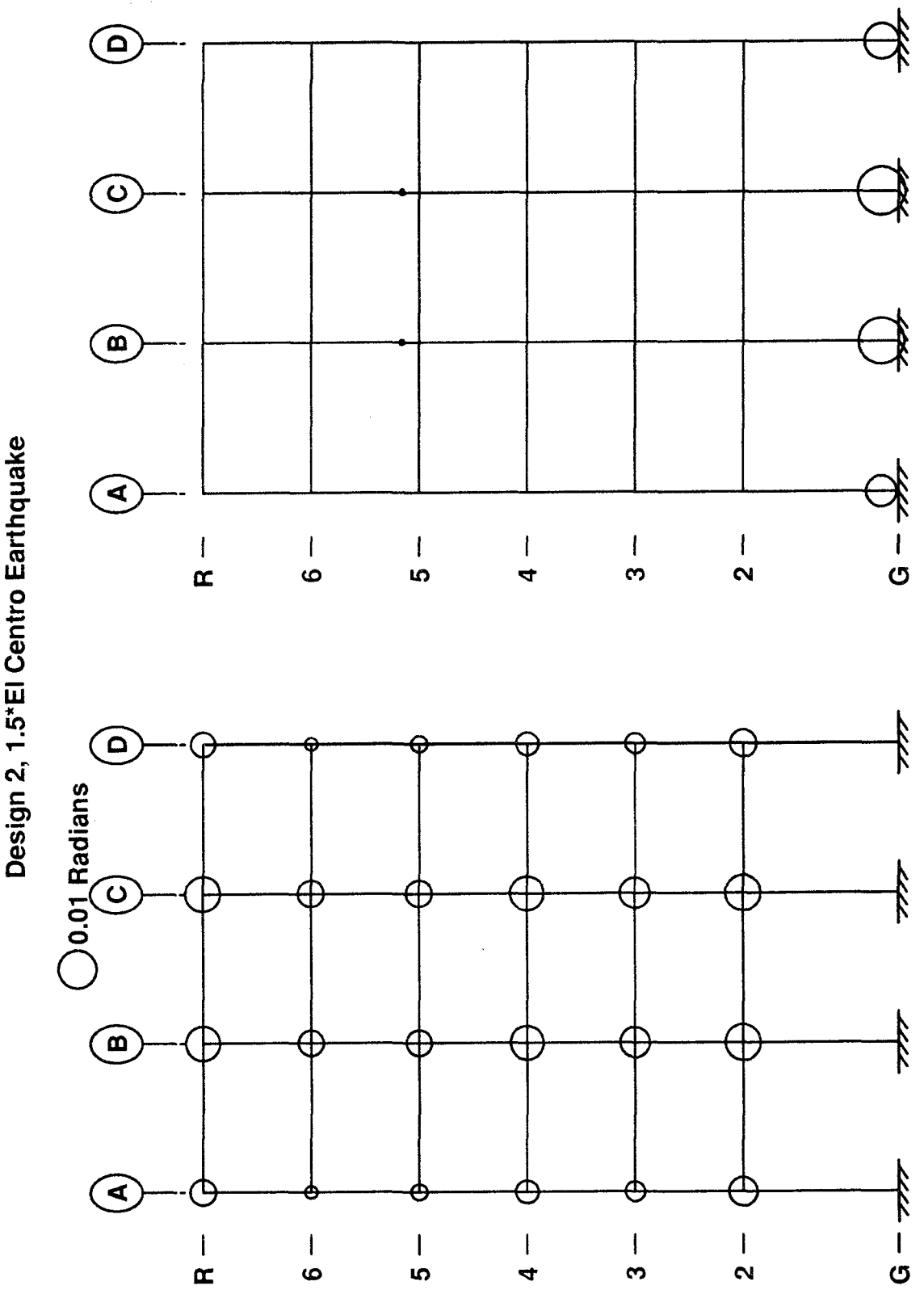

Figure 7.40 Maximum Beam, Column and Panel Zone Joint Plastic Rotations for MRF Design 2

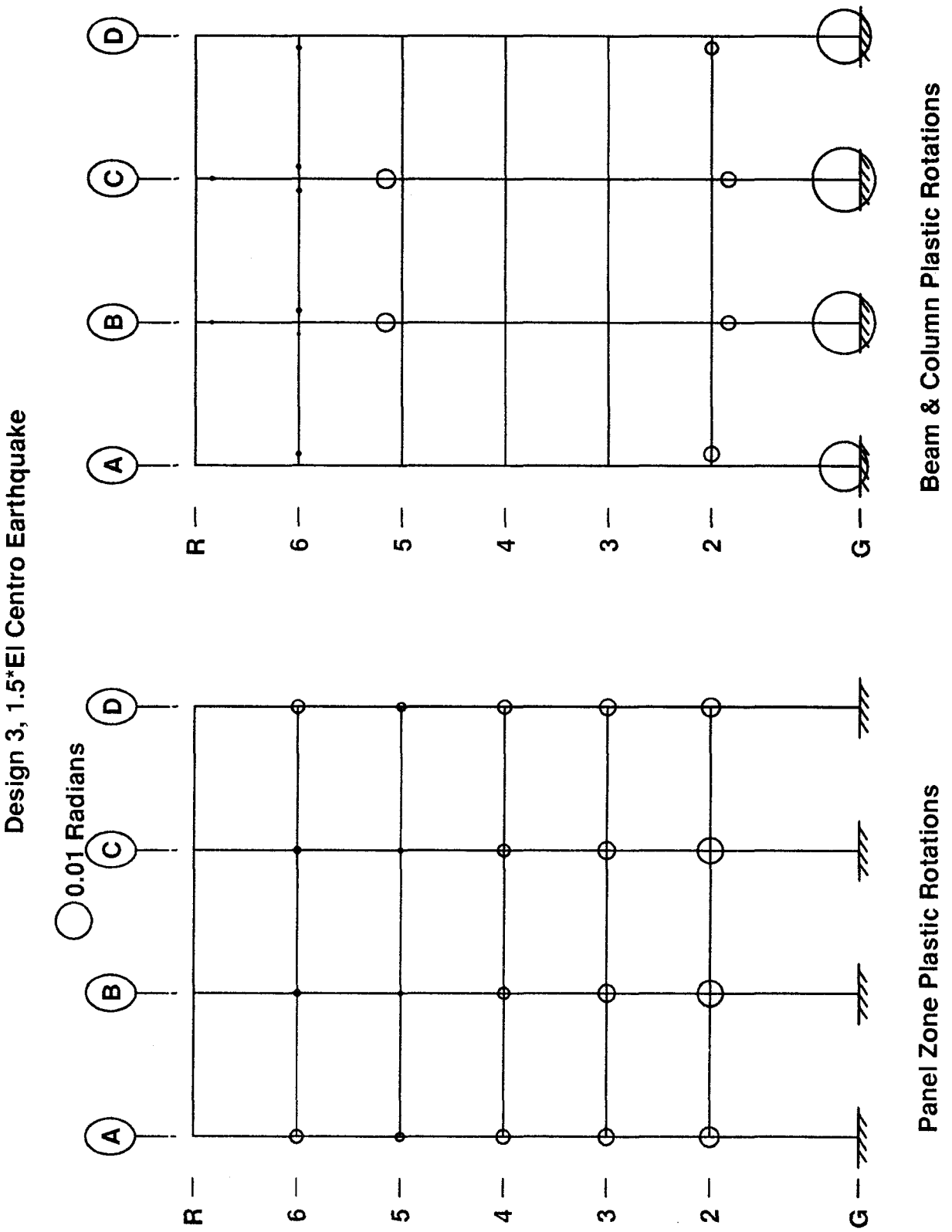

Figure 7.41 Maximum Beam, Column and Panel Zone Joint Plastic Rotations for MRF Design 3

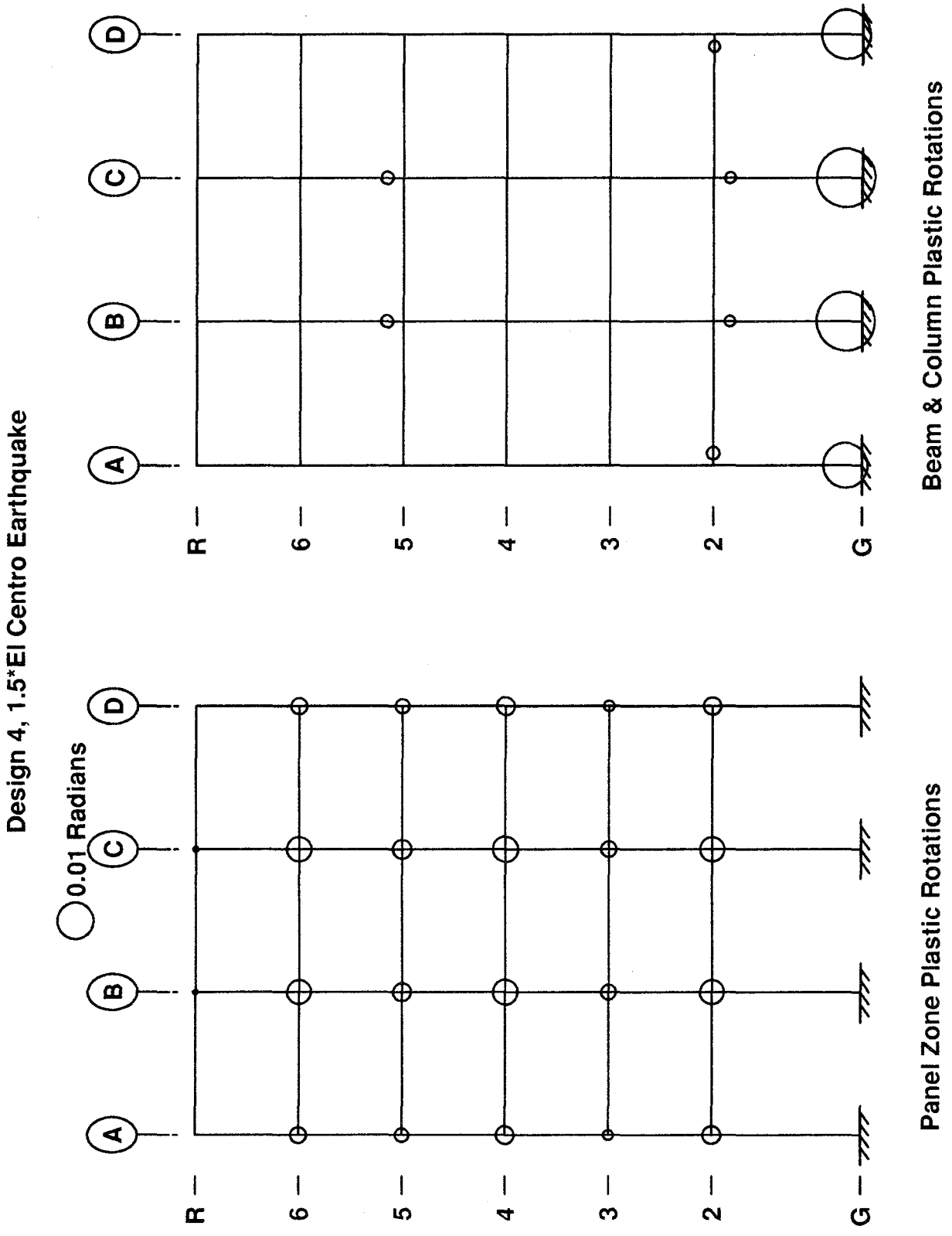

Figure 7.42 Maximum Beam, Column and Panel Zone Joint Plastic Rotations for MRF Design 4

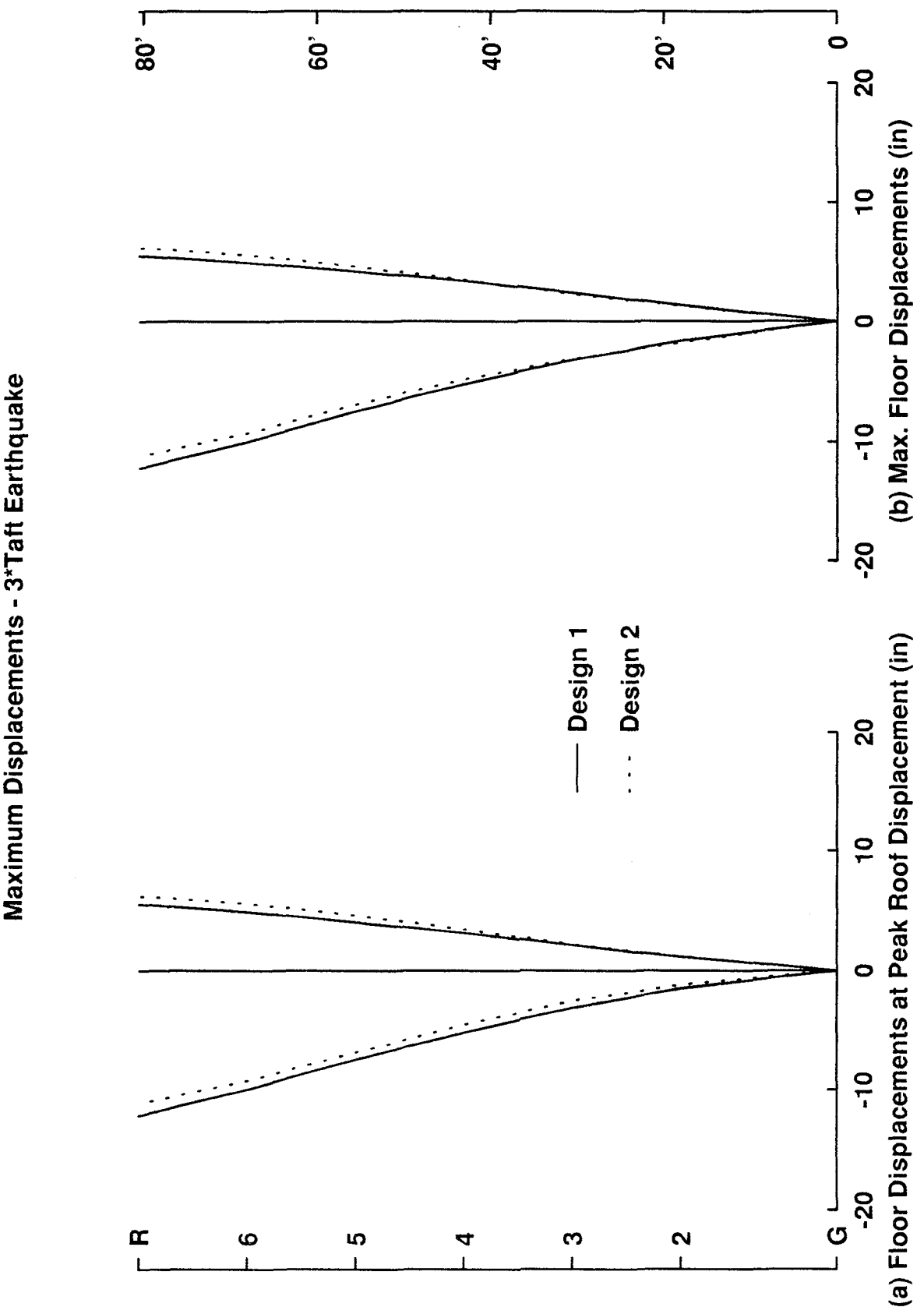

Figure 7.43 Maximum Floor Displacements for MRF Designs 1 and 2 (3*Taft Earthquake)

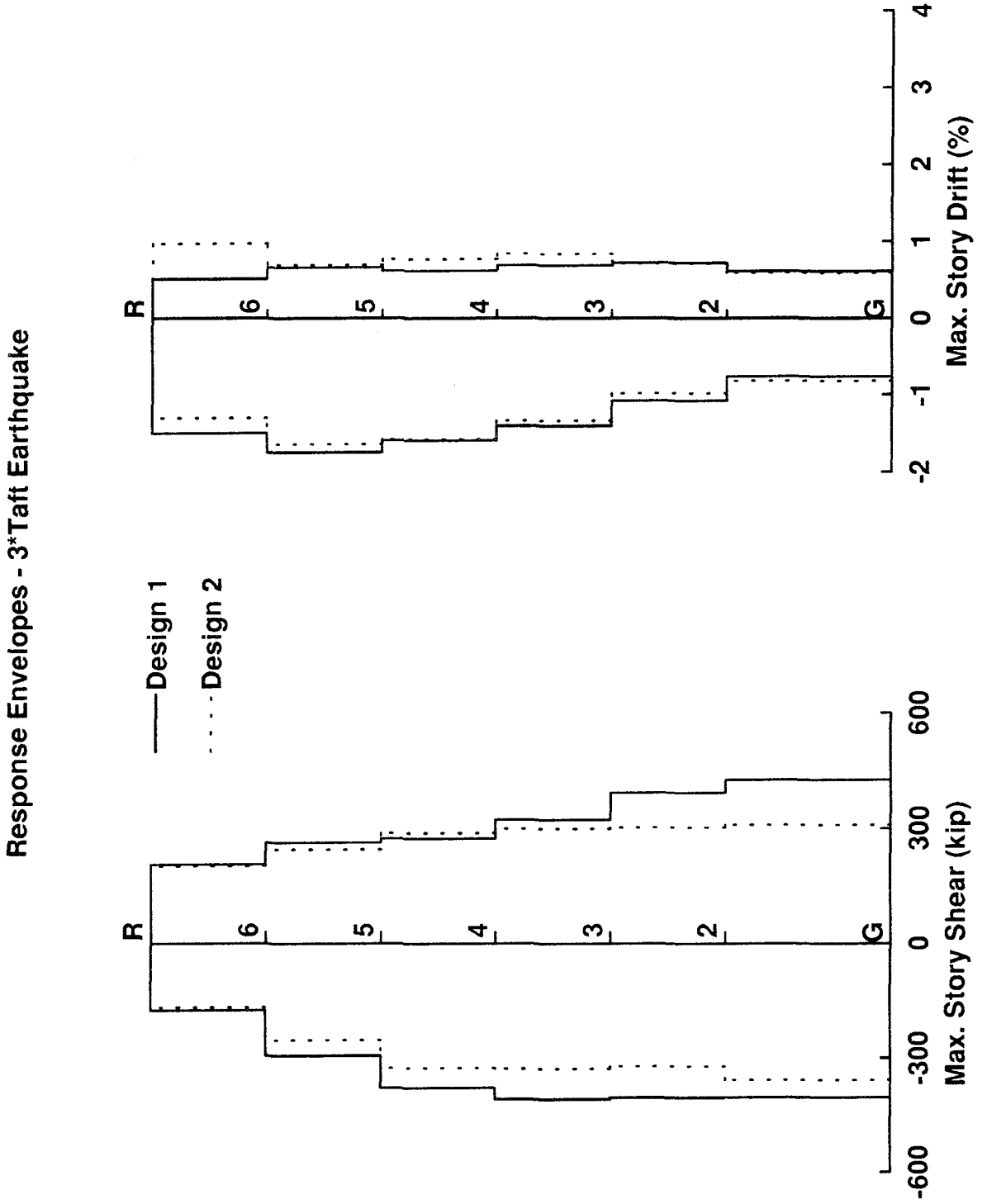

Figure 7.44 Maximum Story Shears and Story Drifts for MRF Designs 1 and 2 (3*Taft Earthquake)

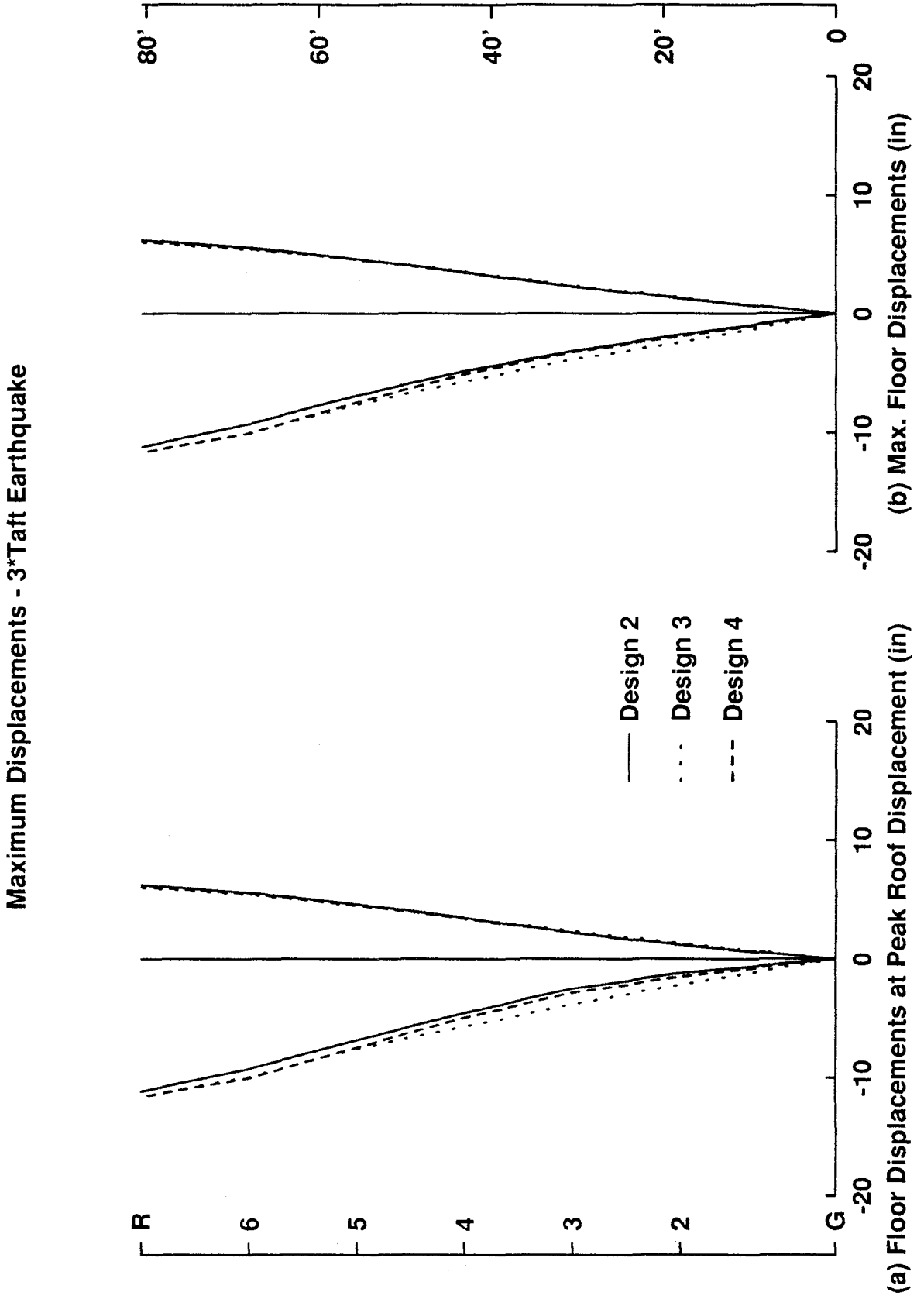

Figure 7.45 Maximum Floor Displacements for MRF Designs 2, 3 and 4 (3*Taft Earthquake)

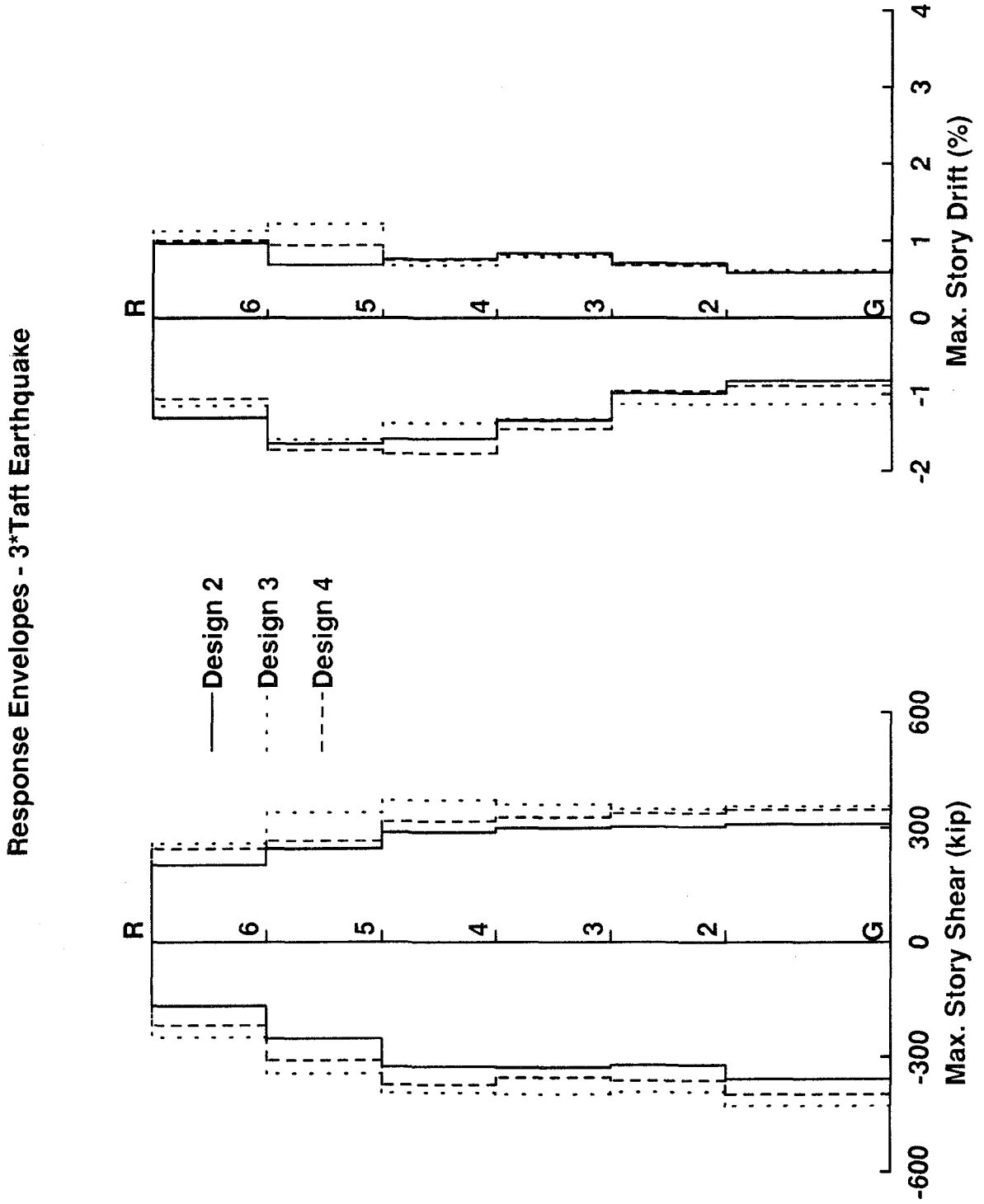

Figure 7.46 Maximum Story Shears and Story Drifts for MRF Designs 2, 3 and 4 (3*Taft Earthquake)

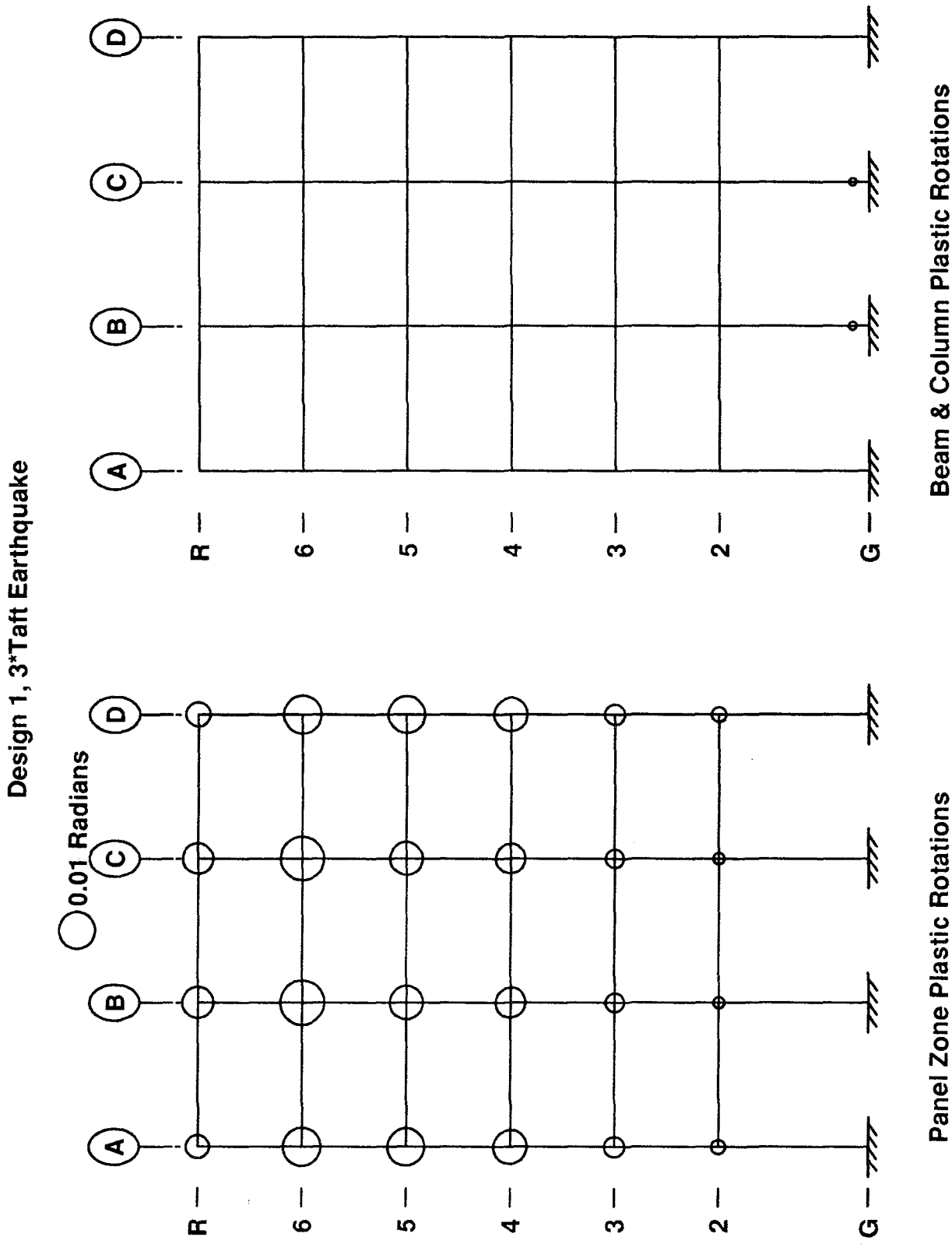

Figure 7.47 Maximum Beam, Column and Panel Zone Joint Plastic Rotations for MRF Design 1

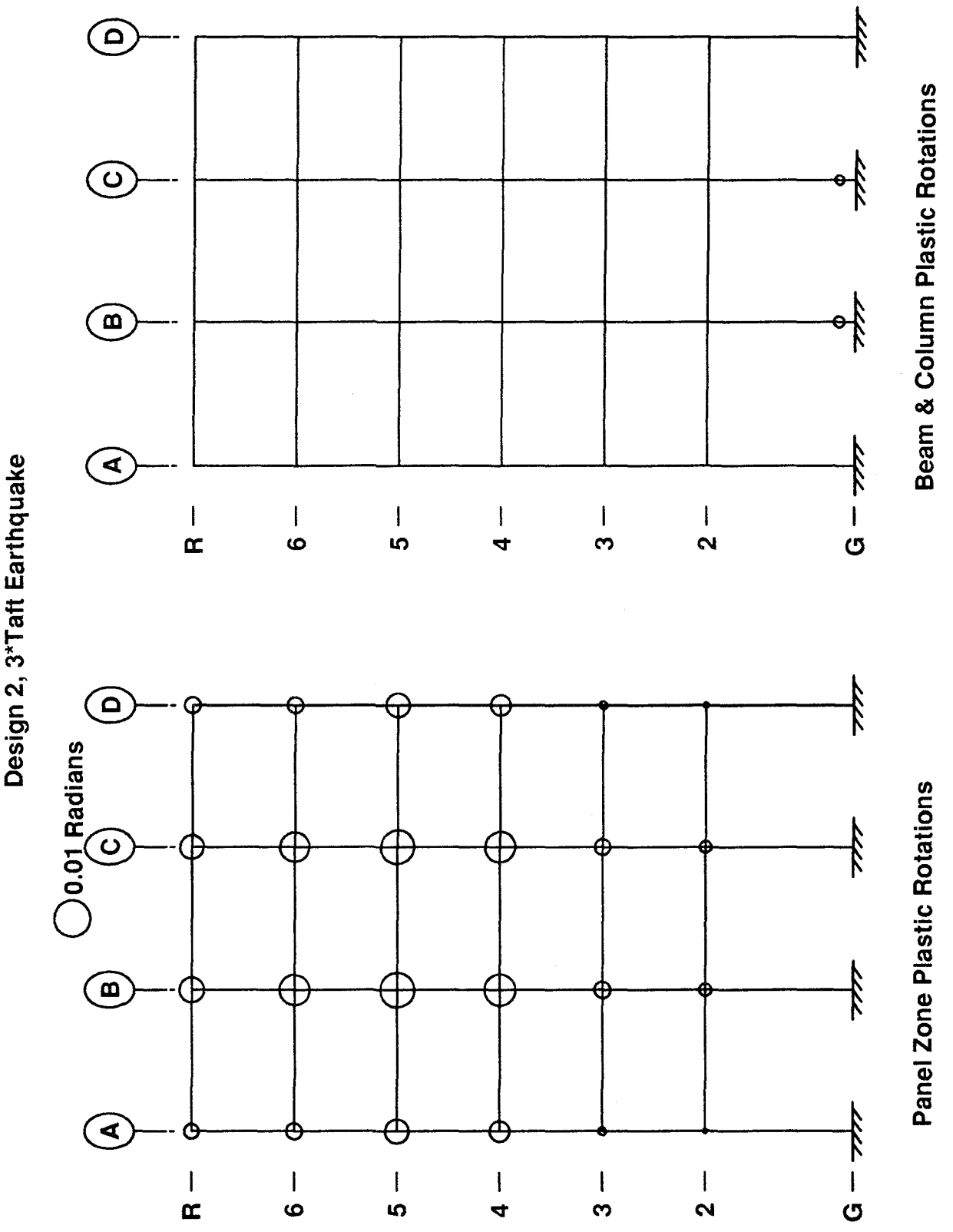

Figure 7.48 Maximum Beam, Column and Panel Zone Joint Plastic Rotations for MRF Design 2

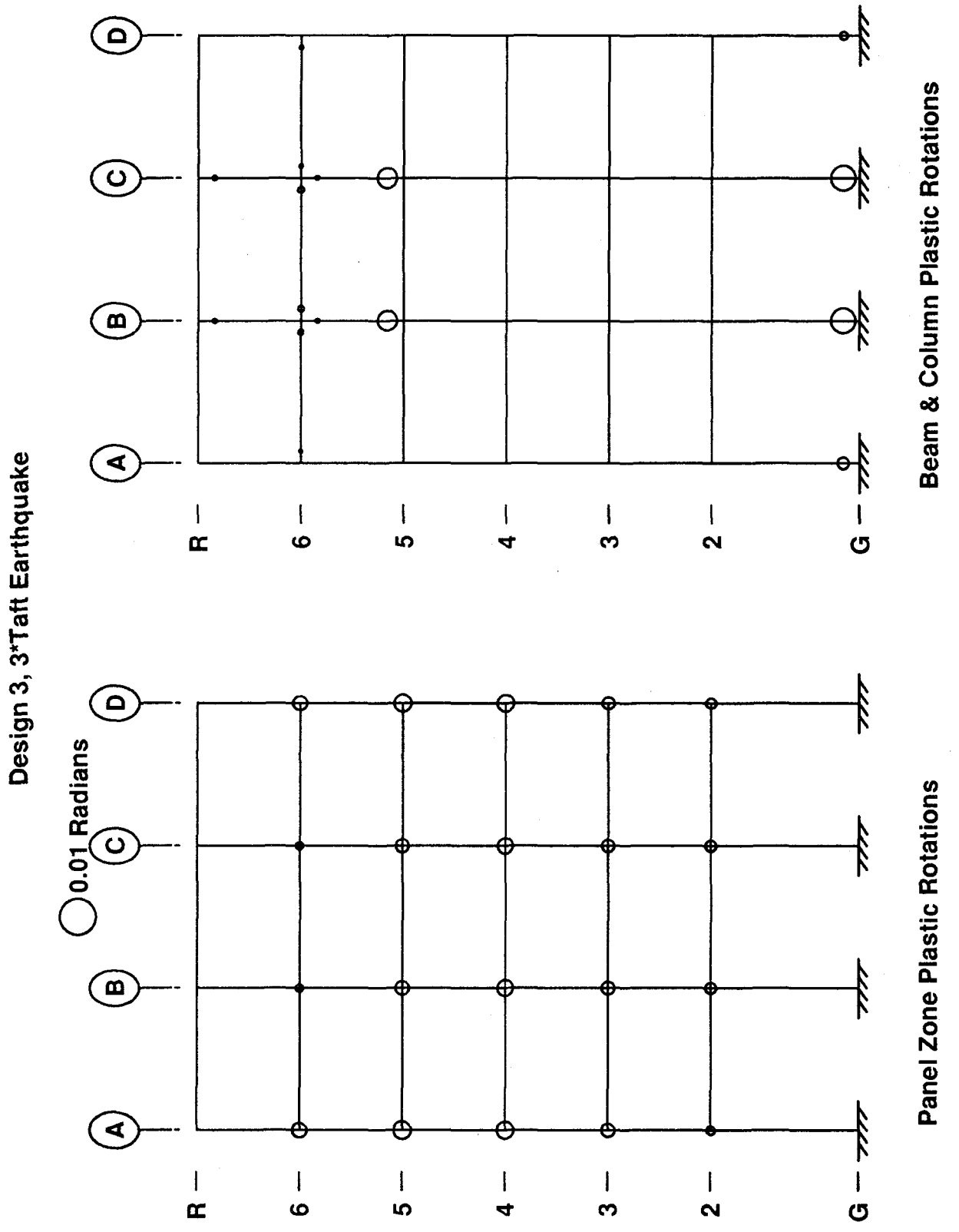

Figure 7.49 Maximum Beam, Column and Panel Zone Joint Plastic Rotations for MRF Design 3

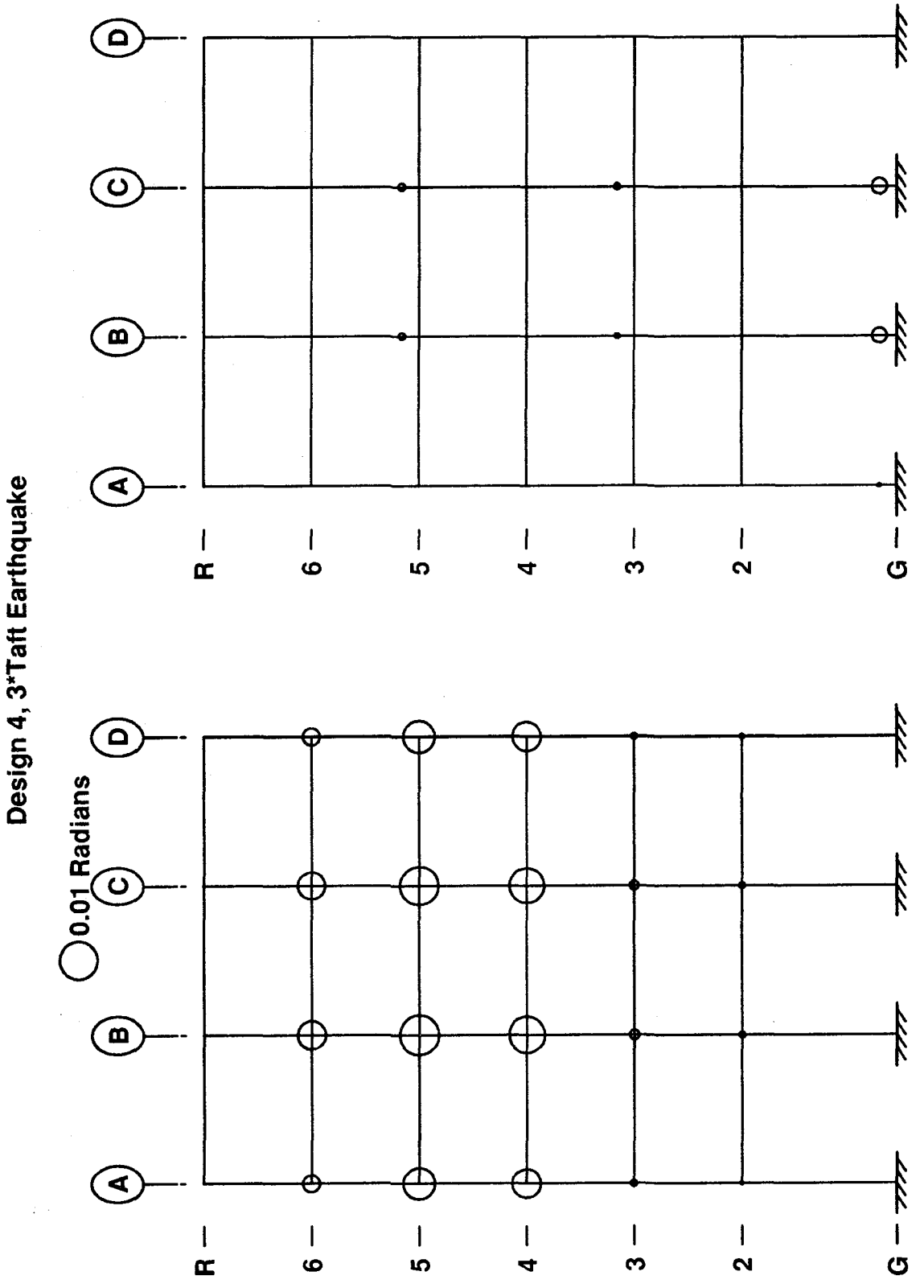

Figure 7.50 Maximum Beam, Column and Panel Zone Joint Plastic Rotations for MRF Design 4

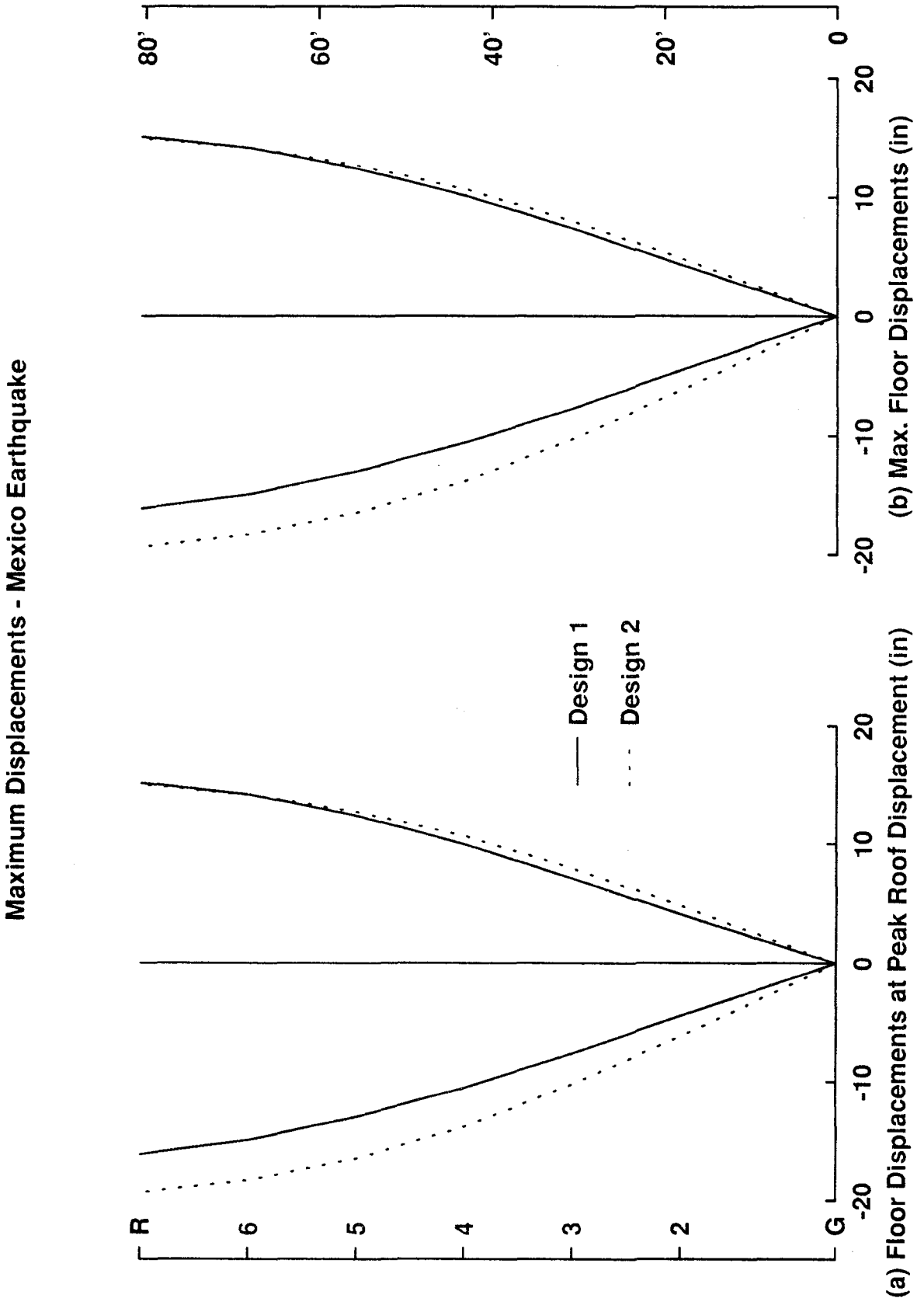

Figure 7.51 Maximum Floor Displacements for MRF Designs 1 and 2 (Mexico Earthquake)

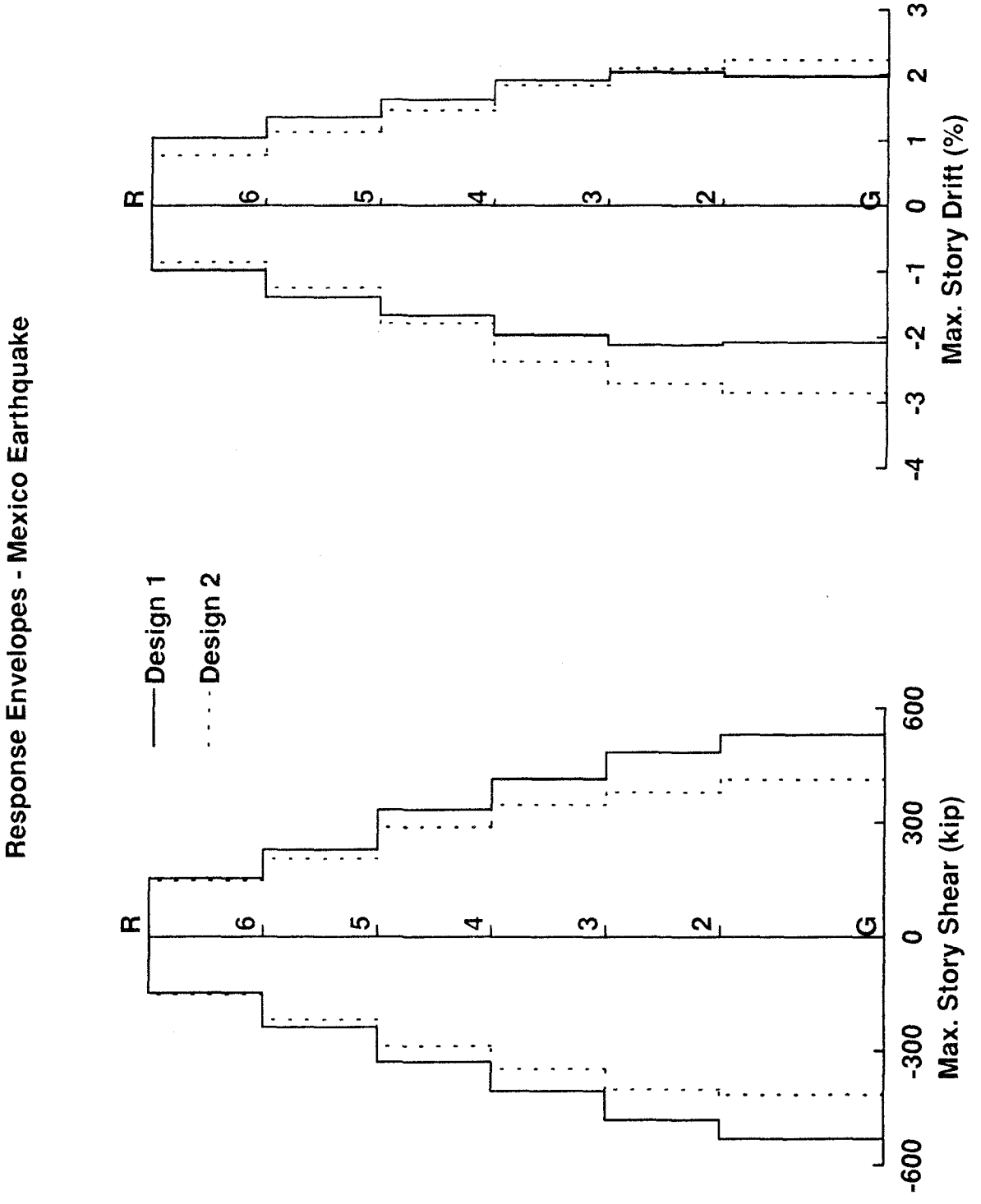

Figure 7.52 Maximum Story Shears and Story Drifts for MRF Designs 1 and 2 (Mexico Earthquake)

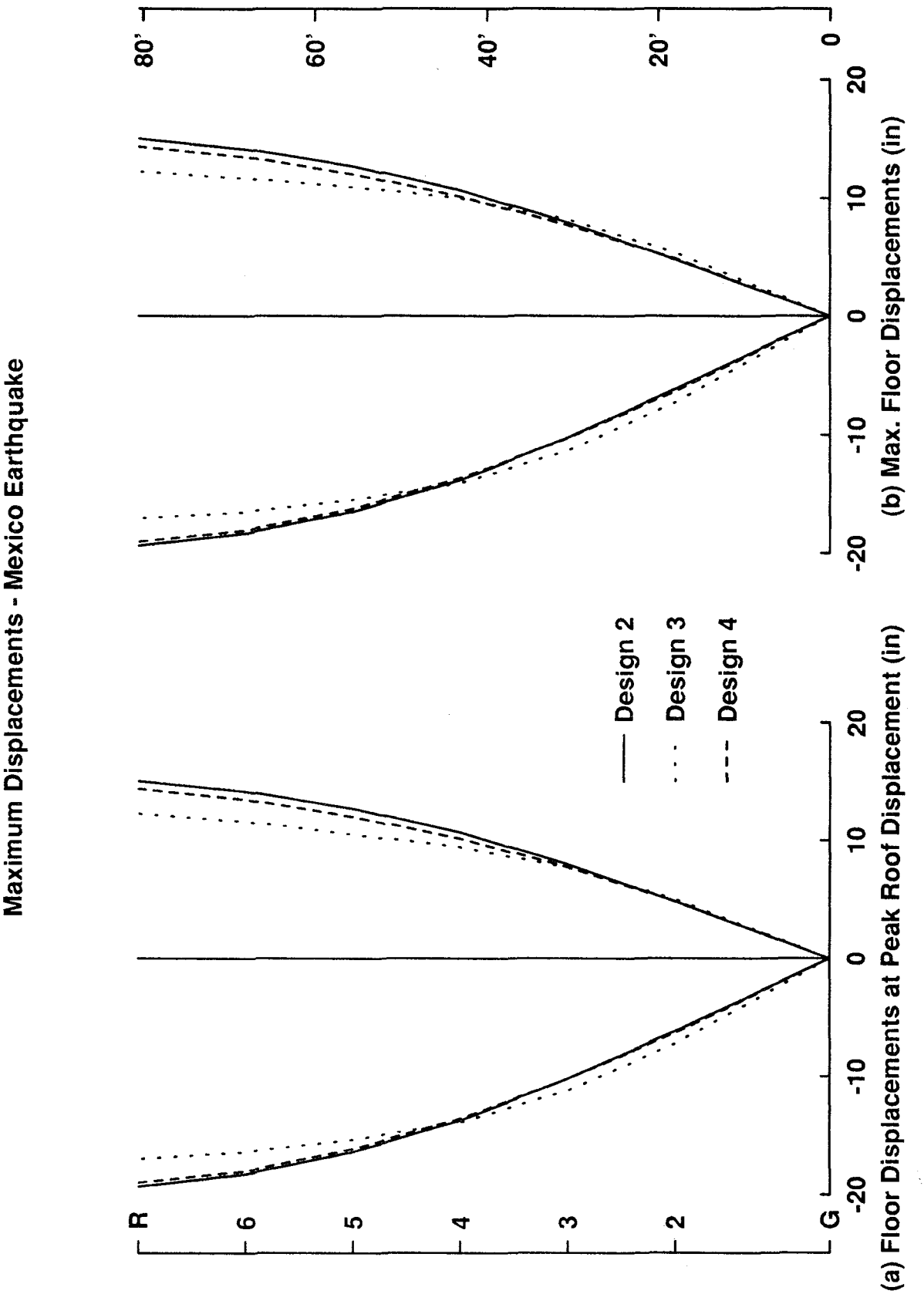

Figure 7.53 Maximum Floor Displacements for MRF Designs 2, 3 and 4 (Mexico Earthquake)

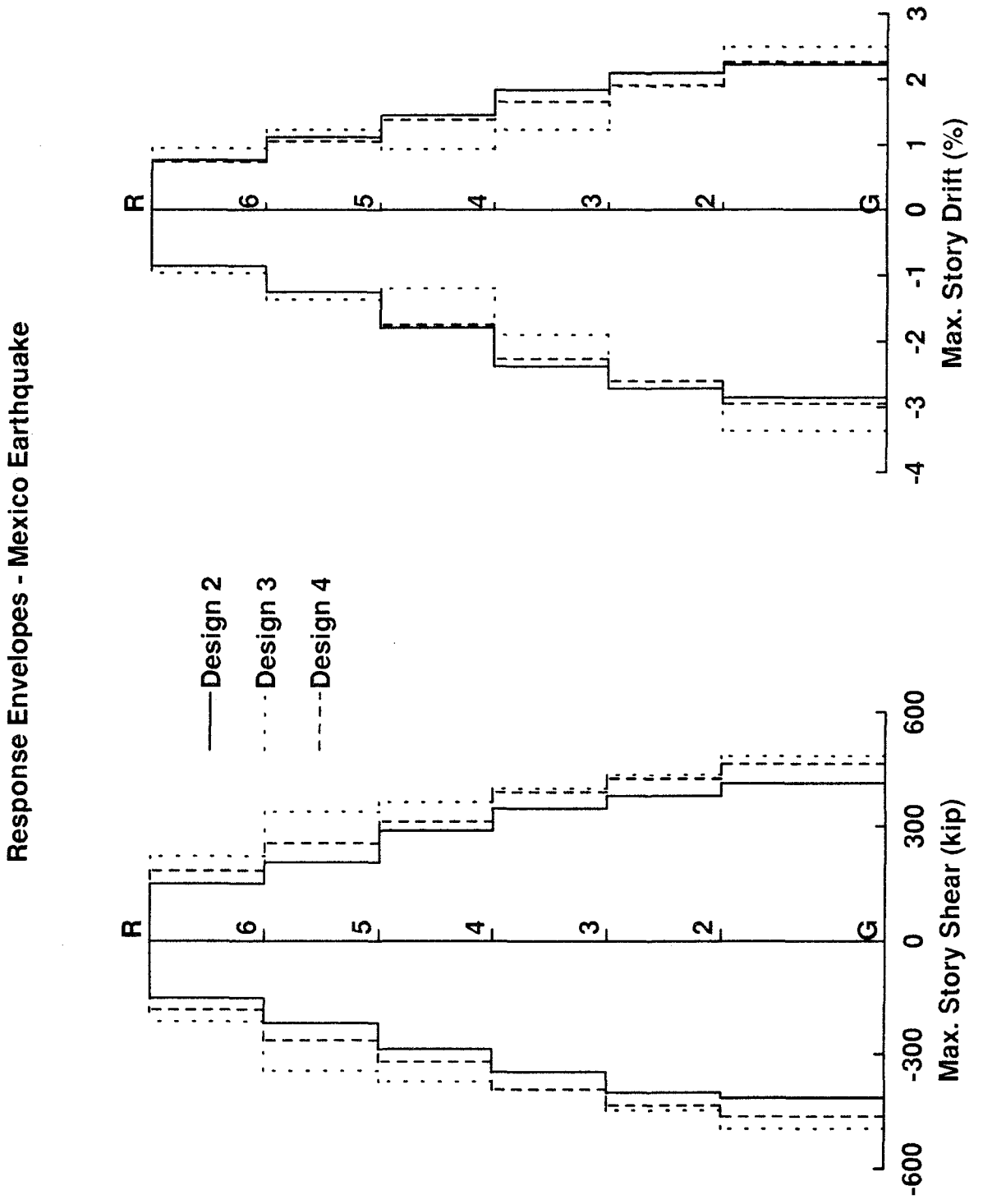

Figure 7.54 Maximum Story Shears and Story Drifts for MRF Designs 2, 3 and 4 (Mexico Earthquake)

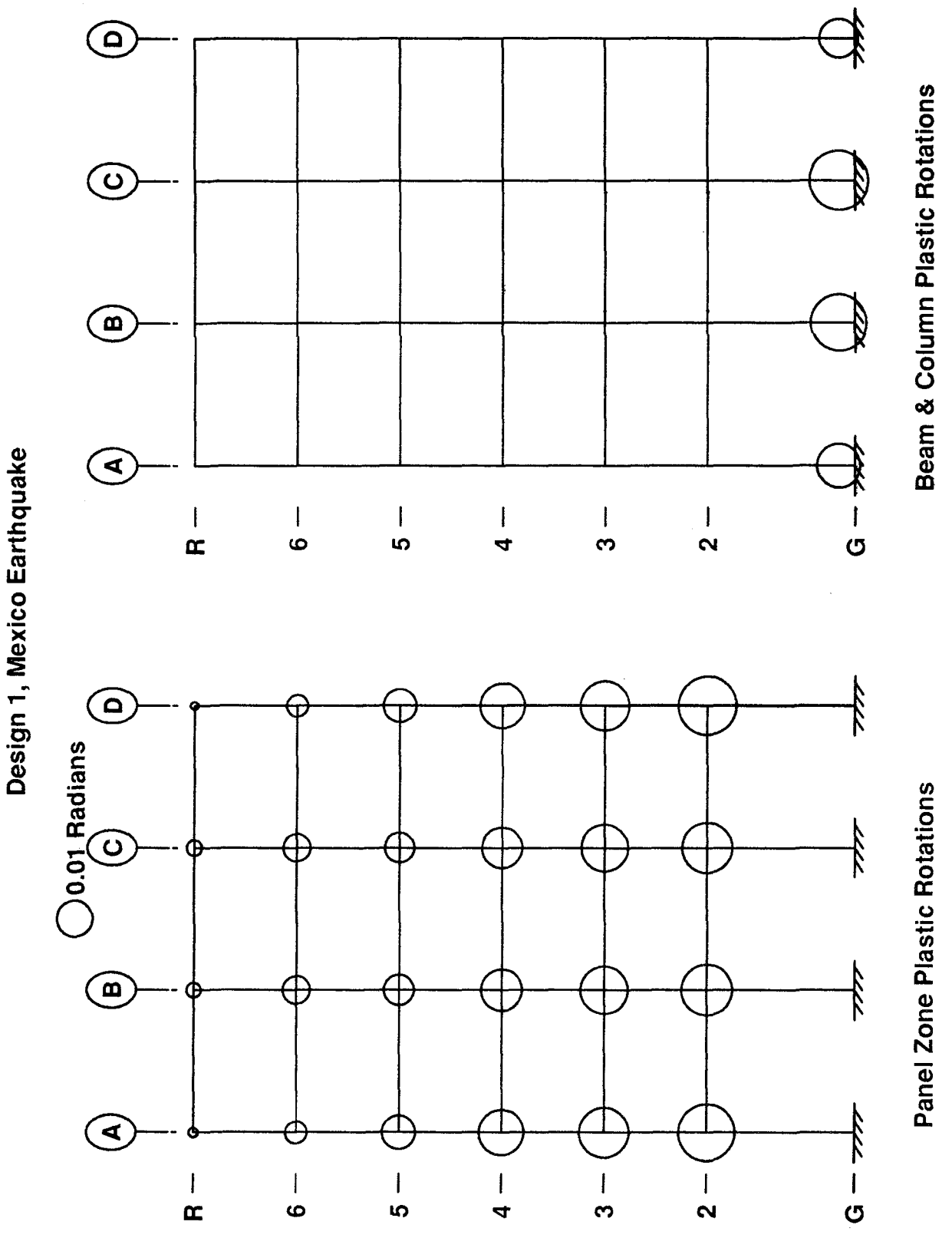

Figure 7.55 Maximum Beam, Column and Panel Zone Joint Plastic Rotations for MRF Design 1

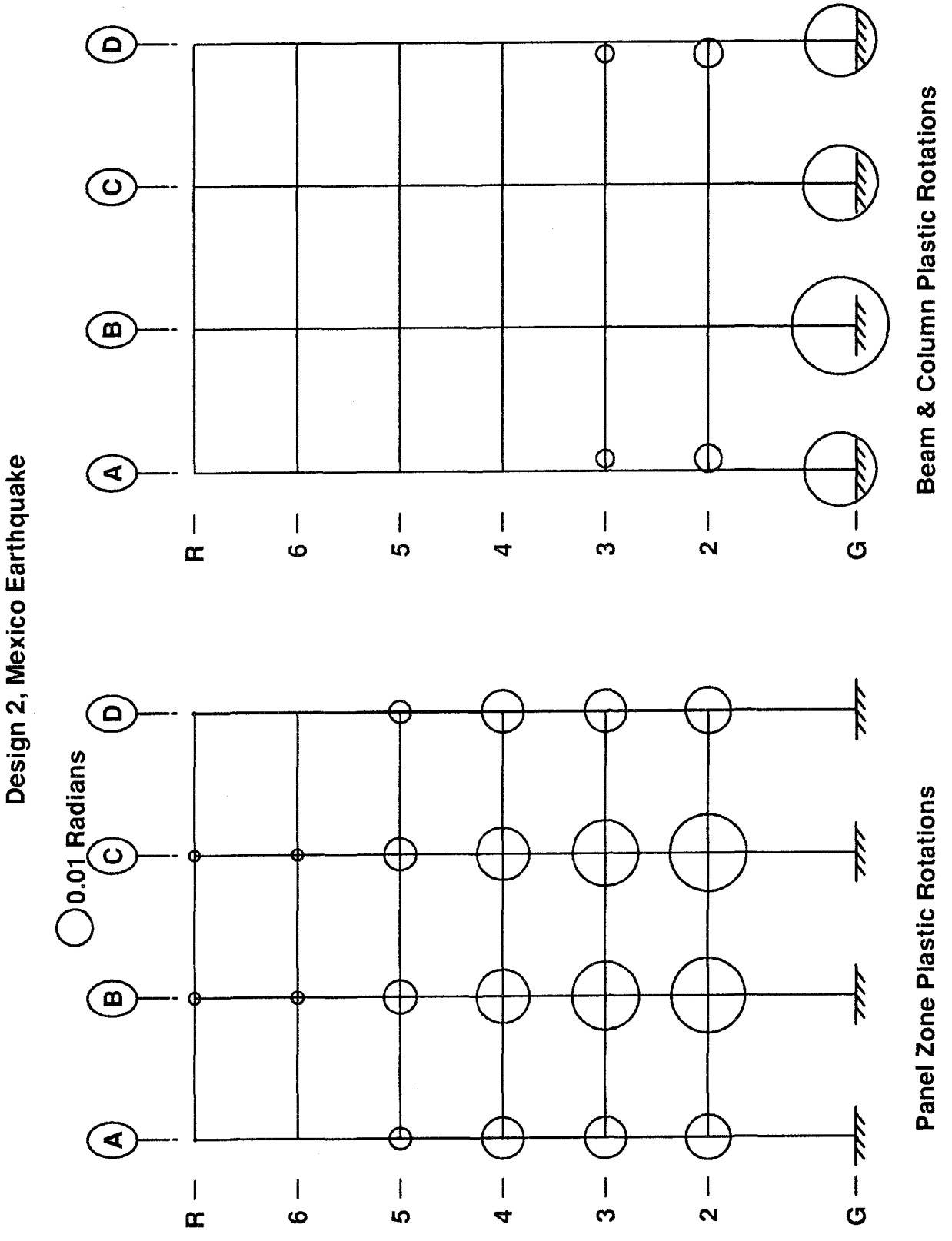

Figure 7.56 Maximum Beam, Column and Panel Zone Joint Plastic Rotations for MRF Design 2

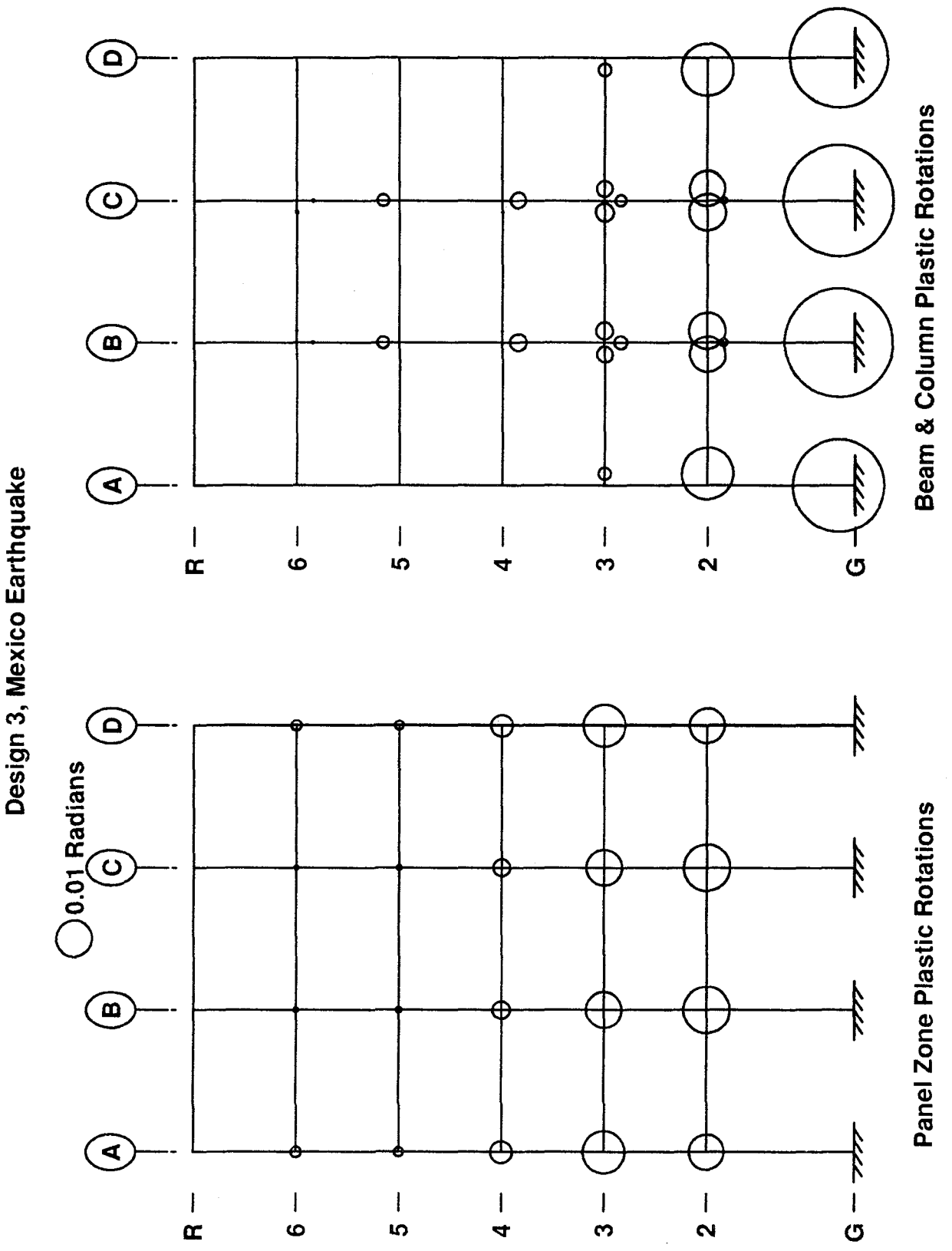

Figure 7.57 Maximum Beam, Column and Panel Zone Joint Plastic Rotations for MRF Design 3

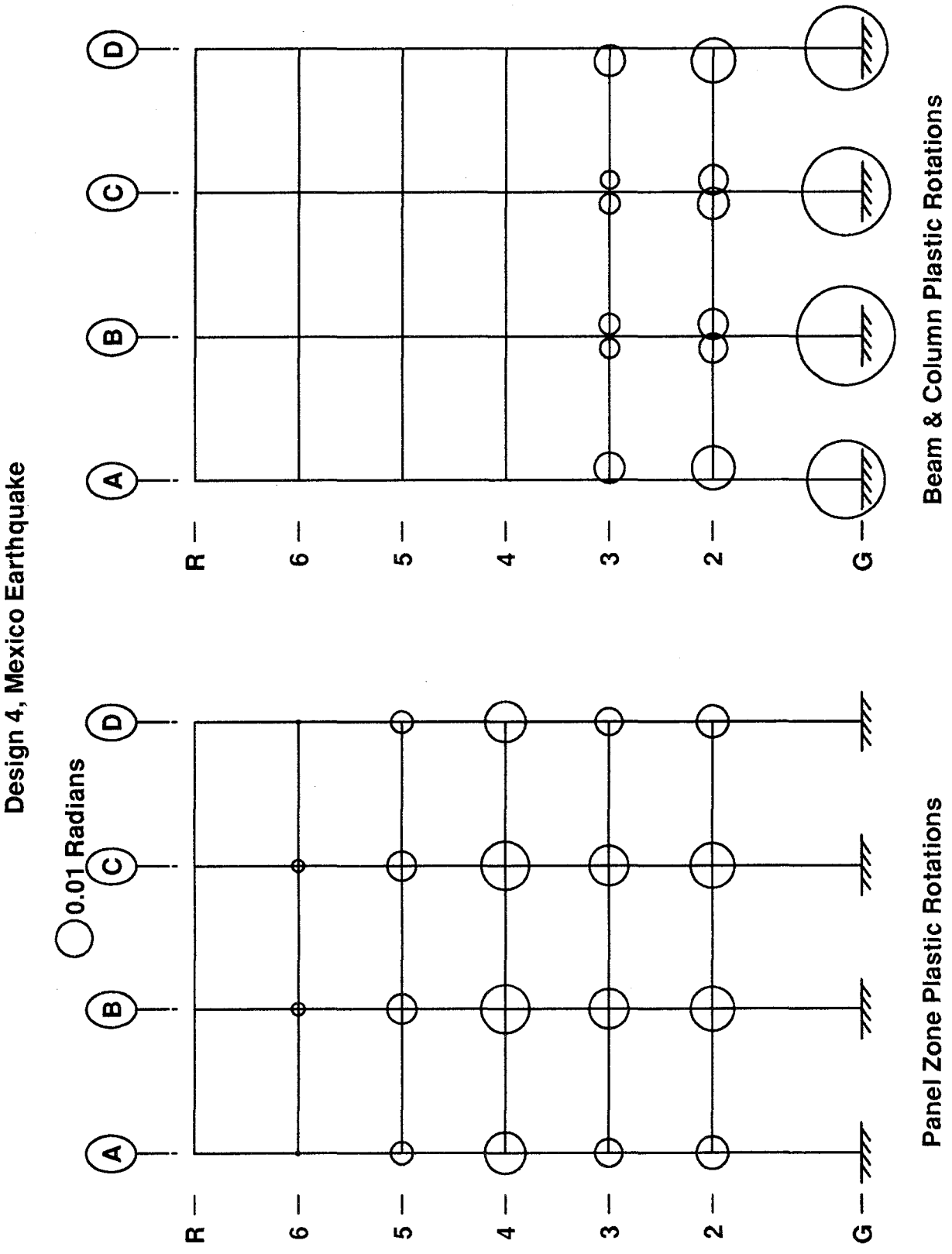

Figure 7.58 Maximum Beam, Column and Panel Zone Joint Plastic Rotations for MRF Design 4

Parkfield, N65E 1966

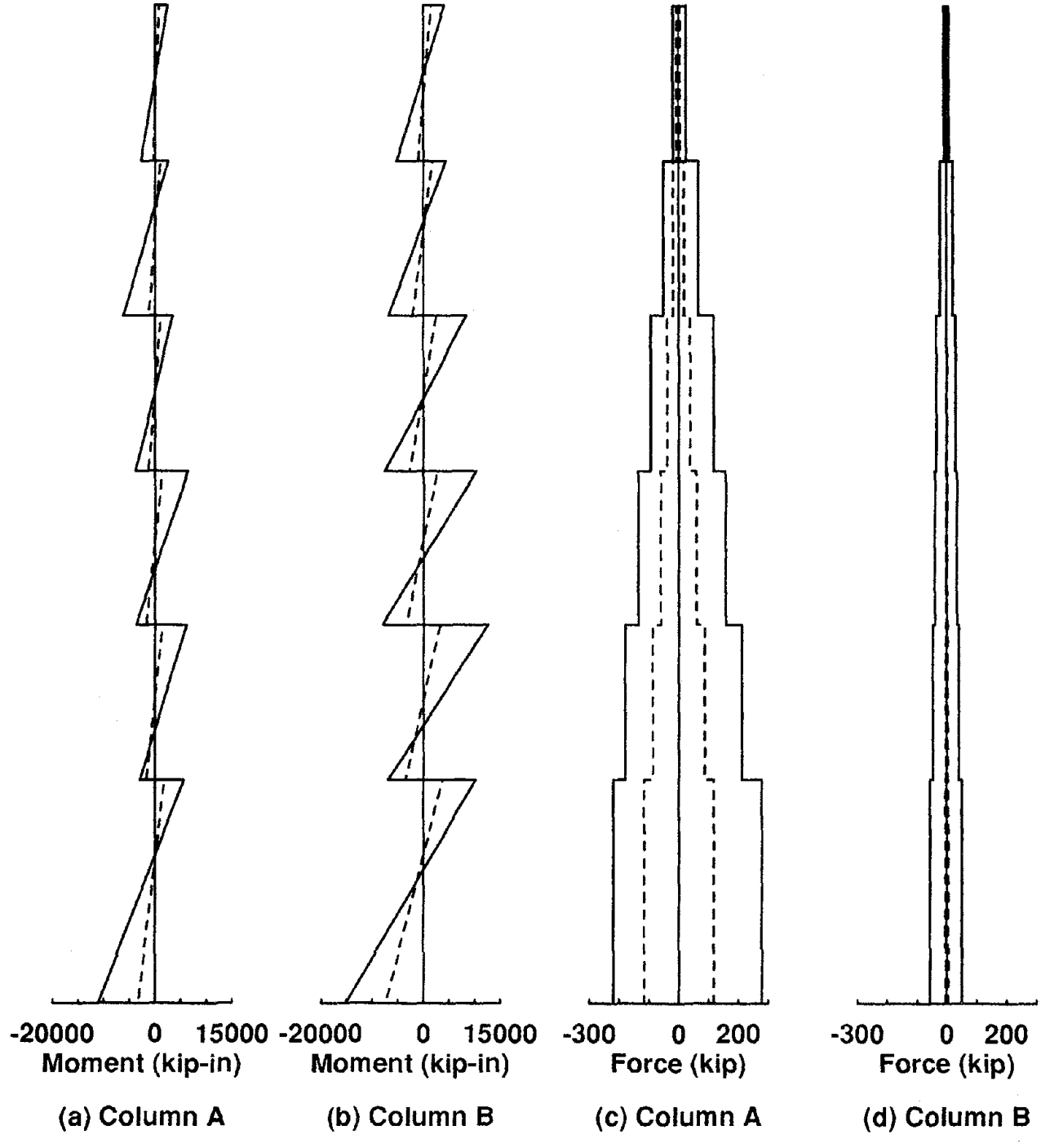

Figure 7.59 Maximum Column Moment and Axial Force Envelopes (Design 2)

Parkfield, N65E 1966
Column Moment Diagrams at Maximum Column Bottom Moments

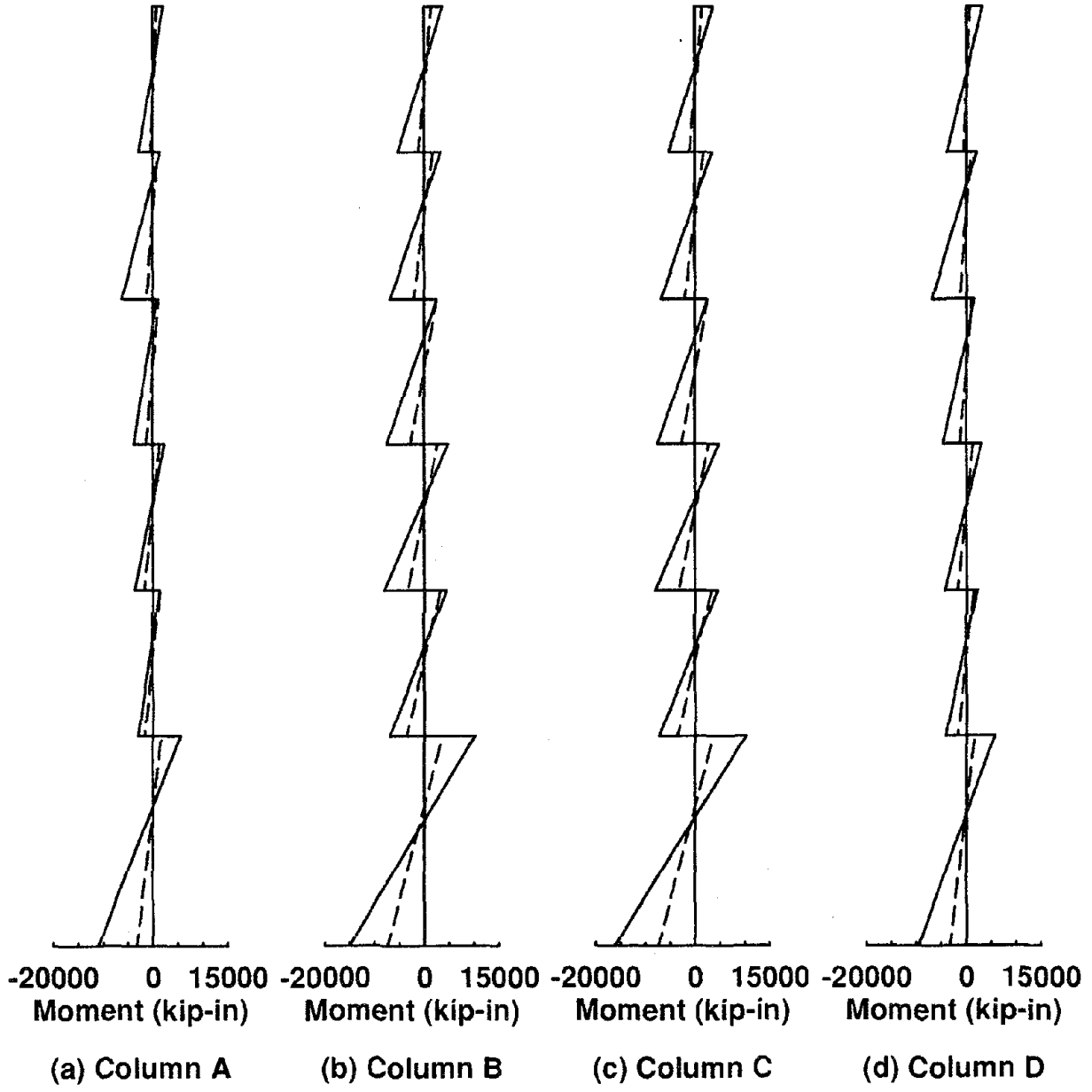

Figure 7.60 Column Moment Diagram at Instant of Maximum Column Bottom End Moment

Parkfield, N65E 1966
Column Moment Diagrams at Maximum Top Column Moments

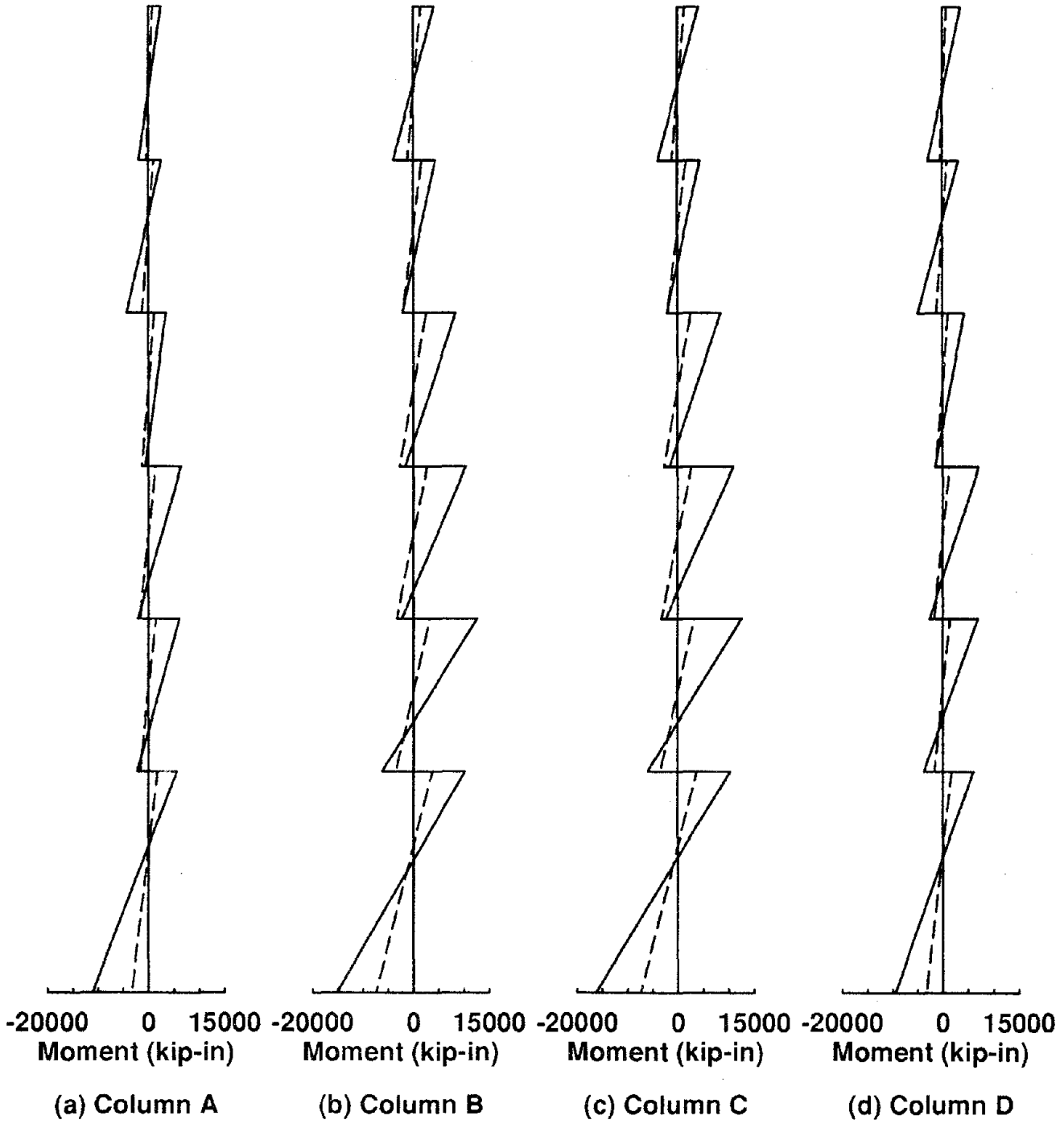

Figure 7.61 Column Moment Diagram at Instant of Maximum Column Top End Moment

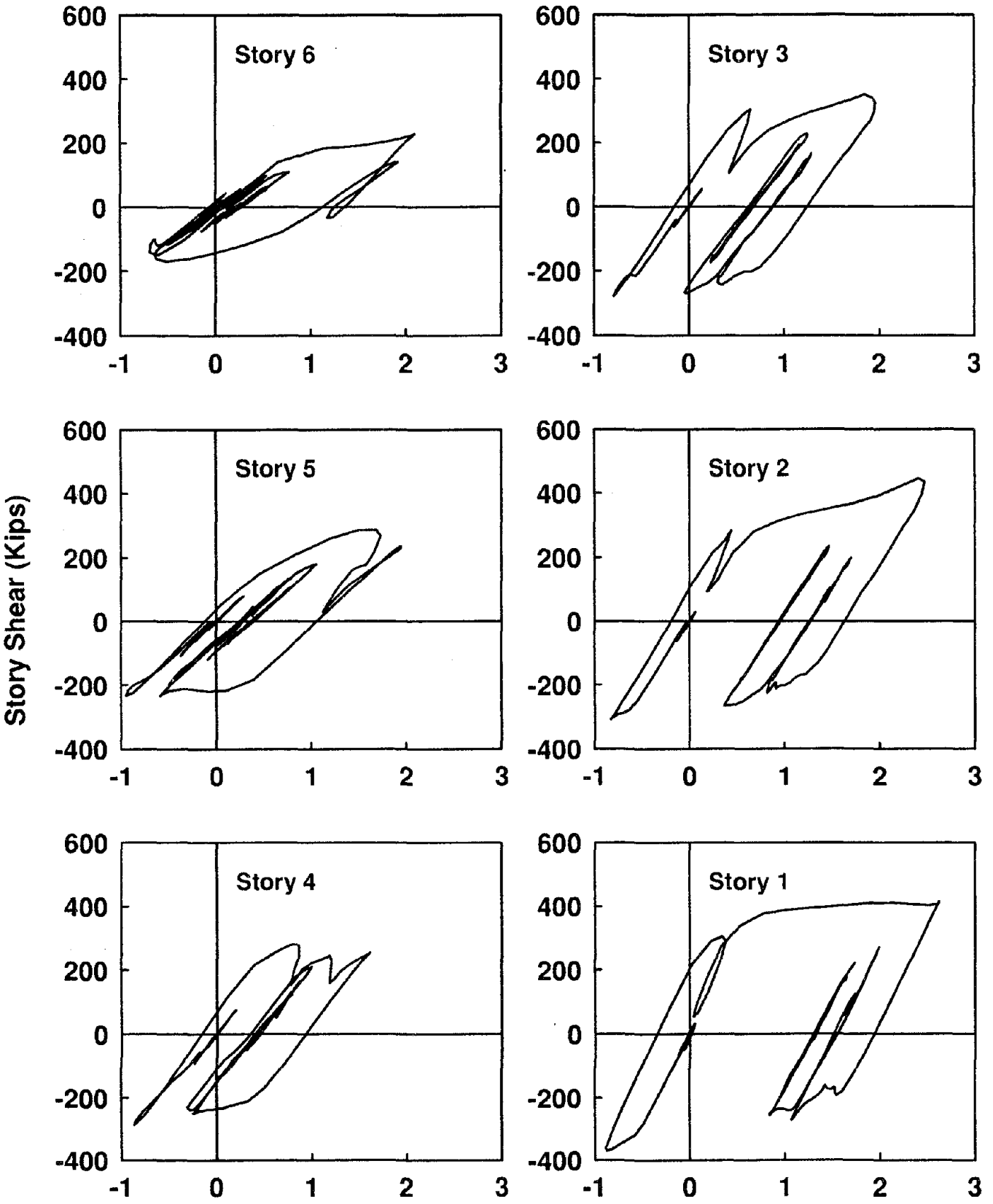

Figure 7.62 Story Shear versus Story Drift Hysteretic Loops (Design 2)

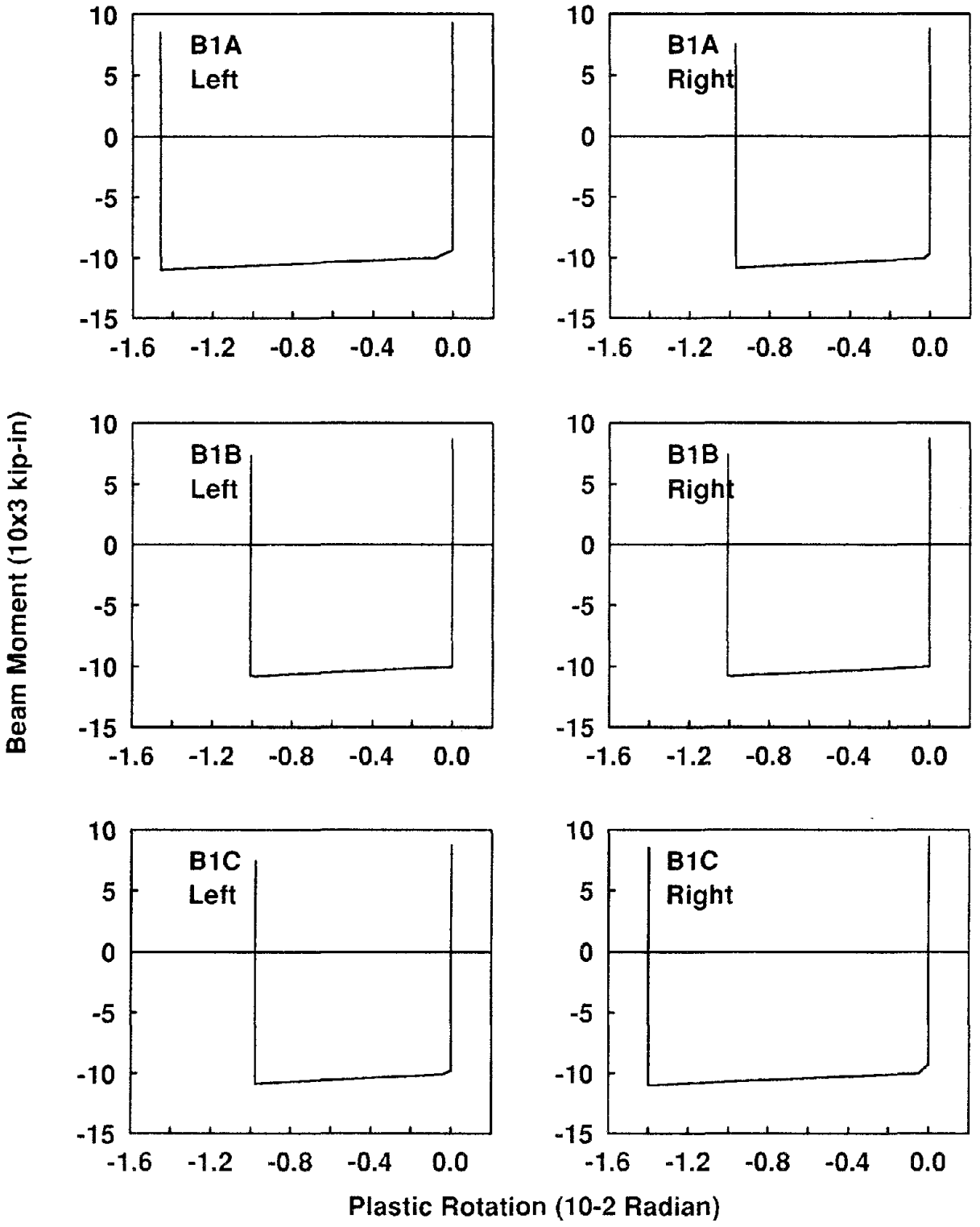

Figure 7.63 Beam End Moment versus Beam Plastic Rotation Hysteretic Loops (Design 3)

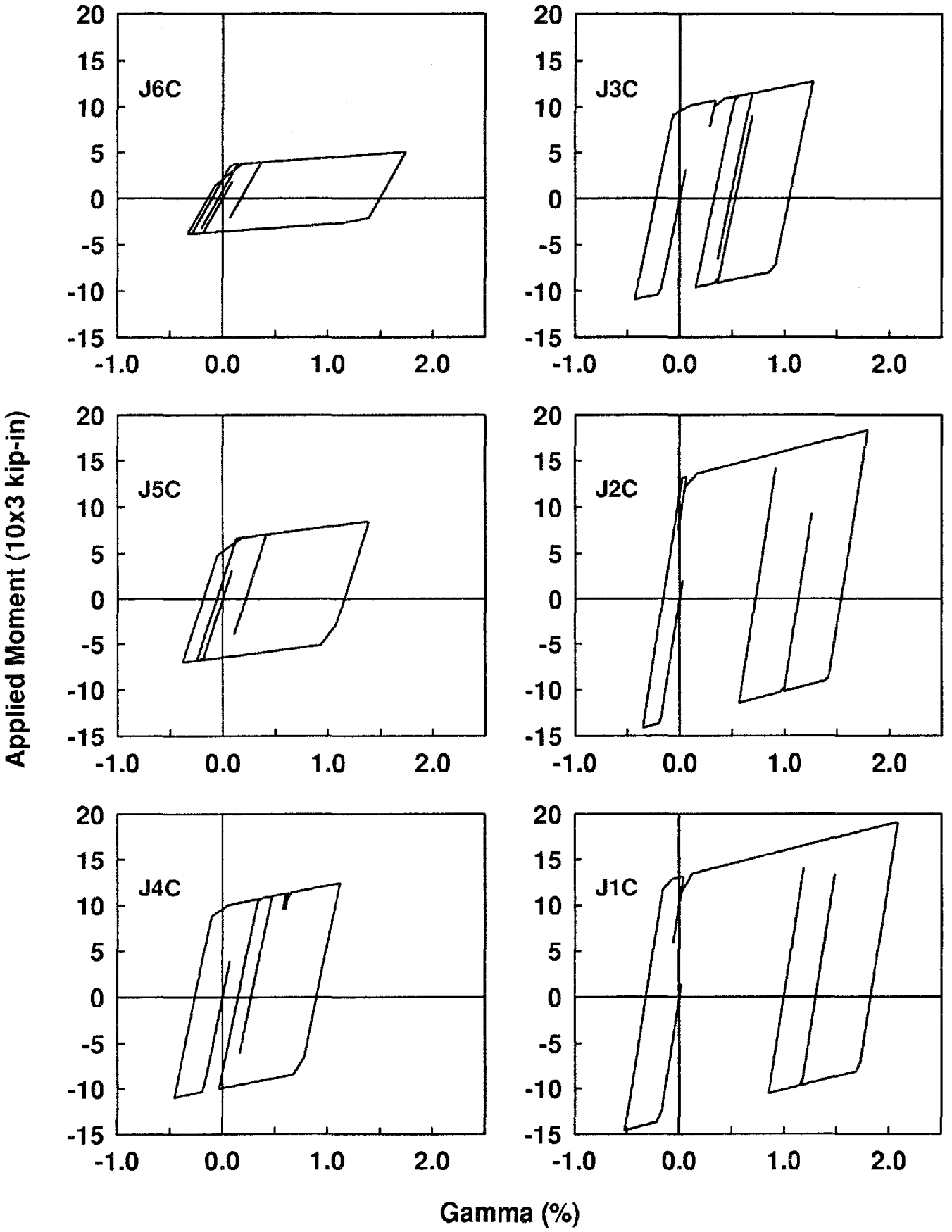

Figure 7.64 Interior Panel Zone Deformation versus Applied Moment Hysteretic Loops (Design 2)

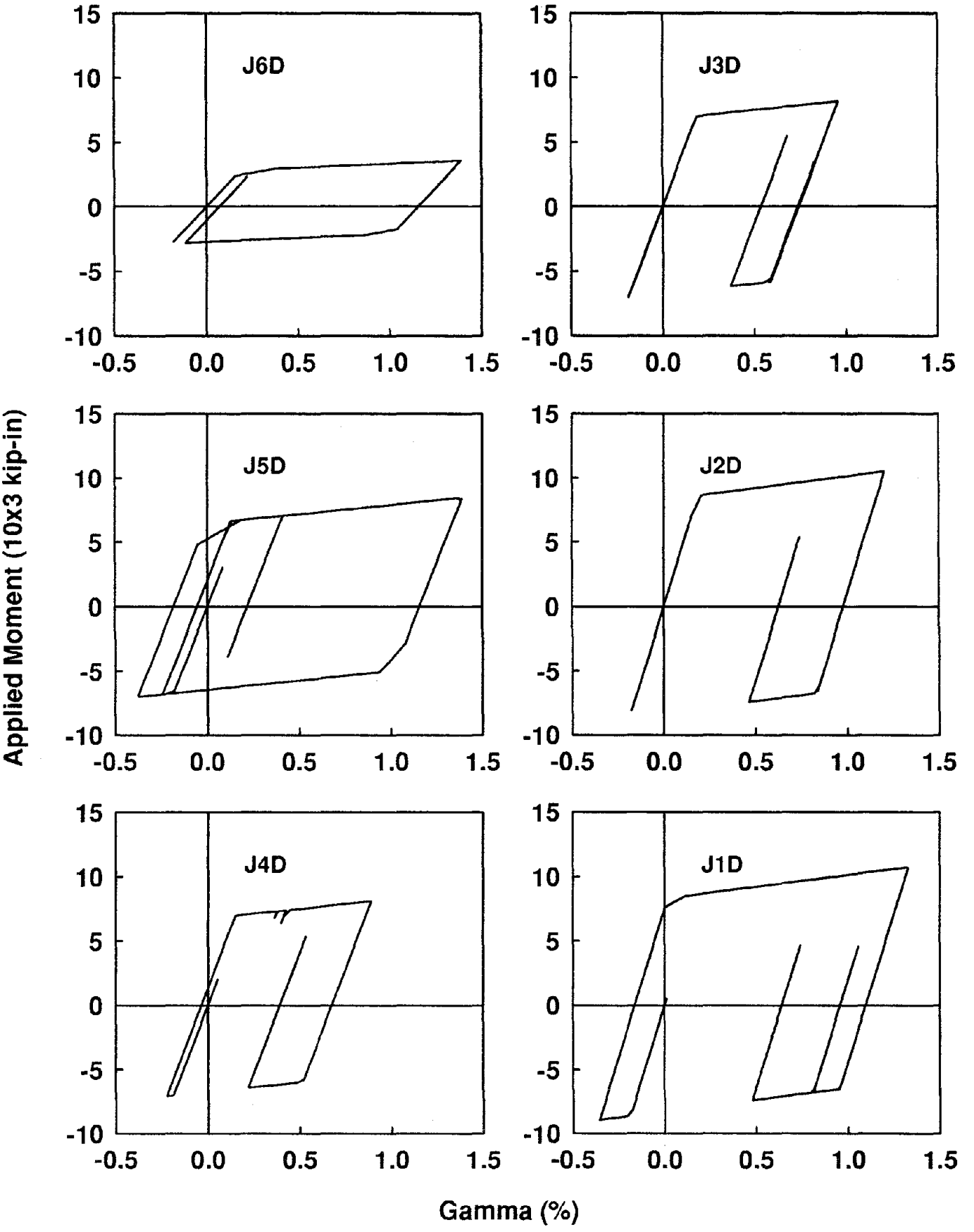

Figure 7.65 Exterior Panel Zone Deformation versus Applied Moment Hysteretic Loops (Design 2)

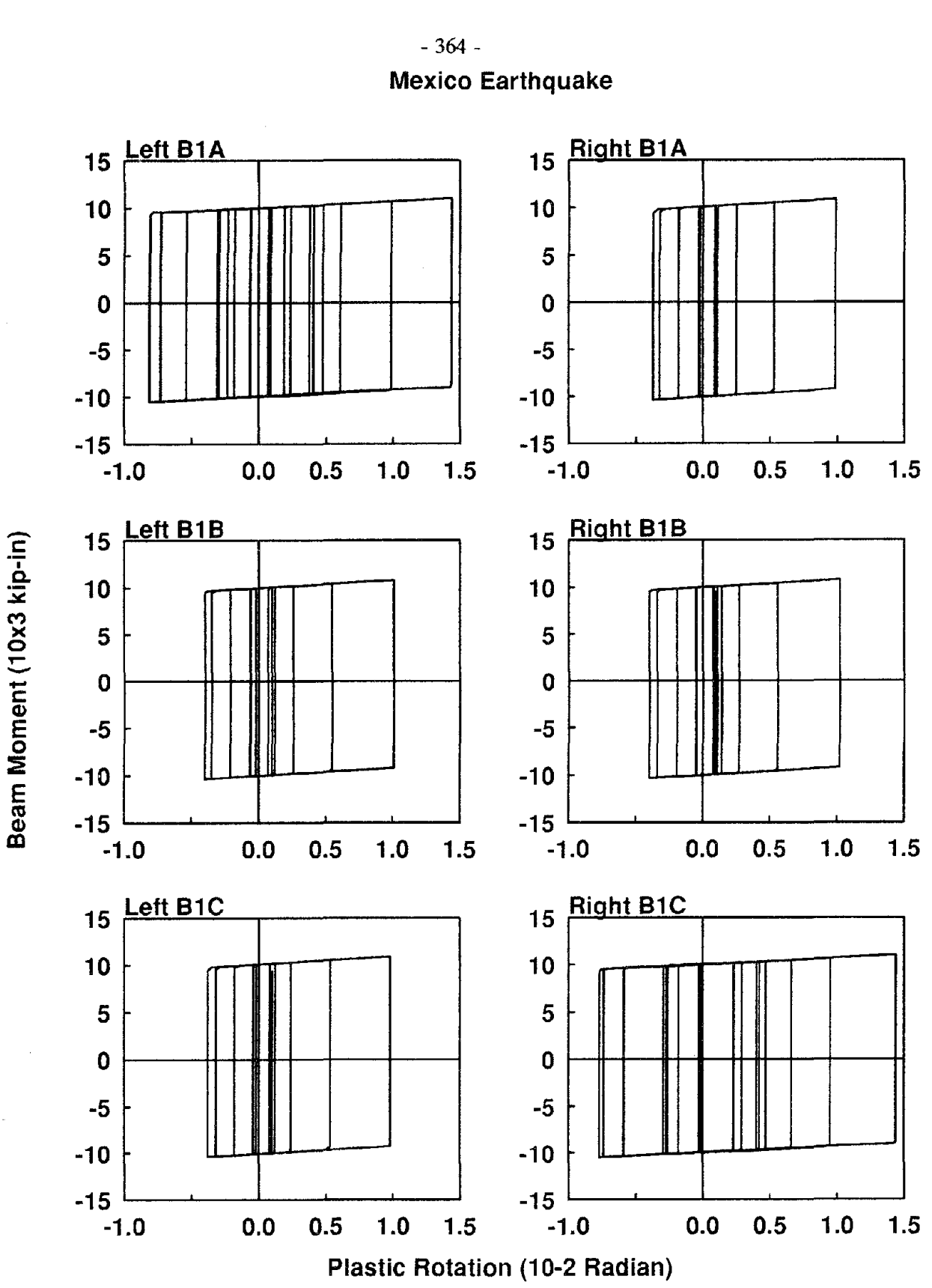

Figure 7.66 Beam End Moment versus Beam Plastic Rotation Hysteretic Loops (Design 2)

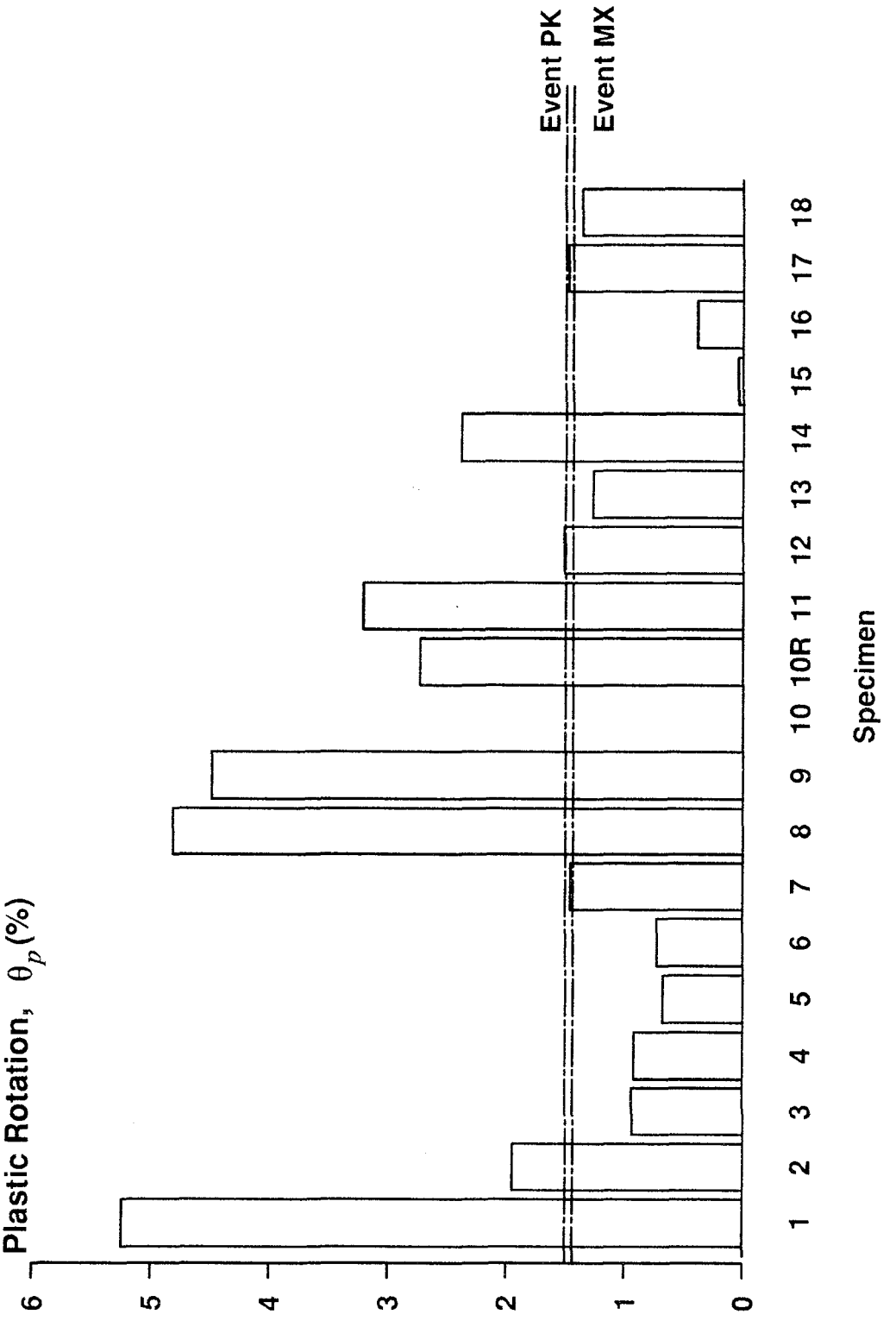

Figure 7.67 Comparison of Beam Plastic Rotation Demand and Supply (Measured from Origin)

Figure 7.68 Comparison of Beam Plastic Rotation Demand and Supply (Measured from Zero-Intercept)

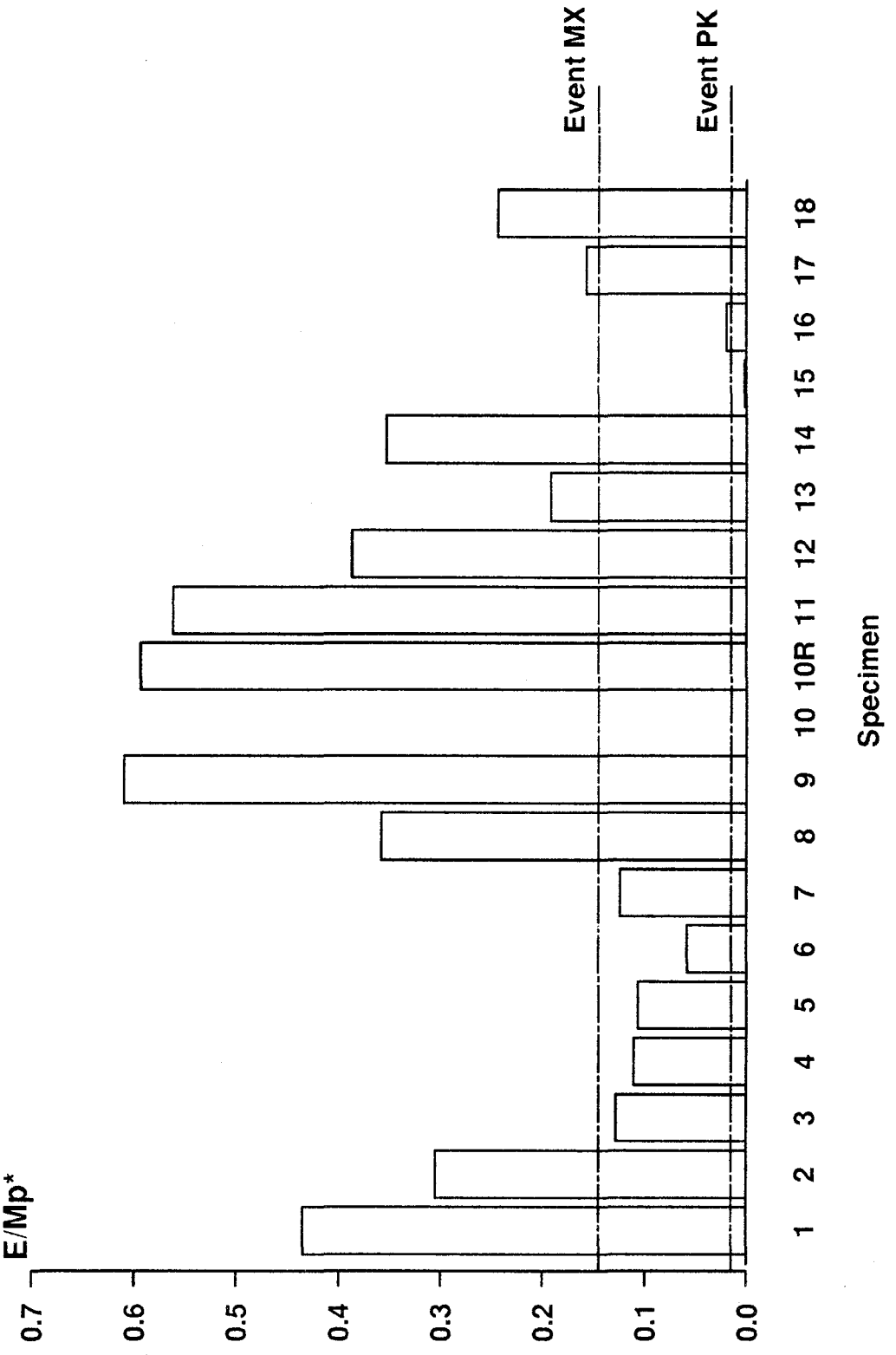

Figure 7.69 Comparison of Normalized Dissipated Energy Demand and Supply

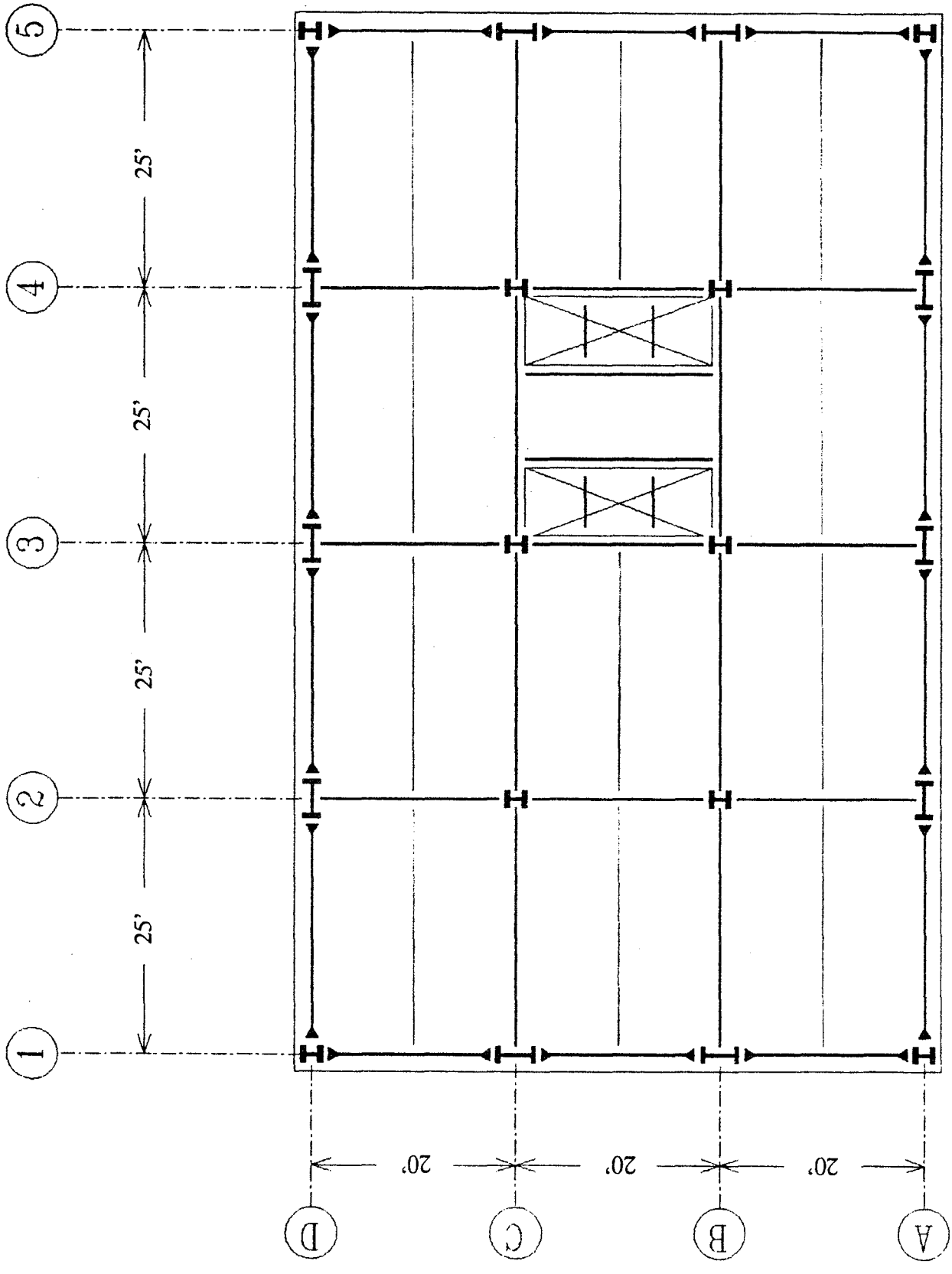

Figure 8.1 Typical Floor Framing Plan for The Twenty-Story Office Building

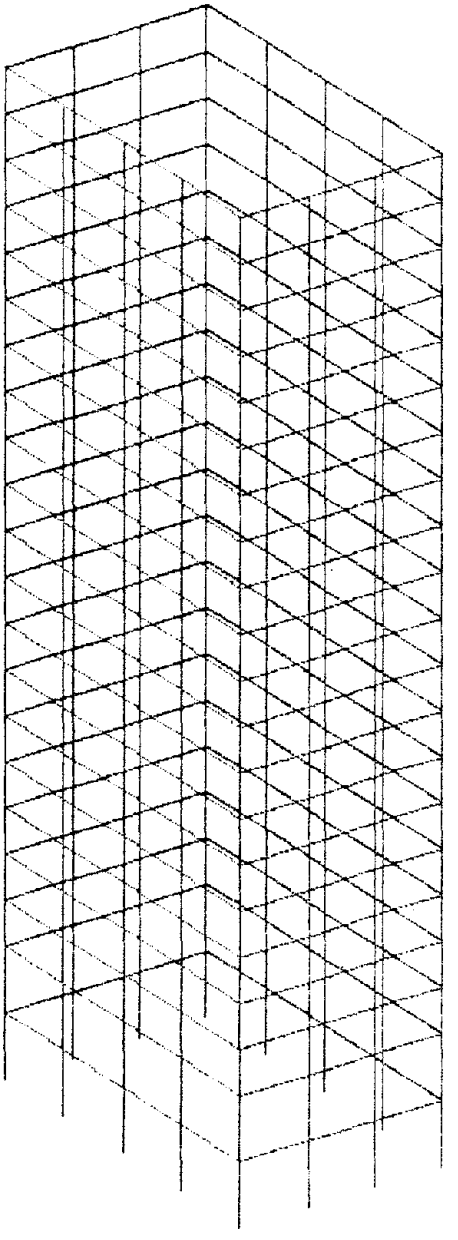

Figure 8.2 Isometric View of The Perimeter Frame

Design 1

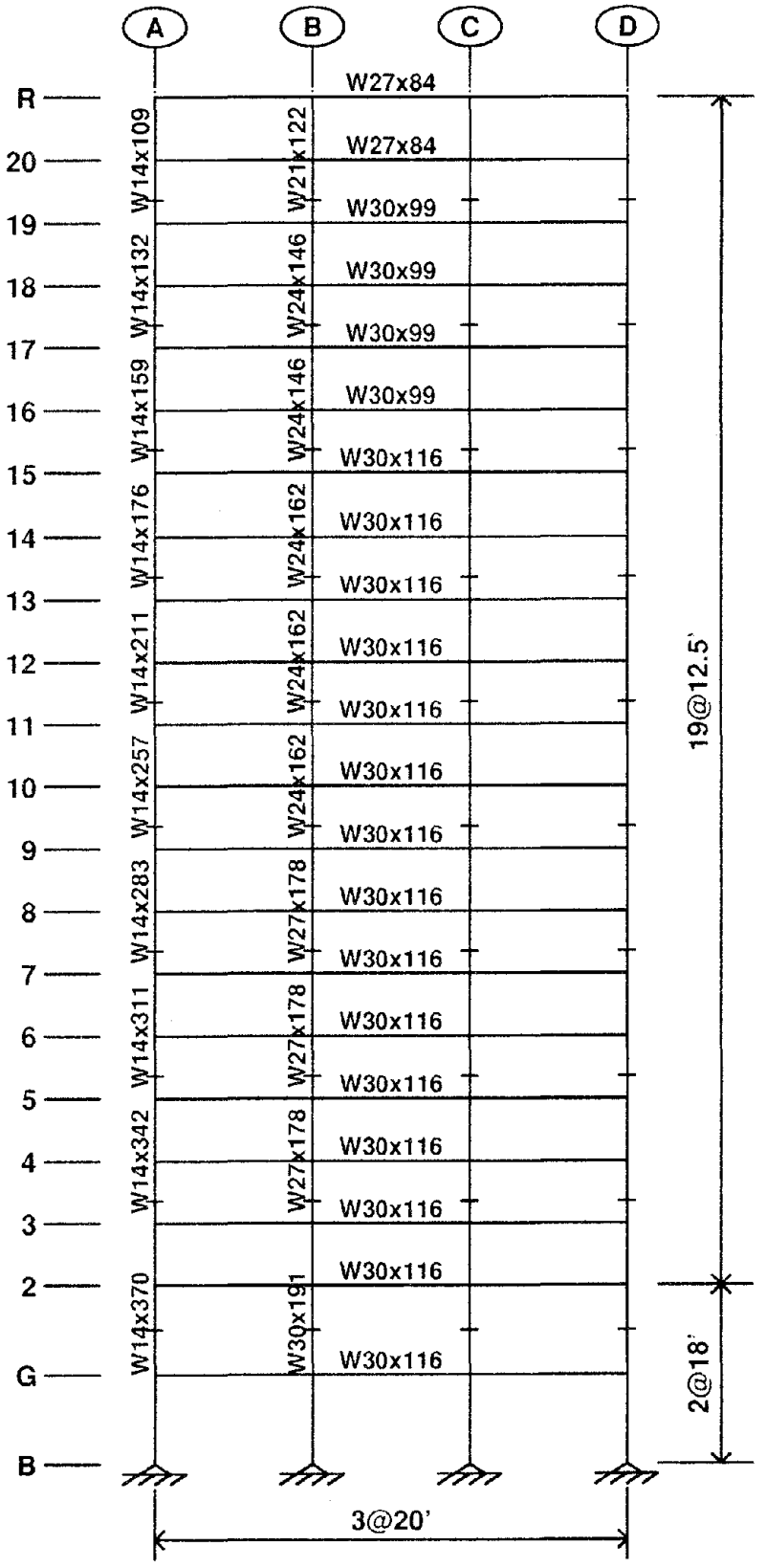

Figure 8.3 Frame Elevation and Member Sizes for MRF Design 1

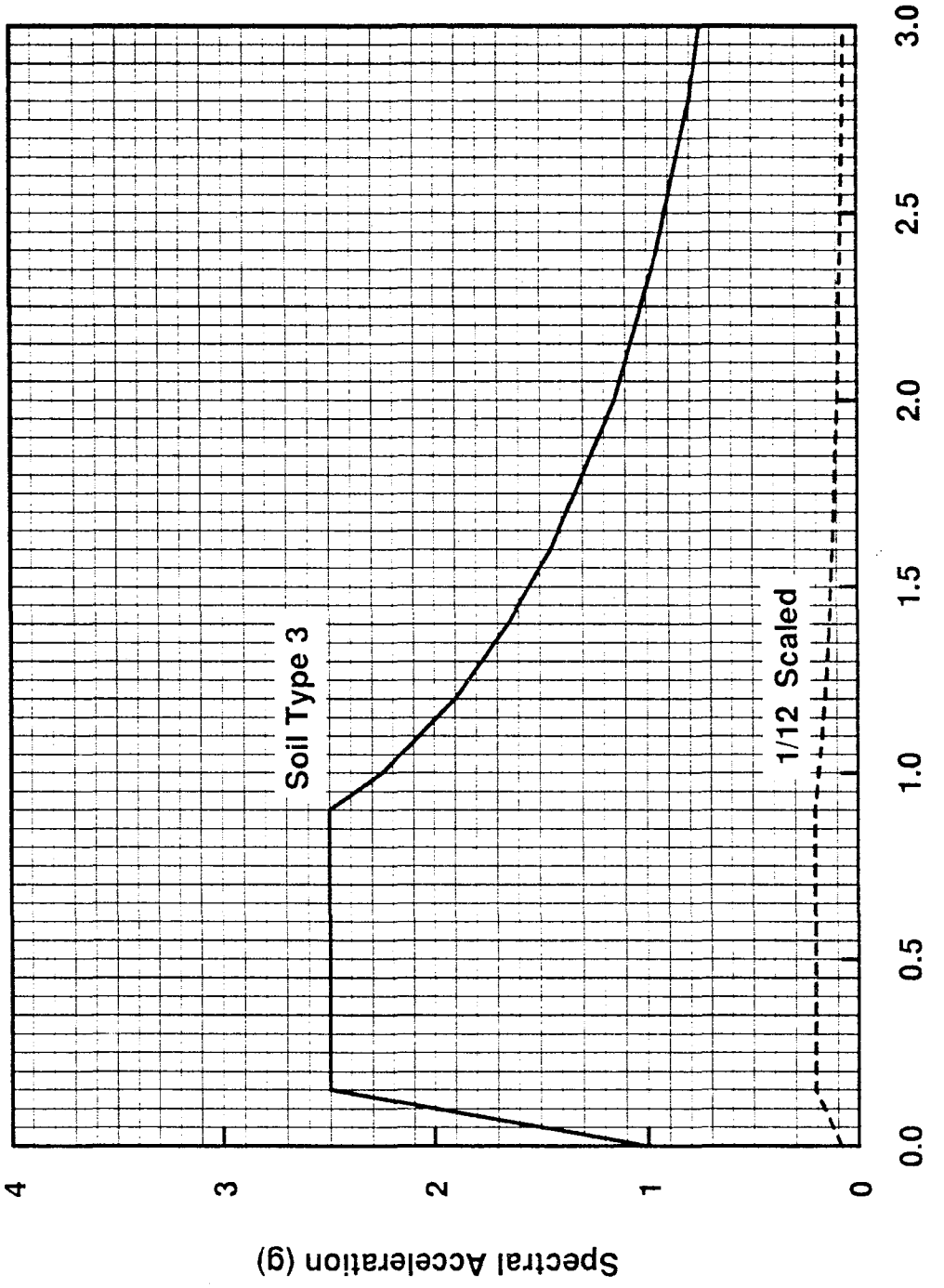

Figure 8.4 Normalized and $\frac{1}{12}$ Scaled Response Spectrum for Soil Type 3

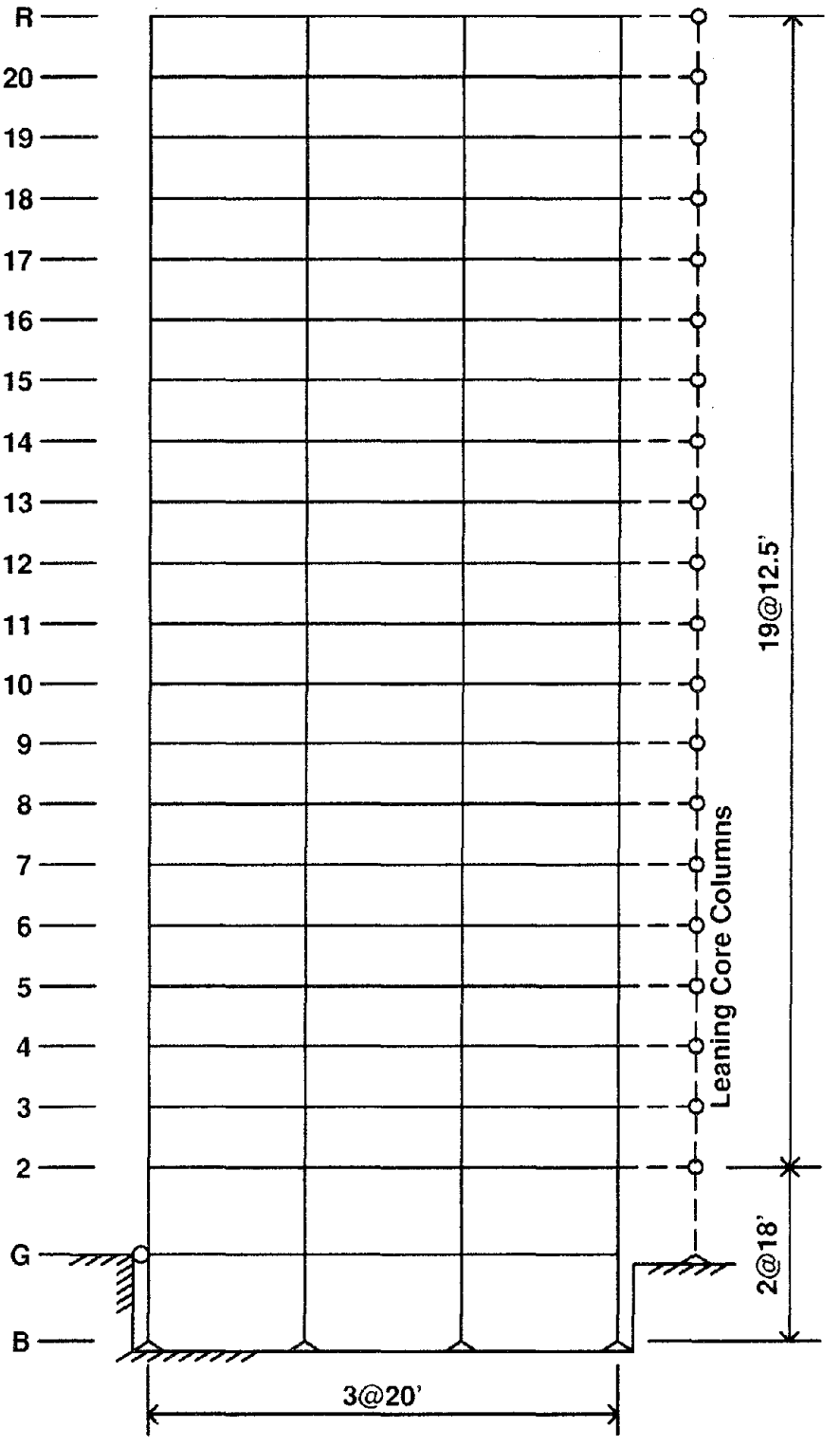

Figure 8.5 Two-Dimensional Frame with The Leaning Core Column Model

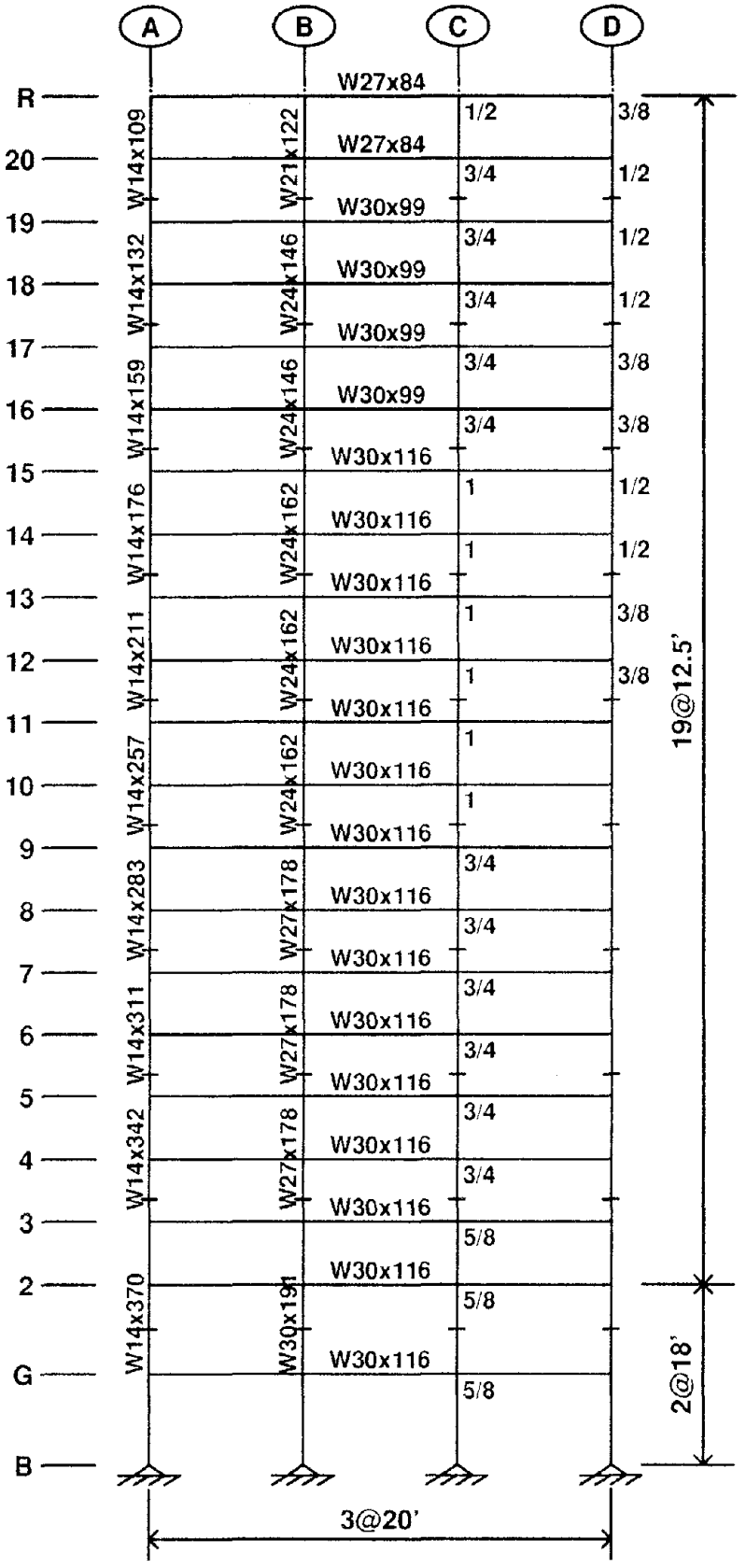

Figure 8.6 Member Sizes and Doubler Plate Thicknesses for MRF Design 2

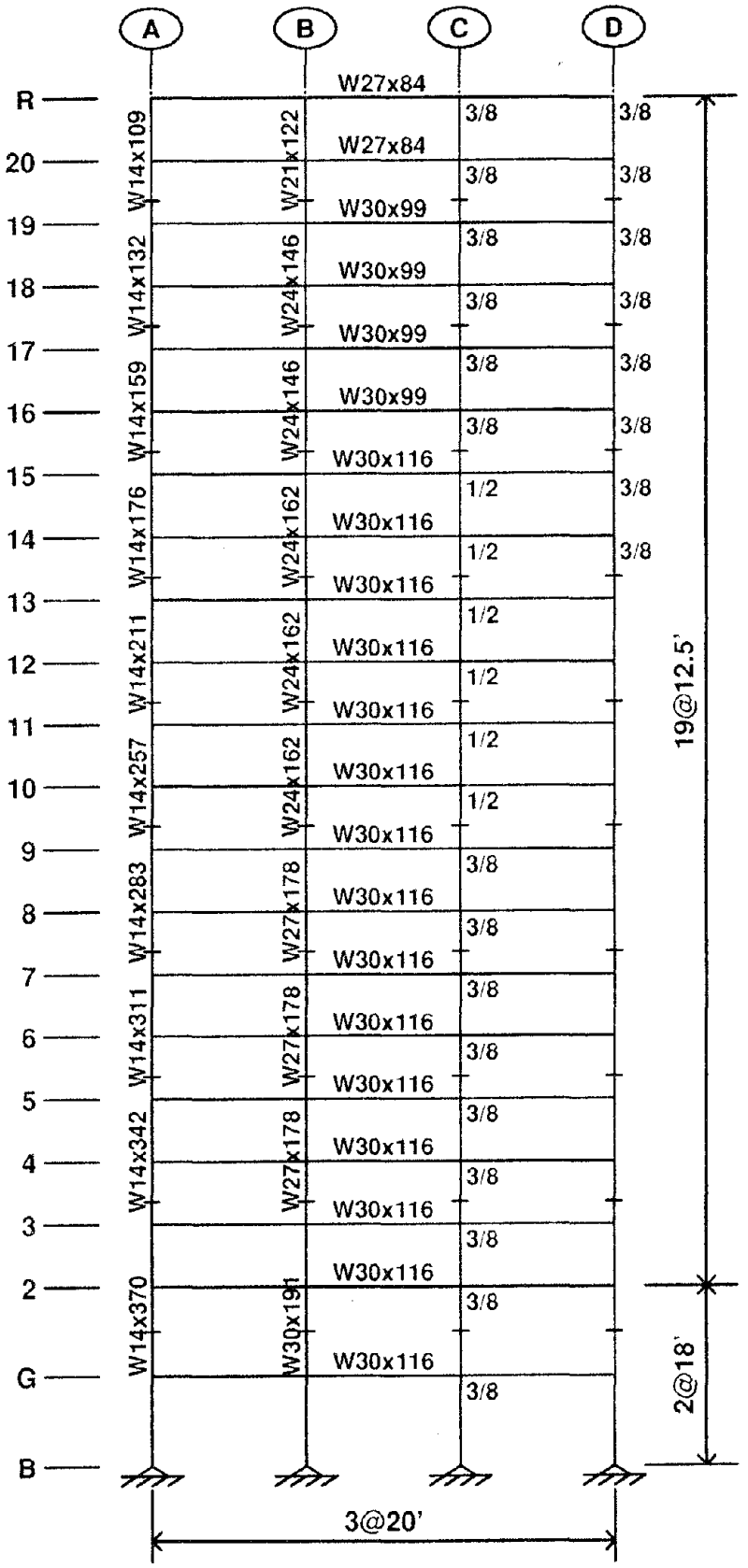

Figure 8.7 Member Sizes and Doubler Plate Thicknesses for MRF Design 3

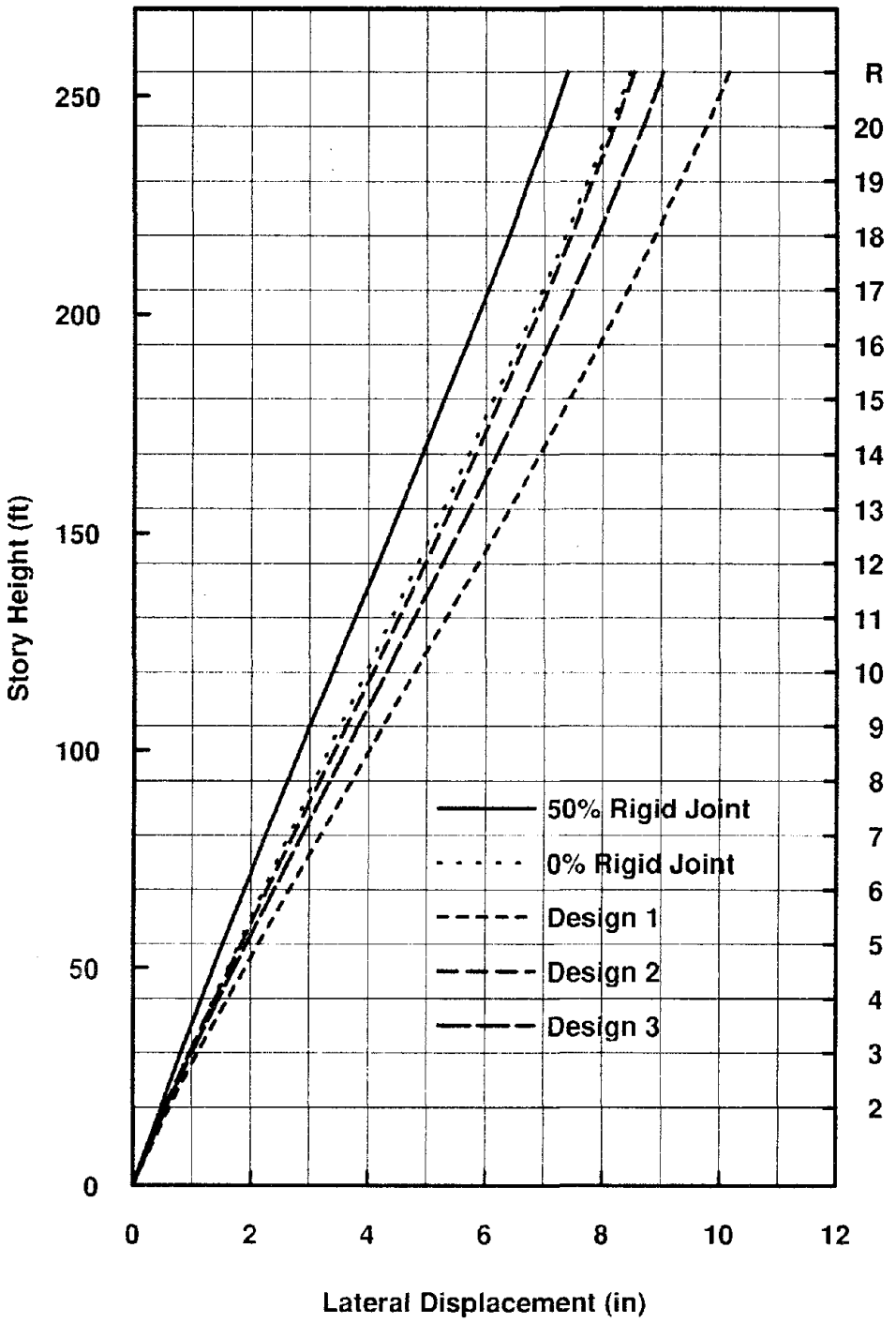

Figure 8.8 Static Lateral Displacements of the MRF Models

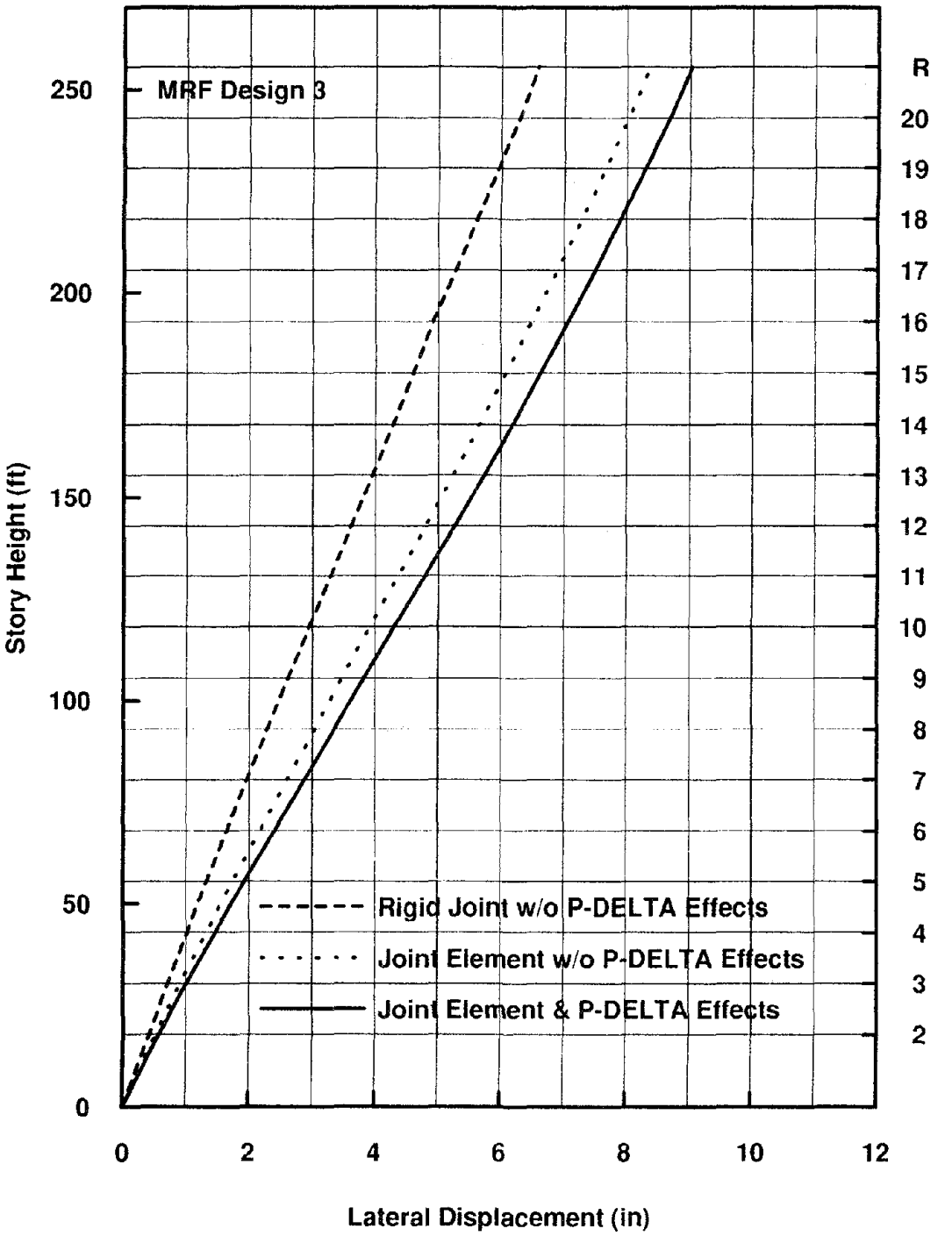

Figure 8.9 Lateral Displacements of The MRF Design 3 under Various Effects

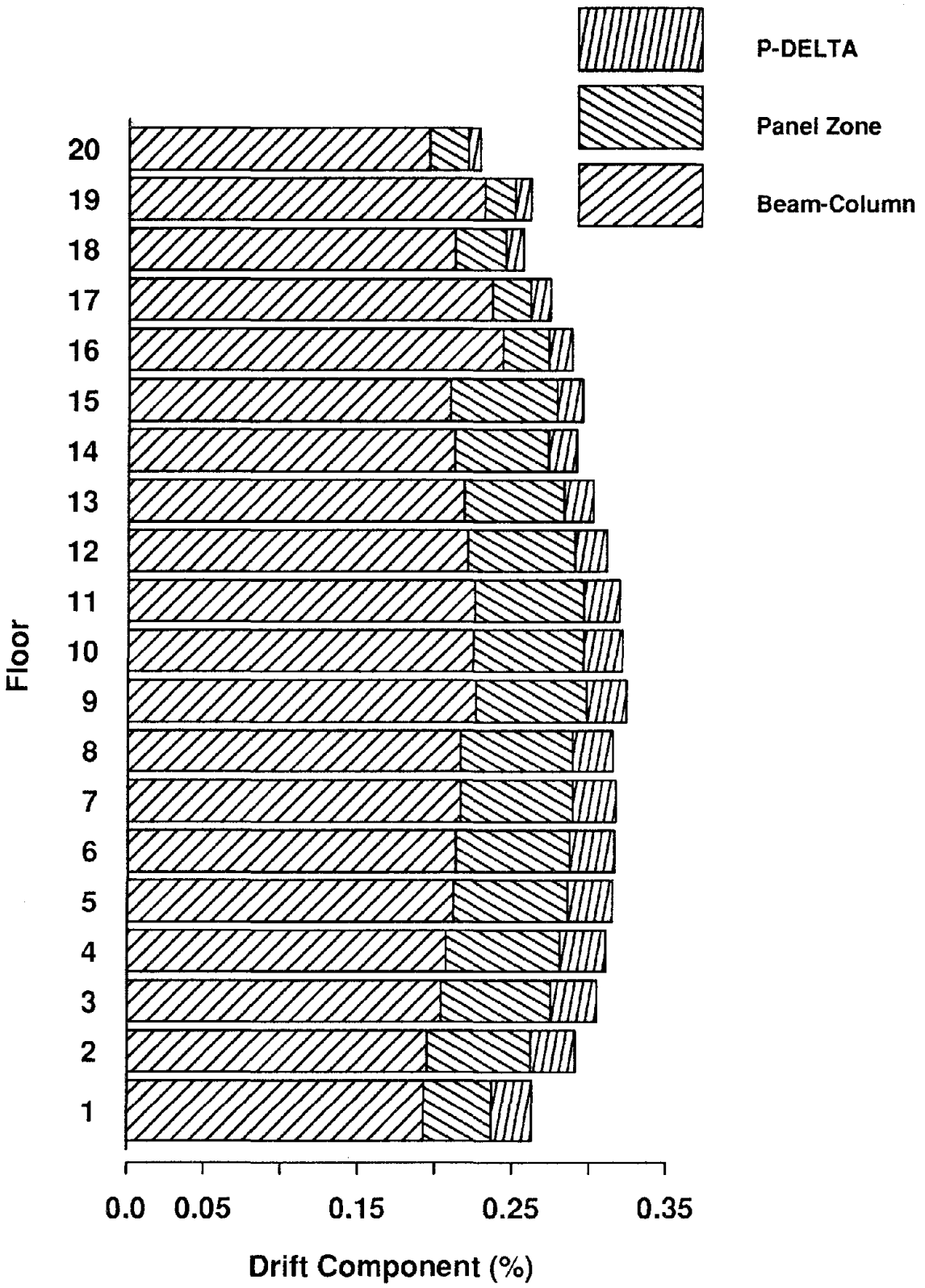

Figure 8.10 Story Drift Components due to Various Effects for MRF Design 3

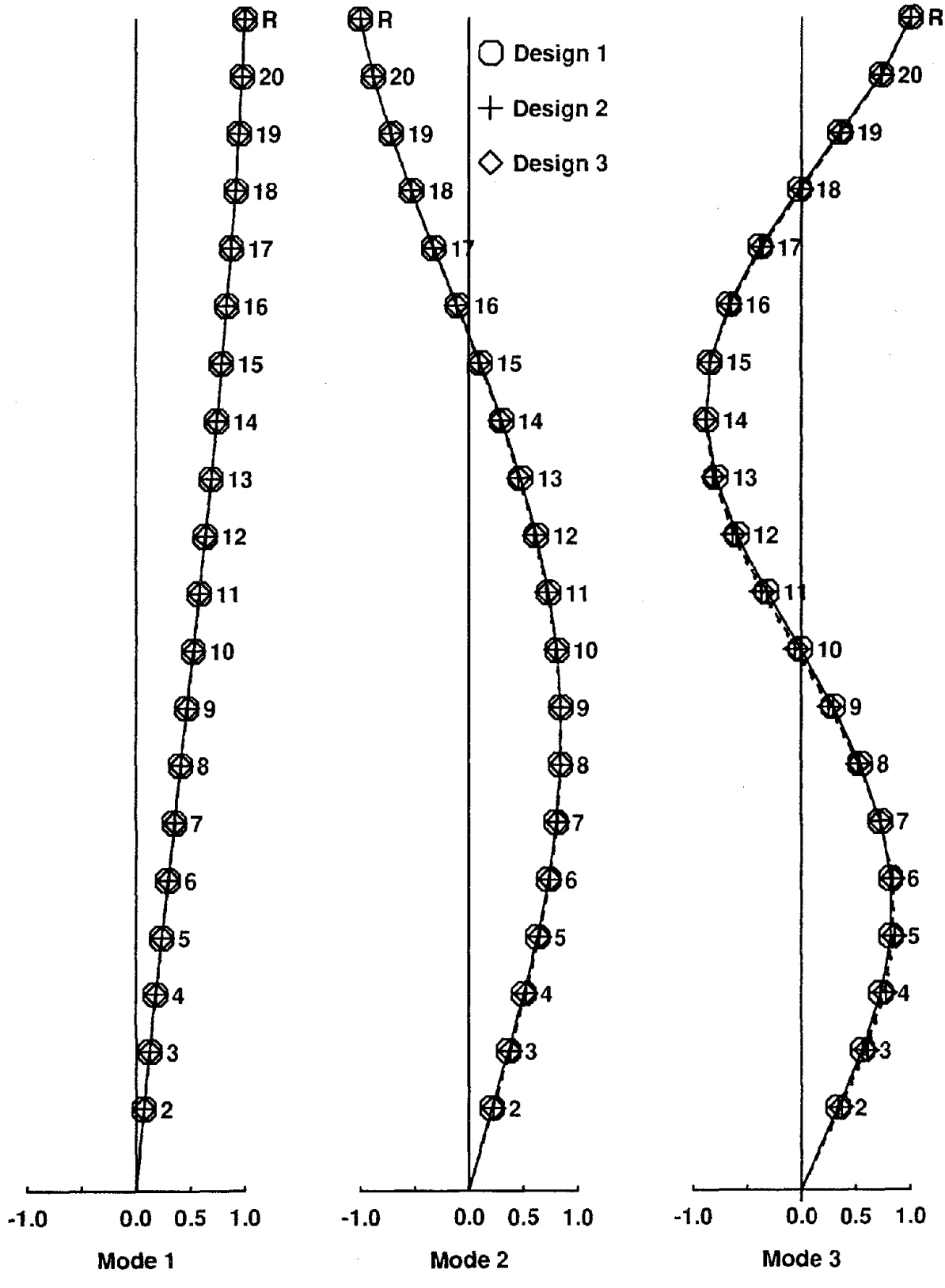

Figure 8.11 Vibration Mode Shapes for MRF Designs 1, 2 and 3

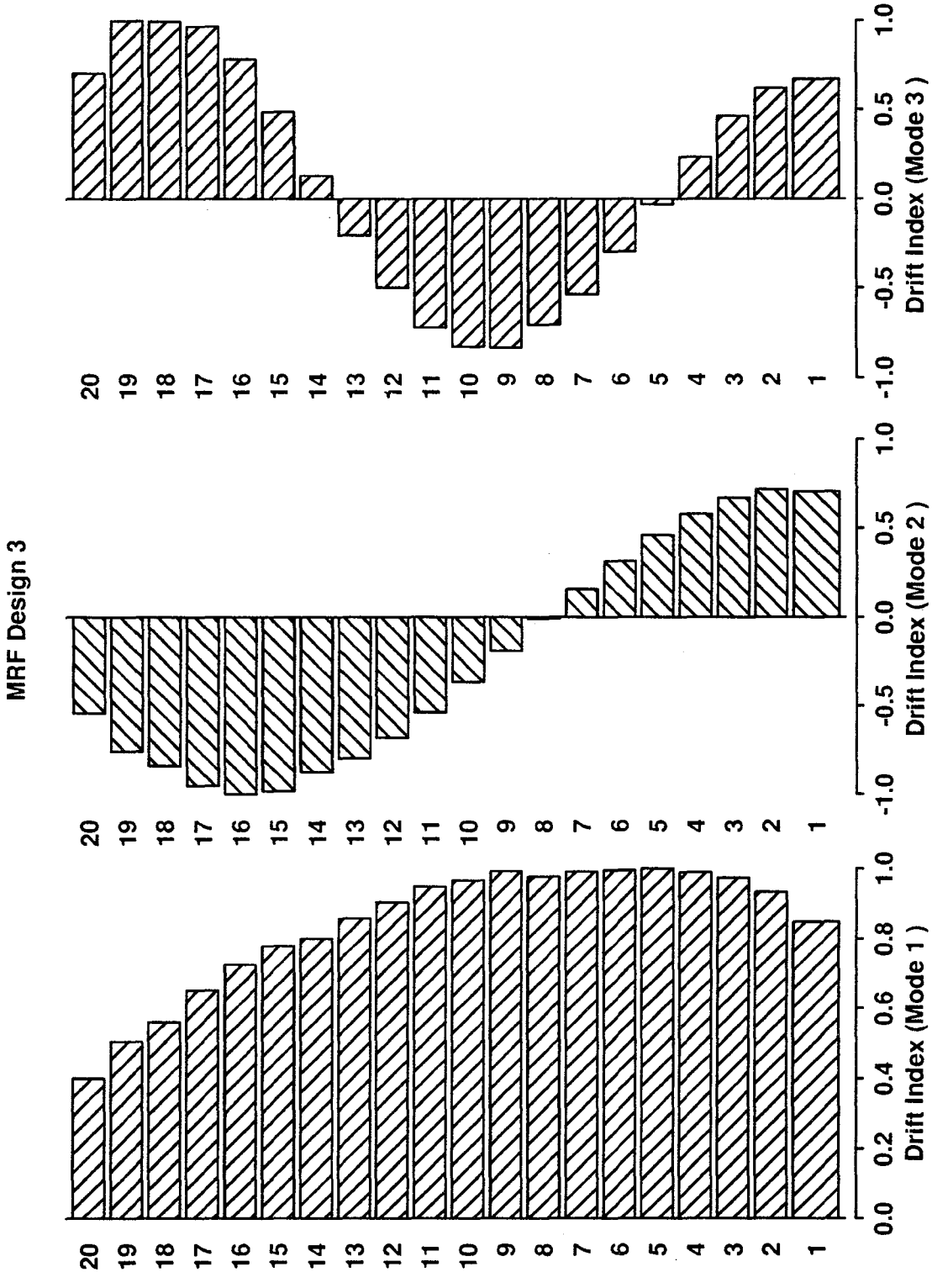

Figure 8.12 Normalized Story Drift Indices for the First Three Modes (MRF Design 3)

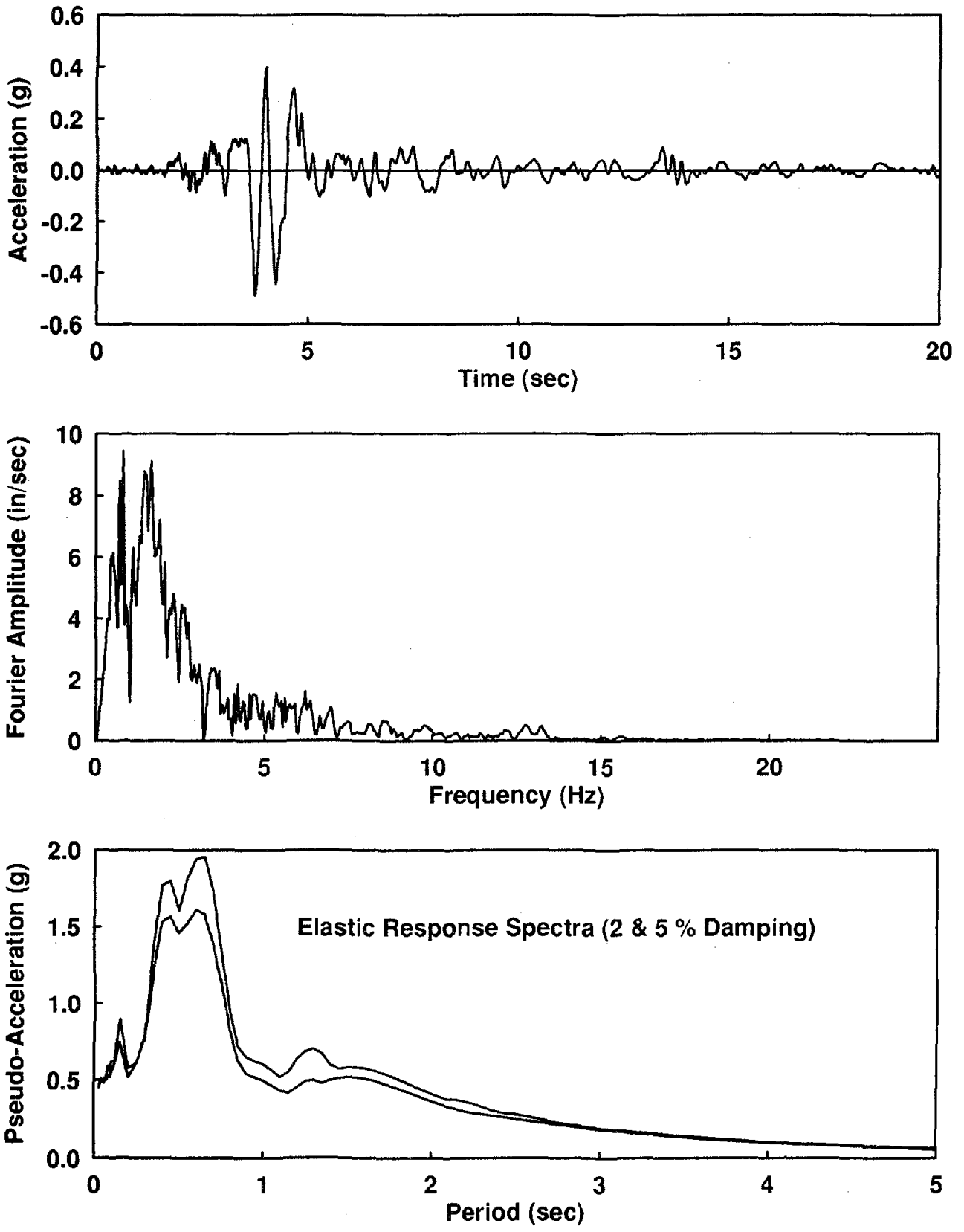

Figure 8.13 Input Ground Acceleration, Fourier Amplitude and Response Spectra

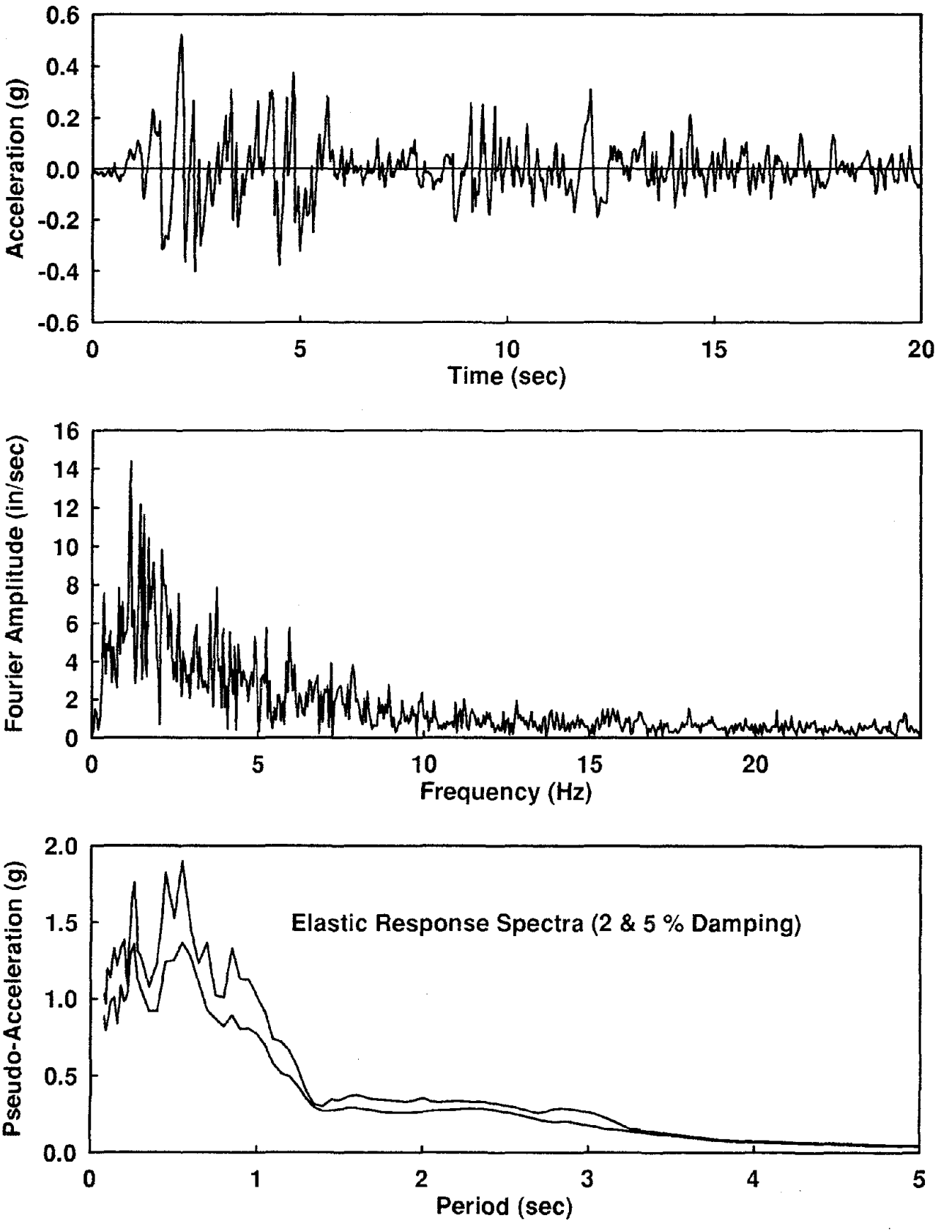

Figure 8.14 Input Ground Acceleration, Fourier Amplitude and Response Spectra

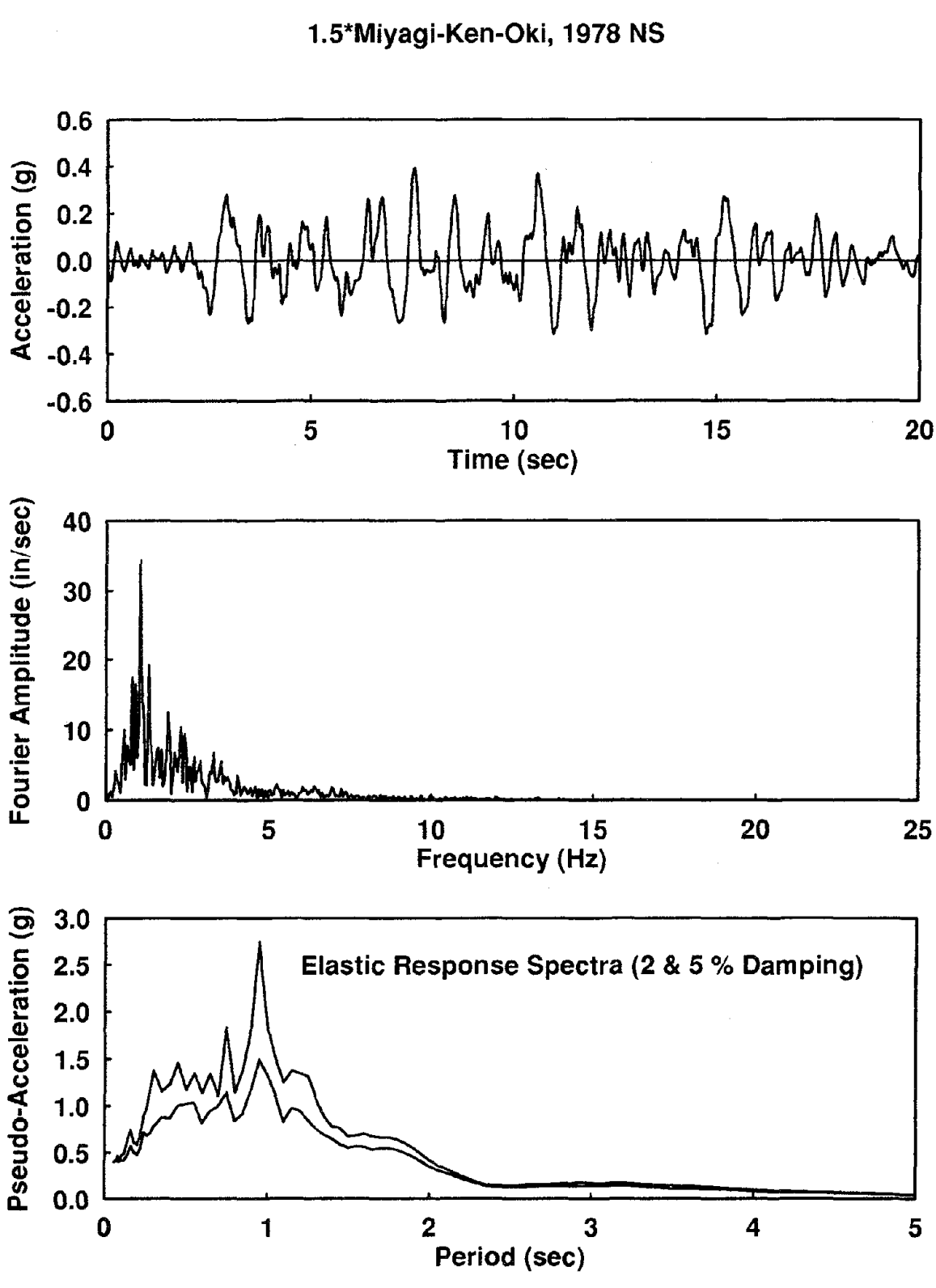

Figure 8.15 Input Ground Acceleration, Fourier Amplitude and Response Spectra

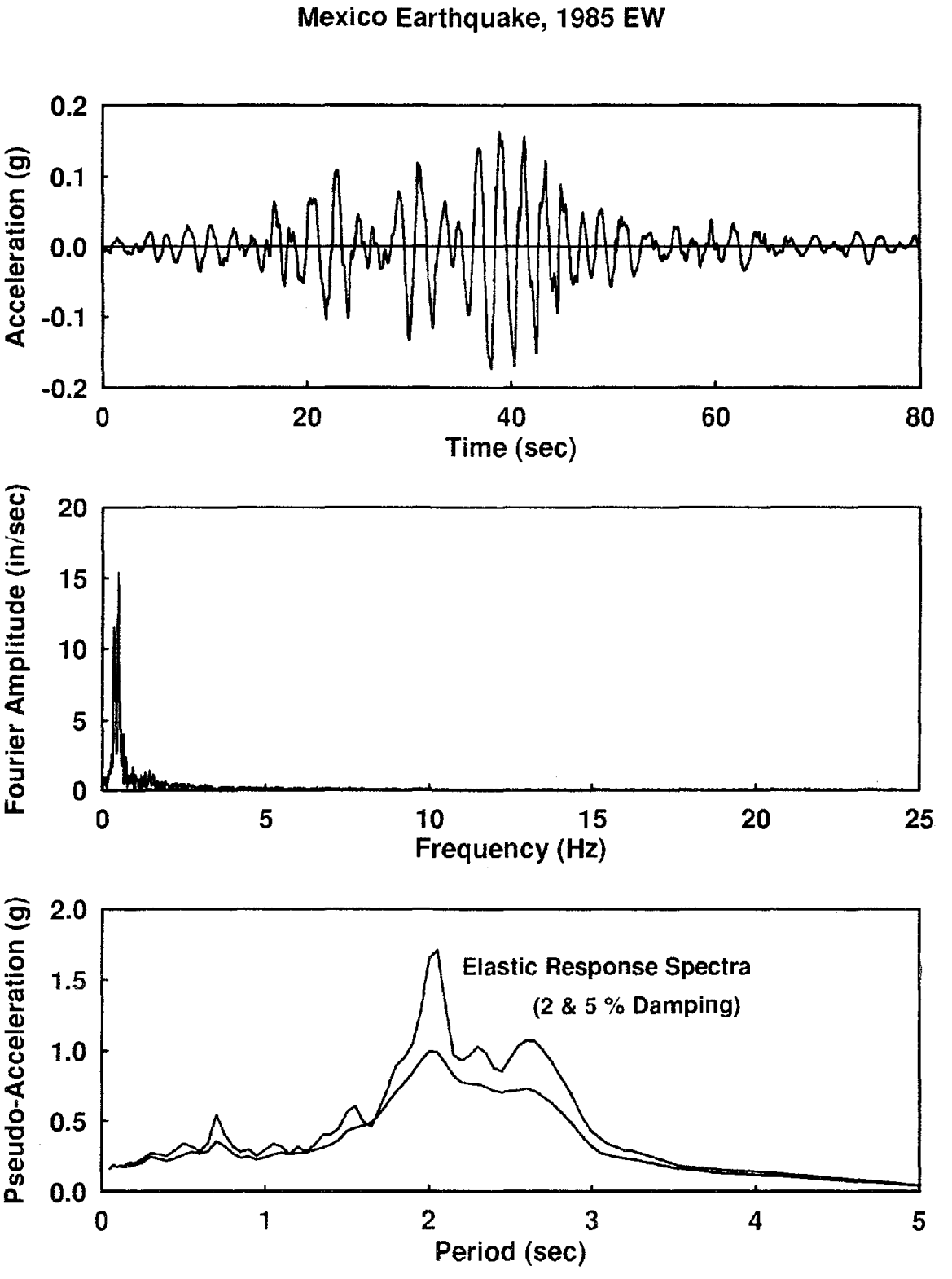

Figure 8.16 Input Ground Acceleration, Fourier Amplitude and Response Spectra

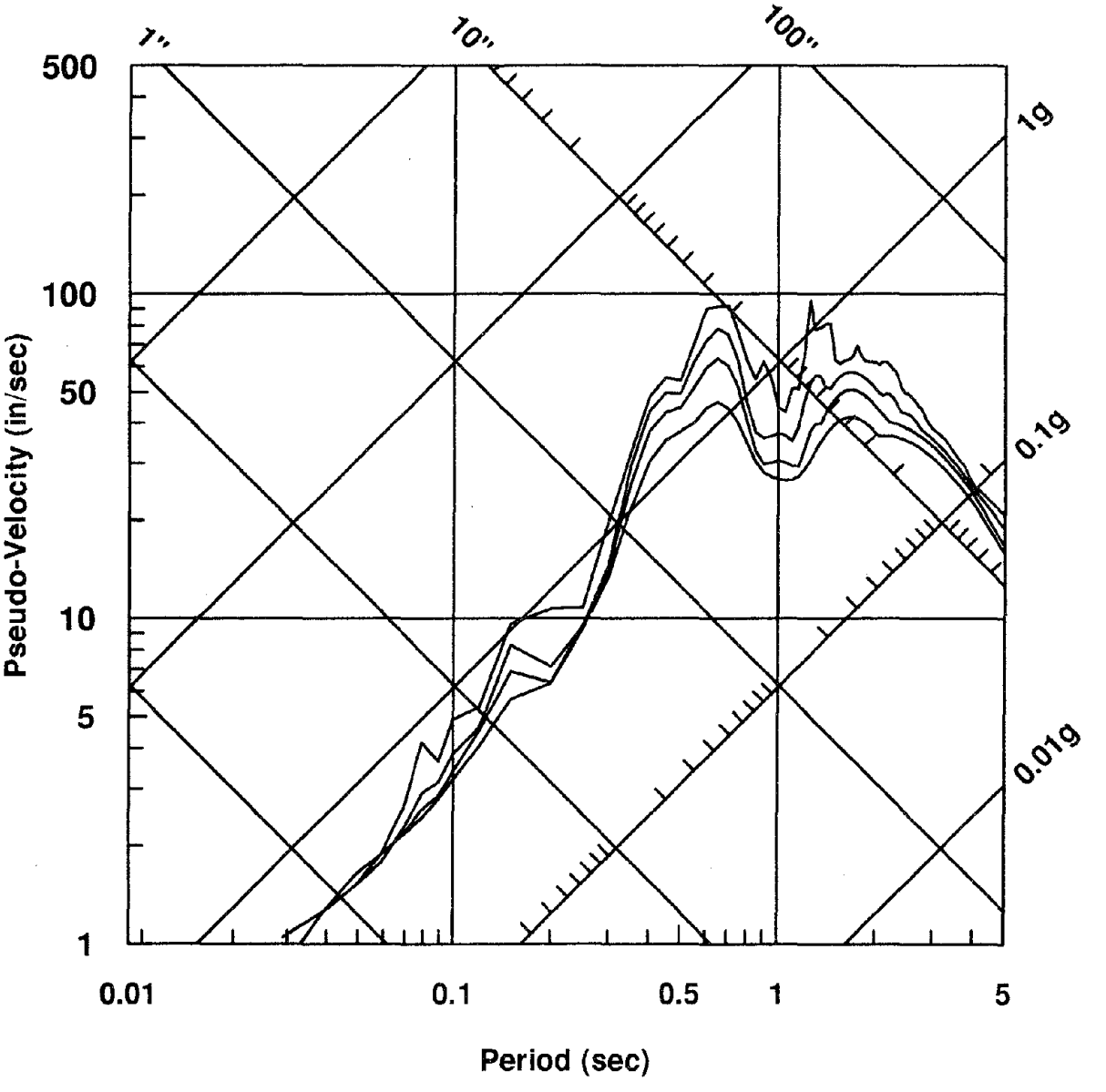

Figure 8.17 Elastic Response Spectra for 0, 2, 5 and 10% Damping

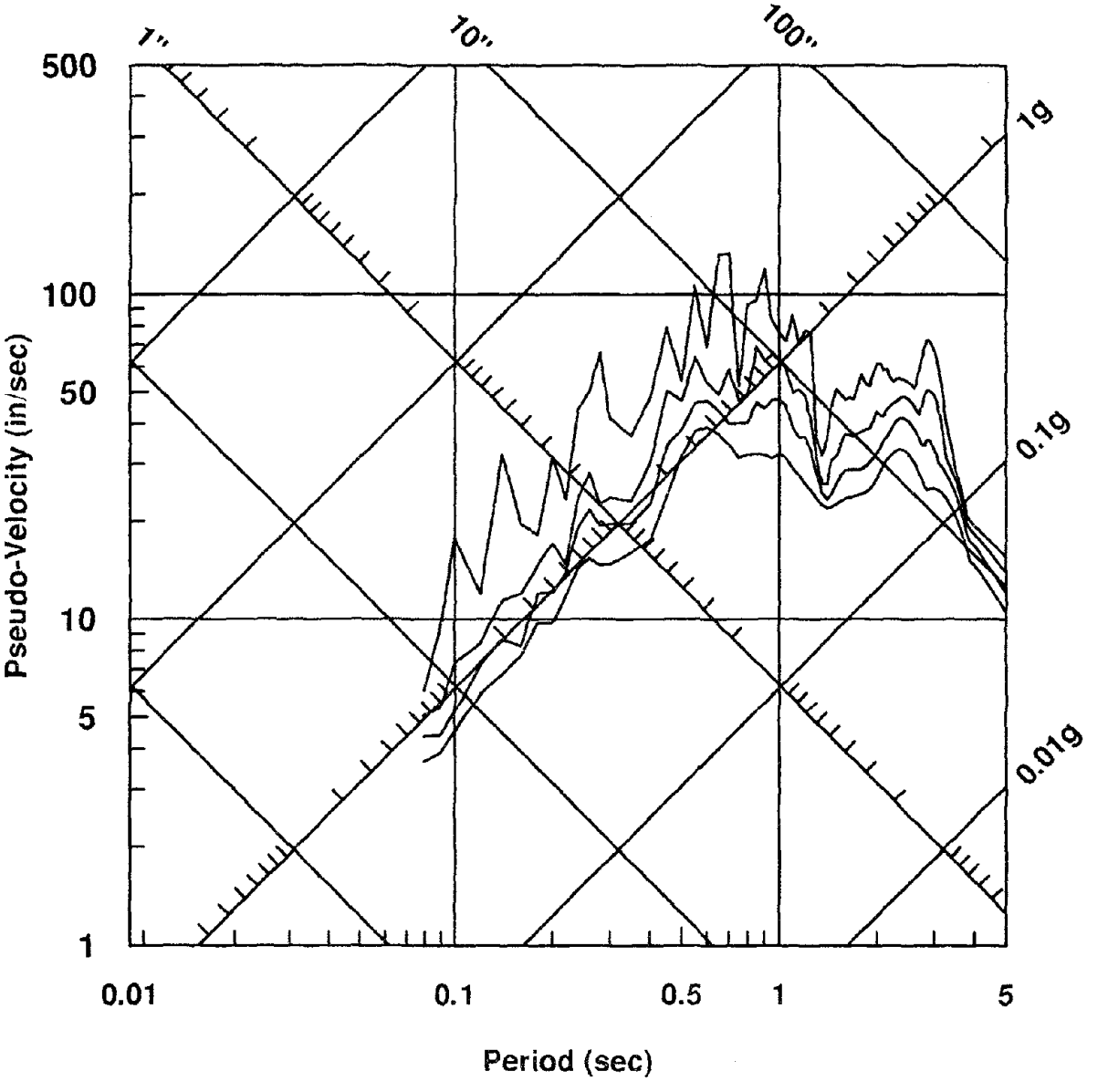

Figure 8.18 Elastic Response Spectra for 0, 2, 5 and 10% Damping

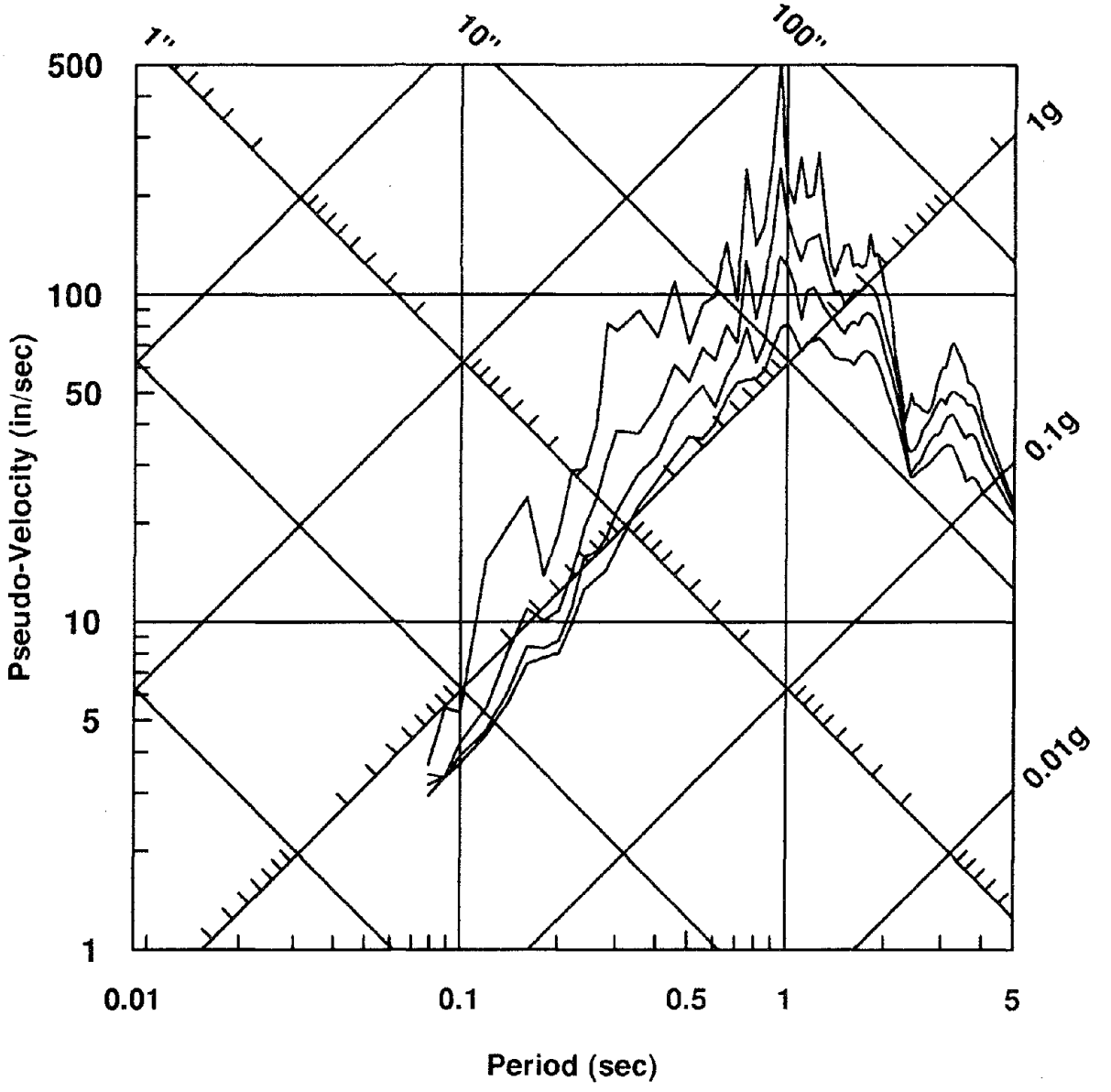

Figure 8.19 Elastic Response Spectra for 0, 2, 5 and 10% Damping

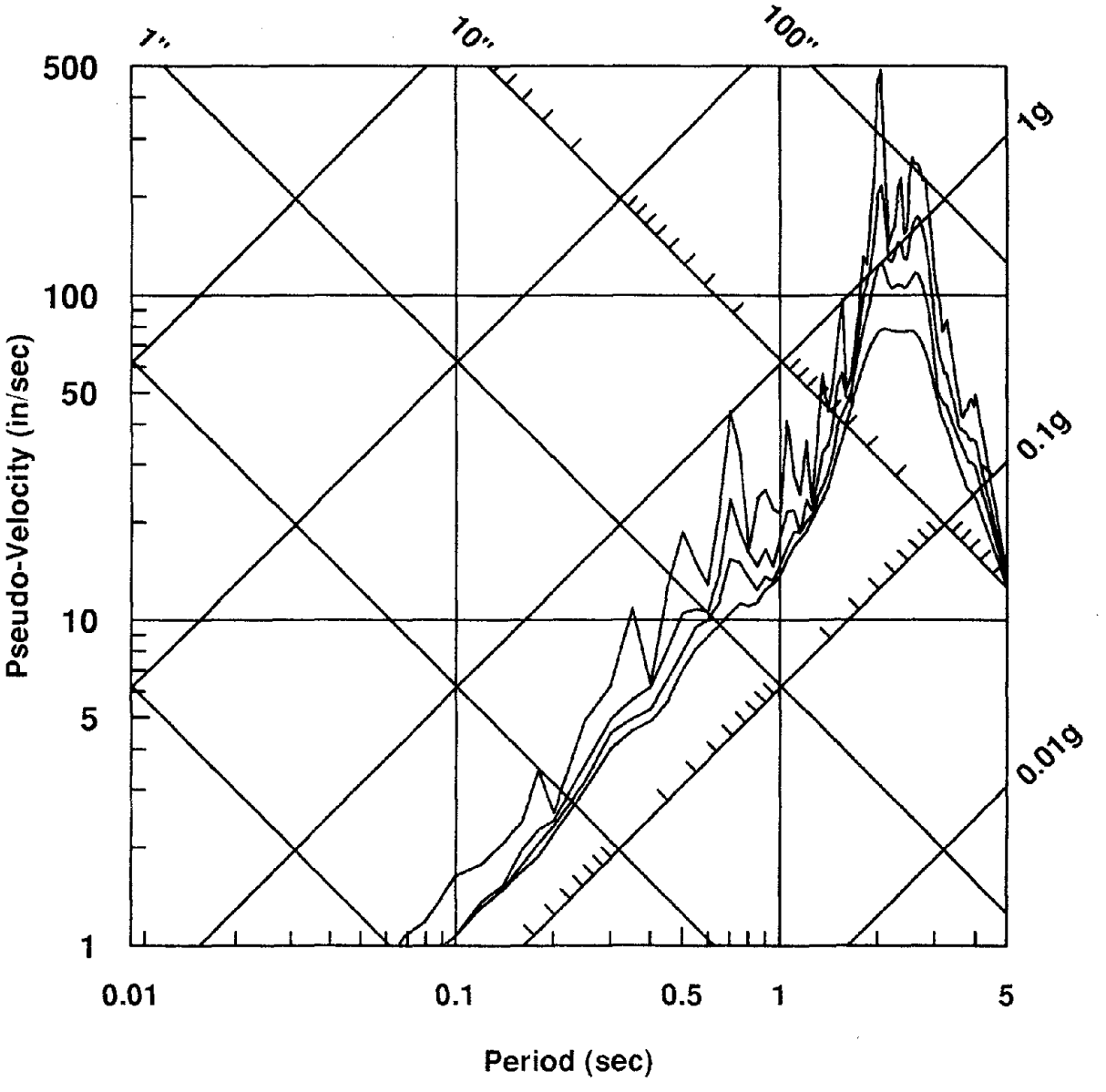

Figure 8.20 Elastic Response Spectra for 0, 2, 5 and 10% Damping

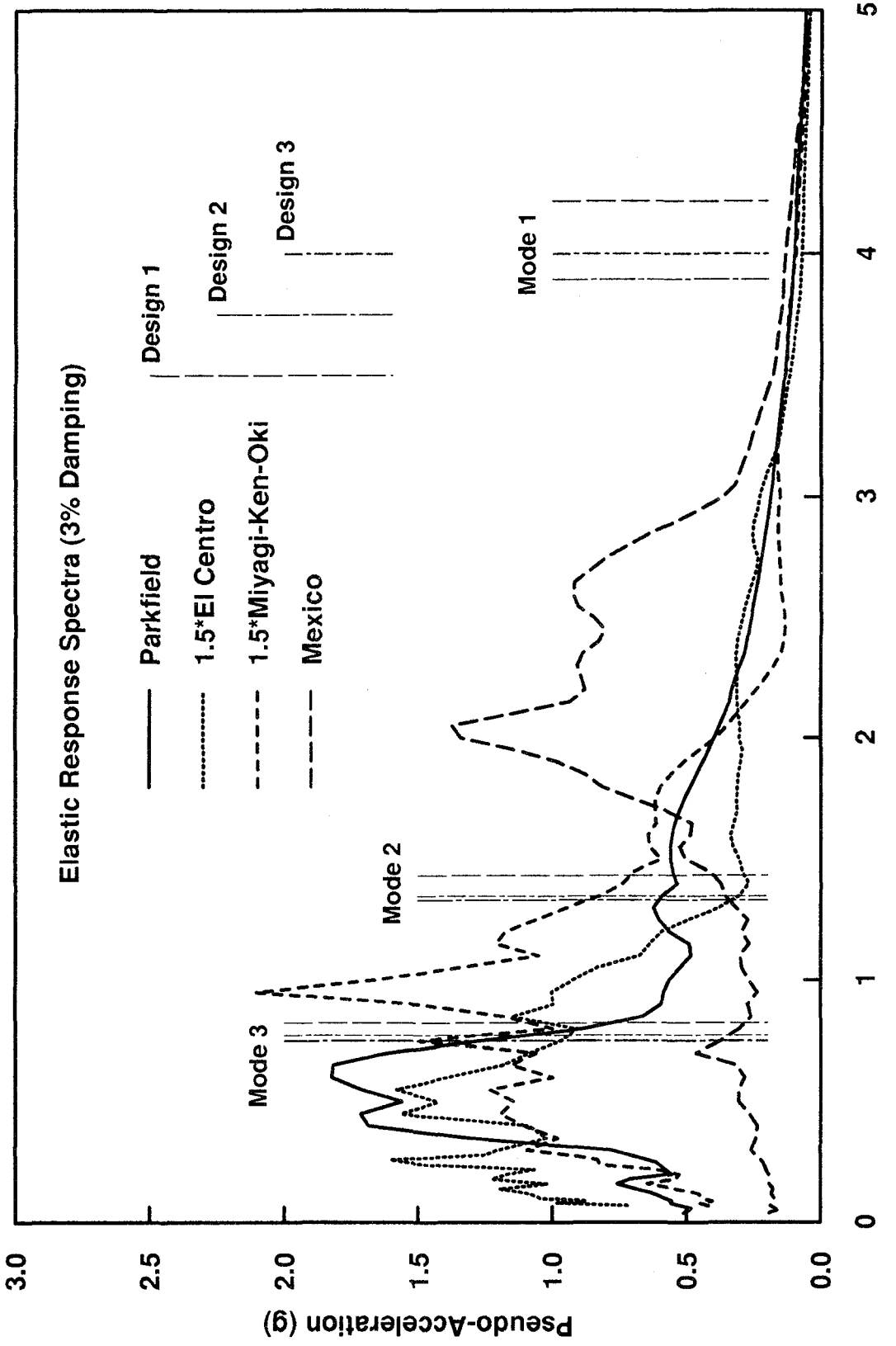

Figure 8.21 Elastic Response Spectra for The Selected Ground Accelerations (3% Damping)

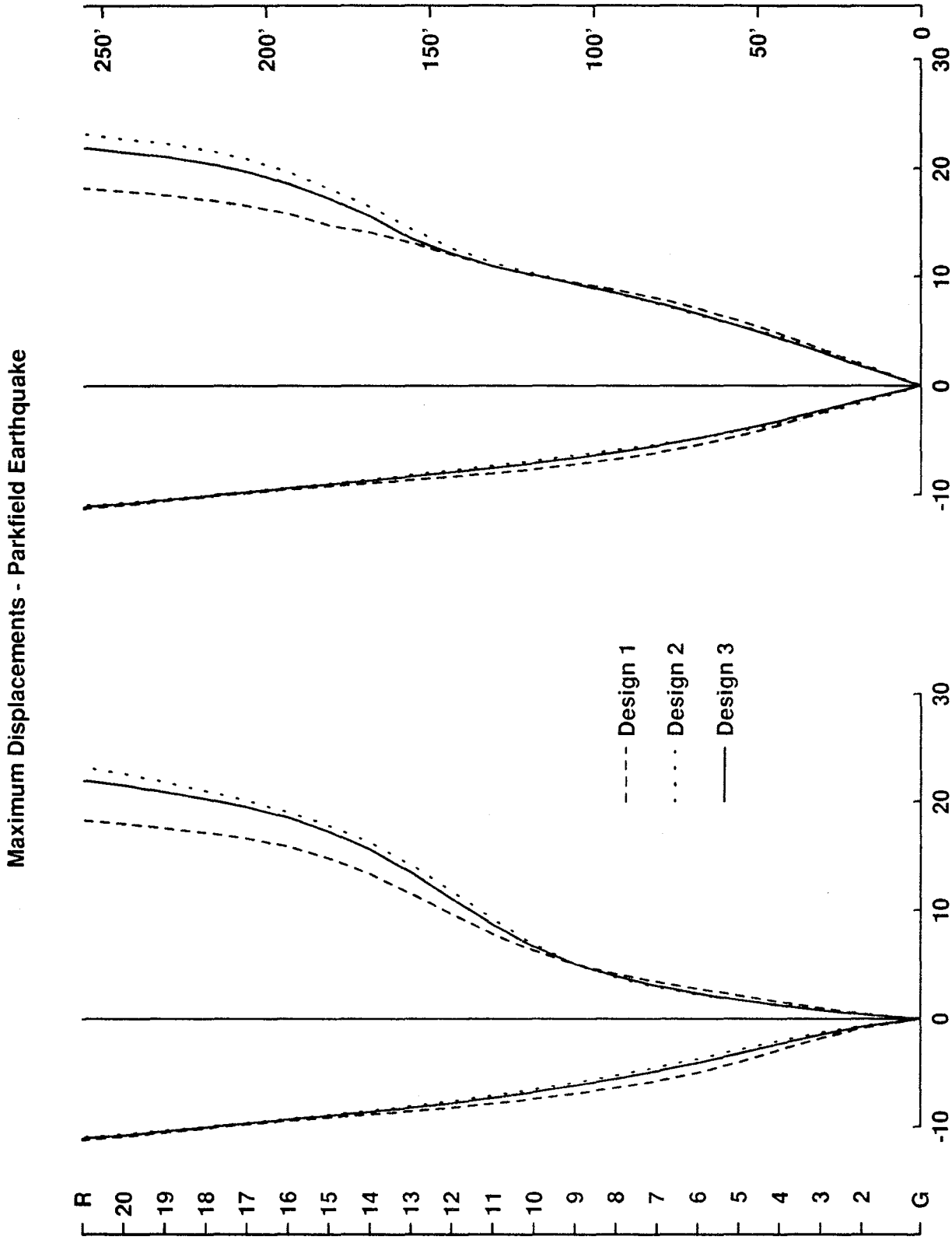

Figure 8.22 Maximum Floor Displacements for MRF Designs 1 2, and 3 (Parkfield Earthquake)

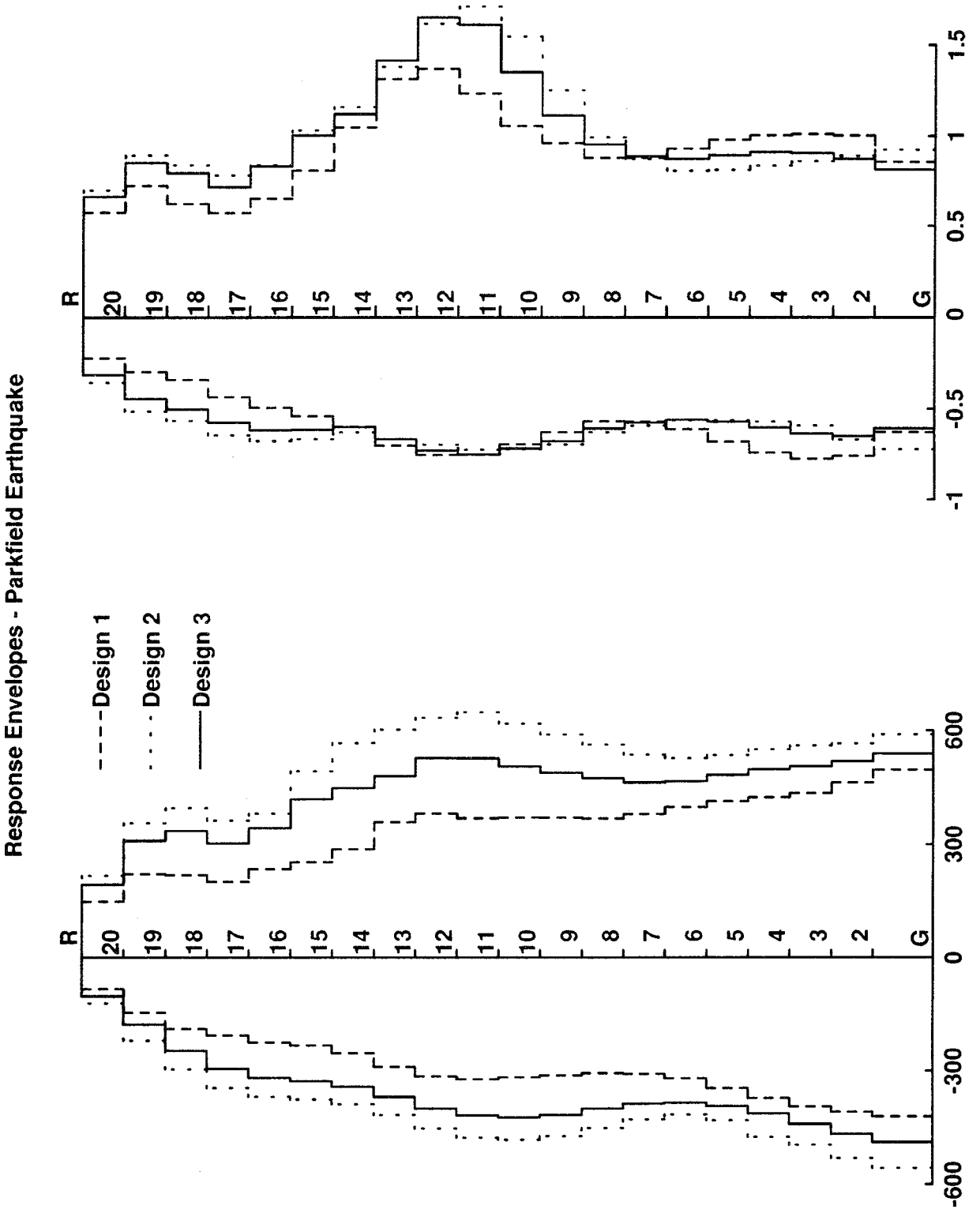

Figure 8.23 Maximum Story Shears and Story Drifts for MRF Designs 1 2, and 3 (Parkfield Earthquake)

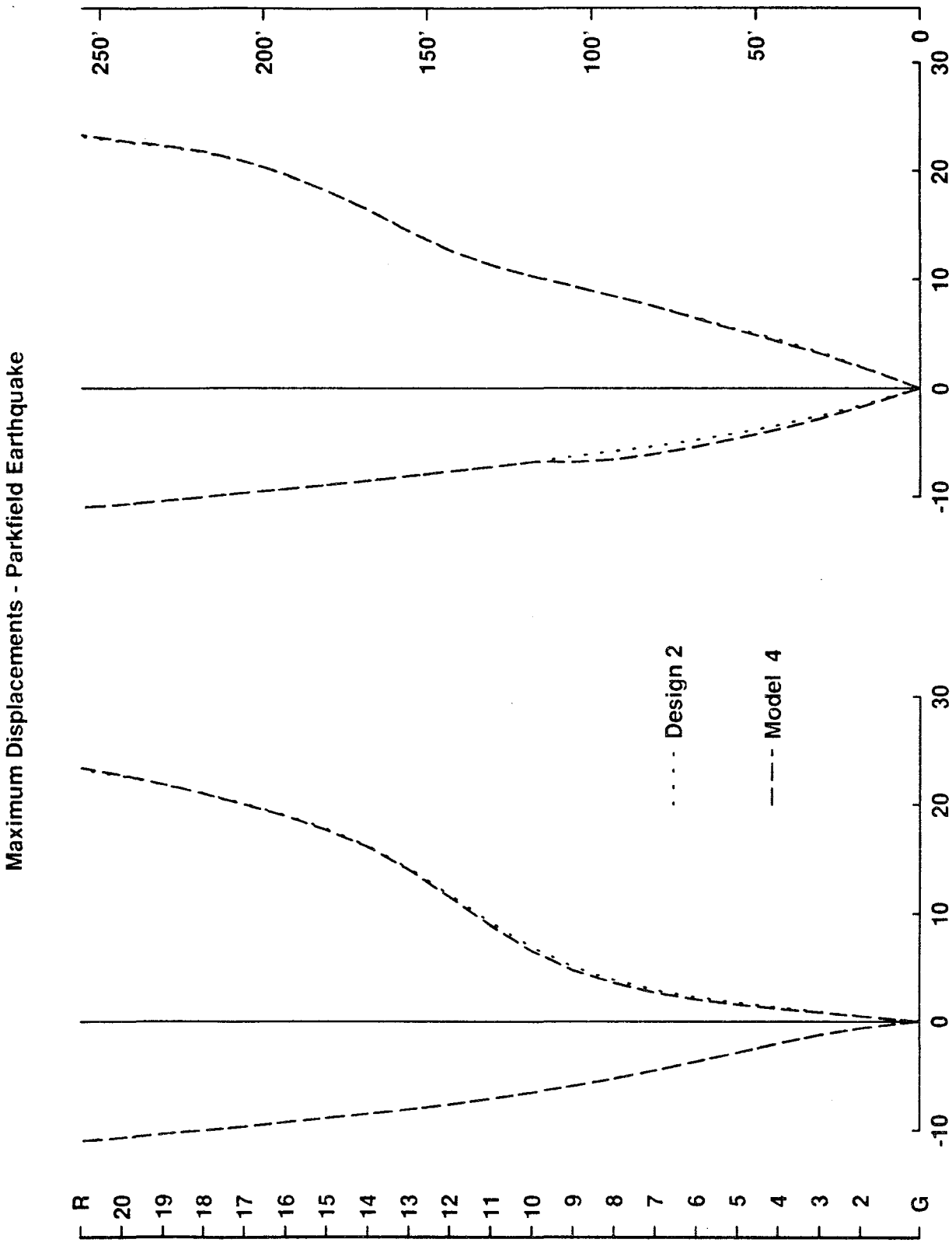

Figure 8.24 Maximum Floor Displacements for MRF Design 2 and Model 4 (Parkfield Earthquake)

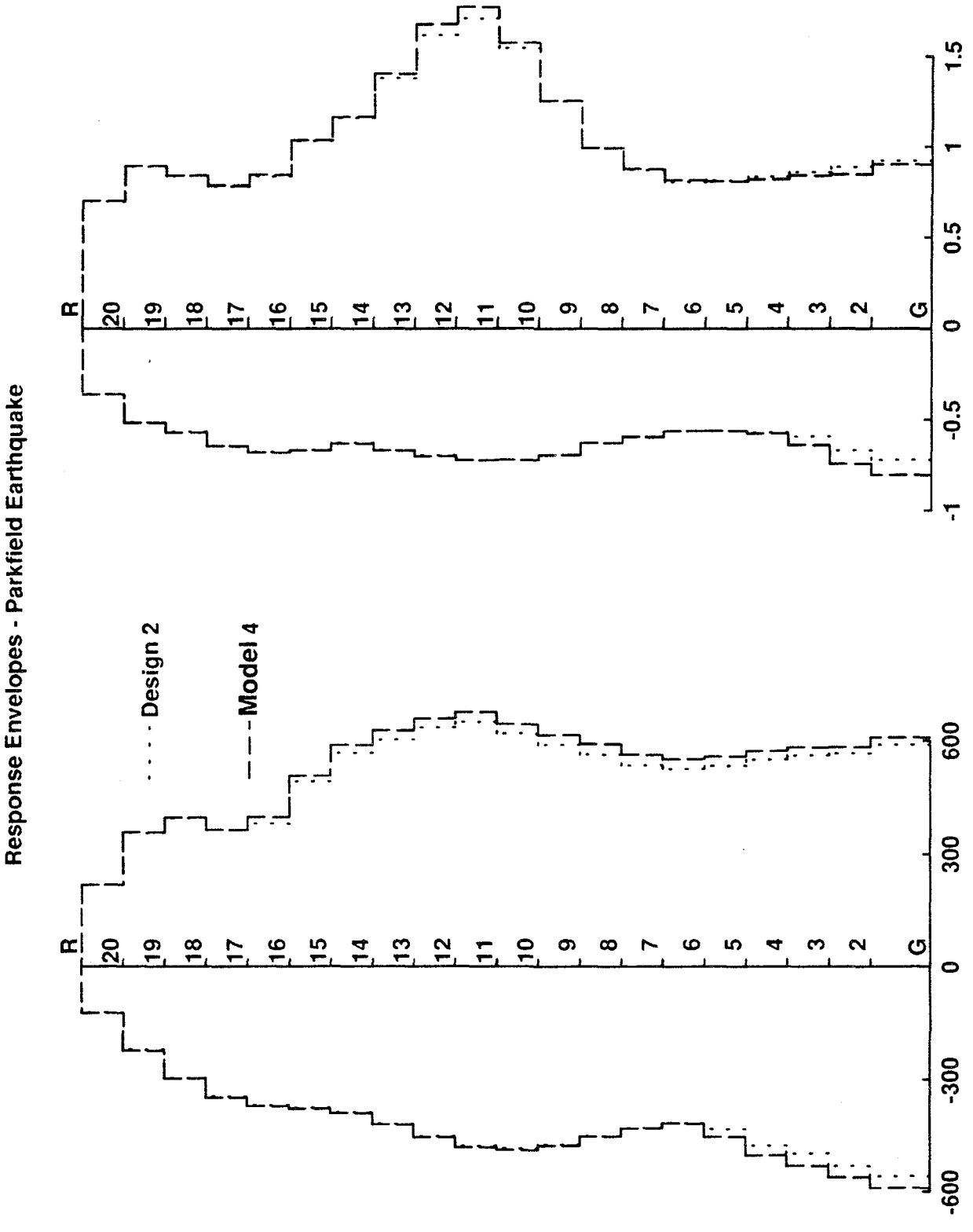

Figure 8.25 Maximum Story Shear and Story Drift for MRF Design 2 and Model 4 (Parkfield Earthquake)

Parkfield Earthquake

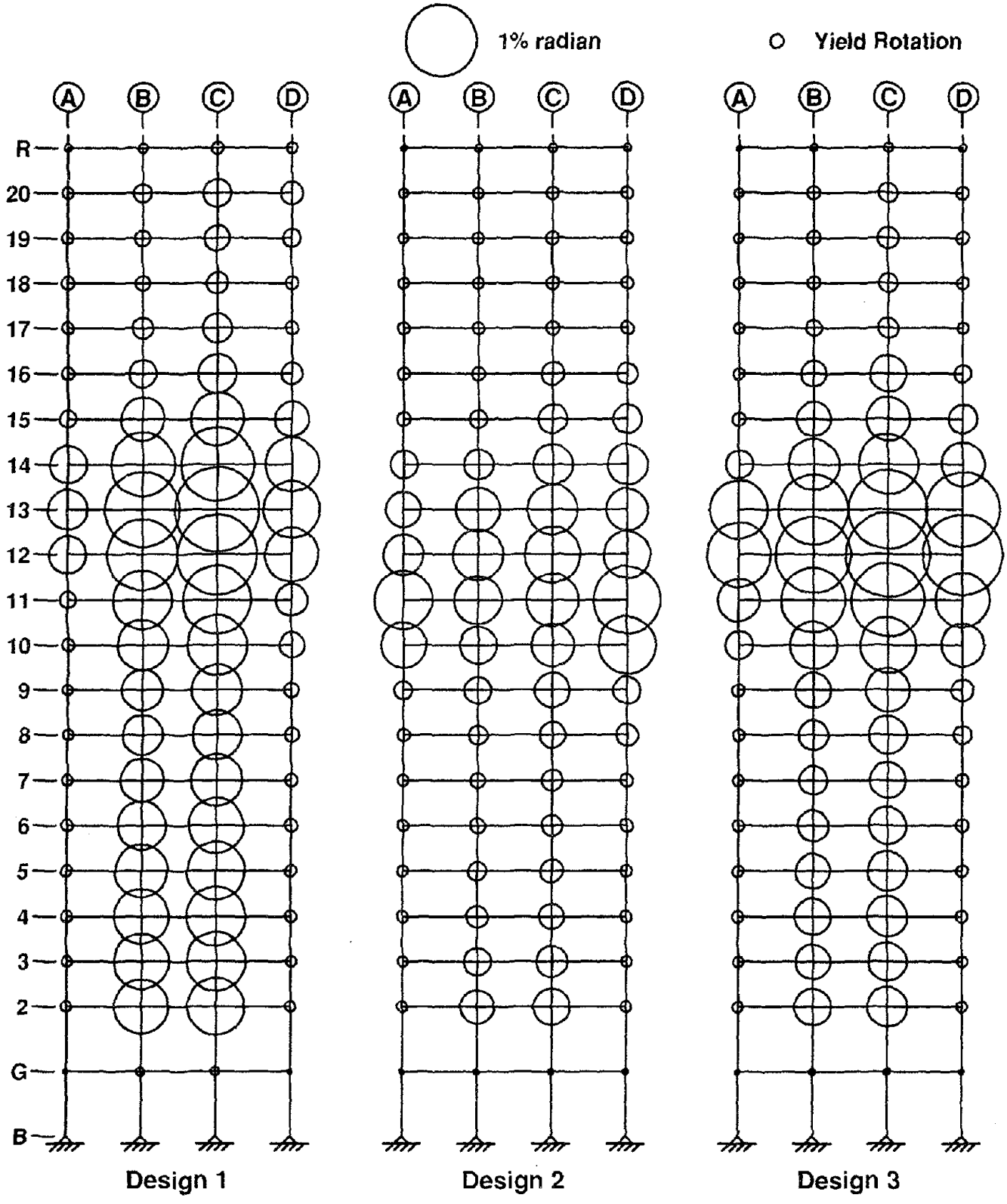

Figure 8.26 Maximum Panel Zone Deformations for MRF Designs 1, 2 and 3

Design 1 - Parkfield Earthquake

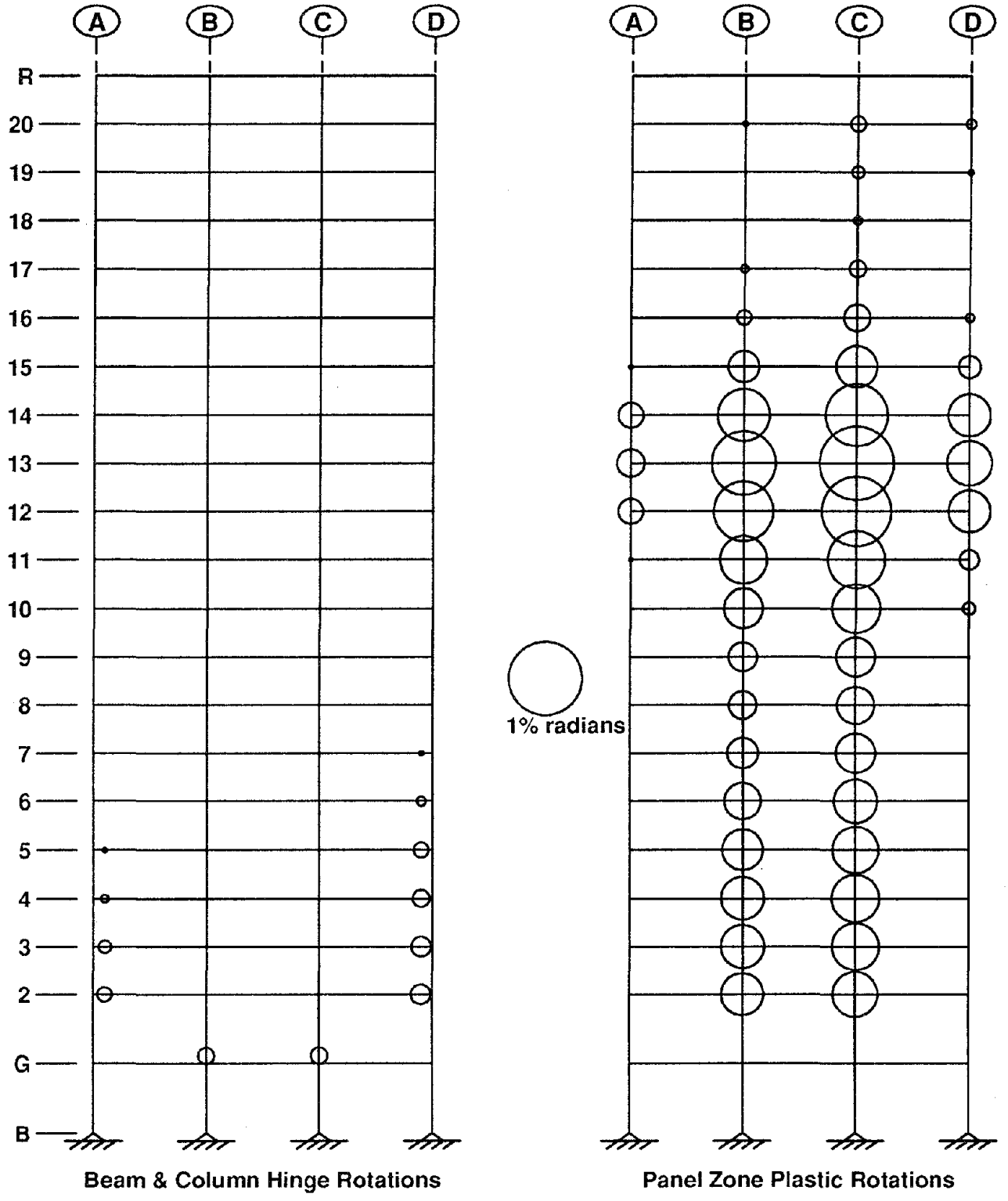

Figure 8.27 Maximum Beam, Column and Panel Zone Joint Plastic Rotations for MRF Design 1

Design 2 - Parkfield Earthquake

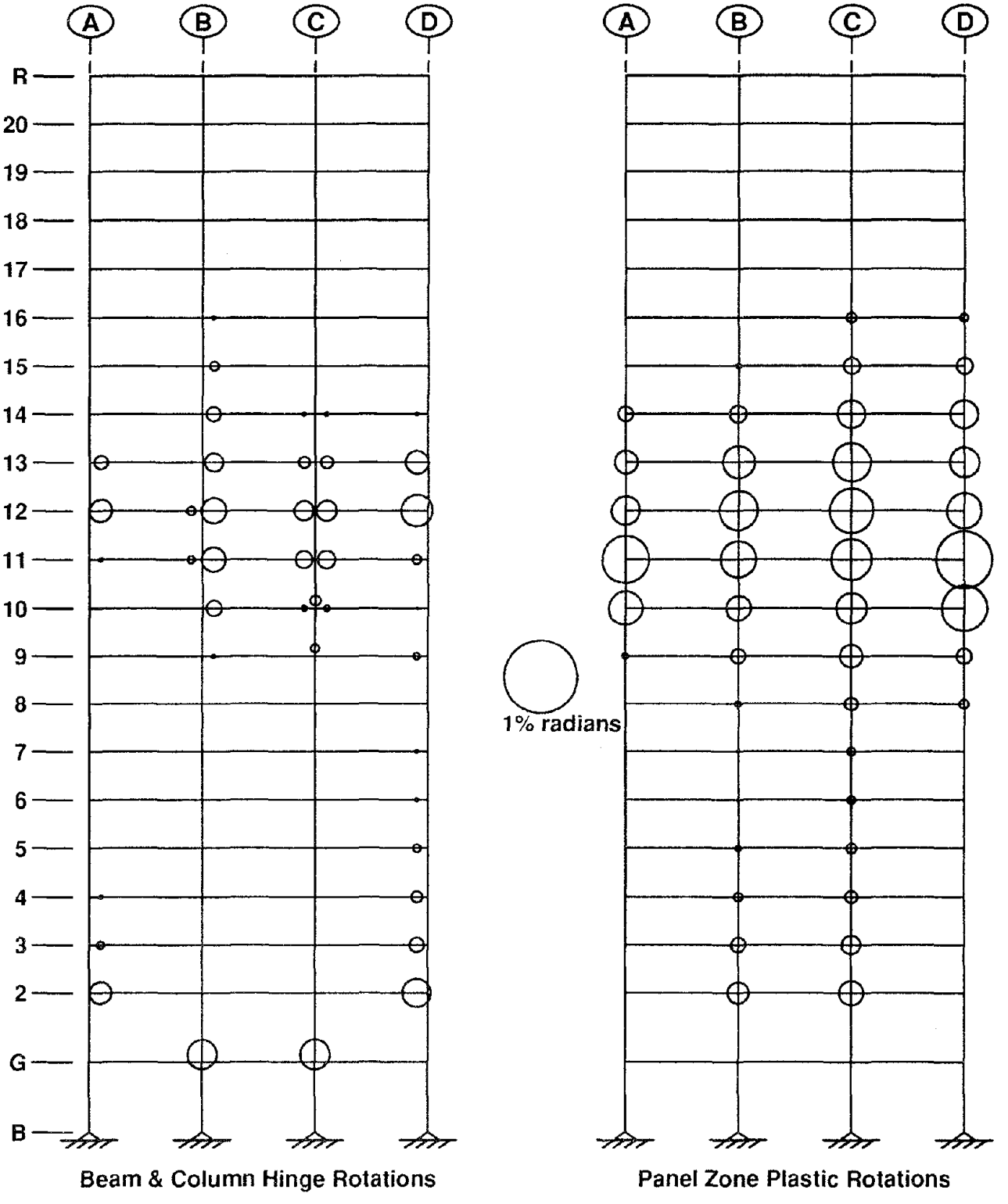

Figure 8.28 Maximum Beam, Column and Panel Zone Joint Plastic Rotations for MRF Design 2

Design 3 - Parkfield Earthquake

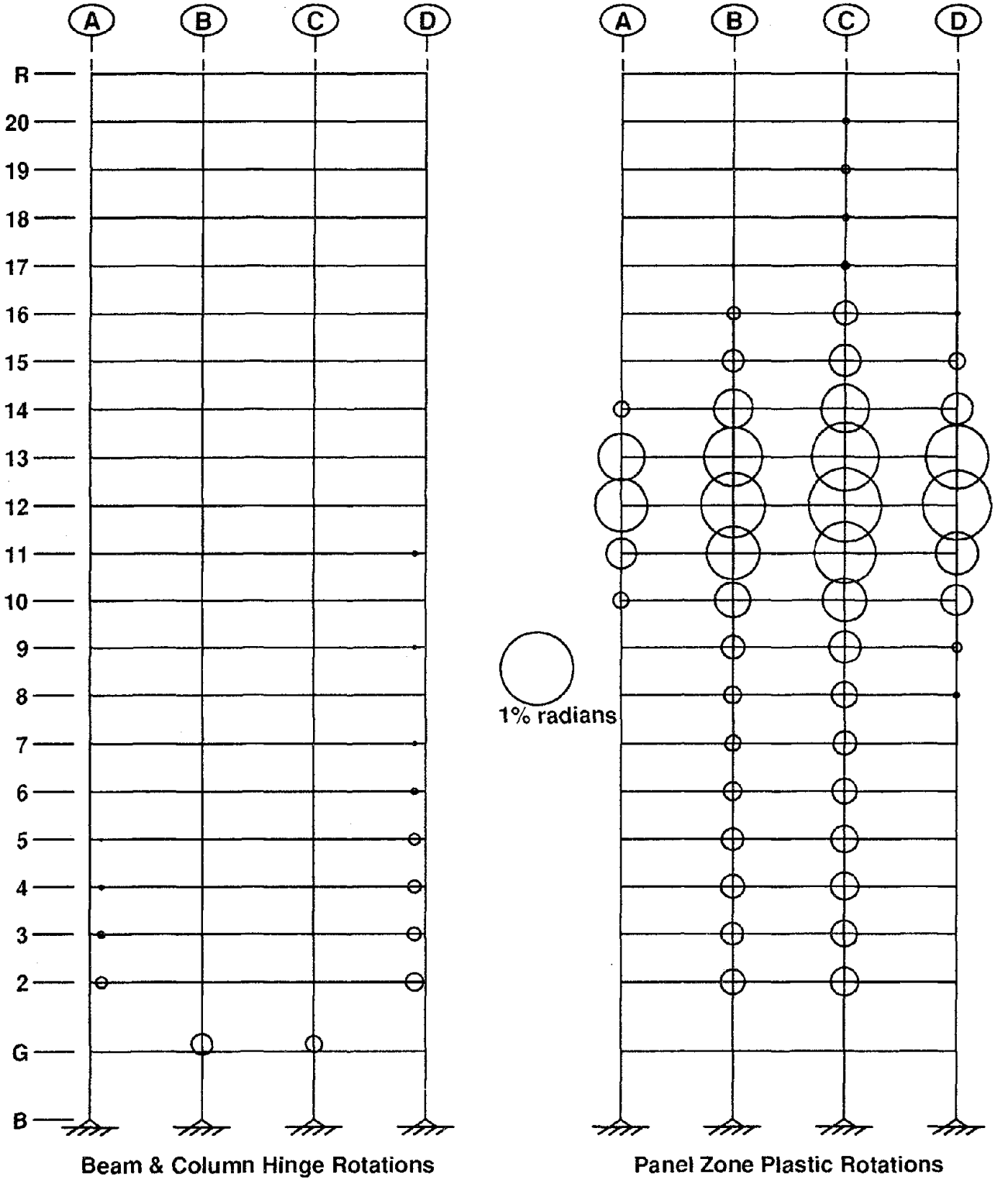

Figure 8.29 Maximum Beam, Column and Panel Zone Joint Plastic Rotations for MRF Design 3

Model 4 - Parkfield Earthquake

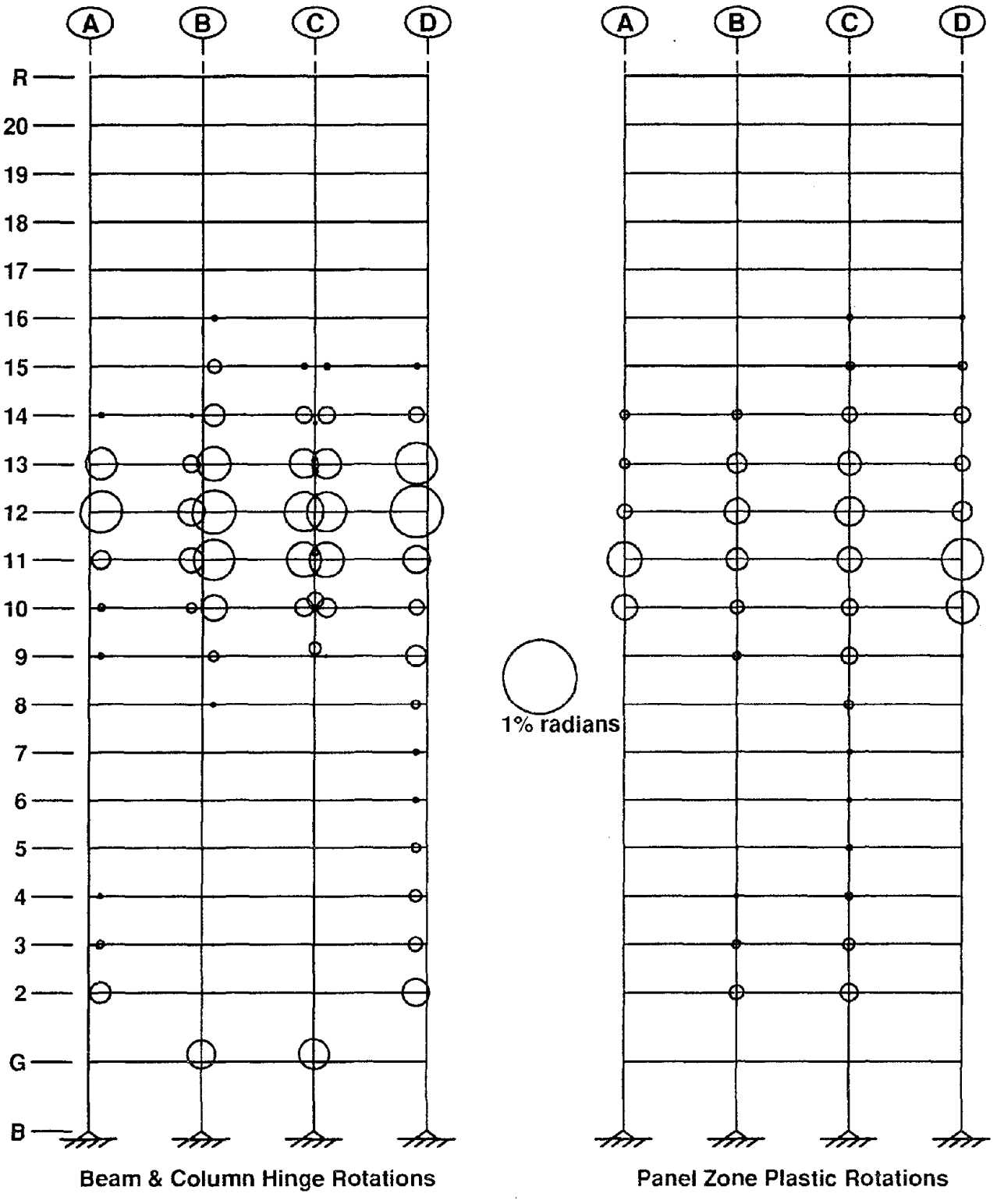

Figure 8.30 Maximum Beam, Column and Panel Zone Joint Plastic Rotations for MRF Model 4

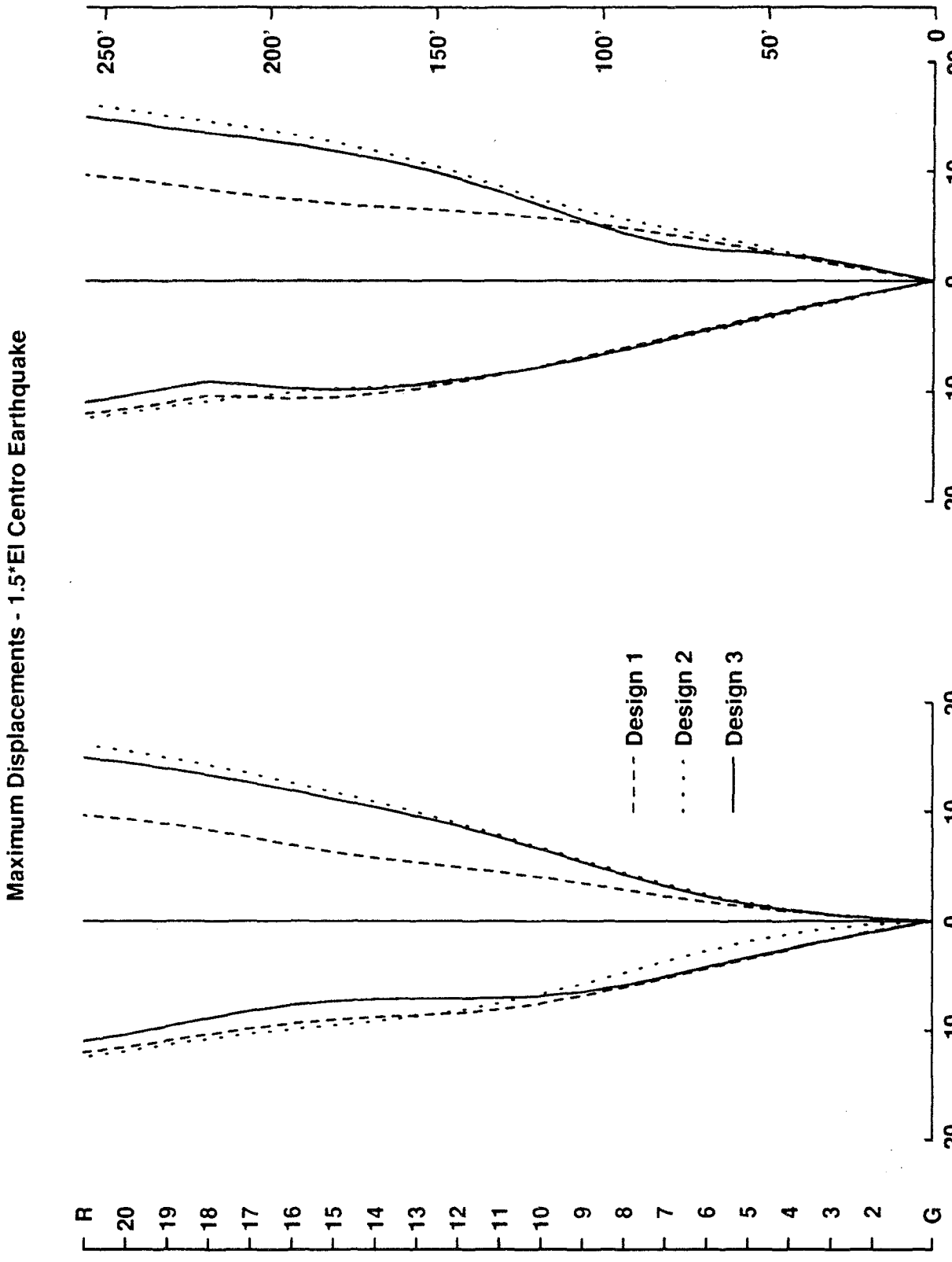

Figure 8.31 Maximum Floor Displacements for MRF Designs 1 2, and 3 (1.5*El Centro Earthquake)

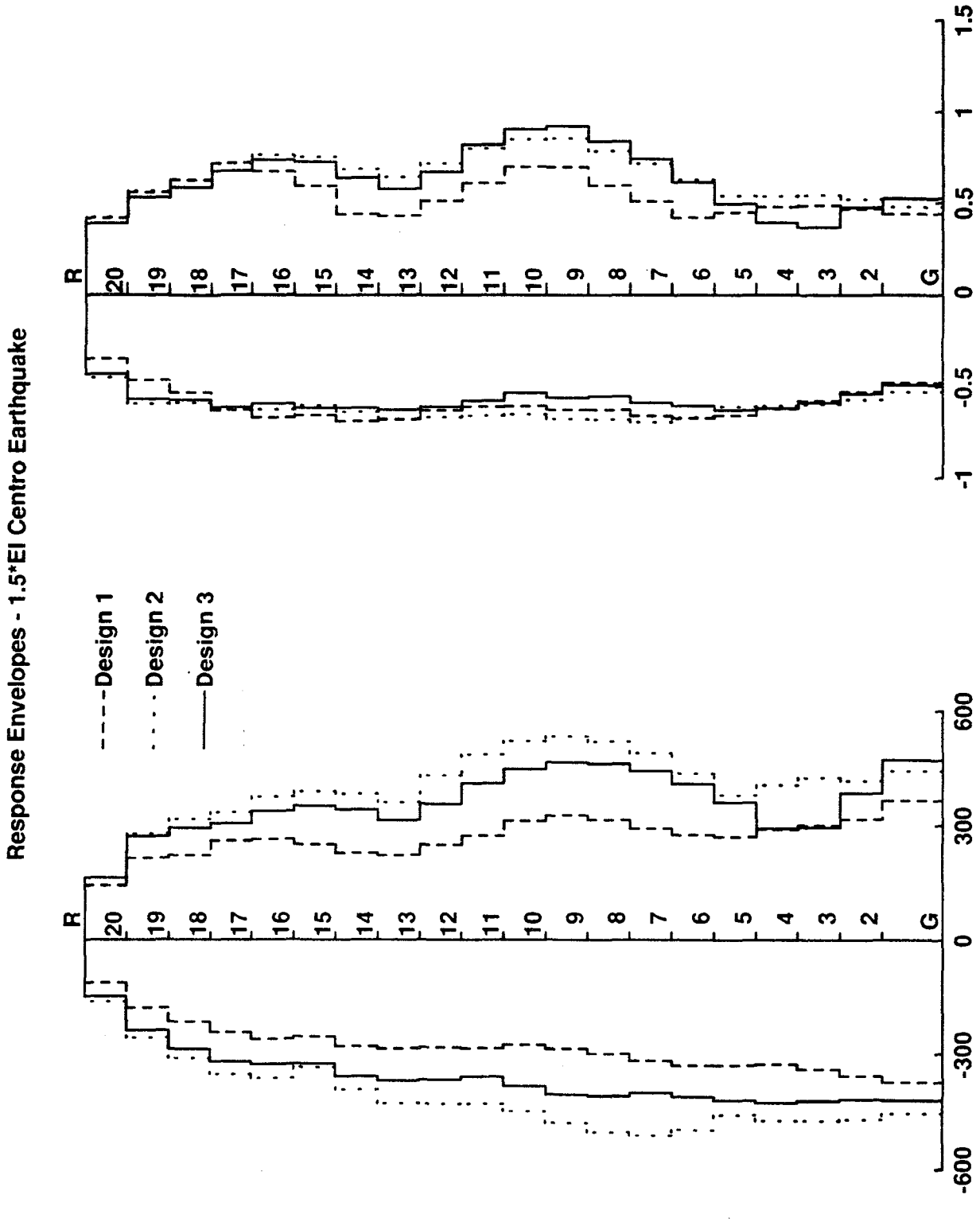

Figure 8.32 Maximum Story Shear and Story Drift for MRF Designs 1 2, and 3 (1.5*El Centro Earthquake)

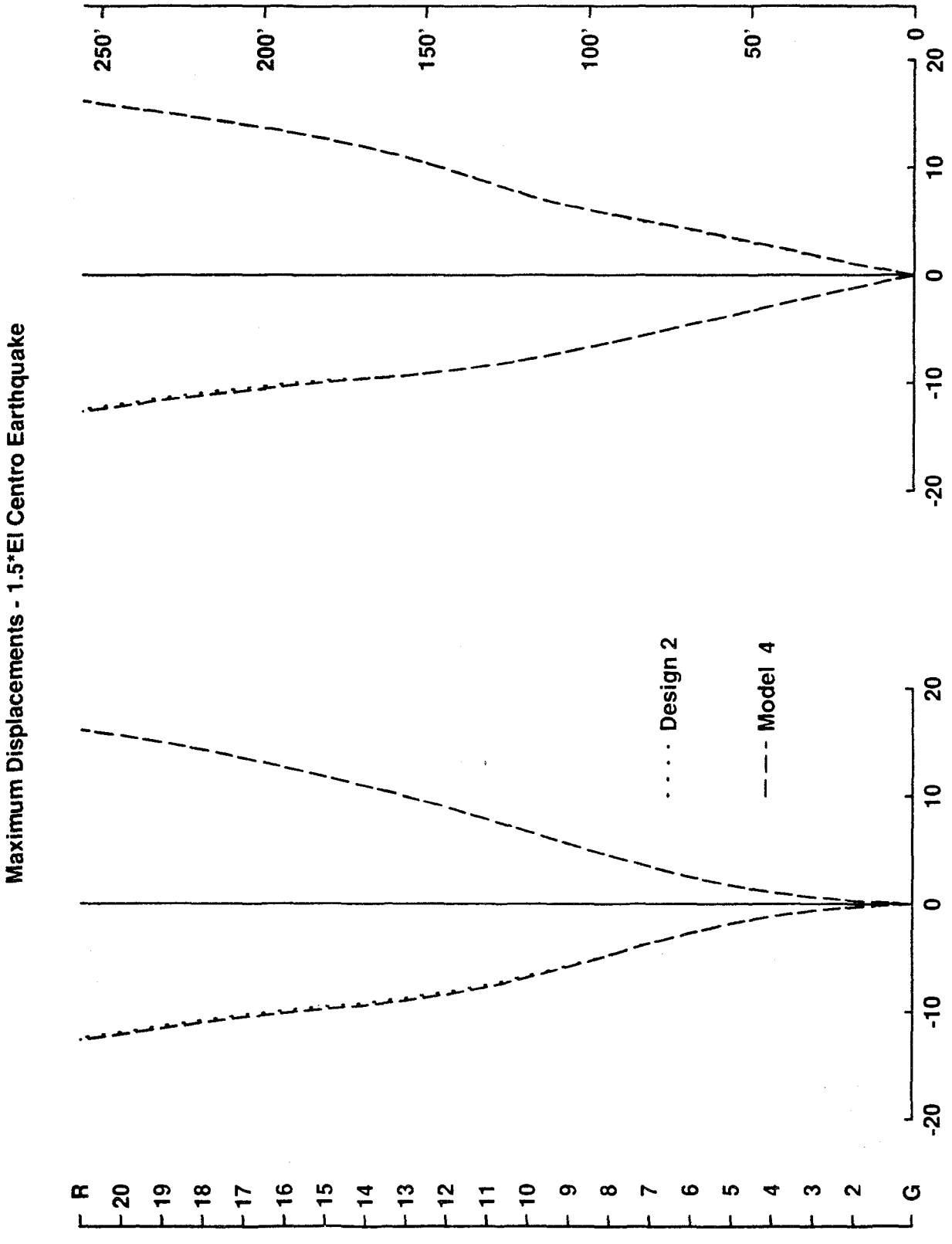

Figure 8.33 Maximum Floor Displacements for MRF Design 2 and Model 4 (1.5*El Centro Earthquake)

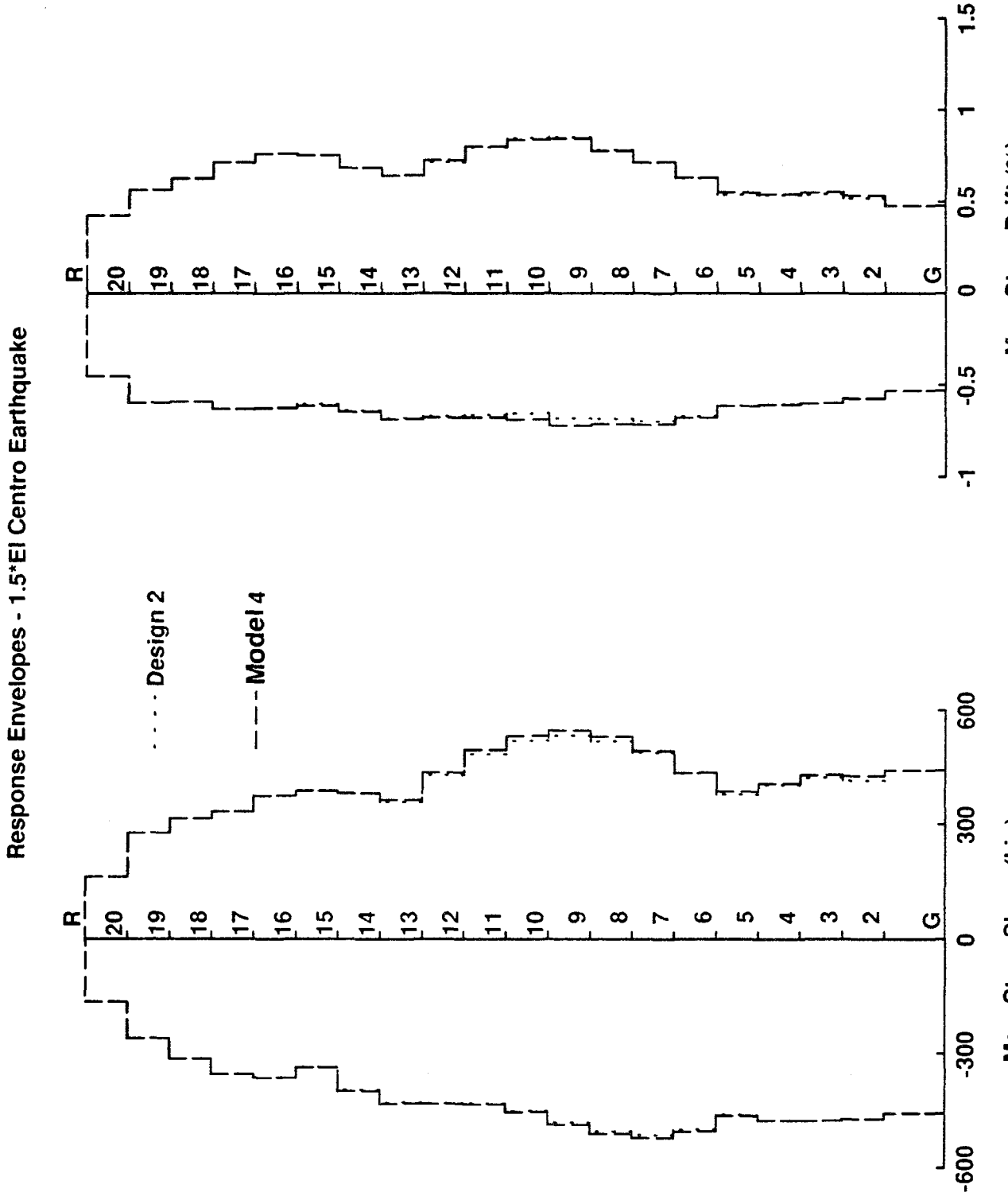

Figure 8.34 Maximum Story Shear and Story Drift for MRF Design 2 and Model 4 (1.5*El Centro Earthquake)

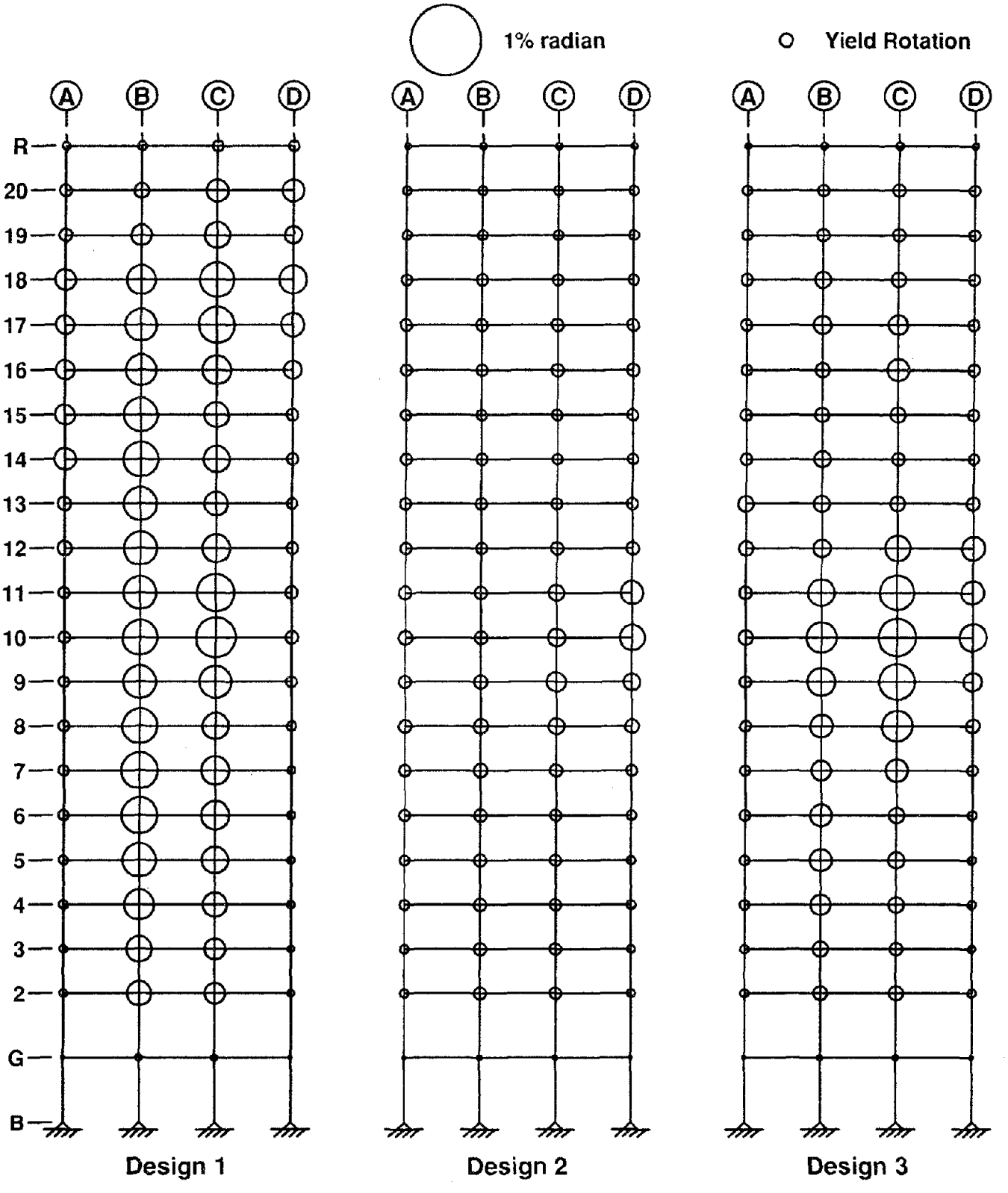

Figure 8.35 Maximum Panel Zone Deformations for MRF Designs 1, 2 and 3

Design 1 - 1.5*El Centro Earthquake

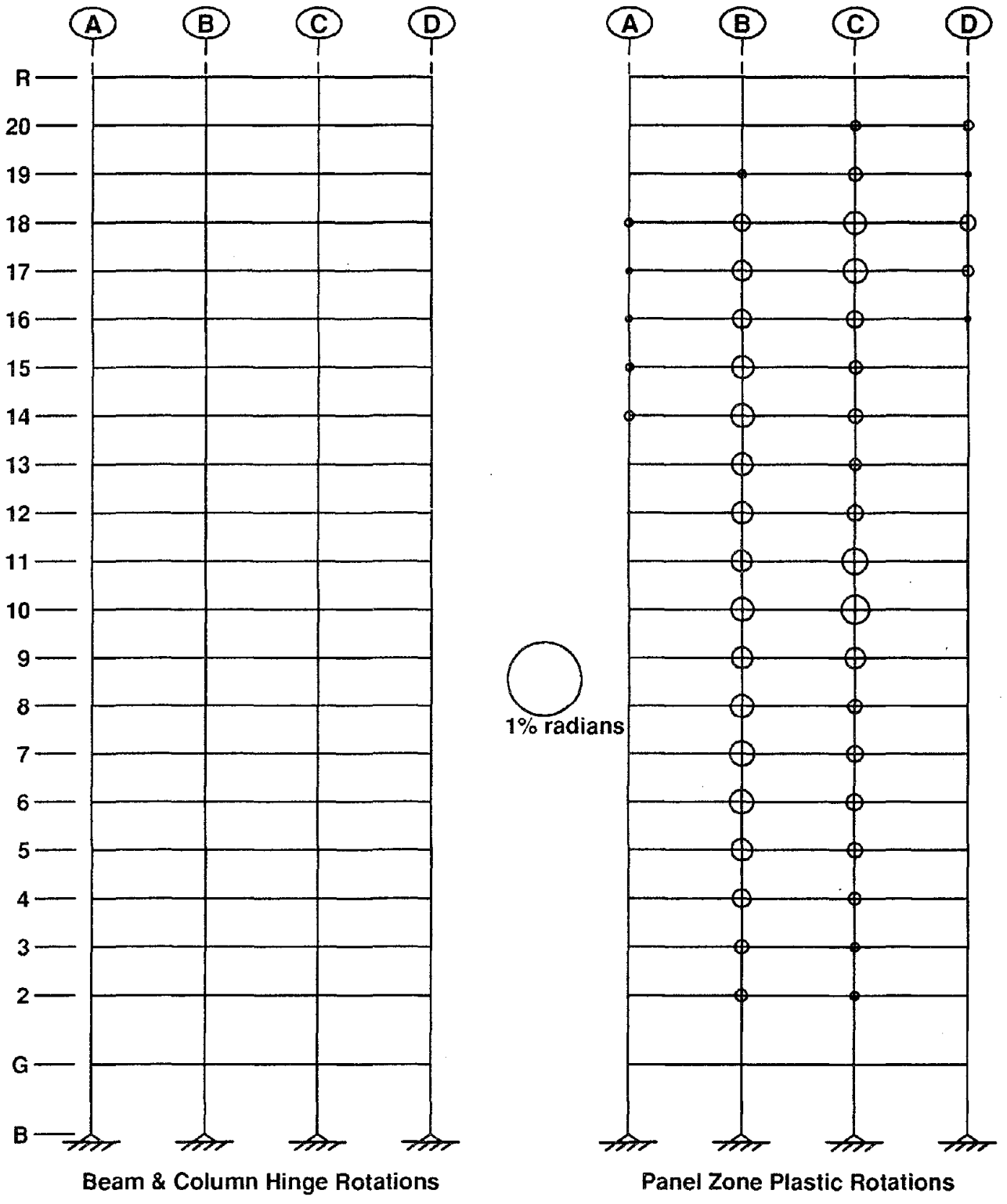

Figure 8.36 Maximum Beam, Column and Panel Zone Joint Plastic Rotations for MRF Design 1

Design 2 - 1.5*El Centro Earthquake

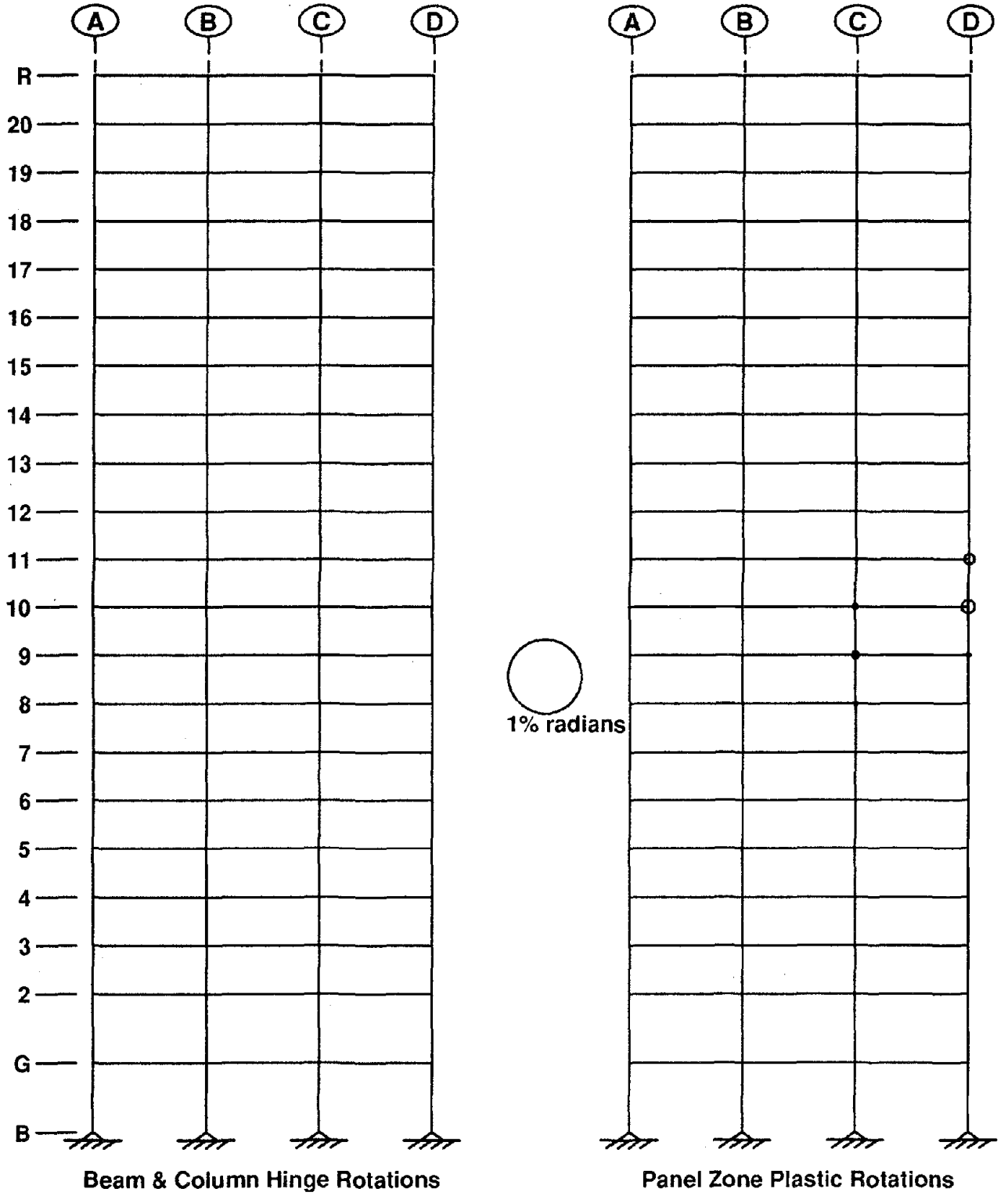

Figure 8.37 Maximum Beam, Column and Panel Zone Joint Plastic Rotations for MRF Design 2

Design 3 - 1.5*El Centro Earthquake

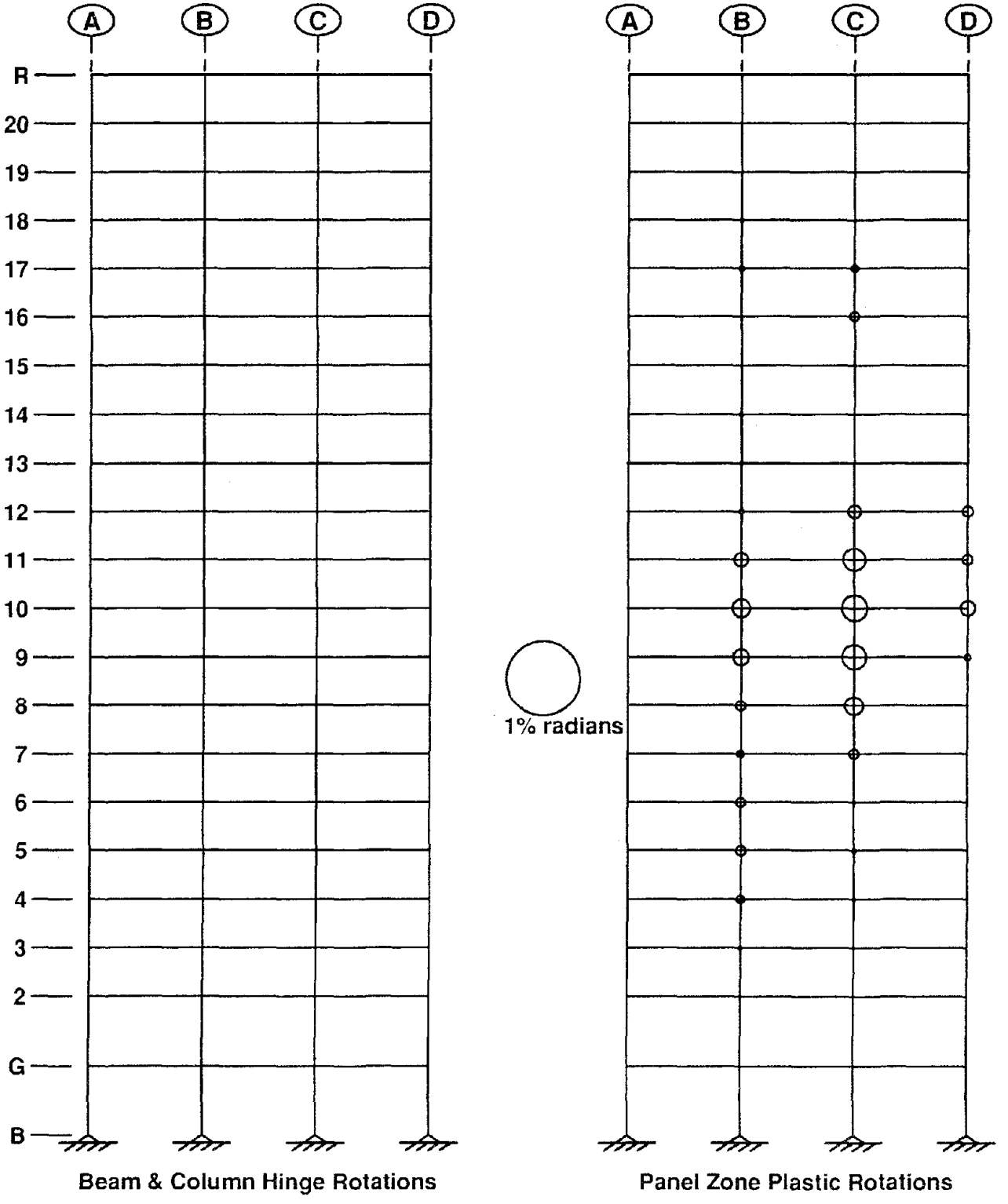

Figure 8.38 Maximum Beam, Column and Panel Zone Joint Plastic Rotations for MRF Design 3

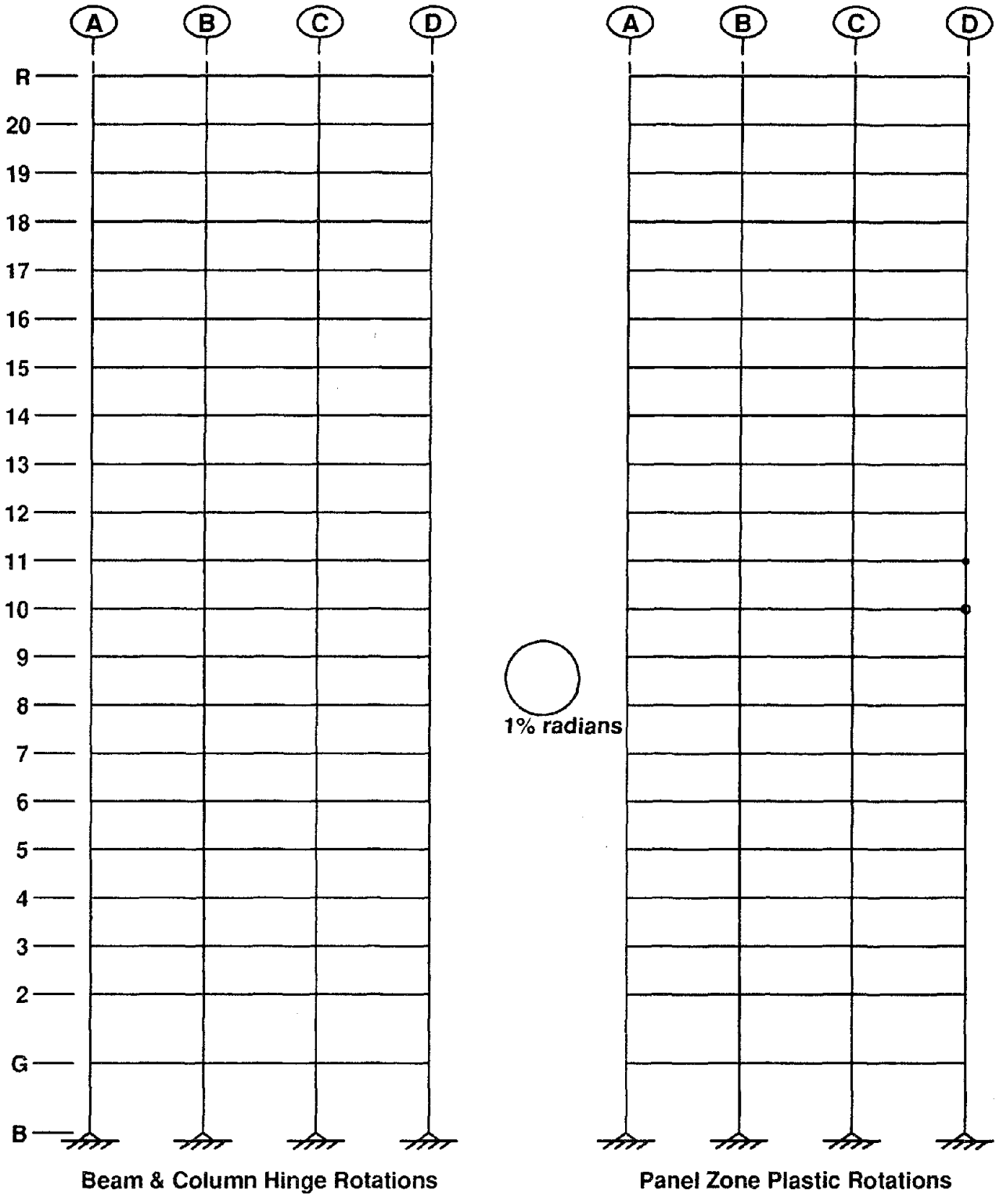

Figure 8.39 Maximum Beam, Column and Panel Zone Joint Plastic Rotations for MRF Model 4

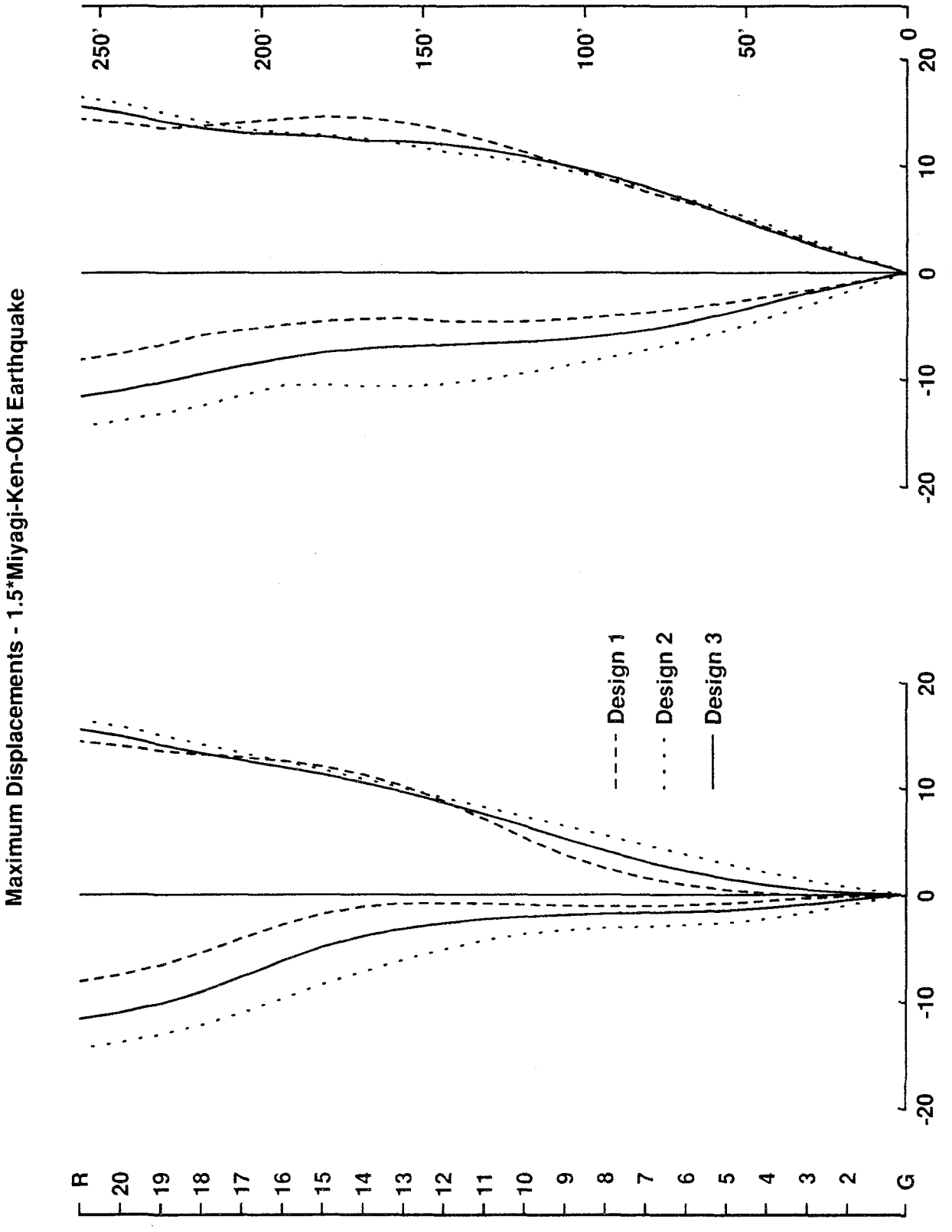

Figure 8.40 Maximum Floor Displacements for MRF Designs 1 2, and 3(1.5*Miyagi-Ken-Oki Earthquake)

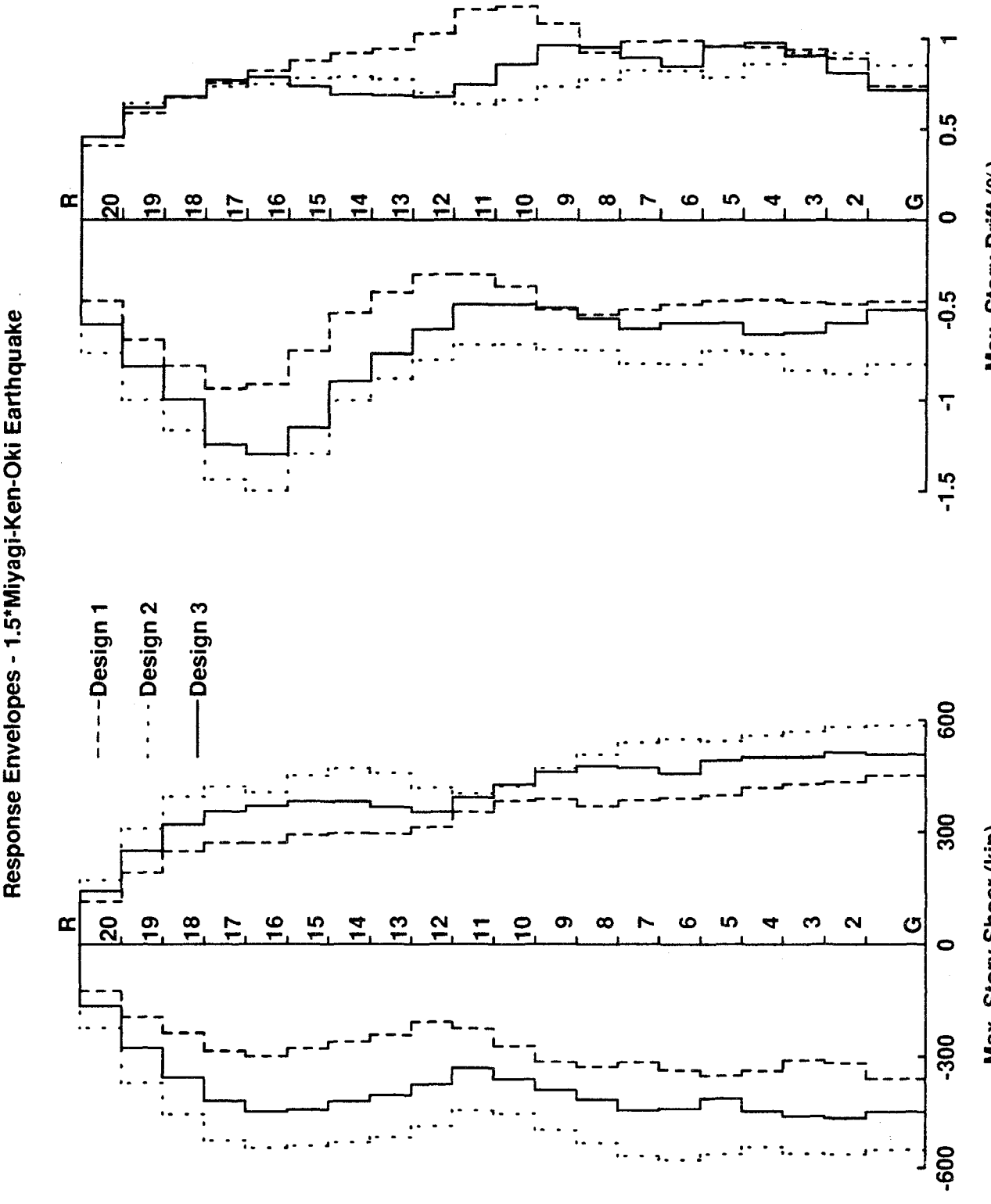

Figure 8.41 Maximum Story Shear and Story Drift for MRF Designs 1 2, and 3 (1.5*Miyagi-Ken-Oki Earthquake)

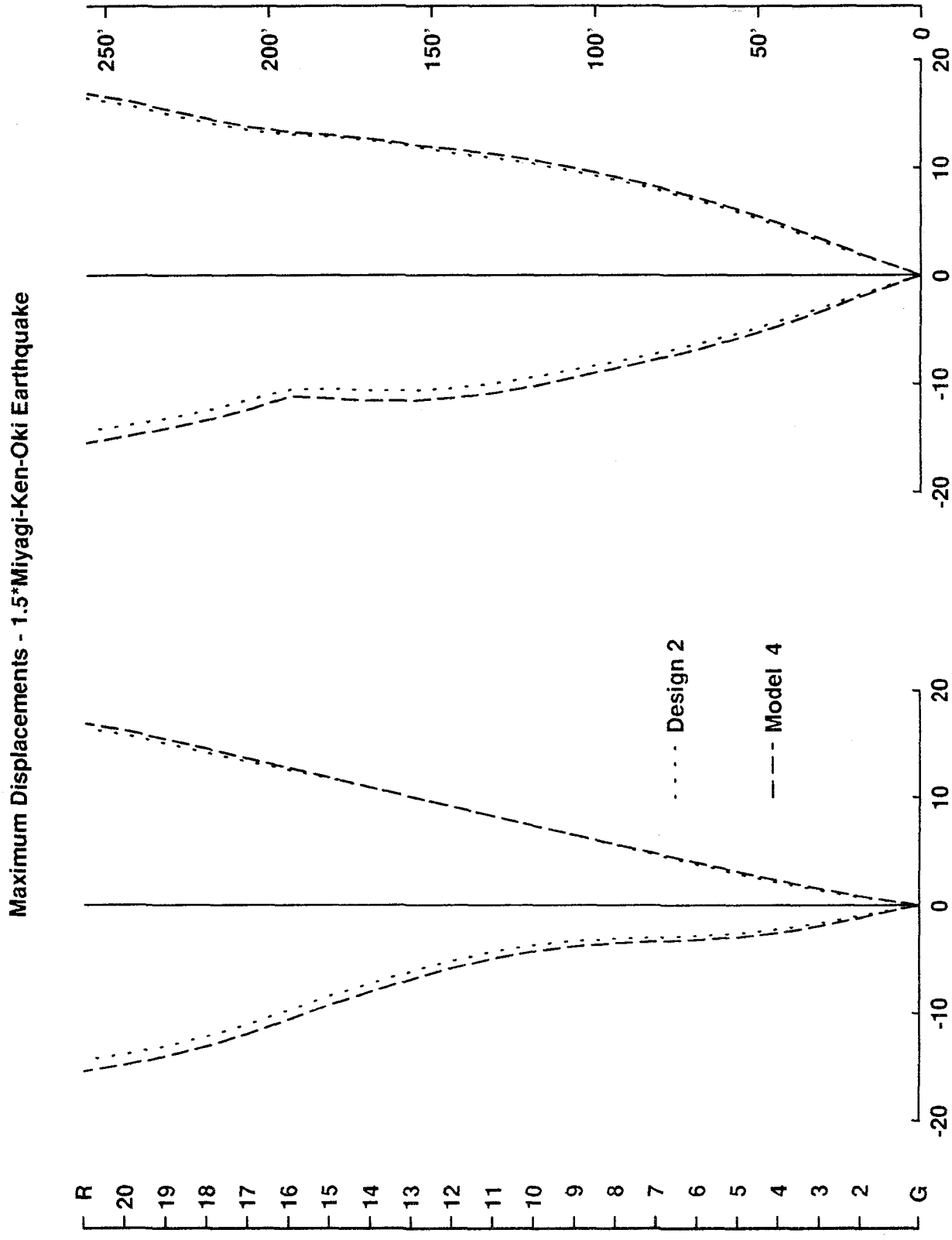

Figure 8.42 Maximum Floor Displacements for MRF Design 2 and Model 4 (1.5*Miyagi-Ken-Oki Earthquake)

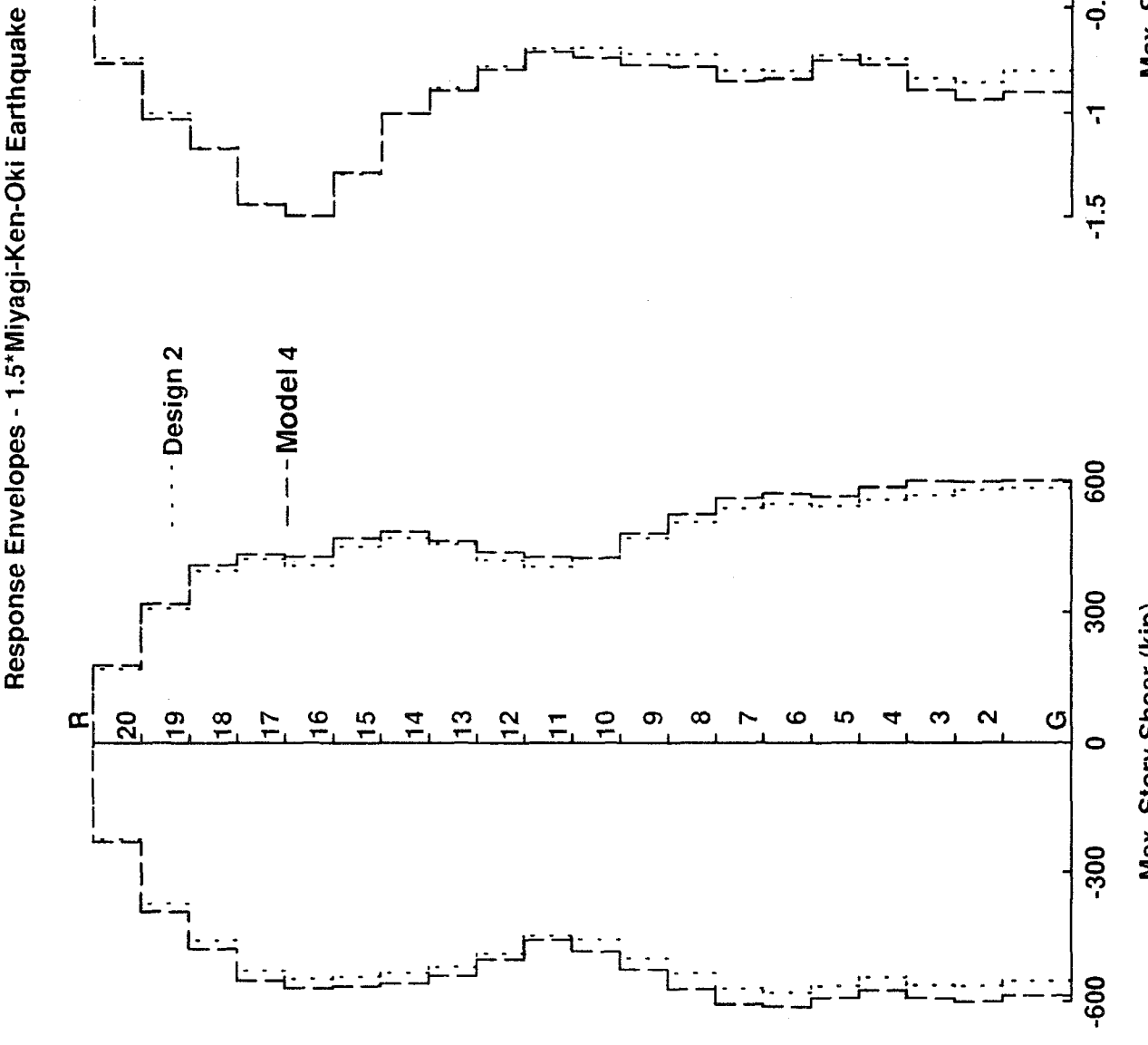

Figure 8.43 Maximum Story Shear and Story Drift for MRF Design 2 and Model 4 (1.5*Miyagi-Ken-Oki Earthquake)

1.5*Miyagi-Ken-Oki Earthquake

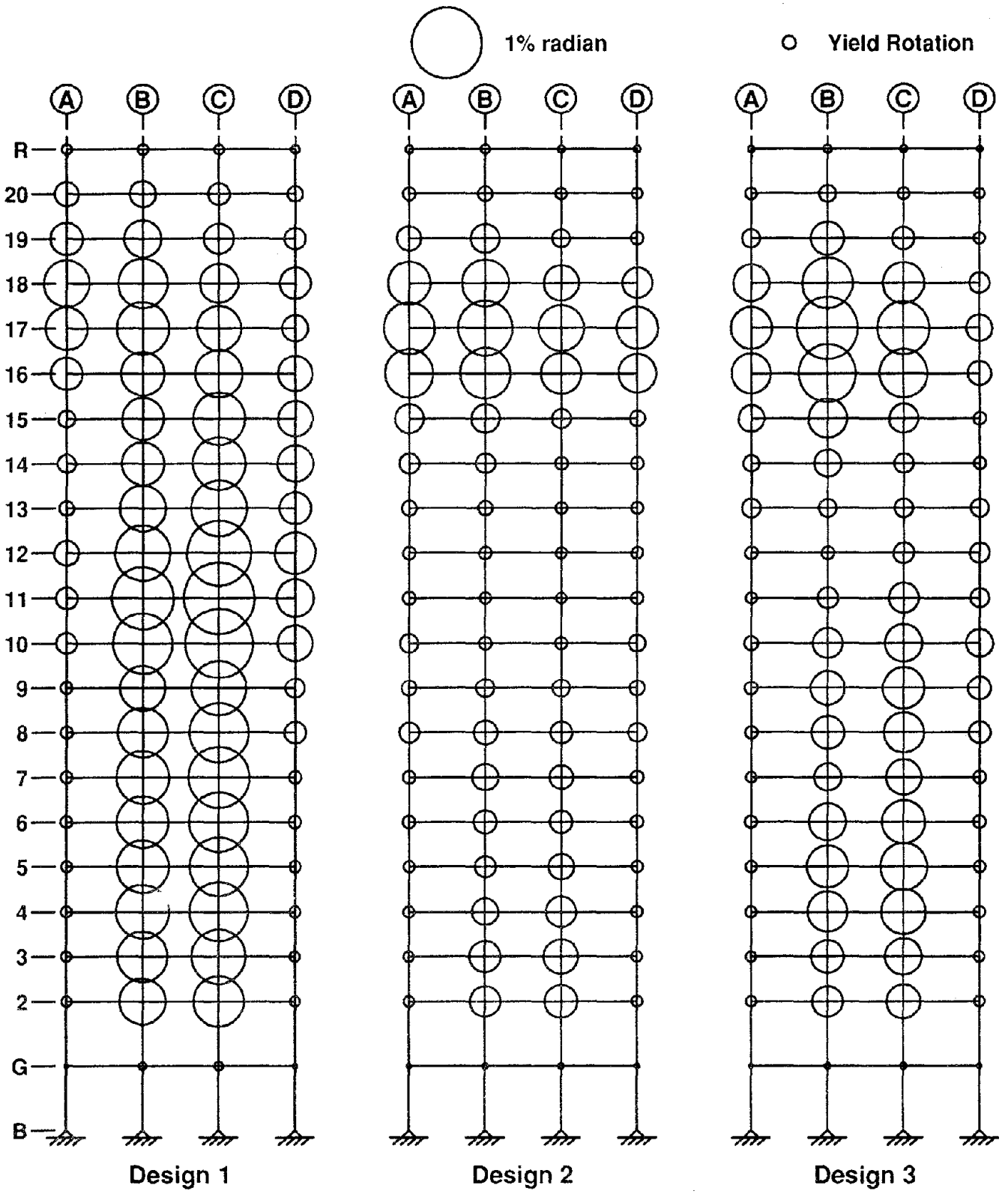

Figure 8.44 Maximum Panel Zone Deformations for MRF Designs 1, 2 and 3

Design 1 - 1.5*Miyagi-Ken-Oki Earthquake

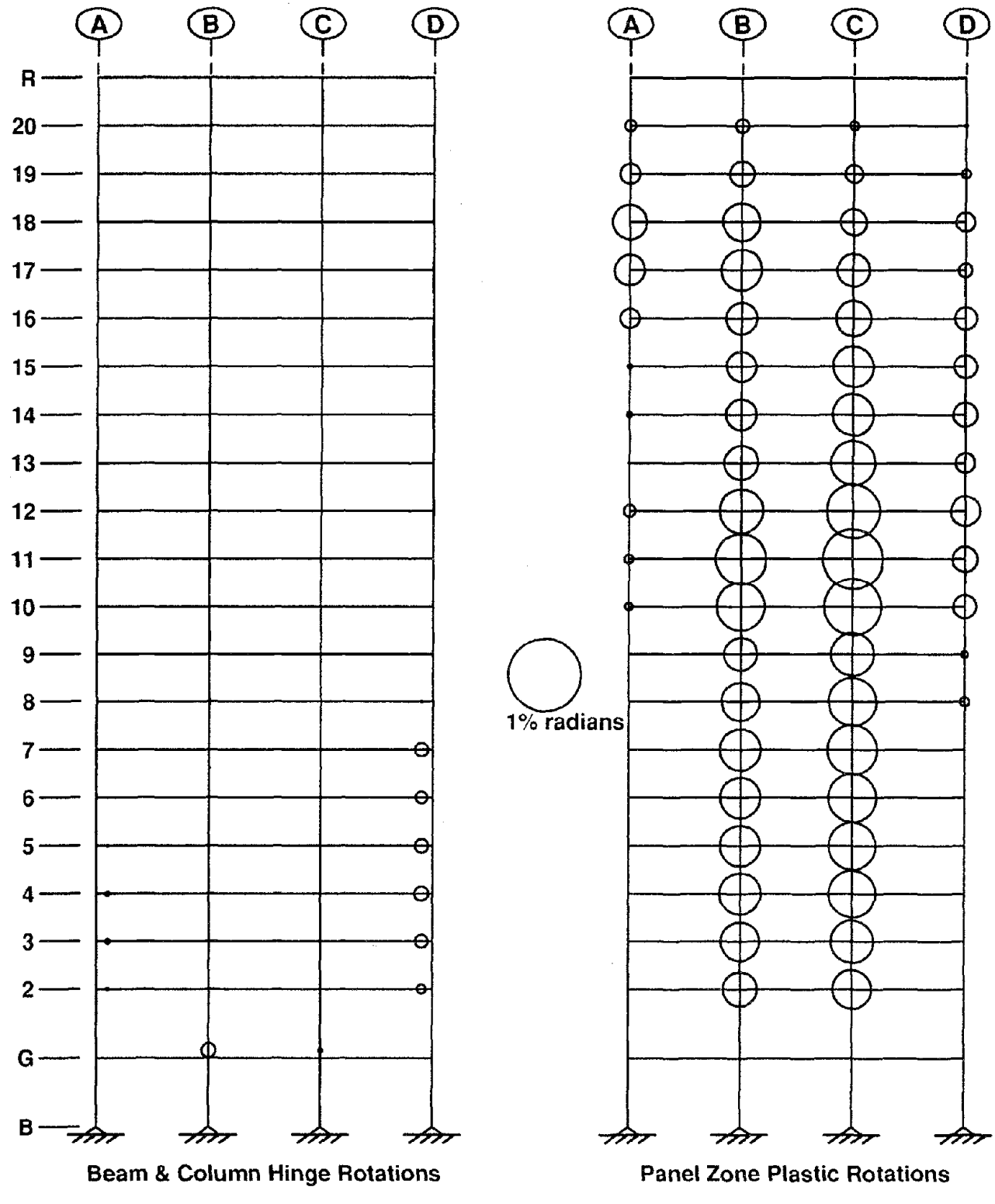

Figure 8.45 Maximum Beam, Column and Panel Zone Joint Plastic Rotations for MRF Design 1

Design 2 - 1.5*Miyagi-Ken-Oki Earthquake

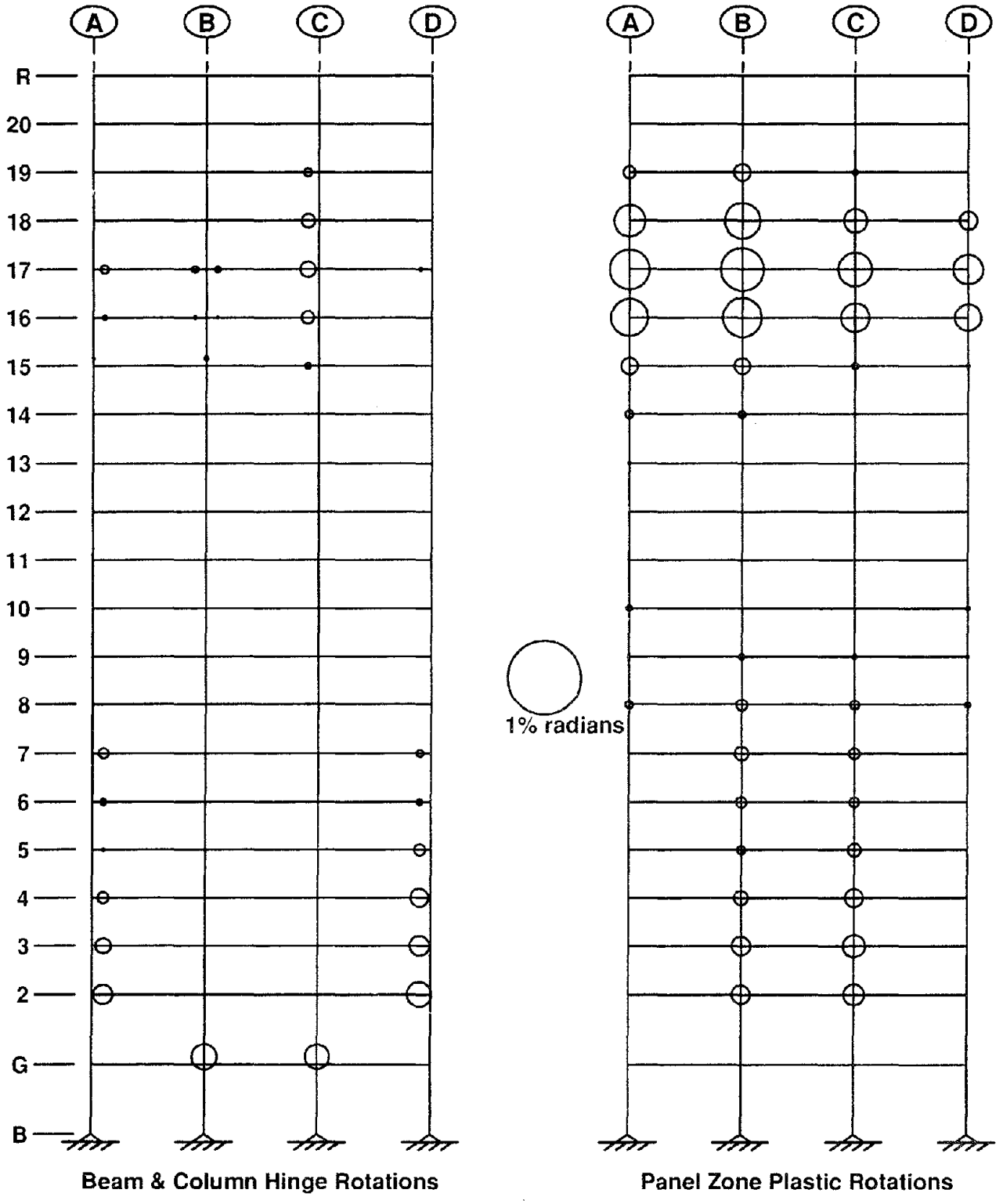

Figure 8.46 Maximum Beam, Column and Panel Zone Joint Plastic Rotations for MRF Design 2

Design 3 - 1.5*Miyagi-Ken-Oki Earthquake

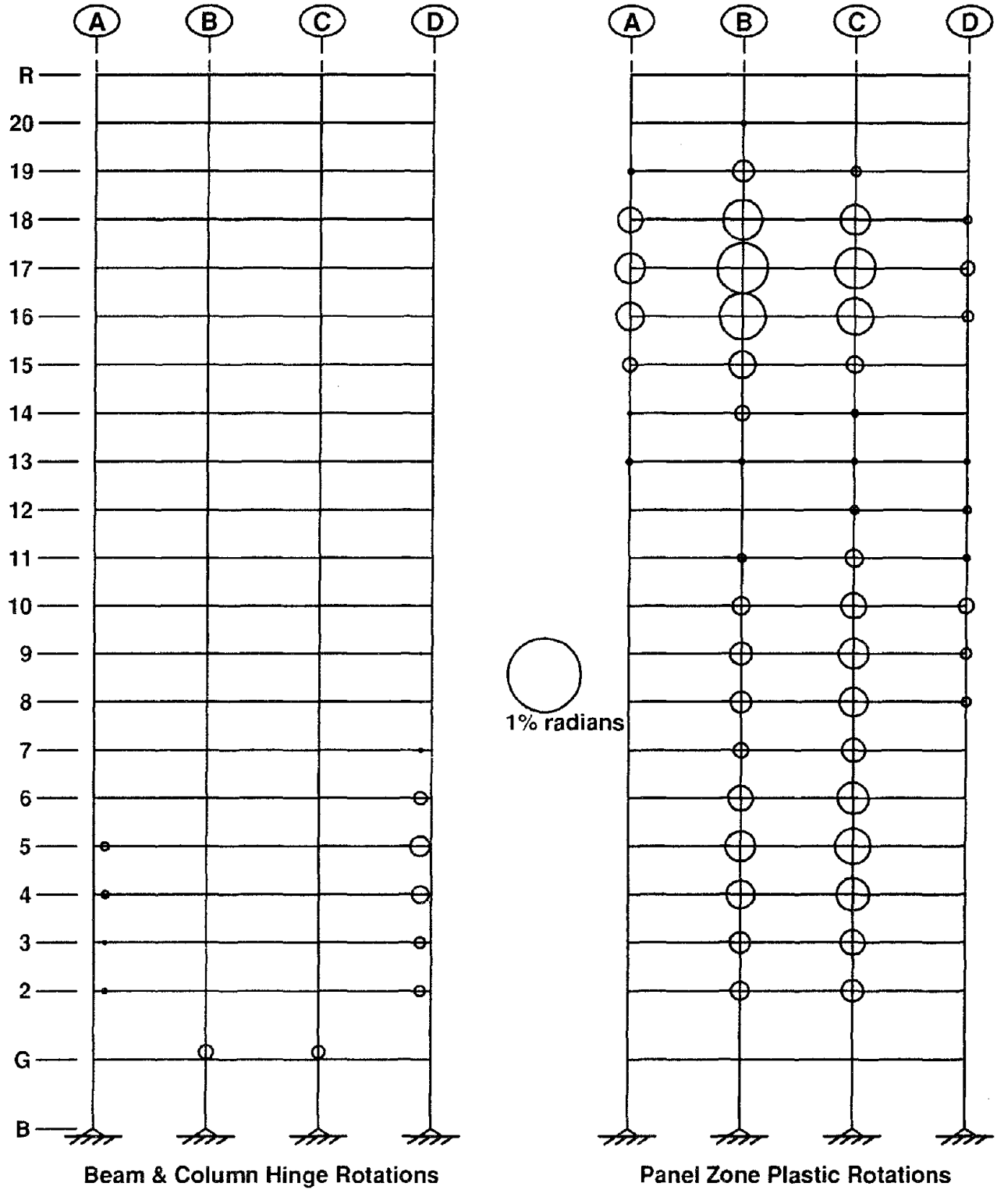

Figure 8.47 Maximum Beam, Column and Panel Zone Joint Plastic Rotations for MRF Design 3

Model 4 - 1.5*Miyagi-Ken-Oki Earthquake

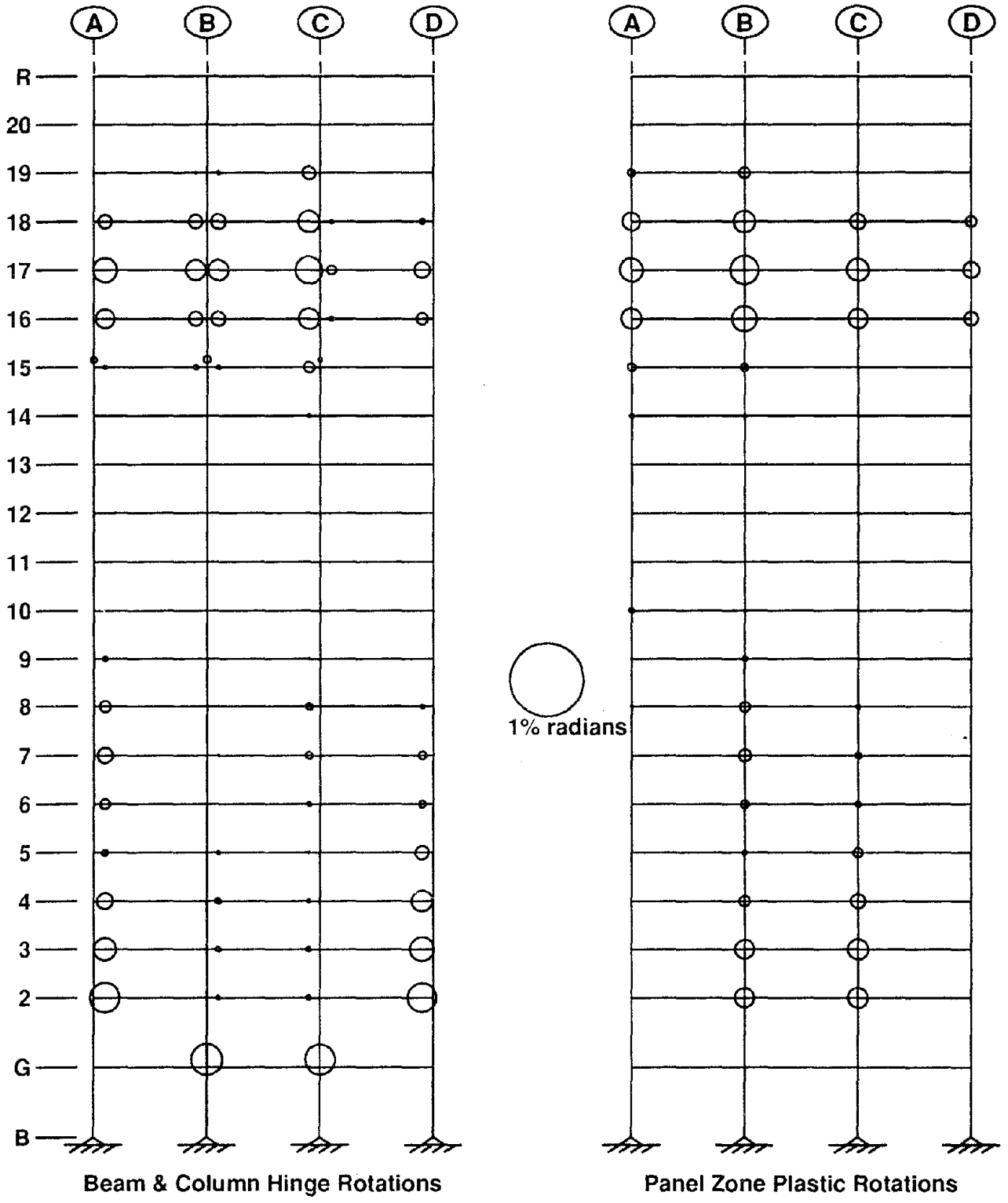

Figure 8.48 Maximum Beam, Column and Panel Zone Joint Plastic Rotations for MRF Model 4

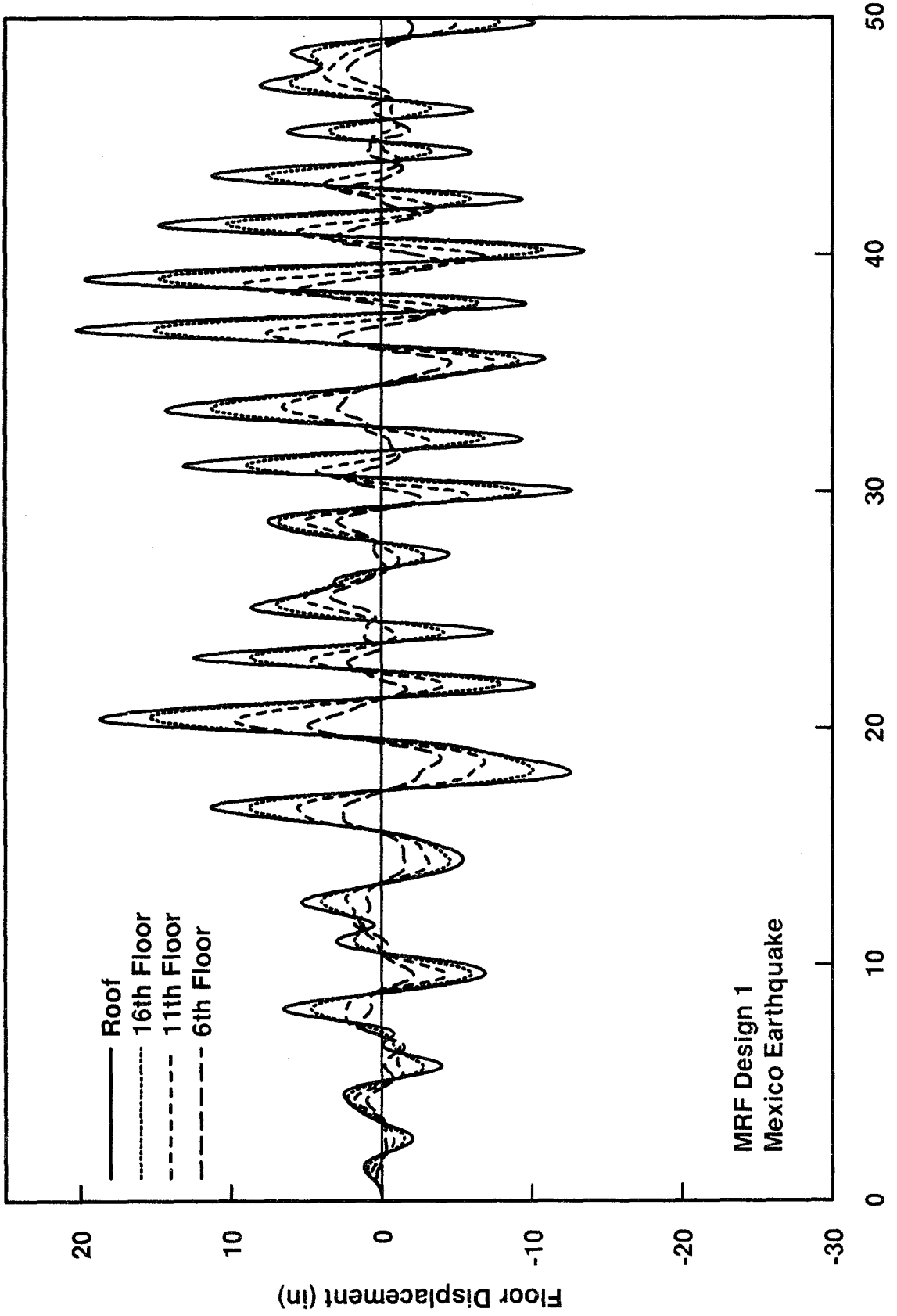

Figure 8.49 Displacement Histories for the 6th, 11th, 16th and Roof Floors of MRF Design 1

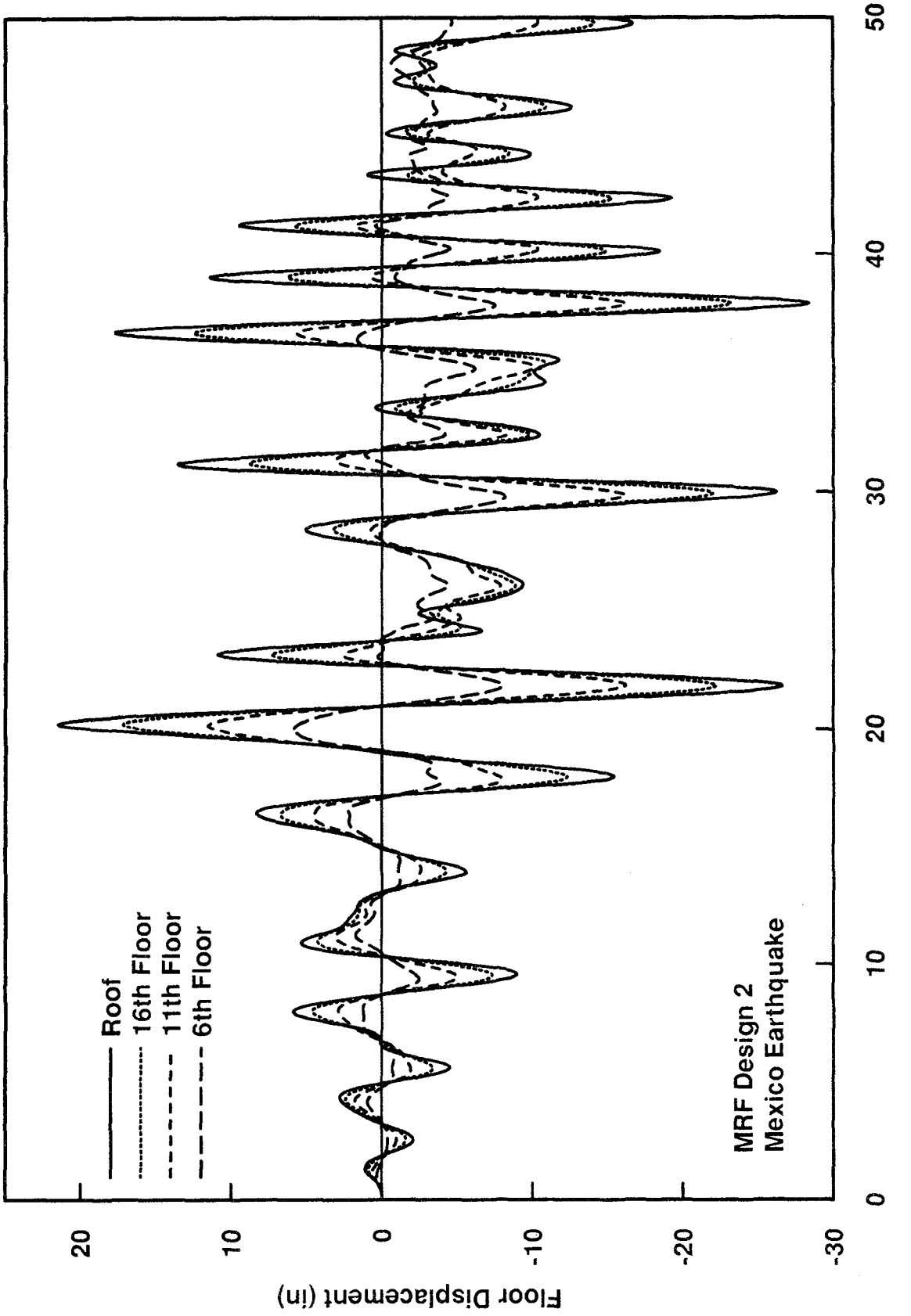

Figure 8.50 Displacement Histories for the 6th, 11th, 16th and Roof Floors of MRF Design 2

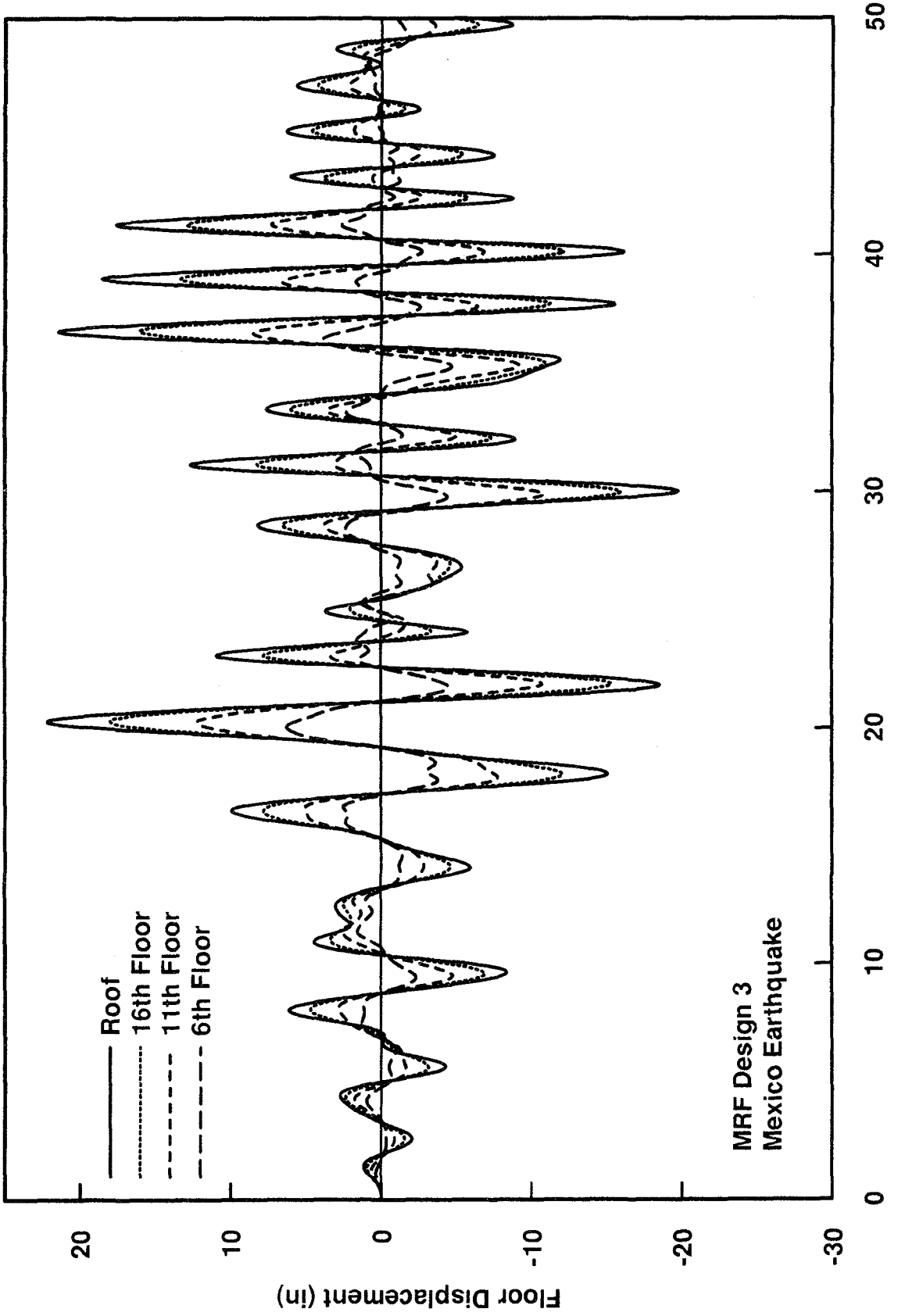

Figure 8.51 Displacement Histories for the 6th, 11th, 16th and Roof Floors of MRF Design 3

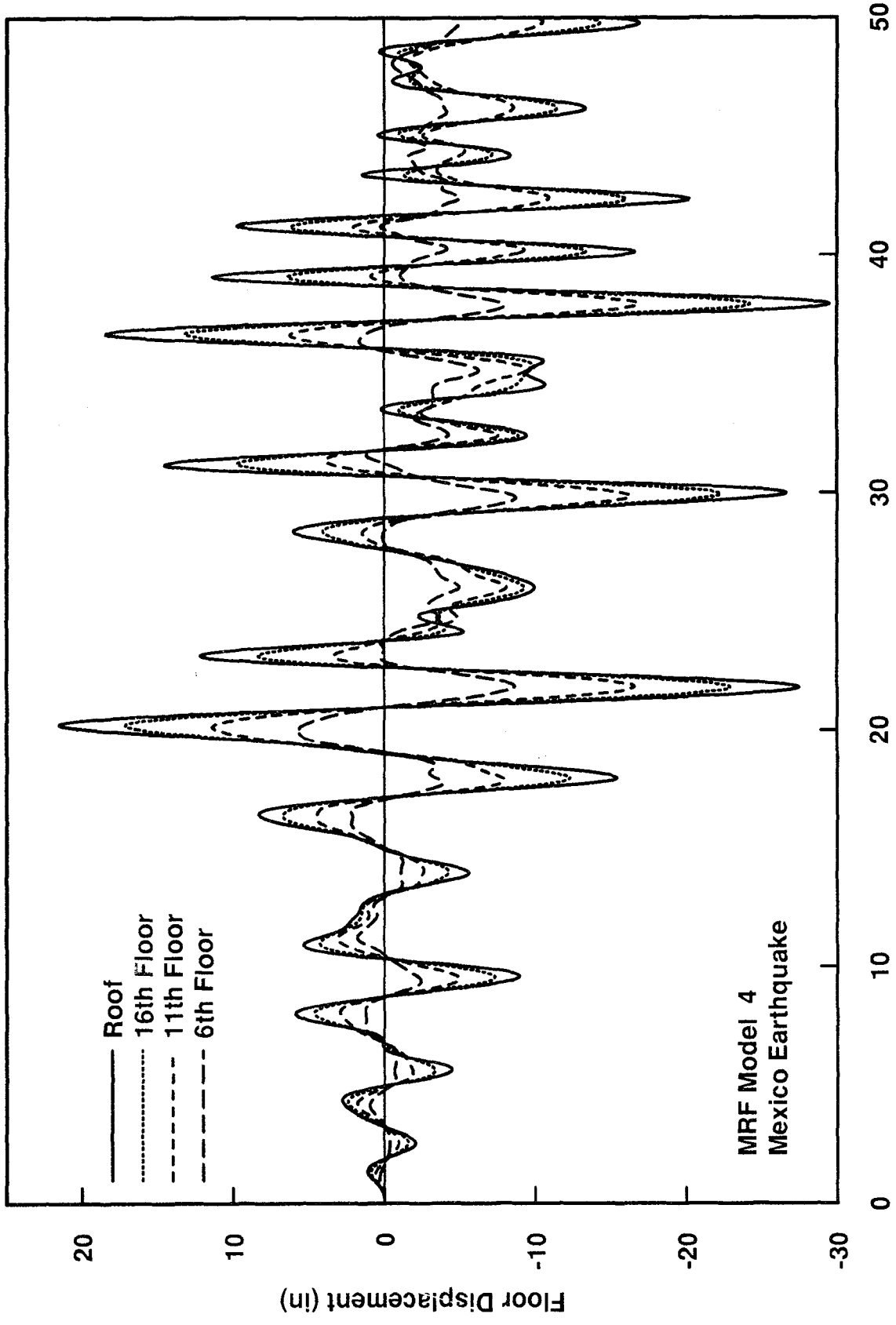

Figure 8.52 Displacement Histories for the 6th, 11th, 16th and Roof Floors of MRF Model 4

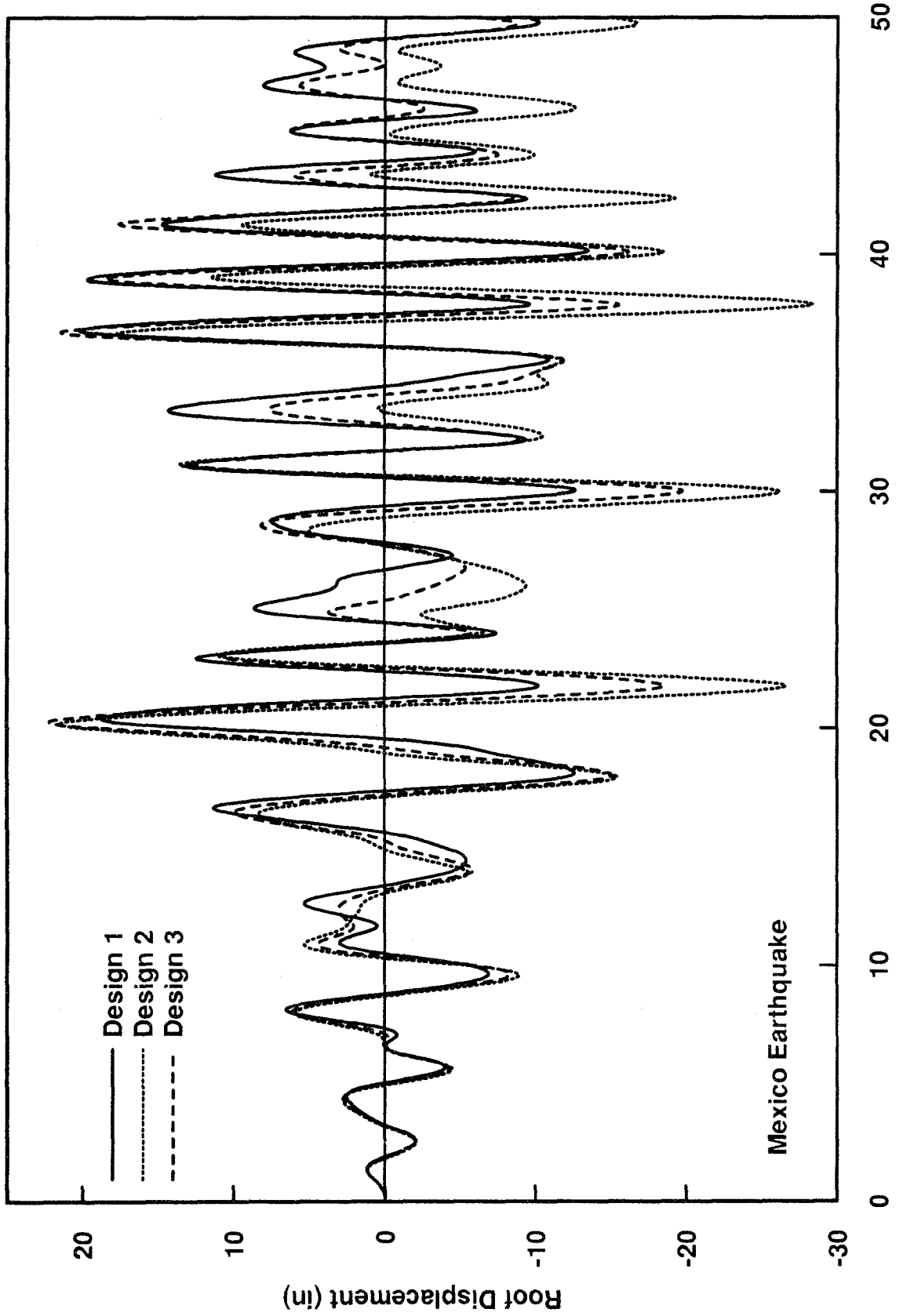

Figure 8.53 Roof Displacement Histories for MRF Designs 1, 2 and 3

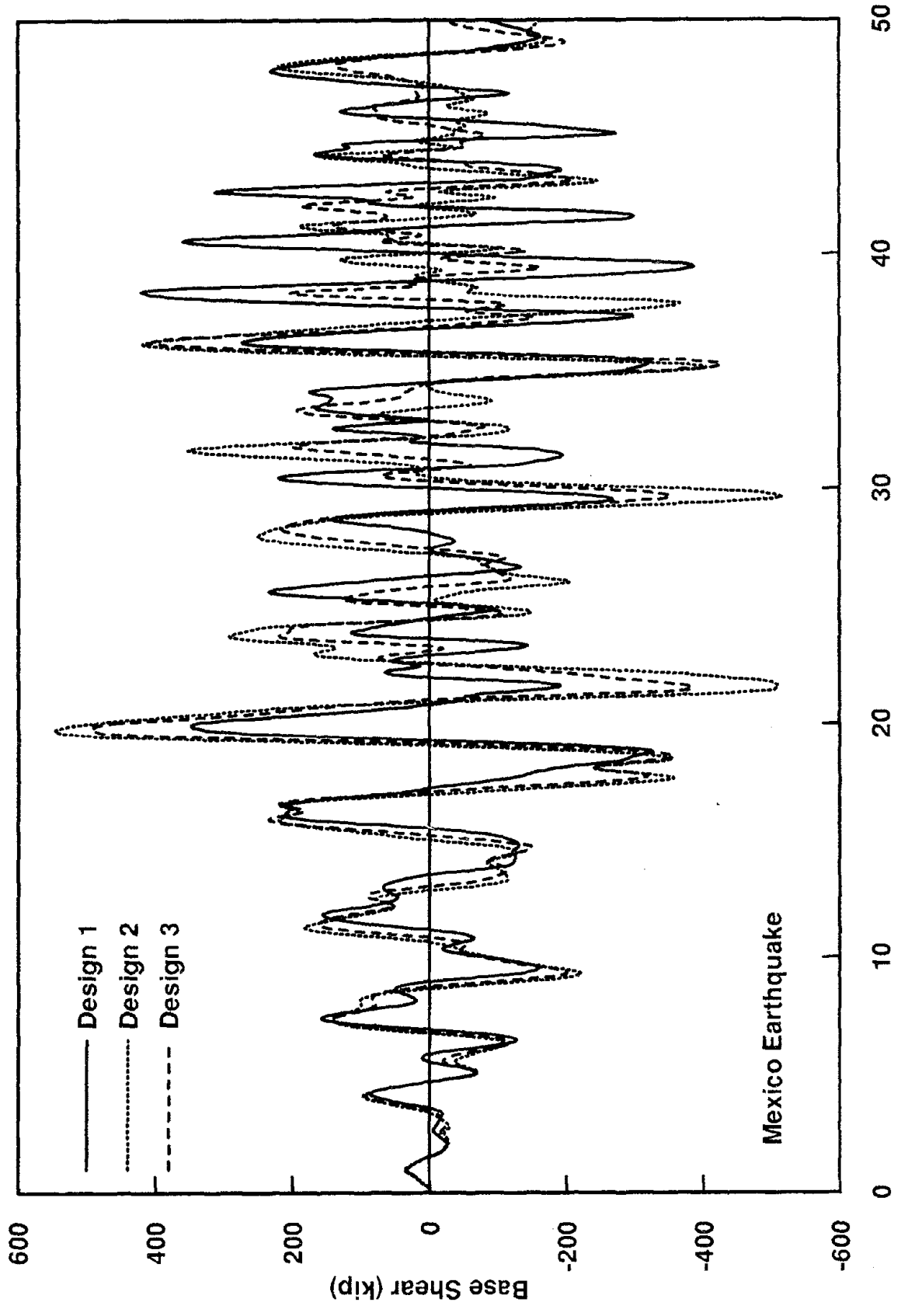

Figure 8.54 Base Shear Histories for MRF Designs Designs 1, 2 and 3

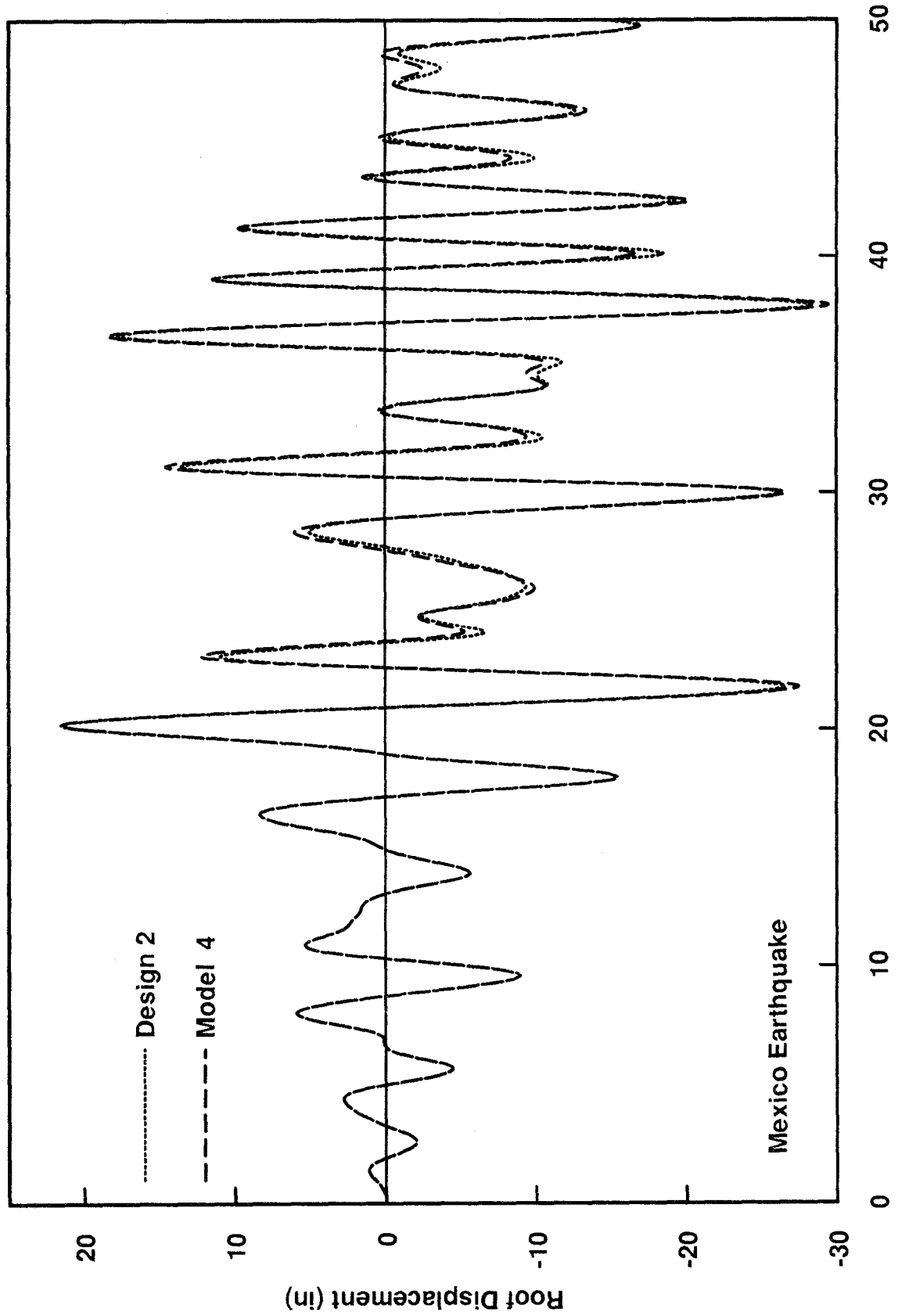

Figure 8.55 Roof Displacement Histories for MRF Designs 2, and Model 4

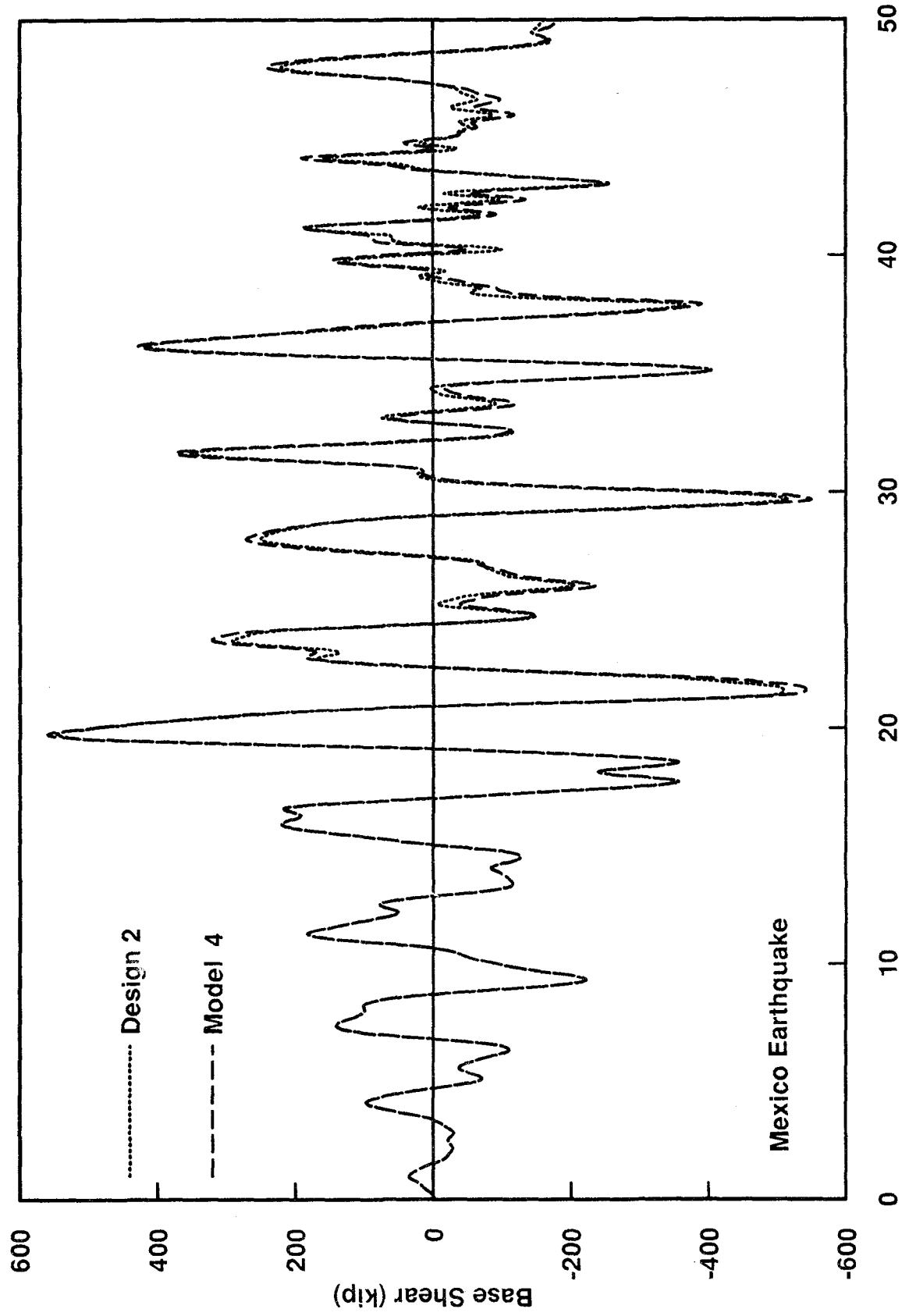

Figure 8.56 Base Shear Histories for MRF Designs 2, and Model 4

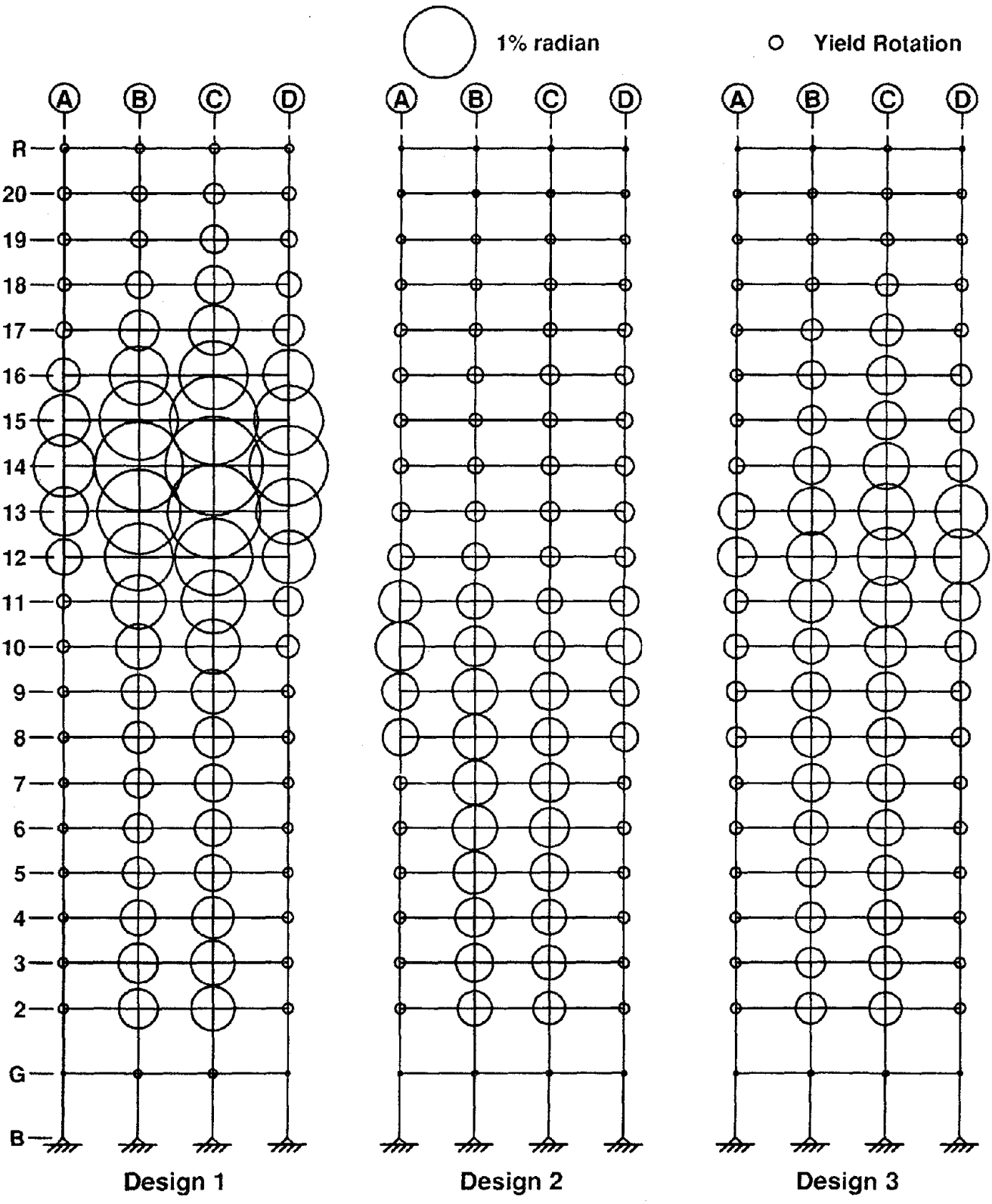

Figure 8.57 Maximum Panel Zone Deformations for MRF Designs 1, 2 and 3

Design 1 - Mexico Earthquake

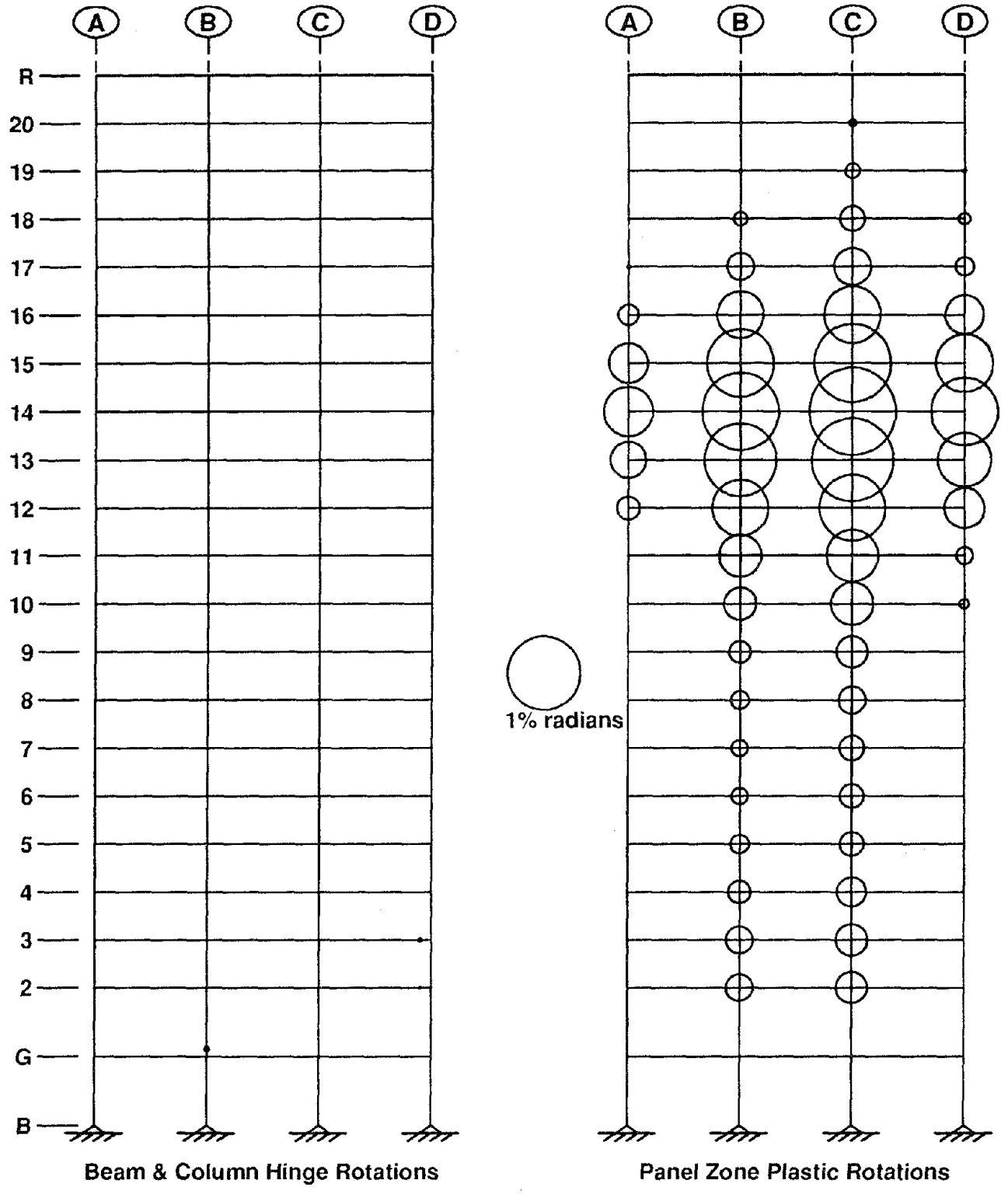

Figure 8.58 Maximum Beam, Column and Panel Zone Joint Plastic Rotations for MRF Design 1

Design 2 - Mexico Earthquake

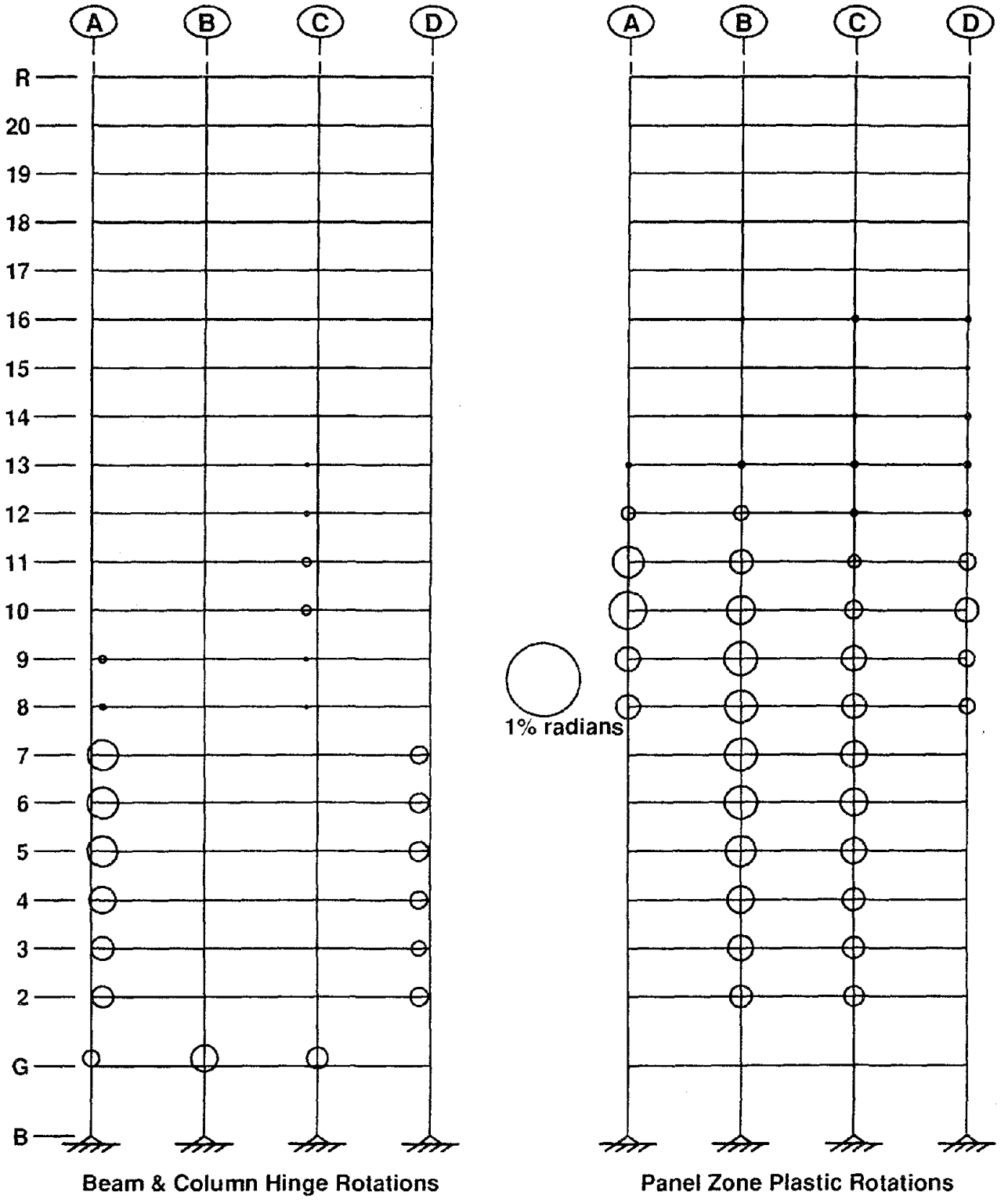

Figure 8.59 Maximum Beam, Column and Panel Zone Joint Plastic Rotations for MRF Design 2

Design 3 - Mexico Earthquake

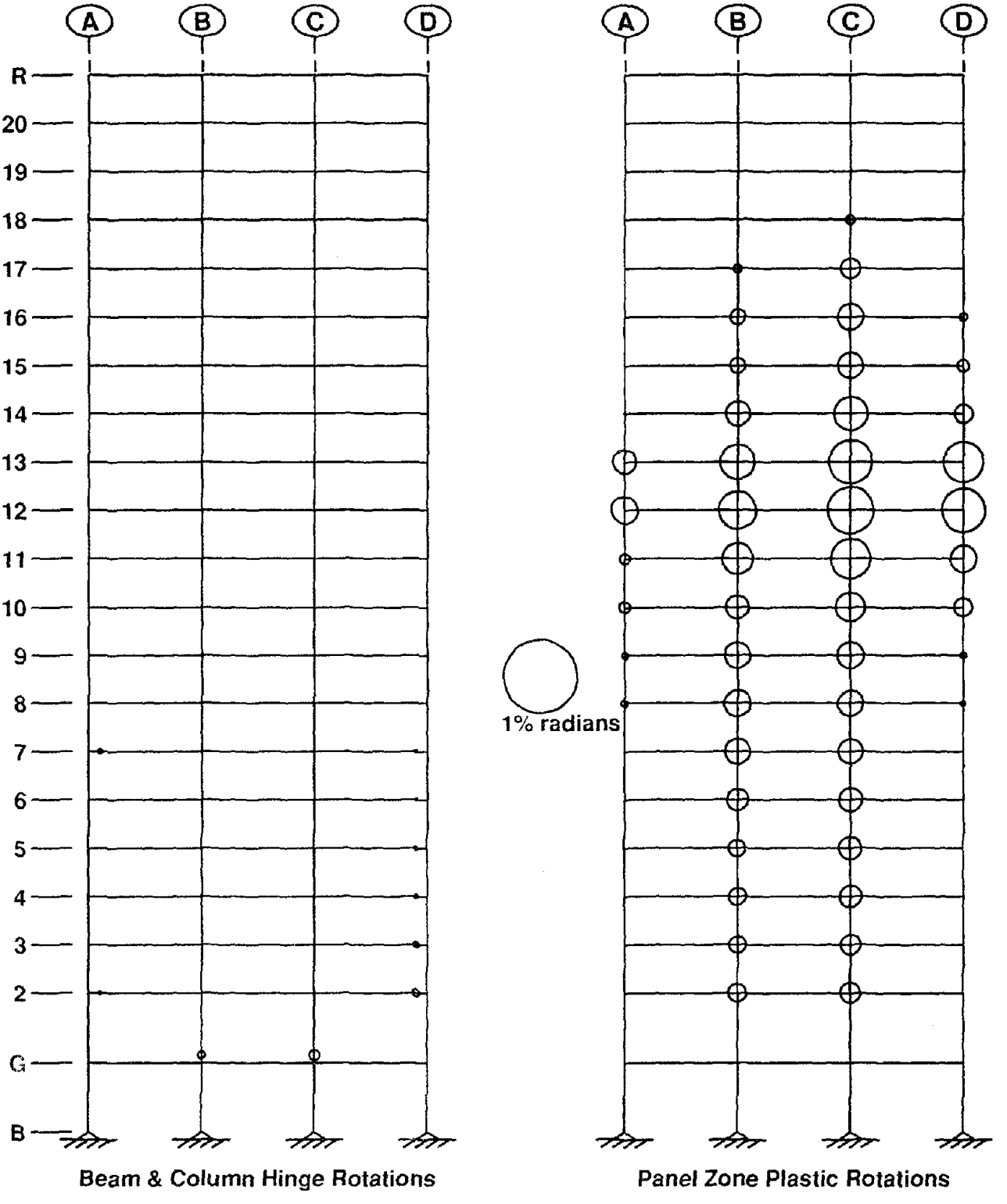

Figure 8.60 Maximum Beam, Column and Panel Zone Joint Plastic Rotations for MRF Design 3

Model 4 - Mexico Earthquake

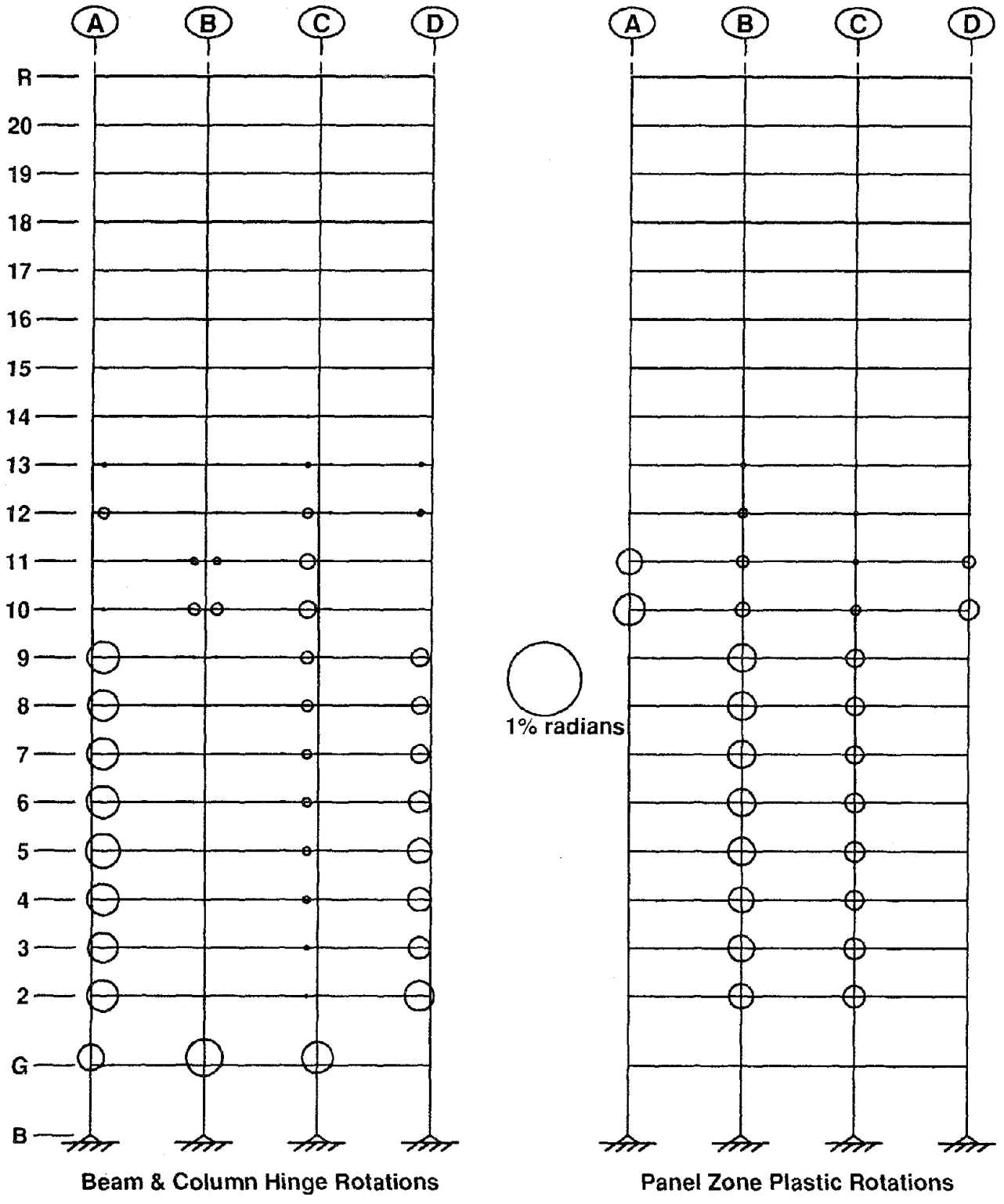

Figure 8.61 Maximum Beam, Column and Panel Zone Joint Plastic Rotations for MRF Model 4

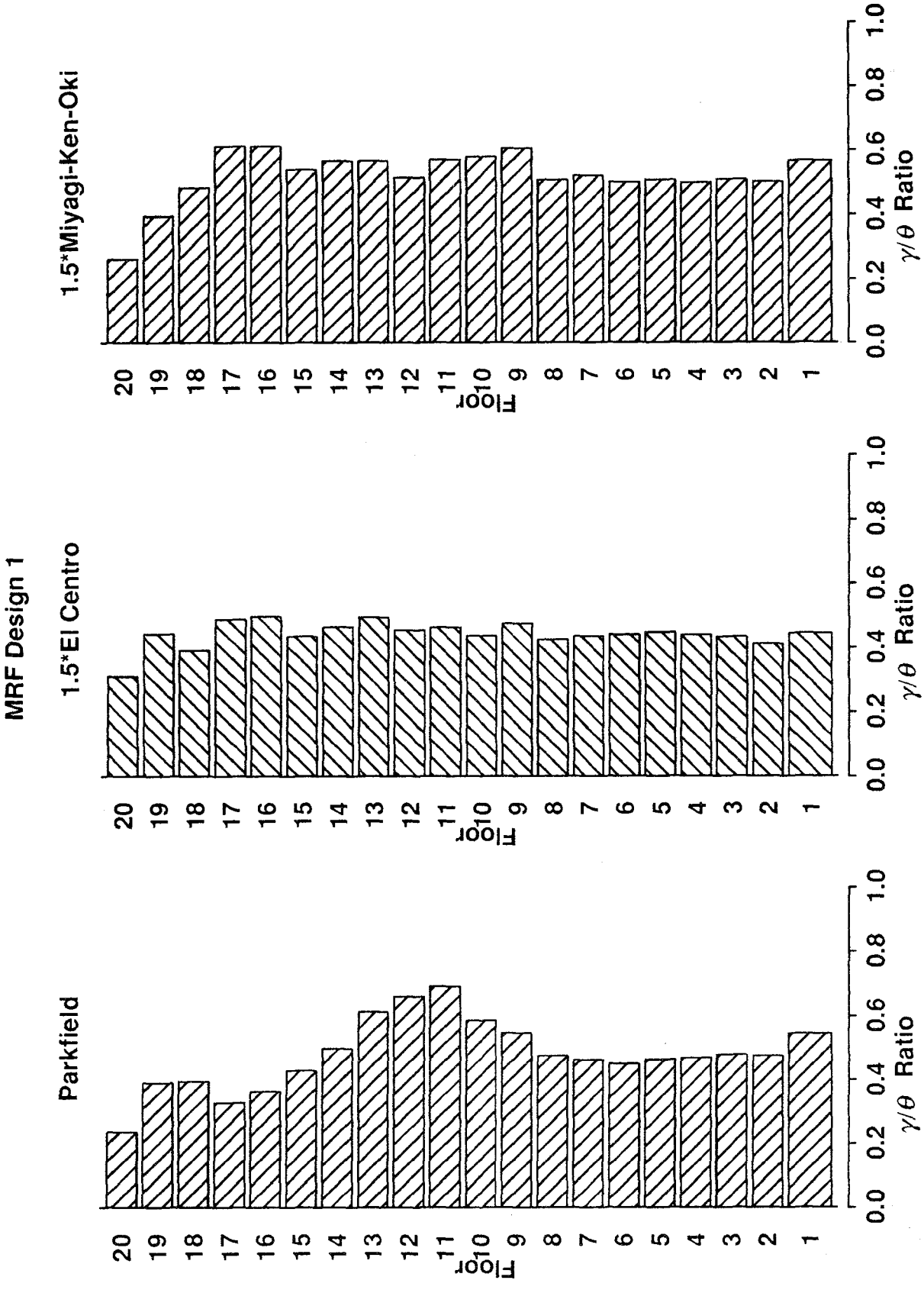

Figure 8.62 Story Panel Zone Deformation to Story Drift, γ/θ, Ratios for MRF Design 1

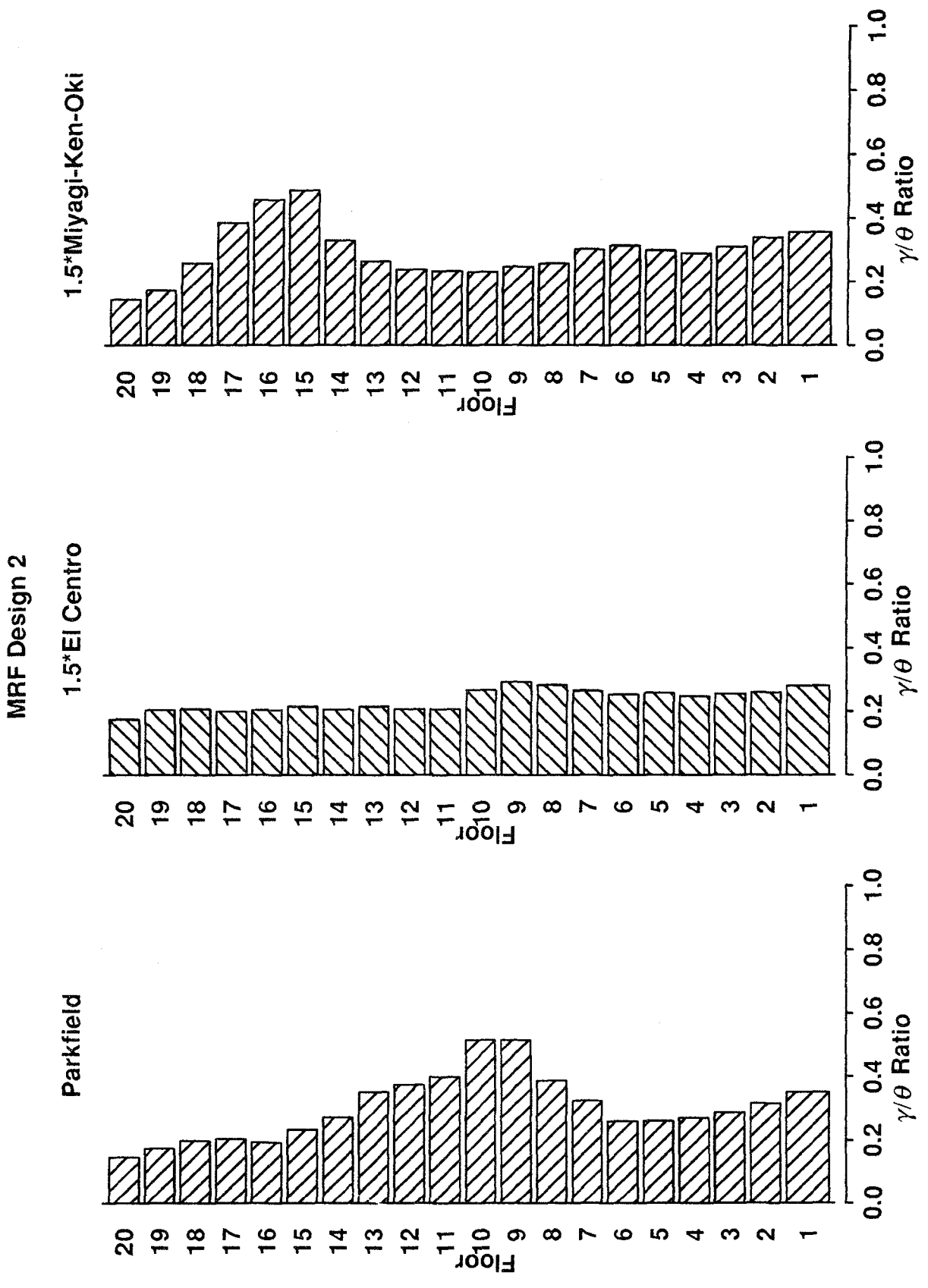

Figure 8.63 Story Panel Zone Deformation to Story Drift, γ/θ, Ratios for MRF Design 2

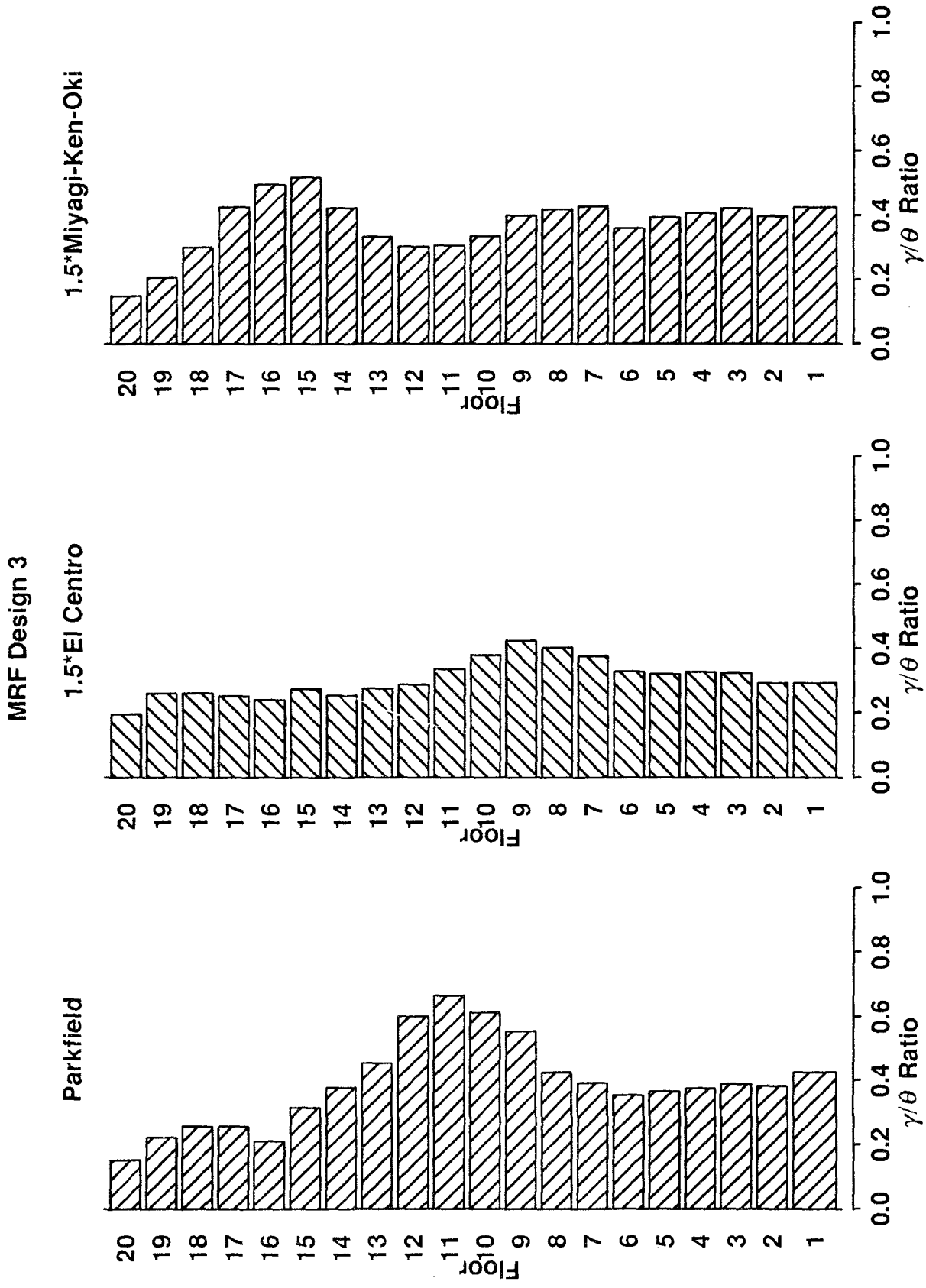

Figure 8.64 Story Panel Zone Deformation to Story Drift, γ/θ, Ratios for MRF Design 3

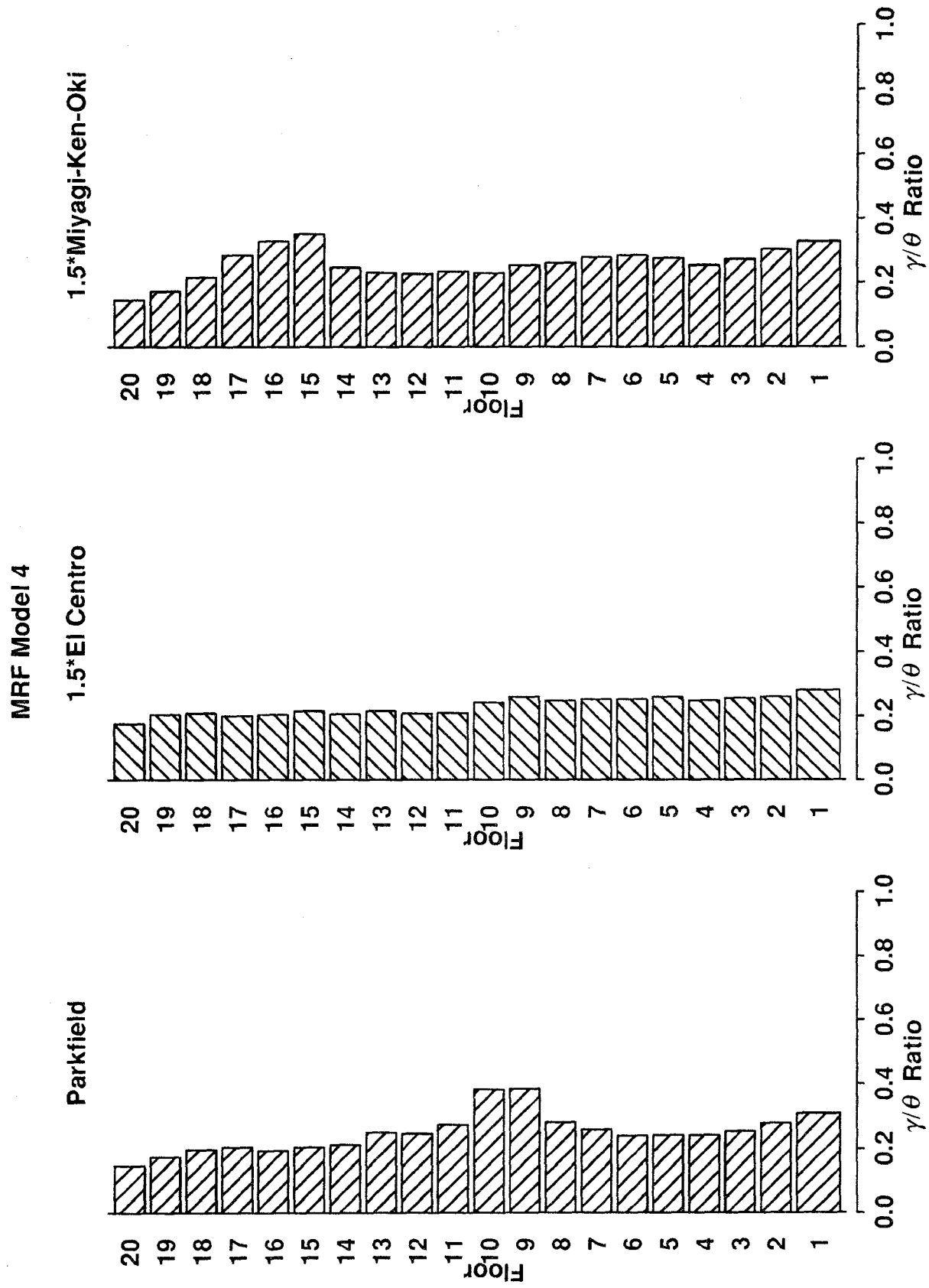

Figure 8.65 Story Panel Zone Deformation to Story Drift, γ/θ, Ratios for MRF Model 4

EARTHQUAKE ENGINEERING RESEARCH CENTER REPORT SERIES

EERC reports are available from the National Information Service for Earthquake Engineering(NISEE) and from the National Technical Information Service(NTIS). Numbers in parentheses are Accession Numbers assigned by the National Technical Information Service; these are followed by a price code. Contact NTIS, 5285 Port Royal Road, Springfield Virginia, 22161 for more information. Reports without Accession Numbers were not available from NTIS at the time of printing. For a current complete list of EERC reports (from EERC 67-1) and availablity information, please contact University of California, EERC, NISEE, 1301 South 46th Street, Richmond, California 94804.

UCB/EERC-80/01 "Earthquake Response of Concrete Gravity Dams Including Hydrodynamic and Foundation Interaction Effects," by Chopra, A.K., Chakrabarti, P. and Gupta, S., January 1980, (AD-A087297)A10.

UCB/EERC-80/02 "Rocking Response of Rigid Blocks to Earthquakes," by Yim, C.S., Chopra, A.K. and Penzien, J., January 1980, (PB80 166 002)A04.

UCB/EERC-80/03 "Optimum Inelastic Design of Seismic-Resistant Reinforced Concrete Frame Structures," by Zagajeski, S.W. and Bertero, V.V., January 1980, (PB80 164 635)A06.

UCB/EERC-80/04 "Effects of Amount and Arrangement of Wall-Panel Reinforcement on Hysteretic Behavior of Reinforced Concrete Walls," by Iliya, R. and Bertero, V.V., February 1980, (PB81 122 525)A09.

UCB/EERC-80/05 "Shaking Table Research on Concrete Dam Models," by Niwa, A. and Clough, R.W., September 1980, (PB81 122 368)A06.

UCB/EERC-80/06 "The Design of Steel Energy-Absorbing Restrainers and their Incorporation into Nuclear Power Plants for Enhanced Safety (Vol 1a): Piping with Energy Absorbing Restrainers: Parameter Study on Small Systems," by Powell, G.H., Oughourlian, C. and Simons, J., June 1980.

UCB/EERC-80/07 "Inelastic Torsional Response of Structures Subjected to Earthquake Ground Motions," by Yamazaki, Y., April 1980, (PB81 122 327)A08.

UCB/EERC-80/08 "Study of X-Braced Steel Frame Structures under Earthquake Simulation," by Ghanaat, Y., April 1980, (PB81 122 335)A11.

UCB/EERC-80/09 "Hybrid Modelling of Soil-Structure Interaction," by Gupta, S., Lin, T.W. and Penzien, J., May 1980, (PB81 122 319)A07.

UCB/EERC-80/10 "General Applicability of a Nonlinear Model of a One Story Steel Frame," by Sveinsson, B.I. and McNiven, H.D., May 1980, (PB81 124 877)A06.

UCB/EERC-80/11 "A Green-Function Method for Wave Interaction with a Submerged Body," by Kioka, W., April 1980, (PB81 122 269)A07.

UCB/EERC-80/12 "Hydrodynamic Pressure and Added Mass for Axisymmetric Bodies.," by Nilrat, F., May 1980, (PB81 122 343)A08.

UCB/EERC-80/13 "Treatment of Non-Linear Drag Forces Acting on Offshore Platforms," by Dao, B.V. and Penzien, J., May 1980, (PB81 153 413)A07.

UCB/EERC-80/14 "2D Plane/Axisymmetric Solid Element (Type 3-Elastic or Elastic-Perfectly Plastic)for the ANSR-II Program," by Mondkar, D.P. and Powell, G.H., July 1980, (PB81 122 350)A03.

UCB/EERC-80/15 "A Response Spectrum Method for Random Vibrations," by Der Kiureghian, A., June 1981, (PB81 122 301)A03.

UCB/EERC-80/16 "Cyclic Inelastic Buckling of Tubular Steel Braces," by Zayas, V.A., Popov, E.P. and Mahin, S.A., June 1981, (PB81 124 885)A10.

UCB/EERC-80/17 "Dynamic Response of Simple Arch Dams Including Hydrodynamic Interaction," by Porter, C.S. and Chopra, A.K., July 1981, (PB81 124 000)A13.

UCB/EERC-80/18 "Experimental Testing of a Friction Damped Aseismic Base Isolation System with Fail-Safe Characteristics," by Kelly, J.M., Beucke, K.E. and Skinner, M.S., July 1980, (PB81 148 595)A04.

UCB/EERC-80/19 "The Design of Steel Energy-Absorbing Restrainers and their Incorporation into Nuclear Power Plants for Enhanced Safety (Vol.1B): Stochastic Seismic Analyses of Nuclear Power Plant Structures and Piping Systems Subjected to Multiple Supported Excitations," by Lee, M.C. and Penzien, J., June 1980, (PB82 201 872)A08.

UCB/EERC-80/20 "The Design of Steel Energy-Absorbing Restrainers and their Incorporation into Nuclear Power Plants for Enhanced Safety (Vol 1C): Numerical Method for Dynamic Substructure Analysis," by Dickens, J.M. and Wilson, E.L., June 1980.

UCB/EERC-80/21 "The Design of Steel Energy-Absorbing Restrainers and their Incorporation into Nuclear Power Plants for Enhanced Safety (Vol 2): Development and Testing of Restraints for Nuclear Piping Systems," by Kelly, J.M. and Skinner, M.S., June 1980.

UCB/EERC-80/22 "3D Solid Element (Type 4-Elastic or Elastic-Perfectly-Plastic) for the ANSR-II Program," by Mondkar, D.P. and Powell, G.H., July 1980, (PB81 123 242)A03.

UCB/EERC-80/23 "Gap-Friction Element (Type 5) for the Ansr-II Program," by Mondkar, D.P. and Powell, G.H., July 1980, (PB81 122 285)A03.

UCB/EERC-80/24 "U-Bar Restraint Element (Type 11) for the ANSR-II Program," by Oughourlian, C. and Powell, G.H., July 1980, (PB81 122 293)A03.

UCB/EERC-80/25 "Testing of a Natural Rubber Base Isolation System by an Explosively Simulated Earthquake," by Kelly, J.M., August 1980, (PB81 201 360)A04.

UCB/EERC-80/26 "Input Identification from Structural Vibrational Response," by Hu, Y., August 1980, (PB81 152 308)A05.

UCB/EERC-80/27 "Cyclic Inelastic Behavior of Steel Offshore Structures," by Zayas, V.A., Mahin, S.A. and Popov, E.P., August 1980, (PB81 196 180)A15.

UCB/EERC-80/28 "Shaking Table Testing of a Reinforced Concrete Frame with Biaxial Response," by Oliva, M.G., October 1980, (PB81 154 304)A10.

UCB/EERC-80/29 "Dynamic Properties of a Twelve-Story Prefabricated Panel Building," by Bouwkamp, J.G., Kollegger, J.P. and Stephen, R.M., October 1980, (PB82 138 777)A07.

UCB/EERC-80/30 "Dynamic Properties of an Eight-Story Prefabricated Panel Building," by Bouwkamp, J.G., Kollegger, J.P. and Stephen, R.M., October 1980, (PB81 200 313)A05.

UCB/EERC-80/31 "Predictive Dynamic Response of Panel Type Structures under Earthquakes," by Kollegger, J.P. and Bouwkamp, J.G., October 1980, (PB81 152 316)A04.

UCB/EERC-80/32 "The Design of Steel Energy-Absorbing Restrainers and their Incorporation into Nuclear Power Plants for Enhanced Safety (Vol 3): Testing of Commercial Steels in Low-Cycle Torsional Fatique," by Spanner, P., Parker, E.R., Jongewaard, E. and Dory, M., 1980.

UCB/EERC-80/33 "The Design of Steel Energy-Absorbing Restrainers and their Incorporation into Nuclear Power Plants for Enhanced Safety (Vol 4): Shaking Table Tests of Piping Systems with Energy-Absorbing Restrainers," by Stiemer, S.F. and Godden, W.G., September 1980, (PB82 201 880)A05.

UCB/EERC-80/34 "The Design of Steel Energy-Absorbing Restrainers and their Incorporation into Nuclear Power Plants for Enhanced Safety (Vol 5): Summary Report," by Spencer, P., 1980.

UCB/EERC-80/35 "Experimental Testing of an Energy-Absorbing Base Isolation System," by Kelly, J.M., Skinner, M.S. and Beucke, K.E., October 1980, (PB81 154 072)A04.

UCB/EERC-80/36 "Simulating and Analyzing Artificial Non-Stationary Earth Ground Motions," by Nau, R.F., Oliver, R.M. and Pister, K.S., October 1980, (PB81 153 397)A04.

UCB/EERC-80/37 "Earthquake Engineering at Berkeley - 1980," by , September 1980, (PB81 205 674)A09.

UCB/EERC-80/38 "Inelastic Seismic Analysis of Large Panel Buildings," by Schricker, V. and Powell, G.H., September 1980, (PB81 154 338)A13.

UCB/EERC-80/39 "Dynamic Response of Embankment, Concrete-Gavity and Arch Dams Including Hydrodynamic Interation," by Hall, J.F. and Chopra, A.K., October 1980, (PB81 152 324)A11.

UCB/EERC-80/40 "Inelastic Buckling of Steel Struts under Cyclic Load Reversal.," by Black, R.G., Wenger, W.A. and Popov, E.P., October 1980, (PB81 154 312)A08.

UCB/EERC-80/41 "Influence of Site Characteristics on Buildings Damage during the October 3,1974 Lima Earthquake," by Repetto, P., Arango, I. and Seed, H.B., September 1980, (PB81 161 739)A05.

UCB/EERC-80/42 "Evaluation of a Shaking Table Test Program on Response Behavior of a Two Story Reinforced Concrete Frame," by Blondet, J.M., Clough, R.W. and Mahin, S.A., December 1980, (PB82 196 544)A11.

UCB/EERC-80/43 "Modelling of Soil-Structure Interaction by Finite and Infinite Elements," by Medina, F., December 1980, (PB81 229 270)A04.

UCB/EERC-81/01 "Control of Seismic Response of Piping Systems and Other Structures by Base Isolation," by Kelly, J.M., January 1981, (PB81 200 735)A05.

UCB/EERC-81/02 "OPTNSR- An Interactive Software System for Optimal Design of Statically and Dynamically Loaded Structures with Nonlinear Response," by Bhatti, M.A., Ciampi, V. and Pister, K.S., January 1981, (PB81 218 851)A09.

UCB/EERC-81/03 "Analysis of Local Variations in Free Field Seismic Ground Motions," by Chen, J.-C., Lysmer, J. and Seed, H.B., January 1981, (AD-A099508)A13.

UCB/EERC-81/04 "Inelastic Structural Modeling of Braced Offshore Platforms for Seismic Loading," by Zayas, V.A., Shing, P.-S.B., Mahin, S.A. and Popov, E.P., January 1981, (PB82 138 777)A07.

UCB/EERC-81/05 "Dynamic Response of Light Equipment in Structures," by Der Kiureghian, A., Sackman, J.L. and Nour-Omid, B., April 1981, (PB81 218 497)A04.

UCB/EERC-81/06 "Preliminary Experimental Investigation of a Broad Base Liquid Storage Tank," by Bouwkamp, J.G., Kollegger, J.P. and Stephen, R.M., May 1981, (PB82 140 385)A03.

UCB/EERC-81/07 "The Seismic Resistant Design of Reinforced Concrete Coupled Structural Walls," by Aktan, A.E. and Bertero, V.V., June 1981, (PB82 113 358)A11.

UCB/EERC-81/08 "Unassigned," by Unassigned, 1981.

UCB/EERC-81/09 "Experimental Behavior of a Spatial Piping System with Steel Energy Absorbers Subjected to a Simulated Differential Seismic Input," by Stiemer, S.F., Godden, W.G. and Kelly, J.M., July 1981, (PB82 201 898)A04.

UCB/EERC-81/10 "Evaluation of Seismic Design Provisions for Masonry in the United States," by Sveinsson, B.I., Mayes, R.L. and McNiven, H.D., August 1981, (PB82 166 075)A08.

UCB/EERC-81/11 "Two-Dimensional Hybrid Modelling of Soil-Structure Interaction," by Tzong, T.-J., Gupta, S. and Penzien, J., August 1981, (PB82 142 118)A04.

UCB/EERC-81/12 "Studies on Effects of Infills in Seismic Resistant R/C Construction," by Brokken, S. and Bertero, V.V., October 1981, (PB82 166 190)A09.

UCB/EERC-81/13 "Linear Models to Predict the Nonlinear Seismic Behavior of a One-Story Steel Frame," by Valdimarsson, H., Shah, A.H. and McNiven, H.D., September 1981, (PB82 138 793)A07.

UCB/EERC-81/14 "TLUSH: A Computer Program for the Three-Dimensional Dynamic Analysis of Earth Dams," by Kagawa, T., Mejia, L.H., Seed, H.B. and Lysmer, J., September 1981, (PB82 139 940)A06.

UCB/EERC-81/15 "Three Dimensional Dynamic Response Analysis of Earth Dams," by Mejia, L.H. and Seed, H.B., September 1981, (PB82 137 274)A12.

UCB/EERC-81/16 "Experimental Study of Lead and Elastomeric Dampers for Base Isolation Systems," by Kelly, J.M. and Hodder, S.B., October 1981, (PB82 166 182)A05.

UCB/EERC-81/17 "The Influence of Base Isolation on the Seismic Response of Light Secondary Equipment," by Kelly, J.M., April 1981, (PB82 255 266)A04.

UCB/EERC-81/18 "Studies on Evaluation of Shaking Table Response Analysis Procedures," by Blondet, J. M., November 1981, (PB82 197 278)A10.

UCB/EERC-81/19 "DELIGHT.STRUCT: A Computer-Aided Design Environment for Structural Engineering," by Balling, R.J., Pister, K.S. and Polak, E., December 1981, (PB82 218 496)A07.

UCB/EERC-81/20 "Optimal Design of Seismic-Resistant Planar Steel Frames," by Balling, R.J., Ciampi, V. and Pister, K.S., December 1981, (PB82 220 179)A07.

UCB/EERC-82/01 "Dynamic Behavior of Ground for Seismic Analysis of Lifeline Systems," by Sato, T. and Der Kiureghian, A., January 1982, (PB82 218 926)A05.

UCB/EERC-82/02 "Shaking Table Tests of a Tubular Steel Frame Model," by Ghanaat, Y. and Clough, R.W., January 1982, (PB82 220 161)A07.

UCB/EERC-82/03 "Behavior of a Piping System under Seismic Excitation: Experimental Investigations of a Spatial Piping System supported by Mechanical Shock Arrestors," by Schneider, S., Lee, H.-M. and Godden, W. G., May 1982, (PB83 172 544)A09.

UCB/EERC-82/04 "New Approaches for the Dynamic Analysis of Large Structural Systems," by Wilson, E.L., June 1982, (PB83 148 080)A05.

UCB/EERC-82/05 "Model Study of Effects of Damage on the Vibration Properties of Steel Offshore Platforms," by Shahrivar, F. and Bouwkamp, J.G., June 1982, (PB83 148 742)A10.

UCB/EERC-82/06 "States of the Art and Pratice in the Optimum Seismic Design and Analytical Response Prediction of R/C Frame Wall Structures," by Aktan, A.E. and Bertero, V.V., July 1982, (PB83 147 736)A05.

UCB/EERC-82/07 "Further Study of the Earthquake Response of a Broad Cylindrical Liquid-Storage Tank Model," by Manos, G.C. and Clough, R.W., July 1982, (PB83 147 744)A11.

UCB/EERC-82/08 "An Evaluation of the Design and Analytical Seismic Response of a Seven Story Reinforced Concrete Frame," by Charney, F.A. and Bertero, V.V., July 1982, (PB83 157 628)A09.

UCB/EERC-82/09 "Fluid-Structure Interactions: Added Mass Computations for Incompressible Fluid," by Kuo, J.S.-H., August 1982, (PB83 156 281)A07.

UCB/EERC-82/10 "Joint-Opening Nonlinear Mechanism: Interface Smeared Crack Model," by Kuo, J.S.-H., August 1982, (PB83 149 195)A05.

UCB/EERC-82/11 "Dynamic Response Analysis of Techi Dam," by Clough, R.W., Stephen, R.M. and Kuo, J.S.-H., August 1982, (PB83 147 496)A06.

UCB/EERC-82/12 "Prediction of the Seismic Response of R/C Frame-Coupled Wall Structures," by Aktan, A.E., Bertero, V.V. and Piazzo, M., August 1982, (PB83 149 203)A09.

UCB/EERC-82/13 "Preliminary Report on the Smart 1 Strong Motion Array in Taiwan," by Bolt, B.A., Loh, C.H., Penzien, J. and Tsai, Y.B., August 1982, (PB83 159 400)A10.

UCB/EERC-82/14 "Seismic Behavior of an Eccentrically X-Braced Steel Structure," by Yang, M.S., September 1982, (PB83 260 778)A12.

UCB/EERC-82/15 "The Performance of Stairways in Earthquakes," by Roha, C., Axley, J.W. and Bertero, V.V., September 1982, (PB83 157 693)A07.

UCB/EERC-82/16 "The Behavior of Submerged Multiple Bodies in Earthquakes," by Liao, W.-G., September 1982, (PB83 158 709)A07.

UCB/EERC-82/17 "Effects of Concrete Types and Loading Conditions on Local Bond-Slip Relationships," by Cowell, A.D., Popov, E.P. and Bertero, V.V., September 1982, (PB83 153 577)A04.

UCB/EERC-82/18 "Mechanical Behavior of Shear Wall Vertical Boundary Members: An Experimental Investigation," by Wagner, M.T. and Bertero, V.V., October 1982, (PB83 159 764)A05.

UCB/EERC-82/19 "Experimental Studies of Multi-support Seismic Loading on Piping Systems," by Kelly, J.M. and Cowell, A.D., November 1982.

UCB/EERC-82/20 "Generalized Plastic Hinge Concepts for 3D Beam-Column Elements," by Chen, P. F.-S. and Powell, G.H., November 1982, (PB83 247 981)A13.

UCB/EERC-82/21 "ANSR-II: General Computer Program for Nonlinear Structural Analysis," by Oughourlian, C.V. and Powell, G.H., November 1982, (PB83 251 330)A12.

UCB/EERC-82/22 "Solution Strategies for Statically Loaded Nonlinear Structures," by Simons, J.W. and Powell, G.H., November 1982, (PB83 197 970)A06.

UCB/EERC-82/23 "Analytical Model of Deformed Bar Anchorages under Generalized Excitations," by Ciampi, V., Eligehausen, R., Bertero, V.V. and Popov, E.P., November 1982, (PB83 169 532)A06.

UCB/EERC-82/24 "A Mathematical Model for the Response of Masonry Walls to Dynamic Excitations," by Sucuoglu, H., Mengi, Y. and McNiven, H.D., November 1982, (PB83 169 011)A07.

UCB/EERC-82/25 "Earthquake Response Considerations of Broad Liquid Storage Tanks," by Cambra, F.J., November 1982, (PB83 251 215)A09.

UCB/EERC-82/26 "Computational Models for Cyclic Plasticity, Rate Dependence and Creep," by Mosaddad, B. and Powell, G.H., November 1982, (PB83 245 829)A08.

UCB/EERC-82/27 "Inelastic Analysis of Piping and Tubular Structures," by Mahasuverachai, M. and Powell, G.H., November 1982, (PB83 249 987)A07.

UCB/EERC-83/01 "The Economic Feasibility of Seismic Rehabilitation of Buildings by Base Isolation," by Kelly, J.M., January 1983, (PB83 197 988)A05.

UCB/EERC-83/02 "Seismic Moment Connections for Moment-Resisting Steel Frames.," by Popov, E.P., January 1983, (PB83 195 412)A04.

UCB/EERC-83/03 "Design of Links and Beam-to-Column Connections for Eccentrically Braced Steel Frames," by Popov, E.P. and Malley, J.O., January 1983, (PB83 194 811)A04.

UCB/EERC-83/04 "Numerical Techniques for the Evaluation of Soil-Structure Interaction Effects in the Time Domain," by Bayo, E. and Wilson, E.L., February 1983, (PB83 245 605)A09.

UCB/EERC-83/05 "A Transducer for Measuring the Internal Forces in the Columns of a Frame-Wall Reinforced Concrete Structure," by Sause, R. and Bertero, V.V., May 1983, (PB84 119 494)A06.

UCB/EERC-83/06 "Dynamic Interactions Between Floating Ice and Offshore Structures," by Croteau, P., May 1983, (PB84 119 486)A16.

UCB/EERC-83/07 "Dynamic Analysis of Multiply Tuned and Arbitrarily Supported Secondary Systems," by Igusa, T. and Der Kiureghian, A., July 1983, (PB84 118 272)A11.

UCB/EERC-83/08 "A Laboratory Study of Submerged Multi-body Systems in Earthquakes," by Ansari, G.R., June 1983, (PB83 261 842)A17.

UCB/EERC-83/09 "Effects of Transient Foundation Uplift on Earthquake Response of Structures," by Yim, C.-S. and Chopra, A.K., June 1983, (PB83 261 396)A07.

UCB/EERC-83/10 "Optimal Design of Friction-Braced Frames under Seismic Loading," by Austin, M.A. and Pister, K.S., June 1983, (PB84 119 288)A06.

UCB/EERC-83/11 "Shaking Table Study of Single-Story Masonry Houses: Dynamic Performance under Three Component Seismic Input and Recommendations," by Manos, G.C., Clough, R.W. and Mayes, R.L., July 1983, (UCB/EERC-83/11)A08.

UCB/EERC-83/12 "Experimental Error Propagation in Pseudodynamic Testing," by Shiing, P.B. and Mahin, S.A., June 1983, (PB84 119 270)A09.

UCB/EERC-83/13 "Experimental and Analytical Predictions of the Mechanical Characteristics of a 1/5-scale Model of a 7-story R/C Frame-Wall Building Structure," by Aktan, A.E., Bertero, V.V., Chowdhury, A.A. and Nagashima, T., June 1983, (PB84 119 213)A07.

UCB/EERC-83/14 "Shaking Table Tests of Large-Panel Precast Concrete Building System Assemblages," by Oliva, M.G. and Clough, R.W., June 1983, (PB86 110 210/AS)A11.

UCB/EERC-83/15 "Seismic Behavior of Active Beam Links in Eccentrically Braced Frames," by Hjelmstad, K.D. and Popov, E.P., July 1983, (PB84 119 676)A09.

UCB/EERC-83/16 "System Identification of Structures with Joint Rotation," by Dimsdale, J.S., July 1983, (PB84 192 210)A06.

UCB/EERC-83/17 "Construction of Inelastic Response Spectra for Single-Degree-of-Freedom Systems," by Mahin, S. and Lin, J., June 1983, (PB84 208 834)A05.

UCB/EERC-83/18 "Interactive Computer Analysis Methods for Predicting the Inelastic Cyclic Behaviour of Structural Sections," by Kaba, S. and Mahin, S., July 1983, (PB84 192 012)A06.

UCB/EERC-83/19 "Effects of Bond Deterioration on Hysteretic Behavior of Reinforced Concrete Joints," by Filippou, F.C., Popov, E.P. and Bertero, V.V., August 1983, (PB84 192 020)A10.

UCB/EERC-83/20 "Analytical and Experimental Correlation of Large-Panel Precast Building System Performance," by Oliva, M.G., Clough, R.W., Velkov, M. and Gavrilovic, P., November 1983.

UCB/EERC-83/21 "Mechanical Characteristics of Materials Used in a 1/5 Scale Model of a 7-Story Reinforced Concrete Test Structure," by Bertero, V.V., Aktan, A.E., Harris, H.G. and Chowdhury, A.A., October 1983, (PB84 193 697)A05.

UCB/EERC-83/22 "Hybrid Modelling of Soil-Structure Interaction in Layered Media," by Tzong, T.-J. and Penzien, J., October 1983, (PB84 192 178)A08.

UCB/EERC-83/23 "Local Bond Stress-Slip Relationships of Deformed Bars under Generalized Excitations," by Eligehausen, R., Popov, E.P. and Bertero, V.V., October 1983, (PB84 192 848)A09.

UCB/EERC-83/24 "Design Considerations for Shear Links in Eccentrically Braced Frames," by Malley, J.O. and Popov, E.P., November 1983, (PB84 192 186)A07.

UCB/EERC-84/01 "Pseudodynamic Test Method for Seismic Performance Evaluation: Theory and Implementation," by Shing, P.-S.B. and Mahin, S.A., January 1984, (PB84 190 644)A08.

UCB/EERC-84/02 "Dynamic Response Behavior of Kiang Hong Dian Dam," by Clough, R.W., Chang, K.-T., Chen, H.-Q. and Stephen, R.M., April 1984, (PB84 209 402)A08.

UCB/EERC-84/03 "Refined Modelling of Reinforced Concrete Columns for Seismic Analysis," by Kaba, S.A. and Mahin, S.A., April 1984, (PB84 234 384)A06.

UCB/EERC-84/04 "A New Floor Response Spectrum Method for Seismic Analysis of Multiply Supported Secondary Systems," by Asfura, A. and Der Kiureghian, A., June 1984, (PB84 239 417)A06.

UCB/EERC-84/05 "Earthquake Simulation Tests and Associated Studies of a 1/5th-scale Model of a 7-Story R/C Frame-Wall Test Structure," by Bertero, V.V., Aktan, A.E., Charney, F.A. and Sause, R., June 1984, (PB84 239 409)A09.

UCB/EERC-84/06 "R/C Structural Walls: Seismic Design for Shear," by Aktan, A.E. and Bertero, V.V., 1984.

UCB/EERC-84/07 "Behavior of Interior and Exterior Flat-Plate Connections subjected to Inelastic Load Reversals," by Zee, H.L. and Moehle, J.P., August 1984, (PB86 117 629/AS)A07.

UCB/EERC-84/08 "Experimental Study of the Seismic Behavior of a Two-Story Flat-Plate Structure," by Moehle, J.P. and Diebold, J.W., August 1984, (PB86 122 553/AS)A12.

UCB/EERC-84/09 "Phenomenological Modeling of Steel Braces under Cyclic Loading," by Ikeda, K., Mahin, S.A. and Dermitzakis, S.N., May 1984, (PB86 132 198/AS)A08.

UCB/EERC-84/10 "Earthquake Analysis and Response of Concrete Gravity Dams," by Fenves, G. and Chopra, A.K., August 1984, (PB85 193 902/AS)A11.

UCB/EERC-84/11 "EAGD-84: A Computer Program for Earthquake Analysis of Concrete Gravity Dams," by Fenves, G. and Chopra, A.K., August 1984, (PB85 193 613/AS)A05.

UCB/EERC-84/12 "A Refined Physical Theory Model for Predicting the Seismic Behavior of Braced Steel Frames," by Ikeda, K. and Mahin, S.A., July 1984, (PB85 191 450/AS)A09.

UCB/EERC-84/13 "Earthquake Engineering Research at Berkeley - 1984," by , August 1984, (PB85 197 341/AS)A10.

UCB/EERC-84/14 "Moduli and Damping Factors for Dynamic Analyses of Cohesionless Soils," by Seed, H.B., Wong, R.T., Idriss, I.M. and Tokimatsu, K., September 1984, (PB85 191 468/AS)A04.

UCB/EERC-84/15 "The Influence of SPT Procedures in Soil Liquefaction Resistance Evaluations," by Seed, H.B., Tokimatsu, K., Harder, L.F. and Chung, R.M., October 1984, (PB85 191 732/AS)A04.

UCB/EERC-84/16 "Simplified Procedures for the Evaluation of Settlements in Sands Due to Earthquake Shaking," by Tokimatsu, K. and Seed, H.B., October 1984, (PB85 197 887/AS)A03.

UCB/EERC-84/17 "Evaluation of Energy Absorption Characteristics of Bridges under Seismic Conditions," by Imbsen, R.A. and Penzien, J., November 1984.

UCB/EERC-84/18 "Structure-Foundation Interactions under Dynamic Loads," by Liu, W.D. and Penzien, J., November 1984, (PB87 124 889/AS)A11.

UCB/EERC-84/19 "Seismic Modelling of Deep Foundations," by Chen, C.-H. and Penzien, J., November 1984, (PB87 124 798/AS)A07.

UCB/EERC-84/20 "Dynamic Response Behavior of Quan Shui Dam," by Clough, R.W., Chang, K.-T., Chen, H.-Q., Stephen, R.M., Ghanaat, Y. and Qi, J.-H., November 1984, (PB86 115177/AS)A07.

UCB/EERC-85/01 "Simplified Methods of Analysis for Earthquake Resistant Design of Buildings," by Cruz, E.F. and Chopra, A.K., February 1985, (PB86 112299/AS)A12.

UCB/EERC-85/02 "Estimation of Seismic Wave Coherency and Rupture Velocity using the SMART 1 Strong-Motion Array Recordings," by Abrahamson, N.A., March 1985, (PB86 214 343)A07.

UCB/EERC-85/03 "Dynamic Properties of a Thirty Story Condominium Tower Building," by Stephen, R.M., Wilson, E.L. and Stander, N., April 1985, (PB86 118965/AS)A06.

UCB/EERC-85/04 "Development of Substructuring Techniques for On-Line Computer Controlled Seismic Performance Testing," by Dermitzakis, S. and Mahin, S., February 1985, (PB86 132941/AS)A08.

UCB/EERC-85/05 "A Simple Model for Reinforcing Bar Anchorages under Cyclic Excitations," by Filippou, F.C., March 1985, (PB86 112 919/AS)A05.

UCB/EERC-85/06 "Racking Behavior of Wood-framed Gypsum Panels under Dynamic Load," by Oliva, M.G., June 1985.

UCB/EERC-85/07 "Earthquake Analysis and Response of Concrete Arch Dams," by Fok, K.-L. and Chopra, A.K., June 1985, (PB86 139672/AS)A10.

UCB/EERC-85/08 "Effect of Inelastic Behavior on the Analysis and Design of Earthquake Resistant Structures," by Lin, J.P. and Mahin, S.A., June 1985, (PB86 135340/AS)A08.

UCB/EERC-85/09 "Earthquake Simulator Testing of a Base-Isolated Bridge Deck," by Kelly, J.M., Buckle, I.G. and Tsai, H.-C., January 1986, (PB87 124 152/AS)A06.

UCB/EERC-85/10 "Simplified Analysis for Earthquake Resistant Design of Concrete Gravity Dams," by Fenves, G. and Chopra, A.K., June 1986, (PB87 124 160/AS)A08.

UCB/EERC-85/11 "Dynamic Interaction Effects in Arch Dams," by Clough, R.W., Chang, K.-T., Chen, H.-Q. and Ghanaat, Y., October 1985, (PB86 135027/AS)A05.

UCB/EERC-85/12 "Dynamic Response of Long Valley Dam in the Mammoth Lake Earthquake Series of May 25-27, 1980," by Lai, S. and Seed, H.B., November 1985, (PB86 142304/AS)A05.

UCB/EERC-85/13 "A Methodology for Computer-Aided Design of Earthquake-Resistant Steel Structures," by Austin, M.A., Pister, K.S. and Mahin, S.A., December 1985, (PB86 159480/AS)A10 .

UCB/EERC-85/14 "Response of Tension-Leg Platforms to Vertical Seismic Excitations," by Liou, G.-S., Penzien, J. and Yeung, R.W., December 1985, (PB87 124 871/AS)A08.

UCB/EERC-85/15 "Cyclic Loading Tests of Masonry Single Piers: Volume 4 - Additional Tests with Height to Width Ratio of 1," by Sveinsson, B., McNiven, H.D. and Sucuoglu, H., December 1985.

UCB/EERC-85/16 "An Experimental Program for Studying the Dynamic Response of a Steel Frame with a Variety of Infill Partitions," by Yanev, B. and McNiven, H.D., December 1985.

UCB/EERC-86/01 "A Study of Seismically Resistant Eccentrically Braced Steel Frame Systems," by Kasai, K. and Popov, E.P., January 1986, (PB87 124 178/AS)A14.

UCB/EERC-86/02 "Design Problems in Soil Liquefaction," by Seed, H.B., February 1986, (PB87 124 186/AS)A03.

UCB/EERC-86/03 "Implications of Recent Earthquakes and Research on Earthquake-Resistant Design and Construction of Buildings," by Bertero, V.V., March 1986, (PB87 124 194/AS)A05.

UCB/EERC-86/04 "The Use of Load Dependent Vectors for Dynamic and Earthquake Analyses," by Leger, P., Wilson, E.L. and Clough, R.W., March 1986, (PB87 124 202/AS)A12.

UCB/EERC-86/05 "Two Beam-To-Column Web Connections," by Tsai, K.-C. and Popov, E.P., April 1986, (PB87 124 301/AS)A04.

UCB/EERC-86/06 "Determination of Penetration Resistance for Coarse-Grained Soils using the Becker Hammer Drill," by Harder, L.F. and Seed, H.B., May 1986, (PB87 124 210/AS)A07.

UCB/EERC-86/07 "A Mathematical Model for Predicting the Nonlinear Response of Unreinforced Masonry Walls to In-Plane Earthquake Excitations," by Mengi, Y. and McNiven, H.D., May 1986, (PB87 124 780/AS)A06.

UCB/EERC-86/08 "The 19 September 1985 Mexico Earthquake: Building Behavior," by Bertero, V.V., July 1986.

UCB/EERC-86/09 "EACD-3D: A Computer Program for Three-Dimensional Earthquake Analysis of Concrete Dams," by Fok, K.-L., Hall, J.F. and Chopra, A.K., July 1986, (PB87 124 228/AS)A08.

UCB/EERC-86/10 "Earthquake Simulation Tests and Associated Studies of a 0.3-Scale Model of a Six-Story Concentrically Braced Steel Structure," by Uang, C.-M. and Bertero, V.V., December 1986, (PB87 163 564/AS)A17.

UCB/EERC-86/11 "Mechanical Characteristics of Base Isolation Bearings for a Bridge Deck Model Test," by Kelly, J.M., Buckle, I.G. and Koh, C.-G., 1987.

UCB/EERC-86/12 "Effects of Axial Load on Elastomeric Isolation Bearings," by Koh, C.-G. and Kelly, J.M., November 1987.

UCB/EERC-87/01 "The FPS Earthquake Resisting System: Experimental Report," by Zayas, V.A., Low, S.S. and Mahin, S.A., June 1987.

UCB/EERC-87/02 "Earthquake Simulator Tests and Associated Studies of a 0.3-Scale Model of a Six-Story Eccentrically Braced Steel Structure," by Whittaker, A., Uang, C.-M. and Bertero, V.V., July 1987.

UCB/EERC-87/03 "A Displacement Control and Uplift Restraint Device for Base-Isolated Structures," by Kelly, J.M., Griffith, M.C. and Aiken, I.D., April 1987.

UCB/EERC-87/04 "Earthquake Simulator Testing of a Combined Sliding Bearing and Rubber Bearing Isolation System," by Kelly, J.M. and Chalhoub, M.S., 1987.

UCB/EERC-87/05 "Three-Dimensional Inelastic Analysis of Reinforced Concrete Frame-Wall Structures," by Moazzami, S. and Bertero, V.V., May 1987.

UCB/EERC-87/06 "Experiments on Eccentrically Braced Frames with Composite Floors," by Ricles, J. and Popov, E., June 1987.

UCB/EERC-87/07 "Dynamic Analysis of Seismically Resistant Eccentrically Braced Frames," by Ricles, J. and Popov, E., June 1987.

UCB/EERC-87/08 "Undrained Cyclic Triaxial Testing of Gravels-The Effect of Membrane Compliance," by Evans, M.D. and Seed, H.B., July 1987.

UCB/EERC-87/09 "Hybrid Solution Techniques for Generalized Pseudo-Dynamic Testing," by Thewalt, C. and Mahin, S.A., July 1987.

UCB/EERC-87/10 "Ultimate Behavior of Butt Welded Splices in Heavy Rolled Steel Sections," by Bruneau, M., Mahin, S.A. and Popov, E.P., July 1987.

UCB/EERC-87/11 "Residual Strength of Sand from Dam Failures in the Chilean Earthquake of March 3, 1985," by De Alba, P., Seed, H.B., Retamal, E. and Seed, R.B., September 1987.

UCB/EERC-87/12 "Inelastic Seismic Response of Structures with Mass or Stiffness Eccentricities in Plan," by Bruneau, M. and Mahin, S.A., September 1987.

UCB/EERC-87/13 "CSTRUCT: An Interactive Computer Environment for the Design and Analysis of Earthquake Resistant Steel Structures," by Austin, M.A., Mahin, S.A. and Pister, K.S., September 1987.

UCB/EERC-87/14 "Experimental Study of Reinforced Concrete Columns Subjected to Multi-Axial Loading," by Low, S.S. and Moehle, J.P., September 1987.

UCB/EERC-87/15 "Relationships between Soil Conditions and Earthquake Ground Motions in Mexico City in the Earthquake of Sept. 19, 1985," by Seed, H.B., Romo, M.P., Sun, J., Jaime, A. and Lysmer, J., October 1987.

UCB EERC-87/16 "Experimental Study of Seismic Response of R. C. Setback Buildings," by Shahrooz, B.M. and Moehle, J.P., October 1987.

UCB/EERC-87/17 "The Effect of Slabs on the Flexural Behavior of Beams," by Pantazopoulou, S.J. and Moehle, J.P., October 1987.

UCB/EERC-87/18 "Design Procedure for R-FBI Bearings," by Mostaghel, N. and Kelly, J.M., November 1987.

UCB/EERC-87/19 "Analytical Models for Predicting the Lateral Response of R C Shear Walls: Evaluation of their Reliability," by Vulcano, A. and Bertero, V.V., November 1987.

UCB/EERC-87/20 "Earthquake Response of Torsionally-Coupled Buildings," by Hejal, R. and Chopra, A.K., December 1987.

UCB/EERC-87/21 "Dynamic Reservoir Interaction with Monticello Dam," by Clough, R.W., Ghanaat, Y. and Qiu, X-F., December 1987.

UCB/EERC-87/22 "Strength Evaluation of Coarse-Grained Soils," by Siddiqi, F.H., Seed, R.B., Chan, C.K., Seed, H.B. and Pyke, R.M., December 1987.

UCB/EERC-88/01 "Seismic Behavior of Concentrically Braced Steel Frames," by Khatib, I., Mahin, S.A. and Pister, K.S., January 1988.

UCB/EERC-88/02 "Experimental Evaluation of Seismic Isolation of Medium-Rise Structures Subject to Uplift," by Griffith, M.C., Kelly, J.M., Coveney, V.A. and Koh, C.G., January 1988.

UCB/EERC-88/03 "Cyclic Behavior of Steel Double Angle Connections," by Astaneh-Asl, A. and Nader, M.N., January 1988.

UCB/EERC-88/04 "Re-evaluation of the Slide in the Lower San Fernando Dam in the Earthquake of Feb. 9, 1971," by Seed, H.B., Seed, R.B., Harder, L.F. and Jong, H.-L., April 1988.

UCB/EERC-88/05 "Experimental Evaluation of Seismic Isolation of a Nine-Story Braced Steel Frame Subject to Uplift," by Griffith, M.C., Kelly, J.M. and Aiken, I.D., May 1988.

UCB/EERC-88/06 "DRAIN-2DX User Guide.," by Allahabadi, R. and Powell, G.H., March 1988.

UCB/EERC-88/07 "Cylindrical Fluid Containers in Base-Isolated Structures," by Chalhoub, M.S. and Kelly, J.M., April 1988.

UCB/EERC-88/08 "Analysis of Near-Source Waves: Separation of Wave Types using Strong Motion Array Recordings," by Darragh, R.B., June 1988.

UCB/EERC-88/09 "Alternatives to Standard Mode Superposition for Analysis of Non-Classically Damped Systems," by Kusainov, A.A. and Clough, R.W., June 1988.

UCB/EERC-88/10 "The Landslide at the Port of Nice on October 16, 1979," by Seed, H.B., Seed, R.B., Schlosser, F., Blondeau, F. and Juran, I., June 1988.

UCB/EERC-88/11 "Liquefaction Potential of Sand Deposits Under Low Levels of Excitation," by Carter, D.P. and Seed, H.B., August 1988.

UCB/EERC-88/12 "Analysis of Nonlinear Response of Reinforced Concrete Frames to Cyclic Load Reversals," by Filippou, F.C. and Issa, A., September 1988.

UCB/EERC-88/13 "Earthquake-Resistant Design of Building Structures: An Energy Approach," by Uang, C.-M. and Bertero, V.V., September 1988.

UCB/EERC-88/14 "An Experimental Study of the Behavior of Dual Steel Systems," by Whittaker, A.S., Uang, C.-M. and Bertero, V.V., September 1988.

UCB/EERC-88/15 "Dynamic Moduli and Damping Ratios for Cohesive Soils," by Sun, J.I., Golesorkhi, R. and Seed, H.B., August 1988.

UCB/EERC-88/16 "Reinforced Concrete Flat Plates Under Lateral Load: An Experimental Study Including Biaxial Effects," by Pan, A. and Moehle, J., November 1988.

UCB/EERC-88/17 "Earthquake Engineering Research at Berkeley - 1988," November 1988.

UCB/EERC-88/18 "Use of Energy as a Design Criterion in Earthquake-Resistant Design," by Uang, C.-M. and Bertereo, V.V., November 1988.

UCB/EERC-88/19 "Steel Beam-Column Joints in Seismic Moment Resisting Frames," by Tsai, K.-C. and Popov, E.P., November 1988.